Development and Validation of a Computational Tool for Fusion Reactors' System Analysis

Zur Erlangung des akademischen Grades
Doktor der Ingenieurwissenschaften
von der KIT-Fakultät für Maschinenbau
Karlsruher Institut für Technologie (KIT)

genehmigte
Dissertation
von

Fabrizio Franza

Tag der mündlichen Prüfung: 7 Juni 2019

Hauptreferent:	Prof. Dr.-Ing. Robert Stieglitz Karlsruher Institut für Technologie (KIT)
Korreferent:	Prof. Dr. habil. Hartmut Zohm Ludwig-Maximilians-Universität München

Abstract

On the roadmap to fusion energy the development and the operation of a demonstration power plant (DEMO) is the next step after ITER, a key facility currently devoted to the exploration of the physics aspects for self-sustained fusion plasmas with sizes and fusion power comparable to those attended in fusion power plants (FPP). Fusion systems codes are essential computational tools aimed to simulate the physics and the engineering features of a FPP. The main objective of a system code is to find one (or more) reactor configurations which simultaneously comply with physics operational limits, engineering constraints and net electric output requirements. As such simulation tools need to scope many design solutions over a large parameter phase space, they rely on rather basic physics and engineering models (mostly at zero or one-dimensional level) and on a relatively large number of input specifications. Within the conceptual design of a FPP, systems codes are interfaced to the detailed transport codes and engineering platforms, which operate in much larger time scales.

To fill the gap between systems and the detailed transport and engineering codes the high-fidelity system/design tool MIRA (Modular Integrated Reactor Analysis) has been developed. MIRA relies on a modular structure and provides a refined FPP system analysis, with the primary goal of generating a more robust plant baseline. It incorporates into a unique computing environment a mathematical algorithm for the utmost tokamak fusion problems, including two-dimensional plasma magnetic equilibrium and core physics, transport of neutron and photon radiations emitted from the plasma and electromagnetic and engineering characterization of the toroidal field (TF) and poloidal field (PF) field coil systems. Most of the implemented modules rely on higher spatial resolution compared to presently available system codes, such as PROCESS.

The multiphysics MIRA approach has been applied to the DEMO 2015 baseline, generated by means of the PROCESS system code. The analysis has been carried out by taking an identical set of input assumptions and requirements (e.g. same fusion power, major radius and aspect ratio) and observing the response on certain figures of merit. This verification study has featured the violation of some constraining conditions imposed on plasma safety factor, TF ripple and plasma burn time.

The DEMO 2015 baseline has been found not in line with all the imposed requirements and constraints, hence necessitates a set of active measures on some of the input parameters. Such measures have been reported in form of parameter scans, where three variables have been identified, such as plasma internal inductance, blanket breeding zone inboard thickness and vacuum vessel/TF coil gap radial outboard width. The addressed sensitivity analyses have shown non-trivial inter-parametric dependencies, never explored in fusion system analyses. For instance, large influences of the plasma internal inductance on safety factor, plasma shape, density and temperature features, peak divertor flux and plasma burn time have been observed. Moreover, an optimal overall breeding blanket + TF coil inboard width has been observed with respect to the maximization of the plasma burn time, representing a meeting point between neutronic tritium breeding and technological limits in central solenoid and TF coils superconducting cables. These outcomes have inspired important changes in the way of designing a tokamak reactor like DEMO, where more extended analyses of the key physics and engineering aspects of the reactor can speed up and improve the design process of a FPP.

Kurzfassung

Auf dem Weg zur kommerziellen Nutzung der Fusionsenergie bilden die Entwicklung und der Betrieb eines Demonstrationskraftwerks (DEMO) den nächsten Schritt nach ITER, einer Schlüsselanlage zur Untersuchung der wichtigsten physikalischen Parameter von sich selbsterhaltenden Fusionsplasmen bei Größen und Leistungen, die mit denen zukünftiger Fusionskraftwerke vergleichbar sind. Fusionssystemcodes sind wichtige Rechenwerkzeuge zur Simulation physikalischer und technischer Merkmale eines Fusionskraftwerks. Ein solcher Code dient zur Bestimmung einer (oder mehrerer) Reaktorkonfiguration(en), die die physikalischen Betriebsgrenzwerte einhalten, technische Beschränkungen berücksichtigen und die Nettoleistungsanforderungen erfüllen. Da diese Werkzeuge zahlreiche Auslegungslösungen über einen groen Parameterphasenraum simulieren sollen, beruhen sie auf grundlegenden physikalischen und technischen Modellen (meist auf Nullniveau oder eindimensional) sowie auf relativ zahlreichen Eingangsspezifikationen. Bei der konzeptionellen Auslegung eines Fusionskraftwerks werden die Systemcodes mit detaillierten Transportcodes und technischen Plattformen, die sich über weit längere Zeiträume erstrecken, verknüpft.

Um die Lücke zwischen Systemcodes und den detaillierten Transportcodes und technischen Codes zu schließen, wurde nun für die modulare integrierte Reaktoranalyse das hochpräzise Auslegungsprogramm MIRA (Modular Integrated Reactor Analysis) entwickelt. MIRA ist modular aufgebaut und ermöglicht eine verbesserte Simulation des Fusionskraftwerks mittels Entwicklung einer robusteren Referenzkonfiguration. Dazu wird in eine einzigartige Rechenumgebung ein mathematischer Algorithmus für die wichtigsten Probleme einer Fusion in einem Tokamakreaktor integriert. Dazu gehören das zweidimensionale Plasmagleichgewicht und die Kernphysik, der Neutronen- und Photonenkernstrahlungstransport sowie die elektromagnetische und technische Charakterisierung der Toroidalfeld- (TF) und Poloidalfeldspulen (PF). Die meisten integrierten Module verfügen über eine höhere räumliche Auflösung als gegenwärtig verfügbare Systemcodes, wie z.B. PROCESS.

Das multiphysikalische Programm MIRA wurde dann auf die mit Hilfe des Codes PROCESS erzeugte Referenzkonfiguration DEMO 2015 angewandt. Für die Analyse wurden identische Modellannahmen und Anforderungen (z.B. die gleiche Fusionsleistung sowie gleiche Radien und Aspect Ratio) gewählt und der Einfluss auf bestimmte Leistungskennwerte beobachtet. Dabei wurde festgestellt, dass einige Anforderungen an den Plasma-Safety-Factor, das Ripple des Toroidalfelds sowie die Plasmabrenndauer nicht erfllt worden waren.

Zusammenfassend stellte sich heraus, dass die Referenzkonfiguration DEMO 2015 nicht allen Anforderungen entspricht und daher einige Eingabeparameter korrigiert werden müssen. Dies geschieht beispielsweise über Parameterscans, bei denen drei Variablen, wie z.B. die innere Induktivität des Plasmas, die Stärke der innenliegenden Blanketbrutzone sowie die Breite des Zwischenraums zwischen Vacuum Vessel und Toroidalfeldspule, bestimmt werden. Die Sensitivitätsanalysen ergaben nichttriviale Abhängigkeiten zwischen den Parametern, die noch nie zuvor mit Fusionssystemanalyse untersucht worden sind. So wurden beispielsweise große Einflüsse der inneren Plasmainduktivität auf den Safety-Factor, die Plasmaform, die Dichte und Temperatur, den maximalen Divertorwärmefluss und die Plasmabrennzeit beobachtet. Auch wurde die optimale Breite des Brutblankets plus Toroidalfeldspule im Hinblick auf eine maximale Plasmabrennzeit bestimmt. Diese ist ein guter Kompromiss zwischen der neutronischen Tritium-Breeding-Ratio und den technischen

Grenzwerten in den zentralen elektromagnetischen und supraleitenden Kabeln. Die Ergebnisse werden zu wichtigen nderungen der Auslegung eines Tokamakreaktors wie DEMO führen. Weitere Analysen der wichtigsten physikalischen und technischen Größen des Reaktors werden zu einer schnelleren und besseren Auslegung des Fusionskraftwerks beitragen.

Contents

List of Acronyms

ASDEX	Axially Symmetric Divertor EXperiment
ANISN	Anisotropic Scattering S_N transport code
BB	Breeding Blanket
BD	Breakdown
BOP	Beginning of Pulse
BoP	Balance of Plant
BSL	Biot-Savart Law
BT	Burn Termination
BTE	Boltzmann Transport Equation
CAD	Computer-aided Design
CCE	Current-carrying Element
CCL	Current-carrying Loop
CEA	Commissariat á l'énergie atomique et aux énergies alternatives
CCFE	Culham Centre for Fusion Energy
CICC	Cable in Conduit Conductor
CoE	Cost of Electricity
CP	Cooling Plate
CS	Central Solenoid
DC	Design Code
DCLL	Dual-Coolant Lithium-Lead
DEMO	Demonstration Fusion Power Plant
DGM	Discontinuous Galerkin Method
DPA	Displacement per Atom
DT	Design Target
EFDA	European Fusion Development Agreement
EFFI	Electromagnetic Fields, Forces and Inductance
EIA	Energy Information Administration
ELM	Edge Localized Mode
EOF	End of Flat-top
EOP	End of Pulse
ESS	Energy Storage System
FE	Finite Element
FEM	Finite Element Method
FENDL	Fusion-Evaluated Nuclear Data Library
FPP	Fusion Power Plant
FPY	Full-Power Year

FW	First Wall
GI	Ground Insulation
GSE	Grad-Shafranov Equation
HCLL	Helium-Cooled Lithium-Lead
HCPB	Helium-Cooled Pebble Beds
H&CD	Heating and Current-Drive
HTS	High Temperature Superconductor
IB	Inboard
IHX	Intermediate Heat Exchanger
IHX	Intermediate Heat Exchange System
IPP	Max Planck Institute for Plasma Physics
IV	Iteration Variable
KERMA	Kinetic Energy Released in MAterials
KIT	Karlsruhe Institute of Technology
JAEA	Japan Atomic Energy Agency
JET	Joint European Torus
LCMS	Last Closed Magnetic Surface
LHS	Left-Hand Side
LTS	Low Temperature Superconductor
MARFE	Multifaceted Asymmetric Radiation From Edge
MCNP	Monte Carlo N-Particle transport code
MHD	Magneto-Hydrodynamic
MIRA	Modular Integrated Reactor Analysis
MMS	Multi-Module-Segment
MoC	Method of Characteristics
MS	Magnetic Surface
NDOF	Number Degrees of Freedom
OB	Outboard
OIS	Outer Inter-coil Structure
OL	Operational Limit
PCS	Power Conversion System
PD	Pump-down
PDE	Partial Differential Equation
PF	Poloidal Field
PFC	Poloidal Field Coil
PHTS	Primary Heat Transfer System
PPCS	Power Plant Conceptual Study
PPPT	Power Plant Physics and Technology

RB Reactor Build
RC CS recharge
R&C Requirements and Constraints
REBCO *Rare-Earth*-Barium-Copper-Oxide
RD Ramp-down
RHS Right-Hand Side
RM Remote Maintenance
RU Ramp-up

SC Systems Code
SOF Start of Flat-top
SOL Scrape-off Layer
SPC Swiss Plasma Center

TBR Tritium Breeding Ratio
TF Toroidal Field
TFC Toroidal Field Coil
TL Technological Limit
TOKEF Tokamak Input generator for EFFI
TOKES Tokamak Equilibrium and Surface processes

V&B Validation and Benchmark
VDE Vertical Displacement Event
VV Vacuum Vessel

WCLL Water-Cooled Lithium Lead
WP Winding Pack

List of Symbols

Latin Symbols

Symbol	Unit	Description
$\mathbf{A}$	[Wb/m]	Vector potential of magnetic field vectorial distribution
A	[-]	Plasma aspect ratio
A_{Cu}	[cm^2]	Copper cross-sectional area in coil cable
A_{cond}	[cm^2]	Total conductor cross-sectional area in coil cable
A_{He}	[cm^2]	Helium coolant cross-sectional area in coil cable
A_p	[m^2]	Plasma poloidal cross section area
A_{sc}	[cm^2]	Superconducting cross-sectional area in coil cable
$A_{tar,i/o}$	[m^2]	Poloidal area of inner/outer divertor target
$A_{wet,i/o}$	[m^2]	Inner/outer divertor wetted area
a	[m]	Plasma aspect minor radius
$\mathbf{B}$	[T]	Vectorial magnetic field distribution
$B_{\max}$	[T]	Maximum allowable operating magnetic field in coil
B_{peak}	[T]	Peak operating magnetic field in coil
$\langle B_p \rangle_l$	[T]	Line-averaged poloidal magnetic field
B_p	[T]	Total poloidal magnetic field
B_r	[T]	Radial magnetic field
B_t	[T]	Toroidal magnetic field at plasma geometric center (or axis)
B_z	[T]	Vertical magnetic field
B_ϕ	[T]	Toroidal magnetic field
$\mathcal{B}_p$	[T/s]	Plasma tritium burning rate
C_{Ejima}	[-]	Ejima coefficient
$\mathcal{C}(\mathbf{I_c})$	[-]	Vector function of PF/CS operational and technological limits
$\mathcal{D}_{bd}$	[-]	Poloidal domain enclosed to the plasma breakdown region
$\mathcal{D}_p$	[-]	Poloidal domain enclosed to the plasma confining region
d_c	[m]	Minimum cassette body thickness $\lvert \mathrm{D_{i,1}D_{i,6}} \rvert$ (see Figure 2.10)
$d_{S,i/o}$	[m]	Inner/outer distance between X- and strike points ($\lvert \mathrm{X_lS_i} \rvert / \lvert \mathrm{X_lS_o} \rvert$) (see Figure 2.10)
d_{strand}	[mm]	Diameter of superconducting strand
E_{fus}	[MeV]	Fusion reaction energy yield
$E_{m,i}$	[GJ]	Magnetic energy stored in the coil i
$\mathrm{EMF_i}$	[-]	Energy Multiplication Factor in reactor component i

List of Latin symbols (continues on next page)

List of Latin symbols (continued from previous page)

Symbol	Unit	Description
$\mathbf{F}$	[MN]	Vectorial total Lorentz force
$F_{z,CS}^{sep,dw}$	[MN]	Down-pulling vertical separating force on CS stack
$F_{z,CS}^{sep,\max}$	[MN]	Maximum vertical separating force on CS stack
$F_{z,CS}^{sep,up}$	[MN]	Up-pulling vertical separating force on CS stack
$F_{z,CS}^{tot}$	[MN]	Total vertical force on CS stack
$F_{z,CS}^{tot,\max}$	[MN]	Maximum vertical force on CS stack
$F_{z,i}$	[MN]	Total vertical force on toroidal current loop i
$F_{z,i\leftarrow j}$	[MN]	Vertical force on toroidal current loop i from loop j
$F_{z,PF}^{g}$	[MN]	Total vertical force on PF coil g
$F_{z,PF}^{\max}$	[MN]	Maximum vertical force on PF coil g
$f(\Psi)$	[MA]	Plasma poloidal current potential
f_{aux}	[-]	Ratio of $\dot{W}_{aux}$ to $\dot{Q}_{th}$
$f_{Cu,srand}$	[-]	Copper fraction in superconducting strand
f_{Cu2sc}	[-]	Copper to superconducting ratio in strand
f_{cryo}	[-]	Ratio of $\dot{W}_{cryo}$ to $\dot{Q}_{th}$
f_{DT}	[-]	Plasma fuel density fraction
f_{GW}	[-]	Greenwald plasma density fraction
f_{He}	[-]	Plasma helium fraction
f_{heat}	[-]	Ratio of τ_{heat} to τ_E
f_i	[-]	Plasma total ion fraction
f_{LH}	[-]	Ratio of transport loss to H-mode threshold power
f_{P2E}	[-]	Particle-to-energy confinement time ratio
f_{pump}^{i}	[MW^{-2}]	Ratio of $\dot{W}_{pump}^{i}$ to $\dot{Q}_{i}^{3}$ in system $i = BB/div/VV$
f_{RU}	[-]	Ratio of τ_{RU} to τ_{res}
f_{rad}	[-]	Fraction of $P_{sep,i/o}$ dissipated through radiation losses in the divertor region
$f_{sep,i/o}$	[-]	Fraction of P_{sep} transported to inner/outer vertical target
$f_{x,i/o}$	[-]	Flux expansion factor at inner/outer divertor target
f_{Z_1}	[-]	Core plasma concentration of seeded impuruty 1
$f_{Z_1,M}$	[-]	Mantle plasma concentration of seeded impuruty 1
f_{Z_2}	[-]	Core plasma concentration of impuruty 2
$f_{Z_2,M}$	[-]	Mantle plasma concentration of impuruty 2
$G_{B_{r/z}}$	[T/A]	Radial/vertical magnetic field Green's function of the Ampere's law in potential form
G_{Ψ}	[Wb/A]	Poloidal magnetic flux Green's function of the Ampere's law in potential form
H	[-]	Plasma confinement enhancement factor
$\mathbf{J}$	[$\mathrm{MA/m}^2$]	Vectorial electric current density distribution
$\mathbf{J}$	[$\mathrm{cm}^{-2}/\mathrm{s}/\mathrm{eV}$]	Neutron/photon particle current vector
J_r	[$\mathrm{MA/m}^2$]	Radial component of current density vectorial distribution

List of Latin symbols (continues on next page)

List of Latin symbols (continued from previous page)

Symbol	Unit	Description
J_z	[MA/m^2]	Axial component of current density vectorial distribution
J_{wp}	[MA/m^2]	Current density in winding pack
$J_{wp}^{\max}$	[MA/m^2]	Maximum current density in winding pack
J_ϕ	[MA/m^2]	Toroidal component of current density vectorial distribution
$J_{\phi,p}$	[MA/m^2]	Plasma toroidal current density
I_{BS}	[MA]	Bootstrap plasma current
I_{CD}	[MA]	Current-drive plasma current
$\mathbf{I_c}$	[MA]	PF/CS coil currents vector
I_c	[MA]	Total coil current
$I_c^{\max}$	[MA]	Maximum coil operating current
I_{crit}	[MA]	Superconducting cable critical current
I_i	[MA]	Turn current of coil i
I_{ind}	[MA]	Inductive plasma current
I_{op}	[kA]	Turn operating current of coil
$I_{op}^{\max}$	[kA]	Allowable maximum turn operating current in coil
I_p	[MA]	Total plasma current
I_{TFC}	[MA]	Total current in a TF coil
$L_{c,i}$	[H]	Cable self-inductance of coil i
L_i	[H]	Self-inductance of a generic coil i
L_p	[H]	Self-inductance of the plasma loop
l_i	[-]	Normalized plasma internal inductance
l_p	[m]	Poloidal length of the opening for the access to divertor cooling pipes and vacuum pump duct $\lvert D_{o,5}D_{o,6}\rvert$ (see Figure 2.10)
$l_{t,i/o}$	[m]	Inner/Outer divertor targets length (see Figure 2.10)
ℓ_p	[m]	Plasma poloidal perimeter
$\mathcal{M}_{i,j}$	[H]	Mutual inductance between coils i and j
$m_{BB,segm}^{i/o}$	[ton]	Mass of inboard/outboard segments per reactor sector
$N_{BB,segm}^{i/o}$	[-]	Number of inboard/outboard segments per reactor sector
N_{bd}	[-]	Number of points on $\partial\mathcal{D}_{bd}$
N_c	[-]	Number of PF/CS coils
N_l	[-]	Number of layers in coil
$N_{l,I/O}$	[-]	Number of layers in in inner/outer TF coil winding pack
N_{sect}	[-]	Number of reactor sectors
N_{strand}^{Cu}	[-]	Number of copper strands in superconducting cable
N_{strand}^{sc}	[-]	Number of superconducting strands in cable
N_{TFC}	[-]	Number of TF coils
N_{tpl}	[-]	Number of turns per layer in coil
$N_{tpl,I/O}$	[-]	Number of turns per layer in in inner/outer TF coil winding pack

List of Latin symbols (continues on next page)

List of Latin symbols (continued from previous page)

Symbol	Unit	Description
N_{turn}	[-]	Number of superconducting turns
$N_{turn}^{\min}$	[-]	Minimum number of superconducting turns
n_e	$[10^{20}/\mathrm{m}^3]$	Plasma electron density
$\overline{n}_e$	$[10^{20}/\mathrm{m}^3]$	Line-averaged plasma electron density
$\langle n_e \rangle$	$[10^{20}/\mathrm{m}^3]$	Volume-averaged plasma electron density
n_D	$[10^{20}/\mathrm{m}^3]$	Plasma deuterium fuel density
n_{DT}	$[10^{20}/\mathrm{m}^3]$	Plasma fuel density
n_{GW}	$[10^{20}/\mathrm{m}^3]$	Plasma Greenwald density
n_T	$[10^{20}/\mathrm{m}^3]$	Plasma tritium fuel density
$n_{e,0}$	$[10^{20}/\mathrm{m}^3]$	Plasma electron density at plasma magnetic axis
$n_{e,ped}$	$[10^{20}/\mathrm{m}^3]$	Plasma electron density at pedestal height
$n_{e,sep}$	$[10^{20}/\mathrm{m}^3]$	Plasma electron density at separatrix
n_i	$[10^{20}/\mathrm{m}^3]$	Atom density of a generic isotope i
P_{add}	[MW]	Plasma additional heating power
P_α	[MW]	Plasma α power
P_{brem}	[MW]	Plasma bremmtrahlung radiation power
P_{CD}	[MW]	Plasma current-drive heating power
P_{nCD}	[MW]	Plasma non-current-drive heating power
P_{con}	[MW]	Plasma advective/conductive transport loss power
$P_{con,i/o}$	[MW]	Transport loss power onto inner/outer divertor target
$P_{div}^{n/\gamma}$	[MW]	Plasma neutron/gamma radiation power onto divertor structures
P_{fus}	[MW]	Plasma fusion power
$P_{fw}^{n/\gamma}$	[MW]	Plasma neutron/gamma radiation power onto FW
$P_{fw/ib}^{n/\gamma}$	[MW]	Plasma neutron/gamma radiation power onto inboard FW
$P_{fw/ob}^{n/\gamma}$	[MW]	Plasma neutron/gamma radiation power onto outboard FW
P_{LH}	[MW]	L-mode to H-mode threshold power
P_{line}	[MW]	Total plasma line radiation power
$P_{line,core}$	[MW]	Plasma core line radiation power
$P_{line,mantle}$	[MW]	Plasma mantle line radiation power
P_{neut}	[MW]	Plasma neutron radiation power
P_{OH}	[MW]	Plasma ohmic heating power
P_{rad}	[MW]	Plasma total radiation loss power
$P_{rad,core}$	[MW]	Plasma core radiation loss power
$P_{radDiv,i/o}$	[MW]	Dissipated radiative power onto inner/outer divertor target
$P_{rad,mantle}$	[MW]	Plasma mantle radiation loss power
$P_{radPlasma,i/o}^{div}$	[MW]	Plasma radiation loss power onto inner/outer divertor target
P_{sep}	[MW]	Plasma power transported across the separatrix
P_{syn}	[MW]	Plasma synchrotron radiation power
p	[Pa]	Plasma pressure distribution
$\langle p \rangle$	[Pa]	Volume-averaged plasma pressure distribution

List of Latin symbols (continues on next page)

List of Latin symbols (continued from previous page)

Symbol	Unit	Description
Q	[-]	Plasma fusion gain
$\dot{Q}_{BB}$	[MW]	Thermal power extracted from breeding blanket
$\dot{Q}_{div}$	[MW]	Thermal power extracted from divertor
$\dot{Q}_{th}$	[MW]	Thermal power transported to BoP
$\dot{Q}_{VV}$	[MW]	Thermal power extracted from vacuum vessel
q	[-]	Plasma safety factor distribution
q_{brem}	[MW/m^3]	Plasma bremsstrahlung radiation power density
q_{cyl}	[-]	Cylindrical plasma safety factor
q_{fus}	[MW/m^3]	Plasma fusion power density
q_{line}	[MW/m^3]	Plasma line radiation power density
q_{neut}	[MW/m^3]	Plasma neutron power density
q_{rad}	[MW/m^3]	Total plasma radiation power density
q_{syn}	[MW/m^3]	Plasma synchrotron radiation power density
q_0	[-]	Plasma safety factor at magnetic axis
q_{95}	[-]	Plasma edge safety factor
q_α	[MW/m^3]	Plasma α power density
R_0	[m]	Plasma major radius
R_{ax}	[m]	Radial coordinate of plasma magnetic axis
R_x^m	[s^{-1}]	Global volumetric reaction rate of the nuclear interaction x in the reactor component m
R_{heat}^m	[MW]	Global heat generation rate in reactor component m
R_{nt}^m	[T/s]	Global tritium production rate in reactor component m
R_p	[Ω]	Plasma resistance
$\mathcal{R}_x$	[m^{-3}/s]	Local volumetric reaction rate of the nuclear interaction x
$\mathcal{R}_{dpa}$	[dpa/fpy]	Local material damage rate
$\mathcal{R}_{dpa,peak}^{fw}$	[dpa/fpy]	Peak neutron damage in Eurofer material (FW)
$\mathcal{R}_{dpa,peak}^{vv}$	[dpa/fpy]	Peak neutron damage in SS316 Eurofer material (VV)
$\mathcal{R}_{heat}$	[W/m^{-3}]	Volumetric heat generation rate
$\mathcal{R}_{heat,peak}^{wp}$	[W/m^{-3}]	Peak volumetric heating in winding pack
$\mathcal{R}_{nt}$	[T/m^{-3}/s]	Volumetric tritium production rate
$\mathcal{R}_x$	[m^{-3}/s]	Local volumetric reaction rate of the nuclear interaction x
r	[m]	Radial coordinate in the global curvilinear coordinate system
$r_{\mathrm{B_{c,1}}}$	[m]	Radial coordinate of uppermost inner and outer BB points (see Figure 2.11)
r_{bd}	[m]	Radial coordinate of plasma breakdown point $\mathbf{X_{bd}}$
$r_{j,k}^m$	[m]	Radial coordinate of radial node j in the reactor component m on the k reactor side $k = i/o$
$r_{X,l/u}$	[m]	Radial coordinate of lowermost/uppermost elevated plasma point (upper/lower X-point)
$r_{wp,i/o}$	[m]	Inboard/outboard radial coordinate of the inner TF coil winding pack (see Figure 4.10)

List of Latin symbols (continues on next page)

List of Latin symbols (continued from previous page)

Symbol	Unit	Description
S	[m^2]	Toroidal surface of a generic core reactor component
S	[m]	Divertor power spreading factor
S_{FW}	[m^2]	First wall toroidal surface
S_p	[m^2]	Plasma toroidal surface
T_{cs}	[K]	Current-sharing temperature
T_{hs}	[K]	Hot spot temperature
T	[keV]	Plasma temperature
TBR	[-]	Tritium Breeding Ratio
$\langle T \rangle$	[keV]	Volume-averaged plasma temperature
$\langle T \rangle_n$	[keV]	Density-averaged plasma temperature
$\mathcal{T}_h$	[-]	Variable for a generic triangular mesh (2D) or tetrahedral mesh (3D)
T_{op}	[K]	Operating temperature of superconducting cable
T_{ped}	[keV]	Plasma temperature at pedestal height
T_{sep}	[keV]	Plasma temperature at separatrix
T_0	[keV]	Plasma temperature at plasma magnetic axis
t_{dump}	[s]	Dump time
U_{loop}	[V]	Plasma loop voltage
V	[m^3]	Volume of a generic core reactor component
V_{dump}	[kV]	Dump voltage
$V_{dump}^{\max}$	[kV]	Maximum allowable dump voltage
V_p	[m^3]	Plasma volume
$\dot{W}_{add}$	[MW]	Electric power to additional heating system
$\dot{W}_{aux}$	[MW]	Electric power to auxiliary plant systems
$\dot{W}_{cryo}$	[MW]	Electric power to cryogenic system
$\dot{W}_{gross}$	[MW]	Gross electric power
$\dot{W}_{net}$	[MW]	Net electric power
$\dot{W}_{pump}$	[MW]	Total electric pumping power
$\dot{W}_{pump}^{i}$	[MW]	Electric pumping power in system $i = BB/div/VV$
$\dot{W}_{rec}$	[MW]	Electric recirculating power
W_{th}	[MJ]	Plasma thermal stored energy
w_{pq}	[-]	Weight of the quadrature formula associated with the discrete ordinate $\mathbf{\Omega}_{pq}$
$\mathbf{S_k}$	[m]	Point k on target plasma boundary
$\mathbf{X_{bd}}$	[m]	Plasma breakdown point
$\mathbf{X_l}$	[m]	Plasma bottom X-point
Z_{ax}	[m]	Vertical coordinate of plasma magnetic axis

List of Latin symbols (continues on next page)

List of Latin symbols (continued from previous page)

Symbol	Unit	Description
Z_{eff}	[-]	Plasma effective charge
z	[m]	Poloidal coordinate in the global curvilinear coordinate system
z_{bd}	[m]	Vertical coordinate of plasma breakdown point $\mathbf{X_{bd}}$
$z_{X,l/u}$	[m]	Axial coordinate of lowermost/uppermost elevated plasma point (upper/lower X-point)

List of Latin symbols

Greek Symbols

Symbol	Unit	Description
α_n	[-]	Alpha coefficient for the plasma electron density profile
α_T	[-]	Alpha coefficient for the plasma temperature profile
$\alpha_{w,i/o}$	[deg]	Inner/outer horizontal angle of the divertor curve segment interfacing the blanket (see Figure 2.10)
β	[-]	Plasma beta coefficient
$\beta_{i/o}$	[deg]	Inner/outer vertical target angles (see Figure 2.10)
β_n	[-]	Beta coefficient for the plasma electron density profile
β_N	[%]	Plasma normalized beta
β_{th}	[%]	Plasma thermal beta
β_p	[%]	Total poloidal plasma beta
$\beta_{p,th}$	[%]	Thermal poloidal plasma beta
β_t	[%]	Total toroidal plasma beta
$\beta_{t,th}$	[%]	Thermal toroidal plasma beta
β_T	[-]	beta coefficient for the plasma temperature profile
Γ_{sep}	[MW/m]	Divertor challenging quantifier
Γ^u_{sep}	[MW/m]	Upper limit on divertor challenging quantifier
$\Gamma^{k,j}_{\perp,av}$	[MW/m^2]	Average wall loading of the $k-$th particle streaming onto the wall boundary $\partial\mathcal{D}_j$ ($k = n,\gamma$ and $j = fw/ib, fw/ob, div$)
$\Gamma^{k,j}_{\perp,\max}$	[MW/m^2]	Peak wall loading of the $k-$th particle streaming onto the wall boundary $\partial\mathcal{D}_j$ ($k = n,\gamma$ and $j = fw/ib, fw/ob, div$)
$\Gamma^{tot,div/k}_{\perp,\max}$	[MW/m^2]	Total peak heat flux on inner/outer divertor target ($k = i/o$)
γ_{beam}	[-]	Ratio of fast beam to thermal particles pressure
γ_{CD}	[A/W m^2]	Global normalized current-drive efficiency
γ_{fast}	[-]	Ratio of fast to thermal particle pressures

List of Greek symbols (continues on next page)

List of Greek symbols (continued from previous page)

Symbol	Unit	Description
$\gamma_{f\alpha}$	[-]	Ratio of non-thermalized fast alpha to thermal particle pressures
$\Delta_{\mathrm{BB-div}}$	[m]	BB-divertor gap thickness ($\lvert \mathrm{B_{o,6}D_{o,5}} \rvert$), the same of IB and OB sides (see Figure 2.11)
$\Delta_{\mathrm{BB,i/o/t}}$	[m]	Inboard/outboard/top BB thickness (see Figure 2.11)
$\Delta^{i/o/tor}_{BB,segm}$	[m]	Inboard/outboard/toroidal extension of the BB segment
$\Delta_{\mathrm{BB-VV,i/o/t}}$	[m]	Inboard/outboard/top thickness of the gap between the BB and the VV
$\Delta^{ib}_{case,I/O/T}$	[m]	Inner/outer/toroidal thickness of inboard TF coil leg casing (see Figure 4.10)
$\Delta^{ob}_{case,I/O/T}$	[m]	Inner/outer/toroidal thickness of outboard TF coil leg casing (see Figure 4.10)
ΔT_{cs}	[K]	Current-sharing temperature margin
$\Delta T^{\min}_{cs}$	[K]	Minimum allowable current-sharing temperature margin
$\Delta_{\mathrm{div-VV}}$	[m]	Offset between the divertor and the VV
Δ_{EP}	[m]	Extension of the equatorial port (see Figure 2.12)
Δ_{gi}	[m]	Thickness of TF coil ground insulator (see Figure 4.10)
Δ_{LP}	[m]	Extension of the lower port (see Figure 2.12)
$\Delta_{\mathrm{SOL,i/o}}$	[m]	Inboard/outboard SOL thickness (see Figure 2.11)
$\Delta_{\mathrm{TFC,i/o/t/b}}$	[m]	Inboard/outboard/top/bottom VV thickness (see Figure 2.13)
Δ_{UP}	[m]	Extension of the upper port (see Figure 2.12)
$\Delta_{\mathrm{VV,i/o/t/b}}$	[m]	Inboard/outboard/top/bottom VV thickness (see Figure 2.12)
$\Delta_{\mathrm{VV-TFC,i/o/t/b}}$	[m]	Inboard/outboard/top/bottom thickness of the gap between the VV and the TFC (see Figure 2.13)
$\delta_{tf}(\mathbf{p})$	[%]	Toroidal field ripple at point $\mathbf{p}$
$\delta_{tf,\max}$	[%]	Maximum toroidal field ripple at plasma separatrix
$\delta_{X,l/u}$	[-]	Upper/lower plasma triangularity at plasma separatrix (see Figure 2.9)
δ_X	[-]	Average triangularity at plasma separatrix (see Figure 2.9)
$\delta r_{wp,I/O}$	[m]	Radial thickness of inner/outer TF coil winding pack (see Figure 4.10)
$\delta y_{wp,I/O}$	[m]	Toroidal thickness of inner/outer TF coil winding pack (see Figure 4.10)
$\partial\mathcal{D}_{bd}$	[-]	Boundary of plasma breakdown region $\mathcal{D}_{bd}$
$\partial\mathcal{D}_p$	[-]	Actual plasma boundary
$\partial\mathcal{D}^t_p$	[-]	Target plasma boundary
η_{add}	[%]	Wall-plug efficiency

List of Greek symbols (continues on next page)

List of Greek symbols (continued from previous page)

Symbol	Unit	Description
η_{gross}	[%]	Gross electric efficiency
θ_{sect}	[deg]	Periodicity toroidal angle of a reactor sector
θ_{vault}	[deg]	TF coil casing vault angle
$\kappa_{X,l/u}$	[-]	Upper/lower plasma elongation at plasma separatrix (see Figure 2.9)
κ_X	[-]	Average plasma elongation at plasma separatrix (see Figure 2.9)
λ_{int}	[mm]	Divertor integral power decay length
λ_q	[mm]	Decay length of heat flux in SOL at mid-equatorial plane
μ_0	[H/m]	Magnetic permeability of vacuum ($4\pi \times 10^{-7}$)
μ_{pq}	[-]	Cosine of the azimuthal angle associated with the discrete ordinate $\mathbf{\Omega}_{pq}$
ξ_p	[-]	Cosine of the polar angle assocuiated with the discrete ordinate $\mathbf{\Omega}_{pq}$
ρ	[-]	Normalized inverse poloidal magnetic flux distribution
ρ_b	[m]	Baffle radius $\lvert D_{c,1}D_{i,4}\rvert$, $\lvert D_{c,2}D_{o,4}\rvert$
ρ_{core}	[-]	Normalized radial coordinate value denoting the core plasma region
ρ_d	[m]	Central dome curvature radius (if dome is selected), or curvature radius of the cassette curve facing the private region $\lvert D_{c,3}D_{i,1}\rvert$ (see Figure 2.10)
ρ_{ped}	[-]	Normalized radial coordinate value denoting the pedestal height
Σ_x	[cm^{-1}]	Macroscopic cross section of the nuclear interaction x
Σ_t	[cm^{-1}]	Macroscopic total cross section
$\sigma_{x,i}$	[barn]	Microscopic cross section of the nuclear interaction x of the isotope i
$\langle \sigma v \rangle$	[m^3/s]	Velocity-averaged thermonuclear fusion reaction rate
σ_{S_p}	[Ω/m]	Plasma conductivity
$\left\langle \sigma_{S_p} \right\rangle$	[Ω/m]	Surface-avegared plasma conductivity
τ_{BT}	[s]	Time duration of plasma burn termination
τ_{burn}	[s]	Time duration of plasma burn
τ_{cycle}	[s]	Time duration of a reactor cycle
τ_{dwell}	[s]	Plasma dwell time

List of Greek symbols (continues on next page)

List of Greek symbols (continued from previous page)

Symbol	Unit	Description
τ_E	[s]	Plasma energy confinement time
τ_{flat}	[s]	Plasma flat-top time duration
τ_{heat}	[s]	Time duration of plasma heating
τ_p^*	[s]	Plasma particle confinement time
$\tau_{RC/PD}$	[s]	Time duration of pumping-down and CS recharge
τ_{RD}	[s]	Time duration of plasma ramp-down
τ_{RU}	[s]	Time duration of plasma rampu-up
τ_{res}	[s]	Plasma resistive time scale at ramp-up
ϕ	[m]	Toroidal coordinate in the global curvilinear coordinate system
ϕ	[$cm^{-2}/s/eV$]	Neutron/photon particle scalar flux
Φ_{fast}	[cm^{-2}/s]	Fast neutron flux density
$\Phi_{fast,peak}^{wp}$	[cm^{-2}/s]	Peak fast neutron flux density on Nb_3Sn superconductor (WP)
Φ_g	[cm^{-2}/s]	Average neutron/photon flux density in the energy group g
Φ_{tot}	[cm^{-2}/s]	Total neutron flux density
$\chi_{k,j}$	[-]	Peaking factor of the $k-$th particle flux onto the boundary $\partial\mathcal{D}_j$ ($k = n, \gamma$, and $j = fw/ib, fw/ob, div$)
Ψ	[Wb]	Poloidal magnetic flux distribution
Ψ_{ax}	[Wb]	Poloidal magnetic flux at plasma magnetic axis
Ψ_b	[Wb]	Poloidal magnetic flux at plasma boundary
Ψ_{bd}	[Wb]	Poloidal magnetic flux at plasma breakdown
Ψ_b^{eof}	[Wb]	Poloidal magnetic flux at plasma boundary at end of flat-top
Ψ_{ind}	[Wb]	Inductive poloidal flux consumed during plasma ramp-up
Ψ_b^{sof}	[Wb]	Poloidal magnetic flux at plasma boundary at start of flat-top
Ψ_{res}	[Wb]	Resistive poloidal flux consumed during plasma ramp-up
ψ	[$cm^{-2}/s/sr/eV$]	Angular neutron/photon flux density
ψ_{pq}	[$cm^{-2}/s/sr$]	In-group angular neutron/photon flux density of discrete ordinate $\boldsymbol{\Omega}_{pq}$
$\overline{\Psi}$	[-]	Normalized poloidal magnetic flux distribution
$\psi_{-/+,l/u}$	[deg]	Inboard/outboard, lower/upper plasma separatrix intersecting angle at lowermost/uppermost elevated plasma points (see Figure 2.9)

List of Greek symbols (continues on next page)

List of Greek symbols (continued from previous page)

Symbol	Unit	Description
$\mathbf{\Omega}_{pq}$	[-]	Discrete ordinate along the azimuthal coordinate q and polar coordinate p.

List of Greek symbols

1. Introduction

According to the World Population Prospects performed and revised in 2017 by the United Nation Department of Economic and Social Affairs [1], approximately 11 billion people in 2100 are expected to live on Earth. The energy supply necessary to sustain such a growth is therefore a key issue for the future of mankind over the next decades. The New Policies Scenario proposed by the U.S. Energy Information Administration (EIA) in the International Energy Outlook (2017 edition) [2] foresees a growth of primary energy demand from 2015 to 2040 by 28 %, with the petroleum and other liquid fuels and natural gas demand rising by 18 and 43 % respectively and coal demand projected to remain near the current level, about 47500 TWh.
Considering that some of the raising economies from the non OECD countries, such as China and India, fulfil the majority of the projected energy demand with high greenhouse gas emissions energy sources [3], the establishment of new energy technologies based on low or null CO_2 emissions is vital, as well as the reinforcement of existing renewable energy sources. This framework becomes even more relevant in view of the climate goal of limiting the global warming to 2 ^{o}C by 2040, according to the Paris Agreement entered into force in November 2016. The accomplishment of such a target depends on many factors, such as the evolution of global economies, world population growth and life standards in the different countries.

In the framework of investigating new and emission free energy technologies, aiming to reduce the global emissions, thermonuclear fusion has been the object of many research activities carried out worldwide over the last decades. The goal is to demonstrate the credibility as a future and viable energy source, the operability of fusion reactors and eventually the applicability at an industrial niveau.
The European Union, by means of the EFDAs socio-economic research into fusion project, has developed a computer model called EFDA Times model [4], providing results about the optimum energy system composition until the year 2100, taking into account of economic life standards, energy market, etc. For example, a scenario assumes accordingly to limit carbon dioxide concentrations up to 450 ppm and estimates the nuclear fusion to account for approximately 1/3 of the total worldwide electricity mix, which is more than any other source. This figure is considered to be robust only assuming the worlds governments to take action against the carbon dioxide emission. If a scenario with no limitations on CO_2 concentrations is assumed fusion cannot be considered economically feasible and the energy market would be still dominated by the fossil fuels.

Recognizing the importance of nuclear fusion in the future, many research facilities have been built over the last decades, e.g. JET [5] in UK and ASDEX Upgrade [6] in Germany. The object is to scope the fusion principles and to mostly investigate the plasma physics fundamentals, such as plasma heating, confinement and stability.
The next step towards the consolidation of fusion energy fundamentals and to the electricity production from fusion energy is characterized by the operation of the fusion machine, based on a self-sustained burning plasma. Such a facility is being developed within an international consortium of partners, i.e. the ITER project [7], where ITER indicates "The Way" in Latin. ITER is a fusion reactor mostly devoted to study the physics aspects for plasmas based on larger sizes and fusion

power, as well as some of the technological challenges which will be part of the realization of a fusion power plant.

The European Union plays a key role in the advancement of nuclear fusion and a long term perspective is needed in order to predict the time scales for the realization of fusion power plants. The EUROfusion Consortium, on behalf of the European Commission, has issued a Roadmap to fusion electricity by 2051 [8]. The scenario pictured in this roadmap sees ITER as the key facility to explore and exploit from 2025 on (official first plasma), before the construction of a demonstration fusion power plant (DEMO), being the last and unique step between ITER and a commercial fusion power plant.

1.1. Introduction to Fusion Energy

In a fusion reaction, atoms of light elements, such as Hydrogen (H), Deuterium (D) and Tritium (T), fuse into heavier particles, along with a net surplus of nuclear energy which can be potentially converted into electricity in large base load power plants. In fusion research, two fusion reactions are normally considered for electricity production: one involves the only presence of deuterium, while the other a mixture of deuterium and tritium. The fuel and its availability needed for both reactions represent two of the main advantages of such technology, as the deuterium is naturally present in ocean water. There is, indeed, one atom of deuterium for every 6700 atoms of hydrogen [9]. However, the majority of currently considered reactors assume the D-T reaction, because of higher reaction rates than D-D reaction, featured also at lower temperatures. This nuclear process is also foreseen for the operation of future next step machines, such as ITER and DEMO. For this reason, throughout the course of this thesis, it will be always referred to D-T as the main burning fuel, unless differently specified. This fusion reaction involves the emission of an alpha particle and a high-energy neutron, producing a net energy amount E_{fus} equal to 17.6 MeV. It can be written as:

$$ {}^{2}_{1}\mathrm{D} + {}^{3}_{1}\mathrm{T} \rightarrow {}^{4}_{2}\mathrm{He}\,(3.5\,\mathrm{MeV}) + \mathrm{n}\,(14.1\,\mathrm{MeV}) \tag{1.1} $$

Based on momentum and energy conservation, the total energy released per fusion reaction E_{fus} consists of 3.5 MeV kinetic energy associated with the He^4 and 14.1 MeV attributed to released neutron energetic content. Since tritium is a radioactive isotope with a half-life of only 12 years, there is no natural reservoir of tritium available on earth, apart from trace amounts formed by the interaction of the atmosphere with cosmic rays.
For this reason it has to be produced on-site, by using the lithium isotopes ^{6}Li and ^{7}Li according to neutron captures reactions $^{6}\mathrm{Li}(\mathrm{n},\alpha)\mathrm{T}$ and $^{7}\mathrm{Li}(\mathrm{n},\mathrm{n}'\alpha)\mathrm{T}$. Fusion is considered to exhibit a relatively low environmental impact and provide potentially a higher safety due to the absence of criticality events.
Compared to fission power plants, it comes with a modest radioactive "legacy" mostly characterized by activated structural materials with decay half-times of the order of hundreds of years.

Concerning the operational aspects of a fusion power plant (FPP), as it can be seen from the D-T Reaction (1.1), the D and T nuclei are positively charged, and thus certain physical conditions are required in order to overcome the Coulomb barrier for them to fuse. These conditions are given by hot plasmas featuring temperatures of hundreds millions of Celsius degrees (or tenths of keV) and certain plasma densities ($\sim 10^{20}$ atom/m^3), where full ionization of hydrogen isotopes along with the condition of plasma take place.
By strong magnetic fields ions and alpha particles can be confined within the plasma region, such

that the kinetic energy allows for fusion while the α particles provide a heat source to maintain high plasma temperatures. Charged particles are influenced by the magnetic field as per Lorentz forces leading the latter to follow the field lines by means of gyro motion [9]. The magnetic confinement is obtained by operating magnetic fields of order of several Tesla with a system of magnetic coils, requiring high electric current densities. To minimize Joulean losses in the magnet winding superconducting coils are used. In fusion research, the majority of experimental devices currently built and under investigations are based on the tokamak geometry, where the main components are in the shape of tori (see Figure 1.1).

In tokamaks, the field lines produced by the current flowing in magnet coils and the plasma surround the toroidal axis, helically. Such a topology, comes from the superposition of a poloidal and a toroidal magnetic field, with charged particles tied to the field lines, wound around the torus toroidally and poloidally. The toroidal component, i.e. along the longitudinal direction of the torus, is required to trap the charged particles, which gyrate perpendicularly around the field lines. For geometric reasons, the magnetic field is found to be non-uniform across the torus, i.e. higher on inner side and smaller on the outer side. This asymmetric field typically leads to an unbalanced force between positively and negatively charged ions and electrons, eventually driving the particles to drift away from their magnetic field lines. Adding an additional transversal poloidal field component, would be the way around to the solution of such problem. Then, the resulting field is twisted into a helix. By this, any charged particle finds itself repeatedly on the upper side and the lower side of the torus, globally, cancelling out the effects of the vertical drifts. In tokamak configuration, a toroidal current flowing in the plasma confining region contributes to provide the poloidal component of the magnetic field.

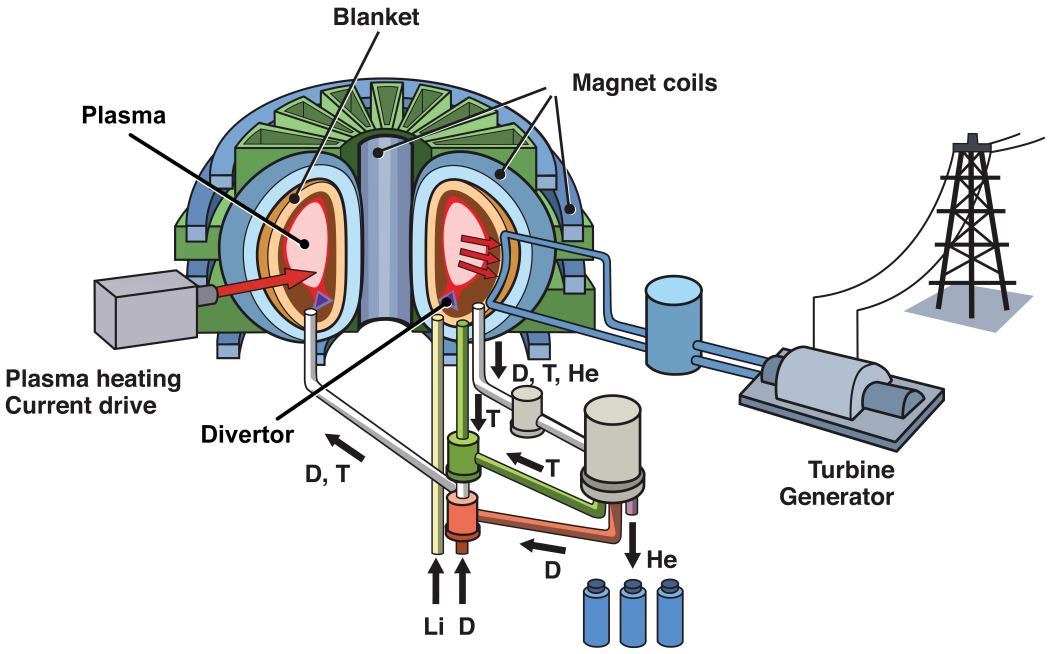

Figure 1.1.: Layout of a future tokamak fusion power plant. Figure reproduced according to [10].

The plasma current can be driven by magnetic induction, internal pressure-dependent transport turbulence mechanisms and additional external current-drive systems. In the former case, a time-varying external solenoidal current is operated to link a loop voltage in the plasma region, inducing

a net toroidal plasma current. In case of internal phenomena an advantageous bootstrap plasma current, parallel to the magnetic field, is generated in presence of pressure gradients [9].
In real D-T burning fusion devices, though, an external heating source is also needed to compensate the unavoidable plasma energy losses given by advective and conductive transport and electromagnetic radiation mechanisms [9]. This external power is provided by the plasma heating and current drive systems, also foreseen for steady state operations of a tokamak reactor, where a non-inductive current drive is required. Indeed, most of the methods used to heat a plasma can also be used to drive current. Diverse solutions are currently investigated to provide external heatings, such as neutral beam injection (NBI), electron-cyclotron resonance heating (ECRH), ion-cyclotron resonance heating (ICRH) and lower hybrid current-drive (LHCD). They differ for the used heating principle and the kind of particles deployed to drive current. In currently investigated fusion power plants, such as DEMO, relatively large fractions of produced electric power are recirculated to feed the external systems, representing a main challenge for their design and for overall plant efficiency.

The energy associated with the fusion D-T reaction-induced alpha and neutron, together with the auxiliary heating, are transferred to the components enveloping the plasma, mainly the breeding blanket and divertor. In both components, some operative coolant, e.g. helium or water, is circulated to cool down the structures and to transfer the thermal energy to a power conversion system, characterized by heat exchangers, steam generators and turbines.
In a FPP the blanket is devoted to the breeding of tritium by means of neutron captures of lithium-containing materials, taking place in solid or liquid breeder materials. This vital system makes use of the high energy neutrons leaving the plasma confining region, without interacting with the magnetic field generated by the magnet coils. As shown in Figure 1.1, tritium is extracted from the breeding blanket and fed to the Fuel Cycle and Vacuum System, where also unburnt deuterons and tritons are processed and re-injected into the plasma.
The high neutron fluxes, foreseen in large fusion power stations, will likely degrade the plasma facing components, particularly the divertor and the breeding blanket. Henceforth, they require frequent replacement. To that end, a remote handling and maintenance system is designed to allow for extraction of irradiated components and reintroduction of the new ones. For the sake of an economic and competitive production of electricity, the time requested by these operations should be minimized, to reduce the impact on the overall plant availability. The latter is intended as the fraction of time in which the plant operates normally and relevant fusion power is produced.

The divertor is another key component in such an operation, as plasma diffuses across the plasma boundary and, after neutralization, the charged particles follow the open magnetic field lines moving toward the divertor targets, where they are pumped out by means of dedicated vacuum pumps.
Alongside the plasma, the superposition of the poloidal and toroidal magnetic fields is featured by the magnet coil systems, respectively characterized by the poloidal and toroidal field coils. Both magnet coils systems carry out multiple functions, such as inductive current-drive, equilibrium, confinement and stability.

The complexity of the physics phenomena occurring in the different reactor components, combined with the extreme operative conditions and the engineering limitations of systems and materials, make nuclear fusion reactors the most complicated systems for electricity production, more than any currently available in the energy market. A proper conceptual design process poses therefore a technical challenge.

1.2. System Analysis to Support the Conceptual Design of EU-DEMO Fusion Power Plant

According to the European strategy to fusion energy [8] DEMO is considered as the single step between ITER and a commercial fusion power plant featuring all the key systems and components and thus, proving the credibility of nuclear fusion as a reliable energy source. For this reason, taking advantage of the progresses potentially (and hopefully) demonstrated by ITER, DEMO shall be properly designed. The design process is divided in different phases, following the definition of the objectives which are directly related to the performances and to the requirements expected by DEMO. In the framework of the European Power Plant Physics and Technology programme (PPPT), addressed by the EUROfusion consortium on behalf of the European Union, certain targets have been defined in the Roadmap to fusion electricity [8], which will have to rely on consolidated technical solutions and proofed materials under high level neutron fluence, possibly extrapolated from the ITER exploitation. The general goals defined for DEMO are:

1. *produce net electricity for the grid at the level of a few hundred MW;*
2. *breed the amount of tritium needed to close its fuel cycle;*
3. *demonstrate all the technologies for the construction of a commercial fusion power plant, ensuring an adequate level of availability over a reasonable time span, e.g. steady state or long pulse.*

As it can be seen, the goals listed above highlight the importance of the successful operation of DEMO from a pure engineering standpoint, along with the physics one; as a matter of fact, the Missions 1 and 2 listed in the roadmap to DEMO [8] foresee the reaching of plasma regimes of operation characterized by high values of fusion gains, minimizing the energy losses and reaching acceptable heat loads on the divertor.

The design process of a fusion device differs from all the other energy sources because of the peculiarities given by the physical processes and the technology solutions, so far observed only in experimental machines. For this reason, the definition of the targets is followed by a conceptual design, where only one or a few design points are actually investigated, aiming to prove the technological feasibility when operating under the required DEMO operative conditions. The final step before the manufacturing and the construction is given by the actual engineering design, where the established conceptual designs (assumed to be mature at this stage of advances) are further elaborated and analysed by means of more detailed analysis tools, but also relying on the exploiting of dedicated experimental devices and mocks-up.

Several DEMO studies have been already carried out in Europe in the framework of the Power Plant Physics and Technology (PPPT) programme, aiming to demonstrate the safety and the socio-economic aspects rather than the technological feasibility of the key systems. One of these studies is the Power Plant Conceptual Study (PPCS) [11], where five different DEMO concepts, operating the same net electric output (1500 MW) and five different blanket concepts, and in general a wide spectrum of reactor possibilities, have been investigated. According to Federici et al. [12], no conceptual design currently exists for DEMO, as the reactor design has not been formalized and the detailed operational requirements are not yet available. However, two different DEMO design options, based on attractiveness, readiness and risk of physics and technical solutions, have been chosen and currently investigated, i.e.:

- Near term DEMO, also called DEMO1, based on rather conservative assumptions in terms of delivery terms, i.e. starting the construction in 20 years from now, plasma operation ($\approx$ 2 hr of actively induced plasma pulse) and of power conversion system, which has to rely on mature and reliable technologies. The latter come along with a power layout featuring values of thermodynamic efficiencies of order of 33 %.
- More advanced DEMO design concept (also defined DEMO2), based on more optimistic (but less mature) physics assumptions, such as steady plasma scenario, driven by acceptably high current-drive fractions.

Both DEMO designs are built upon the "success" of ITER physics and rely on different assumptions, more conservative for DEMO1 and more optimistically advanced for DEMO2, requiring intensive investigations about the physics and technology credibility of the key components and about the uncertainties affecting the design requirements for DEMO.

The conceptual design starts therefore from the definition of these main goals and shall proceed selecting the main DEMO reactor parameters. The approach adopted in the EU-Programme [12], follows different sequential steps, which are iteratively repeated until a certain grade of satisfaction, regarding the consistency and the attractiveness of the integrated design, is met. The procedure is defined in the simplified flowchart of Figure 1.2 (see only the black solid line path for the approach currently adopted in Europe).
The whole process begins with the definition of a set of systems requirements and constraints, which are presumably based on the readiness of physics and technology advances in the key research areas. This section is then followed by an initial specification of the major design features, including reactor sizes and materials and operating conditions.
At this design stage, dedicated computational tools, referred to as fusion reactor *systems codes*, are adopted in such a way that all the key subsystems and components are consistently simulated by means of relatively simple mathematical models (often zero dimensional). These are able to capture the physical phenomena, the technological constraints of materials and the connections among the physics and the engineering worlds. Further details on these dedicated tools are reminded to the next section, as at this point it is important to show their location within the design process and to catch the influence and the impacts they might potentially have on the design.
The results coming from the systems code (SC) are normally used to engineer the obtained geometries, generating a refined three-dimensional characterization of the whole reactor volume, along with the definition of the materials.
The output of this task is normally identified with a dedicated CAD file (Computer-aided Design). Geometries and materials definitions are therefore used to consolidate the results from the SC and to carry out the specific analyses in the design codes (DC), which are based on very detailed three-dimensional and time-dependent numerical models applied to the different physics or technology areas. For instance, these incorporate e.g. plasma magnetohydrodynamics (MHD), reactor neutronics, thermal-hydraulics, electromagnetic and structural analyses.
The process can be considered completed when all components are consistently defined, the operational requirements and constraints are considered to be reliable enough and the technical solutions adopted for each DEMO system are also found to be attractive.

The attractiveness of a DEMO design relies both on the readiness of physics and technologies guidelines but also on the ability to accomplish the initial goals, demonstrating the feasibility for the whole machine and of the entire energy production process. Once this phase is terminated, the engineering design of DEMO, scheduled by 2029 for EU DEMO [8], can be therefore launched. If consistency and/or attractiveness criteria are not accomplished, the set of initially imposed design

features needs to be adjusted and the whole process shall be repeated, from systems to design codes runs. The maturity of the conceptual design is based on the number of iterations currently remaining to finalize the design, which emphasizes therefore the importance of refinement of the analysis tools. One can infer that the level of details of the used tools and codes might affect (and potentially reduce) the number of loops to be sustained in the reported flowchart.

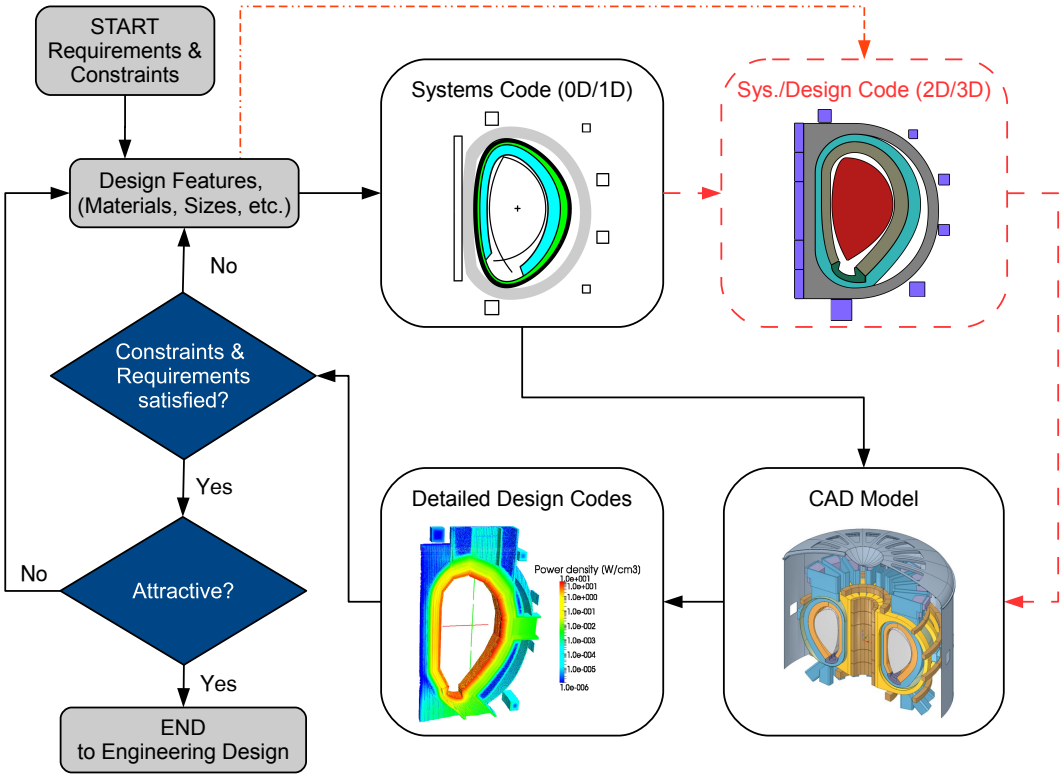

Figure 1.2.: Conceptual design process: the black path represents the approach currently adopted in the EU-DEMO programme, while the red dashed line includes an additional step, where a new concept of advanced systems/design code (proposed here and referred as to system-design code) is introduced in the design loop. The figure in the "Systems Code (0D/1D)" box depicts a DEMO reactor sketch as per PROCESS system code [12], whilst those in "CAD Model" and "Detailed Design Codes" boxes represent, respectively, the DEMO 2015 design CAD model and a related 3D map of nuclear power density, according to the detailed Monte Carlo neutron transport model proposed in [13]. Images reused with the permission of Elsevier.

With regard to systems and design codes, the connections linking these two sides of the design algorithm can be potentially consolidated by complementing or replacing the system code with new concept of system analysis tool, defined here as systems/design code (see red-dashed and red-dotted-dashed line paths in Figure 1.2). The idea behind this computing concept is to provide an integrated fusion reactor system analyses tool characterized by more advanced and detailed SC modules, compared to canonical systems codes. That would allow, therefore, to catch in a unique algorithm several key aspects, both of physics and technology kind, which normally rely on given assumptions rather than on consistent calculations, as they cannot be captured within the existing systems codes environment.

The beneficial effects derive from reducing the modelling gaps between systems and design codes, enriching the set of data flowing toward the detailed physics and engineering platforms and eas-

ing therefore the whole process. The design of DEMO-like fusion power plants coming from this system-design tool, can be expected to be more robust as it includes more precise information concerning the investigated components. This new concept of analysis tool, consequentially, engages longer computing times laying between systems and design code times, from seconds to hours respectively.

Finally, the overall target of this additional (or alternative) step in the design chain is to reduce the number of iterations of the design process. To that end, the problem is addressed by introducing a flexible tool which enhances the quality of the systems analyses and captures and addresses the major issues, requiring larger efforts if they were addressed in design code phase. In this way, more technical solutions might be potentially scoped at a reactor level, elaborating globally the effects of component-specific variations and assumptions.
Moreover, such a tool allows one to study the sensitivity of certain design parameters on a plant scale and thereby to limit the parameter ranges for exploitation only to configurations which do not contradict the key physics and engineering aspects.

1.3. State of the Art of Fusion Reactor Systems Codes

In the frame of the conceptual design of a fusion power plant, many key parameters necessitate to be simultaneously considered and parametrically varied to address their behaviour under diverse operational conditions, e.g. steady state or pulsed regime. In order to investigate these crucial aspects, the systems codes are vital computational tools, currently worldwide used in different fusion R&D programmes. Combining the available documentation, it is possible to come up with two possible definitions of systems codes, reflecting the mathematical and the technical nature of such computing instruments.

- From a mathematical point of view, the systems code can be seen as a tool where all the reactor components are simulated by means of simplified models, often zero dimensional, aiming to explore all the possible configurations and setting the physics and engineering requirements and constraints to be simultaneously met. The latter can be also considered as a system of constrained linear and nonlinear algebraic equalities and inequalities, each describing the governing phenomena occurring in the considered reactor blocks.
- From a pure technical standpoint, it can be defined as an integrated computational code having a modular structure, where each module simulates a reactor system or a component, attaining parameters from the connecting subsystems and passing the calculated ones to others.

Several systems codes have been developed with the ultimate goal of including in the system analyses the key aspects, relevant for the design of fusion plants. They can differ both from modelling or programming specifications, for instance depending on the technical and mathematical details of the implemented models or on the programming language used to write the code. Moreover, a systems code can usually run in two different operational modes: solving and optimization. When the former mode is selected the systems code attempts to find a solution for the entire system, i.e. a design point, consistently with the given inputs and the system requirements and constraints.
In mathematical terms, it is equivalent to solve a system of N equations with $M = N$, where M is the number of variables. Regarding the optimization mode, the target is to find a design point maximizing or minimizing a given figure of merit, such as the reactor size or the cost of electricity. In this case one can find $M > N$. However, if the given solution constitutes a local optimum,

and not a global, other attractive design points might be excluded, presenting therefore a drawback. Henceforth, a third operational mode is also foreseen, i.e. the scan mode, where one or many input parameters are iterated and the solutions are filtered according to the given DEMO-like plant requirements and constraints.

1.3.1. Presently available fusion reactor systems codes

Different systems codes have been developed in Europe, United States and Asia to support the design of fusion reactors, each of them with relatively different targets and research framework, as shortly described hereafter.

ASC. The ARIES system code (ASC) was developed for the US Advanced Reactor Innovation and Evaluation Study (ARIES) program [14], one the key American multi-institutional fusion research activities. It is meant to explore the most influencing parameters in the physics, technology and economic trade space related to the developmental transition from experimental facilities to viable commercial power plants.

HELIOS. The HELIOS code [15] was developed at CEA France and it is a physics-devoted systems code for the modelling of DEMO plasma scenario. Compared to the previously existing systems code, HELIOS has put emphasis mainly on the characterization of the plasma shape and on the numerics related to the geometric plasma parameters, e.g. volume and surface.

KSC. The KAERI system code (KSC) [16] was developed at Korea Atomic Energy Research Institute (KAERI) in to sustain the South Korea National Basic Plan of fusion energy. It is a physics-oriented systems code, meant to investigate the performance of a DEMO plant in terms of plasma parameters.

PROCESS. Developed at Culham Centre for Fusion Energy (CCFE) in UK, the PROCESS code [17, 18] is the reference systems code for EU-DEMO baseline activities [12, 19]. Its features, along with the wide experience of the PROCESS team in this field, make it likely the most suitable code for EU-DEMO studies. Essentially, it depicts many physics and engineering aspects of DEMO, allowing both solving and optimization modes and incorporating a modular structure.

SYCOMORE. After HELIOS, CEA launched a new project for the development of a more comprehensive system analysis tool called SYCOMORE [20]. The SYCOMORE aims at highlighting the key physics and technology aspects for fusion reactors. Concerning the latter category, SYCOMORE attempts to catch additional engineering areas, such as blankets neutronics [21], thermal-hydraulics models [22]) and superconducting coils [23]. With regards to the physics part, the HELIOS code has been incorporated.

TPC. Written, implemented and operated by Japan Atomic Energy Agency (JAEA), the Tokamak Plasma Power Balance Calculation Code (TPC) [24, 25] is based on the ITER Physics Design Guidelines. TPC is one of two systems codes, together with PROCESS, adopted in the framework of the so-called *Broader Approach* [26], which is a ten-year fusion programme carried out by Japan and European Union. That includes different sub-projects and phases, such as the DEMO Design Activity. Within this step, TPC and PROCESS have been benchmarked so that the differences among the two codes were assessed and the different capabilities were evaluated.

TREND. The Tokamak Reactor code for the Evaluation of Next-step Devices code (TREND) [10] has been developed at Max-Planck-Institute for Plasma Physics (IPP) in Garching, Germany.

The main focus of this code is on plasma physics, since the development has been carried out in parallel to work on physics design guidelines for DEMO, with the ultimate goal of evaluating the implications of physics assumptions on a given DEMO reference design. In the frame of a collaboration between KIT and IPP Garching, the system code modelling efforts from Karlsruhe Institute of Technology (KIT) and IPP Garching side have been jointly merged into a unique systems analysis tool, being one of the central elements of this work.

Based on this literature review, the PROCESS and the SYCOMORE have been found the most complete and detailed SCs for DEMO system studies, as the implemented models are suited and kept up-to-date to DEMO design progresses. In the framework of the European DEMO design point development both codes are operated [19, 27] for the characterization of the DEMO design baseline, observed by the different work packages within the PPPT programme. For this reason, many assumptions and results discussed throughout this work are based on specific reference DEMO designs produced by the PROCESS and SYCOMORE codes.

1.3.2. Model outline of existing fusion reactor systems codes

The listed fusion reactor systems analysis tools differ from several aspects, such as software architecture, module structure, modelling sophistication, etc. However, one can also find some key similarities and analogies, especially in terms of phenomenological, mathematical and geometrical details. Systems codes are meant to simulate the plant as a whole and to scope, over a multidimensional parameter phase space, many design solutions. Thus, they are constrained to run on feasibly low time scales and the majority of the systems code modules are mostly zero-dimensional, steady state and often based on scaling laws. Moreover, they rely on diverse design parameters taken as invariants of the plant analysis, leading to an over-determination of the problem treated.
Hence, as the main goal of this work is to propose improved modules for the key physics and engineering areas, an outline on the state of art is necessary to capture the reference state of advances, from which the intent of improvement inspiring this work actually arose. Except for minor differences among the existing fusion system analysis tools, in the following a comprehensive list of modules that can be broadly found among all fusion system codes is reported.

GEOMETRY. It defines the radial/poloidal profiles and calculates the related thickness, surfaces and volumes for the key physical reactor components. It is often based on very primitive shapes of the major confining boundaries but contains no profiling of more elaborated components, such as the divertor.

CORE PLASMA PHYSICS. The key zero dimensional conservation laws for plasma power, particles, current and magnetic flux are consistently solved. Energy and particle confinement times, extrapolated from experimental devices or ITER physics guidelines are used to calculate the advection-conduction transport losses. The radial profiles for ions and electrons density and temperatures are normally inputs, and the calculation of the integral power balance terms is based on purely radial magnetic flux profile.

HEATING and CURRENT DRIVE. From the physics standpoint, the major task is to calculate the injected additional heating power, by the H&CD system, as well as the fractions of plasma currents due non-inductive means, i.e. bootstrap and external current-drive. The former, is typically based on scaling laws, derived from ITER physics guidelines. For NBI and ECRH, several extrapolating laws also are implemented for the calculation of the normalized CD efficiency, relating the driven current in the plasma and the injected associated power. The normalized efficiency

is presented in formulas where it scales with average plasma parameters, such as temperature and density. From an engineering perspective, the technology representation and constraints of these systems are only poorly represented in systems code. The aspects related to integration into a fusion power station are uniquely depicted by the specified wall plug efficiency, denoting the ratio between the plasma heating power and the externally-supplied electric power.

DIVERTOR. Dedicated integral models are used to calculate the power loads on target plates and the divertor lifetime, based on the plasma power exhausted derived from the core plasma physics module and on some scaling law depicting the heat flux deposition on divertor targets. Some systems codes, e.g. PROCESS and SYCOMORE, attempt also to assess the divertor target plasma temperature based on a two-point model, i.e. based on energy and momentum conservation laws.

MAGNETS SYSTEM. The poloidal field and the toroidal field coils (PFC and TFC) are ideally designed in systems codes calculating the nominal currents associated with their operational functions, that is providing a toroidal and poloidal magnetic field dictated by selected plasma stability, shaping and control conditions. The magnets systems models normally calculate coil currents, peak magnetic field, stress and stored magnetic energies. In PROCESS the stresses in the TF coils are evaluated by means of one dimensional homogenized radial linear elasticity model, whilst the coil current densities are based on scaling laws relating coil material-specific superconducting properties. The currents in both coil systems are related to expected magnetic performances, essentially in terms of magnetic field and flux within the plasma confining region. These are based on an integral formalism of Ampere's law in case of TF coils and standard analytical formulas involving elliptic integrals, in case of PF coils, treated as coaxial wires.

BREEDING BLANKET. For the majority of the existing systems codes, there are no direct models for the calculation of the key blanket design parameters, such as tritium breeding ratio (TBR) and nuclear heating power. These are affected by complex three-dimensional effects and strong material heterogeneities, thus necessitating of detailed neutron transport analysis. Recently, the SYCOMORE code introduced a "surrogate" neutronics model [21], derived from one-dimensional and two-dimensional homogenized neutron transport codes, applied to a multitude of design points previously calculated. With regards to the thermal-hydraulics parameters, the PROCESS and SYCOMORE codes include some mathematical algorithms evaluating the blanket material inventories, the calculation of coolant flow rates and temperatures (as per integral energy balance) and the characterization of the coolant pressure drops, for instance based on analytical formulas.

PLANT POWER BALANCE. The zero dimensional steady state power balance is congruently solved for the key plant subsystems at the flat top phase of plasma current, describing the energy flows through the reactor components. The latter basically relates the plasma performances to the power conversion system layout, computing the net electric power to the grid starting from the core fusion power. A multitude of input parameters are usually needed in systems codes to specify the power distribution among different systems (e.g. repartition of plasma neutron and radiation power between blanket and divertor), as well as the efficiencies regarding the energy conversion processes taking place in a FPP, such as the wall-plug and the thermodynamic efficiencies for the auxiliary heating and power conversion systems, respectively. No transient aspects related to pulsed operation is apparently present in any of the reviewed systems codes' power flow modules.

COST. The calculation of costs of electricity (CoE) given by direct and indirect costs is based on several scaling laws for the CoE as a function of some of the key parameters (e.g. net electric power and thermodynamic efficiency). Due to the partial unreadiness of fusion reactor technologies,

it is relatively difficult coming up with reliable fusion plant cost estimations. Thus, these models are often affected by large uncertainties [28].

AVAILABILITY. A fusion plant availability model is implemented in the PROCESS system code. The availability model of PROCESS considers two kinds of unavailability, i.e. the remainder of the availability: a planned and an unplanned unavailability. The planned unavailability relates to the lifetime of components and the time requested for regular replacements, due to the remote maintenance operations. The unplanned unavailability derived from the enhanced failure probability of the major plant systems when approaching their technological limits. The modelling part is addressed by calculating the expected lifetime of blanket and divertor extracting average neutron flux and the peak heat fluxes on blanket and divertor, respectively. These are related to the allowable fluence and cumulative heat deposition. The time to replace both components is based on simplified scaling formulas, whereas, as for the failure rates, assumptions are taken depending on the investigated system.

1.4. Aims for a More Detailed Fusion Reactor Systems Code

Fusion reactor systems codes are vital tools for the conceptual design of DEMO-like power plants. Many systems codes have been developed, trying to consolidate the design points before further elaboration and validation in the actual design process of the reactor components. As systems codes rely on simplifications and assumptions, several iterations between the systems and the design codes are needed, as depicted in Figure 1.2. The whole process is expected to converge to a credible and feasible reactor design point, eventually after an undefined number of iterations.

This aspect led the designers to arise questions and doubts about the level of sophistications of currently existing systems codes and on the impact of the modelling assumptions on the overall design. One can infer that more advanced systems code models, not only can feature more robust and consistent plant system designs, but also reduce the number of iterations in complete the process.

The wide experience gained at KIT on fusion technology has recently highlighted the relatively large gaps between systems codes and design platforms, eventually coming at expenses of the latter, where lower tolerances and correction margins are in general allowed. Referring to the EU-DEMO programme, it is in general challenging to maintain consistency among different labs working on the key physics and engineering areas. To motivate this statement and to help understanding the foundations upon which this work relies, an illustrative example is reported in the following.
The blanket radial build is often fixed in systems codes analysis, assuming a design previously validated by means of detailed neutronics, thermal-hydraulics, structural mechanics and safety analyses, obtained therefore by deploying a considerable amount of manpower and time.
When seeking for a DEMO design point, meeting a set of given requirements and constraints, many parameters might be varied within the hundreds of internal SC iterations, such as fusion power, major radius, etc. At this point, there is no guarantee that the previously defined radial build is adequate to accomplish the breeding and/or shielding criteria required for such a component. Important modifications might be consequently needed in the blanket design phase, where the available radial and poloidal domains are fixed and very tiny margins for corrections are allowed.
Hence, if the neutronic analysis were to be introduced in the systems analyses, the change in the global design would be consistently taken into account and the specific blanket design procedure, from the design codes side, would rely on more robust engineering specifications. In this way the

process could avoid feeding back the design updates to the systems code and repeating again. Introducing therefore a neutronic analysis in the systems code can potentially help to ease the design phase of the specific components and to speed up the entire procedure.

The key aspects mentioned above inspired this study, where a newly developed computational platform for advanced fusion reactor systems analysis is being proposed. The essential points are focused on the ”modularity” and on the ”integration” of physics and engineering modules. For this reason, its name is Modular Integrated Reactor Analysis (MIRA), where new and advanced systems codes modules are implemented and tested.
The ultimate goal is to show the scientific implications of improved calculation algorithms and to show how they affect the fusion reactor globally. The modelling activities are mainly focused on the major technology areas, such as breeding blanket, magnets coils system and plant integration. However, several improvements have been applied to some of the plasma physics fields, such as magnetic equilibrium and confinement under externally applied magnetic field. The outline reported in the previous section emphasizes the limits of existing systems modelling algorithms, often dictated by computing time constraints. Hence, acknowledging the current status of advances in comparison to proposed advanced modelling approach, it is envisaged not to refer to this tool as a standard fusion reactor systems code, but rather as an improved concept, referred as to system/design code.
In this definition, the word ”system” identifies the modular architecture of a comprehensive global reactor simulation, whilst ”design” recalls the depiction of design elements which are normally not taken into consideration in canonical fusion reactors SCs.

One has to bear in mind that, differently from SCs, the DCs allow capturing all the technical aspects and physical phenomena taking place in all the key subsystems, though running on much longer computing times. It can be observed that there is a certain trade-off between level of details and computing times, as these are two entities reversely proportional. Simplified models correspond to relatively quick calculation times, thus potentially running on standard PCs. Three dimensional and transient analyses carried out on longer time scales and necessitate much higher computing power. Therefore, the technical choices made for all the modules, regarding the mathematical sophistication and the adopted tools, are always taken trying to reach a good compromise between results precision and running times, establishing an intermediate level of analyses between system and design codes.

1.5. Organization of the Thesis

This thesis consists of seven main chapters, as described hereafter.
In Chapter 2 a detailed description on the general architecture of the advanced MIRA systems code is given. Besides the functional logics, highlighted for the addressed reactor physical components, large efforts are also devoted to the mathematical characterization of the newly integrated models, divided in physics and engineering parts.

The reactor physics is fully covered in Chapter 3, where algorithms devoted to cover a wide spectrum of topics, including core plasma, divertor physics and magnetic equilibrium.
The engineering part is addressed in Chapter 4, covering the major tokamak reactor technology areas, including blanket neutronics, superconducting coil magnetics and cabling design and plant power balance.
The modelling aspects embraced and proposed throughout this project represent the master innovative features, especially when integrated into a unique computing environment. The major goal is

also to illustrate how these are connected and what are the physics and engineering implications on a given plant design, possibly improving their sophistication at systems level. In Chapters 3 and 4 the analytical and numerical aspects of the implemented models are individually illustrated, with focus on the major simplifying assumptions and the limitations derived from them.

In order to demonstrate the capabilities of the combined package, a complete fusion reactor design is performed and detailed in Chapter 5 for a recent and consolidated DEMO FPP baseline, i.e. EU-DEMO 2015 baseline [29, 30]. The main results are reported for each reactor element, cross-checking the consistency of the results and comparing them with those obtained as per reference PROCESS fusion systems code run. Making use of a more advanced modelling frame for each individual component, several benefits may come from a more detailed representation, for instance observing certain effects which could not be elucidated with "standard" zero dimensional-like systems code approach. These benefits are being illustrated in this section and the physical behaviour of each individual component and of the overall reactor (as a whole) is also detailed.

Chapter 6 refers to a set of parametric studies of global reactor parameters, undertaking several physics and engineering aspects which are not adequately tackled by means of zero dimensional systems codes. As for the plasma, the internal inductance, i.e. an integral parameter referring to the magnetic energy stored within the confining plasma, has been scanned within a reasonable range and evaluated mainly to address the implications on the key core physics variables and on the externally-applied magnetic configuration.
Concerning the major engineering areas, the radial builds of the breeding blanket and the TF coils are scoped to evaluate the response on various impacting design parameters, such as tritium breeding ratio, toroidal field ripple and stored magnetic energy.

Finally, the main results are summarized and commented in Chapter 7, along with an outlook of future modelling activities which could be conducted to continue and improve the current MIRA analysis frame.
Due to the complexity and the multitude of systems defining such an advanced FPP systems code, for the sake of a "fluid" readability of this thesis a part of modelling details was omitted in the main body and reported in Appendix, where the reader is encouraged to attain from for a deeper understanding of the physics and engineering assumptions.

2. Architecture of an Advanced FPP System Code

This chapter presents the models and the methodologies implemented in the system-design code MIRA and how these are connected. The mathematical aspects for each modelling element are individually illustrated, together with a dedicated verification study. The words *Modular* and *Integrated* included in the acronym MIRA are two of its major strength points, implying a high capability to replace and introduce new modules, as well as to keep an "integrated" view of the reactor as a whole. Even though MIRA has been built to operate as a complete fusion reactor system-design code, it can be also used to scan a specific FPP system/component and to evaluate its behaviour in the context of the reactor environment.

2.1. Functional Logics and Elements of a System Code

The definition of a fusion power plant design goes through the consideration of many multi-physics aspects, involving a multitude of reactors systems and components and obeying to different physics and engineering laws. The latter must be properly taken into account when assessing the main specifications for each of these elements, leading thus to a consistent power plant design. A systems code implies a modular structure, where many blocks are embedded in a system data flow in such a way that the information coming from other modules is processed. Subsequently, certain methods are established and new information is returned to the communicating systems parts. It is necessary to define the reactor modules implemented in the system/design code MIRA and the connections in a global systems code run.
This set of information is depicted in the flow chart of Figure 2.1. As it can be seen, the whole procedure begins with the characterization of the requirements and constraints (R&C). Since one of the major goals is to find certain reactor design points, where requirements and constraints are simultaneously verified, it is important to give a comprehensive definition for both.

- *Physics and engineering requirements refer to specific parameters which are supposed to be obtained for a specific fusion power plant design.*
- *Physics and engineering constraints are related to technological and operational limits of all the reactor systems, around which the requirements are expected to be found.*

This definition inherently clarifies the challenging design process of a fusion power plant, identified as the meeting point between physics and engineering. That is precisely a task to perform when running a fusion systems code. Requirements basically pose the question "what do we want from a power plant?", whilst the constraints describe the operational and technological limitations given by plasma physics, materials and the systems engineering layout, restraining the set of solutions answering this question. For example, a requirement can be imposed on the reactor sizes or power output, such as fixing or imposing a lower and/or an upper limit to the major radius or to the fusion power. A constraint can be based on material operational limits, such as the peak heat flux on

the plasma facing components. The materials withstanding loading conditions above their nominal conditions would be damaged, thus losing the structural integrity.

Moving towards the data flow reported in Figure 2.1, the reactor components need to be parametrically initialized. This phase corresponds to the definition of a set of component features, requiring an initial value to allow for a reactor systems analyses. These two sequential steps are depicted by the two containers named as *Components* and *Power Plant* Modules, which are defined as follows.

- In *Component Engineering/Physics* modules, the main reactor systems are established in terms of geometry, physics and/or engineering aspects, materials, R&C. In this block of modules are imposed only those parameters which do not depend on any other reactor components and exclusively come from system-specific features.

- *Reactor Physics* modules, instead, define the set of analyses or methodologies to calculate those parameters depending on more than a single FPP component, being hence contingent on the plant system and on its configuration.

In the first category the main reactor elements, such as plasma, blanket, vacuum vessel and reactor magnet systems, are parametrically defined. In the second one, the modules are concerned with the type of physics or engineering analysis accessing the operational parameters from the defined components. For example, the class *Plasma Magnetic Equilibrium* receives the input specifications from the component modules plasma and reactor coils. At present, MIRA incorporates the plant and components systems modules listed in the two blocks of Figure 2.1. These plant system modules

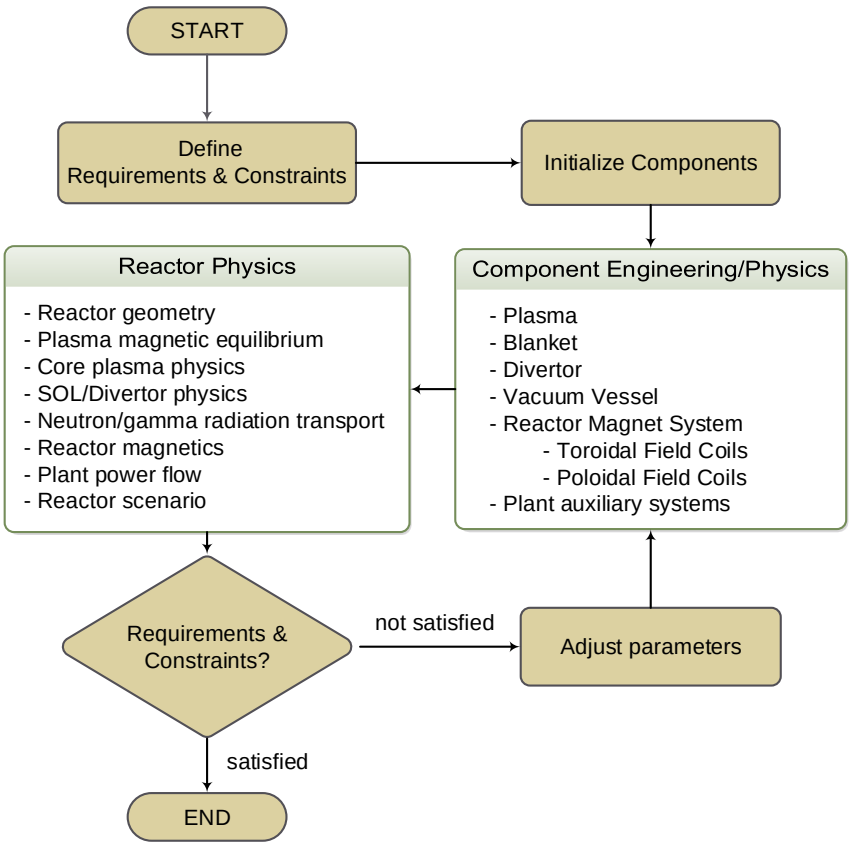

Figure 2.1.: Organizational structure of MIRA.

represent the actual computing core and, for most of them, the innovation angle in the frame of fusion system tool development. Separating component from plant modules is an operative choice derived from the strong synergy between systems in fusion devices, where some of the key reactor parameters involve the simultaneous participation of many interfacing reactor elements, i.e. the component classes.

As shown in Figure 2.1, once all the local and global parameters are calculated, the major R&C are scanned. If one or more are not met, the iteration variables linked to the components modules are being adjusted. At the moment a full plant scale solving logic, which systematically adapts all system variables values based on the violated conditions, is not implemented yet. However, some of the implemented modules, as shown later, feature already some built-in self-consistent method to automatically tune the related parameters, thereby attaining to component or system-specific criteria. The parameters adjustment represents the most challenging part of a fusion reactor system code, due to the mathematical complexity of the algebraic and differential equations of the simulated phenomena and due to the largeness of multidimensional parameter space. A successful run, therefore, terminates when they are all met. These represent a working fusion reactor design point.

2.2. Functional Description of the Core Reactor Physical Components

With reference to Figure 2.2, the physical reactor component systems currently incorporated in MIRA are: plasma, divertor, breeding blanket (BB), vacuum vessel (VV) and the whole tokamak magnets system, consisting of toroidal field coil (TFC) and poloidal field coils (PFC). Axisymmetric toroidal objects like tokamaks are commonly illustrated in the global radial/toroidal/poloidal coordinate system (r, ϕ, z), as shown in the reactor complex.

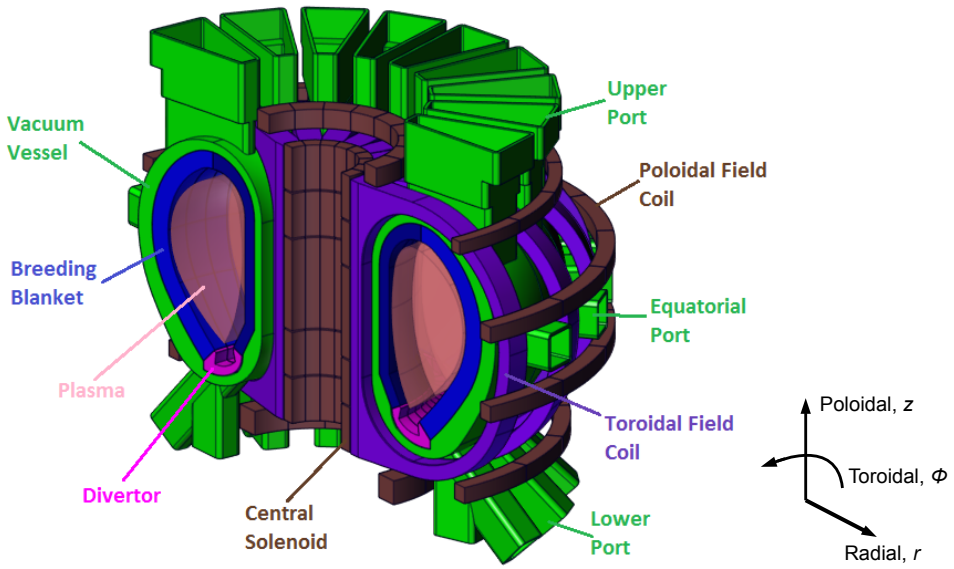

Figure 2.2.: Three dimensional CAD view of the main EU-DEMO 2015 tokamak components, simulated in the system-design code MIRA. Figure reproduced according to [29].

Leaving out momentarily the plasma, whose functional description is portrayed in Sections 3.1 and 3.2, in this section a glimpse on the behavioural aspects of the physical reactor components is outlined. Emphasis is spent on the key functions of such systems and on the engineering solutions currently under investigation for DEMO.

2.2.1. Breeding Blanket engineering solutions for FPP in tokamak configuration

The breeding blanket (BB) is a key nuclear component, occupying more than the 85% of in-vessel surface surrounding the plasma [31]. The blanket has to fulfil the following main functions:

- Tritium breeding. Fusion neutrons are exploited to yield tritium, according to the (n,t) neutron capture reaction occurring in lithium atoms.
- Heat production. The kinetic energy from high energy neutrons is deposited into BB functional materials in form of thermal energy for conversion into electricity.
- Neutron and radiation shielding. The BB and the divertor contribute to the shielding of the vacuum vessel and the superconducting coils from neutron and gamma radiation.

To perform such functions, different key subsystems are necessary, such as:

- *Breeder*, consisting of lithium-containing materials designed to yield a tritium atom via (n,t) neutron capture reactions, occurring in ^{6}Li and ^{7}Li isotopes. Natural lithium contains 7.5 % ^{6}Li and 92.5 % ^{7}Li. However, fusion blankets rely on artificially doped lithium, where the content of ^{6}Li is arbitrarily increased, enhancing the so-called ^{6}Li enrichment. Finally, to process and extract the tritium generated in the breeding material, the blanket is interfaced with a dedicated tritium extraction and recovery system (TERS).
- *Coolant*. Most currently considered designs use a high-pressure fluid pertaining to the Primary Heating Transfer System (PHTS). Primarily, it is responsible of carrying out the thermal energy deposited into the blanket materials by core plasma neutrons, gammas and neutron-induced photons, and transferring it to a power conversion system for electricity production. The BB has to be designed in such a way that all the internal parts subject to surface radiation and neutron volumetric heatings are maintained within material-sustainable limits. The coolant is distributed through the blanket structures through a dedicated manifold system, situated in the rear part of the blanket. The manifold incorporates the back supporting structure as well, designated to provide the mechanical fixations of the BB onto the VV structures.
- *Structural Material*, accommodating the circulation of the coolant through the blanket subsystems and to withstand all the static and dynamic loads which the whole blanket system undergoes throughout its operational phases. These include static and the dynamic pressure, thermal and electromagnetic loads.
- *Neutron Multiplier*, designed to compensate the unavoidable parasitic losses, due to captures in structural materials and streaming through toroidal and poloidal gaps. The neutron multiplier uses mainly $(n,2n)$ reactions.

Various BB layouts, differing for cooling fluid and breeder materials, are part of worldwide fusion research studies. At the moment, four blanket concepts are being investigated within the WPBB R&D programme of the EUROfusion Consortium [31]. These are: helium-cooled pebble beds (HCPB), helium-cooled lithium-lead (HCLL), the water-cooled lithium-lead (WCLL) and the dual-coolant lithium lead (DCLL). As for the blanket structural materials, the reduced activation ferritic-martensitic steel Eurofer is part of the main DEMO design features [19, 32] in Europe.

In order to cover the whole spectrum of breeder/multiplier and coolant solutions, the BB design studies addressed in this work will mainly focus on HCPB and WCLL blankets. A schematic view of the different subsystem is shown in Figure 2.3 for both BB layouts. However, as for neutronic and plant integration aspects, the flexibility of the integrated MIRA packages allows for broader blanket concept scoping studies.

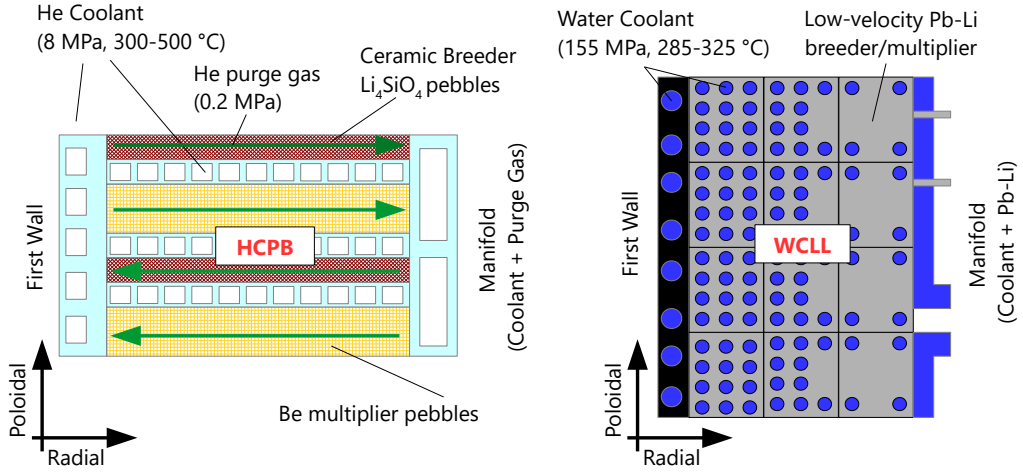

Figure 2.3.: Schematic view of the HCPB and WCLL breeding blanket concepts in the WPBB Project. Figure reproduced according to [33].

The HCPB blanket [34] is based on a solid ternary Li-ceramics as breeder and on beryllium as neutron multiplier. Both are arranged, in forms of radially-arranged pebble beds, in parallel and alternated layers, each separated by a Eurofer steel cooling plate (CP). The breeding materials consists of solid blocks of 60 % lithium orthosilicate (Li_4SiO_4) or alternatively metatitanate (Li_2TiO_3) pebbles [32]. The same disposition is found for the neutron multiplier, based on pure Be or Be-alloys layers of pebbles. The packing of vertically repeated set of breeder and multiplier layers, separated by a CP, are arranged into blanket modules forming a box (7 inboard, 7 outboard) poloidally distributed around the plasma and forming a blanket segment. Three outboard segments and two inboard segments characterize a blanket sector. Such arrangement is put into practice in most of the blanket engineering solutions and refers to as Multi-Module-Segment (MMS). The HCPB operates with a high-pressure 8 MPa helium cooling circuit in a 300-500 °C temperature range, inlet and outlet, respectively. Exploiting the porosity of orthosilicate and beryllium pebbles, a low-pressure 0.2 MPa helium purge gas flows through them to recover tritium and route it to a dedicated external auxiliary system, i.e. the tritium extraction system (TES) [31].

The WCLL BB concept [35, 36] is based on high pressure cooling water, operated at 295-328 °C inlet/outlet temperature and 15.5 MPa pressure, similarly as in pressurized light water fission reactors. Unlike HCPB, it relies on a highly enriched (90 %) liquid metal lead-lithium eutectic alloy, normally labelled Pb-Li, PbLi or LiPb, with a 15.7 % volume content in lithium. The Pb-Li

functions simultaneously as tritium carrier, tritium breeder and neutron multiplier, where lead is the multiplying material. The liquid metal PbLi eutectic alloy enriched at 90 % in ^{6}Li is used as breeding material. The current design presents a repeatable modular layout in poloidal direction, with Eurofer steel stiffeners placed in radial-toroidal and radial-poloidal plane. The cooling water flows through C-shape double wall tubes, situated on the radial-toroidal plane and the liquid PbLi flows radially in the breeding zone (BZ) at relatively low-velocity regime. The first wall and the breeding zone cooling circuits are hydraulically independent, allowing for a redundancy of the cooling operation in off-normal scenarios and a separate regulation of FW and BZ flow rates [37], as well as and a different endeavour use for power conversion purposes [36].

Both blanket concepts feature diverse advantages and critical issues. Solid breeders, for instance, exhibit better tritium breeding and neutron multiplication performances [32], which turns out to be of high interest for reactor size optimisation purposes.

In general, a system code shall provide the means necessary to perform a broad design analysis of the breeding blanket. That, however, should not be pursued only conceiving the blanket as a standalone component, but rather as a system integrated in a reactor environment. MIRA offers several tools to study different design solutions focusing on the key aspects of each option, such as tritium breeding, neutron shielding, power plant performance and space allocation. As a component, the BB is parametrized in terms of an arbitrarily defined number of subsystems, such as FW, BZ and manifold system, each with an inboard/outboard/top thickness and a specified material composition. Such an extended set of data is processed for volume and material mass inventories and for application in a neutronics model; for more details, see Section 4.1.

2.2.2. Tokamak reactor magnet systems: toroidal and poloidal field coils

The magnets system of a tokamak reactor falls into two separate subsystems: the toroidal field (TF) coil and the poloidal field (PF) coil systems.

The PF coils can be thought of as solenoidal current-carrying elements, symmetric around the tokamak axis and serving a number of diverse functions, such as:

- plasma shaping and control;
- establishment and preservation of plasma equilibrium;
- provide inductive current-drive in the plasma confining region.

The set of PF coils designated to the latter function is the central solenoid (CS), which, in relation to the plasma, can be seen as two co-axial loop. Magnetically, they can be admitted as primary and secondary legs of a transformer, respectively. Accordingly, a time-varying current in the CS provides a time-changing magnetic flux through the surface bounding the plasma, provoking an electromotive force which in turn induces the plasma current. The plasma is a quasi-neutral mixture of charged particles, thus, capable of conducting electric currents. Due to its self-inducing and conducting nature, the plasma presents a non-zero electrical resistivity and inductance, which shall be overcome to have a net operating plasma current for a feasibly high time duration, referred to as pulse length. Additionally, this toroidal current interacts with its own magnetic field, yielding a net outward Lorentz radial force, pushing it towards the outer part of the machine. As a result, the plasma tends to displace from its desired position, hence not being steadily manageable.
For this reason, one principle function of the PF coils is to produce a counter inward radial force

produced by a vertical equilibrium field. The coils devoted to this task are the ones in vicinity of the mid-equatorial plane, close to the plasma. In current tokamak magnetic configurations, the plasma takes a vertically elongated shape to attain a large plasma elongation expressed by higher beta values. Such measure is favourable against vertical instabilities and to achieve higher confinement times [38]. Elongated plasmas can be achieved by producing a radial field, which, interacting with the plasma current, generates a vertical force pulling the plasma up-down with respect to the mid plane. The same holds for triangulating the plasma, by applying a proper vertical field. In the DEMO reactor design [29], six PF coils and a stack of five piled-up CS modules are foreseen for its operation, with the ultimate goal of achieving pulse length of at least the $\mathcal{O}$ of 2 hours. As for number, position and electrical current it is worth noting how challenging the selection process can be. Part of this task has to be substantiated by a system code, to identify what are the physics and the engineering limitations of the whole poloidal field magnet system, consisting of plasma and PF/CS coils. MIRA tackles this issue by a dedicated equilibrium plasma module connected to an external PF coil current solver, being addressed in Sections 3.1 and 4.2.2.

Large toroidal magnetic fields in the plasma confining region are also needed, in order to keep the plasma from enduring into a special kind of plasma magneto-hydrodynamic (MHD) instability: the kink instability [9]. Such fields are produced by the TF coils, which in large devices like ITER and DEMO consist of a set of toroidally-distributed curvilinear magnets, winding around the plasma and carrying the same poloidal current. To follow the envelope of the VV and of the other in-vessel components, the TF coils exhibit a D-shape profile, falling into a vertical inboard leg and a curved outboard leg. Since these coils are required to feature large fields they undergo demanding static Lorentz forces, which need to be mapped to ensure the structural integrity during their operating lifetime.

From a functional classification standpoint, a fusion coil element can be structurally broken down into: conductor (or conduit), winding pack (WP) and, for TF coils, steel casing structure (see Figure 2.4−a). The conductor defines the unitary current-carrying element of a magnet, to be wound around the coil perimeter for a certain number of windings. The sum of the currents carried by each of such windings determines the required coil current, derived from the system operational requirements.
In currently investigated large fusion devices, such as ITER and DEMO, both PF and TF coils rely on superconducting materials. Accordingly, the electrical resistivity drops to nearly zero for their bulk temperatures below a critical temperature. Hence, the great advantages derive from the elimination of huge ohmic power dissipation, arising in standard conducting materials like copper. Such a physical state is found only for a relatively narrow region in the magnetic field, temperature and current density phase space, out of which the material goes back to its finite electrical resistivity.
In fusion applications, the most investigated materials are Nb_3Sn and NbTi. The former can work at higher magnetic fields ($\sim$12-13 T), compared to NbTi, which can operate up to 8-10 T. Nb_3Sn, though, is a brittle material, necessitating to be incorporated in a conductor design with a dedicated reinforcement material, such as steel. The current engineering design of the superconducting cables is based on the so-called *Cable in Conduit Conductor* (CICC). This engineering solution is being manufactured for ITER [39] and foreseen for DEMO [40] in magnet cable systems, with Nb_3Sn for TF coils and CS conductors and NbTi for PF coils. This choice is motivated by the different magnetic field strengths where larger field values are expected in TF coils and CS.

The superconducting material is present in wire (or strand) form, twisted several times depending on the design (see Figure 2.4−b). To provide stabilization to the superconductor against unanticipated heating, additional copper stabilizing wires are also included. Alongside, the superconducting

strands are also embedded in a copper matrix. The material ratio between SC and stabilizer represents a very important design parameter for the strand. To bear the Lorentz forces exerted on the conductor, the superconductor/Cu bundles are wrapped in a stainless steel jacket, which, in turn, is wrapped in a electrical turn insulator, made of epoxy resin or glass fiber [41]. The number of superconducting strands is determined from the operating current, lower than the current density by a given safety factor around 0.5. The CICC conductor is cooled by forced flow of supercritical helium (in ITER at 4.5 K and 0.6 MPa [42]), inside the central helium spiral channel and through the void gaps.

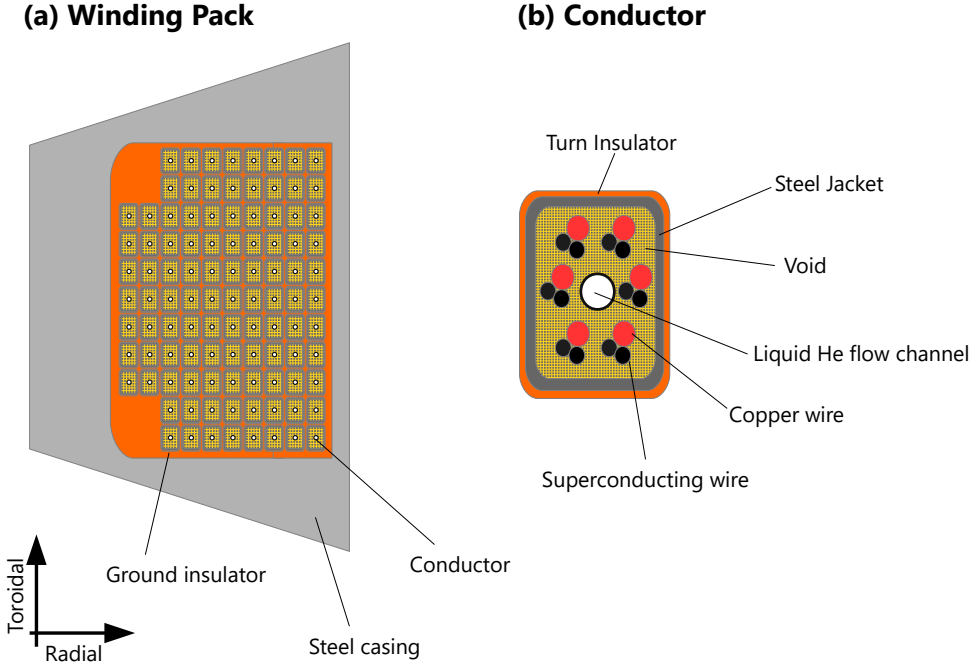

Figure 2.4.: Schematic view of the Cable-in Conduit Conductor arrangement for TF and PF coil tokamak magnet system.

The winding pack contains the wound conductors, each separated by the turn insulator. Broadly, all the windings are wrapped into a large ground insulation, made of glass fiber or epoxy resin, as well. A cross-sectional view for a typical tokamak TF coil inboard leg is shown in Figure 2.4-a. For PF coils and CS, the Lorentz force arising from magnetic interaction with other PF coils and with the TF coils, are borne by the steel jacketing structure. In case of TF coils, instead, a dedicated coil casing structure is needed to counteract the larger and more demanding in-plane and out-of-plane forces detailed in Section 4.2.3. All around the outboard leg of the TF coil, the casing structure takes a rectangular shape, enveloping the ground insulation outer profile. In the inboard straight leg, the shape is trapezoidal to withstand the large inward radial forces by wedging the coil along their side walls.

The current EU-DEMO magnets design activities include three different low temperature superconductor (LTS) concepts of Nb_3Sn-based layouts [40], respectively given by: WP#1 and WP#2 from Swiss Plasma Centre (SPC) and ENEA [43, 44, 45] and WP#3 from CEA [46, 47, 48, 49]. In all cases, the Nb_3Sn superconducting strand design is derived from ITER [50, 51]. Essentially, the diversity of the different solutions pertains to the aspect ratio of the conductor and the material make-up of each subregion, as shown in Figure 2.5.

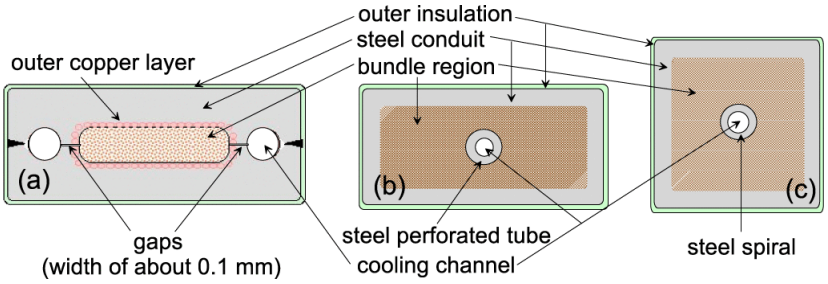

Figure 2.5.: Design options for LTS superconductors of DEMO TF coils and CS: WP#1 from SPC (a), WP#2 from ENEA (b) and WP#3 from CEA (c) [52]. Image reused with the permission of IEEE.

In parallel to the design activities for LTS superconducting coils, the so-called second generation high temperature superconductor (HTS) R&D activities are being also carried out by KIT [41, 53, 54, 55], on a design based on *Rare-Earth*-Barium-Copper-Oxide (REBCO) superconductors. Rare earth can be Y, Nd, Er or others. HTSs exhibit high tensile strength properties and the possibility to operate in large fusion devices. Most importantly, HTSs exhibit larger critical current and temperatures, i.e. the operating current temperatures below which the materials features superconductive behaviour. Consequentially, that offers the possibility to carry massive electrical currents with larger magnetic fields and higher temperature margin.

The EU-DEMO PF/CS coils system is design by CEA with a dedicated design methodology [56]. The design guidelines are largely inherited from ITER, for instance concerning the NbTi strand layout [50, 57] as for the superconducting cable technology.

In MIRA, each coil is modelled as a physical component, whose geometrical representation depends on its type (poloidal or a toroidal field coil). Regarding the PF/CS coils, the user specifies the radial and vertical coordinate of the coil center and radial and poloidal thickness. As for the TF coil, the same construction rules used for BB and VV apply here too, imposing a radial discretization from the plasma outwards. A typical radial nodalization of the TF coils include a subsystem for: inner steel casing, inner ground insulator, WP, outer ground insulator and outer steel case. A more substantiated elucidation is provided in Section 4.2.4. As for the WP element, a conductor design from a data list of conductors already addressed for ITER and DEMO, needs to be prescribed. In the conductor database, different cable engineering solutions are categorized by geometry specifications and superconducting material properties. Details on these aspects are reported in Section 4.2.5.

2.2.3. Functional aspects of the tokamak divertor

The divertor is a plasma facing component of high importance, representing a major interface with the most energetic part of the plasma transport losses, represented by the charged particles leaving the confining region. In tokamak configuration, the magnetic field inside the plasma confining region lies on nested closed magnetic flux surfaces, simply denoted as magnetic surfaces (MS).
In *poloidal divertor* configurations, the magnetic profile is produced by carrying an external toroidal current in the same direction as the plasma current. At some point in the poloidal plane between the two currents a null in the poloidal field component, referred to as magnetic *X-point*, occurs (see Figure 2.6). The MS passing through the X-point is called *separatrix* or last closed magnetic surface (LCMS) [58]. All closed flux surfaces within the separatrix define the plasma confining region, whereas the open flux surfaces outside denote the *scrape-off layer* (SOL) region. The SOL identifies

an unconfined region characterized by open field lines and entered by the charged particles and energy transported out of the confined plasma boundary.
The open magnetic field lines right across the separatrix are precisely ”diverted” to guide these particles and energy fluxes through the SOL into a separate chamber. The particles and heat which flow away perpendicularly through the LCMS are in the SOL region mainly parallel to the magnetic field lines dissipated on the inner and outer vertical targets. On the poloidal plane the inner and the outer *strike points* represent the intersecting spots where the LCMS physically interfaces the vertical targets [58] and the two most critical poloidal locations in terms of impinging heat fluxes. Below the X-point a cold and high-density plasma region, so-called *private region* is formed.
Routing the charged particles in the divertor area allows for controlling the flow of recycling neutrals and impurities, generated from the interactions of charged particles with the structural materials. Accordingly, a fraction of particles interacting with the divertor structures are neutralized, allowing for pumping out in the private region through a vacuum duct.

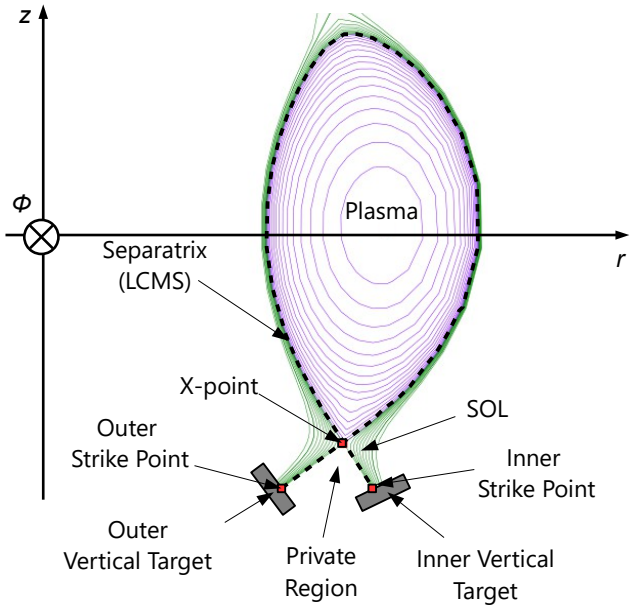

Figure 2.6.: Schematic view of the magnetic configuration in tokamak divertor systems.

As shown in Figure 2.7, illustrating the reference design for ITER, the divertor is composed of some primary physical parts which are depicted in MIRA for the geometric characterization. These refer to [59]:

- inner and outer *vertical targets*, to transfer the particles kinetic and thermal energy into thermal power to an exhaust system,
- inner and outer *baffles*, to protect other components during plasma formation and off-normal transients, e.g. edge-localized modes and vertical plasma displacement,
- *dome*, to endorse the baffling of neutrals in the vacuum duct,
- *cassette*, to accommodate the cooling structures to remove the heat deposited in the aforementioned plasma facing components.

These elements were identified for an ITER-like divertor design, each with a dedicated function to carry on throughout the divertor lifetime.

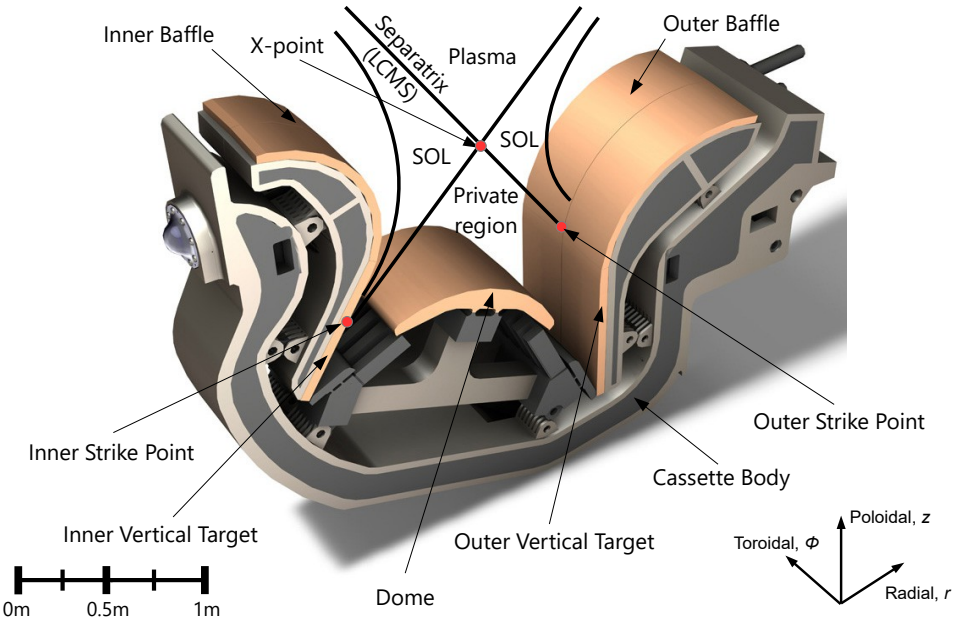

Figure 2.7.: Graphical Description of the ITER tokamak divertor. Reproduced according to [60] (credit: ITER Organization).

In any tokamak configuration, the divertor is envisaged to be toroidally arranged in modules, or cassettes, containing the equipment to withstand the power exhaust. That includes the plasma facing components (targets and baffles) and the cooling structures. The toroidal arrangement in cassettes allows for the replacement during the remote handling operations through dedicated ports penetrating the VV.
For the reference EU-DEMO 2015 design [61, 62, 63], the main body of the cassettes is made of reduced activation ferritic martensitic steel, also known as Eurofer [64], where each cassette is divided into chambers separated by stiffening ribs. Maintaining the structural integrity of the divertor plasma facing components represents one of the most critical challenge for the engineering design of the whole reactor. The baseline material solution for the vertical targets consists of ITER-type tungsten monoblock embedding Copper-Chromium-Zirconium alloy tubes (typically termed CuCrZr). The cooling of the vertical targets and the main cassette body is effectuated by means of two independent water cooling circuits, which operate a different coolant temperatures. The cooling water operates at 3.5-5 MPa pressure and 130-137°C temperature inlet/outlet ranges in the vertical targets loop [65]. In the cassette body loop, 3.5 MPa and 150-180 °C.

2.2.4. Functional description of the vacuum vessel in tokamaks

In thermonuclear fusion devices, high vacuum conditions among plasma operating cycles must be achieved to initiate the D-T reaction. Typically, large volumes of plasma chamber must be evacuated down to $\sim 10^{-5}$ Pa at the initiation of an operating period and pumped down from 10^{-1} to 10^{-3} Pa between operating cycles [66]. As every D-T fusion device is required to pass relatively

large flow rates of tritium through the vacuum pumping system, which can easily migrate through the vast majority of materials, a primary confinement is vital for the safe and economically viable operation. This containment is the vacuum vessel. It provides the primary vacuum containment for the plasma chamber and serves as a safety confinement barrier for radioactive materials. In ITER and DEMO tokamak configurations the VV offers mechanical support to the breeding blanket and the divertor, too. For the current DEMO reactor design [67, 68] the VV is a large double-shell AISI 316L(N) stainless steel structure, actively cooled by 3.15 MPa pressure and 200 °C temperature water flowing between the two steel walls. To bear the water pressure the double-shell structure of the VV is internally reinforced by proper stiffeners, also called ribs.

With reference to Figure 2.2, for recent DEMO designs [67, 69], the VV includes three different sets of dedicated penetrations, also known as ports. These include upper, equatorial and lower ports and are necessary to allow for the following operational tasks:

- remote handling operations (RH), including the extraction and the replacement of the multi-module breeding blanket segments (upper port) and the divertor cassettes (lower port);
- access to the piping system, incorporating the feeding pipes for the coolant and the tritium carrier (upper and lower ports),
- access to the plasma auxiliary heating and current drive (H&CD) systems (equatorial port).

The size of the ports has to account for the volume taken by the different in-vessel components to be accommodated and replaced, as well as the toroidal distance between the adjacent toroidal field coils. The VV has to be sized to offer neutron shielding to the surrounding superconducting coils and shall be also shielded itself to ensure a low neutron-induced material damage throughout its lifetime, being influenced by both blanket and divertor. Since the VV cannot be replaced, the VV ultimately defines the lifetime of the entire reactor.

In the VV component module the radial and the vertical thicknesses of each of the subcomponents are specified as input data sets, following the double-shell stainless steel structure mentioned above. As in the BB module, for each of these VV ”layers” the material composition is prescribed to calculate mass and inventories and perform the core neutron transport analysis.

2.3. Geometric Reactor Core Design

The determination of the space reservation of the plasma and the surrounding physical components is a major goal of a systems code. From a technical standpoint the real target is to compose the two-dimensional radial/poloidal spatial domain of each core reactor component, where the physical borders are constructed combining unitary geometric elements such as lines, arcs and ellipses. All reactor systems obey to their own geometry guidelines for the geometrical characterization. These are either bound to distinct operational conditions, such as a D-shape for TF coils, or simply defined arbitrarily.

The physical reactor components treated by the *geometry* algorithm are: plasma (PLASMA), scrape-off layer (SOL), breeding blanket (BB), vacuum vessel (VV), divertor (DIV), toroidal field coil (TFC), central solenoid (CS) and all the gaps among the mentioned physical components (see Figure 2.8). For the sake of a comprehensive graphical representation, only the gap (GAP) between VV and TFC is marked here.
This sketch represents the 2D radial build of the EU-DEMO 2015 baseline [29, 30], as per MIRA

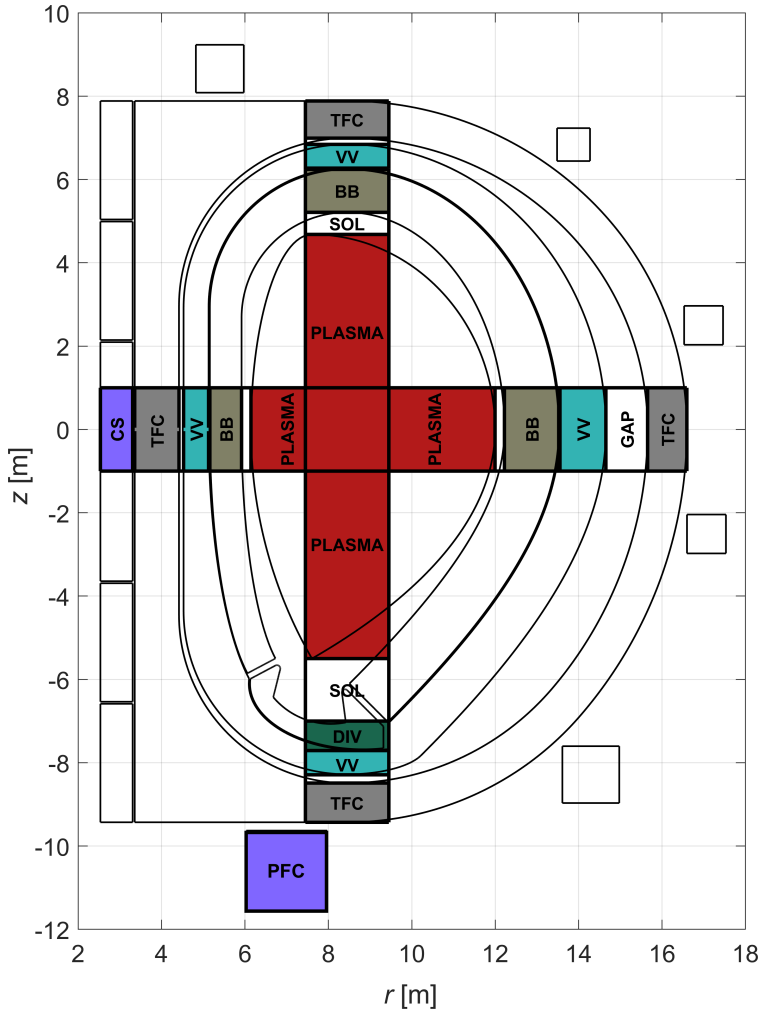

Figure 2.8.: Reactor build sketch of the DEMO 2015 tokamak reactor, as per the MIRA geometry module. The acronyms appearing in the figure stand for: SOL = scrape-off layer, BB = breeding blanket, VV = vacuum vessel, TFC = toroidal field coil, CS = central solenoid.

geometry module. The free parameters of each component (illustrated in the following paragraphs) have been tuned to match, as close as possible, the radial and vertical build information from the PROCESS system code output [30] and the 2D cross section of the DEMO 2015 CAD file [29]. Therefore, the key task of the proposed methodology is to start from a set of radial inboard/outboard and vertical top/bottom thickness of the physical components and find the full 2D vertical cross section.

Depending on the component, certain thicknesses are either calculated internally to match some of the imposed R&C or simply defined by the user. This procedure [70] is also adopted for the EU-DEMO design within the Project Management Unit (PMU) [71]. The innovative aspect of this module, compared to the existing system codes, is to rely on a complete and flexible two-dimensional geometrical frame and, hence, on a more accurate representation of the components in the physics and engineering modules. Moreover, a higher accuracy, in terms of volumes and mass inventories calculation, can be also achieved.

2.3.1. Geometric parametrization of the plasma separatrix in tokamak configuration

The geometric assembling of a tokamak reactor is based on the definition of the plasma profile, precisely the LCMS. Apart from solely physics-devoted applications (e.g. core plasma physics and equilibrium), the separatrix profiles defines a constraining interface with several other reactor systems, such as breeding blanket, divertor and TF and PF coil systems.

For the geometrical definition of an axial-symmetric toroidal object the reference cylindrical global coordinate system (r, ϕ, z) is adopted in fusion application studies. The variable ϕ defines the toroidal direction (or azimuthal angle), whereas the variables (r, z) define the radial and poloidal coordinates. Along this coordinate couplet the geometrical profile of each axisymmetric component is defined. The plasma geometric center is located at a distance R_0 from the tokamak $z-$axis, referred to as major radius and identifying a major input parameter in MIRA. Its vertical coordinate defines the position of the geometrical centre on the mid-plane, located at $z = 0$. The plasma minor radius is identified by the variable a and outlines the radial half-thickness of the plasma at the mid-plane. Parametrically, it is an artificial quantity, since it refers to a circular radius but the plasma geometric cross section is triangulated and elongated. The ratio of plasma major and minor radius is characterized by the aspect ratio A, denoting another major input plasma parameter. The relation between R_0 and A yields the minor radius a, such that

$$a = \frac{R_0}{A}. \tag{2.1}$$

The aspect ratio is one of the foremost parameters for the design of a fusion reactor and its variations have a considerable impact on a variety of reactor systems [12].

The shape of the LCMS poloidal cross section is handled in MIRA by adopting a certain tokamak plasma-like topology, in conformity with the sketch of Figure 2.9. Due to its large parametric flexibility it relies on an up-down elongated and triangulated plasma profile, according to the formalism proposed by J. Johner [15] for the HELIOS system code.

Four sub-domains, taken to be conic arcs, are identified by means of the upper and lower elongations ($\kappa_{X,u}$ and $\kappa_{X,l}$) and of the upper and lower triangularities ($\delta_{X,u}$ and $\delta_{X,l}$). These variables measure the vertical and the horizontal deformations, respectively, from a primitive plasma circular shape, centred in $r = R_0$ and $z = 0$ and with a minor radius a. However, as later outlined in Section 4.2.2, these are preliminarily chosen as "target" values, meaning that the outgoing separatrix profile is imposed as a goal for the equilibrium and confinement model.
The actual plasma shape, however, derives from actual and consistent plasma equilibrium and shaping calculations. The subscript X indicates that these variables are referred to the upper and lower plasma X-points, i.e. X_u and X_l. An X-point defines the space location where inner and outer separatrix lines, identified with indexes "$-$" and "$+$", are intersecting. The inner and outer angles at the upper and lower intersection points are identified by the parameters $\psi_{-,l}$, $\psi_{+,l}$, $\psi_{-,u}$ and $\psi_{+,u}$. In case of so-called single-null configuration, the lower (and unique) X-point is the reference poloidal location to consider for the divertor geometric characterization.
Focusing on single-null divertor configuration, the sum of the lower intersection angles has to yield $\psi_{-,l} + \psi_{+,l} = \pi/2$, whereas in the upper part both $\psi_{-,u}$ and $\psi_{+,u}$ are set to zero.
According to this mathematical formalism the LCMS relies on definition of the normalized radial and vertical coordinates $\xi = (r - R_0)/a$ and $\zeta = z/a$. The latter are parametrically defined for each cross section portion as a function of the given elongations κ, triangularities δ and intersection

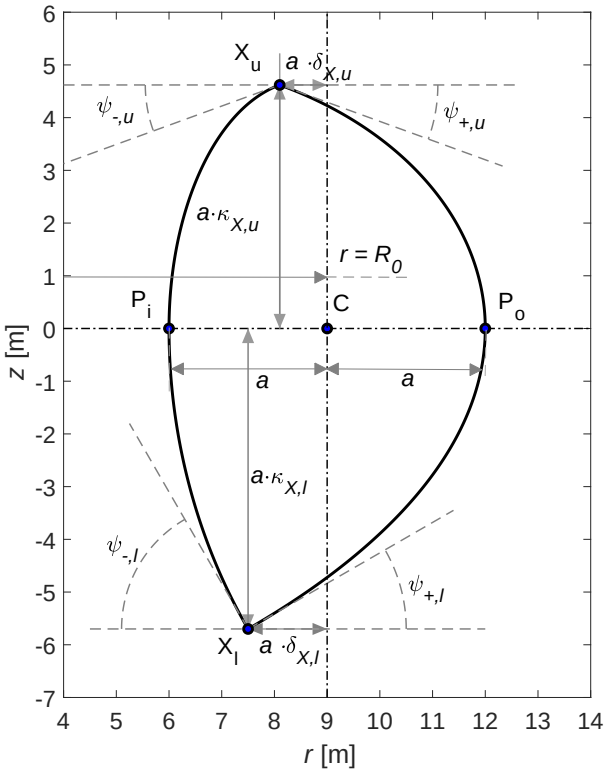

Figure 2.9.: Sketch of the geometrical parametrization for a generic 9-meter-major-radius and plasma cross section, according to the model proposed by Johner [15].

angles ψ.
Due to the vastness of the whole set of equations for ξ and ζ from [15] only a generic set of parametric rules is reported hereafter to show the dependencies of separatrix shape on the listed input variables. In (r,z) coordinates, the plasma boundary is given by:

$$\begin{aligned} r &= R_0 + a \cdot \xi\left(\kappa_{X,u/l}, \delta_{X,u/l}, \psi_{\pm,u/l}\right), \\ z &= a \cdot \zeta\left(\kappa_{X,u/l}, \delta_{X,u/l}, \psi_{\pm,u/l}\right). \end{aligned} \tag{2.2}$$

Accordingly, the coordinate of lower and upper X-points, requested to proceed with the divertor design, can be expressed as:

$$\begin{aligned} r_{x,u/l} &= R_0 + a \cdot \left(1 - \delta_{X,u/l}\right), \\ z_{x,u/l} &= \pm a \cdot \kappa_{X,u/l}, \end{aligned} \tag{2.3}$$

where the subscripts u/l hold for upper or lower X-point respectively. $z_{X,u}$ is the axial coordinate of uppermost elevated plasma point (indicated as upper X-point for convenience) and is taken with the positive sign. $z_{X,l}$ relates to the actual bottom X-point, thus, negative.

Globally, the general definition of plasma triangularity and elongation at X-point δ_X and κ_X are obtained by averaging the upper and lower values pertaining to both, i.e.

$$\mathcal{F}_X = \frac{F_{X,l} + F_{X,u}}{2}, \quad \text{with } \mathcal{F} = \delta, \kappa. \tag{2.4}$$

These two variables, along the plasma volume, are employed as figures of merit for asserting the successful termination of an equilibrium reactor configuration in the devoted modules.

2.3.2. A model for axisymmetric tokamak divertor geometry

Facing the most challenging heating fluxes conditions the divertor is one of the most critical core reactor components. Its physical boundaries have a significant influence on the peak loading conditions and some of the elements appearing in Figure 2.7 have been tentatively included in the MIRA geometry module.
Figure 2.10 shows the 2D cross section of the reference EU-DEMO 2015 divertor configuration reproduced by the MIRA geometry module, including the associated construction points. The central dome is not foreseen for the current configuration.

The divertor geometrical cross section is constructed in MIRA following a sequential order of items, starting from the location of the plasma X-point (X_l). Projecting X_l along the direction identified by the lower intersection angles of the separatrix at X_l ($\psi_{+,l}$ and $\psi_{-,l}$), one can find the position of the inner and outer strike points S_i and S_o, identifying the geometrical points on the radial-poloidal plane where the plasma LCMS strikes the inner and the vertical targets. The distances of the strike points from the bottom X-point, $d_{S,i}$ and $d_{S,o}$, are specified as input parameters and can be driven, for instance, by space reservation constraints in the private region. Selecting a poloidal length of the inner and outer vertical targets $l_{t,i}$ and $l_{t,o}$, as well as their vertical angles β_i and β_o, the targets poloidal contours can be drawn.
The full set of input parameters is listed in Table 2.1 with a detailed description of the identified variables used in the divertor geometry module and illustrated in Figure 2.10.

Relying on a highly parametrized geometric representations offers the possibility to analyze more complex geometric divertor configurations, such as double null, snowflake and super-X divertors [72]. Such a rather elaborate spatial definition of the divertor allows for more enhanced physics modelling of heat fluxes due to core plasma power exhaust (radiation and charged particles) and neutrons, providing a more reliable evaluation of the power flows among the plasma facing components. Moreover, it improves also the geometric refinement of the surrounding and interfacing elements, such as the breeding blanket and the vacuum vessel (Sections 2.3.3 and 2.3.4).

Parameter	Description
$d_{S,i/o}$	Inner/outer distance between X- and strike points ($\lvert X_l S_i \rvert / \lvert X_l S_o \rvert$)
d_c	Minimum cassette body thickness $\lvert D_{i,1} D_{i,6} \rvert$
l_p	Poloidal length of the opening for the access to cooling pipes and vacuum pump duct $\lvert D_{o,5} D_{o,6} \rvert$
$l_{t,i/o}$	Inner/outer target poloidal lengths $\lvert D_{i,1} D_{i,3} \rvert / \lvert D_{o,1} D_{o,3} \rvert$
$\alpha_{w,i/o}$	Inner/outer horizontal angle of the divertor curve segment interfacing the blanket
$\beta_{i/o}$	Inner/outer vertical target angles
ρ_b	Baffle radius $\lvert D_{c,1} D_{i,4} \rvert$, $\lvert D_{c,2} D_{o,4} \rvert$
ρ_d	Central dome curvature radius (if dome is selected), or curvature radius of the cassette curve facing the private region $\lvert D_{c,3} D_{i,1} \rvert$

Table 2.1.: Input data for the divertor geometry module implemented in the MIRA code with reference to the construction points visualized in Figure 2.10.

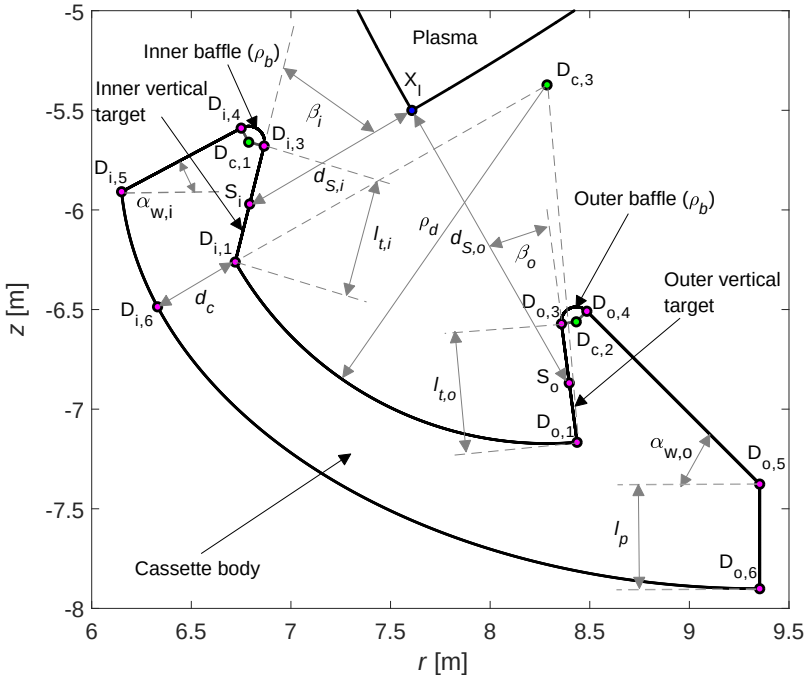

Figure 2.10.: Parametrization of divertor geometry with construction points in evidence (see Table 2.1 for a detailed description of the variables appearing in the figure).

2.3.3. Two-dimensional geometric description of the breeding blanket

The schematic view of the construction points and curves considered in the proposed geometry module is visualized in Figure 2.11. The plasma constructing points are denoted by "P", blanket by "B" and divertor by "D". The subscripts "i" and "o" identify their relations to the inboard (IB) or outboard (OB), whereas "c" indicates that it is a geometrical center for circular of ellipse arcs.

The main requisite for the poloidal definition of the blanket first wall (FW) relies on the minimum inboard, outboard and top distance from the plasma LCMS, i.e. on the overall widths of the SOL $\Delta_{\mathrm{SOL,i/o/t}}$. The SOL thickness is driven by limitations on heat and particle fluxes impinging on the FW surface. With that in mind, the distances between the points $\mathrm{B_{i,5}}$ and $\mathrm{P_o}$ and between $\mathrm{B_{i,2}}$ and $\mathrm{P_i}$ are imposed as input specifications and kept as a required minimum distance along the FW perimeter. The vertical coordinate of top vertical point $\mathrm{B_{i,4}}$ is indeed adjusted so that in proximity of the top elongated point $\mathrm{X_u}$ the FW is restrained from exceeding the lower limit on the minimum Δ_{SOL}.
The reference vertical line centred on the point $\mathrm{B_{c,1}}$ defines the interface between IB and OB blanket segments and can be set by the user. Alternatively, it can be half distance between the top elongated point $\mathrm{X_u}$ and the plasma center $\mathrm{P_c}$, i.e. $r_{\mathrm{B_{c,1}}} = \left(r_{\mathrm{X_u}} + r_{\mathrm{P_c}}\right)/2$.
The procedure for the definition of the FW profile is purely based on geometrical considerations, i.e. setting a lower limit on the distance from the plasma. However, more advanced techniques [71, 73] have been proposed to optimize the FW poloidal profile in terms of minimization of the incident heat loads. Accordingly, the authors proposed to align the FW contour to the magnetic surface at a selected distance in the top/outboard sides of the confined plasma edge. Such considerations, though, have not been addressed within the scope of this work. Nevertheless, the models integrated in MIRA feature already some of the necessary ingredients to perform this operation, for example, providing

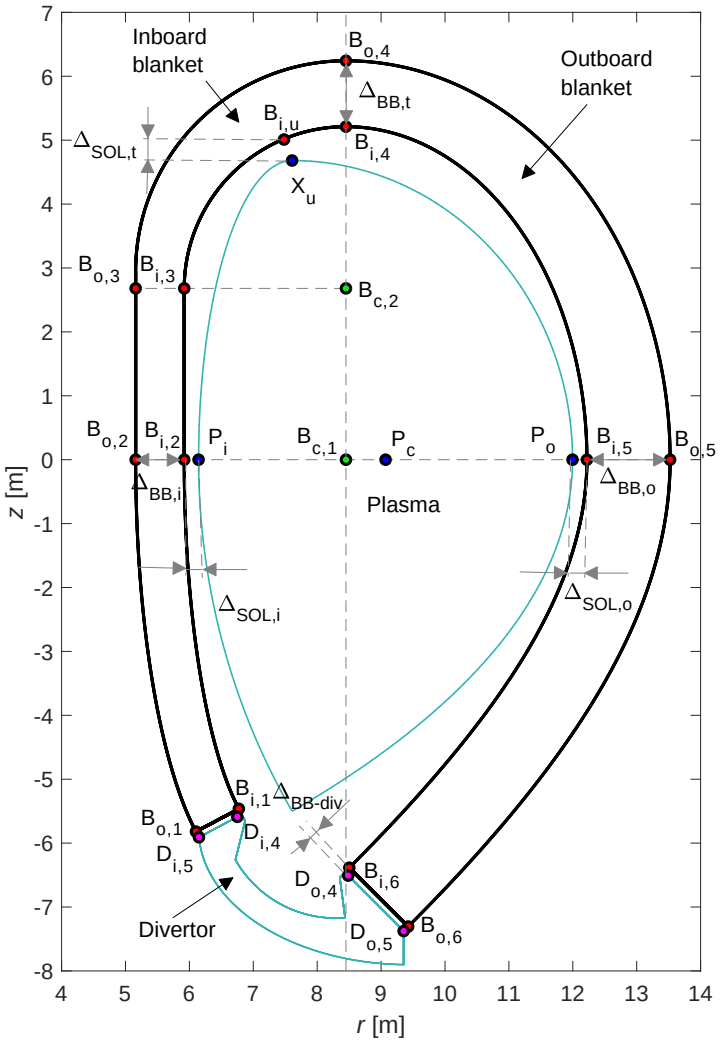

Figure 2.11.: Schematic view of blanket geometry related to DEMO 2015 design [29], according to the MIRA core reactor geometry module (see Table 2.2 for a detailed description of the variables appearing in the figure).

the shape of any poloidal flux surface in the SOL region. Engaging the same methodology described above for the inner blanket profile, denoting the FW shape, the outer profile can be analogously derived. Based on outboard, inboard and top thicknesses of the breeding blanket, $\Delta_{BB,i}$, $\Delta_{BB,o}$ and $\Delta_{BB,t}$ respectively, the same set of curves can be repeated. Therefore, these are obtained upon a given radial discretization of the BB subsystems (FW, breeding zone and manifold regions). Each sub-component is defined in terms of radial inboard, outboard and vertical thickness, as well as in terms of material composition.
Point $B_{c,1}$ individuates the radial location of the interface between IB and OB blanket segments which can be used to evaluate the associated segment masses and volumes.
The full set of geometric input parameters is listed in Table 2.2, with a detailed description in relation to the identified constructions points of Figure 2.11.

The BB segment features are needed to characterize the upper port radial width Δ_{UP} and radial alignment for regular remote handling operations. According to the construction points of Fig-

Parameter	Description
$\Delta_{\mathrm{SOL,i/o/t}}$	Minimum inboard, outboard, top SOL thickness ($\lvert \mathrm{P_iB_{i,2}} \rvert$, $\lvert \mathrm{P_oB_{i,5}} \rvert$, $z_{\mathrm{B_{i,u}}} - z_{\mathrm{X_u}}$)
$\Delta_{\mathrm{BB,i/o/t}}$	Minimum inboard, outboard, top BB thickness ($\lvert \mathrm{B_{i,2}B_{o,2}} \rvert$, $\lvert \mathrm{B_{i,5}B_{o,5}} \rvert$, $\lvert \mathrm{B_{i,4}B_{o,4}} \rvert$).
$r_{\mathrm{B_{c,1}}}$	Radial coordinate of uppermost inner and outer BB points.
$\Delta_{\mathrm{BB-div}}$	BB-divertor gap thickness ($\lvert \mathrm{B_{o,6}D_{o,5}} \rvert$), the same of IB and OB sides.

Table 2.2.: Input data for the breeding blanket geometry module implemented in the MIRA code with reference to the construction points visualized in Figure 2.11.

ure 2.11 the IB and OB radial extensions of the BB segment can be written as:

$$\begin{aligned} \Delta^{i}_{BB,segm} &= \max\left(r_{\mathrm{B_{o,4}}} - r_{\mathrm{B_{o,2}}}, r_{\mathrm{B_{i,1}}} - r_{\mathrm{B_{o,2}}}\right), \\ \Delta^{o}_{BB,segm} &= \max\left(r_{\mathrm{B_{o,5}}} - r_{\mathrm{B_{o,4}}}, r_{\mathrm{B_{o,5}}} - r_{\mathrm{B_{i,6}}}\right). \end{aligned} \tag{2.5}$$

Taking $N^{k}_{BB,segm}$ the number of segments per reactor sector (with k = i/o), the toroidal width to consider for the upper port sizing is given by

$$\Delta^{tor}_{BB,segm} = \theta_{sect} \cdot \max\left(\frac{r_{\mathrm{B_{i,2}}}}{N^{i}_{BB,segm}}, \frac{r_{\mathrm{B_{o,5}}}}{N^{o}_{BB,segm}}\right), \tag{2.6}$$

with

$$\theta_{sect} = \frac{2\pi}{N_{sect}} \tag{2.7}$$

outlining the periodicity toroidal angle of a reactor sector and N_{sect} the total number of sectors, being also the number of TF coils N_{TFC}.

The proposed topological parametrization represents a general methodology to define the blanket boundaries, relying on the radial and vertical composition of BB system. The radial and the poloidal space reservations have a great impact on the main global engineering parameters, such as tritium breeding ratio (TBR) and nuclear heating (NH) power. Details are provided in Section 4.1.3.

2.3.4. Geometric integration of vacuum vessel and ports

In terms of radial and vertical space allocation the geometry rules for profiling the VV in the radial-poloidal plane are inherited from the BB and the divertor (see Figure 2.12). Following the symbol formalism adopted for both components in Figures 2.10 and 2.11 the BB constructing points are denoted by "B", divertor by "D" and the VV by "V".

Imposing inboard, outboard and top gap thickness alongside the BB $\Delta_{\mathrm{BB-VV,i/o/t}}$ and alongside the divertor $\Delta_{\mathrm{div-VV}}$, the VV inner perimeter can be drawn by stretching the BB and the divertor outer boundaries, depending on the poloidal position.
On the inner side of the VV (i.e. facing the plasma), the construction points labelled with capital letter V are obtained by geometric scaling. This offset represents the gap thickness between the VV and BB/divertor, all user inputs. The connecting points to the divertor are denoted by $\mathrm{D_{i,6}}$ and $\mathrm{D_{o,6}}$, whereas for the BB the ones placed on the outer profiles are considered, moving clockwise from $\mathrm{B_{o,1}}$ to $\mathrm{B_{o,6}}$. Having the inboard, outboard, top and bottom VV thicknesses $\Delta_{\mathrm{VV,i/o/t/b}}$, again based on

a radial/vertical internal structure of the VV, the outer contour can be equivalently determined, built from all constructing points spanning from $V_{o,1}$ to $V_{o,7}$ moving counter clockwise.

As shown in the 3D CAD view of Figure 2.2 the VV includes dedicated penetrations called *ports* for the remote handling operations and to provide access to the plasma auxiliary heating system. These are highlighted in Figure 2.12 by dotted lines and include upper, equatorial and lower ports. Geometrically, these are characterized by a poloidal thickness, Δ_{UP}, Δ_{EP} and Δ_{LP}, respectively. The upper and the lower ports thickness are calculated by the VV geometry module such that enough space is guaranteed to extract the BB segment and the divertor cassette, including some margins for manoeuvring actions. The radial extension of the blanket segment is calculated in the BB geometry

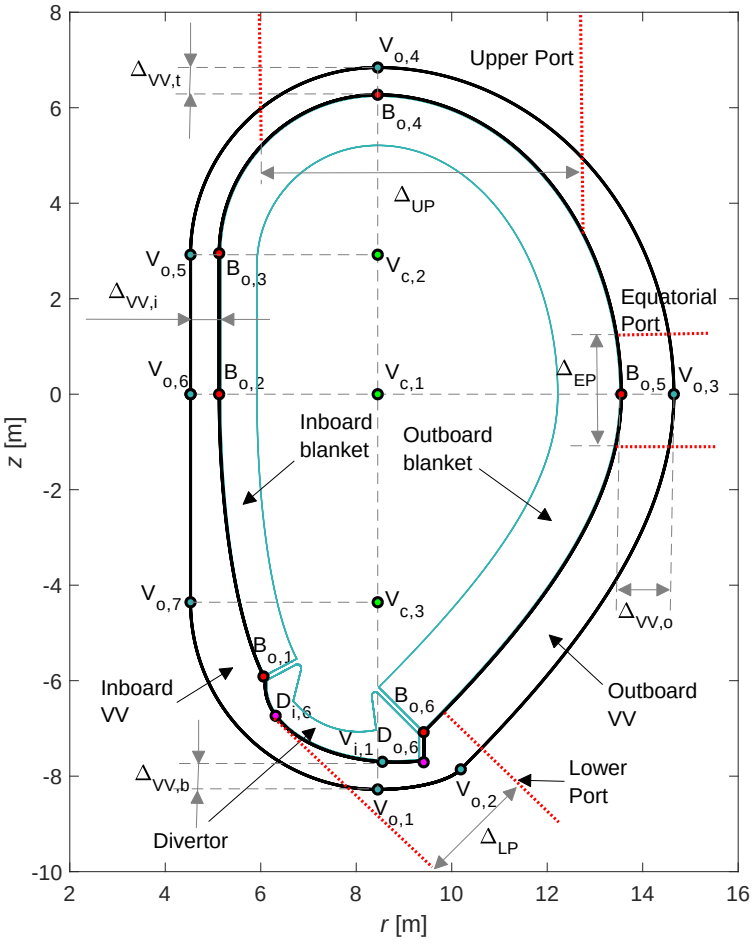

Figure 2.12.: Schematic view of the vacuum vessel geometry related to DEMO 2015 design [29] as per MIRA core reactor geometry module.

module (see Equation (2.5)) and the upper port width becomes

$$\Delta_{UP} = \max(\Delta^{i}_{BB,segm}, \Delta^{o}_{BB,segm}). \tag{2.8}$$

The radial alignment of the upper port is driven by the available inner space between the TF coils. As it can be seen the port has a trapezoidal toroidal cross section, where the minor side shall be larger than the toroidal thickness of the BB segment $\Delta^{tor}_{BB,segm}$. Based on such a constraining limit the port is shifted inwards such that the distance from the tokamak axis is minimized, to push the PF

coils as close as possible to the plasma. The radial location of the upper port shall therefore match the TF coils inter-distance to the maximum BB toroidal segment thickness $\Delta^{tor}_{BB,segm}$. Similarly, the lower port width Δ_{LP} is deduced from the divertor poloidal poloidal shape. The maximum divertor width along the extraction direction is prescribed as the lower port width Δ_{LP}. The equatorial port is taken as a square penetration with identical toroidal and vertical width Δ_{EP}. The cross sectional area is assumed to scale with the required injected power P_{add}. Thus, one can infer that $\Delta_{\mathrm{EP}} \propto \sqrt{P_{add}}$ and

$$\Delta_{\mathrm{EP}}[\mathrm{m}] = \Delta'_{\mathrm{EP}} \sqrt{\frac{P_{add}[\mathrm{MW}]}{P'_{add}}}, \tag{2.9}$$

where $\Delta'_{\mathrm{EP}} = 2.4$ m [29] and $P'_{add} = 50$ MW [27] are the reference equatorial port width and auxiliary heating power of the EU-DEMO 2015 design. The additional heating power P_{add} is calculated in core power radiation model, described in Section 3.2. Vertically, the equatorial port is centred on the mid-equatorial plane. The radial location and the width of vertical port, as well as the thickness of lower port are all specified as input parameters and need to include an additional space for manoeuvring operations and piping access.

The information on the VV profile is mainly adopted for mass and volume inventories and for the reactor neutron/gamma transport modelling. Additionally, the radial and vertical extensions occupied by the ports work as constraining conditions for the position of the PF coils.

2.3.5. Radial/poloidal profiles of TF and PF coil systems

A major task for a tokamak fusion reactor system code is to design the magnet system. Two subsets of reactor coils are foreseen for tokamak configuration: TF and PF coils. The CS is also part of the PF coils system, thus every definition reported in the following for the PF coils, holds for the CS, too.
The geometric definition of both systems is depicted in the schematics of Figure 2.13, with the TF coil constructing points denoted by capital "T" letter and those of the VV with capital "V".
The PF coils are coaxial with the plasma, thus the generic $i-$th coil can be represented by the radial and the axial coordinates of its mass center $r_{m,i}$ and $z_{m,i}$ and the radial and poloidal thickness δr_i and δz_i, respectively.

The TF coils are purely three dimensional elements, thus requiring a geometrical definition, both in radial-poloidal and radial-toroidal directions. The radial-toroidal space reservation is highly influenced by the number of conducting turns which are allocated to operate the required current and by mechanical criteria to cope with the Lorentz forces. These aspects are separately covered in the magnets system module, detailed in Section 4.2.4. Hence, only the main geometry guidelines for the radial-poloidal definition are outlined.
The TF coil radial/poloidal geometric design aspects resides on the so-called D-shape (or "Princeton-D") topology. Splitting the component into four portions, depending on the vertical and radial locations (top/bottom and inboard/outboard), the constraining points for the construction of all arcs are derived from the radial and vertical build specification, as per Figure 2.8. The four inboard, outboard top and bottom gap distances between TF coils and VV, given by $\Delta_{\mathrm{VV-TFC,i/o/b/t}}$ are the control parameters to characterize the inner profile, i.e. towards the plasma side. Having identified the four constraining points on the inner TF coil profile, based on their distance from the VV, the centres and the radii of the four upper and lower outboard circular arcs are found from the equivalent top and bottom ellipse curves, reproduced by means of four-arc approximation method [74]. Repeating the

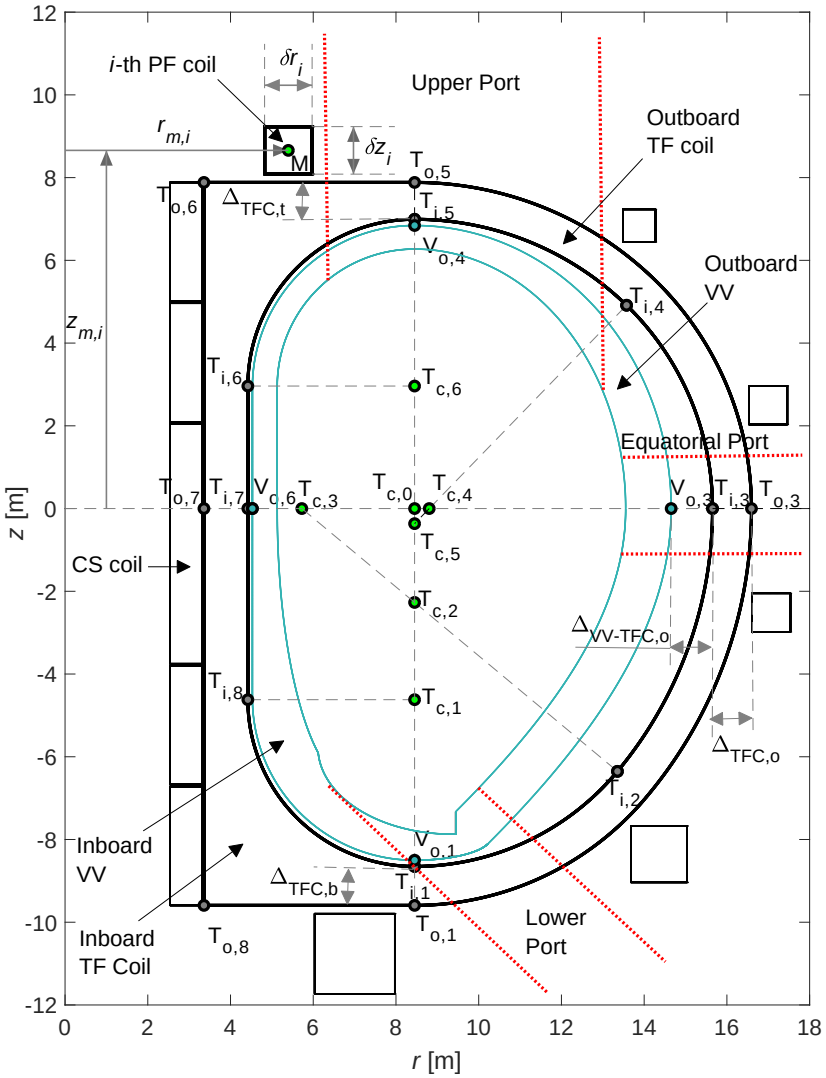

Figure 2.13.: Schematic view of magnet system geometry related to DEMO 2015 design [29], according to the MIRA core reactor geometry module.

same procedure, shifting by a distance as equal as the overall TFC thickness on each space portion $\Delta_{\mathrm{TFC,i/o/t/b}}$, the outer profile can be drawn.

$\Delta_{\mathrm{VV-TFC,i/o/t/b}}$ and $\Delta_{\mathrm{TFC,i/o/t/b}}$ are the input variables for the poloidal geometric characterization of the TF coil and, indirectly, of the PF coils, too. In particular, $\Delta_{\mathrm{TFC,i/o/t/b}}$ are based on the radial and vertical space to allocate to the internal TF coil functional systems, given by the casing, cable winding and insulating regions. For more details see Section 4.2.3.

The Princeton-D geometry concept was introduced in the past by File et al. [75] and further improved by Moses [76] and Erb [77]. Essentially, they provide some guidelines for the construction of an ideal [75] or evenly sectored [76] toroidal conductor, undergoing a constant tension on every curved point of its poloidal contour. Based on that, the tensile unitary forces due to the magnetic pressure f_l, i.e. per unit length, balances the internal mechanical tension T without any bending moments, leading to the condition $T = f_l \cdot \rho$, where ρ is the curvature radius function defined for every point. Accordingly, the condition of constant tension is normally applied to evaluate the TFC

profile.

The approach proposed by J. Erb [77], based on the exact calculation of the toroidal magnetic field for the determination of f_l, has been implemented in the MIRA geometry module.
However, in order to have at disposal more degrees of freedom a set of broader and more general guidelines [53] for the poloidal characterization of the TF coil have been engaged. In summary, these are:

- the TF coil is composed of a straight inboard and a curved outboard leg;
- the outer leg is composed of a set of tangent arcs;
- the sum of all arcs rotation angles shall be 180°.

The three items listed above are graphically illustrated in Figure 2.13.

3. Physics Modelling of an Advanced FPP System Code

Tokamak physics comprises two branches of applications: the core and the SOL physics. The core physics attains to those processes taking place inside the plasma separatrix, involving particle and energy transport in a magnetically confined equilibrium state. The SOL physics, addresses the phenomena occurring in the SOL region, characterized by particles and energy fluxes escaping the confined plasma boundary. The latter interact with the plasma facing components, thus, harming the integrity of the plasma facing components.
In this chapter, three subsections are devoted to the modelling of these aspects. In the first section, the static magnetic equilibrium problem, for a prescribed separatrix shape, is resolved by means of a dedicated two-dimensional stationary model. The aspects related to core power radiation, aimed at quantifying the energy and particle flows deriving from fusion reaction processes, are outlined in the second section. Finally, a SOL/divertor physics part is included in the third section, evaluating the peak heat flux on the divertor targets.

3.1. Magnetic Plasma Confinement in Equilibrium State Description

In existing fusion system codes the main magnetic equilibrium properties are roughly imposed or derived from simplified mathematical and geometrical frames, e.g. cylindrical plasmas. However, the spatial profiles of vertically-elongated magnetic configurations might have a strong impact on the overall performances, such as fusion power. Therefore, a consistent equilibrium and magnetic characterization approach has been introduced in an integrated reactor system analysis in the MIRA magnetic equilibrium model. The major mathematical and coupling aspects are described in the following subsection.

3.1.1. General outline of plasma equilibrium in tokamak configuration

Neglecting the plasma mass inertia and assuming the toroidal rotation of plasma occurring with negligible velocity, the momentum balance equation applied to the plasma relates the pressure gradient forces to the static Lorentz force acting on a unitary volume, such that

$$\nabla p = \mathbf{J} \times \mathbf{B}, \tag{3.1}$$

given the plasma pressure p, the magnetic field (or flux intensity) $\mathbf{B}$ and the plasma electric current density $\mathbf{J}$. The SI system of units will be used throughout this work. For slow processes, such as collisional transport across the magnetic field, the magnetic configuration evolves in time by a set of finite equilibrium states, outlined by Equation (3.1). Furthermore, the current density $\mathbf{J}$ and the

magnetic field **B** must satisfy the two stationary Maxwell's equations identified by the Ampere's law and the divergence-free condition for the magnetic field, reading as:

$$\mu_0 \mathbf{J} = \nabla \times \mathbf{B}, \tag{3.2}$$

and

$$\nabla \cdot \mathbf{B} = 0, \tag{3.3}$$

where $\mu_0 = 4\pi \times 10^{-7}$ H/m is the magnetic permeability of vacuum. From Equation (3.1), it can be verified that $\mathbf{B} \cdot \nabla p = 0$ and $\mathbf{J} \cdot \nabla p = 0$, meaning that both **B** and **J** lie on isobaric surfaces, also known as magnetic flux surfaces (see Figure 3.1) or simply magnetic surfaces (MS). In the cylindrical reference coordinate system (r, ϕ, z), the isobaric surfaces are nested surfaces, each represented by a constant value of poloidal magnetic flux Ψ.

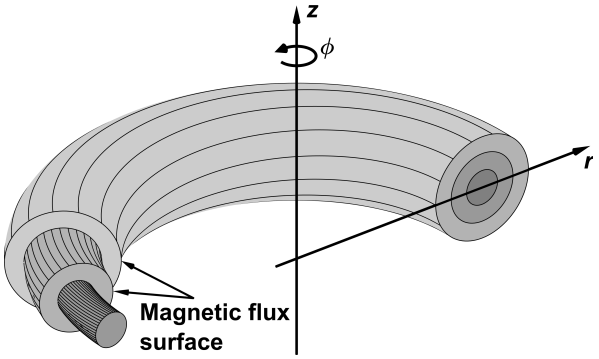

Figure 3.1.: Reference curvilinear coordinate systems for tokamak configuration.

For axially symmetric configurations, meeting Equation (3.3), the poloidal components of the magnetic field can be defined by means of a potential function $\mathbf{A} = \big(0, A_\phi, 0\big)$ such that $\mathbf{B}_p = (B_r, 0, B_z) = \nabla \times \mathbf{A}$. Here, $A_\phi(r,z)$ relates to the poloidal flux $\Psi(r,z)$ such that $\Psi = 2\pi r A_\phi$. The radial and the vertical components of the magnetic field can be therefore defined as

$$B_r = -\frac{1}{2\pi r}\frac{\partial \Psi}{\partial z}, \qquad B_z = \frac{1}{2\pi r}\frac{\partial \Psi}{\partial r}. \tag{3.4}$$

In a similar manner, the poloidal components of the current density J_r and J_z can be found using the scalar function $f = 2\pi r B_\phi / \mu_0$, with the toroidal field B_ϕ acting as a vector potential for **J**. Accordingly, $\nabla \cdot \mathbf{J} = 0$, being referred to as poloidal current and a surface function [78], i.e. $f \equiv f(\Psi)$. As a result, the radial and axial components of **J** can be written as

$$J_r = -\frac{1}{2\pi r}\frac{\partial f}{\partial z}, \qquad J_z = \frac{1}{2\pi r}\frac{\partial f}{\partial r}. \tag{3.5}$$

The problem of static magnetic equilibrium, according to the introduced mathematical formalism, is addressed by the Grad-Shafranov equation (GSE) [79]. In SI units, it reads to [78]:

$$r\frac{\partial}{\partial r}\left(\frac{1}{r}\frac{\partial \Psi}{\partial r}\right) + \frac{\partial^2 \Psi}{\partial z^2} = -2\pi r \mu_0 J_\phi(r, \Psi), \tag{3.6}$$

where J_ϕ is the plasma toroidal current density. Inside the plasma region, $J_\phi \equiv J_{\phi,p}$ can be expressed as the sum of pressure $p(\Psi)$ and poloidal current $f(\Psi)$ contributions, both in terms of gradient on Ψ [78], such that

$$J_{\phi,p}(r, \Psi) = 2\pi r \frac{\mathrm{d}p}{\mathrm{d}\Psi} + \frac{\mu_0}{4\pi r}\frac{\mathrm{d}f^2}{\mathrm{d}\Psi}. \tag{3.7}$$

As a result, the total plasma current I_p is obtained by

$$I_p = \int_{\mathcal{D}_p} J_{\phi,p}\, \mathrm{d}r\mathrm{d}z, \tag{3.8}$$

where $\mathcal{D}_p$ delineates the poloidal domain enclosed to the confining region.

Three additional parameters are largely investigated in plasma equilibrium studies, such as the normalized plasma internal inductance l_i, the plasma beta β and the safety factor q.
The self-inductance of the plasma loop L_p splits into internal and external contributions, $L_{p,e}$ and $L_{p,i}$, with $L_p = L_{p,e} + L_{p,i}$. The plasma internal inductance relates to the magnetic energy associated with the poloidal magnetic field inside the plasma region $\mathcal{D}_p$, such that $\frac{1}{2}L_{p,i}I_p^2 = \frac{1}{2\mu_0}\int_{\mathcal{D}_p} B_p^2 \mathrm{d}V$. Similarly, $L_{p,e}$ refers to the energy stored in the magnetic field outside the LCMS. The normalization of the internal inductance, which leads to the definition of Equation (3.9), takes place dividing $L_{p,i}$ by $\frac{1}{2}\mu_0 R_{ax}$, according to the standard definition used for ITER design [80], yielding

$$l_i = \frac{2}{\mu_0^2 I_p^2 R_{ax}} \int_{\mathcal{D}_p} \left(B_r^2 + B_z^2\right) 2\pi r \mathrm{d}r\mathrm{d}z, \tag{3.9}$$

where R_{ax} is the radial position of the plasma magnetic axis. l_i outlines a key parameter for the magnetic configuration of tokamak plasmas, determining how broad or peaked is the distribution of the toroidal current density [81] inside the confining region. As a consequence, the plasma controllability is highly affected by l_i. Furthermore, according to [82], the biasing difference between internal and external inductance resides in the predominant effects affecting its amplitude. The external inductance solely depends on geometrical effects, while the internal part makes reference to non-geometrical effects, such as frequency-dependent effects. Higher values of l_i, may arise from peaked current density profiles across the confining region, resulting into slow field penetration inside the conductor. This in turn reduces the control and shaping capabilities. The implications of l_i on the overall reactor design are examined in details in Chapter 6.

The plasma beta β can be considered as a dimensionless ratio of plasma pressure to magnetic pressure and reads to:

$$\beta = \frac{p}{\mathbf{B}^2/2\mu_0}. \tag{3.10}$$

Multiple definitions are normally adopted in system codes, depending on which magnetic field component is referred to, i.e. toroidal or poloidal. Moreover, the plasma beta is an integral parameter, thus precise definitions of both numerator and denominator should be specified. For plasma equilibrium studies, the poloidal plasma beta β_p relates the volume-averaged pressure $\langle p \rangle$ to the surface-line-averaged poloidal magnetic field $\langle B_p \rangle_l$, where the integral is performed along the poloidal contour encircling the plasma LCMS $\partial\mathcal{D}_p$. Considering also the integral form of Ampere's law (Equation 3.2), β_p can be written as:

$$\beta_p = \frac{\langle p \rangle}{\langle B_p \rangle_l^2 / 2\mu_0} = 2\mu_0 \frac{\iint_{\mathcal{D}_p} p\, r\mathrm{d}r\mathrm{d}z}{\langle B_p \rangle_l^2 \iint_{\mathcal{D}_p} r\mathrm{d}r\mathrm{d}z}, \quad \langle B_p \rangle_l = \frac{\mu_0 I_p}{\oint_{\partial\mathcal{D}_p} \mathrm{d}l}. \tag{3.11}$$

The plasma beta is a fundamental parameter for the design of a fusion reactor, and thus for system codes. Higher values are more favourable for plasma performances purposes, in terms of fusion

power yield. However, upper limits of β are normally imposed in system codes by stability constraints [10, 17].

The safety factor q is a flux surface function measuring the helical configuration of the magnetic field lines in tokamak plasmas, arising from the superposition of a toroidal and a poloidal magnetic fields. A general definition can be formulated as [78]

$$q(\Psi) = \frac{1}{2\pi} \oint_{\Psi=\text{const}} \frac{1}{r} \frac{B_\phi}{B_p} \mathrm{d}l = \frac{\mu_0}{4\pi^2} f(\Psi) \oint_{\Psi=\text{const}} \frac{1}{r^2} \frac{\mathrm{d}l}{\sqrt{B_r^2 + B_z^2}}, \tag{3.12}$$

where the line integral has to be performed on the poloidal contour around a magnetic surface whose poloidal magnetic flux is constant and equal to Ψ. The helicoidal shape of the magnetic field in a tokamak plasma is needed to compensate several common plasma particle loss mechanisms, known as $\mathbf{E} \times \mathbf{B}$ and $\mathbf{B} \times \nabla \mathbf{B}$ drifts, appearing from non-uniform toroidal magnetic fields in toroidal geometry [9]. The safety factor is a key indicator for the plasma stability.
Higher values of q normally denote a stable plasma, due to the lower twisting of the field lines. q can be expressed for a given value of poloidal flux Ψ, that identifies a magnetic flux surface. In case of single null divertor configuration, the magnetic configuration is characterized by one X-point in vicinity of the divertor region (see point X_1 in Figures 2.9 and 2.10). On this exact location the poloidal magnetic field vanishes and the safety factor there is not defined. A typical choice to overcome this issue is to evaluate q on an a flux surface slightly inside the plasma region. By definition, this is the 95 % flux surface, denoted as edge safety factor q_{95}, where the flux percentage here spans from zero on the magnetic axis to 100 % on the plasma boundary. Near the magnetic axis, instead, a magnetic surface reduces to a point and the safety factor on its vicinity q_0 can be calculated assuming that the flux surface has a very small and circular cross section, according to the relation proposed by Atanasiu et al [78]

$$q_0 = \frac{2\mu_0 f(\Psi_{ax})}{R_{ax}\left(T(\Psi_{ax}) + P(\Psi_{ax}) \cdot R_{ax}^2\right)}, \quad T(\Psi) = \frac{\mu_0^2}{2} \frac{\mathrm{d}f^2}{\mathrm{d}\Psi}, \quad P(\Psi) = 4\pi^2 \mu_0 \frac{\mathrm{d}p}{\mathrm{d}\Psi}. \tag{3.13}$$

A necessary condition to guarantee plasma stability is $q(\Psi) > 1$ across the plasma region. $q_{95} \geq 3$ at the edge of the plasma [66, 83] is also observed as a safe operational limit to prevent the ideal MHD external kink mode ($m = 2, n = 1$) to become unstable and causing a disruption of the plasma [84]. q_0 is usually close to 1 due to the so-called *sawtooth instability* that sets in as soon as q falls below 1 [85]. The sawtooth oscillation is a cyclic instability which is observed when a $q = 1$ surface is present in the plasma, where density, temperature and poloidal flux periodically redistribute following time behaviours which resemble a sawtooth. Hence, the quasi-stationary (i.e. sawtooth-cycle averaged) parameters of tokamak discharges are determined by the sawtooth instability, limiting the peaking of temperature, density, and current density profiles.

In tokamaks, the poloidal magnetic field depends on the total plasma current I_p, according to the integral form of the Ampere's law applying the Stokes theorem

$$\int_{\Sigma_p} \nabla \times \mathbf{B}_p \mathrm{d}\mathbf{\Sigma}_p = \mu_0 \int_{\Sigma_p} \mathbf{J}_{\phi,p} \, \mathrm{d}\mathbf{\Sigma}_p \Rightarrow \oint_{\partial\Sigma_p} \mathbf{B}_p \cdot \mathrm{d}\mathbf{l} = \mu_0 I_p, \tag{3.14}$$

where the integration is at first performed on the LCMS cross-section $\mathbf{\Sigma}_p$ and then on the closed line $\partial\Sigma_p$ enclosing the Σ_p. As a result, the plasma current I_p is correlated to the toroidal field B_ϕ, the safety factor q and the key geometrical parameters. Typically, a formula derived from ITER physics design guidelines [86, 87] is adopted in system codes to calculate I_p for a given toroidal field at

plasma center B_t, major and minor radii (R_0, a) and triangularity and elongation at 95% flux surface $(\kappa_{95}, \delta_{95})$. The plasma current I_p, in [MA] unit, is formulated as

$$I_p = 5\frac{a^2 B_t}{R_0 q_{cyl}} \frac{1+\kappa_{95}^2\left(1+2\delta_{95}^2-1.2\delta_{95}^2\right)}{2}, \tag{3.15}$$

where the cylindrical safety factor q_{cyl} is defined as a function of the inverse aspect ratio $\varepsilon = a/R_0$ by [10]:

$$q_{cyl} = q_{95} \cdot \frac{\left(1-\varepsilon^2\right)^2}{1.17-0.65\varepsilon}. \tag{3.16}$$

The toroidal magnetic field is defined as input parameter. In general, increasing the toroidal field B_t is beneficial from the stability point of view, leading to larger safety factors. However, due to the operational constraints attained to the superconducting cable material, the total magnetic field at conductor cannot exceed the maximum operational field $B_{\max}$.
Making use again of the integral Ampere's law, the toroidal field B_ϕ can be integrated over two toroidal loops at mid-equatorial plane, enclosing the same TFC poloidal current I_{TFC}: one by the plasma center $r = R_0$ and the other by the inboard leg of TF coil winding pack $r = r_{wp,i}$ (for cross-reference, see point $\mathrm{T_{i,7}}$ in Figure 2.13). The integration yields

$$B_t \leq B_{\max}\frac{r_{wp,i}}{R_0}\frac{1}{k_{ripple}}, \tag{3.17}$$

where k_{ripple} is a correction factor, typically $\approx 1.03-1.1$ for ITER and DEMO conductor configuration [23], taking into account of the toroidal field ripple near the innermost and outermost TF coil leg locations.

Another important definition used for equilibrium analysis and throughout this thesis refers to the normalized magnetic flux coordinate $\overline{\Psi}$, defined as

$$\overline{\Psi} = \frac{\Psi-\Psi_b}{\Psi_{ax}-\Psi_b}, \tag{3.18}$$

where Ψ_b and Ψ_{ax} are the poloidal magnetic flux on the plasma boundary and on the magnetic axis. The flux surface functions, such as plasma pressure and safety factor, are often expressed as functions of the normalized flux coordinate $\overline{\Psi}$, rather than the flux Ψ itself.

In existing fusion system codes the magnetic equilibrium parameters are often not treated coherently as also remarked by T. Hartmann [10]. The first observation is about the selection of the key equilibrium and stability parameters, such as safety factor, internal inductance and current density profile. These are frequently chosen in a relatively arbitrary manner. But, it can be verified that they are all strongly tied through their influence in the plasma current density formulation. Moreover, most of the formulas proposed for safety factor and internal inductance are valid only in the limit of cylindrical plasmas, which might digress from real tokamak shapes.

In line of a substantial and massive modelling improvement logics, these aspects motivated the development of a comprehensive two-dimensional equilibrium model, along with its integration in the MIRA system code environment. In the following, a mathematical procedure is proposed for the solution of the GSE from an independent selection of plasma current, poloidal beta and internal inductance.

3.1.2. Solution of Grad-Shafranov equation as per Finite Element Method

For any conductor carrying a toroidal current J_ϕ, solving Equation (3.6) consists of finding the solution of the stationary Maxwell equation in the reference cylindrical coordinate system. In case of tokamak plasmas the additional complexity is to find a toroidal current density distribution $J_{\phi,p}$ fulfilling the main plasma equilibrium, stability and confinement requirements.
These are identified by the plasma current I_p, edge safety factor q_{95}, poloidal beta β_p and internal inductance l_i. Based on Equation (3.7), the toroidal current density inside the plasma region $J_{\phi,p}$ is described by the sum of a pressure and a poloidal current term. Defining a set of polynomial functions for $p(\Psi)$ and $f(\Psi)$, the related coefficients can be adjusted to control the imposed set of plasma parameters $\underline{v} = \left[I_p, \beta_p, l_i, q_{95}\right]$. This approach derives from the set of formulas proposed by Atanasiu et al. [78], chosen for the modelling of plasma magnetic equilibrium problem [88]. Consequently, these have been rearranged as follows. The polynomial expression related to p and f refer to the normalized magnetic flux $\overline{\Psi}$ and yield

$$p(\overline{\Psi}) = \tilde{a}\overline{\Psi}^2 + \tilde{b}\overline{\Psi}^3, \tag{3.19}$$

$$f^2(\overline{\Psi}) = \tilde{c}\overline{\Psi}^2 + \tilde{d}\overline{\Psi}^3 + f_0^2, \tag{3.20}$$

where $f_0 = 2\pi R_0 B_t/\mu_0$ relates to the vacuum toroidal field B_t at plasma axis location R_0. Hence, both pressure and poloidal current takes their extreme values on the plasma axis ($\overline{\Psi} = 1$) and their minimum on the plasma edge ($\overline{\Psi} = 0$). The contribution of the pressure on plasma edge is neglected in this context, although non-null values can be found on the separatrix. Indeed, the pressure profile is typically bound to those of plasma density n and temperature T, such that $p \propto nT$.
For reasons tied to the assumed profile shapes, detailed in Section 3.2, the pressure gradient on the magnetic axis is assumed to be null. Hence, the relation $2\tilde{a} + 3\tilde{b} = 0$ has to hold, too. The expression of Equation (3.7) for $J_{\phi,p}$ can be then reformulated combining Equations (3.19) and (3.20) with the definition of the normalized magnetic flux in Equation (3.18). As a result, it can be defined as

$$J_{\phi,p}(r, \overline{\Psi}) = \frac{K}{2\pi\mu_0}\frac{1}{\Psi_{ax} - \Psi_b}\left[\left(ar + \frac{c}{r}\right)\overline{\Psi} + \left(br + \frac{d}{r}\right)\overline{\Psi}^2\right], \tag{3.21}$$

where

$$a = K \cdot 8\pi^2\mu_0 \cdot \tilde{a}, \quad b = K \cdot 12\pi^2\mu_0 \cdot \tilde{b}, \quad c = K \cdot \mu_0^2 \cdot \tilde{c}, \quad d = K \cdot 3/2\mu_0^2 \cdot \tilde{d}. \tag{3.22}$$

Necessarily, the five coefficients $\underline{w} = [K, a, b, c, d]$, characterizing the profile of $J_{\phi,p}$, have to be calculated in such a way that $J_{\phi,p}\left(\overline{\Psi}, \underline{w}\right) \equiv J_{\phi,p}(\overline{\Psi}, I_p, \beta_p, l_i, q_{95})$. In particular, the parameter K solely depends on the total plasma currents I_p, whereas a, b, c, d are evaluated based on the equality constraints on β_p and l_i and an inequality constraint on q_{95}. The parametrization of Equations (3.19) and (3.20) has been derived from Ref. [78] and modified from quadratic to cubic polynomial expression to impose the two following conditions: null pressure gradient on the magnetic axis and both gradients of p and f null on the plasma boundary, where $\overline{\Psi} = 0$. The latter condition forces the current density $J_{\Phi,p}$ to vanish on $\partial\mathcal{D}_p$, which has been found to increase the shaping capabilities of the PF/CS coils currents. However, the methodology concerned with the achievement of plasma targets $\underline{w}$, remains unchanged.

With reference to Figure 3.2, the plasma equilibrium problem outlined by Equation (3.6) is solved for a fixed shape of LCMS $\partial\mathcal{D}_\mathrm{p}$. A Dirichlet boundary condition $\Psi|_{\partial\mathcal{D}_\mathrm{p}} = \Psi_\mathrm{b}$ is applied by making use of the intrinsic property of magnetic flux surfaces, where Ψ takes a constant value.

The GSE problem can be postulated via the mathematical formalism, referred to as weak formulation. The numerical solution is obtained by means of finite element method (FEM), also known as Galerkin method, a numerical technique to solve various differential problems for arbitrarily complex geometries. A glance on the mathematical fundamentals is provided in Appendix A.

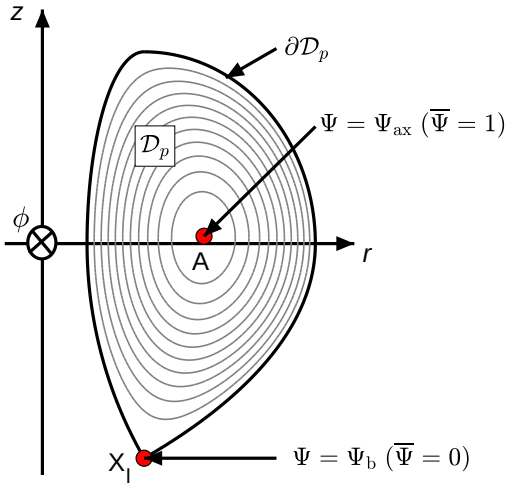

Figure 3.2.: Schematic view of the plasma confining region including the nomenclature used for the FEM model to solve the GSE. Figure reproduced according to [88].

The Grad-Shafranov operator $\Delta^*\Psi$ is a linear combination of the Laplacian operator $\Delta\Psi = \frac{1}{r}\frac{\partial}{\partial r}\left(r\frac{\partial\Psi}{\partial r}\right) + \frac{\partial^2\Psi}{\partial z^2}$, which, in curvilinear axisymmetric coordinate system (r, ϕ, z) can be recast as:

$$\Delta^*\Psi = r\frac{\partial}{\partial r}\left(\frac{1}{r}\frac{\partial\Psi}{\partial r}\right) + \frac{\partial^2\Psi}{\partial z^2} \equiv \Delta\Psi - \frac{2}{r}\frac{\partial\Psi}{\partial r}. \tag{3.23}$$

Accordingly, the GSE can be rewritten as:

$$\Delta^*\Psi \equiv \left(\Delta - \frac{2}{r}\frac{\partial}{\partial r}\right)\Psi(r,z) = -2\pi r\mu_0 J_\phi(r,\Psi). \tag{3.24}$$

Denoting $\mathcal{V} = \{v \in H^1(\mathcal{D}_p) \mid v|_{\partial\mathcal{D}_p} = 0\}$ a functional subspace of the Sobolev space $H^1(\mathcal{D}_p)$, and v as the basis finite element function, the weak formulation is obtained by multiplying Equation (3.24) times v and integrating over the volume $\mathcal{D}_p$, yields

$$\int_{\mathcal{D}_p}\left(\Delta\Psi\cdot v + \frac{2}{r}\frac{\partial\Psi}{\partial r}v\right)\,\mathrm{d}\mathbf{r} = \int_{\mathcal{D}_p} 2\pi r\mu_0 J_{\phi,p} v\,\mathrm{d}\mathbf{r}. \tag{3.25}$$

with $\mathrm{d}\mathbf{r} = 2\pi r\mathrm{d}r\mathrm{d}z$, in cylindrical axisymmetric coordinates. Making use of the first Green's identity, the following rule is applied to delimit the second order derivatives

$$\int_{\mathcal{D}_p}\Delta\Psi\cdot v\,\mathrm{d}\mathbf{r} = -\int_{\mathcal{D}_p}\nabla\Psi\cdot\nabla v\,\mathrm{d}\mathbf{r} + \int_{\partial\mathcal{D}_p} v\,\nabla\Psi\cdot\mathbf{n}\,\mathrm{d}S, \tag{3.26}$$

where $\mathrm{d}S$ is the infinitesimal surface element on $\partial\mathcal{D}_p$ and $\mathbf{n} = [n_r, n_z]$ is the oriented outgoing normal vector on $\partial\mathcal{D}_p$. The surface integral on $\mathrm{d}S$, by definition of the basis function $v \in \mathcal{V}$,

vanishes and the problem of Equation (3.25) turns into finding $\Psi \in \mathcal{V}$ such that:

$$\begin{cases} a(\Psi, v) = \ell(v) \\ \Psi|_{\partial\mathcal{D}_p} = \Psi_{\mathrm{b}} \end{cases} \qquad \forall v \in \mathcal{V}, \tag{3.27}$$

where

$$a(\Psi, v) = \int_{\mathcal{D}_p} \left(\nabla\Psi \cdot \nabla v + \frac{2}{r}\frac{\partial\Psi}{\partial r} v \right) r\mathrm{d}r\mathrm{d}z, \tag{3.28}$$

is the bilinear form and

$$\ell(v) = \int_{\mathcal{D}_p} 2\pi r \mu_0 J_{\phi,p}\, v\, r\mathrm{d}r\mathrm{d}z, \tag{3.29}$$

the linear form of the differential GS equilibrium problem, postulated in weak formulation. An identical expression has been derived by A. Bermúdez et al. [89], where the solving variable is given by toroidal component of the magnetic potential A_ϕ, connected to $\Psi = 2\pi r A_\phi$. In this case the solution is sought on a fixed-boundary equilibrium problem. Finding a similar plasma shape, by means of auxiliary poloidal field coils, is addressed separately in Section 4.2.2.

The approximated numerical solution Ψ_h relies on a triangularization of the two-dimensional domain $\mathcal{D}_p$ into a quasi-uniform mesh $\mathcal{T}_h$, with $h > 0$ identifying a prescribed mesh size h. By definition, the mesh should be constructed such that $\bigcup_{k=1}^{n_t} T_k = \mathcal{T}_h \approx \mathcal{D}_p$. T_k and n_k relate to the $k-$th mesh triangular element and the total number of triangles of the mesh $\mathcal{T}_h$, respectively. Henceforth, the GS equilibrium is resolved as per Galerkin method, with $\Psi_h \in \mathcal{V}_h$ being sought in the continuous finite element subspace $\mathcal{V}_h \subset \mathcal{V}$.
The numerical FE solution to Problem (3.27) turns into finding $\Psi_h \in \mathcal{V}_h$ subject to

$$\begin{cases} a(\Psi_h, v_h) = \ell(v_h) \\ \Psi_h|_{\partial\mathcal{D}_p} = \Psi_{\mathrm{b}} \end{cases} \qquad \forall v_h \in \mathcal{V}_h. \tag{3.30}$$

For a given configuration and a calculated current density $J_{\phi,p}$, Equation (3.30) is being systematically solved within the MIRA equilibrium module exploiting the flexibility of open-source finite element solver `Freefem++` [90].

The target plasma boundary is calculated in the plasma geometry module, based on a precise parametrization pertaining to the plasma major radius, aspect ratio, triangularity and elongation. The triangular $\mathcal{T}_h$, obtained from an imposed mesh size h is also generated by `Freefem++` built-in mesh generator. A verification study has been carried out to authenticate the weak formulation of the GSE, the static equilibrium of plasma and the conservation of magnetic flux, see Appendix E.1. The corroboration of the method has been performed against the analytical solution of the simplest example of magnetic equilibrium in tokamak configuration, i.e. the Solov'ev equilibrium [91]. Additionally, a linear scaling law has been extrapolated to relate the mesh size h to the plasma minor radius a, in order to keep the numerical error below a prescribed limit for every analysed plasma scenario.

The source current density $J_{\phi,p}$ hinges upon $\overline{\Psi}$. Thus, the solution of Equation (3.30) requires an iterative procedure. At the iteration step $n+1$, $J_{\phi,p}$ is expressed as a function of Ψ^n, obtained from the previous iteration. This iterative scheme is based on Picard's method, leading to the following reformulation of Problem (3.30)

$$\begin{cases} a(\Psi_h^{n+1}, v_h) = \ell(v_h, \Psi_h^n) \\ \Psi_h^{n+1}|_{\partial\mathcal{D}_p} = \Psi_{\mathrm{b}} \end{cases} \qquad \forall v_h \in \mathcal{V}_h,\ n = 0, 1, ...N. \tag{3.31}$$

This procedure sets off with an initial guess of $J^0_{\phi,p}$, assuming a flat profile across the poloidal cross section $\mathcal{D}_p$ and yielding the total plasma current I_p. Accordingly, $J^0_{\phi,p} = I_p / \int_{\mathcal{D}_p} \mathrm{d}r\mathrm{d}z$. Solving Problem (3.31) for $J_{\phi,p} \equiv J^0_{\phi,p}$ determines the solution of Ψ^0, defined at the $0-$th iterative step. Afterwards, the actual formulation of $J_{\phi,p}(r, \overline{\Psi})$ can be adopted and the iteration can move forward until specified convergence conditions are met.

When facing the equilibrium problem at a system code level, the major task is to combine the modules entitled to solve the GSE and to calculate the parameters set $\underline{w}$, for the modelling of the plasma current density $J_{\phi,p}$. The whole procedure related to this computation process begins with the definition of the plasma targets, which can be either specified by the user in the plasma module, provided by the data structure, or received from other modules. For example, the poloidal beta β_p is calculated in the core plasma physics module and it depends on plasma density and temperature profiles. The mesh $\mathcal{T}_h$ can be either passed from the plasma geometry module (fixed-boundary) or calculated within a dedicated free-boundary equilibrium solver, later described in Section 4.2.2. In case of fixed-boundary equilibrium the magnetic configuration is found for a prescribed target plasma separatrix $\mathcal{D}^t_p$. In case of free-boundary equilibrium the plasma separatrix domain $\mathcal{D}_p$ is determined by means of externally-applied magnetic fields, operating a set of appropriate toroidal currents in the PF and CS coils such that $\mathcal{D}_p \approx \mathcal{D}^t_p$.

Two concatenate loops are iteratively carried out: one inner loop, linked to the solution of the GSE and one outer loop, to the calculation of the current density parameters.
In order to set-off the inner loop, the initial guess on the poloidal flux Ψ^0 is calculated by imposing uniform current density distribution $J^0_{\phi,p}$. Within the inner loop proportionality constant K, scaling the normalized current distribution $\mathcal{J}_{\phi,p} = J_{\phi,p}/K$ to I_p, is calculated for each iteration step. K forces constant total current and enhances the convergence speed through iterations. The GS equilibrium problem can be finally solved for a fixed set of current density parameters $\underline{w} = [a, b, c, d]$. The inner loop goes on as long as the largest deviation on each mesh node between the $n-$th and $n+1$-th iterations does not meet the imposed convergence tolerance ϵ_g ($\approx 10^{-6}$), $\left|\Psi^{n+1} - \Psi^n\right| \leq \epsilon_g$. For each course of action, until this condition is achieved, the solution of Ψ^n is being updated.
The outer iteration loop is devoted to tune the current density parameters $\underline{w}$ against a prescribed set of plasma parameter targets $\underline{v}^t_{eq} = [I^t_p, \beta^t_p, l^t_i, q^t_{95}]$. Making use of the built-in MATLAB tool `fmincon` the calculation of a, b, c, d is performed via interior point algorithm [92, 93, 94]. A detailed description on the solving aspects is provided in Appendix B. This solving method is suited to the minimization of medium to large scale problems. Here, only the nonlinear equality and inequality constraining conditions, $\left|g_{eq}(a, b, c, d)\right| \leq \varepsilon_p$ and $g(a, b, c, d) \leq 0$ on the plasma targets parameters, are imposed. ϵ_{eq} is an input parameter for the tolerance on the constraint violation ($\approx 10^{-6}$). The two imposed constraints are given by

$$g_{eq}(a, b, c, d) \equiv \underline{v}_{eq}(a, b, c, d) - \underline{v}^t_{eq} = \begin{bmatrix} l_i(a, b, c, d) - l^t_i \\ \beta_p(a, b, c, d) - \beta^t_p \\ a + b \end{bmatrix} = \mathbf{0} \tag{3.32}$$

and

$$g(a, b, c, d) = q^t_{95} - q_{95}(a, b, c, d) \leq 0. \tag{3.33}$$

The last element of the vectorial function g_{eq} denotes the null gradient condition of plasma pressure on the magnetic axis (see Equations (3.19) and (3.22)). The condition on q_{95}, normally $q^t_{95} = 3$, is of inequality type to relax to constraining characteristics and ease the assessment of $\underline{w}$. When the coefficients $\underline{w}$ comply with the imposed constraints on $\underline{v}^t$, the model returns to the data structure a consistent plasma magnetic configuration $\Psi(r, z)$ and $J_{\phi,p}(r, \Psi)$. The plasma kinetic pressure,

corresponding to the specified β_p, is in equilibrium with its own magnetic pressure and the current density peaking guarantees a fixed internal inductance l_i.
The workflow depicting the MIRA plasma magnetic equilibrium computing algorithm is shown in the flowchart of Figure 3.3.

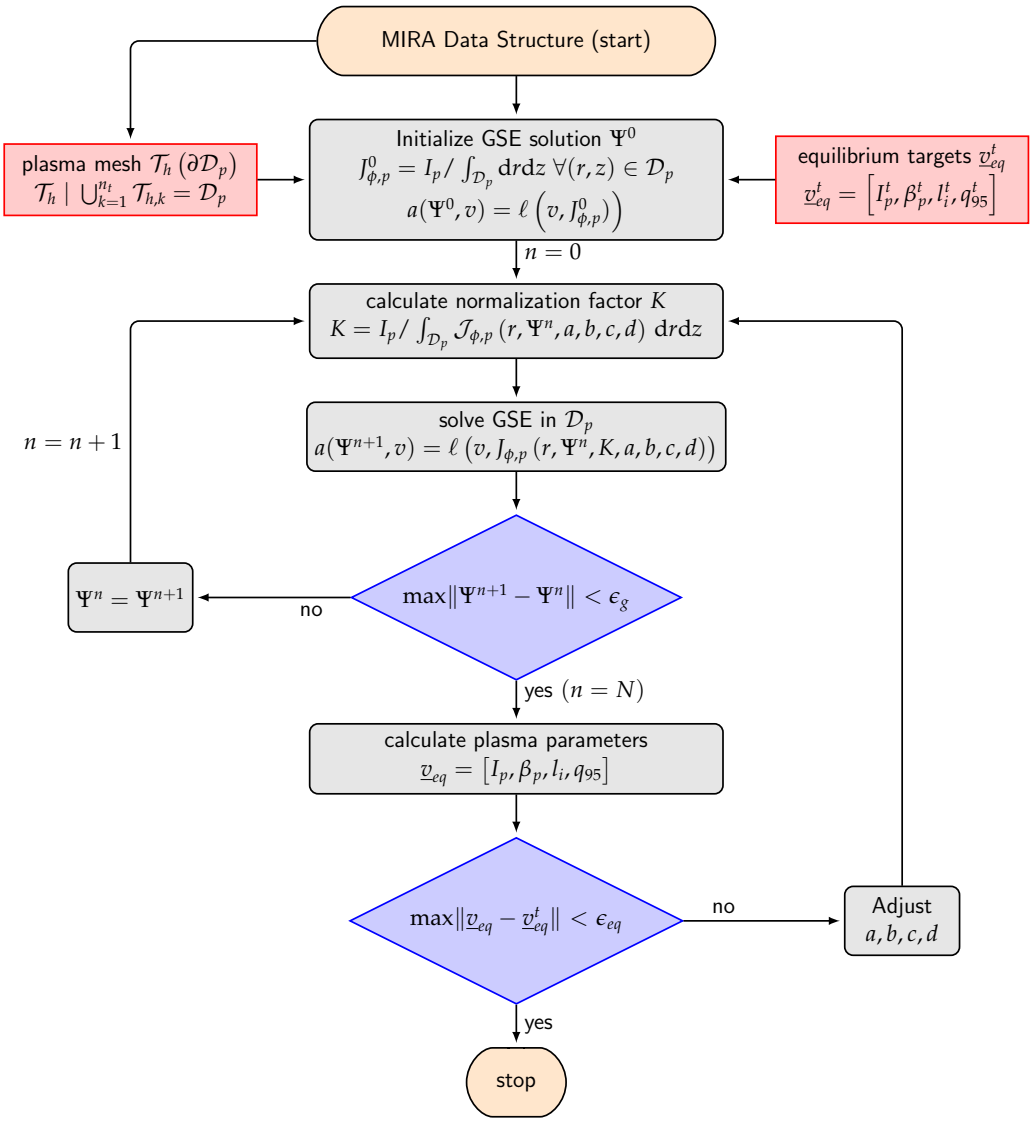

Figure 3.3.: Flowchart of the Grad-Shafranov equilibrium model, integrated in the MIRA system/design tool. Each block is characterized by its shape: ovals relate to start and stop nodes, sharp-corner-rectangles indicate inputs, round-corner-rectangles denote process steps and diamonds refer to process decisions.

Even the fixed-boundary equilibrium, without the coupling with the coil system, can bring beneficial effects to the core plasma physics part, as the assessment of the main integral parameters can unarguably gain from a two-dimensional magnetic configuration. Even though the proposed equilibrium modelling frame features great advances with respect to canonical zero-dimensional system codes approach, it is limited to several simplifying assumptions. Compared to more detailed and

well-established dynamic equilibrium solvers, such as CREATE-NL+ [95], DINA [96], CarMa0NL [97] and TSC [98] codes, this equilibrium model does not include several aspects also relevant for tokamak equilibria. For instance, a full dynamic regime and three-dimensional effects due to passive structures. Furthermore, these equilibrium solvers are also tailed to simulate very fast transient off-normal events, such as edge localized modes (ELMs) and vertical disruption events (VDEs). Certainly, such design-oriented aspects go beyond the goal of a system code and have not been addressed in the proposed equilibrium model.

In a complete MHD fluid theory framework of magnetically confined plasma, the toroidal current density accounts for the sum of three terms, such that $J_{\phi,p} = J^{oh}_{\phi,p} + J^{cd}_{\phi,p} + J^{bs}_{\phi,p}$. $J^{oh}_{\phi,p} \propto \sigma(T)E_\phi$ defines the ohmic term, with σ being the plasma electrical conductivity, T the plasma temperature and E_ϕ the toroidal electric field. $J^{cd}_{\phi,p}$ is the external current-drive term, e.g. obtained by means of neutral beam injection or electron cyclotron current-drive. $J^{bs}_{\phi,p} \propto \sqrt{r/R_0}\nabla p/B_p$ is the bootstrap term [85], relating to a thermoelectric toroidal electric current driven by finite pressure gradient in a toroidal magnetic confinement device.
Hence, a free parametrization of the current density profile based on pure magnetic equilibrium figures of merit is only partly legitimate and hinges upon on a major simplification taken within the modelling frame of MIRA. Ideally, a more complete elaboration of the transport problem in tokamak plasmas should be included to consistently calculate $J_{\phi,p}$ based on plasma equilibrium and transport criteria. For instance, a model based on single-fluid MHD theory [83, 85] yields a set of variables including plasma density n, pressure p, mean velocity $\mathbf{u}$, electric field $\mathbf{E}$, magnetic field $\mathbf{B}$ and current density $\mathbf{J}$.

3.2. Core Power Balance Model

The primary energy source of a fusion reactor derives from the fusion reactions taking place inside the confining region. For this reason, a core plasma physics module is mandatory. The core physics models currently implemented in existing fusion system codes deal with rather simplified analytical assumptions, relying on zero-dimensional and steady state balances for plasma current, power and particles. The models currently implemented in MIRA additionally links the core physics of system codes with the equilibrium model described in Section 3.1.

Here the core physics of the TREND [10] (Tokamak Reactor code for the Evaluation of Next-step Devices) has been considered for integration in MIRA. TREND is implemented with modular code architecture and consists of parts dedicated to geometry, core plasma physics, divertor, power flow, technology and plant costing. Its main focus has been on core plasma physics, since its development was done in parallel to work on physics design guidelines for DEMO [99]. The origin of TREND is a set of equations [100] to estimate the minimum size of DEMO. The integration of TREND has been carried out filtering the modules addressed differently in MIRA, such as magnetic equilibrium, divertor loading and plant power balance. The proposed core physics module is therefore based on the algebraic equations already implemented in TREND, though relying on a calculated two-dimensional magnetic equilibrium configuration inside the confining region. More details may be taken from Appendix C. Essential sub-modules of TREND are:

- Steady state zero dimensional current balance. Each specific current term involved in it, such as inductive current drive I_{ind}, external current drive I_{CD} and bootstrap current I_{BS}, is calculated with respect to steady state plasma current balance $I_p = I_{ind} + I_{CD} + I_{BS}$.

- Pressure properties. It includes a definition for thermal and total plasma pressure, as well as the multiple expressions for the plasma beta, such as toroidal, poloidal, total and normalized beta.
- Steady state zero dimensional particle balance. The atomic densities are calculated for all the atomic species considered in the plasma, i.e. electron, fuel and impurities species. Furthermore, TREND makes use of the plasma quasi neutrality to calculate the effective ion charge number Z_{eff}, a parameter measuring the dilution of the plasma compared to pure hydrogen plasma.

3.2.1. Parametrization of plasma density and temperature profiles

In plasma physics studies the constitutive equations governing the transport of plasma particles, energy and momentum are usually solved by means of sophisticated core and edge transport simulation codes, e.g. ASTRA [101], COREDIV [102], SOLPS [103] and TOKES [104]. Relying on prescribed sets of additional heating and fuelling source terms, as well as applied electric and magnetic fields, they solve various versions of the full set of multi-fluid plasma (MHD) equations. Due to computing time constraints, such demanding simulations are not carried out within a systems code run. Accordingly, certain outputs of transport codes, such as the density and temperatures, are defined as inputs in system codes. This choice holds assuming that the fuelling and heating systems will be capable of reproducing the imposed plasma configuration profiles.

Recalling the normalized magnetic flux coordinate $\overline{\Psi}$ obtained from the equilibrium model, the plasma profiles of density, temperature and pressures are normally parametrized in fusion system codes by means of another independent variable ρ, inversely defined as

$$\rho(r,z) = 1 - \overline{\Psi}(r,z), \tag{3.34}$$

being also referred to as normalized radial coordinate in systems code formalisms. Its value spans from zero on the magnetic axis to one on the periphery. Since the plasma pressure is a magnetic flux function, its profile can be mathematically associated with ρ, i.e. $p = p(\rho)$. The plasma thermal conductivity in tokamak plasma is much larger along the MS than across the MS [9]. For this reason, on a specific flux surface, the plasma is assumed isothermal, hence $T = T(\rho)$. Assuming the plasma as an ideal gas, the plasma pressure pressure scales with density n and temperature T such that $p \propto n_e T$. Henceforth, the density is also taken constant on a MS, $n = n(\rho)$.

Fusion systems codes handle rather simplified formulations of radial profiles, based on the profiles already achieved in experimental tokamak devices. Especially the confinement exhibiting a low and a high confinement mode, L-mode and H-mode, is essential. The H-mode, observed in ASDEX in the 1980s [105], is an increased confinement regime for plasma particles and energy. It is based on a transport barrier at the plasma edge characterized by a reduced turbulence, leading to steep edge gradient of density, temperature and pressure [10]. For taking into account the confinement regime, two kinds of radial profiles are inferred in fusion system codes, the simplified and advanced ones. The former assumes L-mode operation, i.e. neglecting the transport edge barrier, and adopts, for the generic physical quantity x, a simple parabolic profile as

$$x(\rho) = x_0 \cdot \left(1 - \rho^2\right)^{\alpha_x} \quad \text{with } x = n, T, p, \tag{3.35}$$

where x_0 and α_x designate the value of x at plasma center ($\rho = 0$) and the profile coefficient for x respectively.

In case of H-mode confinement regime a more elaborated analytical formulation is needed to reflect the profiles observed in experimental plasma operations. Similarly to some of the presently available fusion system codes (e.g. HELIOS, [15] and PROCESS [17]) the density and temperature radial profiles account for a so-called *pedestal* at plasma edge, identified by the normalized radial coordinate ρ_{ped} and yielding the following expression for $x(\rho)$

$$x(\rho) = \begin{cases} x_{ped} + \left(x_0 - x_{ped}\right)\left(1 - \left(\dfrac{\rho}{\rho_{ped}}\right)^{\beta_x}\right)^{\alpha_x} & \text{for } 0 \leq \rho \leq \rho_{ped}, \\ x_{sep} + \left(x_{ped} - x_{sep}\right)\dfrac{1-\rho}{1-\rho_{ped}} & \text{for } \rho_{ped} < \rho \leq 1. \end{cases} \tag{3.36}$$

The H-mode profile formulation considers a linear decrease within the pedestal region $\rho_{ped} \leq \rho \leq 1$, between the pedestal top x_{ped} and the separatrix x_{sep}. Inside the plasma core ($0 \leq \rho \leq \rho_{ped}$) it relies on more elaborated shapes, introducing a further profile coefficient β_x.

Integrating the radial profiles defined in Equation (3.35) or Equation (3.36), some quantities of great importance for fusion SCs can be computed, such as the volume-averaged $\langle x \rangle$,

$$\langle x \rangle = \frac{1}{V}\int_{\mathcal{D}_p} x(\rho)\mathrm{d}\mathbf{r} = \int_{\mathcal{D}_p} x(\rho(r,z))r\mathrm{d}r\mathrm{d}z \Big/ \int_{\mathcal{D}_p} r\mathrm{d}r\mathrm{d}z \tag{3.37}$$

the line-averaged electron density $\overline{n}_e$

$$\overline{n}_e = \int_0^1 n_e\left(\rho\right)\mathrm{d}\rho, \tag{3.38}$$

and the density normalized averaged-temperature $\langle T \rangle_n$

$$\langle T \rangle_n = \frac{\displaystyle\int_{\mathcal{D}_p} n_e(\rho)\cdot T(\rho)\mathrm{d}\mathbf{r}}{\displaystyle\int_{\mathcal{D}_p} n_e(\rho)\mathrm{d}\mathbf{r}} = \frac{\displaystyle\int_{\mathcal{D}_p} n_e(\rho(r,z))\cdot T(\rho(r,z))r\mathrm{d}r\mathrm{d}z}{\displaystyle\int_{\mathcal{D}_p} n_e(\rho(r,z))r\mathrm{d}r\mathrm{d}z}. \tag{3.39}$$

An example of typical H-mode and L-mode plasma temperature profile configurations is presented in Figure 3.4. In case of H-mode, the profile factors and the values of temperatures at axis, pedestal and separatrix heights are those utilized for the EU-DEMO 2015 baseline and elaborated by the PROCESS system code [30]. The L-mode profile takes the same α_T amplitude and T_0 is calculated such that the volume-averaged temperature $\langle T \rangle$ is the same between the cases. The confinement in H-mode in terms of confinement times τ_E is about twice as high as in L-mode [105]. Hence, despite of the marginal deviations appearing between the two temperature profiles, the heating power needed to achieve such configurations deviate by a factor of 2.

In fusion system codes the volume integration of density and temperature profiles is performed on the normalized coordinate ρ, which normally coincides to a normalized radial coordinate. Hence, two major simplifying assumptions are taken:

(i) all magnetic surfaces feature circular cross-sections and

(ii) the distance between the plasma geometric centre located in $(R_0, 0)$ and the magnetic axis is negligible.

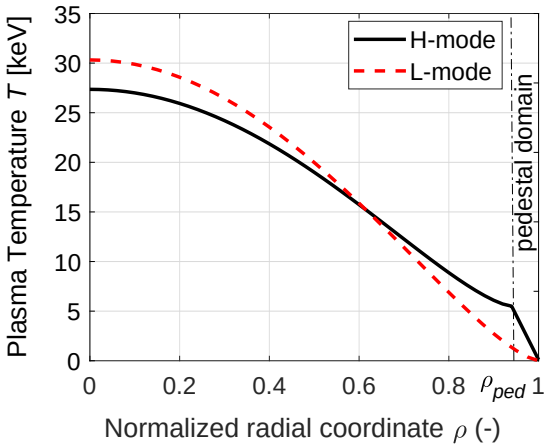

Figure 3.4.: Plasma temperature vs. normalized magnetic flux coordinate ρ for H-mode and L-mode confinement regimes. The H-mode temperature has been obtained from Equation (3.36) and imposing the reference plasma parameters adopted for the EU-DEMO 2015 design [30]. The L-mode profiles assumes the same α_T, while T_0 is such that the volume-averaged temperature $\langle T \rangle$ equates that of H-mode.

As a consequence, system codes "confuse" magnetic with radial coordinate, implying a regular and uniform domain of $\rho \in [0,1]$. However, as shown in Figure 3.2, the poloidal flux spreads across the plasma domain according to a certain two-dimensional distribution, where the magnetic flux surfaces are not equidistant. Nevertheless, systems codes are based on this one-dimensional integration of plasma volume-averaged properties, with relevant implications in the related results. The core physics model implemented in MIRA refuses this simplified frame, and refers to a two-dimensional description of plasma properties, where the introduced integral parameters pertain to a 2D distribution through the whole poloidal domain.

3.2.2. Integral Steady State Core Plasma Power Balance Model

The calculation of the energetic gain from a fusion reactor is a major target for a fusion system code. The plasma is surrounded by other components extracting the energy released by the plasma and associated with different processes, such as radiation, ohmic heating, etc.
The steady state power balance in the confined plasma region implies that the energy content must be constant in time, equalizing energy sources and sinks. The former are characterized by the total plasma heating power P_{heat}, providing thermal energy to the charged plasma particles. This includes the contribution of kinetic alpha particles P_α, the Ohmic heating P_{OH} and the power injected by external auxiliary heating systems P_{add}. Accordingly, $P_{heat} = P_\alpha + P_{add} + P_{OH}$.
The energy losses result from transport losses P_{con} and electromagnetic radiation P_{rad}. The earlier derives from classical and anomalous mass and energy transport processes, occurring in the confined plasma region. Classical processes are based on binary Coulomb collisions while anomalous transport are due to plasma turbulence phenomena, being the driving force to advection and conduction energy losses. Plasma core radiation takes place because of the interactions between charged particles, such as synchrotron and bremsstrahlung radiation. Synchrotron radiation is caused by particle gyration leading to a permanent radial acceleration. The Bremsstrahlung radiation arises from the deceleration of charged particles from their Coulomb elastic collisions [9, 83]. With respect to the Maxwell equations, the acceleration and deceleration of charged particles lead to an emission of

electromagnetic radiation and the related energy content represents an energy loss for plasma internal energy. A further radiation loss mechanism is to large extent attributed to sputtered impurities from the surrounding structures and non-hydrogenic atoms that are quickly ionized in plasmas at electron temperatures of a few eV or more [83]. The radiation emitted from impurity ionization is referred to as *line radiation* and involves elementary atomic process such as electron collisional excitation, radiative de-excitation, electron ionization and radiative recombination. The plasma line radiation is desired to be more relevant in the plasma edge region and largely depends on the charge number Z of involved nuclei [106].

With regard to the energy losses, the transport losses are in general of major importance in the vicinity of the plasma center, while radiation losses, especially due to impurities, have a large impact in the plasma periphery. Henceforth, like in other fusion system codes [10, 15, 17], the overall confining region is split into: core region, where $0 \leq \rho \leq \rho_{core}$ and mantle region, with $\rho_{core} \leq \rho \leq 1$ (see Figure 3.5). This enables a twofold separation of power balance in the plasma domain into core energy balance ① :

$$P_{\alpha} + P_{add} + P_{OH} = P_{rad,core} + P_{con}, \tag{3.40}$$

and mantle energy balance ② :

$$P_{sep} = P_{con} - P_{rad,mantle}. \tag{3.41}$$

P_{sep} identifies the total power flow across the plasma separatrix and the parameter ρ_{core} (input parameter) denotes the flux coordinate interfacing the two domains.
The additional heating power P_{add}, applied by external heating systems, takes into account of the pure heating power P_{nCD} and the power used to drive plasma current P_{CD}. Hence, $P_{add} = P_{CD} + P_{nCD}$. The externally applied power P_{CD} is directly apportioned with the current externally driven in the plasma I_{CD}. A detailed explanation is provided in Appendix C.1. P_{nCD} is being adjusted throughout a MIRA run in such a way that the core power balance of Equation (3.40) is fulfilled. In a narrower sense, P_{nCD} is the remainder of all other source and losses terms, separately calculated. Negative solutions of P_{nCD} represent non-physical design points and can be turned into feasible points by altering free parameters of the core plasma module. For instance, increasing the concentration of the seeded impurity leads to a higher dissipation of radiative losses, with a consequent increase of P_{add}. The ohmic heating power P_{OH} outlines the heating power deposited in the plasma (Joule heating) due to the total electric current I_p flowing in the confining region. Hence, it can written as

$$P_{OH} = U_{loop} I_p \tag{3.42}$$

with U_{loop} denoting the plasma loop voltage (see Equation C.3). The ohmic heating in tokamak plasmas rapidly declines for increasing temperatures. At typical D-T fusion reaction temperatures, it is negligible compared to the other source terms.

The fusion power energy $E_{fus} = 17.6$ MeV, generated from the D-T thermonuclear fusion reaction, is related to the velocity-averaged reaction rate $\langle \sigma v \rangle$ and to the fuel deuterium and tritium densities n_D and n_T. The fusion power density q_{fus} reads to:

$$q_{fus} = n_D n_T \langle \sigma v (T) \rangle E_{fus}, \tag{3.43}$$

where the density are in [m^{-3}], $\langle \sigma v \rangle$ in [m^3/s] and E_{fus} in [MJ]. Both density and temperature are flux functions, thus q_{fus} is also a function of ρ. The deuterium and tritium densities n_D and n_T, assumed to be in equal parts, scale with the electron density n_e by means of the fuel fraction f_{DT}, such that $n_D = n_T = 1/2 f_{DT} n_e$. f_{DT} relates to the plasma dilution and on impurity content. The

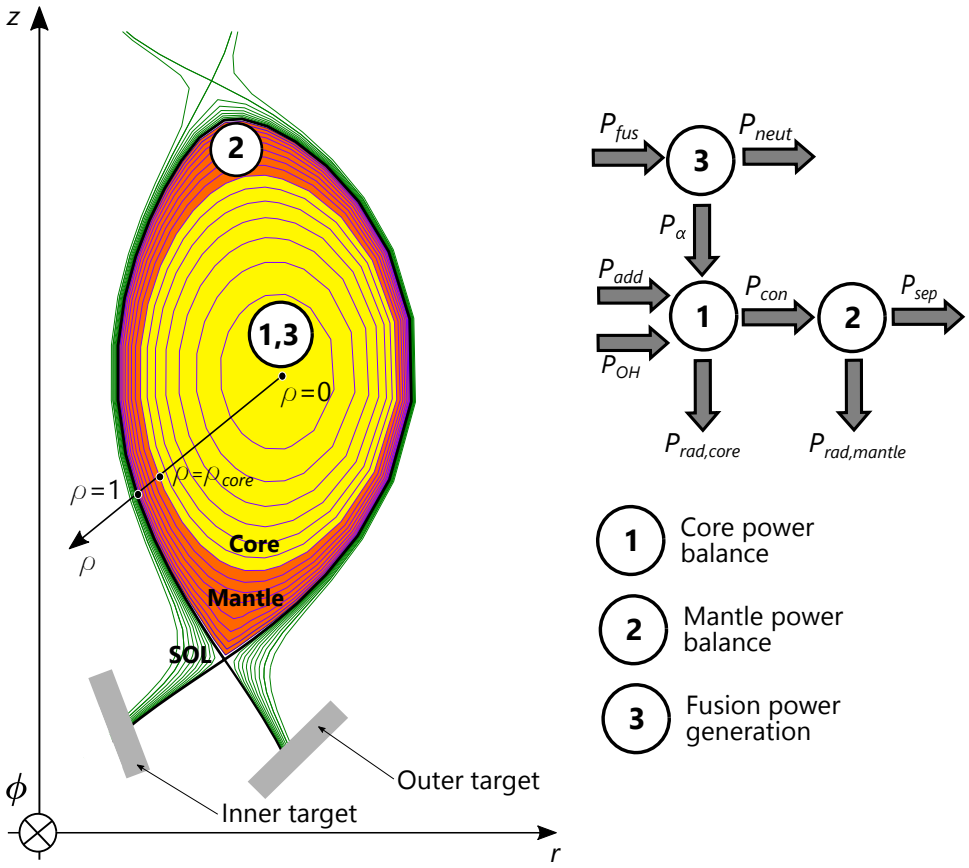

Figure 3.5.: Schematic view of plasma core and mantle power balances. The filled arrows denote the power flows, each associated to a power balance, among the plasma core (1), the plasma mantle (2) and the fusion power generation (3).

fusion reactivity $\langle \sigma v \rangle$ depends on the plasma temperature T, according to theoretical or empirical laws implemented in system and transport codes. Relying on the existing physics background of the TREND system code MIRA adopts the same parametrization, based on a fit proposed by Bosch and Hale [107]. Recasting the definition of deuterium and tritium density on the fuel fraction f_{DT} and recalling the inverse proportionality of alphas and neutrons kinetic energy to the mass number [9], fusion, neutron and the alpha power densities can be written as

$$\begin{aligned} q_{fus}(\rho) &= 1/4\ f_{DT}^2 n_e^2(\rho)\ \langle \sigma v\,(T(\rho))\rangle\ E_{fus}, \\ q_{neut}(\rho) &= 4/5\ q_{fus}(\rho), \\ q_{\alpha}(\rho) &= 1/5\ q_{fus}(\rho). \end{aligned} \tag{3.44}$$

The total fusion power can be evaluated by integrating over the plasma domain $\mathcal{D}_p$

$$P_{fus} = \int_{\mathcal{D}_p} q_{fus}\,(\rho)\,\mathrm{d}\mathbf{r}, \tag{3.45}$$

where the infinitesimal volume integration in $\mathrm{d}\mathbf{r}$ reduces to a double integral on $2\pi r \mathrm{d}r\mathrm{d}z$ in the reference curvilinear coordinate system (r, ϕ, z). Based on Equation (3.44), neutron and alpha and

neutron powers are given by:

$$\begin{aligned} P_{\alpha} &= 1/5 \cdot P_{fus} \\ P_{neut} &= 4/5 \cdot P_{fus}. \end{aligned} \tag{3.46}$$

Fusion, alpha and neutron are strongly bound to the density and temperature profiles and to the poloidal magnetic flux distribution $\Psi(r,z)$, deduced from the equilibrium model.

A figure of merit adopted in system codes to evaluate the ratio of internal to external energy sources is given by the plasma energy gain Q. It relates the fusion power P_{fus} to the sum of additional heating P_{add} and ohmic heating power P_{OH}, such that

$$Q = \frac{P_{fus}}{P_{add} + P_{OH}}. \tag{3.47}$$

The fusion gain can ideally vary between zero to infinity. In case of $Q = 0$ no fusion reaction occurs, while for $Q \to \infty$ identifies a plasma ignition situation, with no external heating power needed to sustain the fusion process. $Q \to \infty$ is an idealized situation, which is excluded by the collisionality of particles. The ITER baseline scenario, for instance, is foreseen to operate with $Q = 10$ [108], whereas for DEMO design, higher values are expected, with $Q \approx 40$ [27, 32].

The total power radiation losses of the confined plasma inside the separatrix is the sum of contributions from the plasma core and the mantle region, $P_{rad} = P_{rad,core} + P_{rad,mantle}$. Since synchrotron and bremsstrahlung radiations occur predominantly in the plasma core, both are assigned exclusively to $P_{rad,core}$, with

$$P_{rad,core} = P_{syn} + P_{brem} + P_{line,core}. \tag{3.48}$$

The radiation power in the mantle region is predominantly characterized by line radiation,

$$P_{rad,mantle} \approx P_{line,mantle}. \tag{3.49}$$

Synchrotron radiation becomes important at high temperature and scales as $P_{syn} \propto B_t^{2.6} n_e T$ [10]. The detailed formulation of P_{syn} is provided in Equation (C.31). The bremsstrahlung power density q_{brem} and total power P_{brem} scales quadratically with n_e and can be enhanced by impurities emission. They can be parametrized as [9, 10]

$$\begin{aligned} q_{brem}(\rho) &= C_B Z_{eff} n_e^2(\rho) \sqrt{T(\rho)}, \\ P_{brem} &= \int_{\mathcal{D}_p} q_{brem}(\rho)\, \mathrm{d}\mathbf{r}, \end{aligned} \tag{3.50}$$

where $C_B = 5.355 \times 10^{-3}$. Z_{eff} defines the effective ion charge number, which takes into account the different ion species and the respective emission contributing to the total bremsstrahlung power.

The radiation emitted by a generic atomic species with charge number Z has a characteristic individual electromagnetic spectrum based on their electronic levels. The associated power density $q_{line,Z}$ is given by

$$q_{line,Z} = n_e n_Z L_Z(T), \tag{3.51}$$

where $L_Z(T)$ is the radiative power loss function, also called luminosity, for the atomic species with charge number Z and n_Z is the related atomic density. The radiative power loss function data, originally derived from Refs. [109, 110], is provided with TREND code package [10] and written

in table format. A linear interpolation is performed to calculate L_Z for any arbitrary temperature included in the application range of each atomic species. Assume n_j and $n_{j,M}$ two variables denoting the density of impurity j in the core and mantle region. If f_j and $f_{j,M}$ are the core and mantle fraction of impurity j, such that $n_j = f_j n_e$ in the core region and $n_{j,M} = f_{j,M} n_e$ in the mantle region, the total line radiation power density q_{line} is given by

$$q_{line}(\rho) = \begin{cases} \sum_j \left(f_j n_e^2(\rho) L_{Z_j}(T(\rho)) - C_B f_j Z_j^2 n_e^2(\rho) \sqrt{T(\rho)} \right) & 0 \leq \rho \leq \rho_{core} \\ \sum_j f_{j,M} n_e^2(\rho) L_{Z_{j,M}}(T(\rho)) & \rho_{core} < \rho \leq 1. \end{cases} \tag{3.52}$$

Since the $L_Z(T)$ data includes a wide spectrum of atomic process, including bremsstrahlung, the latter has been subtracted from the expression of q_{line} within the core sub-domain to avoid multiple counting. All power terms associated with core and mantle line radiation losses can be obtained by integrating over the core and mantle plasma volume with respect to the magnetic flux surface defined by $\rho \equiv \rho_{core}$. Those two power contributions can be written as

$$P_{line,core} = \int_{\mathcal{D}_p(\rho \leq \rho_{core})} q_{line}(\rho) \mathrm{d}\mathbf{r}, \tag{3.53}$$

and

$$P_{line,mantle} = \int_{\mathcal{D}_p(\rho > \rho_{core})} q_{line}(\rho) \mathrm{d}\mathbf{r}, \tag{3.54}$$

with $\rho \in [0,1]$. Overall, the total core radiation power density q_{rad}, and the related total integral power P_{rad}, are defined as

$$\begin{aligned} q_{rad}(\rho) &= q_{brem}(\rho) + q_{syn} + q_{line}(\rho), \\ P_{rad} &= \int_{\mathcal{D}_p} q_{rad} \mathrm{d}\mathbf{r} = P_{brem} + P_{syn} + P_{line,core} + P_{line,mantle}, \end{aligned} \tag{3.55}$$

where the synchrotron power density $q_{syn} = P_{syn}/V_p$ is assumed to be homogeneously distributed across the core plasma cross section and obtained by dividing the total synchrotron power P_{syn} by the core plasma volume V_p.

Since the transport losses P_{con} are hardly predictable, and not yet fully understood, at this level of granularity system codes estimate them by defining a set of scaling laws for the energy confinement time τ_E. Essentially, it depends on plasma sizes, magnetic field and other confinement properties according to several extrapolating laws. Following the TREND modelling frame, the ITER IPB98(y,2) scaling law [108, 111], typically adopted for DEMO system code studies and adapted to high beta and high radiation DEMO scenario [10, 112], is also deployed to evaluate τ_E as function of several plasma variables, i.e. $\tau_E \equiv \tau_E(H, I_p, B_t, P_{con}, \overline{n}_e, R_0, A, \kappa_X)$, where H denotes the *confinement enhancement factor* and M the ion mass number in atomic mass units. A detailed formulation of the adopted τ_E expression is reported in Equation (C.30). τ_E relates the total plasma thermal energy W_{th} to the total energy loss rate P_{con} by means of

$$P_{con} = \frac{W_{th}}{\tau_E}, \tag{3.56}$$

where W_{th} includes the thermal energy content of plasma ion and electrons and can be defined, such that

$$W_{th} = \int_{\mathcal{D}_p} \left(\frac{3}{2} n_e T_e + \sum_j \frac{3}{2} n_j T_j \right) \mathrm{d}\mathbf{r} = \frac{3}{2} \left(1 + f_i\right) \langle n_e \rangle \langle T \rangle_n . \tag{3.57}$$

f_i is the total ion fraction with respect to the electron density n_e and n_j the density of electron and the j impurity. T_e and T_j are related temperatures (assumed equivalent) and $\langle T \rangle_n$ is the density-averaged temperature.

Recent studies [113, 114] have shown that ρ_{core} can be assumed for DEMO in the range $0.6 - 0.75$. Within this interval the calculated $P_{rad,core}$ is expected in DEMO to be larger than in ITER. This leads to a more appropriate definition of $P_{con} = P_{heat} - P_{rad,core}$ to use for evaluating τ_E according to the ITER IPB98(y,2) scaling law (Equation C.30).

3.2.3. Plasma design points with respect to the operational limits

The operation of tokamak plasmas cannot be based on parameters of any arbitrary choice, disregarding the operational limits that somehow restrict the parameters phase space. Therefore, precise plasma limits should be considered within a systems code analysis. From a systems analysis point of view, the goal is to find a set of control parameters complying with main constraining laws dictated by stability and equilibrium criteria.

The operational limits can be classified in two categories, i.e. hard and soft limits [84]. The former refer to the degradation of energy confinement which unavoidably leads to a reduction of fusion power. The latter are concerned with limits preventing the occurrence of catastrophic events like disruptions. These are induced, for instance, by very fast decreases of plasma temperature and current, releasing huge amounts of energy onto plasma facing components, that potentially harm its structural integrity by erosion and melting. The major constraining bounds addressed in most of fusion system codes for the core plasma parameters refer to a dedicated operational limit related to:

- safety factor, to prevent kink and sawtooth MHD instabilities (Section 3.1);
- electron density, to prevent thermal instabilities;
- normalized beta, to avoid pressure-driven MHD instability modes;
- power exhaust, to ensure high confinement regime (H-mode).

The radiation losses affecting the plasma power balance are strongly influenced by the plasma density. As it can be seen from Equations (3.50) and (3.52), the bremsstrahlung radiation and the line radiation scale with n_e^2, becoming therefore important if the density increases. An increase of radiation losses might significantly cool down of plasma, and therefore, reduce the temperature. This phenomenon is particularly enhanced in the edge, where the fusion power plays a minor role and the impurity ions are not fully ionized [84]. A decrease of temperature can sustain the enhancement of radiation losses in the edge region and bring the plasma to thermal instabilities, such as multifaceted asymmetric radiation from the edge (MARFE). The plasma density provides an upper limit preventing such demanding thermal instabilities, which are normally identified in fusion systems codes by

the Greenwald density n_{GW}, reading as [115]

$$n_{GW} = \frac{I_p}{\pi a^2}, \tag{3.58}$$

where n_{GW} is expressed in [10^{20} m^{-3}], I_p in [MA] a in [m]. The Greenwald density originally applied to the line-averaged electron density [10, 15, 17] $\overline{n}_e$, thus the Greenwald fraction $f_{GW} = \overline{n}_e / n_{GW}$ describes the margin on the plasma density. In the meantime, experiments with peaked density profiles showed that it is possible to exceed this empirical limit without necessarily undergoing to any kind of thermal instabilities, revealing an edge density limit as the real limitation [99, 116]. Therefore, the electron density at pedestal height $n_{e,ped}$ should be compared to n_{GW} instead of $\overline{n}_e$, such that $f_{GW,ped} = n_{e,ped} / n_{GW} \leq 1$. In turns this means that the $\overline{n}_e$ can significantly exceed n_{GW}, depending on the peakedness of the density profile, leading to $f_{GW} \leq 1.0 - 1.5$ [99].

Combining the mathematical expression for the fusion power and plasma beta, one can deduce that raising the plasma pressure, i.e. the plasma beta, implies higher values of fusion power, thus of a higher performances. Besides, larger plasma betas express a more efficient use of the externally applied magnetic field in balancing the confined gas pressure with the magnetic pressure. However, due to ideal MHD instabilities modes, i.e. perfectly conducting plasma, an upper limit for pressure and toroidal current is normally observed to prevent the occurrence of some of these modes, such as interchange, ballooning and kink modes [9]. Troyon [117] showed that these maximum values for plasma pressure scale with a combination of plasma current I_p, toroidal field B_t and minor radius a, yielding the definition of the normalized plasma beta β_N

$$\beta_N = \beta_t \Big/ \left(\frac{I_p}{a B_t} \right), \tag{3.59}$$

where β_t indicates the toroidal beta, expressed in [%], B_t in [T], a in [m] and I_p in [MA]. Different fits are used in system codes to observe the limits on β_N [17]. In line with the TREND code, MIRA adopts the same beta limit, based on the scaling law reported by Sauter et al. [118]

$$\beta_N < 4 l_i, \tag{3.60}$$

where l_i indicates the plasma internal inductance, defined in Equation (3.9).

The H-mode confinement regime has proven energy confinement times τ_E largely enhanced compared to those of L-mode regime [10, 106]. The achievement of the H-mode was experimentally found to occur when the applied heating power overcomes a certain threshold limit, defined as L-mode to H-mode threshold power P_{LH}. As the phenomena taking place and contributing this quantity are not yet fully understood, a scaling law was proposed for ITER by Martin et al. [119] and implemented in MIRA, abiding by the TREND code physics module. Accordingly, P_{LH} is defined as

$$P_{LH} = 0.0976 \; M^{-1} \; \overline{n}_e^{0.717} \; B_t^{0.803} \; S^{0.941}, \tag{3.61}$$

where M [amu] is ion mass number, $\overline{n}_e$ [10^{20}m^{-3}] the line-averaged electron density, B_t [T] the toroidal magnetic field and S [m^2] the plasma surface area. The inverse proportionality on M has been integrated to adapt the original scaling, developed mainly with data from deuterium discharges, to the actual D-T operation [10]. The characterization of a consistent plasma design point has to go through an evaluation of the confinement regime, too. Based on experimental observation [99], the power transported across the separatrix P_{sep} (Equation 3.41) has to overcome P_{LH} by a factor

$f_{LH} > 1$ to consider the plasma to operate in high confinement mode. Therefore, the parameter f_{LH}, measuring the quality of the confinement, is defined as

$$f_{LH} = \frac{P_{sep}}{P_{LH}}. \tag{3.62}$$

A sound margin of P_{sep} over P_{LH} is normally observed in system analyses to avoid back-transition to L-mode and compensate the uncertainties of P_{LH}. For the EU-DEMO 2015 design, $f_{LH} \geq 1.2$ has been set as a lower limit for the H-mode threshold limit [27].

3.2.4. A constrained gradient-based solver for tokamak plasma design

In order to achieve a certain amount of fusion power, a tokamak plasma has to operate under specific conditions. Several operational limits have to be considered to prevent MHD instabilities and to preserve a high level confinement regime (H-mode). Therefore, achieving a prescribed fusion power is not the unique goal for a fusion reactor. A system code has the task to find the plasma design point, simultaneously meeting the listed operational limits and fulfilling a set of fixed requirements, mostly on plasma performances. An ideal situation would foresee a direct control on the physical heating and fuelling systems, yielding the desired fusion power and guaranteeing the safe operational conditions.

Additional to the density, beta and H-mode stability and confinement limits, a further constraining condition refers to the *divertor challenging quantifier* Γ_{sep}, defined as

$$\Gamma_{sep} = P_{sep}/R_0. \tag{3.63}$$

The power transported across the separatrix P_{sep}, assumed to be uniquely handled by the divertor, is normalized to the plasma major radius R_0. Γ_{sep} has been proposed as a representative figure of merit for divertor protection [120]. ASDEX Upgrade has already successfully demonstrated $P_{sep}/R_0 = 10$ MW/m. ITER instead is expected to operate at 15 MW/m [99]. For DEMO, 17-20 MW/m is a range assumed for the current designs [27]. Taking a prescribed upper bound for the divertor protection quantifier Γ^u_{sep}, the condition $\Gamma_{sep} \leq \Gamma^u_{sep}$ has been used when seeking for a plasma working point.

A FPP shall provide a minimum net electric power. To meet such criteria, more requirements on fusion power P_{fus} and external additional heating power P_{add} need to be introduced. Large values of P_{fus} coupled to high P_{add} depict a non-efficient operation of a FPP plasma. The approach adopted in MIRA is to set a target value for both fusion and additional heating powers, P^t_{fus} and P^t_{add}.

The complexity of finding a feasible design point can be comprised comparing the dependency of P_{sep} in the power exhaust limit (Equation 3.61) with that in the divertor protection (Equation 3.63). In the former P_{sep} is downwardly limited due to the P_{LH} threshold, whereas, with regard to the divertor limiting condition, P_{sep} is upwardly limited. A system code has to cope with these conditions and has to rely on a systematic approach to find feasible plasma operating points, where the selection of the relatively large set of input plasma parameters can be hardly performed manually. The physics module of MIRA comprises the set of conventional system code plasma physics equations in connection with a gradient-based numerical solver. The magnetic flux-dependent parameters introduced in the physics module are matched with the calculated magnetic configuration $\rho(r,z)$. The full set of constraining conditions includes Greenwald density, beta and power H-mode power exhaust limits, divertor challenging quantifier and required fusion and additional heating power. To achieve a feasible configuration the plasma solver is capable of adjusting as many iteration variables, including:

- electron density and temperature at plasma axis, $n_{e,0}$ and T_0;
- seeded impurity fraction on core and mantle regions, f_{Z_1} and $f_{Z_1,M}$;
- He fraction f_{He};
- fraction of the total plasma current due to current drive (CD) f_{CD} and
- non-thermalized fast particle fraction due to external heating systems γ_{beam}.

The selection of this set of controlling variables has its own rationale based on different attempts to find the optimal solving procedure. Density and temperature at plasma axis permit a direct regulation of the fusion power. Meanwhile, the core and mantle seeded impurity fractions offer two degrees of freedom to comply with power exhaust and divertor protection criteria, particularly in the edge region. Moreover, f_{Z1} can be manipulated to increase the dissipated radiation power in the core and push possible non-physical solutions involving negative non-CD power P_{nCD} towards positive values.

Transport mechanism lead to loss of helium particles from the confining region. Therefore, equivalently to energy loss, a helium particle residence time τ_{He} is also introduced (see Appendix C.3). The helium fraction f_{He} has been introduced as a control variable to keep a constant particle-to-energy confinement time ratio f_{P2E} (Equation C.29). This choice hinges upon the assumption that τ_{He} is similar to the global particle confinement time τ_p^*, which takes into account of particle losses due to transport and pumping mechanisms. Accordingly, it is assumed that $\tau_{He} \approx \tau_p^*$, with τ_p^* being directly apportioned with τ_E.
The CD current fraction f_{CD} allows a direct influence on the plasma current balance satisfy the requirement on the total auxiliary heating power P_{add} and on $P_{nCD} \approx 0$.

The total plasma pressure (and beta) includes a contribution from thermal particles $p_{th} \propto n_e T$ and from fast particles $p_{fast} = p_{f\alpha} + p_{beam}$, consisting of fast alphas and external neutral beams (see Appendix C.2). The fraction of fast beam particles injected by external heating systems γ_{beam} has been found a reasonable control parameters as it relates to an external and controllable system, such as a neutral beam injection system (NBI). As a proof, the system code PROCESS [17] includes a formulation where the fraction of fast beam particles γ_{beam} ($T \gg 10$ keV) to the total fast-to-thermalized particle ratio γ_{fast} scales with $\langle n_{beam} \rangle E_{beam} / B_{tot}^2$, where $\langle n_{beam} \rangle$ and E_{beam} are the average beam particle density and energy and $B_{tot} = \sqrt{B_t^2 + \langle B_p \rangle_l^2}$ the total magnetic field. It can be inferred that the former two parameters can be manipulated for plasma design point identification purposes, with a direct impact on the pressure regime. Henceforth, γ_{beam} an has effective influence on the beta limit condition.

Thus the plasma operating point is determined upon the assumption of a set of target fusion and additional power parameters, along with the stability and high confinement operation limits. To derive a DEMO plasma scenario a solving technique has been developed to compute the set of independent variables $\underline{w}$, simultaneously matching the plasma operational limits and the power requirements. Denoting the complete collection of $n = 7$ plasma iteration variables $\underline{w}$ such that

$$\underline{w} = [n_{e,0},\ T_0,\ f_{He},\ f_{Z_1},\ f_{Z_1,M},\ f_{CD},\ \gamma_{beam}]\,, \tag{3.64}$$

a feasible plasma operating point relates to the solution to the following problem as to

$$\text{find } \underline{w} \text{ subject to } \begin{cases} f_{GW}(\underline{w}) \leq f_{GW}^{u} \\ \beta_N(\underline{w}) \leq 4l_i \\ f_{LH}(\underline{w}) \geq f_{LH}^{l} \\ \Gamma_{sep}(\underline{w}) \leq \Gamma_{sep}^{u} \\ \left| P_{fus}(\underline{w}) - P_{fus}^{t} \right| \leq \epsilon_{fus} \\ \left| f_{P2E}(\underline{w}) - f_{P2E}^{t} \right| \leq \epsilon_{P2E} \\ \left| P_{add}(\underline{w}) - P_{add}^{t} \right| \leq \epsilon_{add} \\ P_{nCD}(\underline{w}) \approx 0 \end{cases}, \tag{3.65}$$

where the superscripts u and l depict the upper and lower limit associated with the named variable and t indicates the target value. ϵ_{fus}, ϵ_{P2E} and ϵ_{add} denote the absolute deviation deployed in the equality constraints on P_{fus}, f_{P2E} and P_{add}. In case of ϵ_{fus} and ϵ_{add} the default value is 0.1 MW and for ϵ_{P2E} is 10^{-3}.
According to this formalism a target is intended more as a required performance, e.g. fusion power, while upper and lower bounds are associated with operational constraints. The group of the conditions to satisfy listed in Equation (3.65) can be recast into the $n-$vector of nonlinear constraint functions $g(\underline{w}) : \mathbb{R}^n \rightarrow \mathbb{R}^n$. As a result, the solution of $\underline{w}$ can be reformulated in a more convenient form as to

$$\text{find } \underline{w} \text{ subject to } \begin{cases} g(\underline{w}) \leq 0 \\ l_b \leq \underline{w} \leq u_b \end{cases}, \tag{3.66}$$

where u_b and l_b are the upper and lower feasibility ranges for the independent variable set.
The rationale to the choice of the operational upper and lower intervals, adopted for each variable of $\underline{w}$, is detailed prior to every performed analysis. All the inequalities are being expressed in a dimensionless form, to apply a uniform constraint violation stopping criteria, such that the condition to meet becomes $\max g(\underline{w}) \leq \epsilon_{cv}$, with ϵ_{cv} being a prescribed constrain violation tolerance.

The solution method is based on Newton-Raphson algorithm [121], derived from the `fmincon` nonlinear programming solver. The Jacobian matrix $J_g(\underline{w})$ of $g(\underline{w})$, cannot be analytically defined, as a number of calculated parameters relies on the numerical solution to the 2D axisymmetric tokamak plasma magnetic equilibrium problem. For this reason, J_g is progressively calculated by means of finite difference method, increasing, though, the computing times. This approach has been proven to find feasible plasma operating points for broadly different plasma magnetic configurations, as illustrated in Chapter 6. Since the problem is characterized by many local and global maxima and minima, the solution of $\underline{w}$ is likely to be influenced by the initial guess $\underline{w}_0$, being a limitation of this approach. However, in order to a find a viable design point within a reasonable number of iterations, whenever a viable plasma design is found, it is made available for the next plasma scenario analysis.

Unlike the existing 0D system codes, the parameters depending on the magnetic configuration are interfaced with the calculated magnetic configuration, as shown in Figure 3.6. The flowchart illustrates the approach to couple the equilibrium solver and the core physics solver.
At first, the MIRA data structure addresses the equilibrium configuration, in terms of a prescribed value of plasma current I_p, poloidal beta β_p, internal inductance l_i and safety factor q_{95}. The solution $\overline{\Psi}(r,z)$ is conveyed to the core physics module, where the normalized radial coordinate $\rho(r,z) = 1 - \overline{\Psi}(r,z)$ is utilized to perform the core physics analysis according to the TREND code

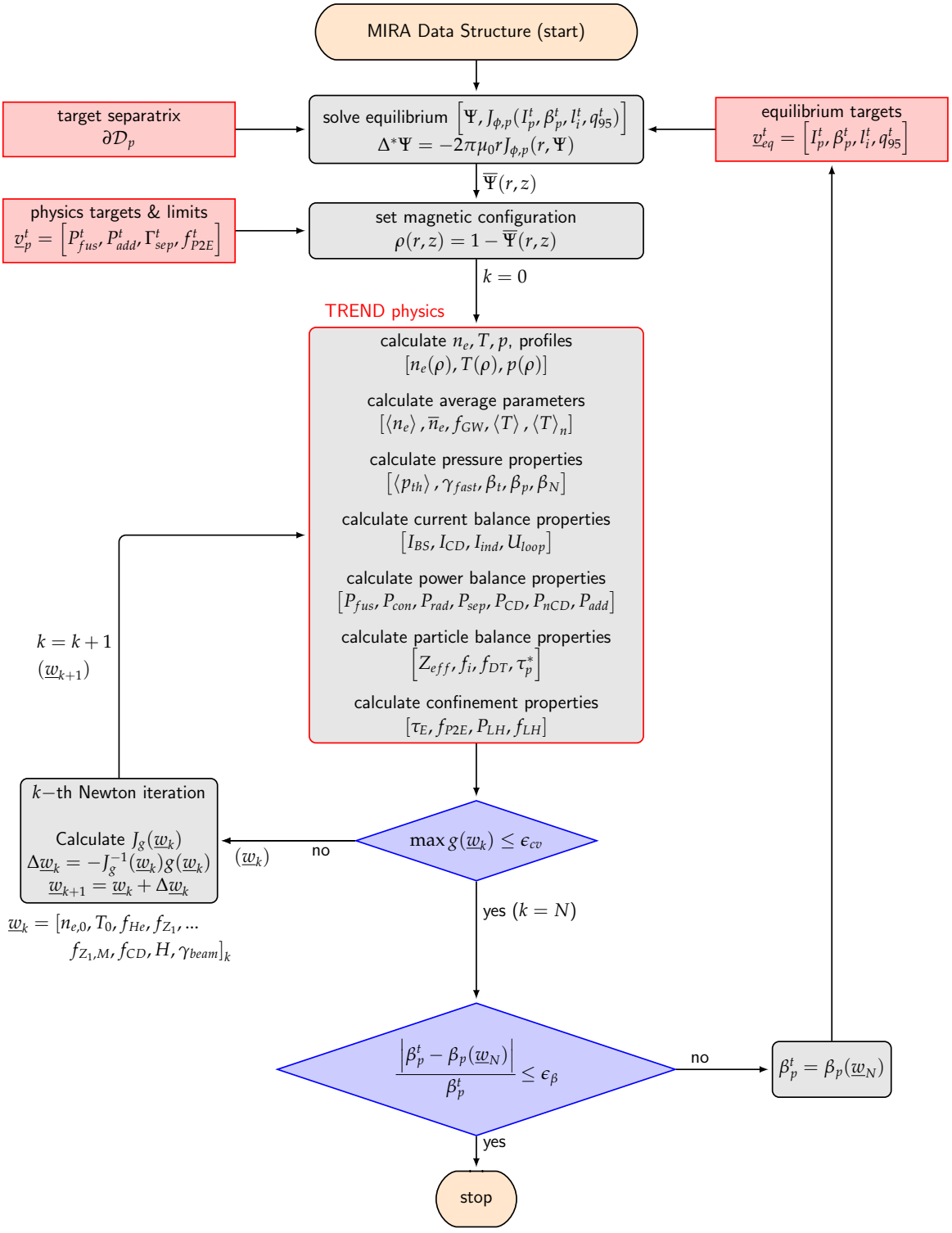

Figure 3.6.: Organizational structure of the coupling between equilibrium and core plasma physics model. Each block is characterized by its shape: ovals relate to start and stop nodes, sharp-corner-rectangles indicate inputs, round-corner-rectangles denote process steps and diamonds refer to process decisions.

physics structure. Additionally, the data structure sets the user-defined core plasma physics targets and the initial guess $\underline{w}_0$ on the plasma iteration variable $\underline{w}$. At every iteration step k, the variables $\underline{w}_k$ are continuously updated on the Jacobian matrix $J_g(\underline{w}_k)$ until the constraint conditions are all met, such that $\max g(\underline{w}_k) \leq \epsilon_{cv}$. The first loop terminates when a viable plasma set of variables $\underline{w}$ is achieved. The magnetic configuration $\overline{\Psi}$, upon which $\underline{w}$ is determined, bases on the target poloidal beta β_p^t takes the form of an initial guess. As β_p directly relates to the total plasma pressure it is also influenced by several iteration variables of $\underline{w}$ (Equation 3.64). Assuming $\underline{w}_N$ the solution of Equation (3.66) achieved after N iterations, the associated poloidal beta $\beta_p(\underline{w}_N)$ becomes the target value to the equilibrium module. Hence, the magnetic configuration $\overline{\Psi}$ attains to a value of β_p which is implicitly contingent on $\overline{\Psi}$. The twofold connection between equilibrium and core physics resides therefore in β_p such that equilibrium and core physics modules iteratively communicate as long as a converging value of β_p is finally obtained. If the relative deviation between the target and the calculated β_p lays below a prescribed tolerance ϵ_β, a fully feasible core plasma configuration is found and the whole process terminates. In this case, feasibility includes the fulfilment of five main blocks of conditions, such as (i) equilibrium with an externally applied magnetic field, (ii) MHD stability limits, (iii) H-mode threshold, (iv) fusion power and (v) additional heating power prerequisites.

As a variety of considered physics parameters rely on the poloidal distribution of Ψ, the internal iterations within the core physics module are clearly expected to be slower than fast zero-dimensional models, such as PROCESS. Nevertheless, this more detailed modelling frame has been proven to provide a more accurate picture of the spatial effects, from which the plasma design can profoundly gain in terms of accuracy. The key innovative aspects of this module, therefore, is to link an equilibrium solver to a core physics module, where the poloidal effects due to the magnetic equilibrium configuration are fed into the core physics module and the shape of plasma profiles are iteratively routed back to the equilibrium model.

3.3. A steady state model for SOL and divertor physics

The plasma facing components addressed in fusion systems codes comprises the divertor structures and the breeding blanket first wall (FW). Since these undergo demanding energy flows, protecting measures involving impurity control and engineering design are required to comply with their material integrity during normal and off-normal reactor operations. The main target of a systems code is to establish a mathematical methodology to correlate the plasma parameters to engineering parameters of such components, such as the geometry.

In a fusion tokamak reactor unburnt fuel ions, electrons, alpha particles and impurity ions are transported across the separatrix. Two possible routes for loading to the plasma facing components are taken, i.e. impinging onto the FW, e.g. blob transport and charge exchange, and tied to the magnetic field lines in SOL, directly to the divertor targets via parallel transport. An evaluation of the heat and particle fluxes transferred across the separatrix through the scrape-off layer, by means of convective and conductive transport mechanism, has to be included in a system design code. The divertor is a major interface with the plasma, where the largest heat fluxes are expected. At present, a DEMO reactor is being designed to operate at 10 MW/m^2 [32, 122], including margins due to transient events and divertor tile misalignments.

The power flows to consider for divertor damage constraints comprise the contributions from core and mantle radiation and convective/conductive power flows transported in SOL, denoted by the steady state power balances at nodes ① and ② in Figure 3.7. Neutrons, instead, can travel through

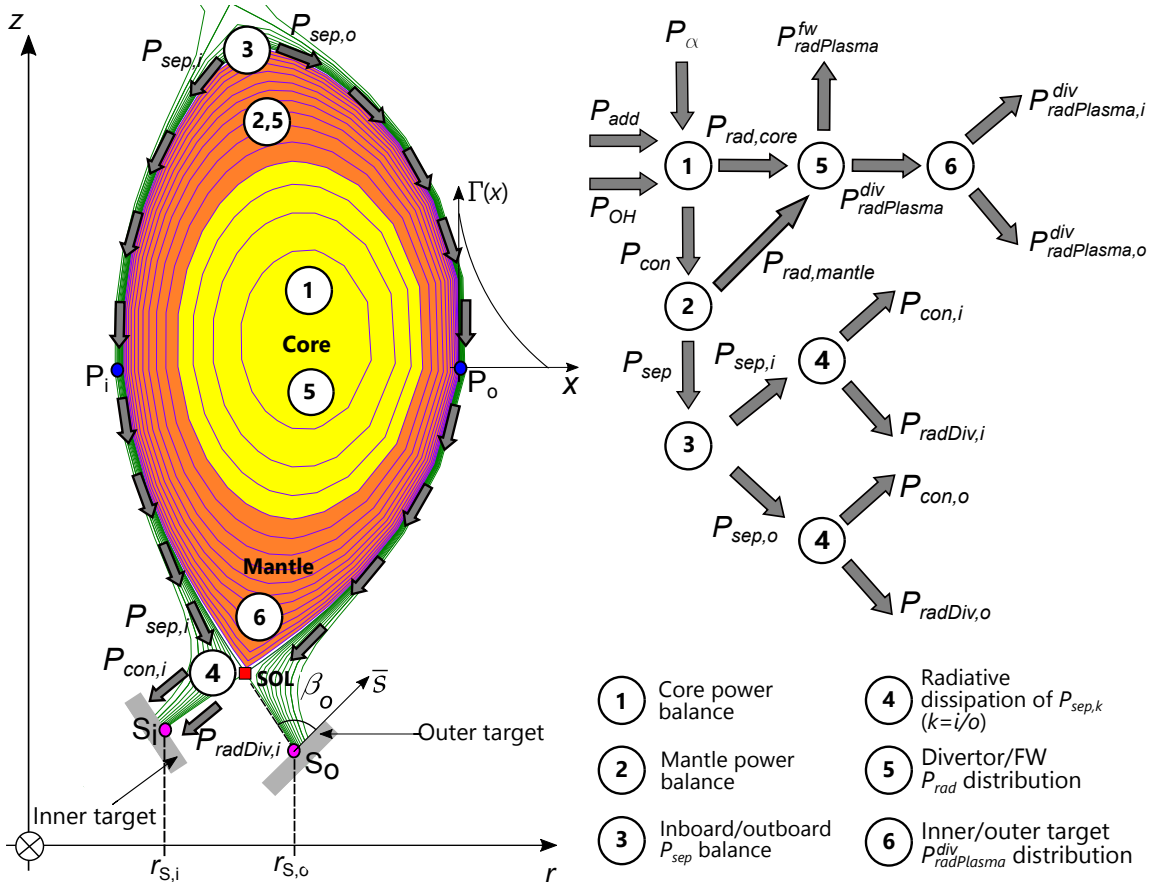

Figure 3.7.: Schematic view of the core and mantle transport and radiation power flows associated with the peak heat flux on the divertor vertical targets. The filled arrows denote the power flows, each associated to a steady state power balance described on the right side and physically located in the left poloidal sketch.

the material bulk, yielding volumetric heating in the structures, while radiation and transport loads deposit energy on the surfaces facing the plasma (see Section 4.1.2).
In the model, the peak flux pertaining to the total power handled by the divertor plates P_{sep} is addressed by a simplified modelling approach. A fraction $f_{sep,k}$, with $k = i/o$, is introduced to account for the repartition of P_{sep} between inner and outer vertical targets. Accordingly, $f_{sep,i} + f_{sep,o} = 1$ and each target handles a transport loss power $P_{sep,k} = P_{sep} \cdot f_{sep,k}$ (node ③). $f_{sep,k}$ is both related to geometric aspects and transport mechanisms tied to confinement regime and magnetic configuration. Hence, it is not a surface fraction. A 2:1 power distribution on outboard/inboard targets is assumed [122], with $f_{sep,o} = 0.66$ without considering the private region and $f_{sep,o} = 0.6$ including the private region [20].

Large values of P_{sep} are critical for the structural integrity of the divertor components, in particular of the vertical targets. Hence, volumetric loss process, such as radiation, are required to dissipate a large fraction of the power transported by the charged particles entering the SOL. Therefore, a reduction of energy and momentum of charged particles reaching the targets denotes a state called *divertor detachment* [58], that can be achieved by injecting in the SOL/divertor region seeding neutral impurities, such as argon, nitrogen and neon [113].
The divertor physics involved in the detachment regime is very complex and includes energy and

momentum loss mechanisms of charged particles due to ionization and recombination processes derived from their interactions with the seeded impurity atoms. As a result fusion system codes rely on a prescribed input radiation fraction f_{rad} accounting for the radiative dissipation $P_{radDiv,k}$ of $P_{sep,k}$ on the divertor target k, indicated only for inner side on node ④ and yielding

$$P_{radDiv,k} = f_{sep,k} \cdot f_{rad} \cdot P_{sep}, \quad k = i/o, \tag{3.67}$$

while the conductive power $P_{con,k}$ on the target k, being the remainder of $P_{radDiv,k}$ from $P_{sep,k}$, can be expressed as:

$$P_{con,k} = f_{sep,k} \cdot (1 - f_{rad}) \cdot P_{sep}, \quad k = i/o. \tag{3.68}$$

The total plasma radiative power P_{rad}, comprising of $P_{rad,core}$ and $P_{rad,mantle}$, spreads over the plasma facing components surfaces, given by the blanket FW and the divertor. Each component experiences a plasma radiation power share, including $P^{fw}_{radPlasma}$ for the FW and $P^{div}_{radPlasma}$ for the divertor (node ⑤). $P^{div}_{radPlasma}$ consists of inner and outer divertor target portions $P^{div}_{radPlasma,i}$ and $P^{div}_{radPlasma,o}$ (node ⑥), both spreading uniformly over the divertor target geometric area $A_{tar,k} = 2\pi r_{S_k} l_{t,k}$. r_{S_k} and $l_{t,k}$ denote the radial coordinate of strike point S_k and the target length of the divertor target k (Figure 2.10)

The conducted power $P_{con,k}$, instead, is conveyed in a few-millimeter thin layer λ_q to the divertor, thus depositing a considerable amount of energy on a very narrow area on the vertical targets $A_{wet,k}$, called *wetted area*. Accordingly, it is assumed that perpendicular to the magnetic field lines the heat flux in the SOL region at the outer midplane Γ falls off exponentially with a decay length λ_q

$$\Gamma(x) = \Gamma_{||} \exp\left(-\frac{x}{\lambda_q}\right), \tag{3.69}$$

where x represents the radial coordinate at the plasma midplane. The processes in the divertor region, including diffusion into the private flux region [123, 124], are represented by a Gaussian distribution $\Gamma(\bar{s})$ whose width S relates to the *power spreading factor* and reads as:

$$\Gamma(\bar{s}) = \frac{\Gamma_0}{2} \cdot \exp\left(\left(\frac{S}{2\lambda_q}\right)^2 - \frac{\bar{s}}{\lambda_q \cdot f_{x,k}}\right) \cdot \operatorname{erfc}\left(\frac{S}{2\lambda_q} - \frac{\bar{s}}{S \cdot f_{x,k}}\right), \quad k = i/o, \tag{3.70}$$

where $\bar{s} \in [-\infty; +\infty]$ indicates the coordinate along the outer target (see Figure 3.7), Γ_{BG} a background heat flux and $\Gamma_{||}$ the peak heat flux at the divertor entrance, relating to Γ_0 such that $\Gamma_{||} = \Gamma_0 / \sin\beta_k$. β_k is the poloidal inclination field line inclination on the target plates (indicated in Figure 3.7 only for the outer target with β_o). The power spreading factor S can be interpreted as a result of the simultaneous contrast between parallel and perpendicular heat diffusion and between point-like particles and gyrating ions, such that following relation for S can be taken as [125]:

$$S = c_{0,r} \frac{r_g}{f_{x,k}} + l_x \sqrt{\frac{\chi_\perp}{\chi_{||}}}, \quad k = i/o, \tag{3.71}$$

where $c_{0,r}$ is a constant to be determined by experiments, $f_{x,k}$ is the flux expansion factor for the divertor target k, detailed shortly afterwards. r_g denotes the ion gyro radius, l_x the connection length between the plasma X-point and divertor targets, $\chi_{||}$ the parallel and $\chi_\perp$ the perpendicular heat diffusivity. While the parallel heat $\chi_{||}$ is associated to the Spitzer-Härm electron conductivity, expressed by an analytical formula, the perpendicular transport coefficient is unknown [125]. Recently, several efforts [125, 126] have been dedicated to the elaboration of experimental data from L-mode and

H-mode operations campaigns on ASDEX Upgrade and JET plasmas, to catch the driving dependencies and derive a set of scaling laws for S. The results showed that S depends on electron density $n_{e,tar}$ and temperature $T_{e,tar}$ at the divertor target, mass number of the main ions M, poloidal field B_p and power transported in SOL P_{sep}. As a result, the scaling derived from ASDEX Upgrade [125] is expressed as:

$$S = 1.42 \cdot \frac{r_g}{f_{x,k}} + 2.11 \cdot T_{e,tar}^{-1.28}\, n_{e,tar}^{0.66}\, M^{-0.84}\, B_p^{-1.33}. \tag{3.72}$$

Since a predictive model to calculate electron density and temperature at divertor targets, based on two-point approach [58], has not been implemented yet, this formula has been implemented in the MIRA divertor physics module. It can be optionally used imposing the additional input parameters associated with $n_{e,tar}$, $T_{e,tar}$ and M. Furthermore, as the SOL physics for DEMO will likely differ from that observed in ASDEX Upgrade, at least in terms of radiation and confinement regime, this formula cannot be trustfully used for DEMO divertor design. In absence of more elaborated scalings, only speculative assumptions could be done on the power spreading factor S for DEMO divertor operating regimes. Wenninger et al. [122] inferred that S scales as R_0/B_p, with R_0 being the major radius and B_p the poloidal field. Based on such an intuitive guess, they estimated a value for S of around 4.5 mm for the near-term EU-DEMO 2015 design. Henceforth, the default option takes $S = 4.5$ mm, though editable as a user-defined parameter.

For λ_q, diverse definitions are available [127, 128]. Based on infrared data from H-mode discharges on JET, DIII-D and ASDEX Updgrade and Alcator C-Mod [124, 127] a scaling law for λ_q has been selected for H-mode operation:

$$\lambda_q[\text{mm}] = (0.73 \pm 0.38) \cdot B_t^{-0.78\pm0.25}\, q_{cyl}^{1.20\pm0.27}\, P_{sep}^{0.10\pm0.11}\, R_0^{0.02\pm0.20}, \tag{3.73}$$

where B_t [T] is the toroidal field at plasma axis, q_{cyl} is the cylindrical safety factor, P_{sep} [MW] is the conducted power in the SOL and R_0 [m] is the plasma major radius. The dependency on R_0, which does not have large effect on λ_q, emphasizes the intrinsic meaning of using the divertor challenge quantifier P_{sep}/R_0 as a constraining condition for core plasma design and for divertor protection purposes. The calculation of $A_{wet,k}$ goes through λ_q and through the *integral power decay length* λ_{int}, relating the total deposited power to the peak heat load. The linear scaling found by T. Eich [127] links λ_q to λ_{int} and yields:

$$\lambda_{int}[\text{mm}] = \frac{\int (\Gamma(\bar{s}) - \Gamma_{BG})\mathrm{d}\bar{s}}{\Gamma_{\max}} \approx \lambda_q + 1.64 \cdot S. \tag{3.74}$$

This is adopted in MIRA. Taking B_p and B for toroidally symmetric poloidal divertor targets, the ratio B_p/B along a SOL flux tube can feature large variations. These must be taken into account for the calculation of the plasma wetted area on divertor targets[58]. For instance, at the outboard midplane $B_p/B \sim 1/3$, while near the X-point, by definition, $B_p/B \to 0$. Near the targets, the wetted area is less elongated than near X-point but still more so than at the midplane. Therefore, in order to assess the expansion of magnetic flux tube $f_{x,k}$ detailed information on the magnetic field distribution are necessary. Subdividing between inboard and outboard plates, i.e. $k = i/o$, $f_{x,k}$ pertains to the poloidal and the total magnetic fields, B_p and B on the k mid-equatorial plane point P_k and on the strike point S_k of the divertor target k, such that [58]

$$f_{x,k} = \frac{B_{p,\mathrm{P_k}}/B_{\mathrm{P_k}}}{B_{p,\mathrm{S_k}}/B_{\mathrm{S_k}}} \qquad k = i/o. \tag{3.75}$$

The radial and vertical coordinates of P_k and S_k are obtained from the plasma and divertor geometry modules. The magnetic field on both inner and outer plasma and divertor locations can be calculated using the full magnetic configuration model integrated in MIRA (see Section 4.2).
Finally, considering the effects of the field line inclination angle β_k on the target plates, the wetted area $A_{wet,k}$ linked to the conducted transport power $P_{con,k}$ can be written as:

$$A_{wet,k} = \frac{2\pi r_{S,k} \cdot \lambda_{int} \cdot f_{x,k}}{\sin \beta_k} \qquad k = i/o, \tag{3.76}$$

and the peak flux on the k target plate $\Gamma_{\perp,\max}^{tot,div/k}$ is derived combining Equations (3.67), (3.68) and (3.76), reading to:

$$\Gamma_{\perp,\max}^{tot,div/k} = P_{sep} \left(\frac{f_{sep,k} \cdot (1 - f_{rad}) \cdot \sin \beta_k}{2\pi r_{S,k} \cdot \lambda_{int} \cdot f_{x,k}} + \frac{f_{sep,k} \cdot f_{rad}}{2\pi r_{S,k} \cdot l_{t,k}} \right) + \Gamma_{\perp,\max}^{\gamma,div/k}, \quad k = i/o, \tag{3.77}$$

where $\Gamma_{\perp,\max}^{\gamma,div/k}$ is the peak heat load due to core photon radiation onto k divertor target (outlined in Equation (4.17)).

The model in MIRA offers a general method to evaluate the peak heat flux on the divertor targets, connecting the plasma and divertor physics to the engineering divertor parameters. In the former category we find the power transported across the separatrix P_{sep} and the radiative power fraction f_{rad}. In the latter, the vertical targets geometrical parameters, including the field line inclination angles β_k and the flux expansion factor $f_{x,k}$. High radiation fraction $f_{rad} \approx 0.8 - 0.9$ are necessary for DEMO divertor scenario to comply with the 10 MW/m^2 heat load technological limit [122], relying on a partially detached divertor configuration. Questions on whether this is achievable in terms of physics and engineering keep arising nowadays [122] considering also that the full detached divertor cannot guarantee a completely safe plasma operation, i.e. with no core radiation cooling, and that the available modelling cannot provide fully predictive capabilities yet [122].

While keeping a simplified modelling approach, compared to more elaborated two-point models [66], the improvements are the more refined geometric representation and the three-dimensional external magnetic configuration model. Unlike the SYCOMORE code, where a built-in divertor load module is available, the expansion factor $f_{x,k}$ can be assessed making use of a calculated magnetic profile and not being specified by the user. Currently, one can already scope diverse divertor design solutions, for instance orienting the targets with different values of β_k or $l_{t,k}$ and adapting the shape of the blanket and of the other core reactor components. However, a more refined SOL and divertor physics modelling basis should be addressed to have a more elaborated simulation of the key target processes, including erosion and sputtering, detachment physics and surface recombination of charged particles on solid divertor surfaces.

Further modelling efforts should be also dedicated to the evaluation of the radiative dissipation of transport loss, mostly to assess the detachment regime conditions and reduce the uncertainties in the power radiative factor f_{rad}. Considering the rather complete and highly flexible environment, even a two-dimensional SOL and divertor physics model, e.g. derived from the TOKES simulation code [104], can be positively admitted for integration in MIRA. In this manner, the approach could be in principle extended to the blanket first wall, such that poloidal shape and segmentation could be consistently adapted.

4. Engineering Modelling of an Advanced FPP System Code

Currently, large efforts are devoted to plasma confinement regimes, which are considered as major challenge to prove fusion as energy source. Even if these aspects will be clarified through ITER, a FPP aims at producing electricity from fusion energy in a viable and economical way. The successful outcome is bound to the engineering feasibility of the major components and systems, from magnets technology to plant integration. In this chapter the main technology aspects are investigated by dedicated modelling parts, integrated in MIRA. In appearance order, these include reactor neutronics, superconducting magnets, temporal description of full pulsed reactor cycle and plant power balance.

4.1. A neutron/gamma radiation transport model of core reactor components

The spatial mapping of neutrons and gamma rays over the physical components surrounding the plasma is necessary for their nuclear design. The design targets and operational limits posed on tritium breeding, energy deposition and neutron radiation shielding must be fulfilled through the engineering design of the system. Within the MIRA modelling activities large efforts have been devoted to the development of a neutron-gamma transport model for tokamak configurations. In particular, this consists of two main sub-modules:

- a two-dimensional transport across the void plasma chamber and
- a one-dimensional model for the radial streaming of neutron and gamma rays across the core reactor components.

The logics of such a decoupling as well as the details of both models are explained subsequently.

4.1.1. Radiation transport in curvilinear coordinate system

The equation governing the transport of neutron and gamma radiations as they pass through materials is given by the Boltzmann transport equation (BTE), which represents a balance of particle gains and losses within a macroscopic incremental volume $\mathrm{d}\mathbf{r}$ about the point $\mathbf{r}$, with incremental energy $\mathrm{d}E$ about energy E and with direction within incremental solid angle $\mathrm{d}\mathbf{\Omega}$ about direction $\mathbf{\Omega}$. The steady state reads as [129]:

$$\begin{aligned}\left[\mathbf{\Omega}\cdot\nabla+\Sigma_t\left(\mathbf{r},E\right)\right]\psi\left(\mathbf{r},\mathbf{\Omega},E\right) &= q\left(\mathbf{r},\mathbf{\Omega},E\right)\\ &= q_{ex}\left(\mathbf{r},\mathbf{\Omega},E\right)+\int \mathrm{d}E'\int \mathrm{d}\mathbf{\Omega}'\Sigma_s(\mathbf{r},\mathbf{\Omega}'\cdot\mathbf{\Omega},E'\rightarrow E)\psi\left(\mathbf{r},\mathbf{\Omega}',E'\right),\end{aligned} \tag{4.1}$$

where the solution is given by the function $\psi\left(\mathbf{r},\mathbf{\Omega},E\right)$, denoting the angular flux density. The first term of the left-hand side (LHS) outlines the streaming term, identifying the particles with energy E

and direction $\mathbf{\Omega}$ leaving the incremental volume $\mathrm{d}\mathbf{r}$ about point $\mathbf{r}$. The second term encompasses all the nuclear interactions of the particles with the bulk material nucleus and that can alter their energy and direction, including scattering, adsorption and multiplication. The total macroscopic nuclear cross section $\Sigma_t(\mathbf{r}, E)$ is defined as a material-related parameter depending on the particle energy. The right-hand side (RHS) indicates the particle source term $q(\mathbf{r}, \mathbf{\Omega}, E)$ comprising of the external volumetric source q_{ex} and the integral source of particles in $\mathrm{d}E\mathrm{d}\mathbf{\Omega}$. This is primarily associated with the inelastic and elastic scattering, with Σ_s identifying the differential macroscopic scattering cross section.
In general, a macroscopic cross section function Σ_x [cm^{-1}] of the x nuclear interaction is obtained by multiplying the microscopic cross section $\sigma_{x,i}$ [barn*] to the $i-$th isotope atom density $n_i(\mathbf{r})$ [barn^{-1} cm^{-1}], such that:

$$\Sigma_x(\mathbf{r}, E, \mathbf{\Omega}) = \sum_i n_i(\mathbf{r}) \cdot \sigma_{x,i}(E, \mathbf{\Omega}). \tag{4.2}$$

The atomic density n_i can be derived from the macroscopic material composition of the matter where particles travel through, while the microscopic cross sections are measured nuclear data and are provided in tabulated data files. The particle phase space of the BTE reads as:

$$\mathcal{X} := \left\{ (\mathbf{r}, \mathbf{\Omega}, E) : \mathbf{r} \in \mathcal{D} \subset \mathbb{R}^3, \mathbf{\Omega} \in \mathcal{S}_2, E \in [0, \infty] \right\}, \tag{4.3}$$

and its inflow boundary subsets

$$\partial\mathcal{X}_- := \left\{ (\mathbf{r}, \mathbf{\Omega}, E) \in \partial\mathcal{D} \times \mathcal{S}_2 \times [0, \infty] \text{, s.t. } \mathbf{\Omega} \cdot \mathbf{n}(\mathbf{r}) < 0 \right\}. \tag{4.4}$$

$\mathcal{D}$ is the volume domain bounded by the boundary $\partial\mathcal{D}$, oriented at each point $r \in \mathcal{D}$ by its unit outward normal field $\mathbf{n}(\mathbf{r})$. $\mathcal{S}_2$ is the unit sphere upon which the angular coordinate $\mathbf{\Omega}$ represents the angular direction of particles. The incoming boundary condition used for neutron and gamma transport problems addressed in this work is defined as

$$\psi(\mathbf{r}, \mathbf{\Omega}, E)|_{\partial\mathcal{X}_-} = \psi_{in}, \tag{4.5}$$

where ψ_{in} is a known function. In case of $\psi_{in} = 0$ it corresponds to the so-called *vacuum boundary conditions*.

The angular flux is rarely used for most purposes and serves only as starting point for calculating two scalar and vectorial fields, widely applied to nuclear applications. These are the *scalar flux*

$$\phi(\mathbf{r}, E) = \int_{\mathcal{S}_2} \psi(\mathbf{r}, \mathbf{\Omega}, E)\mathrm{d}\mathbf{\Omega}, \tag{4.6}$$

and the *current vector*

$$\mathbf{J}(\mathbf{r}, E) = \int_{\mathcal{S}_2} \mathbf{\Omega}\psi(\mathbf{r}, \mathbf{\Omega}, E)\mathrm{d}\mathbf{\Omega}. \tag{4.7}$$

The scalar flux is elaborated to calculate the *local reaction rate* $\mathcal{R}_x$

$$\mathcal{R}_x(\mathbf{r}) = \sum_i n_i(\mathbf{r}) \int_0^\infty \sigma_{x,i}(E)\phi(\mathbf{r}, E)\mathrm{d}E. \tag{4.8}$$

*1 barn = 10^{-24} cm^2

The *global reaction rate* R_x is then obtained by space integration, such that

$$R_x = \int_{\mathcal{D}} \mathcal{R}_x(\mathbf{r}) \mathrm{d}\mathbf{r}. \tag{4.9}$$

The reaction rate can be associated with any secondary particle generation rate, such as breeding tritium atoms in lithium-containing blanket materials, as well as to the energy deposition. The current vector is utilized for boundary crossing purposes. Say, a boundary $\partial\mathcal{D}$ is subject to a current vector $\mathbf{J}$, then the *net current*

$$J_n(\mathbf{r}, E) \equiv \mathbf{n} \cdot \mathbf{J}(\mathbf{r}, E) = \int_{\mathcal{S}_2} \mathbf{n} \cdot \mathbf{\Omega} \psi(\mathbf{r}, \mathbf{\Omega}, E) \mathrm{d}\mathbf{\Omega}, \tag{4.10}$$

indicates the net number of particles per unit area per unit time per unit energy crossing the boundary $\partial\mathcal{D}$ on $\mathbf{r}$, in the positive normal direction of $\mathbf{n}$. Upon this formulation relies the wall loading definition used to estimate the heat fluxes associated with plasma neutrons and gamma rays.

In deterministic transport codes the solution of the BTE is addressed by a multigroup approximation for the energy variable E [129]. This theory splits the whole energy domain $E \in [E_G, E_0]$ into a number N_G of non necessarily-equally spaced intervals. Typically, $E_G = 0$ or around the thermal neutron spectrum $E_G \leq 0.025$ eV. E_0 is large enough to include all the neutron energy values, for fusion applications, not below 14.1 MeV. Accordingly, the energy dependence of the BTE can be removed and Equation (4.1) is solved group-wise for the angular flux $\psi_g(\mathbf{r}, \mathbf{\Omega})$ of the $g-$th energy group $E \in [E_g, E_{g-1}]$, sorted in descendent order as the group index g increases. With such an approximation, the average scalar flux $\Phi_g(\mathbf{r})$ becomes,

$$\Phi_g(\mathbf{r}) = \int_{E_g}^{E_{g-1}} \phi(\mathbf{r}, E) \mathrm{d}E, \tag{4.11}$$

which leads to two important definitions of spectrum-averaged scalar flux, widely adopted in fusion neutronics. These are the *total scalar neutron flux density* Φ_{tot}, covering the whole energy spectrum and the *fast scalar neutron flux density* Φ_{fast}, respectively defined as:

$$\begin{aligned} \Phi_{fast}(\mathbf{r}) &= \int_{E_{fast}}^{E_0} \phi(\mathbf{r}, E) \mathrm{d}E, \\ \Phi_{tot}(\mathbf{r}) &= \int_{E_G}^{E_0} \phi(\mathbf{r}, E) \mathrm{d}E, \end{aligned} \tag{4.12}$$

where $E_{fast} = 0.1$ MeV [130, 131]. In a multigroup energy spectrum, these scalar quantities are obtained by summing over the energy group g, pertaining to the selected energy range.

Unlike the Cartesian coordinate systems, the angles specifying the angular flux do change as the neutrons travel in curvilinear coordinates [129]. This phenomenon, known as angular redistribution, makes the mathematical treatment of the streaming operator more elaborated, as angular derivatives are needed for its description. According to the reference space-angle system, $\hat{e}_z$ represents the polar axis, $\cos^{-1}\xi$ the polar angle and the azimuthal angle is measured from the positive r axis. The angular variable $\mathbf{\Omega}$ can be expressed in terms of μ and η or ξ and ω, with the condition of symmetry on the emission density at $\omega = 0$, i.e. $\psi(r, z, \xi, \omega, E) = \psi(r, z, \xi, -\omega, E)$.

A widely deployed technique in many deterministic transport codes to treat the angular dependency of ψ is the *discrete ordinate approximation*, also called S_N method. Accordingly, for a given order N, the BTE is solved only for a distinct number $K(N)$ of angles Ω_n and can be decoupled into an equivalent number of partial differential equations on the spatial coordinates. The solution has the form of $\psi_n^g(r,z)$, with $n = 1,2,...,K(N)$ being the index associated with the $n-$th angular directions. In curvilinear configurations, due to the angular redistribution, applying the discrete ordinate approximation requires the handling of the streaming operator $\mathbf{\Omega}\cdot\nabla$. Leaving the details of the full description to Appendix D.3, the BTE in (r,z) curvilinear coordinate is decomposed for $K(N)$ ordinates such that [129]:

$$\begin{aligned}\left[\frac{\mu_{pq}}{r}\frac{\partial}{\partial r}r+\frac{2\alpha^p_{q+1/2}}{r\,w_{pq}}+\xi_p\frac{\partial}{\partial z}+\Sigma_t^g(r,z)\right]\psi^g_{pq}(r,z)\\ -\frac{(\alpha^p_{q+1/2}+\alpha^p_{q-1/2})}{r\,w_{pq}}\psi^g_{p,q-1/2}(r,z)=q^g_{pq}(r,z)\end{aligned}\tag{4.13}$$

where $\alpha^p_{q+1/2}$ and $\alpha^p_{q-1/2}$ denote two angular differencing coefficients, associated with the ordinate $\mathbf{\Omega}_{pq}=\left[\mu_{pq},\xi_p\right]$. The formalism proposed by E.E. Lewis et al. [129] has been adopted to map the angular ordinates ordering system. In curvilinear geometry $K(N)=N(N+2)/4$ [129] and the index of the n-th ordinate $\mathbf{\Omega}_n\equiv\mathbf{\Omega}_{pq}$ is replaced by two complementary indexes pq. The first one indicates the value ξ_p associated to $\mathbf{\Omega_{pq}}$, having $\xi_1<\xi_2<...<\xi_N$. The index q refers to the value of μ associated with ξ_p. Therefore, for a fixed value of ξ_p a set of μ values is deduced, such that $\mu_{p1}<\mu_{p2}<...<\mu_{pN_p}$, where $1<N_p<N$. Taking the step differencing approximation $\psi^g_{p,1/2}(r,z)\approx\psi^g_{p,1}(r,z)$, Equation (4.13), for $q=1$, then becomes:

$$\left[\frac{\mu_{p,1}}{r}\frac{\partial}{\partial r}r+\frac{\alpha^p_{3/2}-\alpha^p_{1/2}}{r\,w_{p1}}+\xi_p\frac{\partial}{\partial z}+\Sigma_t^g(r,z)\right]\psi^g_{p,1}(r,z)=q^g_{p,1}(r,z).\tag{4.14}$$

If the angular flux distribution $\psi_{pq}(r,z)$ is known for all the $K(N)=N(N+2)/2$ ordinates, the scalar flux Φ, radial net current J_r and axial net current J_z are calculated by using a quadrature formula, applying the definition of Equations (4.6) and (4.7), with

$$\begin{aligned}\Phi(r,z)&=\frac{1}{4}\sum_{pq}^{K(N)}w_{pq}\,\psi_{pq}(r,z),\\ J_r(r,z)&=\frac{1}{4}\sum_{pq}^{K(N)}w_{pq}\mu_{pq}\,\psi_{pq}(r,z),\\ J_z(r,z)&=\frac{1}{4}\sum_{pq}^{K(N)}w_{pq}\xi_p\,\psi_{pq}(r,z).\end{aligned}\tag{4.15}$$

The weight of the quadrature formula associated with the ordinate $\mathbf{\Omega}_{pq}$ is denoted by the coefficient w_{pq}. In 2D problems Equations (4.13) and (4.14) are solved on four octants for $K(N)=N(N+2)/4$ angular directions $\mathbf{\Omega}_{pq}$, whereas in 1D cylindrical coordinates, the dependences on z and ξ are no longer present. Due to the mirroring condition to the plane perpendicular to the z axis [129], $\psi(r,\mu,\xi)=\psi(r,\mu,-\xi)$, in 1D geometry Equations (4.13) and (4.14) are solved for $K(N)=N(N+2)/8$ angular directions on two octants: $\mu<0,\xi>0$ and $\mu>0$ and $\xi>0$.

A more comprehensive outline on the fundamentals on radiation transport theory is provided in Appendix D.

4.1.2. Neutron/Gamma Radiation Transport Model of the Void Plasma Chamber

A two dimensional modelling methodology for the simulation of neutron and core radiation streaming across the plasma vacuum chamber offers diverse profits. The use of such a transport model aims for a better mapping of neutron and radiation power fluxes onto surrounding plasma facing components, as well as a more robust coupling to the neutron transport model for core reactor components. As depicted in Figure 4.1, the boundary $\partial\mathcal{D}$ of the plasma vacuum chamber domain $\mathcal{D}$, splits into three distinct portions: inboard and outboard blanket FW, $\partial\mathcal{D}_{fw,ib/ob}$ and divertor $\partial\mathcal{D}_{div}$. Subdividing into neutron and photon radiation loading, the generic power flow P_j^k attributed to the volumetric source k onto the boundary portion j can be expressed as follows

$$P_j^k = \int_{\partial\mathcal{D}_j} \left(n_r(r,z) J_r^k(r,z) + n_z(r,z) J_z^k(r,z) \right) 2\pi r \mathrm{d}\ell, \text{ with } \begin{cases} k = n, \gamma \\ j = fw/ib, fw/ob, div. \end{cases} \tag{4.16}$$

J_r^k and J_z^k relate to the radial and vertical the net currents (Equation 4.10) and are derived from the solution to the transport problem of Equation (4.1) for the volumetric source k, i.e. $q_{ex} \equiv q_k$. Both neutron and radiation volumetric sources are derived from the core plasma physics module, with q_{neut} and q_{rad} formulated in Equations (3.44) and (3.55).

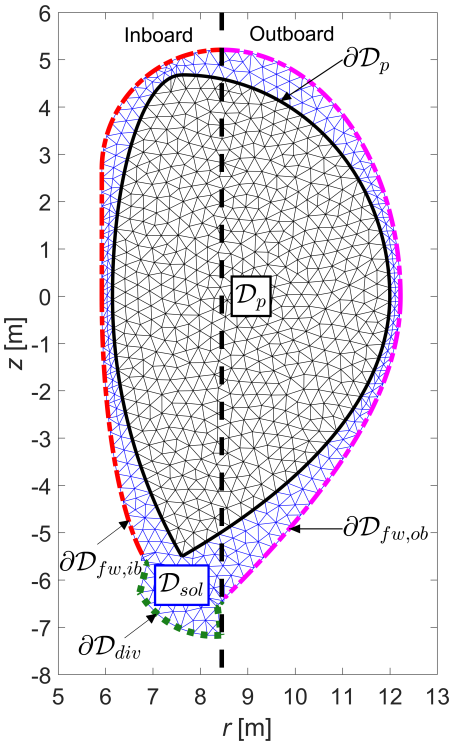

Figure 4.1.: Graphical representation of void plasma chamber domain used for the core neutron and photon transport model. The cross-sectional domain $\mathcal{D}$ is obtained from the union of plasma and SOL domains derived from the DEMO 2015 design. The boundary $\partial\mathcal{D}$, from the inboard and outboard blanket FW and the inner divertor profile.

Figure 4.2 shows a typical formalism adopted in fusion neutronics [130] to map the poloidal profile of the wall loading $\Gamma_\perp^k(\alpha_w)$. That identifies the oriented net current $\mathbf{n} \cdot \mathbf{J}$ over the surface of

the wall boundary portion $\partial\mathcal{D}_w$, such that

$$\Gamma_{\perp}^{k,w} \equiv \Gamma_{\perp}^{k}(\alpha_w)\Big|_{\partial\mathcal{D}_w} = \frac{\int_{\partial\mathcal{D}_w}\left(n_r(r,z)J_r^k(r,z)+n_z(r,z)J_z^k(r,z)\right)2\pi r\mathrm{d}\ell}{\int_{\partial\mathcal{D}_w}2\pi r\mathrm{d}\ell} \quad \text{with } k=n,\gamma \tag{4.17}$$

where $\partial\mathcal{D}_w \subset \partial\mathcal{D}$ is delimited by two increasing poloidal angles $\alpha_{w,i}$ and $\alpha_{w,i+1}$. The angular variable α_w is postulated as the rotation angle, counter-clockwise from the mid-plane,

$$\alpha_w(r,z) = \begin{cases} \tan^{-1}\left(\frac{z}{r-R_0}\right), & \text{for } z \geq 0 \\ \tan^{-1}\left(\frac{z}{r-R_0}\right)+2\pi, & \text{for } z < 0 \end{cases} \quad \forall (r,z) \in \partial\mathcal{D}, \tag{4.18}$$

with R_0 denoting the radial coordinate of the plasma center and $0 \leq \alpha_w \leq 2\pi$.
When discretizing the domain $\mathcal{D}$ by a triangular mesh $\mathcal{T}_h$ (see Figure 4.1) the smallest wall unit $\partial\mathcal{D}_w$, upon which $\Gamma_{\perp}^{k}$ can be assessed, is characterized by any mesh edge on the boundary $\partial\mathcal{D}$.

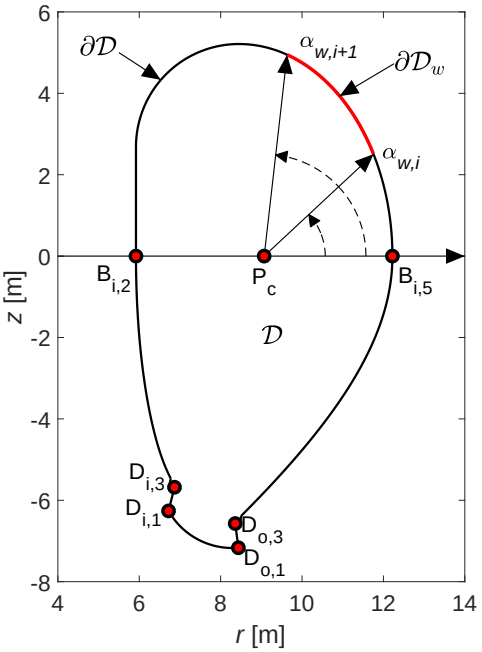

Figure 4.2.: Schematic view of the plasma chamber $\mathcal{D}$, illustrating the variable terminology adopted for assessing the distribution of the wall loading $\Gamma_{\perp}^{k}(\alpha_w)$, with $k=n,\gamma$, onto a certain portion $\partial\mathcal{D}_w$ of the whole wall boundary $\partial\mathcal{D}$. $\partial\mathcal{D}_w$ is identified by two increasing coordinate of the poloidal angle α_w, i.e. $\alpha_{w,i}$ and $\alpha_{w,i+1}$.

The poloidal profile $\Gamma_{\perp}^{k}(\alpha_w)$ is defined piecewise on a set of poloidal wall portions $\partial\mathcal{D}_w$, each represented by a specified incremental angle $\delta\alpha_w$, such that $\alpha_{w,i+1} = \alpha_{w,i} + \delta\alpha_w$.
Predicting the poloidal mapping of the energy flows onto plasma facing components provides a tool to identify the most sensitive spots, as e.g. the peak heat fluxes. The evaluation of the peak heat fluxes is important for plasma surrounding components material to guarantee their structural integrity as well as a proper cooling. Since neutrons travel across the bulk of the materials surrounding the plasma there is no evident limitation for the neutron wall loads but rather for the material damage due to chronic neutron irradiation. On the contrary, this applies to peak radiation wall loadings

on inboard and outboard FW $\Gamma^{\gamma,fw/ib}_{\perp,\max}$ and $\Gamma^{\gamma,fw/ob}_{\perp,\max}$, which shall be kept below an upper limit of 1 MW/m^2 [73, 132].

The so-called *peaking factor* $\chi_{k,j}$ connected to the particle flow k and onto boundary wall element j relates the peak flux $\Gamma^{k,j}_{\perp,\max}$ to the average flux $\Gamma^{k,j}_{\perp,av}$,

$$\chi_{k,j} \equiv \chi_k|_{\partial\mathcal{D}_j} = \frac{\Gamma^{k,j}_{\perp,\max}}{\Gamma^{k,j}_{\perp,av}}, \text{ with } \begin{cases} k = n,\gamma \\ j = fw/ib, fw/ob, div \end{cases}, \tag{4.19}$$

where $\Gamma^{k,j}_{\perp,av}$ is calculated using Equation (4.17) with $\partial\mathcal{D}_j \equiv \partial\mathcal{D}_w$. As illustrated in Figure 4.2 several points poloidally located on the blanket and divertor targets walls are important to assess the peak heat fluxes. Points $\mathrm{B_{i,5}}$ and $\mathrm{B_{i,2}}$, derived from the blanket geometry module, denote the outboard and the inboard FW locations on the mid-equatorial planes, where the peak heat fluxes are expected. Moreover, these two spots are used to sample the angular distribution of angular neutron flux density $\psi(r,\mu)$ for the 1D core reactor neutron transport model, elucidated in Section 4.1.3. As for the divertor wall portion $\partial\mathcal{D}_{div}$, the heat fluxes pertaining to both neutron and photon core radiations are based on the poloidal profile of $\Gamma^k_\perp(\alpha_w)$, separately calculated mesh element-wise for the inboard target $\partial\mathcal{D}_{div,ib}$ in segment $\overline{\mathrm{D_{i,3}D_{i,1}}}$, inner cassette $\partial\mathcal{D}_{div,cass}$ in curve $\overset{\frown}{\mathrm{D_{i,1}D_{o,1}}}$ and outboard target $\partial\mathcal{D}_{div,ob}$ in segment $\overline{\mathrm{D_{o,1}D_{o,3}}}$. Additionally, $\Gamma^{\gamma,\mathrm{div/j}}_{\perp,\max}$, with $j = ib, ob$, must be included in Equation (3.77) for the characterization of the total peak heat flux on the divertor plates.

To solve the transport problem for the simulation of neutron and photon particle streaming across the plasma chamber, some simplifying assumptions are made:

- The domain $\mathcal{D}$ is characterized by the union of the plasma included in the core and SOL regions, surrounded by the blanket first wall and the divertor profile facing the plasma, i.e. comprising of targets, baffles and dome, if any. The BTE for its general steady state form can be solved in the reference curvilinear coordinates $\mathbf{r} = \mathbf{r}(r,z)$, becoming Equation (4.13).
- The plasma core and SOL regions are treated as void gaps, i.e. $n(r,z) = 0$ and $\sigma_t = \sigma_s = 0$). Henceforth, after emission, particles travel in free path to the boundary without altering energy and direction.
- The high energy neutrons and photons can be treated as monoenergetic particles, thus, the energy can be removed from the phase space $\mathcal{X}$. Accordingly, $\psi(r,z,\mathbf{\Omega},E) \equiv \psi(r,z,\mathbf{\Omega})$.
- Neutron and gamma particles are isotropically generated inside the core plasma region, therefore $q(r,z,\mathbf{\Omega},E) \equiv q_{ex}(r,z)$.

Even upon discrete ordinate approximation, a spatial discretization is necessary to solve the two-dimensional BTE numerically, as no direct analytical solution exists for complex arbitrary geometries. Relying already on a finite element PDE solving frame leads to explore PDE solution techniques where the transport polygonal convex domain $\mathcal{D} \subset \mathbb{R}^2$ is approximated by a general, unstructured and quasi-uniform triangular mesh $\mathcal{T}_h$. The mesh size h pertains to its refinement, or coarseness. The problem results into solving the BTE for monoenergetic particles in vacuum media for a generic direction $\mathbf{\Omega}_{pq} = \left[\mu_{pq}, \xi_p\right]$ and in the reference spatial coordinates $\mathbf{r} = (r,z)$. Mathematically, it becomes

$$\begin{cases} \mathbf{\Omega}_{pq} \cdot \nabla\psi_{pq}(r,z) = q_{pq}(r,z), & \text{in } \mathcal{D} \\ \psi_{pq}(r,z) = 0 & \text{on } \partial\mathcal{D}_- \end{cases}, \tag{4.20}$$

where q_{pq} relates to the neutron or photon volumetric source and $\partial\mathcal{D}_- = \{\mathbf{r} \in \partial\mathcal{D} \text{ s.t. } \Omega_{pq} \cdot \mathbf{n} < 0\}$ is the inflow boundary, on which a vacuum boundary condition is imposed. In reference (r,z) curvilinear coordinate system $\mathbf{n}(r,z) = [n_r(r,z), n_z(r,z)]$ defines the outgoing normal versor on $\partial\mathcal{D}$. Problem (4.20) has the form of a convection equation and is a linear first-order hyperbolic PDE. For its numerical solution via FEM, the so-called *discontinuous Galerkin method* (DGM) has been deployed to solve neutron transport problems[133]. It has been shown to provide numerous advantages compared to continuous finite elements, such as the possibility to capture the discontinuities and instabilities which may occur in hyperbolic transport conservation laws [134, 135, 136]. Henceforth, the DGM makes use of the discontinuous finite elements space $\mathcal{W}_h$. It pertains to a quasi-uniform mesh $\mathcal{T}_h$, characterized by n_t mesh cells T_K, each featuring the set of boundary edge ∂T_k. Accordingly, the polynomial basis functions of order lower or equal than r are not required to be globally continuous. Solving Problem (4.20) according to the DGM formalism can be formulated as:

$$\text{find } \psi_h^{pq} \in \mathcal{W}_h \text{ such that} a(\psi_h^{pq}, v_h) = \ell(v_h) \quad \forall v_h \in \mathcal{W}_h, \tag{4.21}$$

where $a(u,v)$ is the bilinear form [136]:

$$\begin{aligned} a(u,v) = &\int_{\mathcal{T}_h} \left(\boldsymbol{\Omega_{pq}} \cdot \nabla u\right) v \, \mathrm{d}\mathbf{r} \\ &+ \sum_{T_k \in \mathcal{T}_h} \sum_{e \in \partial T_k} \int_e \mathcal{H}(u, \boldsymbol{\Omega_{pq}}, \mathbf{n}_k) v \, \mathrm{d}S - \int_{\mathcal{D}_-} |\boldsymbol{\Omega_{pq}} \cdot \mathbf{n}| u \, v \, \mathrm{d}S, \end{aligned} \tag{4.22}$$

and $\ell(v)$ is the linear form,

$$\ell(v) = \int_{\mathcal{T}_h} q_{pq} v \, \mathrm{d}\mathbf{r}, \tag{4.23}$$

of its weak formulation. The *upwind numerical flux* $\mathcal{H}$ is an operator associated with any function $u_h \in \mathcal{W}_h$ and defined on every edge e connecting two mesh elements T_k^+ and T_k^- and with outgoing normal $\mathbf{n}_k$, such that $e = T_k^- \cap T_k^+$. A. Ern and J.-L. Guermond [136] have postulated a general mathematical form valid for each edge e and consistent with the bilinear form of Equation (4.22). It yields:

$$\mathcal{H}(u, \boldsymbol{\Omega_{pq}}, \mathbf{n}_k) = \left(\alpha |\boldsymbol{\Omega_{pq}} \cdot \mathbf{n}_k| - \frac{1}{2} \boldsymbol{\Omega_{pq}} \cdot \mathbf{n}_k\right) [\![u]\!], \tag{4.24}$$

with $[\![u]\!]$ being the *jump* of u across e,

$$[\![u]\!] = u^+ - u^- \tag{4.25}$$

and $u^\pm$ denoting the inflow and outflow *traces* $u|_e$ taken from T_k^+ and T_k^-. This technique ensures coercivity and stability to the solution of Equation (4.21), being a prerequisite for DGMs [136]. The key aspect resides on the jump operator $[\![u]\!]$, which allows to exploit discontinuities across the mesh edges to build an upwind solving scheme and ensure local conservation properties [137]. Note that, due to the vacuum boundary condition of Equation (4.20), the last integral term of Equation (4.22) has to be omitted for solving the mentioned radiation streaming problem. Moreover, the parameter α has received considerable attention in the literature [137]. Working with the specific value $\alpha = \frac{1}{2}$ advocates the aforementioned upwind flux, thus selected for this transport situation. By default, the approximated solution ψ_h^{pq} of all particle transport problems addressed in MIRA analyses is sought in piecewise linear discontinuous finite element space $\mathcal{W}_h$ with polynomial basis functions order $r = 1$. However, quadratic elements can be also specified.

Extracting the streaming operator $\mathbf{\Omega_{pq}} \cdot \nabla$ from Equations (4.13) and (4.14), a bilinear form can be derived for the situations with $q = 1$ and $q > 1$, expressed in reference curvilinear (r, z) geometry and for the set of S_N discrete ordinate $\mathbf{\Omega_{pq}} = [\mu_{pq}, \xi_q]$. Accordingly, the infinitesimal volume and surface can be recast into $\mathrm{d}\mathbf{r} = 2\pi r \mathrm{d}r\mathrm{d}z$ and $\mathrm{d}S = 2\pi r \mathrm{d}\ell$, where $\mathrm{d}\ell$ defines the oriented coordinate along a generic edge e. Hence, for any $p = 1, ...N$ and $\forall q > 1$ the bilinear and linear form $a_{pq}(u, v)$ and $\ell_{pq}(v)$ read as

$$\begin{aligned} a_{pq}(u,v) = \int_{\mathcal{T}_h} \left[\left(\frac{\mu_{pq}}{r} \frac{\partial}{\partial r} r + \frac{2\alpha^p_{q+1/2}}{r\, w_{pq}} + \xi_p \frac{\partial}{\partial z} \right) u \right] v \, r\mathrm{d}r\mathrm{d}z \\ + \sum_{T_k \in \mathcal{T}_h} \sum_{e \in \partial T_k} \int_e \mathcal{H}(u, \mathbf{\Omega_{pq}}, \mathbf{n}_k) v \, r\mathrm{d}\ell, \end{aligned} \tag{4.26}$$

and

$$\ell_{pq}(v) = \int_{\mathcal{T}_h} \left(q_{pq}(r,z) + \frac{\alpha^p_{q+1/2} + \alpha^p_{q-1/2}}{r\, w_{pq}} \psi_{p,q-1/2}(r,z) \right) v \, r\mathrm{d}r\mathrm{d}z, \tag{4.27}$$

while for $q = 1$ and $\forall p \leq N$:

$$\begin{aligned} a_{p,1}(u,v) = \int_{\mathcal{T}_h} \left[\left(\frac{\mu_{p,1}}{r} \frac{\partial}{\partial r} r + \frac{\alpha^p_{3/2} - \alpha^p_{1/2}}{r\, w_{p,1}} + \xi_p \frac{\partial}{\partial z} \right) u \right] v \, r\mathrm{d}r\mathrm{d}z \\ + \sum_{T_k \in \mathcal{T}_h} \sum_{e \in \partial T_k} \int_e \mathcal{H}(u, \mathbf{\Omega_{pq}}, \mathbf{n}_k) v \, r\mathrm{d}\ell \end{aligned} \tag{4.28}$$

and,

$$\ell_{p,1}(v) = \int_{\mathcal{T}_h} q_{p,1}(r,z) v \, r\mathrm{d}r\mathrm{d}z. \tag{4.29}$$

The approximated solution $\psi^{pq}_h \approx \psi_{pq}$ in the discontinuous finite element space $\mathcal{W}_h$, consists of:

$$\text{find } \psi^{pq}_h \in \mathcal{W}_h(\mathcal{T}_h) \text{ such that } \begin{cases} a_{p,1}(\psi^{pq}_h, v_h) = \ell_{p,1}(v_h) & \text{for } q = 1 \\ a_{pq}(\psi^{pq}_h, v_h) = \ell_{pq}(v_h) & \text{for } q > 1 \end{cases} \quad \forall v_h \in \mathcal{W}_h. \tag{4.30}$$

Equations (4.26) to (4.29) are implemented in `Freefem++`, featuring dedicated built-in functions to handle discontinuous finite elements, such as `jump`. `Freefem++` progressively solves the same weak formulation of Problem (4.30) for increasing p and q indexes, and, for diverse values of μ_{pq}, ξ_p, $\alpha^p_{q\pm1/2}$ and $\psi_{p,q-1/2}$. For all Ψ^{pq}_h angular flux distribution the radial and the axial net currents J_r and J_z, are obtained by applying the quadrature formula of Equation (D.26). As a result, the total radiation power on $\partial\mathcal{D}$ and the net wall loading profiles (Equations 4.16 and 4.17) can be assessed.

S_N and DG finite element approximations are largely deployed among many transport codes, such as TRIDENT [138] and FEMRZ [139]. For these numerical methods the available literature and the related solution techniques have been proven well-known and easily reproducible. The handling of the two-dimensional distributions of radial and vertical current J_r and J_z in a finite element environment makes the definition of integral parameters straightforward and simultaneously precise. Canonical zero-dimensional systems codes evaluates only average wall neutron and photon

wall loadings, omitting the possibility to detect the most stressed plasma surrounding regions and, possibly, to re-adapt the shape of the FW and divertor.
The crucial aspects for S_N solution methods are given by the quadrature order N and by the mesh spacing size h. Details are reported in Appendix E.2.

4.1.3. Neutron/Gamma Radiation Transport Model of Core Reactor Components

The neutrons from the D-T reaction must be captured for tritium breeding and thermal heat conversion, requiring a neutronics assessment as part of a system analysis code. Here an extended reactor neutron/gamma transport model is integrated in MIRA.

Radiation interaction with matter in fusion reactors

As neutrons pass through and interact with the surrounding matter they undergo a variety of nuclear reactions, such as scattering and captures reactions yielding the emission of secondary particles or multiple neutrons, like gamma (n,γ), alpha (n,α), tritons (n,t) and multiple neutrons emissions, e.g. $(n,2n)$. All nuclear interactions of neutrons with matter lead to a change of energy and/or flight direction. Neutron-induced gamma rays also interact with reactor materials and are involved in a variety of nuclear processes. In fusion applications light nuclei materials and highly energetic neutrons often presuppose largely anisotropic scattering [140]. This implies the particle streaming to be dependent on the travelling direction, which requires the use of the full kinetic theory and the solution of the BTE. Hence, simplified theories such as diffusion are not adequate for fusion neutronic applications. The design of the core reactor components, especially the functional materials, require account of the main nuclear processes. These are then driven by the following types of neutron interactions:

- tritium breeding;
- neutron multiplication and moderation;
- nuclear heating;
- neutron radiation damage.

Each of these processes corresponds to a design parameter, being evaluated via the transport model.

A key goal of a FPP is to ensure the fuel self-sufficiency by breeding tritium atoms from the (n,t) neutron capture reaction, occurring inside the breeding zone materials of the BB containing lithium atoms. The main T breeding reactions are associated with the ^{6}Li and ^{7}Li isotopes and summarized as:

$$^6_3\mathrm{Li} + \mathrm{n} \rightarrow {}^4_2\mathrm{He} + {}^3_1\mathrm{T} + 4.8\,\mathrm{MeV}, \tag{4.31}$$

$$^7_3\mathrm{Li} + \mathrm{n} \rightarrow {}^4_2\mathrm{He} + {}^3_1\mathrm{T} + \mathrm{n} - 2.5\,\mathrm{MeV}. \tag{4.32}$$

The first reaction provides the largest T breeding contribution, since it exhibits a higher microscopic cross section for low neutron energies and yields an energetic surplus of 4.8 MeV. The ^{7}Li reaction, instead, is a threshold reaction and features a higher σ for fast neutrons (> 6 MeV). For more details see Figure D.5. The tritium breeding capabilities of a BB are identified by the *Tritium Breeding Ratio*

(TBR), i.e. the number of tritium atoms produced per fusion neutron. Taking $\mathcal{R}_{nt}$ the local tritium production rate in the BZ domain $\mathcal{D}_{bz}$, intended as the local reaction rate of the (n,t) captures in lithium isotopes, the TBR can be defined as:

$$\mathrm{TBR} = \frac{\text{T production rate in BZ}}{\text{T burning rate in core plasma}} = \frac{\int_{\mathcal{D}_{bz}} \mathcal{R}_{nt}(\mathbf{r})\mathrm{d}\mathbf{r}}{\mathcal{B}_p}. \tag{4.33}$$

The numerator refers to the global T production rate, which accounts for the T production in lithium atoms only. Applying Equation (4.8), $\mathcal{R}_{nt}$ can be rewritten:

$$\mathcal{R}_{nt}(\mathbf{r}) \left[\frac{\mathrm{T}}{\mathrm{cm}^3\,\mathrm{s}}\right] = n_{^6\mathrm{Li}}(\mathbf{r}) \int_0^\infty \sigma_{n,\alpha}^{^6\mathrm{Li}}(E)\cdot\phi(\mathbf{r},E)\,\mathrm{d}E + n_{^7\mathrm{Li}}(\mathbf{r}) \int_0^\infty \sigma_{n,n'\alpha}^{^7\mathrm{Li}}(E)\cdot\phi(\mathbf{r},E)\,\mathrm{d}E, \tag{4.34}$$

where $n_{^6\mathrm{Li}}$ and $n_{^7\mathrm{Li}}$ indicate the atom density of ^6Li and ^{7}Li. $\sigma_{n,\alpha}^{^6\mathrm{Li}}$ and $\sigma_{n,n'\alpha}^{^7\mathrm{Li}}$ relate to the microscopic cross-sections of T breeding reactions ^{6}Li(n,α)T and ^{7}Li(n, n'α)T and $\phi(r,E)$ is the neutron scalar flux distribution. The denominator of Equation (4.34) indicates the plasma tritium burning rate, corresponding to the neutron generation rate and given by

$$\mathcal{B}_p = \frac{P_{fus}\,[\mathrm{MW}]}{E_{fus}\,[\mathrm{MeV}]} \times e^{-1}, \tag{4.35}$$

with $e = 1.602\times10^{-19}\,\mathrm{MJ/MeV}$, P_{fus} relating to the core fusion power and $E_{fus} = 17.6\,\mathrm{MeV}$ the D-T fusion reaction energy yield. In some cases there are applicative examples where other isotopes interacting with incoming neutrons yield tritium atoms in the products. This is the case, for instance, of beryllium, installed in form of solid pebbles in the HCPB blanket concept. The neutron capture of Be releases a T atom via $^9\mathrm{Be} + \mathrm{n} \rightarrow {}^7\mathrm{Li} + {}^3\mathrm{T} - 10.5\,\mathrm{MeV}$. Since this T production is negligibly small to the BZ it is not considered for T self-sufficiency.

Independently from the blanket concept the neutron multiplier provides an extra-amount of neutrons. These neutrons compensate the parasitic neutron losses occurring inside the blanket components, mostly via adsorption in structural materials [141]. The multiplication involves the interaction of an incoming neutron and the release of one or more extra neutrons from the isotope nucleus, also referred to as $(n,2n)$ reaction. For example, the reaction exploited in beryllium-containing material to multiply neutrons is

$$^9\mathrm{Be} + \mathrm{n} \rightarrow 2^4\mathrm{He} + 2\mathrm{n} - 1.57\,\mathrm{MeV}. \tag{4.36}$$

For the currently pursued blanket design concepts, beryllium and lead are the most promising multiplying materials, as shown in the cross section plot of Figure D.6. Be provides larger $(n,2n)$ microscopic cross section for incoming neutron energies around 5-6 MeV, while Pb for higher energies, near 15 MeV. The neutron multiplier carries out also an important function for an effective "neutron economy" of the breeding blanket: favouring the elastic scattering of the incoming neutrons, which ultimately slows them down. The microscopic cross sections of elastic scattering of Be, Pb and Li are illustrated in Figure D.7. That has a twofold beneficial effects: reduce the high energy neutrons streaming towards the VV and TF coils system and enhance the probability of T breeding from ^{6}Li, more favourable for thermal neutrons.

The streaming of neutrons and gamma through lattice atoms cause interactions leading to a conversion of their kinetic energy into thermal energy. The volumetric heat deposition can be conceived

as a special case of "heat generation rate" $\mathcal{R}_{heat}$, which can be written as [66]:

$$\mathcal{R}_{heat}(\mathbf{r})\left[\frac{\mathrm{W}}{\mathrm{cm}^3}\right] = \sum_j n_j(\mathbf{r}) \int_0^\infty k_j(E)\cdot\phi(\mathbf{r},E)\,\mathrm{d}E, \tag{4.37}$$

with n_j indicating the atomic density for material j and k_j the so-called *KERMA* factor (kinetic energy released in materials):

$$k_j(E)[\mathrm{J\,barn}] = \sum_x \sigma_{x,j}(E)\cdot\overline{E}_{x,j}(E). \tag{4.38}$$

$\sigma_{x,j}$ [barn] is the microscopic cross section in material j of the generic process x, responsible of releasing the energy $\overline{E}_{x,j}$ [J] upon an incident neutron with energy E. As for neutrons these processes include the kinetic energies of recoil nuclei, charged particles emitted instantaneously, charged particles emitted upon radioactive decay and other processes such as internal conversion [66]. Because of exothermal nuclear reactions, that might take place in a typical fusion reactor BB, the energy deposited in materials by a 14.1 MeV fusion neutron ($Q-$value) is likely to exceed its incident original value (typically between $\sim$ 17 to 24 MeV [66]). A large contribution comes from those materials with large $(n,2n)$ cross sections and from lithium due to the (n,α) and (n,γ) neutron captures. With regard to gamma rays, the KERMA factor in material j includes the contributions of positron-electron pair production $\sigma_{pp,j}$, the Compton scattering $\sigma_{cs,j}$ and the photoelectric adsorption $\sigma_{pe,j}$. The sum of all yields the following definition of KERMA factor due to gammas [66]

$$k_j^\gamma(E)\,[\mathrm{J\,barn}] = \sigma_{pe,j}(E)\cdot E + \sigma_{pp,j}(E)\cdot(E-E_{pp}) + \sigma_{cs,j}(E)\cdot E. \tag{4.39}$$

In pair production, $E_{pp} = 1.02$ MeV corresponds to the mass of two electron masses, hence not accountable for deposited heating.
In fusion reactor blankets a significant part of the nuclear heating (NH) power is due to the heat deposited by neutron-induced photons, i.e. from (n,γ) reactions. Due to the large presence of iron in BB structural materials the reaction ^{56}Fe(n,γ)^{57}Fe provides a considerable amount of energy to the whole system (see microscopic cross section plot in Figure D.8). However, large quantities of steel might escalate in too large parasitic neutron captures, leading to substantial penalization of tritium breeding and/or neutron multiplying capabilities of the BB. Similarly to the TBR, the *Energy Multiplication Factor* (EMF) relates the incident neutron energy to the actual amount deposited . If this concept is generally applied to the system i, it can be written as

$$\mathrm{EMF_i} = \frac{\sum_m^{M_i} \int_{\mathcal{D}_{m,i}} \mathcal{R}_{heat}(\mathbf{r})\mathrm{d}\mathbf{r}}{P_{neut,i}}, \tag{4.40}$$

with $P_{neut,i}$ denoting the incident neutron power and M_i the number of regions of the $i-$th system, each enclosed by the volume domain $\mathcal{D}_{m,i}$. If the EMF is evaluated for the whole reactor $P_{neut,i}$ is equivalent to the total neutron power P_{neut}. Otherwise, only the BB with its M_{BB} number of sub-domains can be alternatively used for assessing $\mathrm{EMF_{BB}}$. In that case $P_{neut,i}$ is the sum of the neutron power spreading over the inboard and outboard blanket FW, $P^n_{fw,ib}$ and $P^n_{fw,ob}$, which can evaluated applying the definition of Equation (4.17). In a similar way $\mathrm{EMF_{div}}$ can be assessed for the divertor component, too. Finally, the global nuclear heating power R^m_{heat}, deposited on a generic reactor component m with a spatial domain $\mathcal{D}_m$, reads as:

$$R^m_{heat}[\mathrm{W}] = \int_{\mathcal{D}_m} \mathcal{R}_{heat}(\mathbf{r})\mathrm{d}\mathbf{r}. \tag{4.41}$$

The bombardment of highly energetic neutrons causes severe damage to materials and have to be taken into account in the design. There are many radiation effects that cause damage, including direct heating, gas production and production of lattice defects. Displaced atoms are produced by the energy imparted to the lattice atoms derived from reactions with neutrons, including elastic and inelastic scattering, $(n, 2n)$ and (n, γ) reactions [66]. The material damage due to displaced atoms depends on the total available energy for producing displacements $E_{a,j}$ [MeV barn] and the energy required to displace an atom from its lattice position E_d. The primary recoil atom loses some of its energy ejecting another atom, giving a pair of displacements; each of these generates another pair, and so on, until the kinetic energy is consumed. Locally, the energy rate available for lattice atom displacements is obtained applying the definition of the reaction (Equation 4.8), hence:

$$\mathcal{R}_{dama}(\mathbf{r}) \left[\frac{\mathrm{MeV}}{\mathrm{cm^3 s}}\right] = \sum_j n_j(\mathbf{r}) \cdot \int_0^\infty E_{a,j}(E) \cdot \phi(\mathrm{r}, E)\mathrm{d}E. \tag{4.42}$$

Since the available energy is used up by producing pairs, for a certain material j the number of displaced atoms per unit, time typically indicated as *displacements per atom* (dpa) per full power year (fpy), can be defined as

$$\mathcal{R}_{dpa}(\mathbf{r}) \left[\frac{\mathrm{dpa}}{\mathrm{fpy}}\right] = \frac{1}{\sum_j n_j(\mathbf{r})} \frac{\mathcal{R}_{dama}(\mathbf{r})}{2E_d} \cdot K_t, \tag{4.43}$$

with E_d in [MeV], n_j in [cm^{-3}] and $K_t = 3.1536 \times 10^7$ [s/fpy]. Different values for E_d used in practice are chosen based on empirical evidence, with a wide range found in the literature [142, 143].

One-dimensional neutron/gamma transport model of core reactor components

Nowadays the transport codes used in fusion neutronics rely on detailed Monte Carlo techniques [13] allowing a comprehensive three dimensional mapping of neutron and photon flux densities down to millimeter in spatial resolution. In system/design codes, however, faster solutions are sought in order to scope multiple design solutions. Formerly, when the available computing capabilities could not cope with high demands required by large Monte Carlo simulations, one-and two-dimensional deterministic codes were deployed to perform very preliminary designs of fusion tokamak devices [140, 144, 145].
The goal of a transport model for a fusion reactor system analysis tool is to provide a reliable estimate of the major neutronic parameters. These incorporate: TBR, nuclear heating, scalar neutron fluxes profiles and local atom displacement rate. Ideally, a system code neutronic module should gauge these design variables for an arbitrary reactor configuration, which includes prescribed radial build and material composition specifications for each constituting physical component. To fulfil this task, a 1D deterministic neutron/gamma transport model has been integrated in the MIRA system/design code. The model approximates the reactor physical components with a set of concentric infinite cylinders around the tokamak axis, where each cylinder is characterized by an homogenized mixture of elementary materials.

For the neutronic evaluation each component is geometrically modelled in MIRA by means of its radial and poloidal geometry profiles. Following the schematics of Figure 4.3 each reactor subsystem denoted with the subscript m entails the presence of a inboard and an outboard portion,

moving from the plasma center, outwards. To each of the M core components corresponds a material composition and a set of IB and OB radial thicknesses $\Delta_{m,i}$ and $\Delta_{m,o}$ and a vertical width $\Delta_{m,t}$ provided by the geometric module. To define the physical domain each sub-domain m is radially nodalized yielding a number N_m of inboard and outboard intervals. For each component, a generic j-th interval midpoint is locally mapped for inboard side, $r^m_{j,i}$, and outboard side, $r^m_{j,o}$, with $j = 1, 2, ...N_m$.
In axial direction the layer on the node j of the side k in the component m takes a poloidally-varying thickness, from δr^m_o on the outboard midplane through δr^m_t to δr^m_i on the inboard mid-plane. Say, $\delta r^m_j(\alpha_s)$ describes such a behaviour along the poloidal angle α_s. The lines following the poloidal profile of such a layer (red-dashed inboard, blue dot-dashed outboard) is obtained by applying the component construction rules from the points $(r^m_{j,o}, 0)$, through $(r^m_{\max}, z^m_{j,t})$ to $(r^m_{j,i}, 0)$. The IB and OB portions are separated by $r = r^m_{\max}$, relating to the radial coordinate of the most elongated point for each components. This profile is then subdivided into a number of linear piecewise elements N_S, each with a poloidal length $\delta^{j,m}_{s,k}$.

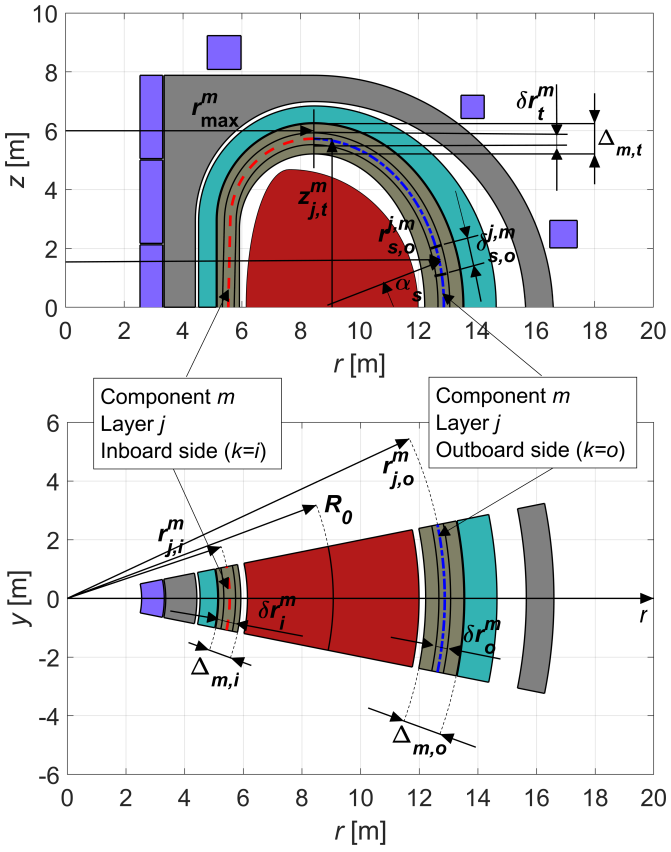

Figure 4.3.: Schematic view of a tokamak reactor with variables and constructions lines used for the one-dimensional neutron transport model.

The transport code ANISN [146] has been interfaced with the MIRA data structure and it is used to solve the BTE in one-dimensional cylindrical coordinates. ANISN is a one-dimensional multigroup discrete ordinates transport code, with anisotropic scattering. Within the MIRA neutron transport model, it is operated to analyse the radial streaming of fusion neutrons and neutron-induced gamma rays across the core reactor components, namely plasma vacuum chamber, BB, VV, TF coils and CS.

The major goal is then to convert the radial and poloidal nodalization of all reactor components into a more suitable set of instructions, readable by ANISN. The radial coordinates related to each component's layer are sorted in a global radial mesh read by ANISN. All nodes are stored in a unique array, such that $r = [r_{1/2}, r_{3/2}, ...r_{J-1/2}, r_{J+1/2}, ...r_{N-1/2}, r_{N+1/2}]$, with $J = 1, 2, ...N$. The mid-point of the interval J lays on $r = r_J$ and $N = \sum_m^M N_m$. For the tokamak-like radial configuration, a vacuum boundary condition is imposed both on left boundary $r = r_{1/2}$ and on the right boundary $r = r_{N+1/2}$. The selection of N_m is based on the selected minimum radial grid size h, a user-defined parameter yielding,

$$N_m = \max\left(\left\lceil \frac{\Delta_{m,i}}{h} \right\rceil, \left\lceil \frac{\Delta_{m,o}}{h} \right\rceil\right), \tag{4.44}$$

with $\lceil x \rceil$ indicating the ceiling function of a generic real number x, returning the least integer greater than or equal to x.

Relying on the multigroup energy approximation (see also Appendix D.2) ANISN needs to associate a material-ordered set of nuclear cross sections within each subregion m. The evaluated nuclear data libraries cannot be directly used in nuclear analyses but they have to be suitably converted to group-wise cross section data, prior to the simulation. A MATXS file [147], short abbreviation for "material cross sections", is one of such multigroup cross section data formats, read by the ANISN code. A multigroup cross section library table suitable for S_N codes is generated with the TRANSX code [148] from the the MATXS file, where the libraries are stored. TRANSX has been incorporated in the integral MIRA package and is interfaced with ANISN for any transport simulations. TRANSX takes the list of the atom density $n_{k,m}$ of the $k-$th isotopic element in $m-$th component. The output file includes $L+1$ cross section tables for each material m, with L denoting the L-th Legendre expansion order of the scattering cross sections used to tally the in-group scattering source term.
An informative glance on the aspects of multigroup approximation and Legendre polynomial expansion of the scattering source term is provided in Appendices D.2 and D.3. The Fusion-Evaluated Nuclear Data Library (FENDL) [149] are recommended for neutron/photon radiation transport analysis in fusion engineering systems [150]. Here, FENDL/MG-3.1b version is accessed by TRANSX. It contains the multigroup cross section data set on the Vitamin J+ energy structures, including 211 groups for neutron and 42 groups for gammas.

In absence of fission reactions the source term in nuclear fusion engineering applications is based on a fixed spatial, angular and energy distribution. ANISN allows for a volumetric isotropic source and an angular description of the neutron source on every radial interval r_J and group energy g. In 1D discrete ordinate transport codes the angular sampling is performed on the set of discrete ordinates μ_{pq}. One-dimensional transport calculations on typical tokamak configurations offer a more credible and reliable assessment if the neutron source is sampled on the scattering angle cosine μ, rather than imposing isotropic volumetric source in the core plasma volume intervals [151]. The solution of 2D void plasma chamber transport model can be employed. The difference between 1D and 2D model resides in the polar angle cosine ξ, vanishing from the BTE. The angular flux density distribution to use for source profiling purposes in ANISN can be extracted from the 2D model for any point $(r, z) \in \mathcal{D}$. The shell source term $\psi_{pq,J}^{shell}$ is simply summed up to the angular flux $\psi_{pq,J}$, calculated by ANISN for the ordinate μ_{pq} in the interval r_J, as given in Equation (D.30). The neutron source is mapped in the 2D model on the BB innermost and the outermost radial nodes on the mid-equatorial plane, identified by points $B_{i,2}$ and $B_{i,2}$ on Figure 4.2 and located at $r_i = r_{1/2,i}^{sol}$ and $r_o = r_{N_{sol}+1/2,o}^{sol}$ in the 1D model mesh grid. The shell source term for direction $\mu = \mu_{pq}$ and radial interval $r = r_k$, with $k =$i/o, can be written as

$$\psi_{pq,k}^{shell,0} = \psi_{pq}(r_k, 0)\big|_{\xi=-\xi_p} + \psi_{pq}(r_k, 0)\big|_{\xi=\xi_p} \quad \text{with } k = i, o. \tag{4.45}$$

Therefore, if the same set of azimuthal S_N quadrature ordinates μ_{pq} is used for 1D reactor and 2D vacuum toroidal chamber transport models $\psi^{shell,0}_{pq,K}$ is obtained by summing the 2D solution $\psi_{pq}(r_K, 0)$ for positive polar angle cosines $\xi = \xi_p$ and negative polar angle cosines $\xi = -\xi_p$. The total neutron source of the 1D problem $S_k = \sum_{pq} |\mu_{pq} w_{pq}| \cdot \psi^{shell,0}_{pq,k}$ is normalized to the peak neutron wall loading $\Gamma^{n,fw/k}_{\perp,\max}$ on the inboard and outboard blanket first wall, expressed in Equation (4.17). The actual shell source for ANISN simulations can be recast into

$$\psi^{shell}_{pq,k} = \psi^{shell,0}_{pq,k} \cdot \frac{\Gamma^{n,fw/k}_{\perp,\max}}{S_k} \quad \text{with } k = i, o. \tag{4.46}$$

Besides the improvements, the 2D transport model is beneficial for whole reactor transport analysis by providing the angular sampling of the neutron source onto the blanket FW.

ANISN solves the BTE returning the following results:

- the neutrons/gamma scalar flux $\phi(r, E)$ and;
- the local reaction rates $\mathcal{R}_x(r)$, including tritium breeding R_{nt}, nuclear heating $\mathcal{R}_{heat}$ and atom displacement rate $\mathcal{R}_{dpa}$.

This pair of spatial-energy distributions is provided in matrix form, since the solving method is based on a multidimensional radial-energy nodalization. Therefore, denoting with J the index relating the N radial nodes r_J and g to the N_G energy groups $\phi(r, E) = \phi(r_J, E_g) \equiv \phi_{J,g}$ and $\mathcal{R}_x(r) = \mathcal{R}_x(r_J) \equiv \mathcal{R}_{x,J}$, with $J = 1, 2, ..., N$ and $g = 1, 2, ...N_G$. The total and fast scalar fluxes on a given radial location r_J are derived by summing column-wise the $J-$th row terms over the energy group.

The global reaction rate R^m_x of a generic nuclear process x in the component m entails the integration over the domain $\mathcal{D}_m$. The method relies on the subdivision of $\mathcal{D}_m$ into a number N_m of inboard and outboard layers. Accordingly, the integration over $\mathcal{D}^k_m$ for the calculation of the global reaction rate R^m_x can be approximated as

$$R^m_{x,k} = \int_{\mathcal{D}^k_m} R_x(\mathbf{r}) \mathrm{d}\mathbf{r} \approx \sum_j^{N_m} \sum_s^{N_S} \mathcal{R}_x(r^m_{j,k}) \cdot \delta r^m_j(\alpha_s) \cdot \delta^{j,m}_{s,k} \cdot 2\pi r^{j,m}_{s,k} \quad \text{with } k = i, o, \tag{4.47}$$

with α_s, $\delta^{j,m}_{s,k}$ and $r^{j,m}_{s,k}$ being the geometric variables used for the radial and the poloidal nodalization, illustrated in Figure 4.3. This estimate of $R^m_{x,k}$ needs further adjustments to account for two different factors: the numerical deviations attributed to the approximated volume integration and the neutron wall loading profile, spanning poloidally alongside the IB and OB sides of the FW. The former aspect can be adjusted recalibrating the individual layer volumes to the actual volume V^m_k. The latter is corrected by applying a dividing factor which corresponds to the neutron wall loading peaking factor $\chi_{\text{neut}}|_{\partial\mathcal{D}_k}$ (Equation 4.19). This supposition is motivated as follows. According to Equation (4.46) the neutron shell source angular distribution on inboard and outboard FW boundaries is normalized to the peak neutron wall loading. This arrangement is conservatively safe for shielding evaluation purposes but too optimistic if applied to the global reaction rates, as it implicitly assumes that around the plasma chamber the wall loading takes its peak value. Therefore, for evaluating the integral variables, the average wall loading $\Gamma^{neut}_{\perp,av}$ on inboard and outboard sides of the reactor is found more appropriate. Dividing by $\chi_{\text{neut}}|_{\partial\mathcal{D}_k}$ yields the desired outcome. Bearing that in mind, the

global reactor rate R_x^m can be then obtained by summing the inboard and outboard contributions and imposing these two corrections. Thus,

$$R_x^m = \sum_k R_{x,k}^m \cdot \frac{V_k^m}{\overline{V}_k^m} \cdot \frac{1}{\chi_{\text{neut}}|_{\partial \mathcal{D}_k}} \quad \text{with } k = i, o, \tag{4.48}$$

where $\overline{V}_k^m$ is the approximated volume of the $k-$th portion of the core region m,

$$\overline{V}_k^m = \sum_j^{N_m} \sum_s^{N_S} \delta r_j^m(\alpha_s) \cdot \delta_{s,j}^m \cdot 2\pi r_{s,k}^{j,m} \quad \text{with } k = i, o. \tag{4.49}$$

A verification and benchmark study has been carried to outline the major errors introduced by the set of assumptions taken for the proposed neutron and gamma transport algorithm, see Appendix E.3. The benchmark has been performed against the Monte Carlo N-Particle transport code (MCNP). The error introduced by the model arises from:

- numerics associated with radial nodalization, discrete ordinates quadrature formula and multi-group energy approximation,
- cylindrical geometry against actual toroidal tokamak topology and
- material mixture homogenization.

In actual 3D tokamak reactor configurations the neutron/gamma streaming is affected by radial, poloidal and toroidal heterogeneities, that an homogenized model cannot depict. There are also neutron streaming effects through void gaps in toroidal direction which have to be accounted for by the actual three-dimensional geometry.
To assess each error contribution dedicated simulation campaigns have been carried out. The main outcome of this exercise is summarized in Table E.9. The overall uncertainties affecting the TBR and the nuclear heating in the most sensitive reactor components have been found around +7-8 %, while larger errors affect the local peak dpa rate in the FW Eurofer, +10 %, and in the VV, +38 %. The nuclear power density at the inner interface of the TF coil winding pack yields similar figures, around 38 %. Generally, the one-dimensionality yields the deviation of the solution to progressively increasing moving from the plasma center, outwards. As a result, both local and integral parameters are more accurate in the vicinity of the plasma domain. Having the blanket near the plasma is therefore a blessing. The largest share of the overall reactor deposited energy derives from that in FW and BZ, where the gap between approximated and exact solution deviate by +3-4 %. Moving outwards the error spins up to +20-30 %. Supposedly, moving further from the neutron source the limitation of the cylindrical approximation no longer fits to the actual tokamak geometry situation.
As a final outcome, for shielding applications, the results on local parameters can trustfully taken "as they are", due to their over-estimative nature. For T-self sufficiency and blanket radial build characterization, the figures on TBR and global nuclear heating power are scaled down by a factor reflecting the estimated errors, i.e. $\sim$7-8 %.

Neutronic requirements and operational limits

To reliably operate a FPP a set of operational neutronic requirements needs to be observed when designing the core reactor components, in particular, the BB and the VV. These requirements have been proposed by Fischer et al. [152] for EU-DEMO plant configurations, and re-adapted here for

observation in more simplified system design code neutronics modelling. Essentially, they are meant to ensure tritium self-sufficiency, adequate shielding protection of superconducting coils and prevent the degradation of steel properties by limiting the neutron-induced irradiation damage.

An operable fuel cycle requires the tritium self-sufficiency. To accomplish this, the *achievable tritium breeding ratio* TBR_a (Equation 4.33) must exceed the *required tritium breeding ratio* TBR_r [153, 154]. Both denotations depend on different plasma physics and technology aspects. In particular, the required TBR shall exceed unity to compensate the parasitic losses throughout the whole fuel cycle from the generation in the BB to use in the plasma chamber, such as the permeation losses. Furthermore, it should provide additional tritium as start-up inventory for further FPPs. The surplus of TBR to associate with the required TBR depends on several plasma physics aspects, e.g. burn-up fraction, and on the fuel cycle efficiency. To cover these aspects a 5 % margin [152, 155] is suggested. The achievable tritium breeding ratio on the other hand is the actual TBR that can be produced in a certain BB system [154], which is affected by several uncertainties, as: system and modelling definition, nuclear data and code. Such uncertainties in currently performed 3D Monte Carlo simulations are estimated to amount to 5 % and mostly include the effects of the vacuum vessel penetrations, typically not integrated into DEMO Monte Carlo models [141]. A TBR design target for DEMO $\mathrm{TBR}_a = 1.10$ is currently pursued in the conceptual design of DEMO within the the PPPT programme.

In a fusion reactor the radiation shielding requirements are necessary to protect the superconducting TF coils and to limit the neutron irradiation damage to structural and functional materials. With regard to the DEMO design goal [152] the limits on the TF coils are imposed in terms of

- fast neutron fluence to the superconducting cable,
- peak nuclear heating in the winding pack,
- radiation damage to the copper stabilizer and
- radiation dose to the epoxy resin insulator.

The fulfilment of such requirements is primarily devoted to the radiation attenuation features of the BB and the VV [130, 131]. The actual limits observed to shield the TF coils are equivalently imposed in terms of scalar fast neutron flux Φ_{fast} and of volumetric deposited power density $\mathcal{R}_{heat}$. According to the radial disposition of the 1D neutronic module the location pertaining to such constraints are placed on the IB and OB inner sides of the TF coil winding pack, i.e. $r = r_{1,i}^{wp}$ and $r = r_{1,o}^{wp}$ (see also Figure 4.3 for the variable formalism). The upper limits imposed for DEMO design are respectively 10^9 [$\mathrm{cm}^2\ \mathrm{s}^{-1}$] and 50 [$\mathrm{W/m}^3$]. The former value identifies the fast neutron flux corresponding to several full power years DEMO lifetime, ∼7-8 fpy, considered as a design assumption for the current EU-DEMO baseline [156].

Similar considerations have been made to pose practical limits to the neutron damage in Eurofer and stainless steels used for BB and VV components. Assuming $20 \div 50$ dpa peak neutron damage limit in the BB Eurofer [32] and 2.75 dpa in the VV SS316 structure [67] over a target lifetime for the BB and the FPP, $t_{\mathrm{life,BB}}$ and $t_{\mathrm{life,FPP}}$, the verification of the constraining limits on neutron damage takes place. The neutron damage in the Eurofer steel is correlated to the target BB lifetime, i.e. ∼2-5 fpy in current DEMO conditions [152]. The 2.75 dpa peak value in the VV, instead, is bound to the entire lifetime envisaged for DEMO, i.e. ∼6-8 fpy [67, 156]. The VV and the superconducting coil lifetime are assumed to be equal since both are irreplaceable in a reactor. Both are then put in combination with the calculated atomic displacement rate $\mathcal{R}_{dpa}(r)$.

The full list of neutronic operational limits is provided in Table 4.1.

Description	Symbol	[Unit]	Value
Tritium Breeding Ratio	TBR	$[-]$	≥ 1.10
Max fast neutron flux on Nb_3Sn superconductor	$\Phi^{wp}_{fast,peak}$	[n/cm^2/s]	$< 10^9$
Max NH in winding pack	$\mathcal{R}^{wp}_{heat,peak}$	[W/m^3]	< 50
Neutron damage in Eurofer (FW)	$\mathcal{R}^{fw}_{dpa,peak}$	[dpa/fpy]	$< (20 \div 50) \Big/ t_{\text{life,BB}}$
Neutron damage in SS316 (VV)	$\mathcal{R}^{vv}_{dpa,peak}$	[dpa/fpy]	$< 2.75 \Big/ t_{\text{life,FPP}}$

Table 4.1.: Neutronic DEMO operational limits observed for system design with MIRA code. $t_{\text{life,BB}}$ and $t_{\text{life,FPP}}$ indicate the lifetime (in fpy) of the BB and the FPP, both input parameters in MIRA. Table reproduced according to [152].

4.2. External Magnetic Field Configuration

In tokamaks the externally-applied magnetic field consists of toroidal and poloidal components, generated by a magnet coil system. A systems code shall characterize the coil system and depict the field and force distributions as function of operational phase. In MIRA each coil is treated as a physical component characterized by a spatial allocation, volume and material composition. Additionally, it is simulated as a current-carrying element (CCE) and scopes the:

- evaluation of the nominal current, based on operational requirements and technological constraints;
- full spatial electromagnetic characterization, including distribution of magnetic field, flux and volumetric forces, as well as stored energy
- coil engineering design, consisting of allocating the superconducting cables in the winding pack and sizing of all coil subsystems (such as casing and ground insulator).

In the following the modelling of the coils is described. For the toroidal and the poloidal field configurations the different electromagnetic aspects are elaborated. Methodologies are also elucidated about the space sizing and allocation of the major coil subsystems, such as winding pack and coil casing.

4.2.1. Magnetostatics in Tokamaks

The quantification of a magnetic field **B** generated by a static time-independent current source **J** is a magnetostatic problem, derived from the two stationary Maxwell's equations. Accordingly, **J** and **B** do not depend on time. In magnetostatic problems the Ampere's law and the magnetic Gauss law (Equations 3.2 and 3.3) are the governing equations. The solution yields the local and global magnetic parameters, such as magnetic field, forces, flux, energy and mutual inductance. In this subsection the theoretical fundamentals are recalled.

Magnetic flux and field in axisymmetric tokamak geometry

A magnet coil can be defined as a CCE closely wound in an arbitrary closed line and transporting an electrical current I. This current is locally identified by the current density vector field distribution $\mathbf{J}$, defined at any spatial location $\mathbf{r}$. The magnetic field $\mathbf{B}$ can be formulated as a magnetic vector potential $\mathbf{A}$, such that $\mathbf{B} = \nabla \times \mathbf{A}$. As a result, the Ampere's law becomes $\Delta\mathbf{A} = -\mu_0\mathbf{J}$, which is a Poisson equation. Its solution can be then written as an integral with the RHS, reading as [89]

$$\mathbf{A}(\mathbf{r}) = \frac{\mu_0}{4\pi}\int\limits_{\mathcal{D}_J} \frac{\mathbf{J}(\mathbf{r}')}{|\mathbf{r}-\mathbf{r}'|}\mathrm{d}\mathbf{r}'. \tag{4.50}$$

Thus, the magnetic field $\mathbf{B}$ is given by

$$\mathbf{B}(\mathbf{r}) = \frac{\mu_0}{4\pi}\int\limits_{\mathcal{D}_J} \frac{\mathbf{J}(\mathbf{r}')\times\left(\mathbf{r}-\mathbf{r}'\right)}{|\mathbf{r}-\mathbf{r}'|^3}\mathrm{d}\mathbf{r}', \tag{4.51}$$

with $\mathrm{d}\mathbf{r}'$ denoting the differential volume of the CCE. Such an integral expression of $\mathbf{B}$ is called *Biot-Savart* law (BSL). The domain $\mathcal{D}_J$ denotes the volume domains of $\mathbf{J}$.

For many applicative cases there exists an analytical solution to Equations (4.50) and (4.51), i.e. for coaxial current-carrying loops (CCL), alternatively called current ring or current filament. A CCL is centred on the vertical axis and carries a current I and its current-carrying cross section is approximated by a point, located at $r = R$ and $z = Z$. In the reference curvilinear coordinates system (r,ϕ,z) and axisymmetric conditions, the vector potential of the magnetic field reduces to the toroidal component A_ϕ and the magnetic field to the radial and axial components, B_r and B_z. On these assumptions the integral of Equation (4.50) is solved by a Green's function G of the differential elliptic operator of $\nabla A_\phi(r,z) = -\mu_0 J_\phi$. G defines the solution of a PDE for a Dirac's delta total current source $I\cdot\delta(r-R,z-Z)$ located at $r = R$ and $z = Z$. A set of formulas to outline $A_\phi(r,z)$, or, more conveniently, the poloidal magnetic flux Ψ, has been derived from the tomakak simulation code TOKES [104] and implemented in MIRA.
TOKES (acronym for "Tokamak Equilibrium and Surface processes") is a physics simulation tool and designed to simulate plasma equilibrium states and surface processes in tokamaks. In MIRA only the part addressing the magnetic field and flux functions is integrated. Due to the linearity of the problem the poloidal flux and field is calculated at any observation point $\mathbf{p} = (r,z)$ for a given number N of CCLs. Each of the current loops carrying a current I_n has a radius R_n and it is axially situated at $z = Z_n$ on the point $\mathbf{P_n} = (R_n, Z_n)$. The poloidal flux Ψ is then given by

$$\Psi(\mathbf{p}) = \sum_n^N I_n G_\Psi(\mathbf{p};\mathbf{P_n}), \tag{4.52}$$

and for the $k-$th component of the magnetic field $\mathbf{B}$ (with $k = r,z$)

$$B_k(\mathbf{p}) = \sum_n^N I_n G_{B_k}(\mathbf{p};\mathbf{P_n}),\ \ k = r,z, \tag{4.53}$$

where $G_\Psi(\mathbf{p};\mathbf{P_n})$ and $G_{B_k}(\mathbf{p};\mathbf{P_n})$ are the Green functions of the Ampere's law in its potential form,

denoting the proportionality constants to the toroidal current I_n. These are summarized as:

$$G_\Psi(\mathbf{p};\mathbf{P_n}) = \mu_0\sqrt{rR_n}\left[\left(\frac{2}{k}-k\right)K(k)-\frac{2}{k}E(k)\right], \tag{4.54}$$

$$G_{B_r}(\mathbf{p};\mathbf{P_n}) = \frac{\mu_0}{4\pi}\frac{k(z-Z_n)}{\sqrt{R_n r^3}}\left[-K(k)+\frac{1-\frac{1}{2}k^2}{1-k^2}E(k)\right], \tag{4.55}$$

$$G_{B_z}(\mathbf{p};\mathbf{P_n}) = \frac{\mu_0}{4\pi}\frac{k}{\sqrt{rR_n}}\left[K(k)+\frac{(R_n+r)k^2-2r}{2r(1-k^2)}E(k)\right], \tag{4.56}$$

where k is defined as

$$k = \sqrt{\frac{4rR_n}{(z-Z_n)^2+(R_n+r)^2}}, \tag{4.57}$$

and $K(k)$ denotes the elliptic integral:

$$K(k) = \int_0^{\frac{\pi}{2}} \frac{\mathrm{d}\varphi}{\sqrt{1-k^2\sin^2\varphi}} \tag{4.58}$$

and $E(k)$ the elliptic integral:

$$E(k) = \int_0^{\frac{\pi}{2}} \sqrt{1-k^2\sin^2\varphi}\,\mathrm{d}\varphi. \tag{4.59}$$

While this filamentary theory is valid for regions remote from the CCL, the singularities associated with it lead to a diverging behaviour in its vicinity. Such singularities can be deduced from Equation (4.57), where for $r \to R_n$ and $z \to Z_n$ $k \to 1$, yielding $K(k) \to \infty$. Hence, more refined solutions of Equations (4.50) and (4.51) for finite-thickness conductors are tackled in Section 4.2.2.

Mutual inductance and magnetic energy

In filamentary current loop approximation a magnet coil can be thought as a combination of multiple CCL, each carrying the same current. Two different coils, say coil i and coil j, can mutually interact with each other, magnetically and mechanically. The interaction leads to the concept of *self-inductance* and *mutual inductance*, i.e. to the ability of storing and exchanging the magnetic energy through the magnetic field generated by their static currents For the stored energy the concept of self-inductance of the coil i is developed assuming that it is composed of N_i turns, each carrying a current $I_{turn,i}$. The total current I_i circulating in the coil i is defined as $I_i = N_i I_{turn,i}$. The self-inductance L_i has to satisfy the following definition of magnetic energy $E_{m,i}$ stored in the coil i

$$E_{m,i} = \frac{1}{2}L_i I_{i,turn}^2 = \int \frac{\mathbf{B}^2}{2\mu_0}\mathrm{d}\mathbf{r}, \tag{4.60}$$

where from Equation (4.53) $\mathbf{B}^2 \propto (N_i I_{turn,i})^2$ and L_i can be untied from the current $I_{turn,i}$. The self-inductance is a pure geometry function with a quadratic dependency on the number of turns N_i. A mathematical definition of L_i for a circular conductor of radius R_i and a cross-sectional area A_i, can be written as [66]

$$L_i = \mu_0 N_i^2 R_i\left[\ln\left(\frac{8R_i}{\sqrt{A_i/\pi}}\right)-1.75\right]. \tag{4.61}$$

Similarly, the concept of mutual inductance $\mathcal{M}_{i,j}$ between the coil i and coil j, which can be conceived as the magnetic flux $\Psi_{j,i}$ linked by the coil circuit j per unit current flowing in the coil i. Making use of the formulation of Ψ from Equations (4.52) and (4.54),

$$\mathcal{M}_{i,j} = \mu_0 N_i N_j \sqrt{R_i R_j} \left[\left(\frac{2}{k} - k \right) K(k) - \frac{2}{k} E(k) \right], \tag{4.62}$$

with k defined as of Equation (4.57) for $r = R_i$, $R = R_j$, $z = Z_i$, $Z = Z_j$ and a number of turns N_i and N_j for the coils i and j. For an arbitrary number N_c of magnetically coupled coil circuits, the total energy E_m stored in the magnetic field is therefore given by the form:

$$E_m = \frac{1}{2} \sum_{i=1}^{N_c} \sum_{j=1}^{N_c} \mathcal{M}_{i,j} I_{turn,i} I_{turn,j} = \frac{1}{2} \mathbf{I}^T \mathcal{M}\, \mathbf{I}, \tag{4.63}$$

where $\mathcal{M}$ is the mutual inductance matrix. Each coefficient is calculated as $\mathcal{M}_{i,j} = \mathcal{M}_{j,i}$ for $i \neq j$ and $M_{i,j} = L_j$ for $i = j$. $\mathbf{I} = [I_{turn,1}, ... I_{turn,N_c}]$ is the column vector containing the turn currents associated with the N_c coils. The stored energy in the conductor is only related to these terms, while the mixed terms identify the share of energy stored in the magnetic field outside the conducting region.

Lorentz forces

Two circular circuits interact also by exerting the same attractive or repulsive forces, derived from the definition of the static Lorentz force. Having a differential volume of conductor $\mathrm{d}\mathbf{r}$, carrying the current density $\mathbf{J}$ and experiencing a magnetic field $\mathbf{B}$, the differential Lorentz force $\mathrm{d}\mathbf{F}$ can be written as

$$\mathrm{d}\mathbf{F} = \mathbf{J} \times \mathbf{B}\, \mathrm{d}\mathbf{r}, \tag{4.64}$$

which, for a circular loop carrying the total toroidal current I linked to $\mathbf{J}$, can be expressed as a differential force per unit length $\mathrm{d}\mathbf{l}$,

$$\mathrm{d}\mathbf{F} = I\, (\mathrm{d}\mathbf{l} \times \mathbf{B}). \tag{4.65}$$

If two coaxial loops carry the currents I_i and I_j, the loop i experiences a magnetic field generated by the loop j $\mathbf{B_j} = (B_{r,j}, B_{z,j})$, which interacting with the current I_i yields the total force $\mathbf{F_{i \leftarrow j}} = -\mathbf{F_{j \leftarrow i}} = F_{r,i \leftarrow j} \hat{n}_r + F_{z,i \leftarrow j} \hat{n}_z$. Based on Equation (4.65) and of the $\mathbf{B}$ field components of Equation (4.53) the mutual force between acts in axial direction reading as

$$F_{z,i \leftarrow j} = B_{r,j} I_i \oint \mathrm{d}l_1 = 2\pi R_i G_{B_r}(\mathbf{p_i}; \mathbf{p_j}) I_j I_i, \tag{4.66}$$

where R_i and R_j are the radii of loops i and j, Z_i and Z_j are axial elevations of CCL i and j, with $\mathbf{p_i} = (R_i, Z_i)$ and $\mathbf{p_j} = (R_j, Z_j)$. Similarly, the vertical force on loop j is given by:

$$F_{z,j \leftarrow i} = B_{r,i} I_j \oint \mathrm{d}l_j = 2\pi R_j G_{B_r}(\mathbf{p_j}; \mathbf{p_i}) I_i I_j. \tag{4.67}$$

It can be verified that $R_j G_{B_r}(\mathbf{p_j}; \mathbf{p_i}) = -R_i G_{B_r}(\mathbf{p_i}; \mathbf{p_i})$ leading to $F_{z,i \leftarrow j} = -F_{z,j \leftarrow i}$. As a result, if the two currents flow in the same directions, the axial forces are attractive; otherwise they are repulsive. In either case the magnitude is the same on both loops. The radial volumetric force acting radially on each loop is due to the vertical magnetic field generated by the circuits and its integral over the whole loop perimeter vanishes. If both loops operate a different current direction, the radial

forces are inward. The contrary occurs if they feature the same current sign. In particular, the radial force acting on a CCL due to its own axial field B_z acts always outwards and is also referred to as *hoop tensile force*, tending to expand the CCL.

The concept of mutual forces can be extended to a linear system of N CCLs. Similarly to the magnetic energy formulation a quadratic form can be derived combining Equations (4.53), (4.55) and (4.66) for the total vertical force $F_{z,i}$ acting on the loop i. This current ring is placed on $\mathbf{p_i} = (r_i, z_i)$ and operates the current I_i. The total vertical force is due to the interaction of its own current with the radial field generated by the other $N-1$ turns, yielding

$$F_{z,i} = \sum_{n \neq i}^{N} F_{z,i \leftarrow n} = I_i \sum_{n \neq i}^{N} G_{F_z}(\mathbf{p_i}; \mathbf{P_n}) I_n, \tag{4.68}$$

where

$$G_{F_z}(\mathbf{p_i}; \mathbf{P_n}) = \frac{\mu_0}{2} \frac{k(z_i - Z_n)}{\sqrt{r_i R_n}} \left[-K(k) + \frac{1 - \frac{1}{2}k^2}{1 - k^2} E(k) \right] \tag{4.69}$$

denotes the equivalent Green function coefficient for the applied vertical force on the CCL i due to field generated by other $N-1$ coaxial loops, each placed on point $\mathbf{P_n} = (R_n, Z_n)$.

Magnetic field, force and inductances in 3D tokamak geometry

Relying on a linear system of coaxial loops simplifies the mathematical handling of the variables stored in the operating currents. For more complex (and non symmetrical) magnets geometries, such as for the TF coils, the solution of the full convolution integrals of Equation (4.51) in the three-dimensional space has to be performed. The computational code EFFI [157, 158], due to its large flexibility and portability, has been used and linked to MIRA. EFFI stands for "Electromagnetic Fields, Forces and Inductance" and assesses at any given spatial location and for an arbitrary system of ironless coils. As illustrated in Figure 4.4, a coil in EFFI can be either constructed from circular arc and/or straight segments of rectangular cross section.

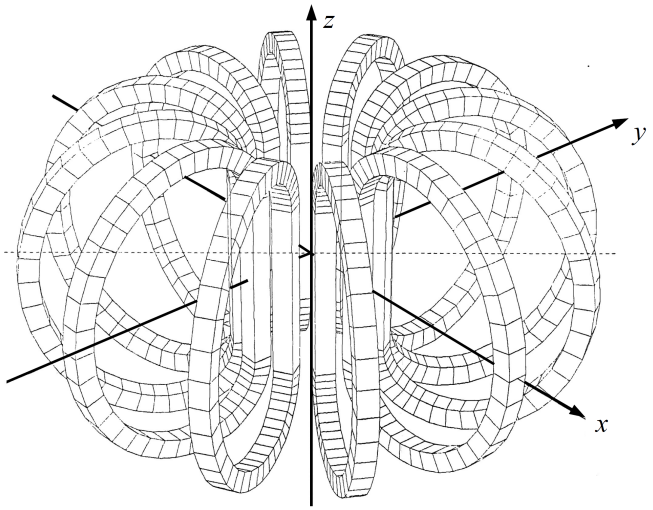

Figure 4.4.: Representation of current-carrying elements system engaged by the Biot-Savart code EFFI for the magnetostatic simulation of any arbitrary set of tokamak TF coils [159].

EFFI is based on the solution of the Biot-Savart law for Cartesian (x, y, z) and Cylindrical (r, ϕ, z) coordinate systems. The code EFFI is coupled to the package TOKEF [159], i.e. a tokamak input generator for EFFI, converting the information on tokamak-like coils geometries in a format readable from EFFI, such as in terms of arcs, loops of straight current elements. In general for any complex magnet system the Biot-Savart law offers the possibility to directly calculate the magnetic field at any given position, without solving the magnetostatic problem for the whole system domain. This is an advantage with respect to more enhanced numerical methods (e.g. finite elements). On the other hand, the size of problem scales with the number of coil elements representing the entire system. For electromagnetic applications within the MIRA magnets module, the use of the EFFI code is restricted to the modelling of the TF coils. Moreover, EFFI refuses the filamentary approximation within the coil cross section, where an homogeneous distribution of $\mathbf{J}$ is considered. Accordingly, inside a conductor of finite sizes, it solves the full three-dimensional integral Biot-Savart equation. Therefore, to avoid the singularity derived from the filamentary theory, EFFI is also deployed to calculate the magnetic field inside PF and TF coils regions. More details on the logics of EFFI and TOKEF in relation to the fusion tokamak magnet system are reported separately for PF and TF coils in the following subsections.

4.2.2. A nonlinear solver for the PF/CS coils current configuration

The external poloidal field configuration required to meet shaping, equilibrium and plasma current induction requirements is obtained by aggregating the contributions from the PF coils and the CS. The PF/CS coils magnet system is composed of a number N_c of physically equivalent circular magnetic circuits, each carrying a current I_c. N_c splits into a number N_{CS} of axially aligned elements included in the CS stack and a number N_{PF} of PF coils. A major goal of a system code is to gauge the current I_c for each of coil. The calculated currents must satisfy a given set of operational requirements on the plasma boundary shape and fulfil the technology and the operational constraints imposed on the physical subcomponents, such as peak field and current density in the superconducting cable and total forces.

A nonlinear current solver for the PF/CS coil system to find one (or more) current configurations and meeting such requirements and constraints is integrated in MIRA. Conceptually it follows the design guidelines engaged in the frame of the PPPT programme for DEMO scenario analysis [160, 161] and integrated in the CREATE-NL+ equilibrium solver [95, 162]. It is worth notice that in the current MIRA coil solver an optimized geometric PF/CS coil configuration is not calculated, but relies on prescribed positions and sizes. A devoted method should deduce a coil configuration whose number, poloidal locations and cross-sections are optimized with respect to, for example, plasma shape requirements and coil stored energy.

The current loops configuration in tokamak poloidal field coil systems

The entire system of toroidal currents can be thought as union of plasma, PF/CS coils and passive structures. Neglecting the effects of the structures, the plasma and the PF/CS coils are magnetically equivalent so that the magnetic properties associated to flux, field and vertical Lorentz forces can be assessed following the filamentary theory for an arbitrary system of coaxial loops, as shown in Figure 4.5.

Say, each PF/CS coil i is characterized by a number of turns N_i, each carrying the same current $I_i = I_{c,i}/N_i$. The turn j of the coil i is then located at point $\mathbf{P_{j,i}}$. Geometrically it consists of a vertical and axial thickness δr_i and δz_i and a pair of mid-point coordinates $r_{m,i}$, $z_{m,i}$. The plasma is conceived as a PF coil including a number N_p of CCLs, each carrying a different toroidal current $I_{p,g}$.
The plasma ring currents can be extracted from the plasma equilibrium model as follows. The Grad-Shafranov equilibrium problem solved for a fixed target plasma domain boundary $\partial\mathcal{D}_p^t$ entails a radial/vertical profile of the plasma toroidal current density $J_{\phi,p}(r,\Psi)$ (Equation 3.7). Such a distribution can be super-imposed onto a rectangular regular mesh grid, where each cell incorporates a CCL in $\mathbf{P_{g,p}} = (r_{g,p}, z_{g,p})$ carrying the current $I_{g,p}$.

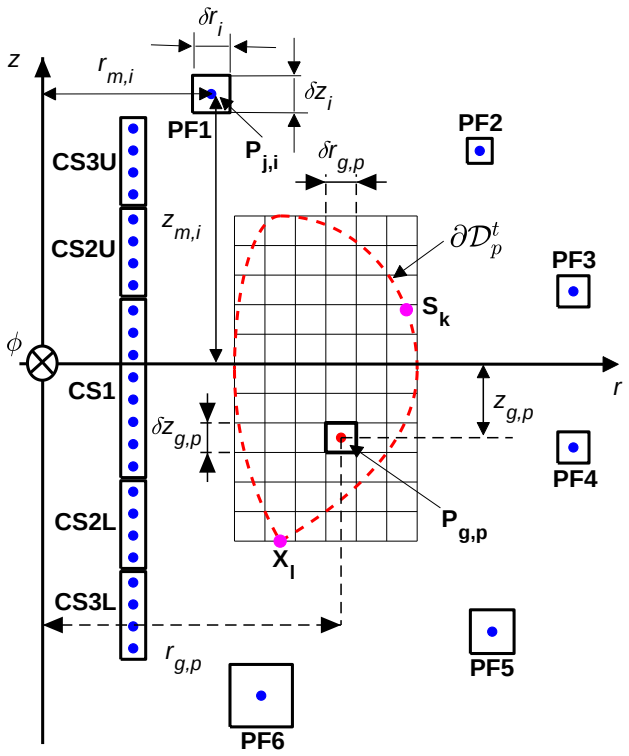

Figure 4.5.: Schematic diagram of PF/CS + plasma Coil systems. The blue dots depict the CCL on the poloidal field coils systems (both for PF coils and CS). The red dot, instead, represents a generic plasma CCL placed on point $\mathbf{P_p} = (r_p, z_p)$. On $\mathbf{S_k}$ it is placed a generic LCMS point, while $\mathbf{X_l}$ indicates the bottom X-point. Figure reproduced according to [88].

The plasma current in the $g-$th loop is tallied by integrating over the differential cross sectional area $\mathrm{d}r\mathrm{d}z$ as

$$I_{g,p} = \int_{\Sigma_{g,p}} J_{\phi,p}(r,\Psi)\mathrm{d}r\mathrm{d}z, \tag{4.70}$$

where $\Sigma_{g,p}$ depicts the rectangular cross section of the plasma cell associated with the current ring in $\mathbf{P_{g,p}}$,

$$\Sigma_{g,p} = \left\{ (r,z) \in \mathcal{D}_p \mid r_{g,p} - \frac{\delta r_{g,p}}{2} \leq r \leq r_{g,p} + \frac{\delta r_{g,p}}{2} \vee z_{g,p} - \frac{\delta z_{g,p}}{2} \leq z \leq z_{g,p} + \frac{\delta z_{g,p}}{2} \right\}. \tag{4.71}$$

As a result, the sum over all the plasma current filaments yields the total plasma current I_p. To have a meaningful spatial mapping of the size of $J_{\phi,p}$, $\delta r_{g,p}$ and $\delta z_{g,p}$ should be comparable to the plasma mesh size h, which $J_{\phi,p}$ depends on. These aspects emphasize the implications of two-dimensional modelling of the plasma to systems and modules which are external to the plasma itself.

In tokamaks the requirements and the constraints imposed on the PF/CS coils to determine the coil currents vector $\mathbf{I_c} = [I_{c,1}, ...I_{c,N_c}]$ are imposed in terms of poloidal flux Ψ, radial and vertical fields B_r and B_z and vertical forces F_z. The poloidal distribution of field and flux has to recreate an imposed value around some key spatial locations in the poloidal plane (r, z) bound to the operational phase of the reactor. The generic magnetic function $\mathcal{F}$, with $\mathcal{F} = \Psi, B_r, B_z$, calculated at a given spatial location $\mathbf{p}$ for the coupled system of plasma and N_c PF/CS coils can be written as a function of $\mathbf{I_c}$ and of the plasma current density distribution $J_{\phi,p}$ such that

$$\mathcal{F}(\mathbf{p}; \mathbf{I_c}, J_{\phi,p}) = \overline{\mathcal{G}}_{\mathcal{F},c}(\mathbf{p})\mathbf{I_c} + \mathcal{G}_{\mathcal{F},p}(\mathbf{p}; J_{\phi,p})I_p, \text{ with } \mathcal{F} = \Psi, B_r, B_z. \tag{4.72}$$

$\overline{\mathcal{G}}_{\mathcal{F},c}(\mathbf{p})$ denotes the $1 \times N_c$ vector, with each element identifying the $\mathcal{F}$ contribution from the coil i at point $\mathbf{p}$ and defined as:

$$\left(\overline{\mathcal{G}}_{\mathcal{F},c}(\mathbf{p})\right)_i = \sum_j^{N_i} \frac{G_{\mathcal{F}}(\mathbf{p}; \mathbf{P_{j,i}})}{N_i} \text{ with } i = 1, 2, ..., N_c, \tag{4.73}$$

where $G_{\mathcal{F}}$ is the associated Green function (Equations 4.54−4.56). The term $\mathcal{G}_{\mathcal{F},p}(\mathbf{p};, J_{\phi,p})I_p$ embeds the share of $\mathcal{F}$ associated with the plasma CCLs only, for sake of analogy with $\overline{\mathcal{G}}_{\mathcal{F},c}$, rearranged with the total plasma I_p in evidence. Similarly, $\mathcal{G}_{\mathcal{F},p}(\mathbf{p})$, can be expressed as

$$\mathcal{G}_{\mathcal{F},p}(\mathbf{p}; J_{\phi,p}) = \sum_g^{N_p} G_{\mathcal{F}}(\mathbf{p}; \mathbf{P_{g,p}}) \frac{I_{g,p}(J_{\phi,p})}{I_p}. \tag{4.74}$$

The vertical force $F_{z,i}$ exerted on the PF/CS coil i by interaction with the other $N_c - 1$ PF/coils and with the plasma can be formulated as a quadratic expression:

$$F_{z,i}(\mathbf{I_c}, J_{\phi,p}) = (\mathbf{I_c})_i \cdot \left(\sum_j^{N_c} \mathcal{G}_{F_z}^{i \leftarrow j} \cdot (\mathbf{I_c})_j + \mathcal{G}_{F_z}^{i \leftarrow p} \left(J_{\phi,p}\right) I_p \right), \tag{4.75}$$

where,

$$\mathcal{G}_{F_z}^{i \leftarrow j} = \frac{1}{N_i N_j} \sum_k^{N_i} \sum_h^{N_j} G_{F_z}(\mathbf{p_{k,i}}; \mathbf{P_{h,j}}), \tag{4.76}$$

is the force on the coil i from coil j per unit current $I_{c,i}$ and unit current $I_{c,j}$, and

$$\mathcal{G}_{F_z}^{i \leftarrow p}\left(J_{\phi,p}\right) = \frac{1}{N_i} \sum_k^{N_i} \sum_g^{N_p} G_{F_z}(\mathbf{p_{k,i}}; \mathbf{P_{g,p}}) \frac{I_{g,p}\left(J_{\phi,p}\right)}{I_p} \tag{4.77}$$

on coil i from the plasma per unit current $I_{c,i}$ and unit current I_p. The equivalent mutual vertical force coefficient G_{F_z} is given by Equation (4.69). The point $\mathbf{p_{k,i}}$ relates to the spatial location pointing to the $k-$th loop of coil i, and that holds also for the point $\mathbf{P_{h,j}}$ to the conductor h on coil j and for $\mathbf{P_{g,p}}$ to the filament g in plasma.

A fusion power plant operating in pulsed mode relies on distinct phases, each characterized by a specific functional role. The design of the PF/CS coil systems is primarily focused on three main time frames during the pulse:

- plasma breakdown (BD),
- start of flat-top (SOF) and
- end of flat-top (EOF).

The time evolution of the currents in the coils defines a *scenario* [38]. Over the different scenario time frames, the PF/CS coils system shall cope with rather diverse operational demands, expressed as flux and field on radial poloidal prescribed spots.

Technology and operational constraints on PF/CS coils

Throughout a tokamak pulse cycle the PF/CS coils system design has to comply with the operational constraints, formulating a set of design parameters within prescribed operation bounds to guarantee a safe operation. These parameters are affiliated to [161]:

- maximum operating current $\mathbf{I_c}_{,\max}$,
- maximum allowable magnetic field $B_{\max}$,
- maximum Lorentz vertical forces, $F_{z,\max}$.

Having assigned maximum radial and axial widths, δr_i and δz_i, the cross-sectional area $A_{c,i} = \delta r_i \delta z_i$ of the $i-$th coil is filled out with a number of turns $N_{turn,i}$, wound according to the cable layout, as shown in Figure 2.4$-$a. This yields the maximum total current $I_{c,i}^{\max}$, which solely depends on the superconducting cable technology adopted for the $i-$th coil. This restricting condition can be directly formulated on the numerical values of coil current solution vector $\mathbf{I_c} = [I_{c,1}, ..., I_{c,N_c}]$, with upper and lower bounds $I_{c,i}^{\max}$ and $-I_{c,i}^{\max}$, leading to

$$-I_{c,i}^{\max} \leq (\mathbf{I_c})_i \leq I_{c,i}^{\max}, \text{ with } i = 1, 2, ..., N_c. \tag{4.78}$$

A superconducting cable cannot exceed a maximum magnetic field limit $B_{\max}$ to maintain a superconducting state. Moreover, since the in-coil magnetic field distribution is likely to feature its largest values at the perimeter of the conducting region, an arbitrary number $N_{\partial\mathcal{D},i}$ of points is selected on the edges defining the poloidal contour. On these positions B is evaluated refusing the filamentary approximation to avoid the numerical singularities near the current loops. Therefore, the constraining bounds due to magnetic field in the current-carrying cross section is:

$$B(\mathbf{p_{j,i}}; \mathbf{I_c}) \leq B_{\max,i}, \text{ with } \begin{cases} i = 1, 2, ..., N_c \\ j = 1, 2, ..., N_{\partial\mathcal{D},i} \end{cases}, \tag{4.79}$$

where $B(\mathbf{p_{j,i}}; \mathbf{I_c}, J_{\phi,p})$ is the calculated magnetic field and $B_{\max,i}$ indicates the allowable peak magnetic field imposed by the superconducting cable for the coil i. This set of B ceiling conditions corresponds to a number $\sum_i^{N_c} N_{\partial\mathcal{D}_i}$ of additional relations to fulfil. The most critical magnetic field limits are verified in the CS stack during the premagnetization phase. For this reason and to reduce the size of the problem the field upper bound conditions on the PF coils can be optionally disabled.

The mutual interactions between PF/CS coils and plasma yield large electromagnetic forces required to be controlled. While the radial tensile forces are radially balanced by the internal jacketing steel structures of the conductors, the vertical components must lay within acceptable values.

A stress analysis has to be performed to ensure the structural integrity of the coils. But, if the combination of coil currents features demanding static forces, the design of internal structures is more complex. Therefore, the mechanical criteria differently applied to the number N_c^{PF} of PF coils and N_c^{CS} of the CS stack are driven by total vertical force F_z arising. For the current DEMO scenario [160, 161] the vertical forces limits are formulated as:

- maximum vertical force on each PF coil;
- maximum total vertical force on the CS stack;
- maximum separation force between the CS stack elements.

In ITER and DEMO the PF coils are anchored directly on the TF coil external casing structure through dedicated supports including flexible plates or sliding interfaces allowing for radial displacements [163]. These attachments can tolerate vertical loads up to a certain prescribed upper limit $F_{z,PF}^{\max}$, creating room for an imposed operational constraint on the $g-$th PF coil,

$$F_{z,PF}^{g}(\mathbf{I_c}, J_{\phi,p}) \leq F_{z,PF}^{\max}, \;\; \text{with}\, g = 1, 2, ...N_c^{PF}. \tag{4.80}$$

A different situation is found in the CS stack, where large vertical forces, might lead to a misalignment between the elements or a vertical separation. For this reason. devoted structural components are designated to cope with these forces. In the ITER CS system both CS supports and a vertical preload structure are foreseen to keep the CS coils in line. The pre-loading is necessary to compensate separating forces arising during start of flat-top, tending to separate the elements from each other. This effect might jeopardize the structural integrity of the ground insulator between modules [163]. A constraining condition is posed on the maximum total vertical force $F_{z,CS}^{tot}$ and on the maximum separation force on the CS modules, both reading as

$$F_{z,CS}^{tot}(\mathbf{I_c}, J_{\phi,p}) = \left| \sum_{i}^{N_c^{CS}} F_{z,i}(\mathbf{I_c}, J_{\phi,p}) \right| \leq F_{z,CS}^{tot,\max}, \tag{4.81}$$

with $F_{z,CS}^{sep,\max}$ denoting the allowable limit on the maximum CS vertical force and

$$\begin{aligned} F_{z,CS}^{sep,up}(\mathbf{I_c}, J_{\phi,p}) &= \max \left[\sum_{i}^{k} F_{z,CS}^{i}(\mathbf{I_c}) \right] \leq F_{z,CS}^{sep,\max}, \\ F_{z,CS}^{sep,dw}(\mathbf{I_c}, J_{\phi,p}) &= \min \left[\sum_{i}^{k} F_{z,CS}^{N_c^{CS}-i+1}(\mathbf{I_c}) \right] \geq -F_{z,CS}^{sep,\max}, \end{aligned} \quad \text{with } k = 1, 2, ..N_c^{CS}. \tag{4.82}$$

$F_{z,CS}^{sep,\max}$ relates to the upper bound linked to allowable separation force between the CS elements, while $F_{z,CS}^{sep,up}$ and $F_{z,CS}^{sep,dw}$ differentiate between the separation loads pulling the elements up and down, respectively.

Finally, the constraining rules to fulfil when calculating the currents in the coils must account for the design, manufacturing and feasibility interconnected with the cable technology, as well as for its operational limits. Summarizing these can be combined into a unique compact formulation,

$$\begin{cases} |(\mathbf{I_c})_i| \leq I_{c,i}^{\max} \\ \mathcal{C}(\mathbf{I_c}, J_{\phi,p}) \leq \mathbf{0} \end{cases} \quad \text{with } i = 1, 2, ..., N_c, \tag{4.83}$$

where,

$$\mathcal{C}(\mathbf{I_c}) = \begin{pmatrix} B(\mathbf{p_{j,i}}; \mathbf{I_c}, J_{\phi,p}) - B_{\max,i} \\ F^{g}_{z,PF}(\mathbf{I_c}, J_{\phi,p}) - F^{\max}_{z,PF} \\ F^{tot}_{z,CS}(\mathbf{I_c}, J_{\phi,p}) - F^{tot,\max}_{z,CS} \\ F^{sep,up}_{z,CS}(\mathbf{I_c}, J_{\phi,p}) - F^{sep,\max}_{z,CS} \\ -F^{sep,dw}_{z,CS}(\mathbf{I_c}, J_{\phi,p}) - F^{sep,\max}_{z,CS} \end{pmatrix} \text{ with } \begin{cases} i = 1,2,...,N_c \\ j = 1,2,...,N_{\partial\mathcal{D},i} \\ g = 1,2,...N^{PF}_c \end{cases} . \tag{4.84}$$

Accordingly, $\mathcal{C}(\mathbf{I_c})$ incorporates a number $N_{\mathcal{C}} = \sum_i^{N_c} N_{\partial\mathcal{D},i} + N^{PF}_c + 3$ of nonlinear conditions to meet when determining $\mathbf{I_c}$.

While the peak magnetic field $B_{\max}$ and the maximum operating current $I^{\max}_c$ are purely hinging upon the selected superconducting cable technological solution, the constraints on the vertical forces are operational. Henceforth, a set of fixed values assumed for the design the DEMO PF/CS coils is given in Table 4.2.

Description	Symbol	[Unit]	Value
Maximum vertical force in PF coils	$F^{\max}_{z,PF}$	[MN]	≤ 450
Maximum vertical force in CS stack	$F^{tot,\max}_{z,CS}$	[MN]	≤ 300
Maximum separation force in the CS stack	$F^{sep,\max}_{z,CS}$	[MN]	≤ 350

Table 4.2.: DEMO vertical force constraints on the PF/CS coils [161].

PF/CS coils current configuration at plasma breakdown

The beginning of a plasma pulse requires a premagnetization of the CS, which has to be brought to its maximum operating current to maximize the poloidal magnetic flux within the torus vacuum chamber. This phase ends with the plasma breakdown (BD) defined as the time duration for the formation of the plasma. At this time $t = t_{bd}$ the plasma chamber is filled with a neutral gas, mostly molecular deuterium. The plasma formation in a tokamak is realized by means of the Townsend avalanche [164], consisting of a ionization of the gas by an externally applied toroidal electric field. Such an electric field is provided by a time variation of the toroidal currents running in the CS. At plasma breakdown the conditions to meet are concerned with the *stray magnetic field*, essentially, due to the curvature of the magnetic field lines at the top and bottom extreme sides of the CS. Ideally the CS is an infinitely vertical solenoid with zero field outside its region and an homogeneous vertical magnetic field inside, given by

$$B_{z,\max} = \mu_0 J^{\max}_{wp} \delta r_{cs}, \tag{4.85}$$

with $J^{\max}_{wp}$ the maximum current density in the CS and δr_{cs} its radial thickness. In actual operating situations the CS must be vertically truncated, typically at the height of the TF coils, yielding a non-null field in the chamber. The breakdown region can be surrounded by a circular poloidal domain $\mathcal{D}_{bd}$, centred on a target BD point $\mathbf{X_{bd}} = (r_{bd}, z_{bd})$ and characterized by a radius ρ_{bd} (see Figure 4.6).

A major task of the PF coils is to keep the magnetic field below a certain limit $B^{\max}_{stray}$ within $\mathcal{D}_{bd}$. For breakdown analyses on the EU-DEMO 2015 baseline [165], the maximum stray field has been assumed around 3 mT and $\mathbf{X_{bd}}$ and targeted to take place in the central outboard area, e.g. $r_{bd} = 9.80$ m and $z_{bd} = 0$. The extension of the BD domain $\mathcal{D}_{bd}$ has been taken for $\rho_{bd} \sim 2$ m. $\mathbf{X_{bd}}$

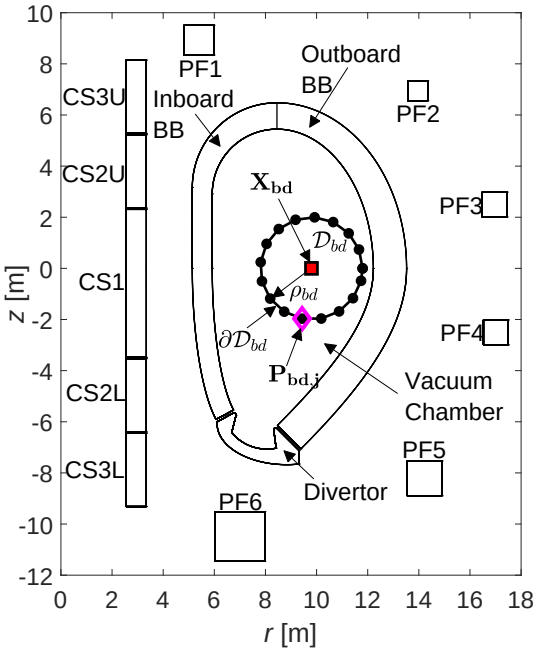

Figure 4.6.: Schematic diagram of the plasma breakdown configuration and the constructing points and variable denoting the circular BD region $\mathcal{D}_{bd}$.

identifies the spot where the poloidal magnetic flux Ψ shall be maximized and it also represents a null point, i.e. $B_r(\mathbf{X_{bd}}) = B_z(\mathbf{X_{bd}}) = 0$. As a result, the stray field criteria can be met by taking a finite number N_{bd} of points $\mathbf{P_{bd,j}}$ on the boundary $\partial\mathcal{D}_{bd}$ and posing an upper limit to the total magnetic field [165]. Combining the maximization of the poloidal flux and the cancellation of both magnetic field components on $\mathbf{X_{bd}}$ to the technological and operational constraints outlined in Equation (4.83) at plasma breakdown, the solution vector $\mathbf{I_c}$ is obtained by solving the nonlinear problem (with no plasma current density $J_{\phi,p}$), formulated as

$$\max_{\mathbf{I_c}} \Psi\left(\mathbf{X_{bd}}; \mathbf{I_c}\right) \text{ subject to } \begin{cases} B_k(\mathbf{X_{bd}}; \mathbf{I_c}) = 0 \\ B(\mathbf{P_{bd,j}}; \mathbf{I_c}) \leq B_{stray}^{\max} \\ |(\mathbf{I_c})_i| \leq I_{c,i}^{\max} \\ \mathcal{C}(\mathbf{I_c}) \leq 0 \end{cases} \text{ with } \begin{cases} i = 1, 2, ..., N_c \\ j = 1, 2, ..., N_{bd} \\ k = r, z \\ \mathbf{P_{bd,j}} \in \partial\mathcal{D}_{bd} \end{cases} . \tag{4.86}$$

This constrained linear and nonlinear optimization problem, is characterized by a number of conditions $N = N_{\mathcal{C}} + N_c + N_{bd} + 2$ and it is being solved via interior point algorithm [166] integrated in the `fmincon` MATLAB solver (see Appendix B).

The proposed methodology has two limitations, both for premagnetization and flat-top phase. First, due to the quadratic dependency on $\mathbf{I_c}$ of the vertical force constraints, the solution is affected by the required initial guess of $\mathbf{I_c^0}$. However, as the coil current solution is meant to reproduce the premagnetization process, i.e. starting from a null-current situation, the solver attempts reproducing the current rising trend up to its peak feasible limit, as the objective function is the poloidal flux Ψ at $\mathbf{X_{bd}}$. Therefore, at least in case of premagnetization the initial guess has been found for a variety of examined cases to negligibly affect the solution. Moreover, calculating the currents for a given flux and field map is an ill-posed problem, where several solutions might exist. For this reason a direct

comparison in terms of coil currents with other equilibrium solver (e.g. CREATE-NL+) has not been addressed.

PF/CS coil current configuration at plasma flat-top

In advanced DEMO scenario modelling [161] the operational requirements on the plasma shape at start of flat-top (SOF) and end of flat-top (EOF) are applied in terms of minimum distance from the blanket first wall as well as in terms of global plasma shape features, such as volume, triangularity and elongation [160]. Such a choice is justified by the fact that at the stage where detailed flat-top equilibria calculations are performed, the profile of the FW is being provided as input of the problem. In a systems code modelling frame the reactor physical components are being built around the plasma separatrix. For this reason, the situation is handled inversely, by imposing a target separatrix shape. Relying on a calculated plasma equilibrium solution on a fixed reference plasma boundary $\partial\mathcal{D}_p^t$ (target plasma boundary) the goal of the external PF/CS coil systems is to reproduce a target plasma boundary as closely as possible, to make the obtained magnetic configuration usable in core plasma physics. The Dirichlet boundary condition applied to Equation (3.30), needs to be realized for externally-applied magnetic flux from PF/CS coil system. Based on the definition of the LCMS the whole tokamak toroidal currents system has to produce a global magnetic configuration so that together with the plasma a poloidal flux on $\partial\mathcal{D}_p^t$ equal to a target value Ψ_b^t is established.

Based on Figure 4.5, the poloidal profile of the target plasma separatrix $\partial\mathcal{D}_p^t$ is discretized in a number N_b of linear piecewise elements. These are framed by an identical number of points $\mathbf{S_k} = (r_{k,b}, z_{k,b})$, for which the poloidal flux Ψ equals Ψ_b^t, so that

$$\Psi(\mathbf{S_k}; \mathbf{I_c}, J_{\phi,p}) = \Psi_b^t \quad \text{with } k = 1, 2..., N_b \tag{4.87}$$

and $J_{\phi,p}$ being the plasma current density. Assuming a single null divertor configuration, three additional constraints have to be imposed to control the position of the bottom X-point $\mathbf{X_l} = (r_X, z_X)$, i.e. $B_r(r_X, z_X) = B_z(r_X, z_X) = 0$. Moreover, as $\mathbf{X_l}$ belongs to $\partial\mathcal{D}_p^t$, the requirement on the poloidal flux Ψ_b^t is to be verified, too. Thus,

$$\begin{cases} B_k(\mathbf{X_l}; \mathbf{I_c}, J_{\phi,p}) = 0 \\ \Psi(\mathbf{X_l}; \mathbf{I_c}, J_{\phi,p}) = \Psi_b^t \end{cases} \quad \text{with } k = r, z. \tag{4.88}$$

"Immobilizing" the bottom X-point appears rather restrictive and not in line with actual operational tokamak situations, where controlled dislocations can be induced to avoid too large and too localized heat fluxes on the divertor targets. In this case a precise location is necessary to design the key divertor elements, which can be drawn only if the radial and axial positions of the X-point have been established.

In order to represent the poloidal shape of $\partial\mathcal{D}_p^t$ a sufficiently large number of points N_b are required. Thereby, the problem becomes over-constrained with N_b expected to be a way larger than N_c. To that end a linear least-square solution of $\mathbf{I_c}$ can be considered. Accordingly, taking $\mathcal{L}(\partial\mathcal{D}_p^t; \mathbf{I_c}, J_{\phi,p})$ an objective function, defined as the squared 2-norm of the residual error $\left|\Psi(\mathbf{S_k}; \mathbf{I_c}, J_{\phi,p}) - \Psi_b^t\right|$ on each point $\mathbf{S_k}$ on $\partial\mathcal{D}_p^t$,

$$\mathcal{L}(\partial\mathcal{D}_p^t; \mathbf{I_c}, J_{\phi,p}) = \frac{1}{2N_b}\sqrt{\sum_{k=1}^{N_b}\left|\Psi(\mathbf{S_k}; \mathbf{I_c}, J_{\phi,p}) - \Psi_b^t\right|^2} \quad \forall \mathbf{S_k} \in \partial\mathcal{D}_p^t, \tag{4.89}$$

the problem would be engaged by minimizing $\mathcal{L}$. Taking $\mathbf{I_c}$, the PF/CS coil currents solution, the overall constrained linear least-square problem is obtained by combining the separatrix target function, the X-point requirements and the coil technological and operational limits. Finally, it can be written as

$$\min_{\mathbf{I_c}} \mathcal{L}\left(\partial\mathcal{D}_p^t; \mathbf{I_c}, J_{\phi,p}\right) \text{ subject to } \begin{cases} B_k(\mathbf{X_l}; \mathbf{I_c}, J_{\phi,p}) = 0 \\ \Psi(\mathbf{X_l}; \mathbf{I_c}, J_{\phi,p}) = \Psi_b^t \\ |(\mathbf{I_c})_i| \leq I_{c,i}^{\max} \\ \mathcal{C}(\mathbf{I_c}, J_{\phi,p}) \leq 0 \end{cases} \quad \text{with} \begin{cases} i = 1, 2, ..., N_c \\ k = r, z \end{cases} . \tag{4.90}$$

Similarly to the breakdown case the solution is found by means of interior point algorithm.

Observing closely the parametric dependencies influencing the solution of Equation (4.90), some coupling measures must be taken to account for the mutual influences between the plasma equilibrium state and the magnetic flux induced by external PF/CS coils. The solution vector $\mathbf{I_c}$ reproduces a global configuration which can hardly replicate the exact profile of $\partial\mathcal{D}_p^t$ due to the large number N_b of flux conditions. N_b, typically ∼20-50, is indeed larger compared to degrees of freedom of the coil resolution problem, $N_c \approx 10$. Hence, the key linking parameter between plasma equilibrium solver and the coil current configuration is the actual plasma separatrix $\partial\mathcal{D}_p$, representing a "magnetic" interface between the plasma and the PF/CS coils. Thus, an iterative approach to simulate the problem in an more holistic fashion is suggested. The plasma equilibrium solver has been fully coupled with the PF/CS coil current solver, according to the operational logics illustrated in the flowchart of Figure 4.7.

The reported data flows and the related connections show a new feature : the core plasma physics.
As remarked in Section 3.2.4, a strong linking between core plasma features and equilibrium has been identified in the poloidal beta β_p, used in the equilibrium configuration as a target parameter for current density shaping purposes. The poloidal beta itself is strongly bound to the pressure regime in the confining region and thus to the overall plasma performances and operational requirements. Therefore, β_p ties the core physics targets to the equilibrium model, while the separatrix shape $\partial\mathcal{D}_p$ links the coil solver to both.

This situation led to an organization of the complete coupling in two iteration loops, referred to as inner and outer loops. At first, the main equilibrium and plasma shape target values are set to initialize the equilibrium model, in terms of plasma domain mesh and an initial guess on the current density. The target separatrix shape is parametrized in the geometry module, but the actual design goals for shaping purposes are represented by the X-point triangularity δ_X, the elongation κ_X and the plasma volume V_p. Plasma triangularity and elongation are constructed from a more elaborated set of plasma geometry specifications, such as upper and lower δ and κ, i.e. $\delta_{X,u/l}$ and $\kappa_{X,u/l}$ and lower intersection angles between inner and outer separatrix lines $\psi_{\pm,u/l}$ (see Figure 2.9). As a consequence, these are the actual parameters to impose an arbitrary plasma geometry scenario within certain feasibility ranges. The equilibrium calculation begins with the initial guess of the poloidal beta β_p, which is being upgraded by the plasma solver in response to the imposed plasma operational requirements and limits. Such a cyclic and mutual repetition of equilibrium and physics takes its exit point when β_p converges to a constant value, within the prescribed tolerance $\epsilon_\beta = 0.01$ %.
The plasma configuration expressed by Ψ and current density $J_{\phi,p}$, is passed to the PF/CS coil system solver to find the "best combination" of $\mathbf{I_c}$, to reproduce $\Psi(r,z) = \Psi_b^t \; \forall\,(r,z) \in \partial\mathcal{D}_p^t$, i.e. the target plasma boundary. The maximum offset between actual and target plasma profiles is taken as

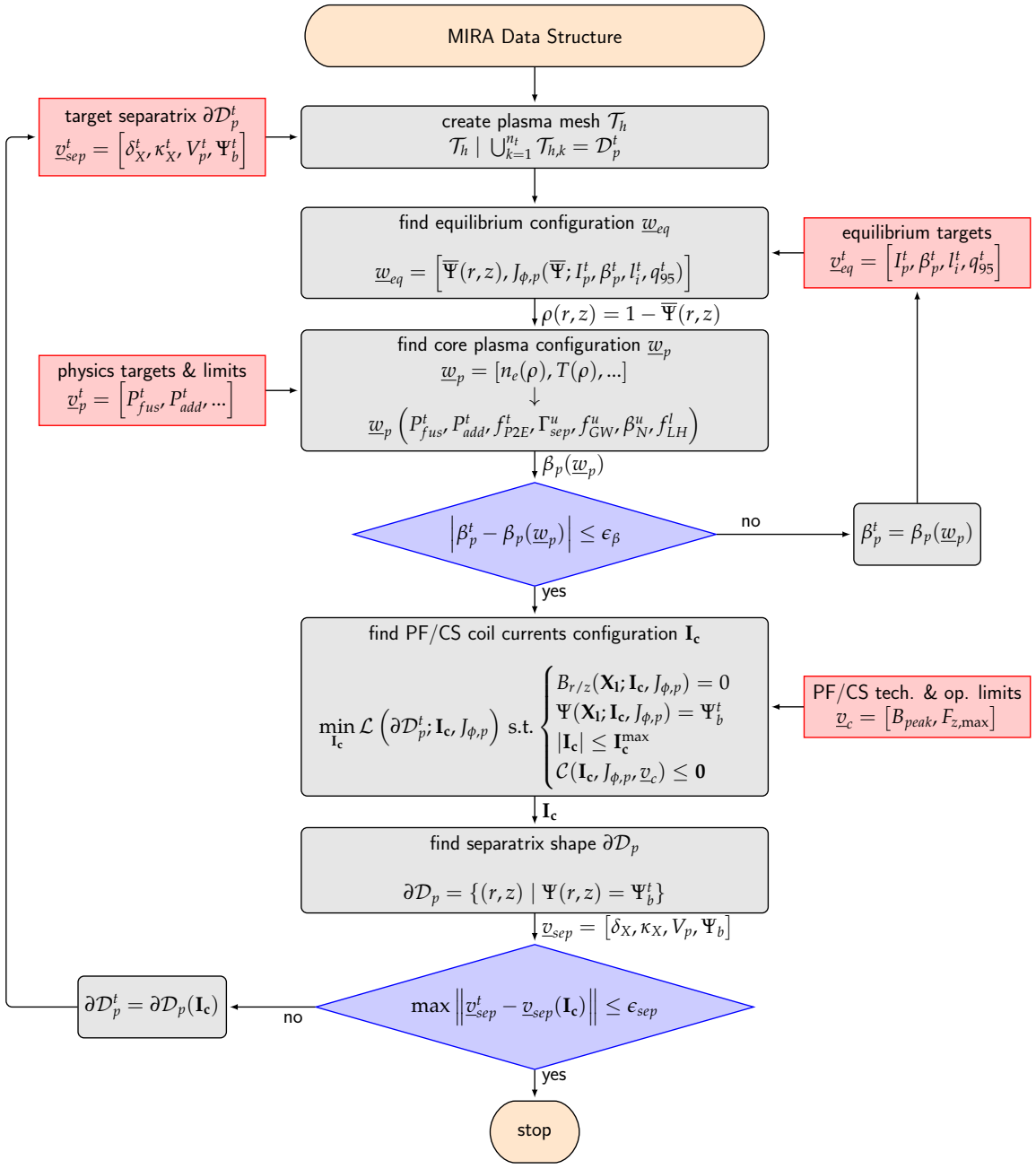

Figure 4.7.: Flow chart for the coupling of plasma equilibrium, core physics and PF/CS coil current solvers. Each block is characterized by its shape: ovals relate to start and stop nodes, sharp-corner-rectangles indicate inputs, round-corner-rectangles denote process steps and diamonds refer to process decisions.

the stopping criteria for the outer loop, controlling the absolute deviation of the actual separatrix parameters $\underline{v}_{sep} = [\delta_X, \kappa_p, V_p]$ with respect to the design goals, given by $\underline{v}_{sep}^t = [\delta_X^t, \kappa_p^t, V_p^t]$. If the largest absolute difference between target and actual values lays within a prescribed tolerance, a complete plasma and PF/CS configuration has been found. Otherwise the new plasma boundary $\partial\mathcal{D}_p^t$ is upgraded and the inner and outer loops are repeated. The extended approach, i.e. including

equilibrium, core physics and coil current solution is engaged within a MIRA run, only to assess the whole reactor configuration at SOF. In other pulse time frames, the core physics solver is by-passed to save computing time.

Looking at the problem from a detailed reactor design angle, the coupled approach relies on rather limited modelling theories compared to advanced transport and equilibrium codes. Nevertheless the modelling frame exhibits a more enhanced mathematical and physics granularity. The most innovative feature is the integrated procedure, where the key core plasma physics and equilibrium issues are coupled and mirrored to engineering aspects affiliated to superconducting magnets technology. This serves as detailed feedback of plasma physics and technology unique to MIRA.

Flat-top length

For pulsed fusion devices the flat-top is the time duration of a reactor pulse, where the plasma current I_p exhibits an almost constant value, defined as t_{sof} and t_{eof}, indicating the time frame for start and end of flat-top. The maximisation of the pulse length τ_{flat} is a priority for a fusion power reactor. With respect to the integral form of Maxwell-Faraday's law, a time variation of the poloidal flux Ψ can be associated to an induced loop voltage U_{loop} in the plasma loop. This a precondition to achieve large inductive currents in the plasma. Exploiting the CS coils, the poloidal magnetic flux Ψ_b is swung down from its starting value at SOF $\Psi_{b,sof}$ to a lower value at EOF $\Psi_{b,eof}$. Assuming that the flux falls slowly and constantly, the flat-top length τ_{flat} can be derived from the Faraday law, to:

$$\frac{\partial \Psi_b}{\partial t} = -U_{loop} \approx \frac{\Psi_{b,eof} - \Psi_{b,sof}}{\tau_{flat}} \Rightarrow \tau_{flat} = \frac{\Psi_{b,sof} - \Psi_{b,eof}}{U_{loop}}, \tag{4.91}$$

where U_{loop} is the plasma loop voltage (for details see Appendix C.1). U_{loop} scales with the plasma resistance R_p and the inductive current I_{ind}. The latter is the remainder of the total plasma current I_p removed from the current drive and bootstrap contributions. The boundary poloidal flux $\Psi_{b,sof}$ at SOF is obtained from the poloidal flux at breakdown $\Psi_{bd} = \Psi(\mathbf{X_{bd}}; \mathbf{I_c})$ subtracting the inductive and the resistive components of the total flux consumption during the ramp-up flux swing. The inductive component Ψ_{ind} depends on the total plasma current I_p and the internal inductance l_i, while the resistive flux Ψ_{res} can be formulated by means of Ejima coefficient C_{Ejima} and I_p, such that [81, 167]:

$$\Psi_{b,sof} = \Psi_{bd} - \Psi_{ind} - \Psi_{res} = \Psi_{bd} - \frac{1}{2}\mu_0 l_i R_{ax} I_p - C_{Ejima}\mu_0 I_p R_0, \tag{4.92}$$

where R_{ax} is the radial coordinate of plasma magnetic axis, extracted from solution $\Psi(r,z)$ to the plasma equilibrium problem, and R_0 is the plasma major radius. Consequentially, $\Psi_{b,sof}$ is adopted as target boundary flux Ψ_b^t at SOF.

Moving forward with the flux swing, Ψ_b is reduced to a feasibly achievable minimum value in accordance to the imposed operational plasma shaping requirements and coils technology constraints. Therefore, splitting the flat-top in a series of quasi stationary state, also called snapshots [161] the equilibrium problem is solved for each of them. This implies two simplifications:

- the core physics solver is disabled and
- the plasma shape is frozen to that of SOF.

Apart from reducing the computing times, those choices are prevalently driven by the fact that $\Psi_{b,eof}$ is mainly affected by the CS coils capabilities to minimize their operating currents without violating any of the technological limitations. Other contributions, such as the variation of the plasma boundary, have been found to provide marginal effects to the determination of $\Psi_{b,eof}$.

The advantage of following a chronological order, when assessing equilibrium configuration, resides in the selection of the PF/CS coils current's initial guess. Beginning with the premagnetization phase, a null-current configuration is assumed. Henceforth, the initial guess at every time step t_i is taken as $\mathbf{I_c}$ calculated on the previous snapshot at $t = t_{i-1}$.

4.2.3. Toroidal magnetic field configuration

The TF coils provide a toroidal magnetic field B_ϕ in the tokamak vacuum chamber. The toroidal magnetic field configuration includes a set of operating parameters, as:

- maximum toroidal field ripple at plasma separatrix,
- static Lorentz forces and
- stored magnetic energy.

These parameters are briefly addressed subsequently.

Magnetic field distribution and toroidal ripple

Assuming B_t the toroidal field to apply to the plasma center at $r = R_0$, with good approximation a $1/r$ dependence of the toroidal field B_ϕ can be derived around the plasma axis, from the integral form of the Maxwell-Ampere's law. Hence, the current carried by each TF coil can be reversely calculated as

$$I_{TFC} = \frac{1}{N_{TFC}} \frac{2\pi R_0}{\mu_0} B_t. \tag{4.93}$$

where N_{TFC} is the number of TF coils. The magnetic field distribution is obtained for a certain geometry profile, a winding pack (WP) cross-sectional layout and a current density vector field J_{TFC}. These aspects are driven by technology considerations. The entire TF coil WP is composed of a series of two WPs, inner and outer. Each has a rectangular radial/toroidal shape to cope with spatial constraints imposed on the inboard leg. It is assumed that these aspects have been fully covered at this point and that the amplitude J^i_{wp} in the $i-$th WP and the spatial distribution of current density vector field $\mathbf{J^i_{wp}}(x,y,z)$, are calculated from I_{TFC}. The poloidal curve $\Gamma^i_{wp}(r,z)$, denoting the D-shape profile of each WP element of the TF coil (see Figure 4.8−a) defines locally the orientation of the poloidal current density vector field $\mathbf{J_{wp}}$, aligned to the local direction $\hat{n}_\parallel$. For this reason, Γ^i_{wp} may be also called "current line".

Relying on an accurate 3D profiling of the magnetic field allows to calculate the *toroidal field ripple*. Because of the discretized nature of the TF coils, the toroidal component of the magnetic field exhibits a ripple, i.e. an oscillation along the toroidal direction ϕ. This effect has negative effects on the plasma stability, potentially causing losses of fast alphas and even affect the confinement of thermal plasma [17].
Therefore, upper limits are typically imposed on the amplitude of the toroidal ripple. At any given

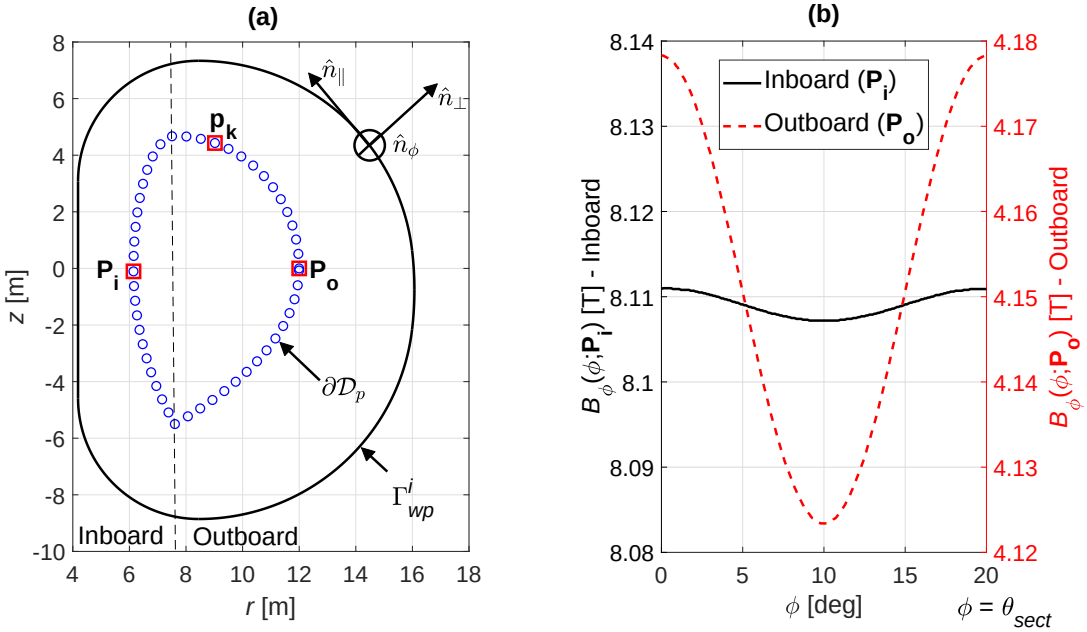

Figure 4.8.: Graphical representation for the calculation of the toroidal field ripple. Subfigure (a) shows the poloidal envelope of the TF coil winding pack Γ^i_{wp} with respect to the set of points $\mathbf{p_k}$ where the ripple δ_{tf} is calculated. Subfigure (b) includes the toroidal distribution of the toroidal field B_ϕ calculated on the EU-DEMO 2015 TF coils system at two radial positions at the mid-equatorial ($z = 0$), located at points $\mathbf{P_i}$ and $\mathbf{P_o}$.

location $\mathbf{p}$ on the (r, z) poloidal plane, the ripple $\delta_{tf}(\mathbf{p})$ is defined as a maximum relative oscillation of the toroidal field B_ϕ within a prescribed range of ϕ, such that [17, 168]

$$\delta_{tf}(\mathbf{p}) = \frac{\max\left(B_\phi(\phi;\mathbf{p})\right) - \min\left(B_\phi(\phi;\mathbf{p})\right)}{\max\left(B_\phi(\phi;\mathbf{p})\right) + \min\left(B_\phi(\phi;\mathbf{p})\right)}, \quad \forall\phi \in [0, \theta_{sect}], \tag{4.94}$$

where, due to the periodicity of the toroidal field over a reactor sector angle θ_{sect}, the reference interval of ϕ is taken between zero and the latter angle. Attaining to plasma stability and confinement issues, the maximum amplitude must be sought within the confining region. Therefore, similarly to Ref. [168], a set of N_δ points $\mathbf{p_k}$ (see Figure 4.8−a) is individuated on the plasma separatrix $\partial\mathcal{D}_p$, provided by the equilibrium model. Accordingly, δ_{tf} is calculated for each of such points and the maximum value $\delta_{tf,\max} = \max\left[\delta_{tf}(\mathbf{p}_1), ..., \delta_{tf}(\mathbf{p}_{N_\delta})\right]$ is considered as the representative value for the verification of the ripple requirement. For current DEMO designs, the limit on $\delta_{tf,\max}$ is fixed to 0.6 % [27].

The different effects of the TF ripple are illustrated in Figure 4.8−b, where B_ϕ has been calculated for the EU-DEMO 2015 TF coil configuration at the plasma mid-plane locations $\mathbf{P_i} = (R_0 - a, 0)$ and $\mathbf{P_o}(R_0 + a, 0)$, depicted in Figure 4.8−a. The curves of Figure 4.8−b exhibit heterogeneous toroidal field fluctuations $\Delta B_\phi(\mathbf{p}) = \max(B_\phi(\phi;\mathbf{p})) - \min(B_\phi(\phi;\mathbf{p}))$ calculated on $\mathbf{p} = \mathbf{P_i}$ and $\mathbf{p} = \mathbf{P_o}$, yielding $\Delta B_\phi(\mathbf{P_o})/\Delta B_\phi(\mathbf{P_i}) \approx 15$.

If the ripple exceeds the allowable limits, action can be taken in two viable directions: increase the number of the coil N_{TFC} and/or push the outer leg far from the plasma. Nevertheless, both solutions are restrained by other considerations. The number of coils cannot be unconditionally enlarged since it reduces the inter-coil space dedicated to equatorial ports. On the other hand, expanding the coil

in radial direction yields the same effect on the PF coils, having negative feedbacks on the shaping performances and on the capital cost, due to the increase of TF coil volume.

The MIRA approach exploits the full spatial resolution of the magnetic factors and is therefore unique in system codes. A more detailed resolution of the toroidal field ripple can be used for a more targeted and design-oriented system analysis.

Lorentz forces and stored energy in TF coils

With respect to the definition of differential Lorentz force definition of Equation (4.64) magnetic fields and electrical currents give rise to static mechanical loads, which must be counteracted by supporting techniques and design of the internal structures. The system of volumetric forces which the TF coils undergo throughout their operation splits in two components:

- in-plane hoop forces $\mathbf{f}_{\perp}$ and
- out-plane bending forces $\mathbf{f}_{\phi}$.

The hoop forces arise from the interaction of the current carried by the coil and its own generated field and thus these the predominant forces scaling up with the total current I_{TFC} and the toroidal field component B_{ϕ}. Equivalently to the PF coils case, these are also purely of tensile kind, meaning that they are exerted outwardly normal to the surface of the coil in the poloidal plane, along the direction $\hat{n}_{\perp}$, as shown in Figure 4.8. In TF coils the magnitude of such forces spans across the current line Γ^{i}_{wp}, due to the inhomogeneous toroidal field in radial direction. Locally, on the i-th WP, $\mathbf{f}^{i}_{\perp}$ can be decomposed into a radial and axial components, $f^{i}_{r,wp}$ and $f^{i}_{z,wp}$, oriented along the global radial and vertical directions $\hat{n}_r$ and $\hat{n}_z$. Accordingly, $\mathbf{f}^{i}_{\perp}$ reads as

$$\mathbf{f}^{i}_{\perp,wp}(\mathbf{r}) = f^{i}_{r,wp}(\mathbf{r})\hat{n}_r + f^{i}_{z,wp}(\mathbf{r})\hat{n}_z. \tag{4.95}$$

Mapping the spatial resolution of volumetric Lorentz force $f^{i}_{k,wp}(x,y,z)$ from EFFI 3D magnetostatic analysis, with $k = x,y,z$ as Cartesian coordinate, the total force is obtained from the integral,

$$F_{k,TFC} = \sum_{i} \int_{\mathcal{D}_{wp,i}} f^{i}_{k,wp}(x,y,z)\mathrm{d}x\mathrm{d}y\mathrm{d}z \;\text{ with } k = x,y,z. \tag{4.96}$$

Since the toroidal field $B_y \approx B_{\phi}$ is larger on the innermost side of the winding pack, there is a net inward centering force $F_{x,TFC}$ pushing each of the N_{TFC} coils towards the tokamak axis. In this case $F_{k,TFC}$ approximates the total radial force $F_{r,TFC}$, derived from the in-plane volumetric radial force $f^{i}_{r,wp}$ (Equation 4.95).

There are operating situations where the information on integral forces is more useful if limited to portions of the coil domain, rather than on the entire magnet. That is the case of vertical separation force and out-of-plane forces. By definition of hoop forces, the net axial force integrated over the coil domain yields zero. Locally, the axial volumetric force produces an internal tensile load, mostly borne by the steel jacketing structure of the conductor. As this is an in-plane force component, i.e. acting outwards normally to the current line direction, it may be thought as a separating force $F_{v,TFC}$ pulling the coil up-down with respect to the mid plane. Hence, the axial forces over the upper and lower halves of the coil, respectively $z \geq 0$ and $z \leq 0$, is reacted internally by the tensile forces $F^{up}_{z,TFC}$ and $F^{dw}_{z,TFC}$. Along with the the hoop forces the whole combination of in-plane loads must

embody the vertical forces applied by the PF coils too, as they directly support on the TF coil casing structure.
The out-of-plane forces are deduced from the magnetic interaction between the TF coils current and the poloidal magnetic field generated by the PF/CS coils and the plasma. The radial current density of the $i-$th coil WP varies between $-J_{wp,i}$ and $+J_{wp,i}$. When this electric current sees a vertical poloidal field it yields a perpendicular force along y, also swiping sign poloidally. This force produces a torque about the mid-plane, to be counteracted by a set of dedicated systems, bounding all coils in the outer leg side reciprocally along the torus. These are referred to as outer inter-coil structure (OIS). Such bending moment depends on the poloidal field configuration and therefore can oscillate during a complete pulse, leading also to fatigue. Similarly to the vertical separation this forces can be also split between upper and lower half of the coil. As a result, a common expression can be shared between $F_{v,TFC}$ and the integral bending force $F_{b,TFC}$, such that

$$F_{v/b,TFC} = \frac{F^{up}_{z/y,TFC} + \left|F^{dw}_{z/y,TFC}\right|}{2} = \frac{\sum_i \left(\int\limits_{\mathcal{D}^{up}_{wp,i}} f^i_{z/y,wp}(\mathbf{r})\mathrm{d}\mathbf{r} + \left| \int\limits_{\mathcal{D}^{dw}_{wp,i}} f^i_{z/y,wp}(\mathbf{r})\mathrm{d}\mathbf{r} \right| \right)}{2}, \quad (4.97)$$

with the z force component used for the vertical force $F_{v,TFC}$ and the y component for the bending out-of-plane force $F_{b,TFC}$. There are no operational or technology requirements directly associated with integral Lorentz forces in TF coils, as the structural integrity has to be assessed through dedicated stress analyses.

Although the issue has been addressed in the past [70], a complete and coherent stress model is currently not available in the MIRA magnets module. However, the full 3D shaping of the volumetric forces, coupled to an advanced engineering design of the winding pack cross sectional space poses the basis of an advanced 2D or even 3D structural mechanics model, to close the TFC design loop. Hence, the absence of a stress model is by now the only limitation of the magnet system modelling part of MIRA. This modelling gap will be filled with some justified engineering assumptions, explicated in conjunction with the performed simulation studies.

The three-dimensional spatial resolution of the magnetic field $\mathbf{B}$ allows to calculate the total stored magnetic energy. The method consists of integrating the magnetic pressure $\mathbf{B}^2/2\mu_0$ over a large half-circular enclosing domain $\mathcal{D}_e$, that is toroidally bounded by a toroidal sector angle θ_{sect} and, radially, large enough so that the magnetic field vanishes, fairly outside the TF coil outer radius. The magnetic energy stored in a singular TF coil $E_{c,TFC}$ and in the entire magnetic field $E_{m,TFC}$ can be written as

$$\begin{aligned} E_{c,TFC} &= \int\limits_{\mathcal{D}_e} \frac{\mathbf{B}^2}{2\mu_0}\mathrm{d}\mathbf{r}, \\ E_{m,TFC} &= N_{TFC} \cdot E_{c,TFC}. \end{aligned} \quad (4.98)$$

From a 3D spatial resolution of the magnetic quantities, precise estimations of field, force and energy are obtained for the plasma, PF/CS and TF coil system, which is unique for a system analysis tool.

4.2.4. Spatial arrangement of the magnet coils functional components

An important aspect to consider in system code magnets modelling is to find a set of functional logics to accommodate all the functional components, characterizing a superconducting coil. To

comply with the magnetic fields and electromagnetic loads three subsystems must be designed. At a coil macroscopic level, these include:

- winding pack (WP);
- ground insulator (GI);
- steel casing.

In the following the specifics are reported for the winding pack and steel casing cross-sectional layouts, differently approached for PF coils, CS and TF coils.

Winding pack scheme of PF/CS coils

For both PF and TF coil systems, the elementary unit of a magnet coil is represented by its conducting cable, wound around the coil perimeter. The latter identifies the electric current trajectory. A coil has a certain cross-sectional space, denoting the WP, to carry the required current I_c. This space needs to be outlined to respond to the current demands, taking into account of the cable technological constraints and the constraining conditions imposed by space limitations.

The WP layout identifies the disposition of the number of superconducting turns N_{turn}, each carrying the current I_{op}. According to the turn winding configuration shown in Figure 4.9, to extend to both TF and PF coils, the WP is defined by a total number of turns N_{turn}, wound on two different levels: on layers, along a cross direction, and on turns, along a radial direction. The cross and the radial directions are denoted further by the subscripts c and r.

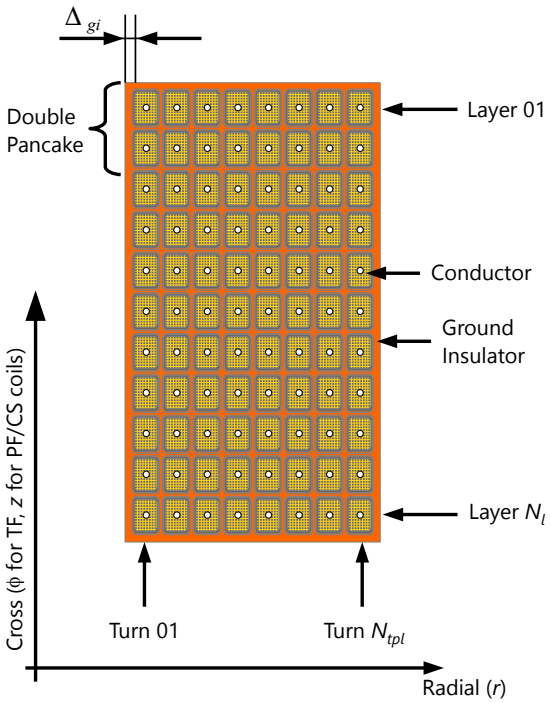

Figure 4.9.: Schematic view of pancake winding arrangement of superconducting cables in a rectangular tokamak coil winding pack.

With respect to the global tokamak reference coordinate system, the cross direction points axially in case of PF coils and toroidally in case of TF coils. Based on a ITER-like winding scheme [42], the number of coil turns along the cross direction outlines the number of layers N_l, or in magnet coils formalism, the number of double pancakes. By using a double (or higher multiple) pancake winding configuration the conductor joints are always placed at the outer pancake diameter and therefore the heat generated within joints, experiencing a lower magnetic field, does not impact the conductor temperature [169]. A pancake incorporates two layers. Radially, it refers to the number of turns per layer N_{tpl}. A coil with such a configuration yields an equivalent total number of turns N_{turn} given by

$$N_{turn} = N_l \cdot N_{tpl}, \tag{4.99}$$

with N_l and N_{tpl} to be calculated according to specific modelling exigencies, i.e. differing from PF coils, CS, and TF coils.

For the PF coils and the CS, N_{turn} can be evaluated in two different ways: in connection with the total current I_c, or based on the maximum cross-sectional space, derived from a set of maximum radial and cross widths, $\delta r_{\max}$ and $\delta c_{\max}$. A minimum number of turns can be assessed to produce the required current I_c

$$N_{turn}^{\min} = \left\lceil \frac{I_c}{I_{op}^{\max}} \right\rceil, \tag{4.100}$$

where $I_{op,\max}$ indicates the maximum turn operating current, depending on the critical current density J_c of the superconductive cable. A detailed description on critical superconducting conditions will be illustrated in Section 4.2.5. Taking the WP with rectangular cross section and $AR = \delta c / \delta r$ denoting an aspect ratio of the PF coil, the number of layers and turns per layer, along with the radial and cross sizes, can be evaluated by solving the following systems of constrained equations,

$$\begin{cases} N_l \cdot N_{tpl} \geq N_{turn}^{\min} \\ N_l = \left\lceil \dfrac{\delta c}{\delta c_{turn}} \right\rceil \\ N_{tpl} = \left\lceil \dfrac{\delta r}{\delta r_{turn}} \right\rceil \\ \delta z = AR \cdot \delta r \end{cases} \tag{4.101}$$

where δr_{turn} and δc_{turn} indicate the turn width in radial and cross direction. The unknown parameters are N_l, N_{tpl}, δr and δc. In case of imposed maximum space, the winding scheme is straightforward,

$$\begin{aligned} N_l^{\max} &= \left\lfloor \frac{\delta c_{\max}}{\delta c_{turn}} \right\rfloor \\ N_{tpl}^{\max} &= \left\lfloor \frac{\delta r_{\max}}{\delta r_{turn}} \right\rfloor. \end{aligned} \tag{4.102}$$

Moreover, the definition of the maximum coil current $I_c^{\max}$ can be equivalently utilized,

$$I_c^{\max} = N_l^{\max} N_{tpl}^{\max} I_{op}^{\max}. \tag{4.103}$$

Both approaches are suited to the design of the winding pack for the PF coils and the CS, with the cross direction c equivalent to the axial direction z. Including the extra-space required by the ground

insulator, the total radial and axial thickness can be written as

$$\begin{aligned} \delta r &= N_{tpl,i}\delta r_{turn} + 2\Delta_{gi}, \\ \delta c &= N_l \delta c_{turn} + 2\Delta_{gi}, \end{aligned} \tag{4.104}$$

yielding the definition of the current density J_{wp} in the WP,

$$J_{wp} = \frac{N_{turn} I_{op}}{(\delta r - 2\Delta_{gi})(\delta z - 2\Delta_{gi})}. \tag{4.105}$$

The CS consists of a number of independent modules, each characterized by the same radial thickness δr_{CS}. Vertically, it is truncated at the top and bottom levels of the TF coil straight leg, hence the total CS stack height is defined as:

$$\delta z_{CS} = z_{TFC}^{\max} - z_{TFC}^{\min}. \tag{4.106}$$

The radial thickness of the WP in the CS is also evaluated by means of analytical formula, idealizing the CS as an infinite solenoidal conductor along the axial direction z. Taking $J_{wp}^{\max}$ the maximum WP current density in the CS its radial thickness δr_{CS} is reversely calculated from Equation (4.85) taking $B_{z,\max}$ equivalent to the allowable peak magnetic field in the conductor $B_{\max}$,

$$\delta r_{CS} = \frac{B_{\max}}{\mu_0 J_{wp}^{\max}}. \tag{4.107}$$

The max WP current density $J_{wp}^{\max}$ is extracted imposing a fixed conductor concept,

$$J_{wp}^{\max}\left[\frac{\mathrm{A}}{\mathrm{m}^2}\right] = I_{op}[\mathrm{A}] \left\lfloor \frac{1}{\delta r_{turn}[\mathrm{m}]} \right\rfloor \left\lfloor \frac{1}{\delta c_{turn}[\mathrm{m}]} \right\rfloor. \tag{4.108}$$

The CS stack incorporates a vertical support structure to cope with the vertical forces arising from operation. To constantly keep in contact all the CS modules the ITER CS reference design [163] the vertical support structure applies a pre-compression in axial direction.

Winding pack and casing layout of TF coils

The TF coils have to withstand radial, vertical and out-of-plane forces, for which a thick full steel casing structure is being built around the winding pack (WP), as shown in Figure 4.10.
At the plasma side the case is subdivided into inner, outer and toroidal case, denoted by the capital-case subscripts I, O and T. The inner side faces the plasma. The largest mechanical load on the TF coils comes from the radial forces, which are counteracted by wedging the straight leg casing and forming a self-supporting vault. The outcome of such a solution is a different layout for the casing cross section from inboard and outboard leg, lower-case superscripts i and o. Accordingly, to each case portion and to both inboard and outboard corresponds a fixed thickness $\Delta_{case,j}^{k}$ with $j = I, O, T$ and $k = ib, ob$. The toroidal edges of the steel casing are influenced by the vault angle θ_{vault} defining a half-sector angle

$$\theta_{vault} = \frac{\pi}{N_{sect}}, \tag{4.109}$$

with N_{sect} being the number of sectors, equivalent to the number of TF coils N_{TFC}.

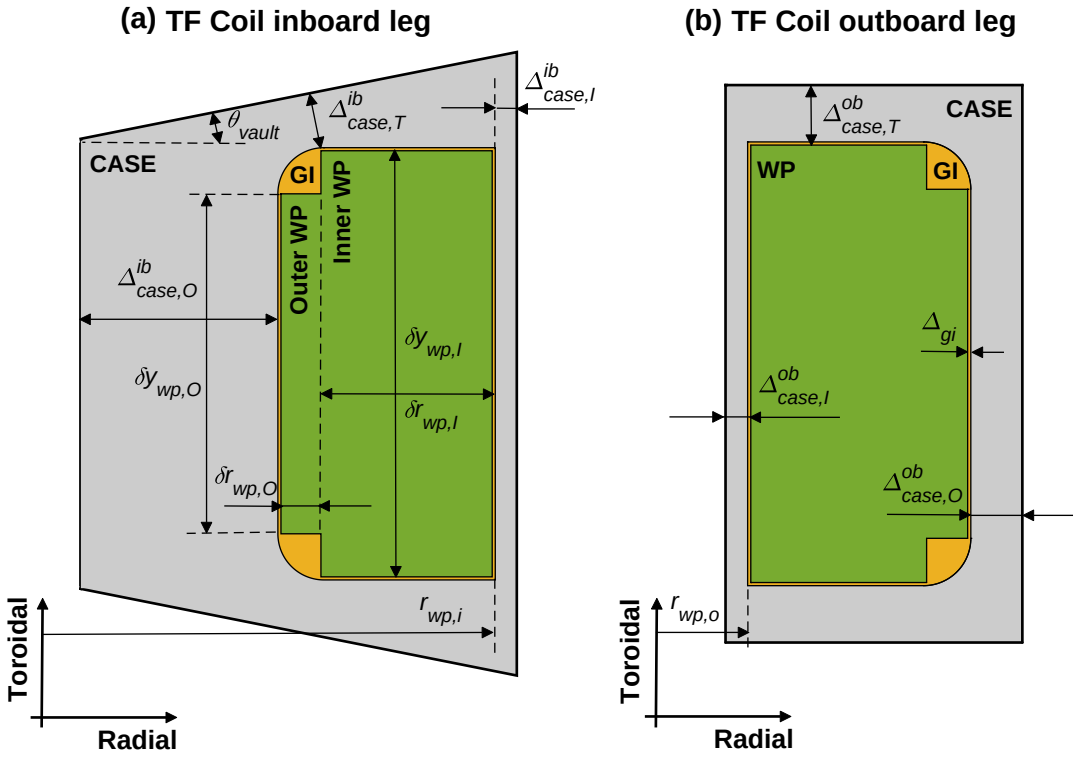

Figure 4.10.: Layout and related parametrization for the cross section of the inboard (a) and outboard (b) TF coil legs.

The method to solve the winding scheme for the TF coils differs from the PF/CS coils. The TF coil WP is organized in a double inner and the outer WP, each characterized by a radial and toroidal thickness $\delta r_{wp,I/O}$ and $\delta y_{wp,I/O}$. Thus N_l and N_{tpl} are evaluated for both. This singularity involves an additional condition on the limited space in toroidal direction, where, due to the wedging of the steel casing, a minimum toroidal thickness $\Delta^{ib}_{case,T}$ shall be reserved. This is addressed by introducing a solution vector $\underline{w} = [N_{l,I}, N_{tpl,I}, N_{l,O}, N_{tpl,O}]$ for the optimization problem,

$$\max_{\underline{w}} N_{l,I} \text{ subject to } \begin{cases} \mathcal{N}_{turn}(\underline{w}) \geq 0 \\ \mathcal{Y}_{wp,I}(\underline{w}) \leq 0 \end{cases}, \tag{4.110}$$

where the number of layers in the inner WP $N_{l,I}$ has to be maximized, so that all turns are packed towards the plasma side, and, more importantly, minimize the overall WP radial thickness $\delta r_{wp} = \delta r_{wp,I} + \delta r_{wp,O}$. The function $\mathcal{N}_{turn}(\underline{w})$ relates to total number of TFC coil turns and reads as

$$\mathcal{N}_{turn}(\underline{w}) = N_{l,I} \cdot N_{tpl,I} + N_{l,O} \cdot N_{tpl,O} - \left\lceil \frac{I_{TFC}}{I_{op}} \right\rceil, \tag{4.111}$$

where I_{TFC} outlines the total TFC current. The reduced toroidal thickness of the TF coil at the inner side of the inner WP, $r = r_{wp,i}$, due to the trapezoidal shape of the TFC casing, turns into an inequality constraint affecting the total toroidal thickness $\delta y_{wp,I}$ and the number of layers $N_{l,I}$. It

depends on the function $\mathcal{Y}_{wp,I}(\underline{w})$, which outlines the maximum available toroidal width fill with turn layers. $\mathcal{Y}_{wp,I}$ can be expressed as

$$\mathcal{Y}_{wp,I}(\underline{w}) = N_{l,I} \cdot \delta c_{turn} - \left[2\left(r_{wp,i} - \Delta_{gi} - N_{tpl,I}\delta r_{turn}\right)\tan\theta_{vault} - 2\Delta_{gi} - 2\frac{\Delta^{ib}_{case,T}}{\cos\theta_{vault}} \right]. \quad (4.112)$$

The radial and toroidal space allocation of the WP is directly related to the layout of the coil cable.

4.2.5. Design verification of the superconducting cable

A superconducting cable is modelled in MIRA according to the conductor design parameters listed in Table 4.3. The premise is to validate the manufactured engineering design with MIRA results. The rationale is to improve the geometric and the material composition and to scope multiple cable technologies for a given reactor magnet system.

Parameter	[Unit]	Variable
Maximum allowable magnetic field	[T]	$B_{\max}$
Maximum operating temperature at field peak	[K]	T_{op}
Maximum operating strain	[%]	ϵ_{op}
Minimum temperature margin	[K]	$\Delta T_{cs}^{\min}$
Helium (coolant) fraction in conductor	[%]	f_{He}
Copper to superconducting ratio in strand	[%]	f_{Cu2sc}
Strand diameter	[mm]	d_{strand}
Number of superconducting strands in conductor	[-]	N^{sc}_{strand}
Number of Copper stabilizer strands in conductor	[-]	N^{Cu}_{strand}
Helium coolant channel diameter	[mm]	d_{ch}
Radial/cross width of cable space	[mm]	$\delta r_{turn,c}/\delta c_{turn,c}$
Steel jacket thickness	[mm]	$\delta_{turn,j}$
Turn insulator thickness	[mm]	$\delta_{turn,ins}$

Table 4.3.: Input parameters for the modelling of the superconducting cables the MIRA magnet module.

Accordingly, the overall turn radial and cross widths δr_{turn} and δc_{turn} can be defined as

$$\delta x_{turn} = \delta x_{turn,c} + 2\left(\delta_{turn,j} + \delta_{turn,ins}\right), \quad \text{with } x = r, c. \quad (4.113)$$

Based on the technological solutions currently investigated for ITER and DEMO, only a limited number of options have been integrated up to now in the superconducting cable database, listed in Table 4.4. At present all conductors are uniquely based on low temperature superconductors (LTS).

The main turn specifications include a set of conductor material-related properties, e.g. void fraction f_{He}, superconducting strand diameter d_{strand}, copper to superconducting ratio in the strand f_{Cu2sc} and the number of copper and SC strands. Some others refer to the operating conditions, such as operating current I_{op}, maximum allowable operating magnetic field $B_{\max}$ and temperature. Moreover, the majority of the conductors can be drawn as a concentric multilayer square or rectangular structure, with edged corners. As a result, the cross-sectional geometrical layout information include the radial and the cross thickness and edge curvature radii of cooling channel, conducting cross section, steel jacketing and a turn insulator.

Cable ID	Cable description	Source
TF_ENEA	LTS DEMO TFC cable design from ENEA	[54, 170, 171]
CS_SPC	LTS DEMO CS cable design from SPC	[49, 172]
CS_CEA	LTS DEMO CS cable design from CEA	[56, 173]
PF5_CEA	LTS DEMO PFC5 cable design from CEA	[56, 174]
PF1_ENEA	LTS DEMO PFC1 cable design from ENEA	[175]
PF4_ENEA	LTS DEMO PFC4 cable design from ENEA	[175]
PF1_ITER	LTS ITER PFC1 cable design	[163, 169]

Table 4.4.: Superconducting cable design solutions included in the MIRA magnet module database.

To safely operate a superconductive magnet, its superconductivity needs to be maintained during the plant operation. Hence, the cable should operate far from its critical current density $J_c(B, T, \epsilon)$, parametrized as a function of magnetic field B, temperature T and, for Nb_3Sn, mechanical strain ϵ. Two scaling laws derived from ITER magnets design [51, 176], one for Nb_3Sn and one for NbTi superconductive strands, are used for the calculation of J_c. Based on the description of the input parameters in Table 4.3, the first operational limitation is identified by the maximum operating current $I_{op,\max}$

$$I_{op}^{\max} = I_{crit} \cdot f_{Iop2Ic}, \tag{4.114}$$

where I_{crit} denotes the total critical current of the cable

$$I_{crit} = J_c(B_{\max}, T_{op}, \epsilon_{op}) A_{cs}(1 - f_{He})(1 - f_{Cu}), \tag{4.115}$$

A_{sc} represents the superconducting cross-sectional area

$$A_{sc} = \pi \frac{d_{strand}^2}{4} \left(1 - f_{Cu,strand}\right) N_{strand}^{sc}, \tag{4.116}$$

$f_{Cu,strand}$ defines the total fraction of copper

$$f_{Cu,strand} = \frac{f_{Cu2sc}}{1 + f_{Cu2sc}}, \tag{4.117}$$

and f_{Iop2Ic} is the critical current ratio I_{op}/I_c and it is normally found around 0.5-0.6 [53]. A preliminary verification entails the comparison of the actual I_{op} to the maximum operating current $I_{op,\max}$, such that $I_{op} \leq I_{op,\max}$. The cross sectional area A_{Cu} tied to the conductor stability and quench protection of the conductor can be written as:

$$A_{Cu} = A_{sc} f_{Cu2sc} + \pi \frac{d_{strand}^2}{4} N_{strand}^{Cu}. \tag{4.118}$$

The copper cross section area must be added to the area occupied by the He coolant A_{He},

$$A_{He} = \frac{f_{He}}{1 - f_{He}} \left(A_{sc} + A_{Cu}\right), \tag{4.119}$$

where f_{He} is the He coolant fraction. Thus, the total conductor cross section A_{cond} is given by

$$A_{cond} = A_{sc} + A_{Cu} + A_{He}. \tag{4.120}$$

The operating point of the conductor, defined by the triplet $[I_{op}, T_{op}, B_{peak}]$, with B_{peak} indicating the actual peak magnetic field, must comply with the so-called *current-sharing temperature limit*,

also known as *temperature margin*. The temperature margin is the difference between the current sharing temperature T_{cs}, at which the critical current I_c equals the actual current I_{op}, and the actual temperature T_{op} [23, 53]. Such a condition can be mathematically written as

$$\Delta T_{cs} = T_{cs} - T_{op} \geq \Delta T_{cs}^{\min}, \tag{4.121}$$

where T_{cs} is the solution to following algebraic equation, relating I_{crit} and I_{op} such that

$$I_{crit}(B_{peak}, T_{cs}, \epsilon_{op}) = I_{op}. \tag{4.122}$$

Further important design criteria of the conductor are given by the *stability* and the *quench protection* of the magnet. Superconducting and copper wires embedded in a unique conduit matrix can be thought as two electric circuits operating in parallel with very large differences in their ohmic resistance, $R_{cs} \ll R_{Cu}$. In case of off-normal events, for instance due to loss of coolant, local increase of nuclear heating or AC losses, the temperature of the superconducting cross section can escalate to hazardous conditions, changing the physical state from super to normal conductor. In case of quench detection, the magnetic energy stored in the coil E_c is dissipated through a series of dump resistors, characterized by a resistance R_{dump}. The current in the superconductor is dumped exponentially after a delay time τ_{delay}, necessary to detect the quench and to initiate the energy discharge. This is depicted by the following exponential decay law

$$I_{op}(t) = I_{op,0} \exp\left(-\frac{R_{dump}}{L_c} \cdot t\right), \; t \geq \tau_{delay}, \tag{4.123}$$

with a time constant $\tau_{dump} = L_c / R_{dump}$ representing the time scale of the energy discharge process, where L_c is the effective self-inductance of the coil and R_{dump} the resistance of the dump resistors. During the decay time a volumetric resistive heating is locally deposited and can potentially propagate enlarging the normal conducting region. Therefore, if the copper cross-sectional area A_{Cu} is large enough than that of superconductor, i.e. $A_{Cu} \gg A_{sc}$, the copper can provide intrinsic stabilization against unanticipated heating events, so that its resistance becomes much smaller than that of the quenched superconducting wire. Any events involving the loss of superconductivity are referred to as *quench*.

If the effects from a quench event are compensated by a prompt action of the cooling system, then the superconductivity can be recovered. Should this latter condition not be sufficient, alternative measures must be taken to protect the magnet. To this end, relying on constant monitoring of the voltages, one applied technique is to distribute the heat through the whole system and thereby limit the maximum hotspot temperature T_{hs}. The superconducting coil circuit is coupled to a second one made of dump resistors, parametrized by a total resistance R_{dump}, to resistively dissipate the stored energy outside the magnet. The adiabatic hotspot criteria is based on a maximum temperature imposed as an upper temperature bound to fulfil during a thermal transient with no cooling function available, where the heat is uniquely dissipated by the thermal capacity of superconductor and copper materials. Assuming thermal equilibrium between the two systems, the governing heat balance equation, applied to a unitary length of conductor, can be written as [46]

$$\sum_k \rho_k(T) c_{v,k}(T) A_k \frac{\mathrm{d}T}{\mathrm{d}t} = \Omega_{Cu}(T) \frac{I_{op}^2(t)}{A_{Cu}}, \;\; \text{with } k = \mathrm{sc}, \mathrm{Cu}, \tag{4.124}$$

where ρ_k, $c_{v,k}$ and A_k are the density, the specific heat capacity and the cross sectional area of the system k, with k denoting the superconductor sc or the copper Cu, and Ω_{Cu} is the electric

resistivity of copper. The volumetric heating per unit length is given by the Joule dissipative power, $\Omega_{Cu}/A_{Cu}I_{op}^2$, conservatively assumed to be entirely deposited in the copper stabilizer. Solving Equation (4.124) by means of separation of variables [46], the dumping time τ_{dump} to reach the maximum hotspot adiabatic temperature T_{hs} is calculated. The ITER hotspot criteria suggests that during a quench the adiabatic hotspot temperature should not exceed 150 K [53], while larger values $\sim$250 K have been recently used for DEMO superconducting cable design [47]. Mathematically, it is equivalent to integrate the T-related expression from T_{op} to T_{hs} and the time-related part $I_{op}^2(t)$ from $t = 0$ to $t = t_{dump}$. The latter is the unknown to the following expression:

$$A_{Cu}\int_{T_{op}}^{T_{hs}}\left(\frac{\sum_k \rho_k(T)c_{v,k}(T)A_k}{\Omega_{Cu}(T)}\right)\mathrm{d}T = \int_0^{t_{dump}} I_{op}^2(t)\mathrm{d}t, \text{ with } k = \mathrm{sc}, \mathrm{Cu}. \tag{4.125}$$

To simplify this expression, the exponential dump of the current can be neglected, i.e. imposing a constant current $I_{op,0}$ throughout the whole transient, thereby eliminating the dependence on the discharge time constant τ_{dump}. As a result, t_{dump} can be calculated as

$$t_{dump} = \frac{A_{Cu}}{I_{op,0}^2}\int_{T_{op}}^{T_{hs}}\left(\frac{\sum_k \rho_k(T)c_{v,k}(T)A_k}{\Omega_{Cu}(T)}\right)\mathrm{d}T. \tag{4.126}$$

Since the stored magnetic energy $E_c = \frac{1}{2}L_c I_{op}^2$ is related to the voltage developed by the quench V_c, the following expression holds for V_c

$$V_{dump} = \frac{2E_c}{t_{dump}I_{op}}, \tag{4.127}$$

where the required condition for protecting the magnet from quench can be set as an upper limit to the peak voltage, such that

$$V_{dump} \leq V_{dump}^{\max}. \tag{4.128}$$

$V_{dump}^{\max}$ defines an admissible maximum voltage during the discharge, about $\sim$10 kV for ITER and DEMO [23, 48]. The importance of a large copper cross-sectional area A_{Cu} can be associated with its thermal inertia and vital contribution to slow down the temperature rise in case of unanticipated heating, eventually leading to a quench.
The dump voltage can be reformulated as a function of the operating current I_{op}, combining the quadratic dependency of I_{op} on E_c and of Equations (4.126) and (4.127), yielding

$$V_{dump} = \frac{L_c}{A_{Cu}\int_{T_{op}}^{T_{hs}}\left(\frac{\sum_k \rho_k(T)c_{v,k}(T)A_k}{\Omega_{Cu}(T)}\right)\mathrm{d}T}\cdot I_{op}^3. \tag{4.129}$$

This formulates an additional upper limit on the maximum operating current to fulfil the quench protection criteria of Equation (4.128). Referring to inequality expression of Equation (4.114), $I_{op,\max}$ can be rearranged as follows:

$$I_{op}^{\max} = \min\left[f_{Iop2Ic}\cdot I_c, \left(\frac{V_{dump}^{\max}}{L_c}A_{Cu}\int_{T_{op}}^{T_{hs}}\left(\frac{\sum_k \rho_k(T)c_{v,k}(T)A_k}{\Omega_{Cu}(T)}\right)\mathrm{d}T\right)^{1/3}\right]. \tag{4.130}$$

As a result, the admissible operating operating is also driven by geometric and winding features, identified by the self-inductance L_c and number of winding turns N_{turn}, and by materials specifications.
The expression of $I_{op,i}^{\max}$ for the generic PF/CS coil i determines the total maximum current $I_{c,i}^{\max}$ as per Equation (4.103), to adopt when calculating the coil current configuration $\mathbf{I_c}$ as solution to the problem of Equation (4.90).

4.3. Reactor Model Integration into Plant System

Producing a few hundreds megawatts of net electric power in steady state or long pulse plasma operation mode is a high level requirement of the EU-DEMO plant. A tokamak reactor features many physics and engineering challenges. However, the integration of the reactor into a plant system gives rise to additional complexities, requiring additional design issues at a plant level. Based on the electricity production and pulse operation mode requirements, a fusion systems code shall evaluate two key plant parameters:

- the net electric power and
- the pulse burn time.

In the following subsections, the modelling aspects on reactor pulse dynamics and plant power balance are illustrated. The pulse cycle phases and the methodologies addressed to calculate the time duration are derived from the system code TREND [10], integrated in MIRA for core plasma physics modelling.

4.3.1. Temporal description of a full pulsed reactor cycle

A power plant operation of pulsed and steady state devices consists of different phases schematically shown in Figure 4.11. The difference between pulsed and steady reactor resides in the time duration τ_{burn} for useful power production, i.e. the burn phase. Ideally, for steady state tokamaks there are no upper limits, while for pulsed devices it depends on the performances of the current inductive means, inherently integrated in the poloidal field magnets system.

At present, two hour long pulses are posed as a design goal for the near term DEMO [32], while for future power plants it may be extended up to ten hours (or more).
The time onset for the beginning of pulse (BOP) $t = t_{BOP}$ has been arbitrarily set to the start of the CS recharge, where the toroidal currents in CS coil circuits are being ramped up to their maximum operating value for preparing to the plasma breakdown (BD). The time $\tau_{RC,i}$ to linearly rise the current in the circuit of the CS coil i, with $i = 1, 2, ..., N_c^{CS}$ is influenced by the maximum power supply voltage during its recharge $V_{i,RC}^{\max}$ [177]. Hence, the equation governing the dynamics of the N_c^{CS} CS circuits, coupled to the N_c PF + CS coils circuits, is given by Maxwell-Faraday's law

$$V_i = L_i \frac{dI_{op,i}}{dt} + \sum_{j \neq i}^{N_c} \mathcal{M}_{i,j} \frac{dI_{op,j}}{dt} \leq V_{i,RC}^{\max}, \quad \text{with } i = 1, 2, ...N_c^{CS}, \tag{4.131}$$

where L_i and $\mathcal{M}_{i,j}$ are the self-and mutual inductances and $I_{op,i}(t)$ the time evolution of the operating current in the $i-$th CS coil circuit during the premagnetization. $I_{op,i}$ derives from the total coil

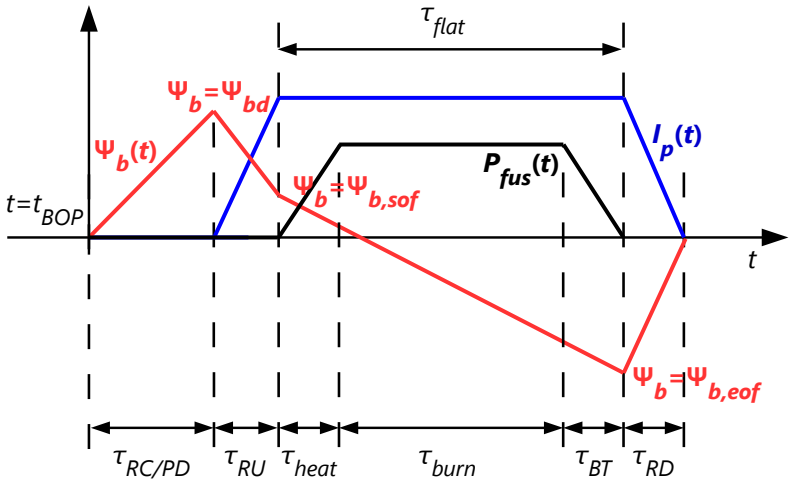

Figure 4.11.: Illustration of the dynamical phases considered for a time cycle in pulsed tokamaks. The acronyms appearing in the figure stand for: BOP = beginning of pulse, RC = CS recharge, PD = pump-down, RU = ramp-up, BT = burn termination and RD = ramp-down.

current $I_{c,i}$ at breakdown and from the number of turns $N_{turn,i}$, such that $I_{op,i} = I_{c,i}/N_{turn,i}$. The time waveform is assumed linear between the BOP and BD. Extrapolating from ITER inductive scenario [80] all coils at BOP are assumed fairly around a zero current condition $I_{c,i}^{BOP} = 0$. Therefore, taking $\Delta I_{op,i} \equiv I_{op,i}^{BD} = I_{c,i}^{BD}/N_{turn,i}$ as the current range between BOP and BD, the recharge time $\tau_{RC,i}$ circuit i and the largest value τ_{RC} amongst all can be formulated as

$$\tau_{RC,i} \geq \frac{L_i \Delta I_{op,i}^{RC} + \sum_{j \neq i}^{N_c} \mathcal{M}_{i,j} \Delta I_{op,j}^{RC}}{V_{i,RC}^{\max}} \quad \text{with } i = 1,2,...N_c^{CS}, \tag{4.132}$$

$$\tau_{RC} = \max\left[\tau_{RC,1},...,\tau_{RC,N_c^{CS}}\right].$$

During the pump-down (PD) unburnt fuel particles, fusion ash and other exhausts are removed from the toroidal vacuum chamber by means of high vacuum pumps. A 20 min time scale is set as design target for the pump-down time of current DEMO designs [178]. At present, no dependencies on plasma exhaust content and available pumping conditions are available for determining the PD time τ_{PD}, which is therefore an input parameter.
Preferably, in parallel to the CS recharge, PD phase should take place as well, to expedite the preparation to the pulse. However, it is hard to state firmly whether pump-down and CS recharge can be fully overlapped, thus high vacuum conditions must be established priorly. Techniques are under discussion to prevent breakdowns by dedicated magnetic field control, with the possibility to operate the outgassing partly simultaneously to the CS recharge. A formulation has been proposed [10] to consider a fraction f_{PD} of the pump-down not usable for overlapping to τ_{RC}, as vacuum is to be guaranteed before the CS recharge starts. According to this assumption, the complete duration $\tau_{RC/PD}$ can be written as

$$\tau_{RC/PD} = f_{PD}\tau_{PD} + \max\left[(1 - f_{PD})\tau_{PD}, \tau_{RC}\right], \tag{4.133}$$

with $f_{PD} \sim 0.25$ [10]. The plasma takes life at the beginning of the ramp-up phase (RU), right at the breakdown time. During the ramp-up the plasma current grows with a constant growth-rate $\dot{I}_p$, such

that $\dot{I}_p = I_p/\tau_{RU}$ and τ_{RU} relating to the ramp-up time duration. $\dot{I}_p$ can be approximately expected to be in the ranges of ITER's, i.e. 0.15 [MA/s] [80]. However, lower bounds, mostly depending on the characteristic resistive time scale τ_{res}, are proposed to impose a requirement on the plasma current RU, with τ_{res} being defined as [10]

$$\tau_{res} = \mu_0 a^2 \langle\sigma\rangle_{S_p} \left(\frac{\langle T_{RU}\rangle}{\langle T\rangle}\right)^{1.5}, \tag{4.134}$$

where a is the plasma minor radius, $\langle T\rangle$ and $\langle T_{RU}\rangle$ are the flat-top and RU average plasma temperatures and $\langle\sigma\rangle_{S_p}$ is the plasma Spitzer resistivity. The major aspects on the key plasma electric properties are outlined in Appendix C.1. τ_{RU} should exceed τ_{res} by a specified factor $f_{RU} \sim 3-10$ [10], such that

$$\tau_{RU} \geq f_{RU} \cdot \tau_{res}. \tag{4.135}$$

After being ramped-up, a net current of cold plasma ($\langle T_{RU}\rangle \approx 0.6$ keV [10]) flows all around the torus. The fusion reaction, however, takes place only above certain threshold temperatures linked to the thermal energy W_{th}. To establish the conditions for power generation after the ramp-up an external heating is necessary to provide the plasma with the energy W_{th}. The energy confinement time τ_E has been introduced to cope with the lack of a deep understanding of the process involved in transport losses mechanisms to quantify the transport loss energy rate $P_{con} = W_{th}/\tau_E$. Similarly, the plasma heating time scale τ_{heat} needed to achieve W_{th} is assumed to scale linearly with the energy confinement time τ_E [10]. Introducing a proportionality factor f_{heat}, τ_{heat} is outlined as

$$\tau_{heat} = f_{heat} \cdot \tau_E, \tag{4.136}$$

with $f_{heat} \approx 5$ [10]. The flat-top length τ_{flat} is calculated in Equation (4.91) and driven only by the inductive capabilities of the magnet system and the plasma conductivity. The plasma conductivity depends on its dilution (impurity fractions), temperature and geometry. The burn phase τ_{burn} is the cycle time slot in which a significant amount of fusion power is obtained for net electricity production, i.e the flat-top length reduced by the other pulse length contributions accounting for heating and burn termination τ_{BT}. Hence it is given by:

$$\tau_{burn} = \tau_{flat} - \tau_{heat} - \tau_{BT}, \tag{4.137}$$

where τ_{BT} is the time foreseen to initiate a controlled plasma ramp-down, safely. That includes tuning some parameters, such as the plasma density, to avoid plasma disruptions [10]. Similarly to the heating phase, in this case a linear scaling relation is presumed on the particle confinement time τ_p^*, such that $\tau_{BT} = f_{BT} \cdot \tau_p^*$. Combining τ_E with τ_p^* through the ratio f_{P2E}, a formulation of τ_{BT} is given by [10]

$$\tau_{BT} = f_{P2E} \cdot \tau_{heat}, \tag{4.138}$$

where $f_{BT} \approx f_{heat}$ is assumed. Finally, the time-scale for the plasma ramp-down (RD) of the plasma current, as in other system code studies [18, 179], is requested to come along with the requirements imposed to the RU time τ_{RU}. Thus,

$$\tau_{RD} \approx \tau_{RU}. \tag{4.139}$$

A final definition to characterize the whole cycle is the so-called *dwell time*, given by

$$\tau_{dwell} = \tau_{RC/PD} + \tau_{RU} + \tau_{heat} + \tau_{BT} + \tau_{RD}. \tag{4.140}$$

It is obtained by subtracting from the entire cycle length τ_{cycle} the burn time τ_{burn}. It represents the duration where no fusion power is featured. τ_{cycle} can be formulated as:

$$\tau_{cycle} = \tau_{burn} + \tau_{dwell}. \tag{4.141}$$

The ratio of burn to cycle time reminds of a plant availability concept, which should also include remote maintenance interruptions. These are very important aspects to demonstrate the economic viability of DEMO and of FPPs.

4.3.2. A model for steady state plant power balance

Establishing a relation between the primary fusion energy source and the net electricity output is the goal of the power balance model. The fusion power finds different conversion mechanisms before providing net electricity to the grid. Two major intermediate plant systems are responsible for such a process:

- the reactor physical components with the energy source terms P_{fus} and P_{add} and
- the converting systems in the so-called balance of plant (BoP) ultimately yielding a net electric power $\dot{W}_{net}$ (see Figure 4.12).

The fusion power P_{fus} splits into alpha and neutron power, with highly energetic fusion neutrons carrying 80 % of such a power, depicted here as P_{neut}. Neutrons leave the plasma confining region and deposit their kinetic energy onto the surrounding plasma facing components, splitting into $P^n_{fw} = P^n_{fw/ib} + P^n_{fw/ob}$ and P^n_{div} . The small fraction of neutrons leaving the vacuum chamber through gaps and reaching the vacuum vessel is neglected. The kinetic energy rate attaining to the alpha fusion products P_α together with the additional external heating power P_{add} provides heating power to the plasma for the sustainment of the fusion reaction. In steady state configuration this heating source power is balanced by radiation power P_{rad} and transport loss power P_{sep}. The latter is associated with direct energy or highly energetic particle fluxes. Similarly to neutrons, core plasma photons are isotropically distributed to blanket FW and divertor surrounding structures, identified by the $P^\gamma_{fw} = P^\gamma_{fw/ib} + P^\gamma_{fw/ob}$ and P^γ_{div} power terms. P_{sep} is the power crossing the separatrix and conducted via the scrape-off layer to the divertor targets along the magnetic field lines. Based on analyses on static and dynamic wall loads for DEMO [180] 15 % of P_{sep} is transported to the wall as ions propagating with structures of dense plasma called blobs. For $P_{sep} \approx 150$ MW [27] about ~ 20 MW are directed to the blanket with almost no impact on the overall plant power balance. The blobs generate localized peak heat fluxes, which MIRA cannot handle at present.
All core plasma power parameters are provided by the core plasma physics module (Section 3.2). The FW and the divertor contributions from total neutron and electromagnetic radiation power are calculated in the vacuum chamber radiation transport model (Equation 4.16). Existing systems codes, typically rely on input parameters to estimate the FW and divertor power repartition. In MIRA, instead, these are calculated for a specified shape of FW and divertor and for a 2D spatial resolution of the volumetric neutrons and photons sources.

The thermal powers originating from plasma neutrons, photons and charged particles heat loads are transported to the surrounding structures, contributing to increase the internal energy of the bulk materials. Because of exoergic nuclear reactions in the BB systems, the energy deposited by fusion neutrons overcomes the incoming value by the energy multiplication factor EMF. Concerning the

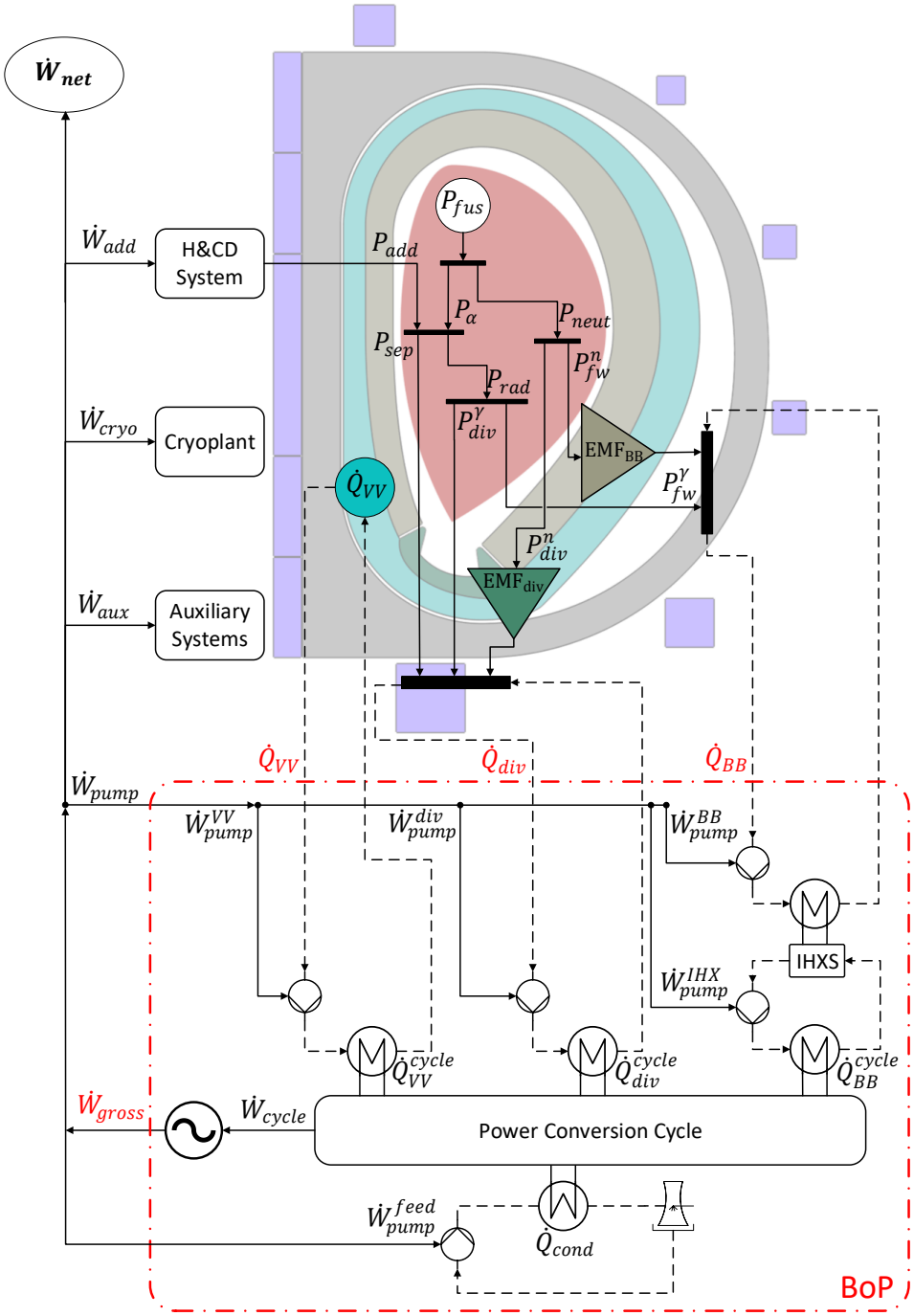

Figure 4.12.: Graphical scheme of the plant integral power balance model implemented in MIRA. The solid-line and the dashed-line arrows indicate power and the fluid flows, respectively.

BB system, the thermal loads originating from the plasma are composed of neutron-induced nuclear heating power and radiation losses, such that

$$\dot{Q}_{BB} = \sum_{m}^{M_{BB}} R^{m}_{heat} + P^{\gamma}_{fw/ib} + P^{\gamma}_{fw/ob} = \mathrm{EMF_{BB}} P^{n}_{fw} + P^{\gamma}_{fw}, \tag{4.142}$$

where M_{BB} is the number of subsystems m radially distributed in the BB region. R^{m}_{heat} is the global

nuclear heating power deposited within a generic reactor component m and $\mathrm{EMF_{BB}}$ is the EMF applied to the BB systems only. In this case, only the FW incoming neutron power P^n_{fw} enters the denominator of the EMF definition (Equation 4.40). All values of R^m_{heat} are calculated and provided by the radiation transport model as well as the inboard and outboard radiation wall loadings $P^\gamma_{fw/ib}$ and $P^\gamma_{fw/ob}$.
Similar considerations hold for the thermal power deposited to the divertor components, originating from neutrons, core and SOL radiation and high localized loads from the transport losses P_{sep}. The total thermal power $\dot{Q}_{div}$ can be estimated by

$$\dot{Q}_{div} = P_{sep} + \mathrm{EMF_{div}}\, P^n_{div} + P^\gamma_{div}, \tag{4.143}$$

where, due to the lack of the divertor in the core transport model, the divertor EMF must be imposed as input parameter. $\mathrm{EMF_{div}}$ has been found around $\sim$1.5 from detailed neutronic analyses [181] on the recent EU-DEMO 2015 baseline. Such large values might be alleged by the fact that the EMF definition involves the neutrons generated in the plasma. But, a fraction of the divertor boundary interfaces the BB, thus a large fraction of neutrons, presumably, also comes from the BB side wall. A third thermal input contributing to the BoP is the thermal power $\dot{Q}_{VV}$ in the vacuum vessel generated by nuclear heating power in the M_{VV} VV structures,

$$\dot{Q}_{VV} = \sum_{m}^{M_{VV}} R^m_{heat}. \tag{4.144}$$

The overall thermal source $\dot{Q}_{th}$ in the BoP is given by the sum of these three contributions, with

$$\dot{Q}_{th} = \dot{Q}_{BB} + \dot{Q}_{div} + \dot{Q}_{VV}. \tag{4.145}$$

In a conventional power plant layout, the primary energy source is extracted by a high temperature coolant, circulating in a primary heat transport system (PHTS), consisting of the operated flow and the associated piping and pumping equipment. The heat from the PHTS is then transferred to a power conversion system (PCS), where a combination of power generation machinery and heat exchangers is installed. To cope with the different power levels at the different operation modes, alternating between burn and dwell times, solutions with an intermediate heat exchange system (IHXS) are firmly evaluated for current DEMO designs [182]. The IHXS includes an energy storage system (ESS) which, during burn phase, stores a certain fraction of the BB thermal power ($\sim$20 % [183]) into a high thermal capacity working fluid, e.g molten salts. During the dwell time this energy reservoir feeds the PCS. In the PCS a secondary working fluid flows through a series of steady-flow devices, such as turbines and condensers, creating a direct thermodynamic cycle for the generation of mechanical work and electricity generation in a generator. In current BoP DEMO solutions [184, 185] a low-grade heat contribution of $\dot{Q}_{th}$ given by $\dot{Q}_{div}$ and $\dot{Q}_{VV}$ is used in recuperative processes (e.g. preheating of secondary coolant) to enhance the mean thermodynamic cycle temperature. System codes rely on the definition of the *gross electrical efficiency* for the characterization of the total gross electric power $\dot{W}_{gross}$ in relation to the whole heat source $\dot{Q}_{th}$, reading as [186]:

$$\eta_{gross} = \frac{\dot{W}_{gross}}{\dot{Q}_{th}}. \tag{4.146}$$

η_{gross} can be defined as a multiplication arrangement of other efficiencies, such as conversion efficiency in the generator $\eta_{gen} = \dot{W}_{gross}/\dot{W}_{cycle}$, thermodynamic cycle efficiency $\eta_{cycle} = \dot{W}_{cycle}/(\dot{Q}^{cycle}_{VV} + \dot{Q}^{cycle}_{div} + \dot{Q}^{cycle}_{BB})$ and conversion efficiency in the coolants circulators. Currently, the definition of all

these terms is omitted and η_{gross} is uniquely considered as input parameter. The net electric power delivered to the grid $\dot{W}_{net}$ is the remainder of $\dot{W}_{gross}$, reduced by all the electric consumptions to operate the FPP, denoting the recirculating power. The three largest contributions are:

- pumping power $\dot{W}_{pump}$, to carry the high pressure coolant through the BB, divertor and VV structures, as well as through the BoP piping and heat exchangers,
- the power $\dot{W}_{add}$ supplied to the additional H&CD systems and
- the power $\dot{W}_{cryo}$ to run the cryogenics plant.

The pumping power features non-trivial challenges when estimated in a rather modelling environment, such as systems code. Assume a situation where an hydraulic circuit with a working fluid (for simplicity assumed incompressible) is operated at a certain mass flow rate $\dot{m}$. The circuit presents a variety of hydraulic localized and distributed resistances associated with a pressure drop Δp requiring pumping power W_{pump}. Assuming isentropic pumping, this can be simply evaluated as [187]

$$\dot{W}_{pump} = \frac{\dot{m}}{\rho}\Delta p, \tag{4.147}$$

where ρ is the mass density of the fluid, assumed constant prior and after the pumping sections. The evaluation of Δp depends on many technical aspects, largely influenced by the thermal-hydraulics features of the BB cooling structures, as well as of the PHTS piping geometry. A calculation within a simplified systems code power flow model might lead to over or underestimations. By definition, both localized and distributed pressure losses scale quadratically with the averaged velocity v and linearly with the density ρ of the fluid, such that $\Delta p \propto \rho v^2$. Since $v \propto \dot{m}$, the pumping power has a trend in the third power of $\dot{m}$, $v \propto \dot{m}^3$. For all BB, divertor and VV systems, $\dot{m}$ is linearly driven by the thermal power $\dot{Q}_i$ to remove by carrying such a coolant mass flow rate, with $\dot{m} \propto \dot{Q}_i$ and $i =$ indicating the generic component among the mentioned ones. As for the pumping power $\dot{W}_{pump}$, the third power scaling turns out to hold on Q_i, such that $\dot{W}^i_{pump} \propto \dot{Q}^3_i$. The following simplified relation expresses the electric pumping power transferred to the coolant of the i-th system and the total power $\dot{W}_{pump}$

$$\begin{aligned} \dot{W}^i_{pump} &= \left(\frac{\dot{W}^i_{pump,ref}}{\dot{Q}^3_{i,ref}}\right) \cdot \dot{Q}^3_i = f^i_{pump} \cdot Q^3_i \\ \dot{W}_{pump} &= \sum_i W^i_{pump} \end{aligned}, \quad \text{with } i = \text{BB, div, VV, IHX.} \tag{4.148}$$

Estimating f^i_{pump} from $\dot{W}^i_{pump,ref}$ and $\dot{Q}^i_{i,ref}$, both derived from a chosen reference DEMO BoP layout, $\dot{W}_{pump}$ can be consistently guessed within a MIRA plant systems analyses. Due to the relatively low flow rates and the large densities, the pumping power consumptions in the VV and IHX cooling circuits are neglected.

To comply with the plasma additional heating power demands P_{add}, the external electric source $\dot{W}_{add}$ power must be provided to the H&CD system, such that

$$\dot{W}_{add} = \frac{P_{add}}{\eta_{add}}, \tag{4.149}$$

where η_{add} is the so-called *wall plug efficiency*, outlined as the conversion ratio between electric to pure plasma heating power. The entity of η_{add} pertains to the deployed plasma heating technology

and complex physics aspects. Values of η_{add} around $\sim 0.4-0.5$ are currently assumed for EU-DEMO studies [27].

The tokamak cryogenic system serves a number of components operating at cryogenic temperatures, such as the superconducting magnets and, if present, the vacuum system cryopumps based on cryosorption or cryocondensation principle. Ideally, all cryogenic power consumptions should be separately evaluated, based on each static and dynamic thermal loads affecting the different systems. In practice, relying also on a rather low maturity level of the cryoplant design at DEMO-relevant scales, such a sophistication can hardly be fulfilled within system codes. Therefore, scaling parameters must be sought, for instance, assuming a proportionality with the overall thermal power $\dot{Q}_{th}$. The rationale behind this conjecture is the following. Presumably, a higher thermal capability of the plant would consequentially escalate into larger thermal loads on the superconducting coils, hence on higher cryogenic power consumption. As a result, the total electric cryogenic power $\dot{W}_{cryo}$ can be written as

$$\dot{W}_{cryo} = f_{cryo} \cdot \dot{Q}_{th}, \tag{4.150}$$

with f_{cryo} being an input parameter derived from more substantiated calculations. In several cases [27, 188], values around $\sim 20-30$ MW are found for total thermal fusion reactor powers near $2300-2400$ MW. f_{cryo} can be estimated to be in the range of $0.83-1.3$ %.

Additional electricity demands are found for other plant systems, such as magnets power supply, tritium handling and diagnostics. Once more, only speculative assumptions can be currently done on these electric power consumptions. Typically, a fraction f_{aux} is taken so that the total power $\dot{W}_{aux}$ linearly scales with the total thermal power $\dot{Q}_{th}$,

$$\dot{W}_{aux} = f_{aux} \cdot \dot{Q}_{th}, \tag{4.151}$$

where very diverse assumptions have been taken so far for f_{aux}, with values spanning from 0.3 % [188] to 3.7 % [27]. Conservatively, figures closer to the upper bound are being chosen for all systems studies addressed within this thesis. The ultimate expression for the net electric power to the grid is obtained subtracting from W_{gross} all listed electrical demands,

$$\dot{W}_{net} = \dot{W}_{gross} - \dot{W}_{rec}, \tag{4.152}$$

with $\dot{W}_{net}$ denoting the reference value to compare to the imposed net electric power requirements and $\dot{W}_{rec}$ the total electric recirculating power, given by

$$\dot{W}_{rec} = \dot{W}_{pump} + \dot{W}_{add} + \dot{W}_{cryo} + \dot{W}_{aux} \tag{4.153}$$

Modelling refinement to enhance the areas associated with the BoP equipments, with the evaluation of the wall-plug efficiency and a with more elaborated temporal descriptions of power supplies and demands are topics of major importance for future works.

5. Analysis of a Generic DEMO-Fusion Reactor Design

System codes can be exploited in a variety of different ways to scope possible power plant solutions. Ideally, these tools should be able to provide one (or more) optimized reactor configurations with respect to some key figures of merit, simultaneously meeting the operational and technological requirements and constraints.
Currently, MIRA does not feature optimization capabilities nor fully integrated plant solving logics (except from the core plasma physics and equilibrium solvers), hence relying on the manual manipulation of most of the input parameters.

Relying on the MIRA architecture and model structure, the goal of this chapter is to analyse a consolidated DEMO FPP design, issued by the systems code PROCESS. For all plant systems and components, the key variables describing the analysed DEMO base case are reported and correlated to those featured by PROCESS. Such a task is performed in two steps:

- a detailed definition of the inputs, requirements and constraints and
- a complete MIRA output configuration.

Both operations are addressed Sections 5.1 and 5.2 and both are structured following the module-wise logics adopted for theoretical description of Chapters 2, 3 and 4.

The primary goal of this chapter is to verify MIRA with established system codes as PROCESS by means of code-to-code comparison.
The second target is to demonstrate that MIRA, due to higher spatial resolution and more refined spatial granularity, demonstrates superior analysis features and reactor scales, allowing also for time dependent problems. The fulfillment of both features allows then a consistent analysis of reactor core components designs and their sensitivities, being subject of Chapter 6.

5.1. MIRA Input Configuration of the EU-DEMO 2015 Baseline

The EU-DEMO 2015 baseline [32] has been used as the base case to test and elucidate the capabilities of the MIRA integral package. The source inputs are given by the full PROCESS code output [27, 30] and the 3D CAD model of the tokamak complex [29]. For the sake of a compact notation, it will be referred henceforth as DEMO baseline.

This plant baseline features performance similar to ITER (Q $\sim$10-30) with conceivable improvements in physics and technology, such as H&CD systems and BoP sound technologies. The top level requirements include indicative ranges for $\dot{W}_{net}$ and a lower bound for TBR and τ_{burn}. Additionally, requirements are imposed on the additional heating power P_{add}, to comply with the near-term DEMO design conservative performance assumptions.
The HCPB and WCLL breeding blanket solutions have been adopted as the reference technologies to cover the entire spectrum of breeding, multiplying and cooling materials. Low activation steel has

been selected as blanket structural material, with imposed dpa limit of 20 dpa throughout its lifetime. Two BB concepts operating different coolants require two distinct engineering layouts for the BoP, each featuring η_{gross}, respectively based on a helium-coolant and a water-coolant PHTS. Those base on a prescribed value η_{gross}, derived from existing DEMO BoP designs. As a part of the BoP, a high pressure water loop is deployed to recover the heat deposited in the divertor structure and send it to the PCS.

Low temperature superconductors working at 12-13 T are based on Nb_3Sn and operated in CS and TF coils have been assumed for the analysis of the DEMO 2015 baseline and low field NbTi strands ($\sim$5-6 T) in the PF coil system.

The major design requirements and features adopted within the frame of this DEMO base case study are reported in Table 5.1.

Main design requirements
− Net electric power $\dot{W}_{net}$ $\sim$300-500 MW
− High grade thermal power $\dot{Q}_{th} \sim 2000$ MW
− Tritium self-sufficiency, $TBR_r \geq 1.10$
− Inductive long pulse operation mode, $\tau_{burn} \geq 2$ hr
− Additional heating power, $P_{add} \sim 50$ MW
Main design features
− 18 toroidal sectors, $N_{sect} = 18$
− Helium and water cooled breeding blanket candidates, HCPB/WCLL
− Single-null water cooled divertor
− Low activation Eurofer steel as blanket structural material
− He and water cooled PHTS with IHXS and Rankine cycle in PCS, η_{gross} $\sim$30 %
− LTS, with Nb_3Sn in TF/CS coils ($B_{\max}$ $\sim$12 T) and NbTi in PF coils ($B_{\max}$ $\sim$5 T)

Table 5.1.: Main design features and top level requirements of the EU-DEMO 2015 baseline [32, 40, 182].

The complete list of core plasma physics and magnetic equilibrium fixed input parameters is reported in Table 5.2. The major radius, aspect ratio, elongation and triangularity are used by the geometry module to build the plasma cross sectional profile. These geometric parameters relate to a target separatrix shape, which are achieved by means of the external PF coils currents.
With regard to the plasma profiles and plasma impurities content, several input variables have been extracted from the PROCESS baseline, in order to allow for a comparison. These include the density and temperature at separatrix and pedestal heights, profile factors and the tungsten impurity level in the core and the mantle region.
Temperature and density profiles are normally extracted from more elaborated 1D/2D plasma transport and equilibrium simulation tools. Therefore, it is implicitly assumed that their use in system codes can be still justified within certain margins and so does in the MIRA core physics module. The 85 % of the Greenwald density is assumed for the density at pedestal height [27, 122] to comply with the DEMO edge density limits.
Similar considerations can be extended to c_{Ejima} and H. Due to the large impact of the H-factor on the energy and the particle confinement properties it has kept fixed to 1.1 to be in line with the DEMO 2015 baseline.
Strict margins have been imposed to the fusion power P_{fus}, the additional heating power P_{add} and the particle-to-energy confinement ratio f_{P2E}. The rationale is elucidated as follows.
The goal is to find a plasma operating point, meeting the operational limits and the imposed design

Description	Symbol	Unit	Value
Plasma major radius	R_0	[m]	9.07
Plasma aspect ratio	A	[-]	3.1
Electron density at separatrix	$n_{e,sep}$	[10^{20} m^{-3}]	0.2
Electron density profile factors	α_n / β_n	[-]	1/2
Temperature at pedestal	T_{ped}	[keV]	5.5
Temperature at separatrix	T_{sep}	[keV]	0.1
Temperature profile factors	α_T / β_T	[-]	1.45/2
Pedestal height	ρ_{ped}	[-]	0.94
Charge number of seeded impurity 1 (Xenon)	Z_1	[-]	54
Charge number of impurity 2 (tungsten)	Z_2	[-]	74
Core/mantle concentration of impurity 2	$f_{Z_2} / f_{Z_2,M}$	[-]	5.0×10^{-5}
Ejima coefficient	c_{Ejima}	[-]	0.3
H-factor	H	[-]	1.1
Normalized current drive efficiency	γ_{CD}	[10^{20} A/W/m^2]	0.271
Target upper/lower elongation at X-point	$\kappa^t_{X,u/l}$	[-]	1.68/1.88
Target upper/lower triangularity at X-point	$\delta^t_{X,u/l}$	[-]	0.5/0.5
Target fusion power	P^t_{fus}	[MW]	2037 ± 1
Target additional heating power	P^t_{add}	[MW]	50 ± 0.1
Target particle-to-energy ratio	f^t_{P2E}	[-]	6.542 ± 0.001
Target internal inductance	l^t_i	[-]	1.155
Lower bound of safety factor at axis	q^l_0	[-]	1
Lower bound of safety factor at 95 % flux	q^l_{95}	[-]	3
Upper bound of divertor challenge quantifier	Γ^u_{sep}	[MW/m]	17
Upper bound of Greenwald density fraction	f^u_{GW}	[-]	1.2
Lower bound of LH-transition factor	f^l_{LH}	[-]	1.2

Table 5.2.: List of fixed core plasma input parameters and design targets adopted for the analysis of the EU-DEMO 2015 baseline.

targets, that is based on a calculated 2D magnetic equilibrium configuration, derived from a set of prescribed equilibrium variables, including internal inductance, plasma beta and safety factor. Existing systems codes, such as PROCESS, on the other hand, work with fixed and imposed safety factors, without any link to these variables. This substantial variance necessitates a benchmark to analyse if the same features are obtained in terms of power and energy and particle confinement performances for the same imposed operational limits on density, divertor challenge quantifier and LH transition and normalized beta.

The input specifications related to the SOL and the divertor physics modelling are devoted to the geometric and to all divertor design parameters, both related to its geometric and heat flux parametrizations.
The approach is tailored to the current DEMO divertor design that foresees a compact and dome-less layout to maximize the plasma coverage and the tritium breeding capabilities. The input variables have been manually adjusted to match the divertor poloidal cross section given by the 3D tokamak complex, being also used as reference space domain for the actual engineering design.
The same holds for the inboard, outboard and top SOL widths in relation to the inner profile of the blanket first wall. A minimum distance of the FW from the separatrix on the mid-equatorial plane,

however, is normally posed as a constraining condition to find the optimal separatrix shape in plasma equilibrium calculations [161].
Currently it is challenging to find a set of values for the radiative fraction f_{rad} and the power spreading S usable with large degrees of confidence to compute the peak heat flux on divertor targets (Equation 3.77). f_{rad} has been extracted also from the PROCESS code output, where it has been imposed, too. Concerning S, 4.5 mm is currently assumed for DEMO [122].
The full set of input parameters tied to SOL and divertor modelling parts is given in Table 5.3.

Description	Symbol	Unit	Value
Inboard/outboard/top SOL thickness	$\Delta_{\mathrm{SOL,i/o/t}}$	[m]	0.225/0.225/0.53
Inner/outer distance between X and strike point	$d_{S,i/o}$	[m]	0.95/1.6
Minimum cassette body thickness	d_c	[m]	0.45
Length of the opening for pipes and vacuum pump duct	l_p	[m]	0.5
Inner/outer target poloidal lengths	$l_{t,i/o}$	[m]	0.6/0.6
Inner/outer horizontal angle interfacing the blanket	$\alpha_{w,i/o}$	[deg]	40/45
Inner/outer vertical target angle	$\beta_{i/o}$	[deg]	46/22.5
Baffle radius	ρ_b	[m]	0.08
Curvature radius of the inner cassette curve	ρ_d	[m]	1.8
Power spreading factor	S	[mm]	4.5
Radiative power dissipative fraction	f_{rad}	[-]	0.3
Neutron energy multiplication factor	$\mathrm{EMF_{div}}$	[-]	1.5

Table 5.3.: List of divertor and SOL input parameters of the EU-DEMO 2015 baseline.

The operating temperatures and pressure associated with the BB and the VV of the DEMO 2015 baseline are listed in Table 5.4, including HCPB and WCLL BB solutions. They have been taken according to the current HCPB and WCLL EU-DEMO blanket design solutions [34, 35]. The operating temperature and pressure are needed to calculate the coolant mass densities, the mass inventory and the atom densities for the neutronic analysis. The mass densities and the isotopic compositions of each listed material are derived from Refs. [189, 190, 191].

	BB (HCPB)	BB (WCLL)	VV
IB/OB segments per sector	2/3	2/3	n.a.*
Breeder/Multiplier	Li_4SiO_4/Be pebble beds	Pb-Li eutectic alloy	n.a.
Coolant	Helium	Water	Water
Inlet/outlet coolant temperatures	300-500 °C	285-325 °C	190-200 °C
Coolant pressure	8 MPa	15.5 MPa	3.15 MPa
Structural material	Eurofer	Eurofer	SS316
^{6}Li enrichment	0.6	0.9	n.a.

Table 5.4.: HCPB and WCLL blanket and vacuum vessel design features adopted for the EU-DEMO 2015 baseline.

MIRA allows for geometric characterization of the spatial profiles of the reactor physical components. Moving radially outwards the BB includes a tungsten armour, the first wall (FW), the breeding zone (BZ) and all the piping and supporting structures, i.e. back plates and manifolds. The VV has a water-cooled double-shell stainless structure and it is separated from the BB by a 3 cm gap.

*not applicable

Starting from the first wall armour the detailed radial reactor build is reported in Table 5.5 for the BB and the VV. Each subsystem includes an inboard and an outboard thickness, $\Delta_{m,i}$ and $\Delta_{m,o}$, and a volume fraction for each constituting material. The top and bottom widths are by default the average values between inboard and outboard. This applies to all components except of the VV, where $\Delta_{VV,t}$ and $\Delta_{VV,b}$ take nearly the same amplitude as the inboard.

Region	$\Delta_{m,i}$ [cm] HCPB/WCLL	$\Delta_{m,o}$ [cm] HCPB/WCLL	Material	Vol. Fract. [%] HCPB/WCLL
W Armour	0.2/0.2	0.2/0.2	Tungsten	99.0
			Void	1.0
First Wall	2.5/2.5	2.5/2.5	Eurofer	64.4/82.0
			Helium	34.6/0.0
			Water	0.0/17.0
			Void	1.0/1.0
Breeding Zone	23/47	52/80	Li_4SiO_4	21.0/0.0
			PbLi	0.0/78.0
			Eurofer	14.0/18.0
			Be pebbles	54.5/0.0
			Helium	9.5/0.0
			Water	0.0/2.0
			Void	1.0/1.0
Back plates	8.5/7.5	8.5/7.5	Eurofer	40.9/96.7
			PbLi	0.0/1.3
			Helium	58.1/0.0
			Water	0.0/1.0
			Void	1.0/1.0
Manifold	44.8/20.8	66.8/39.8	Eurofer	60.1/80.7
			PbLi	0.0/4.05
			Helium	38.9/0.0
			Water	0.0/10.5
			Void	1.0/1.0
GAP BB/VV	3.0	3.0	Void	100.0
VV inner shell	5.0	5.0	SS316	100.0
VV cool. shell	52.0	102.0	SS316	60.0
			Water	40.0
VV outer shell	5.0	5.0	SS316	100.0

Table 5.5.: Radial subdivision and material composition of the BB and the VV adopted for the EU-DEMO 2015 baseline.

The radial discretization and material composition are derived from Refs. [181] and [191] for HCPB and WCLL. Since both BB concepts rely on a MMS structure in poloidal and toroidal directions, each module is separated by void gaps and enclosed by actively cooled steel structures, denoting the module box. For a generic blanket module the box comprises two vertical caps (top and bottom) and two lateral side walls, hydraulically connected with the first wall. Therefore, with respect to the original input material compositions, the volume fractions have been modified to account for a non-null void fraction and for the enhanced steel and coolant volume fractions due to the presence of poloidal caps and side walls. From CAD measurements the poloidal and toroidal void gaps have

been evaluated to about 1 % in all BB subregions equally redistributed among the other materials. With regard to extra coolant and Eurofer box steel fractions, the volume compositions have been recalculated averaging on the total poloidal and toroidal thicknesses.
The space reservation and the material composition of the VV have been obtained from the HCPB MCNP DEMO neutronic module [190].

A set of input parameters is needed to represent the TF, PF and CS coils magnet system. The cross section of the inboard and the outboard legs of the TF coil rely on imposed wideness of the casing and ground insulation structures, which drives the overall radial and vertical build of the coil. These two subcomponents are built around the winding pack. Table 5.6 lists the thicknesses Δ_{case} associated with the inner, outer and toroidal external cases and with the ground insulator, Δ_{gi}.
These TF coil casing variables are inboard and outboard thickness for each of these elements and a constant width for the epoxy resin ground insulator.

Parameter	Symbol	Unit	Value
Inboard leg toroidal case thickness	$\Delta^{ib}_{case,T}$	[cm]	10
Outboard leg toroidal case thickness	$\Delta^{ob}_{case,T}$	[cm]	10
Inboard leg outer case thickness	$\Delta^{ib}_{case,O}$	[cm]	51
Outboard leg outer case thickness	$\Delta^{ob}_{case,O}$	[cm]	22.5
Inboard leg inner case thickness	$\Delta^{ib}_{case,I}$	[cm]	4
Outboard leg inner case thickness	$\Delta^{ob}_{case,I}$	[cm]	19
Ground insulation thickness	Δ_{gi}	[cm]	0.8

Table 5.6.: TF coil casing and ground insulator thickness adopted for the EU-DEMO 2015 baseline [192].

The TF coil radial, vertical thickness and the material mixture in each TF coil region are reported in Table 5.7. A void gap (11 cm on the inboard and 100 cm on the outboard) is located between the TF coil and the VV. The inboard and outboard widths, as well as the top and bottom's (both 12 cm), are deduced from the PROCESS output. The outboard and the top thicknesses are key parameters for the design of the TF coils, since they represent a manoeuvring figure to control the TF ripple on the plasma separatrix.
The WP width and its material mixture are purely tentative at this stage, as they are being updated based on the required operating current I_{TFC} and on the physical space needed to accommodate the necessary number of turns. The WP tentative thickness derives from the PROCESS code output, while the material mixes are taken from the HCPB MCNP DEMO neutronic module [190].

The PF and the CS coils are axisymmetric elements. For all eleven coils, consisting of six PF coils and a five element CS stack in the DEMO 2015 design, the quadruplet of parameters composed of the radial and axial coordinate of its mid-point and their radial and vertical widths are reported in Table 5.8. The mid-point coordinates relate to the variables r_m and z_m and the widths to δr and δz. The naming nomenclature and positioning order of all coils is shown in Figure 4.5. The PF/CS coils geometric parameters are derived from the tokamak complex and adjusted to take into account of the upper and lower port position and TF coil poloidal shape. Since the PF coils directly support on the TF coils casing structure, the position can be adjusted such that they are kept within a controlled distance. From CAD measurements it has been found around 10 cm.

For all coil systems, the cable concept can be selected from the full list data bank of conductors (see Table 4.4). The cable engineering layouts have been identified following different logics, including best performances in terms of peak fields, compactness and maximum operating current.

Region	$\Delta_{m,i}$ [cm]	$\Delta_{m,o}$ [cm]	Material	Vol. Fract. [%]
GAP VV/TFC	12.0	98.0	Void	100.0
TFC inner case	$\Delta^{ib}_{case,I}$	$\Delta^{ob}_{case,I}$	SS316	100.0
TFC inner GI	Δ_{gi}	Δ_{gi}	Epoxy resin	100.0
TFC WP	44.2	44.2	Epoxy resin	18.0
			Nb_3Sn	2.9
			Bronze	7.3
			Copper	11.7
			Liquid He	16.8
			SS316	43.3
TFC outer GI	Δ_{gi}	Δ_{gi}	Epoxy resin	100.0
TFC outer case	$\Delta^{ib}_{case,O}$	$\Delta^{ob}_{case,O}$	SS316	100.0

Table 5.7.: Radial subdivision and material composition of the TF coil adopted for the EU-DEMO 2015 baseline.

	r_m [m]	z_m [m]	δr [m]	δz [m]
CS3U	2.9	+6.66	0.8	2.81
CS2U	2.9	+3.75	0.8	2.81
CS1	2.9	-0.61	0.8	5.71
CS2L	2.9	-4.97	0.8	2.81
CS3L	2.9	-7.88	0.8	2.81
PF1	5.4	+8.82	1.2	1.2
PF2	14.0	+7.0	0.8	0.8
PF3	17.0	+2.5	1.0	1.0
PF4	17.0	-2.5	1.0	1.0
PF5	14.4	-8.40	1.4	1.4
PF6	7.0	-10.45	2.0	2.0

Table 5.8.: DEMO PF/CS coils size and position adopted for the EU-DEMO 2015 baseline.

Such an approach is aimed at demonstrating the benefits from exploiting a sound and optimized cable design rather than parametrizing in a simplified fashion the cabling features within the system analysis, as performed in existing fusion system codes.
The engineering models of the superconducting magnets integrated so far are capable of ensuring that current, field and temperature margin operating values are within the prescribed limits and check whether the conductor is protected against quench. If any of those conditions is not met, no action is taken to change the features of the cable, except of reducing the operating current and, possibly, increase the number of turns. All coil engineering parameters are listed in Table 5.9.

All input specifications associated with the plant power balance and the reactor cycle pulse modelling parts are listed in Table 5.10. Since the selected DEMO 2015 baseline relies on a long pulse inductive operation a set of input specifications must be provided to the modelling of the temporal operating cycles (Section 4.3.1). The pump-down time τ_{PD} has been chosen assuming the 20-min outgoassing time DEMO design goal [178] and on the value indicated in the baseline (30 min). The max voltage during the premagnetization has been assigned to yield CS recharge times of few hundreds of seconds, in line with the achievable active power consumptions at plasma breakdown [179]. The input specifications associated with the plant power balance model (Section 4.3.2) are speci-

Parameter	[Unit]	TF coils	PF coils	CS
Cable ID	[-]	TF_ENEA	PF5_CEA	CS_CEA
Superconducting material	[-]	Nb_3Sn	NbTi	Nb_3Sn
$B_{\max}$	[T]	12.44	5.67	13.7
T_{op}	[K]	5	4.7	4.6
ϵ_{op}	[%]	-0.55	n.a.	-0.51
$\Delta T_{cs,\min}$	[K]	1.5	1.5	1.5
T_{hs}	[K]	250	250	250
f_{He}	[%]	26	29	29
f_{Cu2sc}	[-]	1.0	1.41	0.97
d_{strand}	[mm]	1.0	0.73	0.885
N^{sc}_{strand}	[-]	720	689	659
N^{Cu}_{strand}	[-]	603	470	596
d_{ch}	[mm]	7.0	12	10
$\delta r_{turn,c} / \delta c_{turn,c}$	[mm]	33.8/68.9	28.85/28.85	33.4/33.4
$\delta_{turn,j}$	[mm]	3.9	16	12.8
$\delta_{turn,ins}$	[mm]	1.5	2	1
Δ_{gi}	[mm]	8	8	8
$V^{\max}_{dump}$	[kV]	10	5.5	10

Table 5.9.: List of of operating and design parameters of the superconducting cables deployed for the analysis of the EU-DEMO 2015 baseline.

Parameter	Symbol	Unit	HCPB	WCLL	Source
PD time fraction not usable for overlapping with CS recharge	f_{PD}	[-]	0.25	0.25	[10]
Ramp-up time factor	f_{RU}	[-]	10	5	[10]
Heating time factor	f_{heat}	[-]	5	5	[10]
Pump-down time scale	τ_{PD}	[min]	30	30	
Max voltage during CS recharge	$V^{\max}_{i,RC}$	[V]	1000	1000	
Gross electrical efficiency	η_{gross}	[-]	0.30	0.26	[183, 193]
Wall-plug efficiency	η_{add}	[-]	0.4	0.4	[27, 179]
BB pumping power factor	f^{BB}_{pump}	[MW^{-2}]	1.29×10^{-8}	1.85×10^{-9}	[182]
Divertor pumping power factor	f^{div}_{pump}	[MW^{-2}]	2.38×10^{-6}	2.38×10^{-6}	[185]
Cryogenic power fraction	f_{cryo}	[-]	0.013	0.013	[27]
Auxiliary system power fraction	f_{aux}	[-]	0.037	0.037	[27]

Table 5.10.: List of DEMO parameters for the power flow module and cycle dynamic models of MIRA based on the HCPB and WCLL EU-DEMO 2015 BoP designs

fied both for HCPB and WCLL concepts. The gross thermodynamic and the wall plug efficiencies are sensitive parameters and affected by many technological and engineering aspects, including the design of BoP subcomponents, temperature and pressure of the cooling fluids and plasma heating technology. The gross electrical efficiencies η_{gross} have been obtained from recent DEMO BoP design activities [182, 183, 184, 185]. In order to make these assumptions reliably deployable within a reactor system analysis the interfacing variables such as primary thermal input Q_{th} and P_{add} have been kept within limited ranges, fixing both fusion power and additional heating power in the core

plasma solver. Therefore, the assumptions taken on η_{gross} and η_{add} still hold for diverse plant configurations, for instance in terms of reactor sizes of magnetic field.
Concerning the indicated pumping, cryogenic and auxiliary system power factors, the selected coefficients have been calculated from the cited references, based on the power terms involved in the associated studies. Based on the definitions of Equations (4.148), (4.150) and (4.151) the respective coefficients f_{pump}, f_{cryo} and f_{aux} have been calculated based on the reported values of $\dot{Q}_{th}$, $\dot{W}_{pump}$, $\dot{W}_{cryo}$ and $\dot{W}_{aux}$.

5.2. MIRA Verification and Analysis of the EU-DEMO 2015 Baseline

In this section, the results obtained from a complete MIRA simulation on the DEMO base case, based on the full set of input parameters reported in the previous section, are illustrated and discussed.
The outcome of this MIRA run is broken down into modules, following the theoretical description order of Chapters 2, 3 and 4.
Browsing through the different subsections, the key features will be illustrated and the main deviations from the baseline, represented by the PROCESS output, will be analysed and physics arguments are elaborated elucidating shortcomings being present in former studies.

5.2.1. Reactor geometric configuration and mass inventory parameters

The radial-poloidal sketch of the simulated reactor physical components and generated by the geometric module is depicted in Figure 5.1, along with a superimposition of the poloidal cut extracted from the CAD model of the baseline tokamak complex. The MIRA reactor build and the tokamak complex almost coincide with the CAD model in all the displayed components. The largest gaps are found in the bottom outboard portion of the VV and bottom inboard leg of the BB. These are basically derived from the imposed parametrization, which are driven by simple geometric rules from a radial and vertical construction of the reactor.
As for the BB inboard leg, an ellipse branch instead of a double straight segment is clearly a minor simplification that does not provoke substantial perturbations in terms of FW surface, BB volumes and peak neutron and photon radiation fluxes.
Figure 5.1 demonstrates a tangible refinement of the geometric details, bringing the traditional system code environment closer to the engineering platform. Compared to the same reactor build generated by the PROCESS system code (see Figure 1.2 within the box "system code"), additional design-oriented ingredients can be also noted, such as the presence of the divertor, the subdivision of the CS in five elements and a more realistic shape of the TF coils and the VV.

A set of BB geometric parameters and material inventories is listed in Table 5.11. It includes both for HCPB and WCLL blankets the calculated volume V_{BB}, FW area A_{FW} and the full set of material amounts, denoted with $m_{BB,k}$, with k denoting the generic BB $k-$th material mix. Also the BB inboard and outboard segment masses, $m^{i}_{BB,segm}$ and $m^{o}_{BB,segm}$ are listed.
A direct benchmark with the PROCESS output could not be carried out due to the unbalanced level of geometric and engineering details among MIRA and PROCESS. Moreover, some of the BB materials (e.g. Li_2O) appearing in the PROCESS configuration do not find any matching part in the

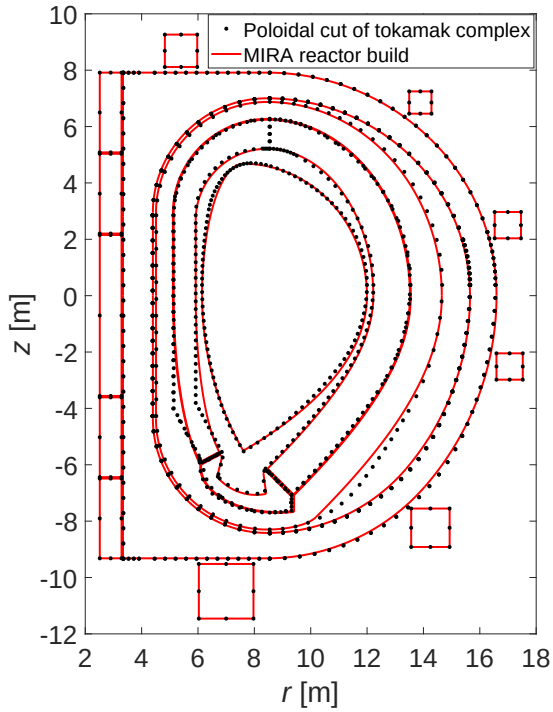

Figure 5.1.: Reactor sketch of the EU-DEMO 2015 Baseline: comparison between MIRA and poloidal cut of 3D tokamak complex, extracted from the 3D DEMO baseline CAD model.

Parameter	Symbol	Unit	MIRA HCPB	PPPT-WPBB HCPB	MIRA WCLL	PPPT-WPBB WCLL
BB volume	V_{BB}	[m^3]	1851	1691	1851	1830
FW area	S_{FW}	[m^2]	1498	1454	1498	1438
BB IB/OB segment mass	$m^{i/o}_{BB,segm}$	[ton]	42.1/90.5	39.9/89.6	38.7/75.1	39.1/71.2
BB mass inventories	$m_{BB,k}$					
$k =$ Tungsten		[ton]	57.4	66.2	57.4	49.8
$k =$ Eurofer		[ton]	5724.1	5606	5390	5203
$k =$ Be pebbles		[ton]	418.9	411	n.a.	n.a.
$k =$ Li_4SiO_4		[ton]	198.3	192	n.a.	n.a.
$k =$ PbLi		[ton]	n.a.	n.a.	8748	8854
$k =$ Helium		[ton]	28.7	32.36	0	n.a.
$k =$ Water		[ton]	0	0	165	146.4

Table 5.11.: Evaluated BB geometric and mass inventories of the EU-DEMO 2015 baseline: comparison between MIRA results and reference HCPB and WCLL blanket designs, addressed within the frame of the WPBB in the PPPT programme [181, 191].

reference EU-DEMO blanket designs. In light of this situation, volume and mass inventories have been compared to those extracted from the PPPT-WPBB design activities carried out for HCPB and WCLL blankets [181, 191]. A blind comparison with detailed BB design features allows a verification of the material composition and of the geometry and material mass inventories models.

Having built the blanket profile parametrization and the material composition on existing and consolidated BB designs has yielded volume, FW area and the material compositions in rather good

agreement. The deviations are below 5 % in most of the cases. Exceptions have emerged for tungsten (in both concepts) and water (WCLL), where deviation up to 15 % are noticed. In terms of global inventories, however, they represent a minor contribution.
Diverging volumes and FW areas, between HCPB and WCLL, are derived from different poloidal blanket segmentation and space allocation of the BB modules within the global BB space reservation provided by the tokamak complex. These BB design aspects are not yet part of the geometric modelling of MIRA and, accordingly, the BB geometric features are identical for HCPB and WCLL.

Two inboard and three outboard segments are currently being considered for the BB toroidal discretization. These are very crucial figures when interfaced with a remote maintenance (RM) pattern, to which the number of IB and OB segments represents a fundamental input. The IB and the OB segment masses play a key role, since RM structures must be able to lift and dislocate across the weight within the vacuum chamber with prescribed tolerances.
Relying on the geometric and material definition flexibility $m^{i/o}_{BB,segm}$ is the remainder of the inboard and outboard total masses from the fluid part, i.e. helium, water and PbLi. Moreover, the evaluation is performed by limiting the control volume only to the segment fraction, i.e., according to Table 5.5, one-half and one-third of sector for inboard and outboard, respectively. Comparing the reference segment mass values a similar outcome is observed.
As the segment mass has a great impact on the RM and on the off-normal plant operations in light of potential improvements involving advanced plant availability model with RM aspects, these features are made already available. Alternatively, if specific operational constraints are posed on the BB segments mass, the MIRA data structure is already capable of coping with this additional design restriction.

5.2.2. Core plasma physics and equilibrium configurations

In the following the plasma magnetic equilibrium, fuel and impurities concentration, power balance and current balance properties are illustrated and correlated to the major deviations from the DEMO baseline, determined by the PROCESS system code. When applicable, these are put in relation to their operational limits (OL) and design targets (DT) and it is indicated whether the parameter variable denotes an iteration variable (IV) of the plasma solver. The comparison of each calculated variable between MIRA and PROCESS is performed in terms of $\text{Deviation} = (\text{MIRA} - \text{PROCESS})$ $/\text{PROCESS}$.

The plasma geometric and equilibrium parameters are summarized in Table 5.12. The calculated plasma volume, surface, triangularity and elongation are associated with the fixed target separatrix input parameters listed in Table 5.2. However, the geometric features related to actual plasma shape obtained via full PF/CS coil current solving procedure will be illustrated in the subsection dedicated to the plasma scenario analysis. All other geometric factors have been found in very good agreement with PROCESS except of δ_{95}, which deviates by nearly 15 % from the baseline. In fusion systems codes κ_{95} and δ_{95} are extracted from ITER Physics Design Guidelines [87], linearly scaling with κ_X and δ_X. In MIRA these are both calculated from an equilibrium magnetic configuration. Since both κ and δ participate in a wide number of calculated physics parameters, such as energy confinement time τ_E (Equation C.30), plasma current I_p (Equation 3.8) and plasma conductivity (Equation C.6), a more accurate evaluation can provide considerable gain to the system analysis. The same applies to fusion power since κ_X has been recently established to have large implications on $P_{fus} \propto \kappa_X^{5.4}$ [27].
The toroidal magnetic field at plasma center B_t has been evaluated according to Equation (3.17) and

Parameter (Symbol)	Unit	MIRA	PROCESS	Deviation [%]	Limit
Plasma volume (V_p)	[m^3]	2458	2502	-1.8	
Plasma surface (S_p)	[m^2]	1417	1428	-0.8	
Plasma poloidal cross section (A_p)	[m^2]	44.37	44.79	-0.9	
Plasma poloidal perimeter (ℓ_p)	[m]	25.81	25.77	+0.2	
Elongation at 95% flux surface (κ_{95})	[-]	1.57	1.59	-1.3	
Triangularity 95% flux surface (δ_{95})	[-]	0.28	0.33	-15.2	
Magnetic field at plasma center (B_t)	[T]	5.493	5.667	-3.1	
Total toroidal current (I_p)	[MA]	19.26	19.60	-1.7	
Safety factor at axis (q_0)	[-]	0.55	1.00	-45.0	≥ 1 (OL)
Safety factor at 95 % flux (q_{95})	[-]	3.17	3.25	-2.5	≥ 3 (OL)
Internal inductance (l_i)	[-]	1.155	1.155		≈ 1.155 (DT)
Total poloidal beta (β_p)	[%]	122.4	110.7	+10.6	
Thermal poloidal beta ($\beta_{p,th}$)	[%]	97.1	95.1	+2.1	
Total toroidal beta (β_t)	[%]	3.57	3.15	+13.3	
Thermal toroidal beta ($\beta_{t,th}$)	[%]	2.83	2.70	+4.8	
Total plasma beta (β_{th})	[%]	2.75	2.63	+4.6	
Thermal plasma beta (β)	[%]	3.46	3.06	+13.1	
Normalized beta (β_N)	[%]	2.98	2.59	+15.1	$\leq 4l_i$ (OL)
Fast to thermal beta (γ_{fast})	[-]	0.26	0.16	+62.5	
Fast alpha to thermal beta ($\gamma_{f\alpha}$)	[-]	0.21	0.14	+50.0	
Neutral beam to thermal beta (γ_{beam})	[-]	0.047	0.026	+80.8	(IV)

Table 5.12.: Computed plasma geometry and magnetic equilibrium parameters of the EU-DEMO 2015 baseline: comparison between MIRA and PROCESS results. When applicable, the notes indicate for each parameter if it represents a design target (DT), an operational limit (OL) or an iteration variable (IV) of the plasma solver.

adjusted on the peak field at TF coil conductor. The calculated value has featured a 3 % reduction compared to the PROCESS DEMO baseline. Since B_t has large influences on several plasma features, such as the fusion power $P_{fus} \propto B_t^4$ [100], even such small perturbations can perpetrate important consequences to the whole plasma operating conditions. These deviations from depict another indicator of the impacts (and of the beneficial effects) deduced from a more comprehensive set of physics and engineering models. The magnetic field-related aspects, associated with the full external magnetic field configuration, will be illustrated in Section 5.2.6.
An additional major outcome on this subsection pertains to the safety factor q_0 at plasma centrer, found by far below its lower operational limit, hence denoting an unstable plasma configuration. In system codes q_0 is fixed to 1 while q_{95} is used as iteration variable to match the MHD stability condition in the plasma current formulation (Equation 3.15). In MIRA q_0 and q_{95} are congruently calculated according to two-dimensional plasma magnetic equilibrium aspects.
In light of this situation, action must be taken on the independent parameters directly acting on the magnetic plasma profile, such as on the plasma current density shape. The best candidate has been identified in the internal inductance l_i, to which a dedicated parameter scan will be dedicated in Chapter 6.

A final observation resides in the non-thermalized particles contribution to the plasma beta, given by their ratios to the thermal beta, $\gamma_{f\alpha}$ and γ_{beam}. Their sum yields the ratio of fast particles to thermal beta γ_{fast}, which directly affects the total plasma beta β_p, hence the pressure regime

(Equation C.18). The complex phenomena involved in the plasma particle thermalization can hardly be dealt in a system code environment. Thus, $\gamma_{f\alpha}$ and γ_{beam} are typically evaluated from scaling laws. As for $\gamma_{f\alpha}$, the fitting function implemented in MIRA, extracted from the TREND code, relies on the scaling given by the ITER Physics Design Guidelines [87], reported in Equation (C.17). It expresses $\gamma_{f\alpha}$ as a function of the fuel fraction f_{DT} and the density-averaged temperature $\langle T \rangle_n$. γ_{beam}, instead, has been set in the plasma solver as an iteration variable. In PROCESS γ_{beam} is evaluated as a combination of input parameters, such as neutral beam energy and rate, that can be anyway advocated to NBI system control parameters, hence, to iteration variables. As f_{DT} and $\langle T \rangle_n$ have been found relatively close such pronounced divergences on $\gamma_{f\alpha}$ (50 %), therefore, can be largely attributed to the usage of different modelling approaches. The fast beam contribution, although exhibiting similar distances from PROCESS, has a much smaller impact on γ_{fast}.

The largest deviations in the plasma profile and core power balance properties are attributed to the electron density, in particular at plasma axis $n_{e,0}$ (≈ -7 %), while marginal differences have been obtained for the temperature properties, as listed in Table 5.13.

Parameter (Symbol)	Unit	MIRA	PROCESS	Deviation [%]	Limit
Electron density at axis ($n_{e,0}$)	[10^{20}/m^3]	0.944	1.014	-6.9	(IV)
Electron density at pedestal ($n_{e,Ped}$)	[10^{20}/m^3]	0.609	0.678	-10.2	
Vol.-averaged electron density ($\langle n_e \rangle$)	[10^{20}/m^3]	0.729	0.798	-8.6	
Line-averaged electron density ($\overline{n}_e$)	[10^{20}/m^3]	0.806	0.874	-7.8	
Greenwald density (n_{GW})	[10^{20}/m^3]	0.716	0.728	-1.6	
Greenwald density fraction (f_{GW})	[-]	1.126	1.200	-6.2	$\leq$ 1.2 (OL)
Temperature at axis (T_0)	[keV]	26.85	27.36	-1.9	(IV)
Volume-averaged temperature ($\langle T \rangle$)	[keV]	13.48	13.12	+2.7	
Density-averaged temperature ($\langle T \rangle_n$)	[keV]	15.34	14.41	+6.5	
Fusion power (P_{fus})	[MW]	2037	2037		$\approx$ 2037 (DT)
Neutron power (P_{neut})	[MW]	1630	1629	+0.1	
Alpha power (P_α)	[MW]	407	408	-0.2	
Fusion gain (Q)	[-]	39.9	39.9		
CD power (P_{CD})	[MW]	49.9	50.0	-0.2	
Additional heating power (P_{add})	[MW]	49.9	50.0	-0.2	$\approx$ 50 (DT)
Ohmic heating power (P_{OH})	[MW]	1.01	1.11	-9.0	
Core radiation power ($P_{rad,core}$)	[MW]	124.2	132.6	-6.3	
Mantle radiation power ($P_{rad,mantle}$)	[MW]	180.0	172.9	+4.1	
Radiation power (P_{rad})	[MW]	304.2	305.5	-0.4	
Transport loss power (P_{con})	[MW]	335.3	327.1	+2.5	
Power across the separatrix (P_{sep})	[MW]	154.1	154.2	-0.1	
Divertor challenge quantifier (Γ_{sep})	[MW/m]	16.99	17.00	-0.1	$\leq$ 17 (OL)
Energy confinement time (τ_E)	[s]	3.74	4.23	-11.6	
LH-transition factor (f_{LH})	[-]	1.27	1.27		$\geq$ 1.2 (OL)

Table 5.13.: Calculated plasma profile and power balance properties of the EU-DEMO 2015 baseline: comparison between MIRA and PROCESS results.

The pedestal density has been set proportional to the Greenwald density n_{GW}, hence it differs from that of PROCESS because of the diverse plasma current I_p, derived from the offset in B_t. The disparity of electron density between MIRA and PROCESS is a central point in relation to the reper-

cussions originated by the modelling approximations limiting the core plasma physics capabilities of fusion systems codes. In PROCESS the electron density is being pushed towards its upper bound dictated by the Greenwald density limit, $f_{GW} \leq 1.2$, whereas in MIRA this limit is not approached. The plasma design targets have been fixed for the fusion power and the additional heating power (the same as PROCESS) and also forcing the solver to enhance the power transported across the separatrix P_{sep} towards its upper limit. As it turns out the sought plasma operating point is achieved without densities advancing towards its upper operational Greenwald ceiling. It can be verified that the same temperature profiles and rather diverse densities profiles yielded an identical fusion powers. Combining the distances from PROCESS exhibited by B_t, I_p and all profiles variables, the largest deviations in the power balance properties have been found for τ_E, i.e. -11.6 %. Smaller distances have emerged from the calculated plasma losses, such as $P_{rad,core}$, $P_{rad,mantle}$ and P_{con}, since a target value has been imposed on Γ_{sep} and on P_{add}, i.e. on the plasma heating and loss.

Zero-dimensional system codes rely on a fixed magnetic coordinate coincident to the radial normalized coordinate defined as $\rho = r/a$. Accordingly, $\rho = 0$ represents the magnetic axis (normally coincident to the plasma center) and $\rho = 1$ identifies the plasma LCMS and the magnetic flux surfaces are equally spaced from each other. But, in real tokamak magnetic configurations there are non-negligible two-dimensional effects, such as the Shafranov shift of the magnetic axis, affecting the spatial distribution of the plasma thermophysical properties within the confining region.
These effects can be visualized in Figure 5.2−a, where 10 calculated magnetic flux surfaces are superimposed to the same number of fixed flux surfaces, described by the parametric equation proposed by C. Fausser [194] (see Equation E.18). Starting from the magnetic axis A the first calculated MS (i.e. $\rho = 0.1$) embeds almost completely the first two fixed MSs, i.e $\rho = 0.1$ and $\rho = 0.2$. As electron density and temperatures profiles are defined with descending profiles on ρ, in case of calculated poloidal magnetic flux the hotter and denser plasma regions are spread over a wider region compared to the fixed case, leading to large density differences between MIRA and PROCESS for the same fusion power. Moving towards the periphery the calculated flux lines tend to squeeze and come closer with respect to the linearly spaced ones.

This situation can be depicted by the normalized cumulative coordinate $\overline{V}_p$, displayed in Figure 5.2−b as a function of ρ for both analysed cases. $\overline{V}_p$ is defined for a given flux coordinate ρ' and corresponds to the plasma volume, normalized to the total plasma volume V_p contained within the MS delineated by ρ' such that $\mathcal{D}_p(\rho') = \{(r,z) \mid \rho(r,z) \leq \rho'\}$. It is given by

$$\overline{V}_p(\rho') = \frac{1}{V_p} \int_{\mathcal{D}_p(\rho')} 2\pi r \mathrm{d}r\mathrm{d}z. \tag{5.1}$$

$\overline{V}_p$ calculated is larger than the fixed for a large fraction of the whole domain, approximately for $\rho < 0.7$. For $\rho > 0.7$ $\overline{V}_p$ calculated is lower than the fixed. As it will be demonstrated in Chapter 6 within the sensitivity study of l_i, these effects have consequences on many core plasma physics parameters addressed in fusion system codes. The built-in equilibrium solver reveals to be effective in view of modelling plasma physics refinement.

A considerable offset has been observed in the core seeded impurity concentration f_{Z_1}, while rather similar values have been found for the same impurity content in the core (see Table 5.14).
Both core and mantle radiation powers exhibit quite small deviations due to the divertor challenge quantifier constraint $\Gamma_{sep} \leq \Gamma^u_{sep}$, willingly brought to its upper limit, for the sake of a blinder comparison. It can be deduced that, obtaining very similar core radiation powers with rather heterogeneous core impurity contents is an outcome most likely tied to the spatial effects. Accordingly, the

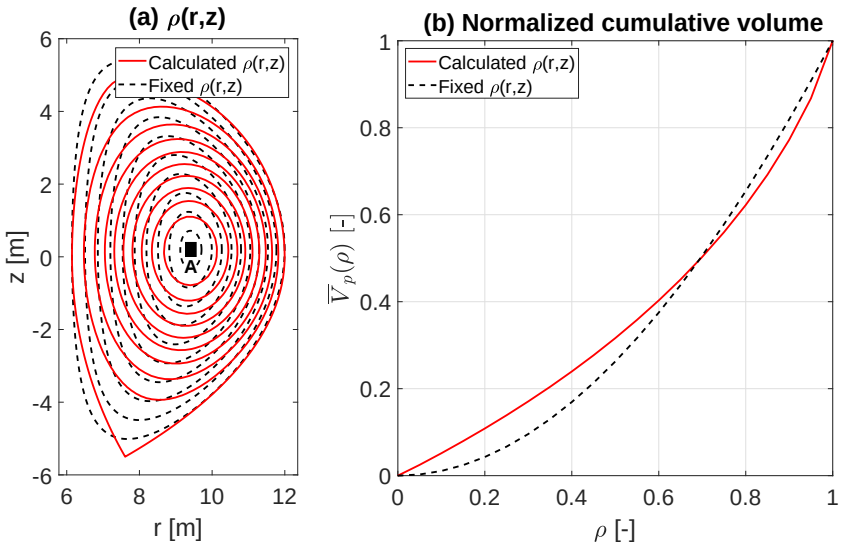

Figure 5.2.: Comparison of poloidal magnetic flux distribution in case of calculated vs. fixed magnetic configuration. Subfigure (a) depicts the two-dimensional spatial profiles of ten iso-poloidal magnetic flux surfaces, taken for equally spaced values of ρ. (b) displays the distributions of the normalized cumulative volume for both cases.

Parameter (Symbol)	Unit	MIRA	PROCESS	Deviation [%]	Limit
Plasma effective charge (Z_{eff})	[-]	2.217	2.584	-14.2	
Thermal ion concentration (f_i)	[-]	0.894	0.875	+2.2	
Fuel concentration (f_{DT})	[-]	0.796	0.769	+3.5	
Helium fraction (f_{He})	[-]	0.099	0.1	-1.0	(IV)
Core seeded impurity conc. (f_{Z_1})	[-]	5.34×10^{-5}	3.89×10^{-4}	-86.3	(IV)
Mantle seeded impurity conc. ($f_{Z_1,M}$)	[-]	3.97×10^{-4}	3.89×10^{-4}	+2.1	(IV)
Particle-to-energy ratio (f_{P2E})	[-]	6.543	6.542	+0.07	$\approx$ 6.542 (DT)

Table 5.14.: Calculated plasma fuel and impurities content parameters of the EU-DEMO 2015 baseline: comparison between MIRA and PROCESS results.

volume integration of the line radiation power density $q_{line} \sim f_{Z_j} n_e^2(\rho) L_{Z_j}(\rho)$ undergoes the effects of the non-uniform spreading of the magnetic flux surfaces, hence of n_e and T.
Moreover, the baseline does not seem to distinguish between core and mantle regions, thus handling a unique variable for the seeded impurity amounts. Hence, with respect to the radiation power parameters a direct comparison with PROCESS can hardly be performed.

The total plasma current repartition has featured a large mismatch about the bootstrap and the inductive current fractions (see Table 5.15). The MIRA and PROCESS current drive fractions f_{CD} are quite alike due to the forced 50 MW design target on the additional heating power P_{add}, to be uniquely provided in form of CD power.
The bootstrap fraction is computed in systems code by choosing a scaling function among a variety of available ones, e.g. H.R. Wilson [195] and Andrade [81]. The former is outlined in Equation (C.8) and set as default one in TREND, hence, in MIRA too. Currently, the extrapolation law used by PROCESS, reported by Sauter et al [196], has not been integrated neither in TREND nor in MIRA. Therefore, the computed discrepancies arises from this very specific modelling assumption. Independently from whichever formula is being exploited the lower bootstrap fractions are mostly

Parameter (Symbol)	Unit	MIRA	PROCESS	Deviation [%]
Loop voltage (U_{loop})	[V]	0.053	0.057	-7.0
Plasma resistance (R_p)	[Ω]	4.13×10^{-9}	5.22×10^{-9}	-20.9
Plasma inductance (L_p)	[H]	1.99×10^{-5}	1.62×10^{-5}	+22.8
CD current fraction (f_{CD})	[-]	0.106	0.095	+11.6
Inductive current fraction (f_{ind})	[-]	0.662	0.557	+18.9
Bootstrap current fraction (f_{BS})	[-]	0.232	0.348	-33.3
Resistive flux consumption at RU (Ψ_{res})	[Wb]	65.86	67.04	-1.8
Inductive flux consumption at RU (Ψ_{ind})	[Wb]	126.8	129	-1.7

Table 5.15.: Calculated plasma current and magnetic flux balance properties of the EU-DEMO 2015 baseline: comparison between MIRA and PROCESS results.

attributed to the lower safety factor at plasma axis q_0, which participates in most of the attainable fitting laws. q_0 has been found well below its expected unitary lower limit (Table 5.12), appointed to 1 in PROCESS with no further connection with any other plasma parameters.
In terms of loop voltage, only marginal differences have been attained. This response finds justifications in a lower plasma resistance, that balances the larger inductive fraction f_{ind}, yielded by the smaller f_{BS}.
The reduced amplitude of the plasma resistance originates from the modelling treatment of the Spitzer surface-averaged conductivity σ_{Sp} and its dependency on the plasma temperature T (Equation C.6). σ_{Sp} is expressed as a function of the density-averaged temperature $\langle T\rangle_n$, whereas in PROCESS [17] the volume-averaged temperature $\langle T\rangle$ is used. Both discrepancies on the bootstrap current and those on the plasma resistance have a major impact on the physics-related features and on the integral plant parameters, such as $\tau_{burn} \sim \tau_{flat} \propto 1/(R_p I_p f_{ind}) \propto 1/(R_p I_p \cdot (1 - f_{BS} - f_{CD}))$.

5.2.3. Core power radiation and divertor physics configurations

This subsection is devoted to the results associated with the loading conditions on BB and divertor, subdividing the results by plasma facing components and type of heating source, according the devoted model outline addressed in Sections 3.3 and 4.1.2.

The FW and the divertor heat fluxes and loads attributed to the core plasma neutron and gamma radiation have been calculated according to the blanket FW and divertor shapes visualized in Figure 5.1 and the neutron and photon power densities q_{neut} and q_{rad}, derived from P_{neut} and P_{rad} reported in Table 5.13. The radiation power density q_{rad} is based on the density and temperature profiles and it does not account for local high impurity concentrations which takes place around the divertor private region to mitigate the highly localized peak heat fluxes. The volumetric source is based only on a distinction between core and mantle region, in which the impurity content is considered homogeneous. For this reason, the radiation peak fluxes have to be taken rather tentatively, especially in the divertor region.
A direct comparison with the baseline can be only conducted for a limited amount of parameters, as the average neutron and gamma wall loadings, where good agreement is found as shown in Table 5.16. For some others it was not possible to extract the necessary values, which are expressed as function of other surrogate ones, such as the total incident power to FW and divertor. In PROCESS the power extracted from divertor and FW is transported as the sum of P_{rad} and P_{sep} (with no sign of neutron power) which is entirely transferred to the blanket internal structures. This approach does

Parameter (Symbol)	Unit	MIRA $k = n/\gamma$	PROCESS $k = n/\gamma$	Deviation [%] $k = n/\gamma$
FW peak wall load ($\Gamma^{k,fw}_{\perp,\max}$)	[MW/m^2]	1.48/0.23		
Divertor peak wall load ($\Gamma^{k,div}_{\perp,\max}$)	[MW/m^2]	0.68/0.15		
FW average wall load ($\Gamma^{k,fw}_{\perp,av}$)	[MW/m^2]	1.05/0.19	1.05/0.215	0.0/-11.6
Divertor average wall load ($\Gamma^{k,div}_{\perp,av}$)	[MW/m^2]	0.331/0.074		
FW peaking factor ($\chi_{k,fw}$)	[-]	1.41/1.16		
Divertor peaking factor ($\chi_{k,div}$)	[-]	2.09/2.07		
FW incident power (P^k_{fw})	[MW]	1569/290		
Divertor incident power (P^k_{div})	[MW]	61/14		

Table 5.16.: Computed core neutron and gamma power radiation parameters of the EU-DEMO 2015 baseline.

not allow to reconstruct the power to blanket and divertor individually.
As for the technological limits the unique restraining condition is imposed on $\Gamma^{\gamma,fw}_{\perp,\max}$, found below its upper limit currently considered for DEMO, i.e. 1 MW/m^2 [73].

Compared to the traditional zero-dimensional system code approach, the radiation transport model allows for a detailed poloidal mapping of the incoming power among the plasma facing components and a precise evaluation of the peak heat fluxes. Systems codes rely on prescribed peaking factors $\chi_{k,j}$, combining the average to the peak heat fluxes (Equation 4.19). However, as both neutrons and gammas spread their kinetic energy rather uniformly across the vacuum chamber, the peaking factor can be predicted within rather narrow confidence intervals (see Figure 5.3). The two curves depict the distributions of plasma core neutron and photon wall loading functions across the poloidal angle α_w (Equations 4.17 and 4.18).

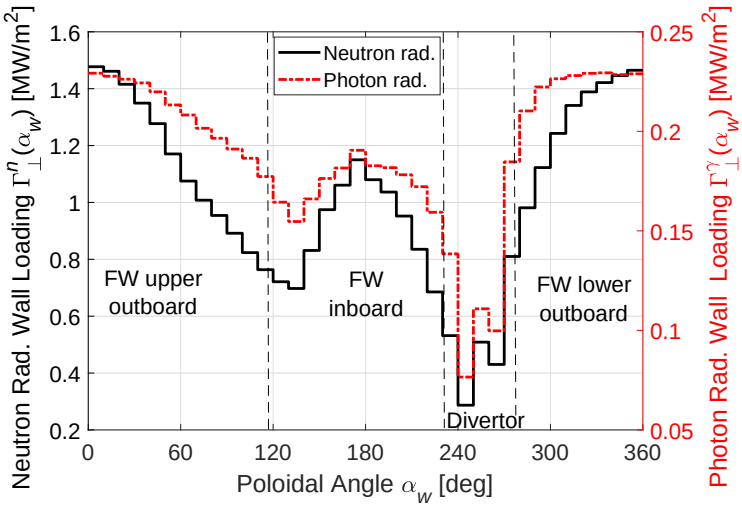

Figure 5.3.: Poloidal distribution of neutron and gamma radiation wall loadings of the EU-DEMO 2015 baseline, as per MIRA simulation.

Similarly, the total incoming power repartition between the first wall and the divertor is evaluated by means of input coefficients, splitting the neutron and the gamma power impinging on the two

systems. In this case, this power distribution depends on the shape of both components and their plasma surrounding features, which vary according to the FW and divertor design layouts. One of the advantages of MIRA is the parametrization of the divertor and the blanket poloidal profiles. Accordingly, the input specification of power core neutron and gamma radiation power distribution between BB and divertor is avoided, improving the mapping of the power flow across the reactor and plant systems.

The PROCESS divertor peak heat flux model contains features which are not integrated yet in MIRA, such as effective charge, density and temperature in the private region. As the SOL/divertor physics model (Section 3.3) is oriented to an estimation of the peak heat flux on divertor targets, it represents the ultimate figure of merit to analyse and compare. All results related to this modelling part are listed in Table 5.17.

Parameter (Symbol)	Unit	MIRA	PROCESS	Deviation [%]	Limit
Divertor area (A_{div})	[m^2]	175.6	185.2	-5.2	
Power decay length (λ_q)	[mm]	1.08			
Integral power decay length (λ_{int})	[mm]	8.5			
Flux tube expansion ($f_{x,i/o}$)	[-]	5.64/4.20			
B_p/B_t at strike point ($(B_p/B_t)_{i/o}$)	[-]	0.032/0.083	0.072	-55.6/+15.3	
IB/OB peak heat flux ($\Gamma_{\perp,\max}^{tot,div}$)	[MW/m^2]	6.33/7.33	6.52	-2.9/+12.4	$\leq$ 10.0 (TL)

Table 5.17.: Calculated SOL and divertor physics parameters of the EU-DEMO 2015 baseline: comparison between MIRA and PROCESS results. (TL) denotes a technological limit.

The inboard and outboard ratios of poloidal to toroidal field B_p/B_t at strike point, which indirectly appear in the definition of the expansion factor of the magnetic flux tube $f_{x,i/o}$ (Equation 3.75), show similar results of MIRA and PROCESS. The main reason for this comparison has been to verify that the magnetic properties are congruent, which could be confirmed. A direct juxtaposition of $f_{x,i/o}$ between MIRA and PROCESS is not feasible, as the ratio could not be retrieved from the PROCESS output, as well as λ_{int} and λ_q. The reasons can be attributed to the different modelling approaches, for which no available sourcing information have been found in literature. In terms of peak divertor heat flux MIRA and PROCESS exhibit similar values, both below the 10 MW/m^2 design limit.
Large uncertainties affect its assessment, in particular on the radiative dissipative power fraction power f_{rad} and on the power spreading factor S, which are both inputs.
In view of future improvements, efforts on divertor physics modelling improvement might tentatively compensate such lacks of substantiated information. However, considerable enlightenment can be only achieved after ITER operation. Compared to presently available system codes, some marginal advances have been achieved from the full reactor magnetic configuration, precisely in calculating $f_{x,i}$ and $f_{x,o}$ with modest accuracy.

5.2.4. Reactor neutronics configuration

The computed neutronic features from the core transport model (Section 4.1.3) are reported in Table 5.18 for HCPB and the WCLL BB designs. The deviations have not been reported because in the DEMO 2015 baseline output of the PROCESS code there is no evident mentioning of a blanket layout.The evaluated integral figures have been found in good agreement both with the PROCESS baseline (when applicable) and with detailed Monte Carlo analyses.
In case of HCPB blanket the reference design value of the TBR is 1.207 [34], while the NH powers in

Parameter (Symbol)	Unit	MIRA HCPB	MIRA WCLL	PROCESS	Limit
Required TBR (TBR_r)	[-]	1.20	1.14		$\geq$ 1.1 (DT)
BB EMF (EMF_{BB})	[-]	1.29	1.16	1.18	
BB NH power (R^{BB}_{heat})	[MW]	2026	1814	1826	
VV NH power (R^{VV}_{heat})	[MW]	48.1	6.9	4.1	
Divertor NH power (R^{div}_{heat})	[MW]	91.5	91.5	n.a.	
Peak WP fast neutron flux ($\Phi^{wp}_{fast,peak}$)	[n/cm^2/s]	2.85×10^8	2.15×10^7	2.24×10^8	$\leq 10^9$ (TL)
Peak WP nuclear heating ($\mathcal{R}^{wp}_{heat,peak}$)	[W/m^3]	32.2	3.8	20.6	$\leq$ 50 (TL)
Peak FW dpa rate ($\mathcal{R}^{fw}_{dpa,peak}$)	[dpa/fpy]	10.6	10.4	10.5	$\leq$ 10 (TL)
Peak VV dpa rate ($\mathcal{R}^{vv}_{dpa,peak}$)	[dpa/fpy]	0.17	0.021		$\leq$ 0.34 (OL)

Table 5.18.: Computed core reactor neutronics parameters of the EU-DEMO 2015 baseline: comparison between MIRA and PROCESS results.

the BB, VV and divertor are around 2031 MW, 46 MW and 112 MW, respectively [131]. In WCLL the calculated TBR and the deposited BB nuclear heating power are equal to 1.127 and 1807 MW, respectively [35], while the power deposited to the divertor components is near 92 MW [197].
The HCPB design solution features better energy multiplications compared to WCLL, due to the larger neutron multiplications in beryllium pebble beds and hence better T breeding performance. In terms of shielding, instead, the hierarchies between the two BBs are inverted, with the WCLL blanket yielding flux densities that are nearly one order of magnitude lower. Both BBs have been found capable of meeting the imposed fast neutron flux density shielding criteria limit and also that on the admissible volumetric heating $\mathcal{R}^{wp}_{heat,peak}$.
The results on atom displacement rates in the BB and VV structural materials cover the peak displacement rates in FW Eurofer steel and in the VV steel material. Concerning the FW, both HCPB and WCLL feature very similar values, though slightly above their lower technological bound. Because of the different shielding capabilities in the BB region, the material damage in the VV $\mathcal{R}^{vv}_{dpa,peak}$ exhibits higher values for the HCPB compared to the WCLL BB by one order of magnitude.

Only a limited amount of parameters could be directly correlated to the baseline, due to PROCESS neutronic modelling limitations (compared to MIRA). Since PROCESS does not refer to a design solution where the materials and thermal-hydraulic features are aligned to BB designs, a cross referencing of the parameters is challenging. In PROCESS R^{BB}_{heat} bases on an input EMF for the BB and lays in rather narrow deviations when compared to the MIRA WCLL case.

A graphical illustration of the neutron flux density indicating the diverse neutron and gamma radiation shielding responses as a function of the radial distance from the inboard FW is visualized in Figure 5.4 for HCPB and WCLL blankets. The origin is set on the inboard FW, such that $\Delta r_{ib,fw} = r^{fw}_{1,i} - r$. In the inboard region the available space is limited compared to that in the outboard and, therefore, it is considered more critical for shielding performances. Both curves exhibit that the allowable maximum fast neutron flux density on the TF coil winding pack $\Phi^{wp}_{fast,\max}$ set to 10^9 [n/cm^2/s] is not exceeded.
Starting from the peak flux density in the FW armour, each subregion provides a different damping, derived from the different material compositions. The more pronounced flux attenuation in the WCLL BB solution is mostly attributed to wider neutron moderation capacities of water compared

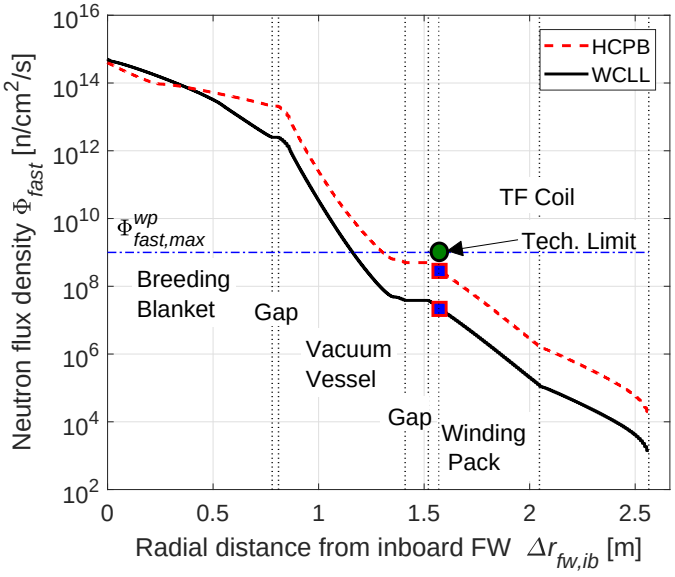

Figure 5.4.: Calculated fast neutron flux density Φ_{fast} vs reverse inboard radial coordinate $\Delta r_{fw,ib}$ for the HCPB and WCLL blanket designs (EU-DEMO 2015 baseline).

to the helium coolant and to the better neutron scattering in Pb than Be.

The major improvements of the neutronic module implemented in MIRA can be underlined by the flexibility in the definition of the radial composition and of the material mixture of the components which allows to analyse TBR and shielding simultaneously, being not feasible in PROCESS.

5.2.5. Plasma scenario and PF/CS coils configuration

The analysed plasma scenario involves the static equilibrium states at plasma breakdown (BD), start of flat-top (SOF) and the end of the flat top (EOF). Depending on the operational phase a proper combination of PF/CS coil currents has been found, according to integrated nonlinear PF/CS coil solver (Section 4.2.2). The numerical results are listed in Table 5.19.
A verification of the MIRA scenario modeling has been addressed in [88] by means of code-to-code comparison with the DEMO 2015 baseline results as per CREATE equilibrium solver [160]. The results have showed a very good agreement on all the calculated parameters, where all deviations are below 7 %. Here a verification against CREATE results is not feasible because the analyses have been conducted with a different internal inductance ($l_i = 0.8$ instead of 1.155 from PROCESS) and lower current density and peak magnetic field limits, fixed for all coils to 12.5 MA/m^2 and 12.5 T. At plasma BD, the reference poloidal flux Ψ_{bd} has been maximized keeping the stray field in the breakdown area B_{stray} below the upper limit $B^{\max}_{stray}$ (fixed to 3 mT) and fulfilling the technological and operational limits of the PF/CS coil systems. The calculated peak stray magnetic field B^{peak}_{stray} within this area has been found below the imposed upper limit.

At plasma flat-top the geometric features are given by the separatrix geometric parameters, including triangularity, elongation, volume, radial and poloidal locations of the plasma bottom X-point $(r_{X,l}, z_{X,l})$, of the magnetic axis (R_{ax}, Z_{ax}) and their respective poloidal magnetic fluxes, Ψ_{ax} and Ψ_b. Both at SOF and EOF these should be maintained as steady as possible to ensure almost constant

Description	Symbol	Unit	BD	SOF	EOF	Limit
Poloidal flux at breakdown	Ψ_{bd}	[Wb]	333.7			
Peak stray field in the BD region	B_{stray}^{peak}	[mT]	2.98			$\leq$ 3 (OL)
Plasma bottom X-point / $r-$coord.	$r_{X,l}$	[m]		7.62	7.62	$\approx$ 7.62 (DT)
Plasma bottom X-point / $z-$coord.	$z_{X,l}$	[m]		-5.52	-5.52	$\approx$ -5.52 (DT)
Plasma magnetic axis / $r-$coord.	R_{ax}	[m]		9.42	9.41	
Plasma magnetic axis / $z-$coord.	Z_{ax}	[m]		0.16	0.17	
Poloidal flux at magnetic axis	Ψ_{ax}	[Wb]		343.9	84.2	
Poloidal flux at plasma boundary	Ψ_{b}	[Wb]		142.2	-115.9	
Triangularity at plasma X-point	δ_X	[-]		0.46	0.45	$\approx$ 0.5 (DT)
Triangularity at 95 flux surface	δ_{95}	[-]		0.29	0.28	
Elongation at plasma X-point	κ_X	[-]		1.78	1.78	$\approx$ 1.78 (DT)
Elongation at 95 flux surface	κ_{95}	[-]		1.58	1.58	
Plasma volume	V_p	[m^3]		2494.8	2496.6	$\approx$ 2458.4 (DT)

Table 5.19.: Computed plasma breakdown and flat-top configurations of the EU-DEMO 2015 baseline . The major variables are reported for the plasma breakdown (BD), start of flat-top (SOF) and end of flat-top (EOF).

plasma performances. The numerical results indicate that this is achieved with minor oscillations for κ and V_p, yielding marginal deviations between SOF and EOF and very close match with the respective design target. The same response has been identified for all other magnetic configuration features, including (R_{ax}, Z_{ax}) and the poloidal flux difference $\Psi_{ax} - \Psi_b$, constantly around 200 Wb in both plasma snapshots.

The plasma triangularity has been found lower than the imposed DT value, approximately by 10%. δ_X has been proven to be a challenging parameter to control with accurate precision, compared to κ_X and V_p. Several reasons play a role in such a pronounced divergence, including reduced shaping capabilities of the coils, possibly tied the large l_i target and to the geometric parametrization used for the target separatrix profile. This cannot be indiscriminately used for any arbitrary values of κ_X and δ_X. As a result, certain limits are observed on the maximum elongation and triangularity that can be achieved for a given set of PF/CS coils, namely as a function of the aspect ratio A, but also of l_i [10, 99]. Accordingly, there is a maximum achievable value for both, above which the PF coils cannot cope with.

Important considerations have been addressed on the poloidal flux on the plasma separatrix at EOF $\Psi_{b,eof}$ to be brought down for maximizing the flat-top pulse length τ_{flat}. With regard to the listed value, the PF/CS current solver has stopped the forced diminishing of $\Psi_{b,eof}$ at around -120 Wb, where the residual error $\mathcal{L}$ on the target separatrix (Equation 4.89) has diverged and endured into a substantial overstepping of the imposed marginal changes on δ_X, κ_X and V_p from those calculated at SOF.

The magnetic configurations calculated at plasma breakdown and both SOF and EOF snapshots are depicted in Figure 5.5$-$a and b. In subfigure (a) the solid lines have been extracted for equally spaced values of poloidal flux $\Psi(r,z)$ between Ψ_{bd} and $\Psi_{bd} - 0.5$ Wb to emphasize the large area covered by rather flat distribution of Ψ. The dashed and the circle marked contours depict the magnetic field line contour at $B_{stray}^{\max}$ and the boundary $\partial\mathcal{D}_{bd}$ of the selected breakdown area. The former curve embraces the latter, meaning that the constraining condition on $B \leq B_{stray}^{\max}$ within $\mathcal{D}_{bd}$ has

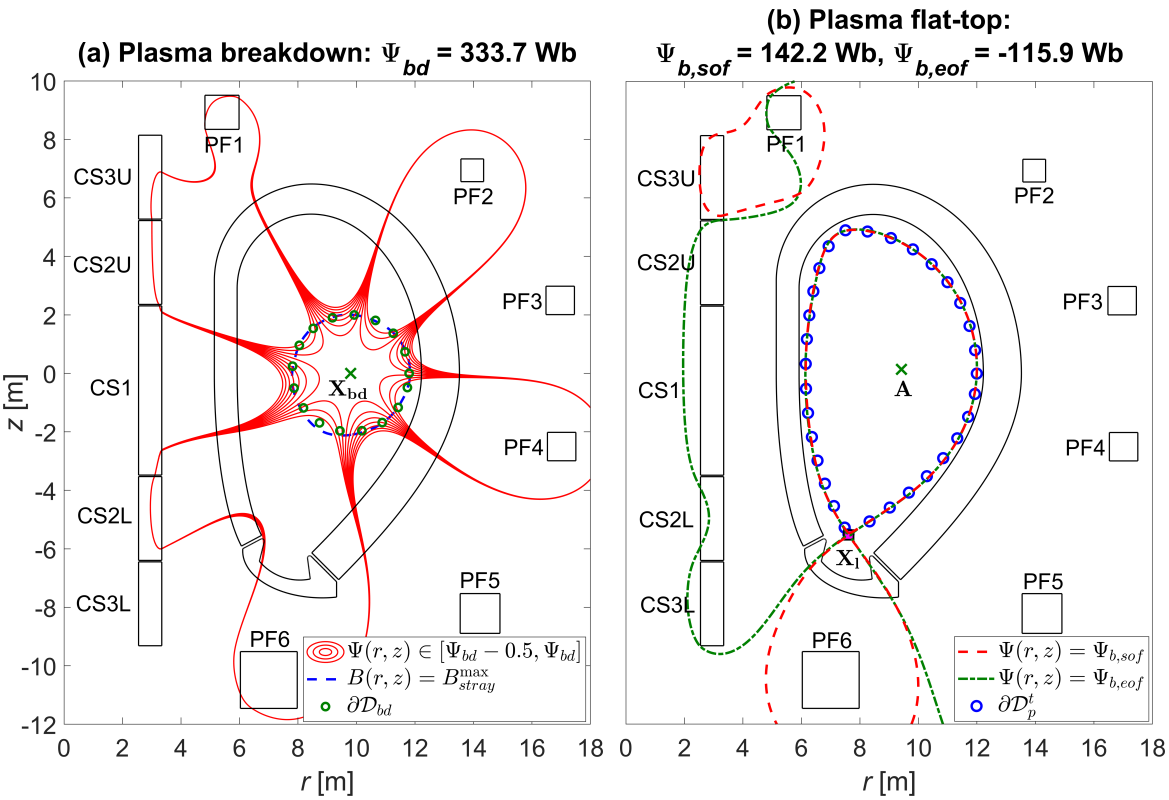

Figure 5.5.: Calculated spatial magnetic configurations of the EU-DEMO 2015 baseline at plasma breakdown (a) and at plasma equilibrium during the flat-top (b). Both plots spans on the same $z-$axis, appearing in Subfigure (a).

been successfully met. Subfigure (b) illustrates the contour lines characterizing the flux surfaces at $\Psi = \Psi_{b,sof}$ and $\Psi = \Psi_{b,eof}$, identified by the dashed and the dash-dot lines. Both profiles are put in relation to the target LCMS shape, driven by the shape parametrization introduced in Section 2.3.1 and displayed with circle markers.
Within the plasma separatrix domain either SOF and EOF curves are genuinely overlapped, confirming the narrow deviations of the geometric features between the two flat-top snapshots listed in Table 5.19. Very small differences are detected across the whole plasma boundary, with poloidal distances from $\partial\mathcal{D}_p^t$ everywhere below 10 cm, in particular on the innermost, outermost and topmost regions of the plasma shape, where a minimum SOL thickness should be guaranteed.
All points taken on the Ψ_b flux contour have been certified to observe the minimum distance from the BB FW, consisting of the SOL widths Δ_{SOL} listed in Table 5.3.

The PF/CS coil current I_c, peak field B_{peak} and vertical force F_z configurations obtained for the analysed cycle time frames are reported in Table 5.20. Each variable, reported for all coils, is related to the imposed operational and technological limits, outlined in Equations (4.83) and (4.84). The coil currents and the peak field features approach their maximum admissible values at breakdown and EOF, since those correspond to the most demanding poloidal flux situations. The current limits are driven by superconducting cable engineering aspects.

The exploitation of the full range of currents for the CS stack coils does not take place in any of the analysed static cases, due to multiple reasons. At plasma BD, the current in central element CS1 and the peak field on coils CS3U and CS2L saturate and the PF/CS coils currents cannot longer

Parameter	Symbol	Unit	BD	SOF	EOF	Limit
Total current in CS3U	$I_{c,CS3U}$	[MA]	+35.18	+27.23	+9.65	±37.73 (TL)
Total current in CS2U	$I_{c,CS2U}$	[MA]	+31.78	-0.39	-27.11	±37.73 (TL)
Total current in CS1	$I_{c,CS1}$	[MA]	**+55.16**	-12.50	**-55.25**	±55.25 (TL)
Total current in CS2L	$I_{c,CS2L}$	[MA]	+34.50	+21.04	-2.91	±37.73 (TL)
Total current in CS3L	$I_{c,CS3L}$	[MA]	+26.79	-7.30	**-36.24**	±37.73 (TL)
Total current in PF1	$I_{c,PF1}$	[MA]	+11.59	+6.61	-6.29	±13.77 (TL)
Total current in PF2	$I_{c,PF2}$	[MA]	+2.98	-2.12	-4.09	±6.12 (TL)
Total current in PF3	$I_{c,PF3}$	[MA]	-0.46	-6.62	-6.41	±7.77 (TL)
Total current in PF4	$I_{c,PF4}$	[MA]	+1.65	-5.81	-6.65	±7.76 (TL)
Total current in PF5	$I_{c,PF5}$	[MA]	+0.23	-7.01	-8.24	±10.81 (TL)
Total current in PF6	$I_{c,PF6}$	[MA]	+13.55	**+19.73**	+12.28	±19.76 (TL)
Peak magnetic field in CS3U	$B_{peak,CS3U}$	[T]	**13.70**	8.45	7.30	$\leq$ 13.70 (TL)
Peak magnetic field in CS2U	$B_{peak,CS2U}$	[T]	**13.32**	6.28	9.44	$\leq$ 13.70 (TL)
Peak magnetic field in CS1	$B_{peak,CS1}$	[T]	12.54	5.19	9.93	$\leq$ 13.70 (TL)
Peak magnetic field in CS2L	$B_{peak,CS2L}$	[T]	13.70	6.28	7.58	$\leq$ 13.70 (TL)
Peak magnetic field in CS3L	$B_{peak,CS3L}$	[T]	12.11	5.19	10.31	$\leq$ 13.70 (TL)
Peak magnetic field in PF1	$B_{peak,PF1}$	[T]	5.25	2.71	2.90	$\leq$ 5.67 (TL)
Peak magnetic field in PF2	$B_{peak,PF2}$	[T]	1.45	1.44	2.32	$\leq$ 5.67 (TL)
Peak magnetic field in PF3	$B_{peak,PF3}$	[T]	0.23	2.84	2.71	$\leq$ 5.67 (TL)
Peak magnetic field in PF4	$B_{peak,PF4}$	[T]	0.61	2.53	2.79	$\leq$ 5.67 (TL)
Peak magnetic field in PF5	$B_{peak,PF5}$	[T]	0.20	2.40	2.70	$\leq$ 5.67 (TL)
Peak magnetic field in PF6	$B_{peak,PF6}$	[T]	3.62	4.41	2.76	$\leq$ 5.67 (TL)
Vertical force in PF1	$F_{z,PF1}$	[MN]	**-443.8**	-130.9	-30.05	±450 (OL)
Vertical force in PF2	$F_{z,PF2}$	[MN]	-31.2	-16.2	-62.93	±450 (OL)
Vertical force in PF3	$F_{z,PF3}$	[MN]	+1.3	-95.0	-103.9	±450 (OL)
Vertical force in PF4	$F_{z,PF4}$	[MN]	+2.5	+43.9	+48.6	±450 (OL)
Vertical force in PF5	$F_{z,PF5}$	[MN]	+2.4	+81.4	+164.9	±450 (OL)
Vertical force in PF6	$F_{z,PF6}$	[MN]	+345.9	+76.2	-218.6	±450 (OL)
Max up separation force in CS	$F_{z,CS}^{sep,up}$	[MN]	127.8	+184.9	+279.9	$\leq$ 350 (OL)
Max down separation force in CS	$F_{z,CS}^{sep,dw}$	[MN]	127.8	-144.9	-79.0	$\geq$ 350 (OL)
Total vertical force in CS	$F_{z,CS}^{tot}$	[MN]	127.8	+40.0	+200.9	$\leq$ 300 (OL)

Table 5.20.: Evaluated Breakdown, SOF and EOF PF/CS coils current, peak field and vertical forces configurations of the EU-DEMO 2015 baseline. Values in bold font weight denote the configurations where the technological limits are reached or close to be reached.

increase to bring up the poloidal flux at $\mathbf{X_{bd}}$ and simultaneously satisfy the stray field criteria. At the EOF two coils approach their current operational ceiling value (CS1 and CS3L), while maintaining broadly sound margins in terms of peak fields. In this case the worse performances of the CS in making use of the fully available current swing are mostly driven by a large value of l_i, compared to DEMO reference values (~ 0.8) [160].
A substantial amplitude of l_i yields a peaked plasma current density $J_{p,\phi}$, which can be associated with a filamentary current. In relation to a triangulated and elongated plasma shape, however, this situation is less favourable than a condition where the plasma current density spreads across the confining region and follows the reference LCMS profile. Accordingly, in the vicinity of the periphery,

the flux and field contributions to the shaping tasks from the plasma are more effective for broad than peaked distributions of $J_{p,\phi}$. As a result, a reduction of l_i allows for better plasma separatrix modelling performances and a consequential reduction of $\Psi_{b,eof}$.
Therefore, the analysis provides indications that the baseline is not optimal in terms of l_i. l_i has large implications across several key reactor and it is marginally included in presently available systems codes, highlighting the importance of its inclusion in plasma equilibrium modelling.

The vertical Lorentz force criteria are not exceed for both PF and CS coils systems. As for the PF coils, the most demanding conditions are observed for the coils PF1 and PF6 at the plasma breakdown, where, due to the large operating currents, compared to remaining four coils, they experience rather large attractive forces, respectively pulling them down and up.
The divertor coil PF6 experiences always demanding features, especially during the flat-top, since it provides the null-field at the bottom X-point.
Safe margins have been also achieved for the separation and the total vertical force on the CS, as expected from their fairly considerable separating gap between the operating CS currents and peak fields and their upper bounds.

The plasma scenario results presented in this subsection are intended to illustrate the levels of details with respect to the physics and technology in tokamak magnetic equilibrium, being by now not accessible in system codes. A direct comparison with the PROCESS DEMO baseline could therefore not be entirely established, because:

- PROCESS considers a system of six PF coils and one unique CS element, instead of five elements. From ITER scenario studies [80], it was demonstrated that a multi-element CS is vital for plasma shaping and control performances. As a result, it must hold for DEMO, too.
- PROCESS does not account for any shaping criteria when finding the coil currents configuration, but purely limited to achieving a vertical equilibrium field $B_V(I_p, R_0, a, \beta_p, l_i)$ [17], applicable to large aspect ratio plasma equilibria [83], on a finite number of points at the plasma mid-plane.
- The radial and vertical locations of the PF coils in PROCESS are not adjusted in relation to their distance from the TF coils, as shown also in the sketch of Figure 1.2. As a result, some of them is located quite far from the TF coils, which, apart from being rather unrealistic, represents a different coils layout from that assumed for this case study.

If the scenario analysis is compared to the reference SOF and EOF CREATE equilibria, several similarities can be found.

The reference PF/CS coils cable operating parameters derived from the global current and field coils operating conditions evaluated in the scenario analysis are listed in Table 5.21. The results include selected demanding values among breakdown, SOF and EOF for operating current I_{op}, dump voltage V_{dump} and temperature margin ΔT_{cs}. Additionally, the maximum admissible operating current $I_{op}^{\max}$, the number of turn N_{turn}, the self-inductance L_c and the stored energy E_c are provided. Analysing the numerical values and combining them to the cable design limits listed in Table 5.9 all conductor design criteria are found fully met for all pulse operational phases. The operating current I_{op} is always below or equal to $I_{op}^{\max}$, $V_{dump} \leq V_{dump}^{\max}$ and $\Delta T_{cs} \geq \Delta T_{cs}^{\min}$.
Despite of the same cable technology, the coil CS1 have exhibited lower amplitudes of $I_{op}^{\max}$ compared to the other CS elements. Predominant effects related to the larger L_c impose an upper limit on $I_{op}^{\max}$ (Equation 4.130) tied to the quench protection criterion and not to the critical current I_c, yielding $I_{op}^{\max} \propto 1/L_c^{1/3}$. L_c scales quadratically with the number of turns N_{turn} (Equation 4.61). As

	I_{op} [kA]	I_{op}^{max} [kA]	V_{dump} [kV]	V_{dump}^{max} [kV]	ΔT_{cs} [K]	ΔT_{cs}^{min} [K]	N_{turn}[-]	L_c [H]	E_c [GJ]
CS3U	58.84	63.10	7.76	10.0	1.65	1.5	598	1.86	3.21
CS2U	53.14	63.10	5.71	10.0	2.15	1.5	598	1.85	2.62
CS1	**45.70**	45.71	9.99	10.0	2.97	1.5	1209	5.10	5.33
CS2L	57.70	63.10	7.31	10.0	1.69	1.5	598	1.86	3.09
CS3L	60.60	63.10	8.47	10.0	3.29	1.5	598	1.86	3.41
PF1	35.76	42.48	2.65	5.5	1.77	1.5	324	1.73	1.10
PF2	28.42	42.48	1.05	5.5	3.16	1.5	144	1.36	0.55
PF3	29.40	34.52	3.40	5.5	2.92	1.5	225	3.98	1.72
PF4	29.57	34.48	3.47	5.5	2.95	1.5	225	4.00	1.75
PF5	18.69	24.51	2.44	5.5	3.07	1.5	441	11.13	1.95
PF6	**21.92**	21.95	5.48	5.5	2.69	1.5	900	15.51	3.72

Table 5.21.: Evaluated reference superconducting cable engineering features of the PF/CS coil conductor, calculated for the EU-DEMO 2015 baseline. For I_{op} and V_{dump} the peak values have been selected among breakdown, SOF and EOF. Analogously, for ΔT_{cs} the smallest one is indicated.

a result, a larger number of windings (in CS1 nearly twice as the other ones) enhances the capabilities to store magnetic energy, though more challenging to dump in case of quench. Splitting the coil CS1 in two separate coil circuits is an option to circumvent this issue. It offers also the possibility to operate with larger poloidal fluxes across all pulse phases.

5.2.6. TF Coil output configuration parameters

Here the operating features and the design parameters associated with the TF coils system are addressed. The simulation results associated with the current, field, force, energy TF coils operating conditions are reported in Table 5.22.
An important deviation from the baseline pertains to the toroidal magnetic field at plasma center B_t, which has faced a reduction from 5.667 to 5.493 T to meet the technological constraining condition on the peak magnetic field at the TF coil conductor $B_{peak,TFC}$. In PROCESS the peak field at TF coil conductor is tied to B_t by means of the $B_\phi \propto 1/r$ dependency (Equation 3.17). Furthermore, a correction factor derived from Biot-Savart law [17] is additionally applied to account for the toroidal field ripple effects near the inboard leg. This formulation does not account for the small contribution of the PF coils (approximately 0.1 T) and of the TF coil shape, making it not entirely applicable to depict such ripple implications. Relying on the 3D magnetostatic analysis, including both TF and PF coils systems, it has been observed that adopting B_t from the baseline would yield $B_{peak,TFC} =$ 12.73 T, that is larger than the 12.44 T limit and even broader than that estimated by PROCESS, i.e 12.32 T.
In order not exceed this upper bound, a 3 % lower amplitude of B_t has been imposed, leading to value of $B_{peak,TFC}$ very close to PROCESS's. This situation denotes an exemplary case of alterations of a key design parameter (in this case the toroidal field) driven by more refined design-oriented analyses. As a consequence, it points out the importance of a thorough and robust check before moving to the detailed design activities of the TF coil system.

Considering the rather simplified modelling approach adopted in PROCESS, the $\sim$10 % deviation observed for L_c is most likely modelling-related. Accordingly, the $B_\phi \propto 1/r$ law is used in PROCESS to calculate the toroidal flux through the TF coil inner vacuum area per unitary current,

Parameter (Symbol)	Unit	MIRA	PROCESS	Deviation [%]	Limit
Toroidal field at plasma centrer (B_t)	[T]	5.49	5.67	-3.2	
Peak magnetic field at TFC ($B_{peak,TFC}$)	[T]	12.36	12.32	+0.3	$\leq$ 12.44 (TL)
TF coil current ($I_{c,TFC}$)	[MA]	13.84	14.28	-3.1	
TF coil turn current ($I_{op,TFC}$)	[kA]	70.61	65.00	+8.6	$\leq$ 70.8 (TL)
Number of turns ($N_{turn,TFC}$)	[-]	196	220	-10.9	
Inner WP radial thickness ($\delta r_{wp,I}$)	[cm]	25.7	23.5	+9.4	
Inner WP toroidal thickness ($\delta y_{wp,I}$)	[cm]	115.1	132.6	-13.2	
Outer WP radial thickness ($\delta r_{wp,O}$)	[cm]	22.1	23.5	-6.0	
Outer WP toroidal thickness ($\delta y_{wp,O}$)	[cm]	100.7	124.3	-19.0	
Max toroidal field ripple ($\delta_{tf,\max}$)	[%]	0.678	0.600	+13.0	$\leq$ 0.6 (OL)
TF coil self-inductance ($L_{c,TFC}$)	[H]	3.16	3.57	-11.5	
TF coil stored magnetic energy ($E_{c,TFC}$)	[GJ]	7.89	7.54	+4.6	
Dump voltage (V_{dump})	[kV]	9.08	7.73	+17.5	$\leq$ 10 (OL)
Current sharing T margin (ΔT_{cs})	[K]	1.78	2.68	-33.6	$\geq$ 1.5 (TL)
Total centering force ($F_{x,TFC}$)	[MN]	-762.7			
Vertical separation force ($F_{v,TFC}$)	[MN]	480.6	502.8	-4.4	
Bending out-of-plane force/BD ($F^{bd}_{b,TFC}$)	[MN]	5.83			
Bending out-of-plane force/SOF ($F^{sof}_{b,TFC}$)	[MN]	21.26			
Bending out-of-plane force/EOF ($F^{eof}_{b,TFC}$)	[MN]	23.64			

Table 5.22.: Calculated TF coil magnetic electromagnetic and engineering parameters of the EU-DEMO 2015 baseline: comparison between MIRA and PROCESS results.

precisely the self-inductance L_c. This B_ϕ expression is integrated over the radial and vertical domain enclosed by the TF coil. As a result, the toroidal opening of the coils is neglected, bringing to an overestimation of linked toroidal flux, hence of L_c. A reliable estimation of L_c is relevant for calculating the stored energy E_c and to assess all the aspects tied to it.

Although both total current I_c and self-inductance L_c are significantly lower, the stored magnetic energy E_c has been proven larger than the PROCESS's. This result is related to the larger turn current $I_{op,TFC}$, since $E_c \propto I^2_{op}$.
The ITER-like TF coil cable has been taken in PROCESS as a reference design, thereby fixing the operating current to its nominal value. Nevertheless, even if more conservative, this modus operandi excludes the exploitation of the cable engineering design improvements recently achieved for DEMO.
In the specific analysed DEMO baseline, this escalated into a more effective use the available superconducting cable technology, as demonstrated by the computed amplitudes of inner and outer WP's radial and toroidal thicknesses δr_{wp} and δy_{wp} and by the number of turns N_{turn}. For a total current I_c just 4 % below the baseline's (due to the lower B_t), N_{turn} has decreased by approximately 11 %. An even more pronounced feedback is observed for the WP toroidal widths $\delta y_{wp,I}$ and $\delta y_{wp,O}$, which are scaled down to 20 % in contrast to an almost identical radial width $\delta r_{wp} = \delta r_{wp,I} + \delta r_{wp,O}$.

Among the static integral Lorentz force terms, only the vertical separation force $F_{v,TFC}$ could be uniquely correlated to the DEMO baseline. The results show a 4.4 % reduction due to ideal toroidal solenoid modelling of Lorentz forces and to the lower total TF coil current $I_{c,TFC}$. In PROCESS, the Lorentz force per unit coil length f_L is calculated taking the $B_\phi \propto 1/r$ law and its arithmetical average value inside the conductor, assuming a linear decrease radially outwards from its peak value

to zero across the WP cross section. Accordingly, $f_L \propto I^2_{c,TFC}/r$ [18], which yields the vertical force on the upper part of the coil after integrating over the radial coordinate from the inboard to the outboard leg's radial coordinates and thereby leading to a logarithmic dependency on r. By approaching the problem in this manner, the actual radial, poloidal and toroidal geometric features of the coil are somewhat neglected, along with the local effects of the magnetic field in the vicinity of the inboard and the outboard leg on the mid-plane due to the TF ripple. These deviate from the $1/r$ assumption on B_ϕ and consequently the Lorentz vertical forces are undervalued, too.
The total radial and bending forces $F_{x,TFC}$ and $F_{b,TFC}$ have been also calculated. However, the limited direct modelling capabilities of existing systems codes prevent a comparison to the DEMO baseline. The centering force F_x depicts the largest contribution in amplitude and it mostly concerns the inboard region. The bending force $F_{b,TFC}$, more relevant at flat-top due to its plasma poloidal field contribution, exhibits much lower amplitudes and it affects mainly the outboard side of the coil.

The maximum TF ripple on the plasma separatrix $\delta_{tf,\max}$ has been found 13 % above its upper limit (0.6 %) The maximum TF ripple can be mapped along the plasma separatrix perimeter ℓ_p, as shown in Figure 5.6−a. The perimeter ℓ_p is illustrated in Figure 5.6−b, showing its counter-clockwise orientation in poloidal direction starting from the bottom X-point X.

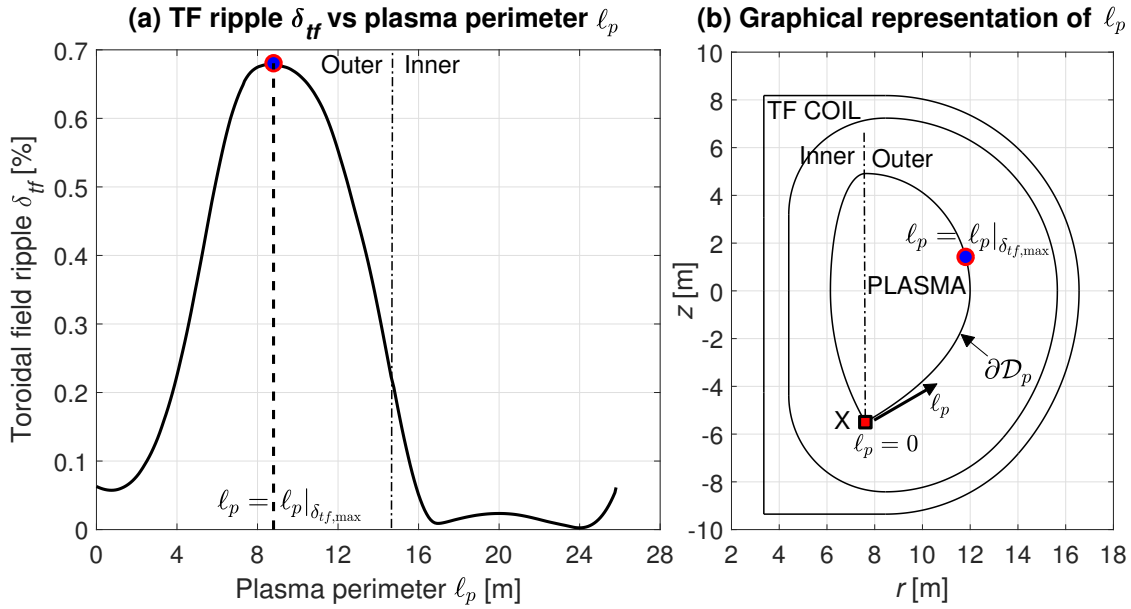

Figure 5.6.: TF ripple poloidal distribution calculated for the EU-DEMO 2015 baseline as per MIRA magnetostatic analysis. In Subfigure (a) δ_{tf} is plotted against the poloidal perimeter ℓ_p, graphically illustrated in Subfigure (b) along with the poloidal profiles of the plasma separatrix and of the TF coil.

Based on this formalism, the outboard branch of the plasma boundary precedes the inboard's. The poloidal location of $\delta_{tf,\max}$, marked at $\ell_p = \ell_p|_{\delta_{tf,\max}}$, is also graphically depicted with a circular mark in Figure 5.6−b and overlapped to the $\partial\mathcal{D}_p$ contour. The peak value is identified nearly above the mid-plane on the outer region of the plasma, since, around this area, the TF coils approach the plasma, by reducing the poloidal distance from it. Simultaneously, moving along ℓ_p the TF coils also tend to come closer among themselves, reducing the effects of the TF ripple. This alternating behaviour of distance of the coils from the plasma and tightness of the coils, that concurrently in-

crease and decrease moving along ℓ_p, is repeated on the inboard side, too. In this case, though, much lower amplitudes are obtained, due to the much higher compactness compared to the outboard's. As a result, the local maximum depicted on the inboard leg is around 0.023 %, i.e. nearly 30 times smaller than $\delta_{tf,\max}$.
The obtained TF ripple response finds qualitative confirmations also in detailed ripple calculations performed in Ref. [198] for older DEMO designs, operating with a higher aspect ratio.

Exceeding the imposed ripple design limit forces to take action to eliminate such a plasma requirement violation. A possible way consists of pushing outwards the TF coil outboard leg, which is equivalent to widening the outboard thicknesses of the gap between the VV and the TF coils $\Delta_{\mathrm{VV-TFC,o}}$. This operation has been performed within the scope of the parametric studies addressed in Chapter 6.

Such design-oriented operations normally are not entirely allowed according to the ripple extrapolation laws deployed in PROCESS, since these are restrained to only a few number of input parameters, including radial coordinate of the inboard and outboard legs, number of TF coils, WP width and thickness.

5.2.7. Reactor cycle output configuration

The DEMO operation is based on diverse time phases, defining a reactor cycle, as elucidated in Section 4.3.1. The computed values associated with the time scales involved in each pulse phase of the DEMO 2015 baseline are reported in Table 5.23. Compared to PROCESS, differences have been identified in the notation of some of the time scales definition, developed by a shifted beginning of the pulse. The pump-down time is referred in PROCESS to as "dwell time", while the dwell time, calculated by Equation (4.140), is denoted as "down time". Taking into account of these notational divergences, the involved numerical values have been adjusted.

Parameter (Symbol)	Unit	MIRA	PROCESS	Deviation [%]	Limit
Time to recharge the CS (τ_{RC})	[s]	363	30	+1110.0	
Pump-down time (τ_{PD})	[s]	1800	1800	0.0	$\geq$ 1200 (TL)
Time for CS recharge/pump-down ($\tau_{RC/PD}$)	[s]	1800			
Ramp-up time (τ_{RU})	[s]	157	30	+423.3	$\geq$ 131 (OL)
Heating time (τ_{heat})	[s]	19	10	+90.0	
Burn time (τ_{burn})	[s]	4768	7200	-33.8	$\geq$ 7200 (DT)
Time for burn termination (τ_{BT})	[s]	123			
Flat-top time (τ_{flat})	[s]	4909	7230	-32.1	
Ramp-down time (τ_{RD})	[s]	157	30	+423.3	$\geq$ 131 (OL)
Dwell time (τ_{dwell})	[s]	2256	1890	+19.4	
Total cycle duration (τ_{cycle})	[s]	7024	9103	-22.8	

Table 5.23.: List of computed parameters describing the reactor cycle of the DEMO 2015 baseline, according to the MIRA pulse temporal description model: the results are compared to those calculated by PROCESS.

In long-pulse DEMO devices, a reliable estimation of the burn time is important to establish the fulfilment of the high level requirement imposed on τ_{burn}, expected to be larger than or equal to two hours. As it turns out, this requirement has been proven to be far from being achieved, with a

calculated $\tau_{burn} \approx 80$ min found lower by nearly 33 % than that yielded by PROCESS. The same result is observed in the flat-top duration τ_{flat}, too. This discrepancy is related to plasma scenario-oriented aspects.

The currently available fusion systems codes, including PROCESS, prescribe the total available flux swing as a joint contribution of the CS and of the PF coils, calculated as follows. The total available flux from the central solenoid, Ψ_{CS}, is assumed to scale with the maximum admissible field $B_{\max}$ (depending on superconducting material limitations) and with the radial extension r_{CS}, such that $\Psi_{CS} \approx 2\pi r_{CS}^2 B_{\max}$. A multiplying factor two is applied supposing that the available flux swing spans from the negative and the positive value of the poloidal flux. Hence, it is purely restrained to geometric and peak field features. The share of poloidal flux of the PF coils Ψ_{PF}, instead, is assumed to be linked to the vertical equilibrium B_V and to the major radius R_0, such that $\Psi_{PF} \propto B_V R_0^2$. The sum of inductive and resistive dissipative fluxes, Ψ_{ind} and Ψ_{res}, is available for the flat-top $\Delta\Psi_{flat}$, given by $\Delta\Psi_{flat} = \Psi_{CS} + \Psi_{PF} - \Psi_{ind} - \Psi_{res}$. Even if fairly idealized and far too simplified, this methodology is based on poloidal flux conservation over a reactor cycle and generally applicable for pulsed system fusion applications. The questionable assumption, however, might be tied to the twofold counting of CS available flux in the definition of Ψ_{CS}. Implicitly, it is equivalent to assume that Ψ_{CS} is ramped down to $-\Psi_{bd}$ at EOF disregarding the limitations due to current, field and forces constraints and the strict plasma shaping requirements. The numerical values of Ψ_{bd}, $\Psi_{b,sof}$ and $\Psi_{b,eof}$ listed in Table 5.19 present a much diverse picture of the real situation, with a poloidal flux at EOF $\Psi_{b,eof}$ nearly 1/3 of Ψ_{bd} (in modulus). Essentially, this is the main cause to such large discrepancies on τ_{flat} and, therefore, on τ_{burn}.

The divergence on τ_{flat} compared to the baseline depicts a situation where a considerable refinement of the physics and mathematical sophistication involved in the systems modelling impact in a significant manner on a major plant performance requirement. Therefore, countermeasures must be taken to increase τ_{flat}, either increasing $\Delta\Psi_{flat}$ or/and decreasing the plasma loop voltage U_{loop}. The most effective technique acting in both directions is the reduction of the internal inductance l_i, as illustrated by a parametric investigation in Chapter 6.
Other cycle time variables reported in Table 5.23 exhibit considerable disparities between MIRA and PROCESS. Those include the ramp-up and ramp-down time τ_{RU} and τ_{RD}, the CS recharge time τ_{RC} and the heating time τ_{heat}. These are all input parameters in PROCESS and, therefore, cannot be attributed to any modelling heterogeneity. The amplitude of τ_{RC}, however, has been recently re-evaluated to 500 s by authors from the PROCESS team [179], compatibly to reasonable electric power consumptions, and thus of the same order as calculated by MIRA. The same holds for ramp-up and ramp-down time scales, both 194 s, in line with maximum plasma current rate derived from ITER, around 0.1 MA/s, and also in line with the MIRA results.

5.2.8. Plant power balance output configuration

The computed plant power balance specifications are listed in Table 5.24, both for HCPB and WCLL blanket configurations. These are then correlated to the same set of results issued by PROCESS system code for the analysed DEMO baseline. The most relevant offsets are those related to the net electric power $\dot{W}_{net}$, inherited from the gaps observed in the gross electric power $\dot{W}_{gross}$. However, very heterogeneous assumptions have been taken for the gross electrical efficiency η_{gross}, which, in the baseline, is extensively larger around 20 % in case of HCPB and 30 % in case of WCLL.

Description	Symbol	Unit	MIRA HCPB	MIRA WCLL	PROCESS	Limit
Total thermal power	$\dot{Q}_{th}$	[MW]	2624.0	2371.0	2436.0	
Gross electric power	$\dot{W}_{gross}$	[MW]	787.2	616.4	913.0	
Gross plant efficiency	η_{gross}	[%]	30.0	26.0	37.4	
Additional heating electric power	$\dot{W}_{add}$	[MW]	124.8	124.8	125.0	
Electric pumping power	$\dot{W}_{pump}$	[MW]	165.9	22.8	155.0	
Cryogenic electric power	$\dot{W}_{cryo}$	[MW]	34.1	30.8	28.8	
Auxiliary systems electric power	$\dot{W}_{aux}$	[MW]	97.1	87.7	104.7	
Electric recirculating power	$\dot{W}_{rec}$	[MW]	421.9	266.1	413.5	
Net electric power	$\dot{W}_{net}$	[MW]	365.3	350.3	500	$\approx$ 300-500 (DT)

Table 5.24.: List of calculated parameters related to the main plant power balance features of the DEMO 2015 baseline: comparison between MIRA and PROCESS results.

Ideally, such large gross efficiencies (37.4 %) could be potentially achieved deploying high temperature helium coolant, with no energy storage system (ESS) and full recover of the thermal power deposited in the divertor [11, 199]. Considering the currently established necessity to operate with the ESS [182] and the rather premature status of progress of the BoP solutions presently scoped, relying on such ideal and favourable situations represents an idealized upper limit. Even with the more conservative and DEMO design-based assumptions on η_{gross} the design goal on $\dot{W}_{net}$ appear to be satisfied.
The larger nuclear heating power achieved by the HCPB is partly "compensated" by the more pronounced electric pumping power consumption, attributed to the much smaller average fluid operating specific density. This leads to a similar net electric power yield for both designs, making them exploitable rather similarly.

6. Sensitivity of Global Reactor Parameters on Key Design Elements

In Chapter 5 several conflicts with key design parameters have been observed, arising from the application of more sophisticated physics and engineering models to simulate the tokamak reactor system. Among these parameters some did not comply with the imposed operational limits and requirements, including the safety factor at plasma magnetic axis q_0, the burn time τ_{burn} and the TF ripple $\delta_{tf,\max}$. Moreover, margins have been found in relation to the T breeding and shielding criteria, making room for possible actions in terms of radial build refinements and optimization.
The violation of these operational limits has inspired different parametric studies, where a wide set of variables has been scanned and examined. The major objectives of these studies are to quantify the response on some of key design elements, and, simultaneously, seek a set of DEMO operating points that meet all the imposed constraining conditions.

The figures extracted and selected for this chapter depict those which have exhibited the largest sensitivities on the infringed constraints and led to a successful identification of a DEMO 2015 baseline coherently in line with all the imposed design targets and limits. Moreover, these parametric scans allow capturing and exploring some of the utmost system dependencies which could not be acquired and observed via traditional 0D/1D modelling approach, pursued by presently available system codes and that drive considerably the design of a tokamak reactor.
Henceforth, the parametric investigation proposed for this chapter includes the study of:

- plasma internal inductance l_i;
- inboard thickness of the breeding blanket breeding zone $\Delta_{\mathrm{BZ,i}}$;
- outboard thickness of the VV-TF coil gap $\Delta_{\mathrm{VV-TFC,o}}$.

This chapter comprises of three different sections, individually devoted to each of the aforementioned scanned reactor variables. The rationales behind their choice will be elucidated during the course of the elaboration for each of them.

6.1. Parametric Scan of the Plasma Internal Inductance

The plasma internal inductance (Equation 3.9) is an integral parameter tied to the plasma current density distribution $J_{\phi,p}$, since it impacts the inductive plasma current drive. A reduction of l_i from the value issued by PROCESS for the analysed DEMO baseline, i.e. $l_i = 1.155$, has been observed to promote a significant increase of τ_{burn}, found well below its two-hour design target. Moreover, the PROCESS l_i amplitude has been found to be in disagreement with those associated with ITER [80] and DEMO [161] plasma flat-top scenario analyses, around $0.7 - 0.8$.
In order to cover the wide a spectrum of l_i spanning from such more realistic situations to the PROCESS's, the parametric study has been effectuated by dropping the plasma internal inductance from 1.2 to 0.7, with an increment of $\delta l_i = 0.05$. This step size has been found to appropriately catch all relevant behaviours with no significant oscillations in-between the calculated design points. The

major goal of this parametric scan is to highlight the major impacts of the plasma magnetic configuration on some of the key reactor design features. However, in a general transport problem for magnetically-confined plasmas l_i is not a fixed parameter but it is calculated, since the profile of $J_{\phi,p}$ is theoretically a solution variable.
The following core physics assumptions have been taken for all analysed l_i operating points.

- The fusion and the additional heating powers, P_{fus} and P_{add}, have been kept constant to the assumed baseline design target, respectively 2037 and 50 MW. The latter is reached by uniquely deploying CD power, such that $P_{add} \equiv P_{CD}$ and $P_{nCD} \approx 0$.
- The power transported across the separatrix P_{sep} has been frozen to the value calculated in the baseline analysis (Table 5.13) and compelling with the divertor challenging limit $\Gamma_{sep} \leq \Gamma^{u}_{sep} = 17$ MW/n. This ensures constant integral loading conditions and allows to have a blind-l_i-based comparison on the peak major heat loads on the plasma facing components.
- The ratio of beam to thermal particle γ_{beam} and the core concentration of the seeded impurity f_{Z_1} are no longer used as iteration variables in the plasma solver and assumed constant to calculated baseline values reported in Table 5.12 and Table 5.14. The rationale behind the last item has been driven by a willingly imposed simplification of the core plasma solving problem, for as the number of plasma iteration variables have been slightly reduced.
- All operating points have been calculated for a constant and DEMO 2015 baseline-devoted plasma current I_p, toroidal field B_t and fixed separatrix shape $\partial\mathcal{D}_p$, corresponding to the target separatrix profile.

Additionally, the same l_i scan has been repeated by ignoring the key plasma operational limits (OL) and the listed design targets (DT), to map the key core physics effects uniquely attributed to the magnetic configuration. The major calculated profiles are reported in Appendix F.1 and, when necessary, are referenced to elucidate some of the results obtained in this section.

The total magnetic energy associated with the plasma current includes an internal and the external parts, depending on the integral contribution inside and outside the confining region. For a fixed total plasma current I_p a small internal energy contribution, i.e. small l_i, yields broader current density profiles, lower close the magnetic axis and larger near the separatrix. Thus, smaller amplitudes of l_i leads to a widening of the flux surfaces, because of the wider distributions of $J_{\phi,p}$. For each value of l_i the coefficients a, b, c, d appearing in the $J_{\phi,p}$ parametrization of Equation (3.21) are numerically adapted to fulfil the requirements and limits imposed on l_i, I_p, β_p and q_{95}.

The two-dimensional ballooning of the poloidal flux driven by the reduction of l_i are visualized in Figure 6.1. The plot depicts different curves tied to different values of ρ and l_i, for a fixed plasma separatrix characterized by the same $\kappa_{X,u/l}$ and $\delta_{X,u/l}$. In particular, the magnetic flux surfaces at $\rho = \rho_{core} \equiv 0.6$ and $\rho = 0.95$ are considered for $l_i = 1.2$ and $l_i = 0.7$. In both ρ situations the flux surface at $l_i = 0.7$ envelopes the one taken at $l_i = 1.2$.

The topology of the flux surfaces associated with the different l_i-driven magnetic configurations is expressed by a continuous reduction of the plasma elongation and triangularity at 95 % flux surface κ_{95} and δ_{95}, which are illustrated in Figures 6.2−a and b. Smaller amplitudes of l_i yield a widening of the flux surfaces, because of the more extended distributions of $J_{\phi,p}$. In particular, δ_{95} and κ_{95} scale up by nearly 26 % and 5 % for l_i decreasing from 1.2 to 0.7.
In presently available systems codes κ_{95} and δ_{95} have a substantial impact on a variety of fitting and extrapolating core physics functions, used to calculate several key parameters. Among these are the plasma current I_p and the Spitzer plasma conductivity σ_{S_p} (Equations 3.8 and C.6). However, κ_{95}

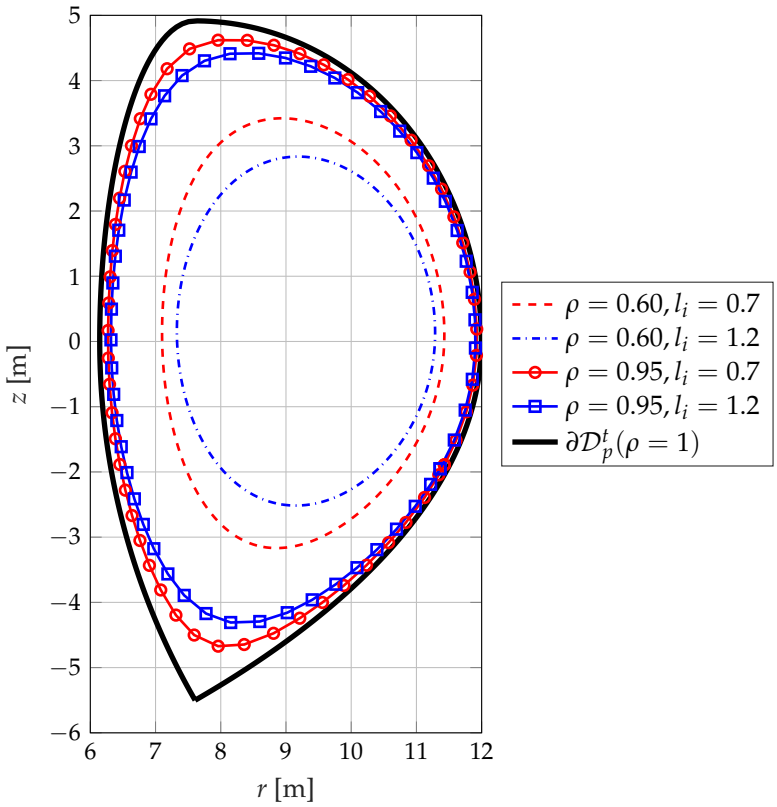

Figure 6.1.: Radial-poloidal profiles of magnetic flux surfaces selected for different values of normalized poloidal flux ρ and plasma internal inductance l_i. The contour at $\rho = 0.60$ depicts the boundary of the core-mantle regions, i.e. $\rho_{core} = 0.60$.

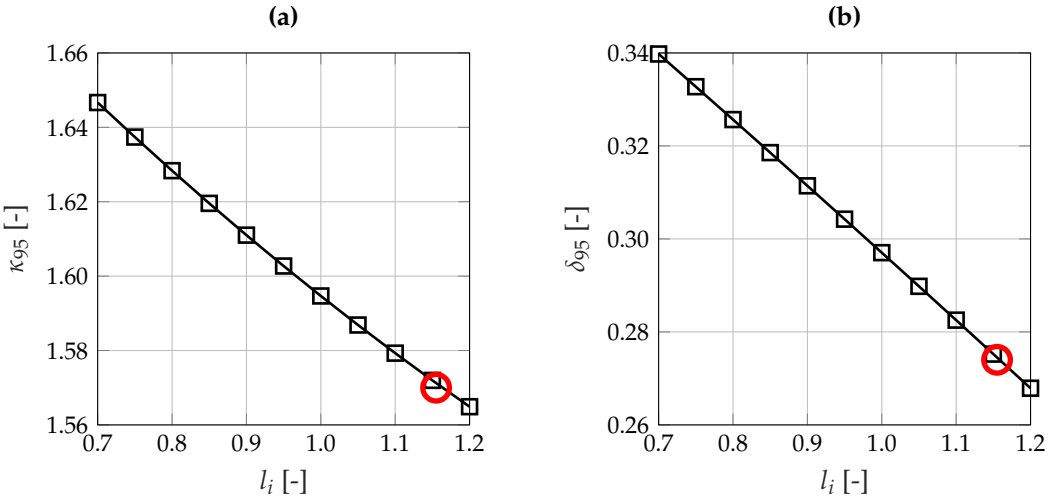

Figure 6.2.: Evolution of magnetic flux surface geometric distribution for variations of internal inductance l_i: (a) elongation at 95 % flux surface κ_{95} and (b) triangularity at 95 % flux surface δ_{95}. The circle marks the DEMO1 2015 baseline, evaluated by MIRA.

and δ_{95} are based on ITER Physics Guidelines scaling formulas and they are expressed as functions of κ_X and δ_X [17].

A revision of the plasma internal inductance has shown to be a viable option to cope with the violated operational limit imposed on the safety factor at plasma axis q_0. Combining the integral definitions of l_i and q and their dependencies on the poloidal field B_p, it emerges that a reduction of the plasma internal inductance yields a rise of q. In particular, $l_i \propto \int_{\mathcal{D}_p} B_p^2 \mathrm{d}\mathbf{r}$ and $q(\rho') \propto \oint_{\partial\mathcal{D}_{\rho'}} \frac{1}{B_p} \mathrm{d}l$, with $\partial\mathcal{D}_{\rho'}$ denoting the geometric boundary of the flux surface at $\rho = \rho'$.

The impact on q_0 and q_{95} for the imposed variations of l_i are depicted in Figure 6.3 and combined to their lower operational limits.

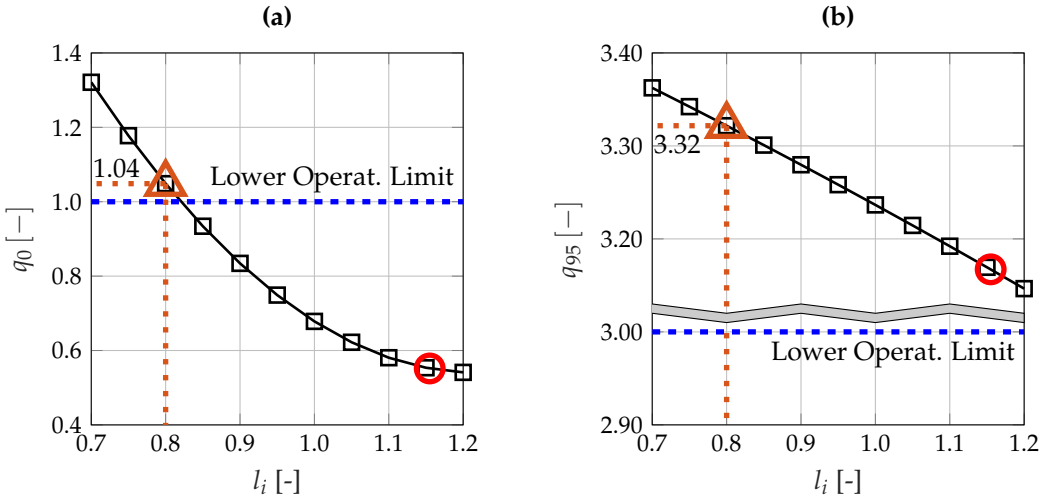

Figure 6.3.: Calculated plasma safety factors for variations of plasma internal inductance l_i: (a) safety factor at magnetic axis q_0 and (b) safety factor at 95 % flux surface q_{95}. The circle marks the DEMO1 2015 baseline, evaluated by MIRA. The orange triangle marker denotes the design point at $l_i = 0.8$ fulfilling the q_0 limit.

The axis safety factor approaches and overcomes its lower bound at $l_i = 0.8$ (see orange triangle marker) and growing by nearly 2.4 times for l_i declining from 1.2 to 0.7. As for q_{95}, the full spread is retained to about the 6 % of the baseline's for the analysed span of l_i, largely above the constraining lower limit (see the orange triangle marker, indicating $q_{95} = 3.32$ for the same $l_i = 0.8$ ordinate).
Both q_0 and q_{95} play a fundamental role in the characterization of a stable plasma design and cannot disregard the two-dimensional magnetic ties derived from the resolution of the Grad-Shafranov equilibrium problem. In particular, a simple input specification of q_0 is not a sufficient condition to a stable plasma state. q_0 necessitates a direct link to the major magnetic features, including toroidal and poloidal magnetic field components, total plasma current and toroidal current density profiles.

The implications on the major plasma power balance of different magnetic flux profiles configurations have been addressed in Section 5.2.2. The same considerations can be extended to interpret the effects on the plasma density and temperatures profiles variables yielded by distinct values of l_i. Lower plasma internal inductances lead to a widening of the core regions towards the periphery, increasing their integral contribution. As a result, keeping unaltered the electron density and temperature profiles $n_e(\rho)$ and $T(\rho)$, their volume-averaged amplitudes $\langle n_e \rangle$ and $\langle T \rangle$ increase. Furthermore, because of a more peaked profile of $T(\rho)$, depicted by a larger α profile coefficient, the temperature is more sensitive to variations of l_i in the evaluated l_i range.
In case of constrained parametric scan, i.e. keeping the plasma OL enabled, the solver adjusts all iteration variables, including $n_{e,0}$ and T_0, to fulfil the constraints and compensate the increase of $\langle n_e \rangle$

and $\langle T \rangle$ induced by the reduction of l_i. The distribution of the axis and volume-averaged electron density and temperature for constrained and unconstrained l_i scans are illustrated in Figures 6.4−a to d.

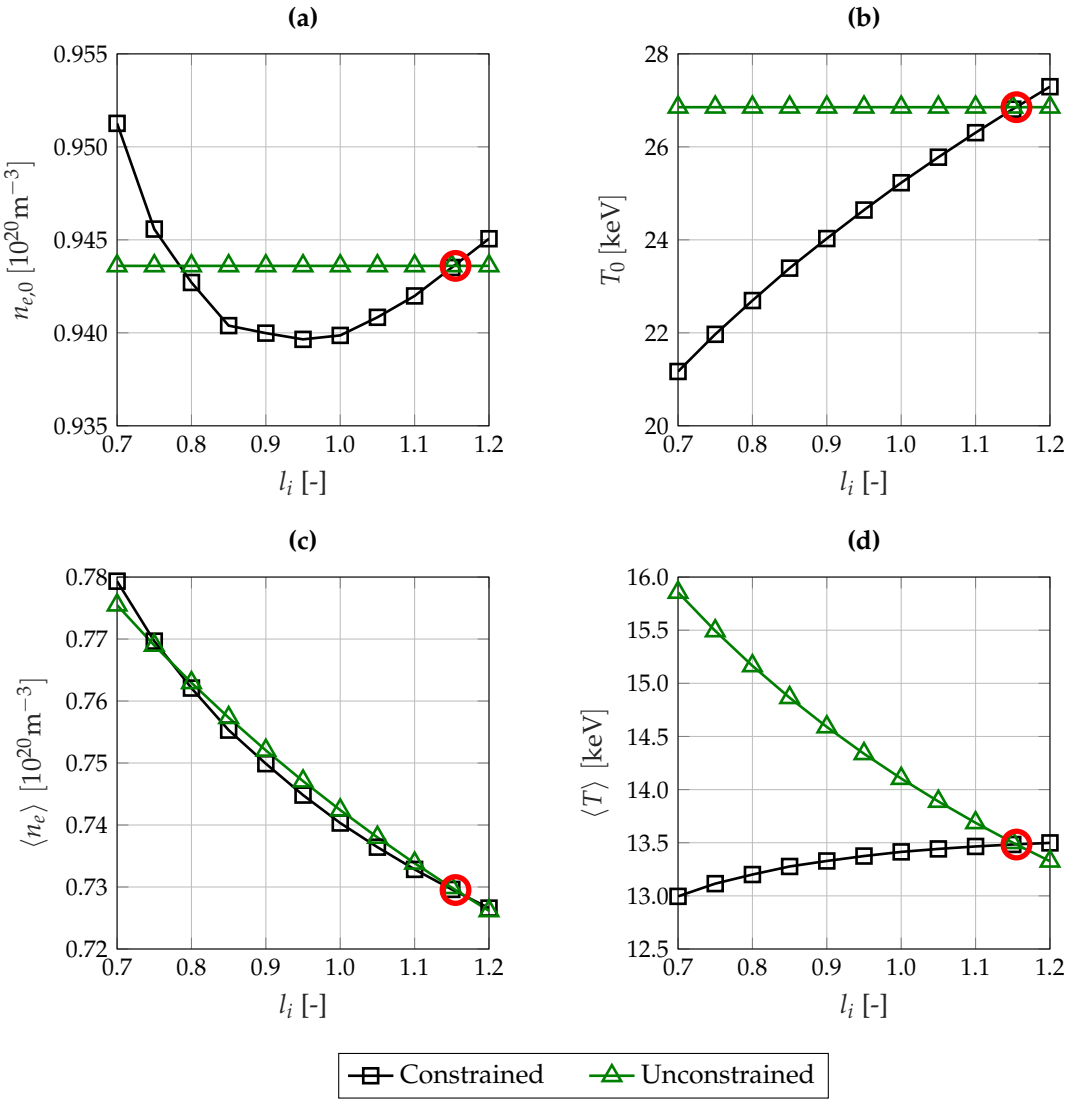

Figure 6.4.: Computed distribution of plasma profile properties for constrained and unconstrained variations of the plasma internal inductance l_i: (a) electron density at magnetic axis $n_{e,0}$, (b) plasma temperature at axis T_0, (c) volume-averaged electron density $\langle n_e \rangle$ and (d) volume-averaged plasma temperature $\langle T \rangle$. The circle marks the DEMO1 2015 baseline, as per MIRA analysis.

In case of constrained scan, $n_{e,0}$ features limited oscillations (below 1 %) compared to T_0 (20 % drop from the baseline value) and exhibits a minimum around $l_i = 0.95$. According to Figure F.1, the reduction of $n_{e,0}$ is associated with a reduction of τ_E as l_i falls because of the dependency on the line-averaged electron density $\overline{n}_e$ (Equation C.30). But, the local minimum is shifted for τ_E to larger values of l_i (≈ 1.05) compared to $n_{e,0}$. For $l_i > 1.05$ both $n_{e,0}$ and τ_E rise with increasing l_i.
As for $\langle n_e \rangle$ and $\langle T \rangle$, the situation appears to be reversed, with a rise of $\langle n_e \rangle$ by nearly 7 % in case of constrained and unconstrained scans and an opposite behaviour of $\langle T \rangle$ for the two cases. In case of constrained plasma operation $\langle T \rangle$ reduces by approximately 4 % as l_i falls, while for unconstrained

study it exhibits a 21 % rise from the baseline point.
When constraining the plasma with almost constant P_{fus} the solver drives $n_{e,0}$ and T_0 such that $\langle n_e \rangle$ and $\langle T \rangle$ are kept nearly constant too. Hence, the distributions of T_0 and $n_{e,0}$ on l_i compensate the reduction of $\langle T \rangle$ driven by the perturbations on the poloidal flux configurations.

Figure 6.5 displays the distributions of the core plasma power balance terms for variations of l_i in case of constrained and unconstrained l_i parametric studies.

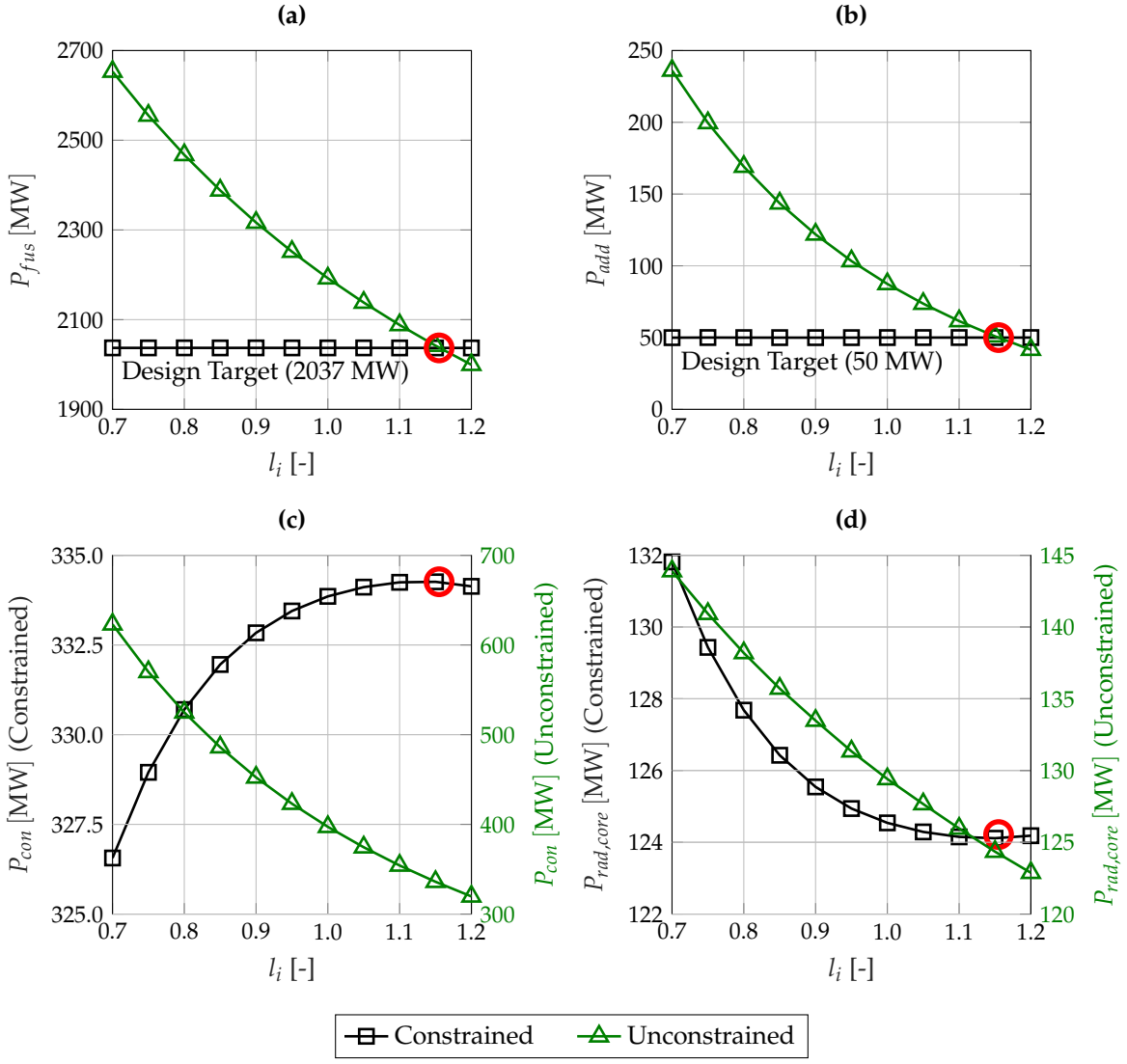

Figure 6.5.: Calculated values of core plasma power balance for constrained and unconstrained variations of the plasma internal inductance l_i: (a) fusion power P_{fus}, (b) additional heating power P_{add}, (c) advective/conductive transport loss power P_{con} and (d) core radiation power $P_{rad,core}$. The circle marks the DEMO1 2015 baseline evaluated by MIRA.

For the unconstrained study P_{fus} and P_{add} experience large deviations from the baseline configuration. In this case P_{fus} is subject to the responses of n_e and T (Equation 3.44) such that $P_{fus} \propto \langle n_e \rangle^2 \cdot \langle \sigma v \rangle$, with $\langle \sigma v \rangle$ denoting the volume-averaged fusion reactivity. The latter is assumed to scale with T^2 for T below 20 keV [112], hence, as first approximation, $P_{fus} \propto \langle n_e \rangle^2 \cdot \langle T \rangle^2$. In case

of unconstrained study, this leads to the global 30 % increment of P_{fus} as l_i drops (Figure 6.5−a). The same considerations hold for the unconstrained distributions of P_{con} and $P_{rad,core}$ (Figures 6.5−c and d), witnessing a considerable rise, too (Equations 3.56 and 3.50). For the unconstrained condition the growing distributions of P_{add} (Figures 6.5−b) resides in the external heating power to inject in the plasma to equate the core power balance $P_\alpha + P_{add} + P_{OH} = P_{con} + P_{rad,core}$ based on the calculated $P_\alpha \propto P_{fus}$, P_{con} and $P_{rad,core}$, all exhibiting incrementing behaviour for decreasing l_i.
In case of constrained configuration, since $P_\alpha \propto P_{fus}$ and P_{add} are bound to fixed values, the plasma engages a power balance configuration where $P_{con} + P_{rad,core} \approx$ const, both affected by $\langle n_e \rangle$ and $\langle T \rangle$. In particular, $P_{rad,core}$ is uniquely bound to the behaviours of n_e and T, since f_{Z_1} has been kept constant. Here $P_{brem} \propto n_e^2\sqrt{T}$ depicts the major contribution of $P_{rad,core}$ leading to the nearly 8-MW drop and rise of P_{con} and $P_{rad,core}$ from the baseline value for l_i going down to 0.7.

Combining the core and the mantle power balances (Equations 3.40 and 3.41) yields $P_\alpha + P_{add} + P_{OH} = P_{rad} + P_{sep}$, where $P_{rad} = P_{rad,core} + P_{rad,mantle} \approx$ const. Therefore, in case of constrained l_i scan P_{rad} is forced to be nearly constant for imposed variations of l_i, because of the constraints on P_{fus}, P_{add} and P_{sep}, with $P_{sep} = P_{con} - P_{rad,mantle}$ being associated with the OL on the divertor challenging quantifier Γ_{sep}.
The linking variable between the core and the mantle plasma power balances is $P_{rad,mantle}$. The constrained and unconstrained distributions of P_{sep} and $P_{rad,mantle}$ are depicted in Figure 6.6.

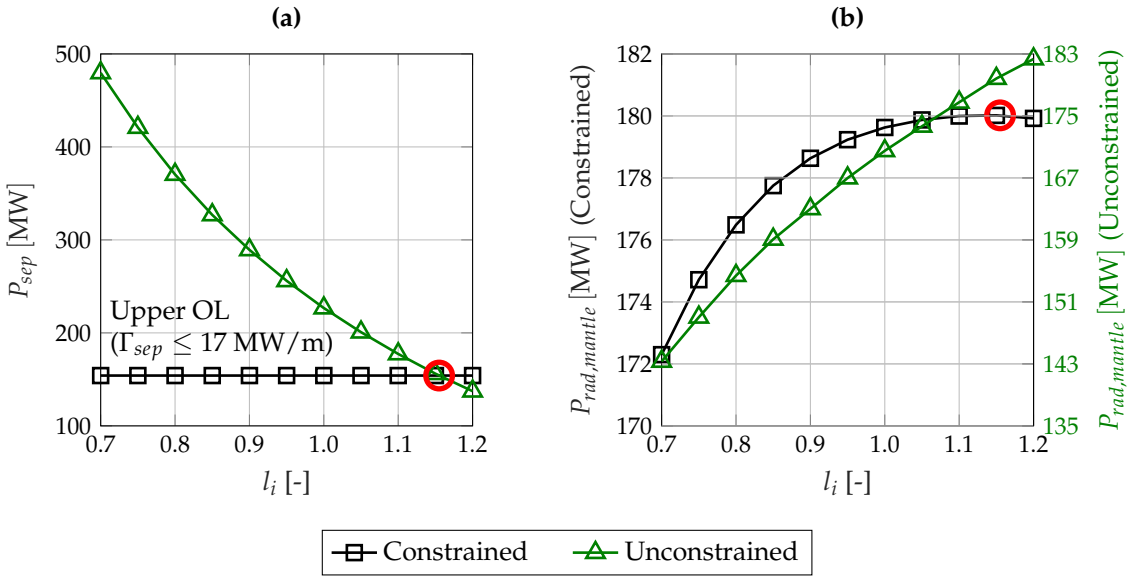

Figure 6.6.: Calculated values of mantle plasma power balance for constrained and unconstrained variations of the plasma internal inductance l_i: (a) power transported across the separatrix P_{sep} and (b) mantle radiation power $P_{rad,mantle}$. The circle marks the DEMO1 2015 baseline evaluated by MIRA.

The ballooning of the flux surfaces towards the separatrix for decreasing l_i (Figure 6.1) yields a reduced mantle region volume, hence smaller $P_{rad,mantle}$ as shown by the unconstrained curve of Figure 6.6−b. In case of unconstrained scan P_{sep} exhibits a rise for decreasing values of l_i and experiences the increment of P_{con} (Figure 6.5−c, unconstrained) and the reduction of $P_{rad,mantle}$, for l_i falling from its baseline value. When P_{sep} is being forced invariant to l_i, the plasma solver adjusts the mantle seeded impurity concentration $f_{Z1,M}$ such that $P_{rad,mantle}$ features constant amplitudes of P_{rad} and P_{sep}.

The reverse behaviours exhibited by constrained and unconstrained studies for some of the illustrated variables (e.g. P_{con} and $\langle T \rangle$) highlight the necessity of a constrained plasma solver in a fusion system code. Henceforth, the results will be illustrated without reporting the unconstrained case, since it depicts non-feasible design points with respect to the imposted OL and DT, as denoted by P_{sep} laying above its upper limit across the l_i domain.

The full set of plasma particle balance properties analysed in the parametric scan consists of helium fraction f_{He}, mantle seeded impurity concentrations $f_{Z_1,M}$, fuel fraction f_{DT} and plasma effective charge Z_{eff}. The core seeded impurity concentration f_{Z1} has been fixed constant to the calculated baseline value 5.34×10^{-5}. The distributions of all these variables as function of l_i are reported in Figure 6.7.

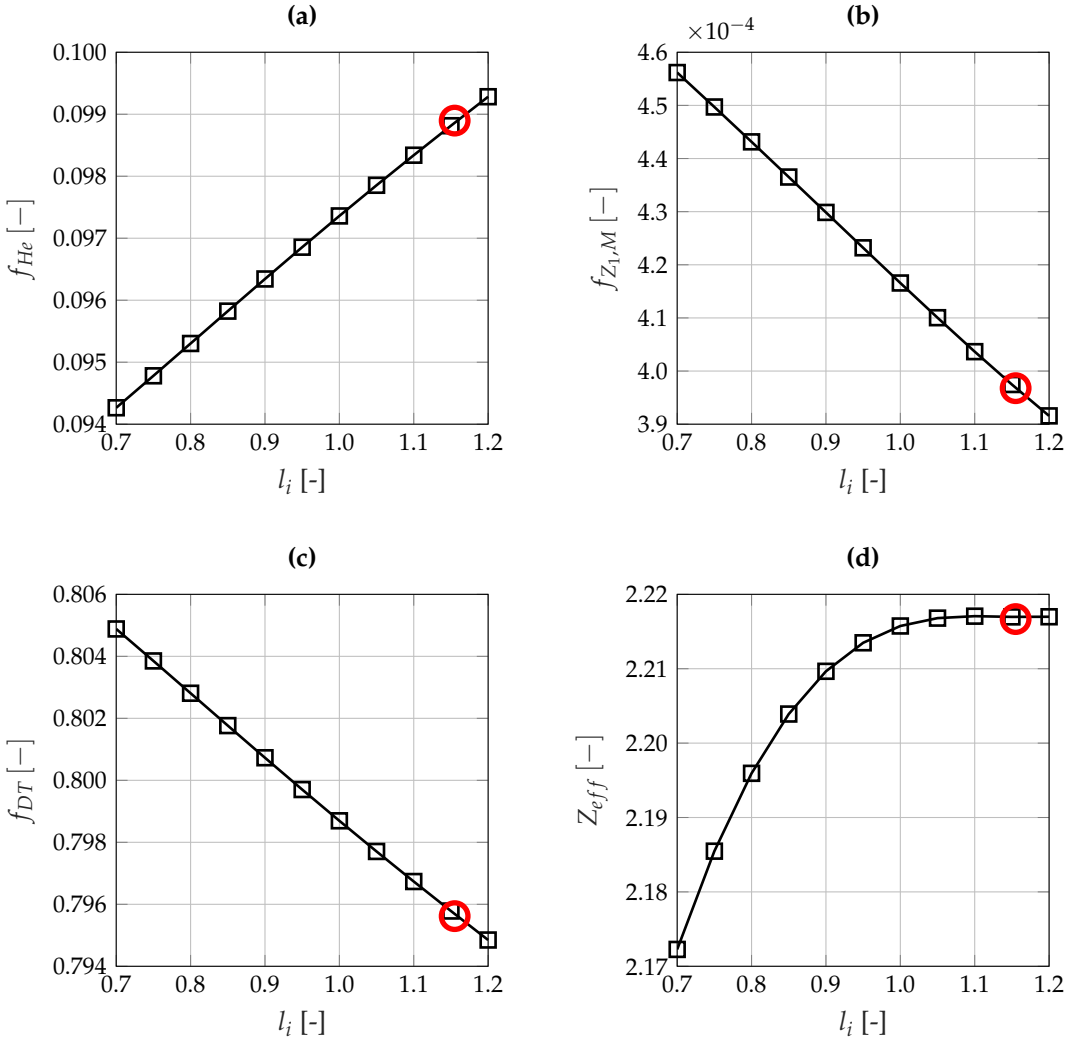

Figure 6.7.: Evaluated distributions of plasma particle balance properties for constrained variations of the plasma internal inductance l_i: (a) helium fraction f_{He}, (b) seeded impurity concentration in the plasma mantle region $f_{Z_1,M}$, (c) core fuel fraction f_{DT} and (d) plasma effective charge Z_{eff}. The red circle marks the DEMO1 2015 baseline, evaluated by MIRA.

f_{He} and $f_{Z1,M}$ are tuned by the plasma solver to fulfil the constraining conditions $P_{sep} \approx 154.1$ MW and $f_{P2E} = \tau_p^* / \tau_E \approx 6.542$. The volume-averaged helium density $\langle n_{He} \rangle = f_{He} \cdot \langle n_e \rangle$ is influenced

by P_{fus}, plasma volume and helium particle confinement time τ_p^* (Equation C.28), thus on τ_E, too. Therefore, fixing P_{fus} and V_p to constant values, f_{He} is influenced by the profiles of $\langle n_e \rangle$ and τ_E (Figures 6.4−a and F.1) and exhibits a 5.2 % decrement.
$f_{Z1,M}$ features a 16.5 % linear increment as l_i decreases. To satisfy the imposed target on P_{sep} the solver acts principally on $P_{rad,mantle}$ by manipulating $f_{Z1,M}$. According to Equation (3.52), $P_{rad,mantle} = P_{line,mantle} \propto f_{Z1,M}$. Hence, the distribution of $f_{Z_1,M}$ for decreasing l_i is mostly associated to the profile of $P_{rad,mantle}$ for the constrained configuration, which globally reduces by nearly 8 MW to fulfil the criteria on P_{sep} and P_{rad} (Figure 6.6−b, constrained). However, a global increase of $f_{Z_1,M}$ is obtained to compensate the larger reduction of $P_{rad,mantle}$ arising from the decrease of l_i, approximately 40 MW (see Figure 6.6−b, unconstrained).
As the DT fuel fraction depicts the remainder of helium and impurities fractions (Equation C.26), f_{DT} exhibits a 5% increment deduced from the distributions of f_{He} and $f_{Z1,M}$.
The behaviour of the plasma effective charge Z_{eff} reproduces the situations of f_{He}, $f_{Z_1,M}$ and f_{DT}, all featuring different rising and diminishing behaviours. Accordingly, the rising effects of $f_{Z_1,M}$ are compensated by the linear decrease of f_{He}, which takes place in the entire plasma domain (core and mantle). Z_{eff} experiences a 2 % reduction from the baseline estimation for decreasing l_i.

Since the internal inductance affects the magnetic configuration inside the confining region the plasma current balance properties are also to experience such effects. These are given by external current drive f_{CD}, bootstrap f_{BS} and induction f_{ind} current fractions. Their distributions on the internal inductance l_i are displayed in Figure 6.8.

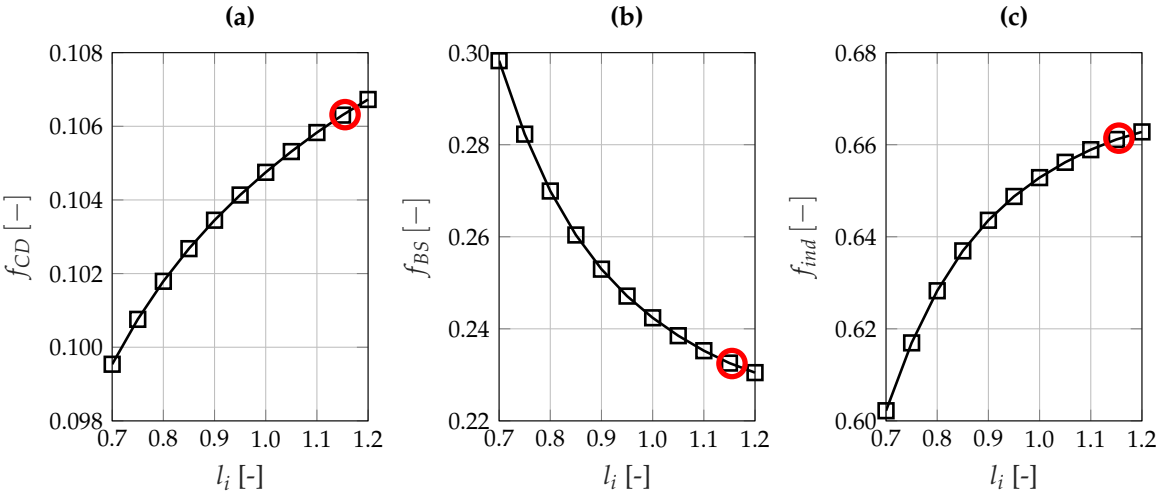

Figure 6.8.: Calculated values of plasma current and magnetic flux balance properties for constrained variations of the plasma internal inductance l_i: (a) external current-drive fraction f_{CD}, (b) bootstrap current fraction f_{BS} and (c) inductive current fraction f_{ind}. The circle marks the DEMO1 2015 baseline evaluated by MIRA.

The design target on P_{add} (50 MW) has been achieved by means of CD power P_{CD}. According to Equation (C.11), P_{CD} linearly scales to f_{CD} and $\langle n_e \rangle$ and inverse proportional to the normalized current drive efficiency γ_{CD}, thus to $\langle T \rangle$ (Equation C.12). Therefore, as l_i falls, to keep P_{CD} steady f_{CD} is expected to decrease to counterbalance the growth of $\langle n_e \rangle$ and the fall of $\langle T \rangle$ (Figures 6.4−c and d). Globally, f_{CD} reduces by nearly 5 % from its baseline value for l_i falling from 1.2 to 0.7.
The bootstrap plasma current is based on the occurring of complex phenomena associated with the transport parallel to magnetic field involving a wide number of plasma physics aspects, such as mag-

netic configuration, collisionality and pressure gradient [196]. Accordingly, the calculated distribution of f_{BS} (Equation C.8) hinges upon the complex linear and nonlinear dependencies on plasma profiles and safety factor variables, including q_0, q_{95}, $n_{e,0}$, $\langle n_e \rangle$ T_0, $\langle T \rangle$ and Z_{eff}. These feature incrementing (q_0, q_{95}, $n_{e,0}$, $\langle n_e \rangle$) and decrementing (T_0, $\langle T \rangle$, Z_{eff}) behaviours for reducing l_i. However, the largest sensitivity on f_{BS} has been observed for q_0, being the most influencing parameter according to adopted f_{BS} scaling. As $l_i \propto B_p^2$ drops, f_{BS} increases since $J_{\phi,p}^{bs} \propto 1/B_p$ [85] and experiences a 27 % increment. This ultimately represents a benefit for the machine because it reduces the requirements on the external CD power and on the inductive current. Since $f_{ind} = 1 - f_{BS} - f_{CD}$, combining the responses of f_{BS} and f_{CD} the overall inductive current fraction decreases by circa 10 %.

The distributions of the plasma resistance R_p and loop voltage U_{loop} on l_i are visualized in Figure 6.9.

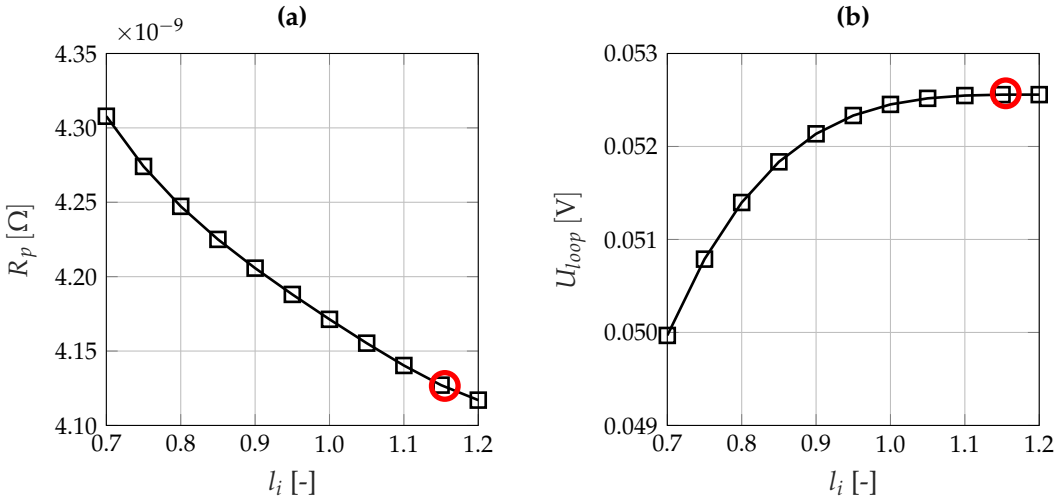

Figure 6.9.: Computed distributions of plasma loop voltage properties for constrained variations of the plasma internal inductance l_i: (a) plasma resistance R_p and (b) loop voltage U_{loop}. The circle marks the DEMO1 2015 baseline evaluated by MIRA.

The amplitude of U_{loop} is jointly influenced by f_{ind} and the plasma resistance R_p, such that $U_{loop} \propto f_{ind} R_p$. The resistance R_p depends on κ_{95}, $\langle T \rangle$ and Z_{eff} (Equations C.4 and C.6) leading to a 5 % rise for decreasing l_i. This partly counterbalances the gains achievable in terms of U_{loop} derived from the boost f_{ind} and leads to an overall 5.1 % dump of U_{loop} as l_i diminishes. The plasma loop voltage U_{loop} is a vital physics parameter playing a central role in inductive fusion machine, as directly linked to the flat-top length τ_{flat}, hence to τ_{burn}, too (Equation 4.91).

A topological modification of the magnetic flux surfaces with varying l_i has ramifications inside and outside the confining region. A variation of l_i corresponds to a change of the applied flux at plasma boundary Ψ_b, thus to a different magnetic field distribution. Therefore, the peak heat flux on divertor targets experience such magnetic field effects derived from the reduction of l_i.
The distributions of the poloidal magnetic field $B_{p,\mathrm{S_k}}$ and $B_{p,\mathrm{P_k}}$ ($k = i/o$) calculated at strike points $\mathrm{S_k}$ (Figure 2.10) and the plasma mid-equatorial plane $\mathrm{P_k}$ (Figure 2.11), of the expansion factor of the magnetic flux tube $f_{x,k}$ and of the peak divertor heat flux $\Gamma_{\perp,\max}^{div/i}$, are visualized in Figure 6.10. These are reported for the plasma SOF configuration but at EOF they present a very similar behaviour. Moving from the baseline design point down to $l_i = 0.7$ $B_{p,\mathrm{S_k}}$ features a substantial increment (40.1 % inboard, 17.8 % outboard), while of $B_{p,\mathrm{P_k}}$ decreases by 13 % and 16 % on inboard and outboard.

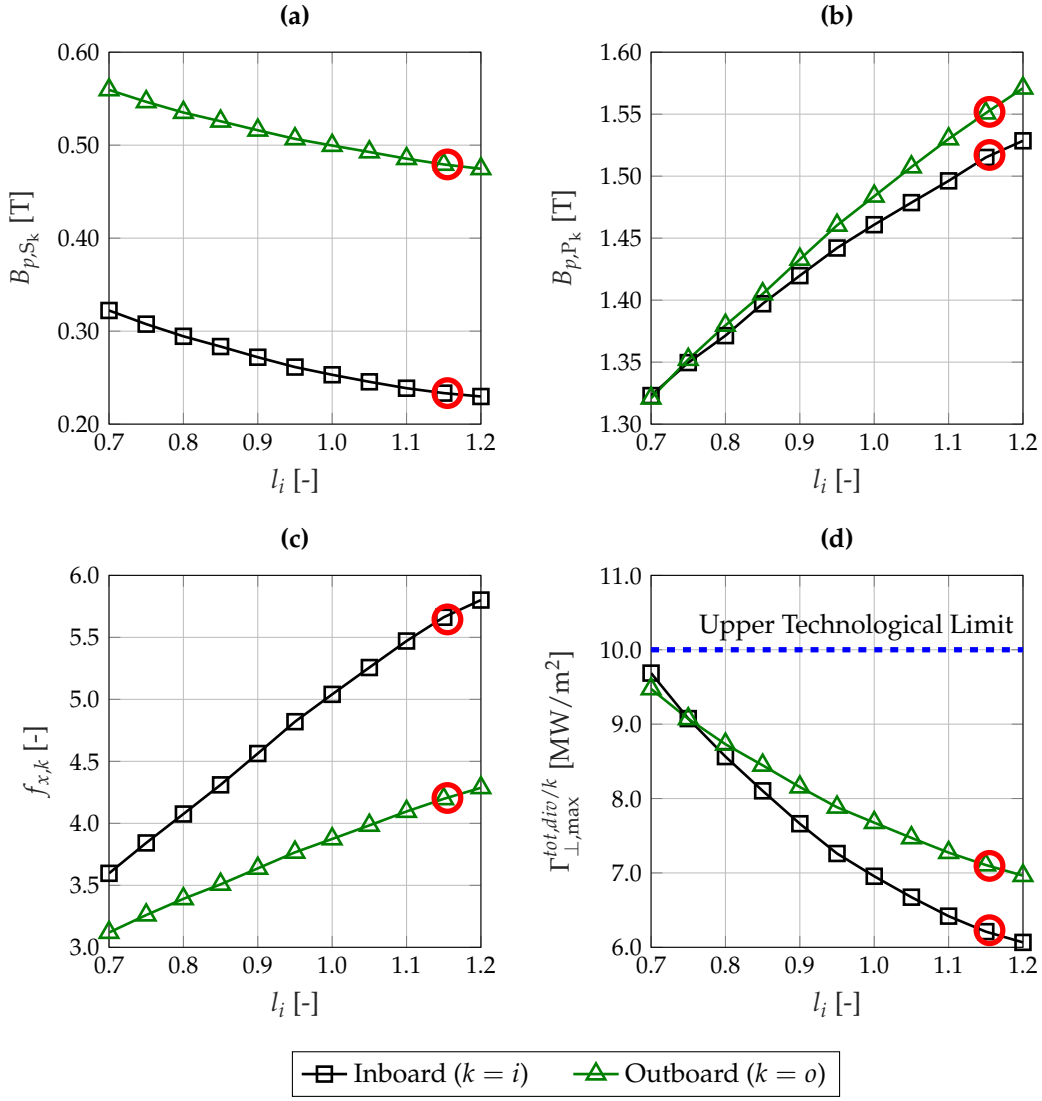

Figure 6.10.: Calculated values of divertor heat load properties for variations of the plasma internal inductance l_i: (a) poloidal magnetic field at divertor strike point B_{p,S_k}, (b) poloidal field at plasma equatorial mid-plane B_{p,P_k}, (c) expansion factor of the magnetic flux tube $f_{x,k}$ and (d) peak heat load on the divertor target $\Gamma^{tot,div/k}_{\perp,max}$ ($k = i/o$). The circle marks the DEMO1 2015 baseline evaluated by MIRA.

The behaviour of is B_{p,S_k} is attributed to the rise of $\Psi_{b,sof}$, due to the linear dependency of Ψ_{ind} on l_i (Equation 4.92). Ultimately, this yields larger PF/CS coil currents, hence larger fields outside the separatrix. The decline of B_{p,P_k}, instead, is driven by the heterogeneous profiles of Ψ inside the separatrix, emerging from the lowering of l_i. Broader distributions of the current density $J_{\phi,p}$ produce higher spreadings of Ψ, reducing the spatial gradients, hence the poloidal field.

B_{p,S_k} and B_{p,P_k} determine the expansion factors $f_{x,k}$, acting on the peak divertor heat flux $\Gamma^{div/k}_{\perp,max}$ (Equations 3.75 and 3.77). Such magnetic field effects on l_i lead to a major decline of the inboard and outboard expansion factors by nearly 40 % and 30 % for decreasing l_i. This has entangled a nearly 60 % rise of $\Gamma^{div/i}_{\perp,max}$ and 36 % of $\Gamma^{div/o}_{\perp,max}$. Even though the different field and flux conditions

endure such enlarged values of $\Gamma^{div/k}_{\perp,\max}$, the 10 MW/m^2 technological limit is being satisfied within the whole l_i analysed domain.
Having posed a specific requirement on P_{sep} allows a quantification of these non-core physics-related influences on the peak divertor flux, by handling the same transported input power. Additionally, this large sensitivity of the divertor wall loading conditions on such purely two-dimensional aspects highlights the importance of their quantification in a tokamak reactor system analysis.

Marginal perturbations have been also observed on the neutron wall loading conditions onto inboard and outboard blanket first wall. A widening of the flux surface implicates a more uniform redistribution of the high energy neutrons, isotropically generated inside the core plasma region. As a consequence, the peak FW inboard and outboard neutron wall loadings, $\Gamma^{n,fw/ib}_{\perp,\max}$ and $\Gamma^{n,fw/ob}_{\perp,\max}$, have been noticed to go down from the baseline amplitudes by 2 % and 4 %. The related parametric scans are displayed in Figure F.2.

Another major objective of reducing l_i is to achieve a two-hour τ_{burn} requirement. In order to succeed, two viable solutions have been examined for a reduced plasma internal inductance: diminish Ψ_{ind} to increase $\Psi_{b,sof}$ and reduce $\Psi_{b,eof}$. Both distributions are pictured in Figure 6.11, confirming the achievement of the anticipated target.

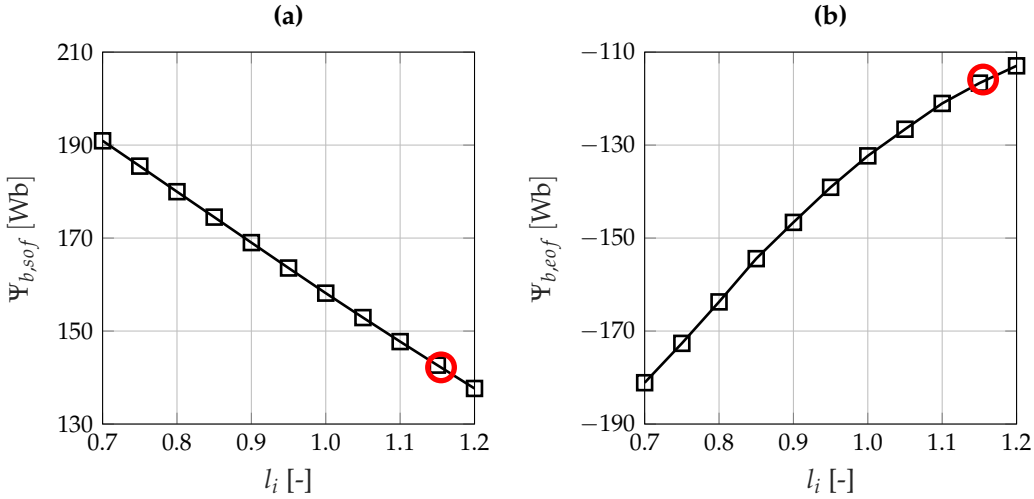

Figure 6.11.: Evaluated distributions of externally-applied poloidal flux at plasma separatrix for variations of the plasma internal inductance l_i: (a) plasma boundary flux at SOF $\Psi_{b,sof}$ and (b) plasma boundary flux at EOF $\Psi_{b,eof}$. The circle marks the DEMO1 2015 baseline, as per MIRA analysis.

The linear behaviour of $\Psi_{b,sof}$ proves the response attended from Equation (4.92), where a lower poloidal flux is consumed at plasma ramp-up. In this specific case, a 33 % augment of the baseline value has been found for l_i decreasing to 0.7. $\Psi_{b,eof}$ shows a decreasing behaviour which finds its ground in the better overlapping of $J_{\phi,p}$ with respect to the target separatrix profile, when lower plasma internal inductances are deployed. In the limit of higher l_i and peaked $J_{\phi,p}$ profiles the total plasma current qualitatively approaches the conduct of a singular current filament, since it condenses large fractions of current around the magnetic axis. These conditions deviate from the actual elongated and D-shape typical single null tokamak plasma topologies. In case of smaller l_i, instead, $J_{\phi,p}$ retains coarser distributions and globally spreads the total current more homogeneously over the whole confining domain. This denotes a situation much closer to the target condition, hence easier to form with the external coil systems.

In this way, lower values of l_i justify the smaller plasma boundary fluxes (in absolute value), for nearly constant poloidal betas and constant total current. The entity of such beneficial effects fairly amounts to a 56 % widening of the baseline's $\Psi_{b,eof}$ modulus, down to the lower end of l_i.

Shaping single null plasmas involves the selection of the target separatrix contour $\partial\mathcal{D}_p^t$, characterized by the target triangularities and elongations δ_X^t and κ_X^t (see Figures 6.12−a and b).

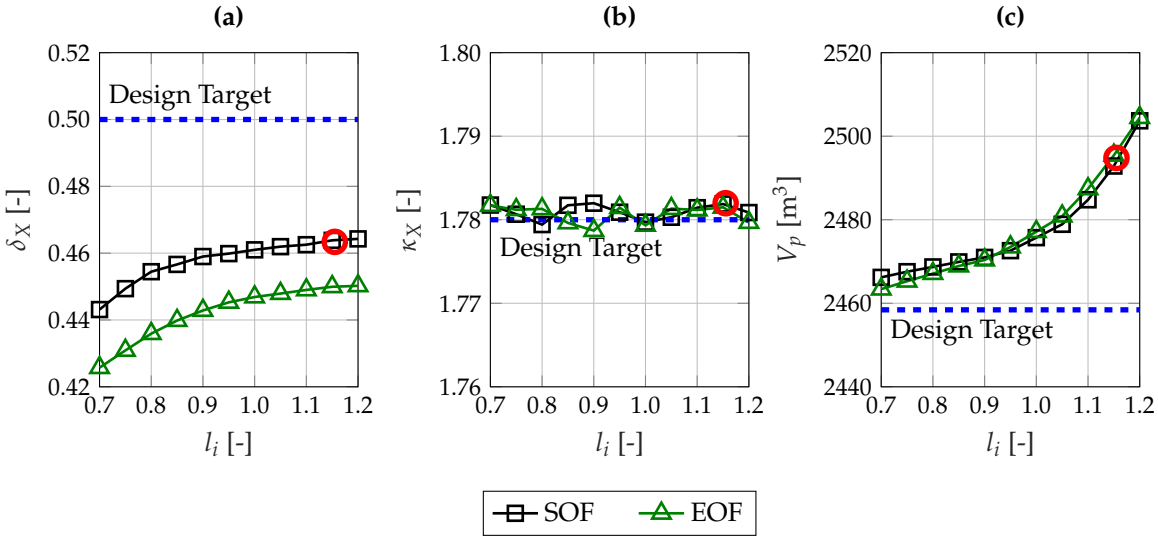

Figure 6.12.: Computed distributions of plasma shape properties at SOF and EOF for variations of the plasma internal inductance l_i: (a) plasma triangularity δ_X, (b) plasma elongation κ_X and (c) plasma volume V_p. The circle marks the DEMO1 2015 baseline evaluated by MIRA.

The parametric scan has exhibited low decreasing responses of δ_X for diminishing values of l_i, whereas κ_X is largely satisfied. Furthermore, both at SOF and EOF, the plasma triangularity (δ_X^{sof} and δ_X^{eof}) is below its target value $\delta_X^t = 0.5$. The negative decreasing behaviour of δ_X is driven by the growth of $\Psi_{b,sof}$ and $\Psi_{b,eof}$, hence by more demanding conditions of the plasma shaping. The imposed δ_X^t target is derived from the DEMO 2015 baseline generated by PROCESS, where it is prescribed as an input parameter. Based on more 2D detailed plasma equilibrium analyses performed by MIRA this target could be not fulfilled for the entire range of l_i. It can be inferred that the selected target plasma triangularity should rely on physics and technological operational limits depending on the plasma geometric features and on the PF/CS coils capabilities [10, 99].
In terms of plasma volume V_p, improvements are observed for reducing l_i amplitudes (see Figure 6.12−c). Across the whole l_i range V_p exceeds the target value and approaches it for smaller l_i. The target plasma volume refers to the same set of design goal imposed by δ_X and κ_X and therefore obeys to the same physical limitations.

The distribution of τ_{burn} for varying plasma internal inductance l_i is displayed in Figure 6.13. A 53 % increase from the baseline design point for lowering l_i can be observed. The profile is deduced combining the response of U_{loop} with the widening of flat-top available flux swing $\Psi_{b,sof} - \Psi_{b,eof}$ The two-hour design target is accomplished for l_i at its inferior limit in the analysed interval, $l_i = 0.7$. The overall rise amounts to 2550 s, emphasizing the large sensitivity of τ_{burn} on l_i and its implications in fusion tokamak devices running in pulsed mode.

The large reference PROCESS plasma internal inductance value $l_i = 1.155$ limits the fulfilment of the q_0 constraint and of the τ_{burn} design target. As a result, if lower l_i amplitudes are assumed,

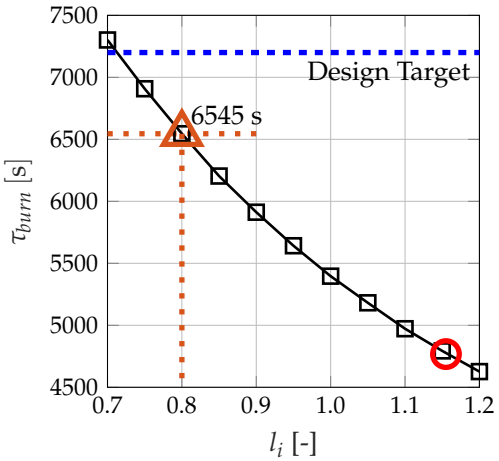

Figure 6.13.: Computed distribution of the plasma burn time τ_{burn} for variations of the plasma internal inductance l_i. The circle marks the DEMO1 2015 baseline evaluated by MIRA. The triangle denotes the design point at $l_i = 0.8$ fulfilling the q_0 limit.

e.g. $l_i = 0.7 - 0.8$, both criteria can be verified. To remain consistent with the ITER and DEMO reference equilibria a revised value of $l_i = 0.8$ is henceforth assumed. Further counteractive measures will be taken in the next section, as the selected l_i design point provides a burn time up to around 6500 s, which is still below the two-hour target.

6.2. Parametric Scan of the Inboard Breeding Zone Thickness

The inboard width $\Delta_{\mathrm{BZ,i}}$ of the BB breeding zone (see Figure 6.14) has emerged as a promising and viable solution to exploit the large surplus of TBR for optimizing the overall reactor radial build on the inboard side. Since the reactor radial build parametric responses are evaluated relatively to the baseline design point, a relative width $\delta_{m,j}$ is used. $\delta_{m,j}$ is defined as:

$$\delta_{m,j} = \Delta_{m,j} - \Delta^*_{m,j}, \tag{6.1}$$

where the subscript m relates to the reactor component and j indicates the inboard or outboard side ($j = i/o$). Accordingly, $\Delta_{m,j}$ refers to the thickness of the scanned design point and $\Delta^*_{m,j}$ to the baseline's.
Relying on the DEMO 2015 baseline revised with $l_i = 0.8$, the scanning variable is therefore characterized by the relative width $\delta_{\mathrm{BZ,i}}$, decreasing from 0 cm to -20 cm, with a 2 cm decrement. Furthermore, the parametric scan has been performed both for HCPB and WCLL blanket design solutions, taking the top BZ width $\Delta_{\mathrm{BZ,t}}$ as the averaged between inboard and outboard. The remaining reactor components' radial specifications are left unchanged. In addition, the two BB layouts rely on rather heterogeneous reference baseline BZ width $\Delta^*_{\mathrm{BZ,i}}$, i.e. 23 cm for HCPB and 47 cm for WCLL.

The neutronic analyses performed on HCPB and WCLL blankets have both shown a TBR excess from the 1.10 design goal (1.20 and 1.14) and a sound shielding margins for the fast neutron flux and peak nuclear power density criteria, observed at TF coil winding pack. In this way, a reduction of $\Delta_{\mathrm{BZ,i}}$ allows a closer position of the CS coils with respect to the plasma, thereby increasing the available poloidal flux through the different plasma scenario operational phases.

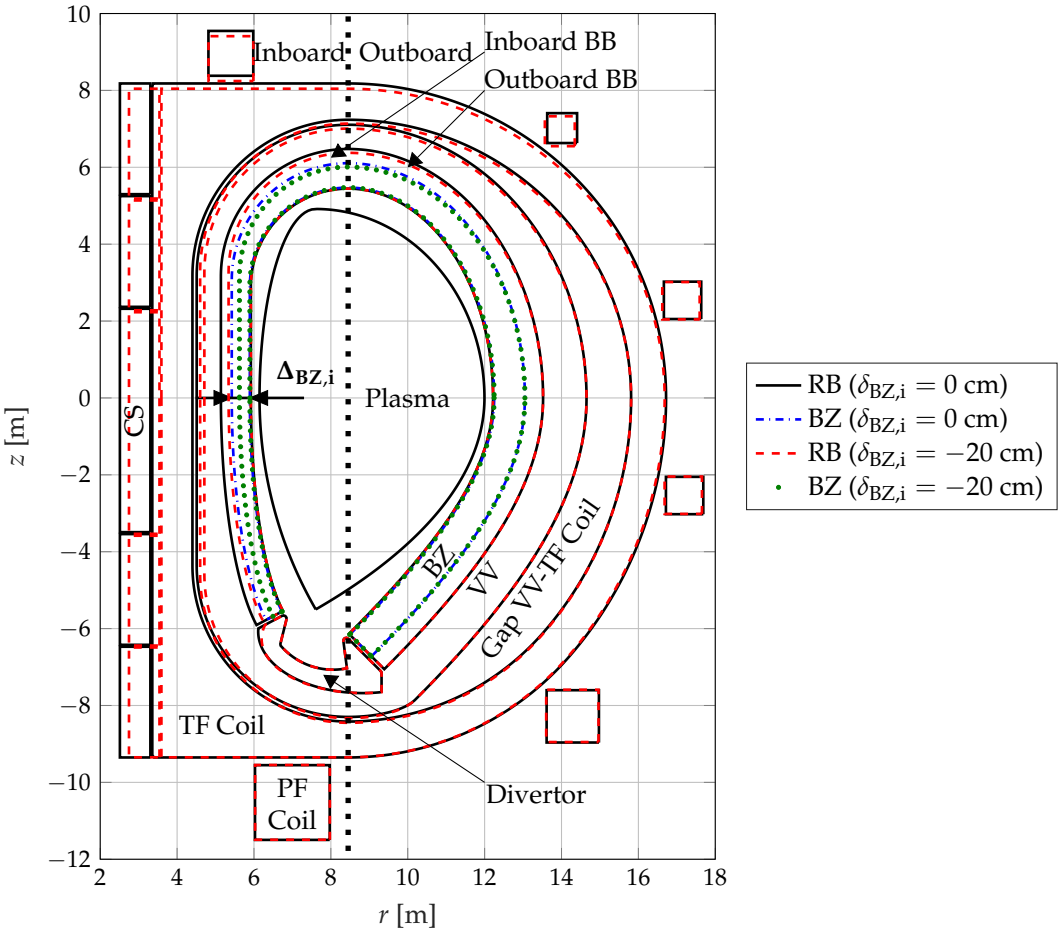

Figure 6.14.: Comparison of MIRA reactor builds (RB) related to two different values BZ inboard relative thickness $\delta_{BZ,i}$: 0 cm (solid contours) and -20 cm (dashed contours). The dashed-dotted and the dotted lines depict the BZ profiles associated with $\delta_{BZ,i} = 0$ cm and $\delta_{BZ,i} = -20$ cm.

These predictions are confirmed by the two sub-plots of Figure 6.15, depicting the poloidal flux at plasma breakdown Ψ_{bd} and at the plasma boundary during the EOF. Since l_i, c_{Ejima}, R_0 and I_p have been kept constant, the flux consumption during the plasma ramp-up remains unchanged and the plasma boundary flux at SOF $\Psi_{b,sof}$ (not reported) experiences the same incremental behaviour shown for Ψ_{bd}. Ψ_{bd} rises by nearly 13 Wb across the whole $\delta_{BZ,i}$ interval and, qualitatively, a very alike response (in modulus) takes place for $\Psi_{b,eof}$, which drops by approximately 40 Wb within the same gap of $\delta_{BZ,i}$.
The diverse growth rates of Ψ_{bd} and Ψ_b^{eof} are driven by three different aspects

- varying distance of the CS elements from the plasma vacuum chamber,
- change of the CS and PF coils operating currents (mostly for Ψ_{bd}) and
- alteration of the CS coil currents technological limits.

Applying the definition of Ψ and B_z in axisymmetric curvilinear coordinates to the CS elements, both scale quadratically with the radial extension of the CS. Thus, lessening the inboard width yields

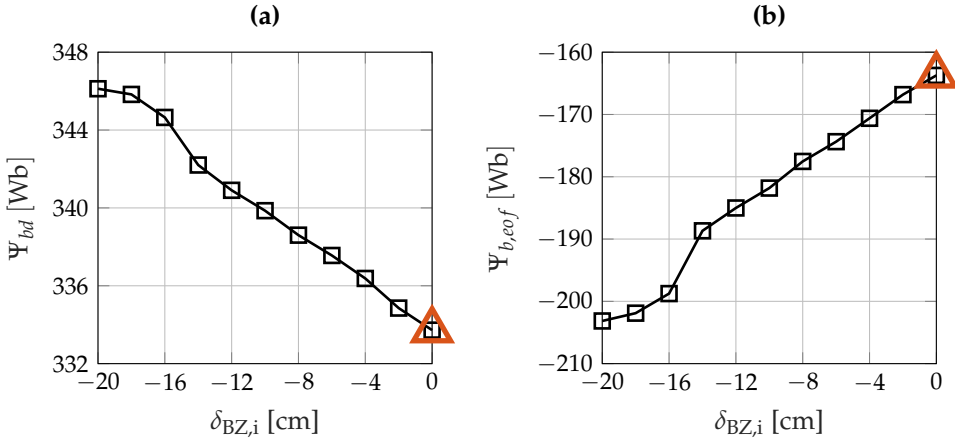

Figure 6.15.: Computed values of plasma poloidal magnetic flux properties for variations of the relative inboard BZ width $\delta_{BZ,i}$: (a) poloidal flux at plasma breakdown Ψ_b and (b) plasma boundary flux at EOF $\Psi_{b,eof}$. The triangles mark the reference DEMO1 2015 baseline modified to $l_i = 0.8$.

an enlarged CS radius leading to a quadratic gain of Ψ and B_z. On the other hand, they also depend linearly on total operating current, which exhibits also alterations for the scoped reactor design points. For the plasma breakdown pulse frame, some of the CS coils feature an increasing behaviour for a decreasing inboard BZ width, while some others decline (full set of CS and PF coils currents are shown in Figures F.3 and F.4). Overall, the total current in the CS stack $I_{c,CS} = \sum_k I_{c,CSk}$ has dropped from nearly 183 MA to 151 MA to accommodate the field and current coil limits, as well as the stray field in the breakdown area. This indicates an advantage in terms of operating conditions of the CS with larger margins with respect to the superconducting coils current limits.

If the quench stability limit overcomes that on the critical current (Equation 4.130) the allowable operating current is tied to the stored energy, hence on the self-inductance of the cable L_c. As a result, expanding the CS drops the total maximum current $I_c^{\max}$, as confirmed by the distributions of CS3U and CS2L coils current of Figure 6.16−a.
These two coils depict the two most extreme cases. Similar considerations can be found for the remaining CS stack elements and at the flat-top configurations too. The predominance of quench stability limit over the critical current limit takes place at $\delta_{BZ,i} = -8$ cm, as highlighted by the blue-dashed line of Figures 6.16−a and b. If $\delta_{BZ,i}$ is further reduced $I_c^{\max}$ drops linearly down to $\delta_{BZ,i} = -14$ cm, because of the growing effects tied to L_c. The change of falling rate between $\delta_{BZ,i} = -14$ cm to -16 cm, will be discussed shortly further in this section.
Combining the coil operating currents and peak magnetic field profiles alters the solution from a field-constrained to current-constrained problem. This transition appears at $\delta_{BZ,i} = -14$ cm, where the $B_{\max}$ upper bound stops from being reached and the $I_c^{\max}$ one drives the CS coil current combination instead. Accordingly, the operating currents $I_{c,CS3U}$ and $I_{c,CS2L}$ perfectly match the related upper limits, down to the lower end of the $\delta_{BZ,i}$. The positive flux gains from operating with a closer CS are partially cancelled by the smaller operating currents, justifying the diminishing growth and fall rates of Ψ_{bd} and $\Psi_{b,eof}$ for $\delta_{BZ,i} \leq -16$ cm.

The change of slope of $I_c^{\max}$ taking place at $\delta_{BZ,i} = -14$ cm contains important additional design insights. Pushing the CS inwards forces the TF coil as well to come closer to the plasma. Since the parametric scan has been performed keeping B_t fixed to the calculated baseline value, the total operating current $I_{c,TFC}$ does not experience any deviation from its reference amplitude.

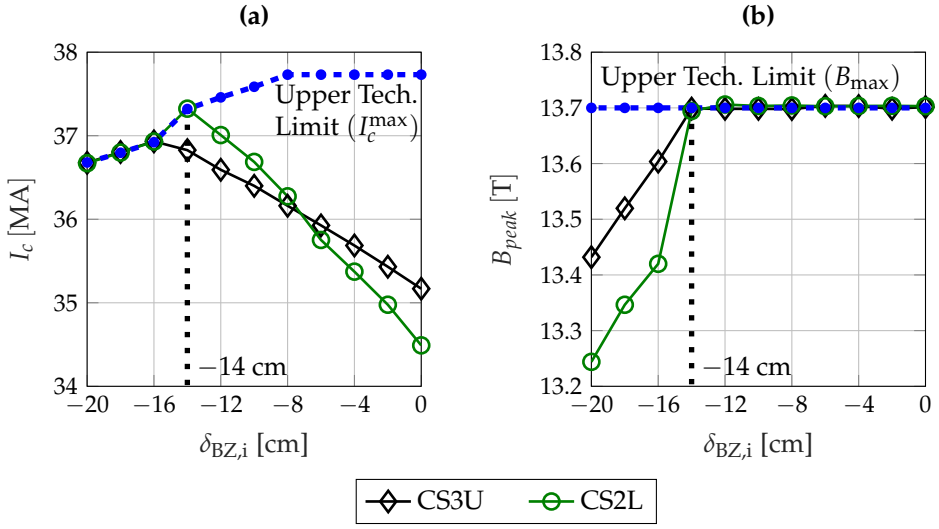

Figure 6.16.: Evaluated distribution of total/maximum operating current $I_c / I_c^{\max}$ (a) and peak/maximum magnetic field $B_{peak} / B_{\max}$ (b) for variations of the relative inboard BZ thickness $\delta_{BZ,i}$ and for different CS coils.

Hence, the total number of cable windings N_{turn} remains unaltered. However, the inward radial dislocation of the TF coil inboard leg provoke a modification to the inner and the outer WP's number of layers N_l and of turns per layer N_{tpl} configurations engaged by the coil packing algorithm. Due to the wedging shape of the steel casing the whole inboard WP gains space in toroidal direction to guarantee the minimum case toroidal thickness (see Figure 6.17 and Table 6.1).

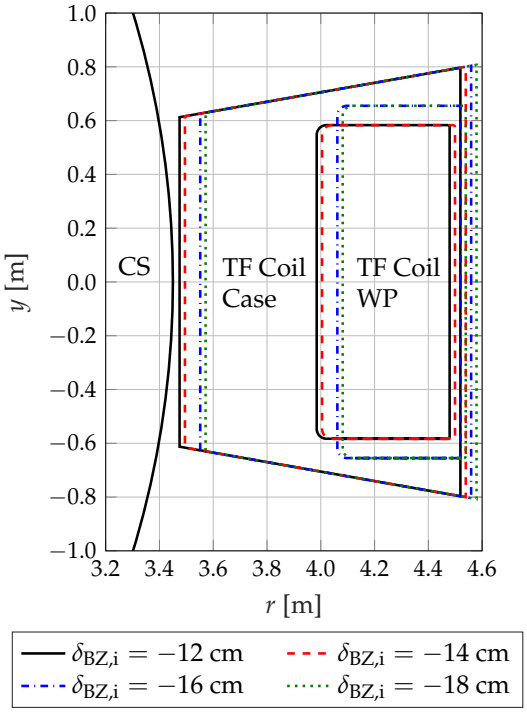

Figure 6.17.: Cross-sectional view of the DEMO baseline's TF coil case for different relative inboard BZ thicknesses $\delta_{BZ,i}$.

$\delta_{\mathrm{BZ,i}}$ [cm]	N_{turn} [-]	$N_{l,I}$ [-]	$N_{tpl,I}$ [-]	$N_{l,O}$ [-]	$N_{tpl,O}$ [-]
-12	196	16	7	14	6
-14	196	16	7	14	6
-16	196	18	7	14	5
-18	196	18	7	14	5

Table 6.1.: TF coil cable winding layouts for different relative inboard BZ thicknesses $\delta_{\mathrm{BZ,i}}$.

When advancing from $\delta_{\mathrm{BZ,i}} = -14$ cm to $\delta_{\mathrm{BZ,i}} = -16$ cm the total number of turns N_{turn} is achieved with an outer turn per layer less and two inner layers more, i.e. one on the upper part ($y > 0$) and the other one on the lower part. Ultimately, this implies a smaller radial width δr_{wp} and a larger toroidal width δy_{wp} of the WP, with an extra δr_{turn} inward shift of the CS towards the vacuum chamber approximately around 5 cm. For constant N_{turn}, the combination of layer and turns per layer faces the aforementioned transition, with $N_{l,i}$ gaining two elements and $N_{tpl,O}$ loosing a turn per layer for $\delta_{BZ,i}$ decreasing from -14 to -16 cm.

The combined gains of poloidal magnetic flux available at plasma flat-top from Ψ_{bd} (equivalently obtained for $\Psi_{b,sof}$) and of $\Psi_{b,eof}$ culminate into a beneficial gain in terms of τ_{flat} and hence of τ_{burn} (see Figure 6.18).

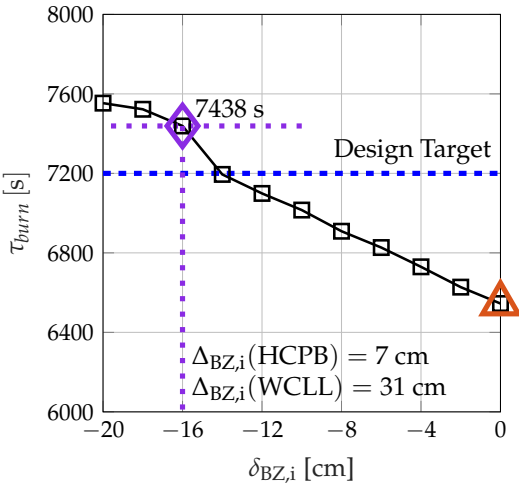

Figure 6.18.: Calculated evolution of plasma burn time τ_{burn} for variations of the relative inboard BZ width $\delta_{\mathrm{BZ,i}}$. The orange triangle marks the reference DEMO1 2015 baseline modified to $l_i = 0.8$. The blue violet diamond marker denotes the largest BZ inboard thickness design point complying with the two-hour τ_{burn} design target.

The fulfilment of the imposed design targets occurs at $\tau_{burn} = 7438$ s and can be finally reached for a BZ radial inboard thickness reduction of 16 cm, as highlighted by the blue violet diamond marker. This denotes a newly revisited DEMO design point coping with the q_0, $\delta_{tf,\max}$ and τ_{burn} operational limits and design targets, found not in line with their upper and lower bounds. To this BZ configuration correspond different $\Delta_{\mathrm{BZ,i}}$ values for HCPB and WCLL blankets, i.e. 7 and 31 cm, respectively. A further growth is achieved going down to $\delta_{\mathrm{BZ,i}} = -20$ cm, with τ_{burn} around 7500 s.
In case of HCPB, questions might arise on the engineering feasibility of such a small BZ thickness with respect to heat recovery and primary and secondary stress issues. However, these go beyond the goals of this parametric study, intended to characterize the sensitivity on other key global design elements, including τ_{burn}.

Varying the inboard BZ thickness impacts the geometric and cabling layout of the TF coils, inducing modifications to the coil electromagnetic properties. If the inboard leg alters the conducting cross section and its radial locations, the spatial magnetic field distribution features other peak values, maximum ripple, Lorentz force and stored energy.
Keeping B_t fixed to the calculated baseline value (Table 5.12), a radial shift of the inboard TF coil leg towards the plasma leads to an increase of its radial position, hence to a reduction of the peak magnetic field $B_{peak,TFC}$. Similar considerations can be made for the net inward force $F_{x,TFC}$ and for the stored magnetic energy $E_{c,TFC}$, both declining due to reduced toroidal fields and total TF coil volume. The situations on the peak field $B_{peak,TFC}$ and $E_{c,TFC}$ is displayed on Figure 6.19−a and b.

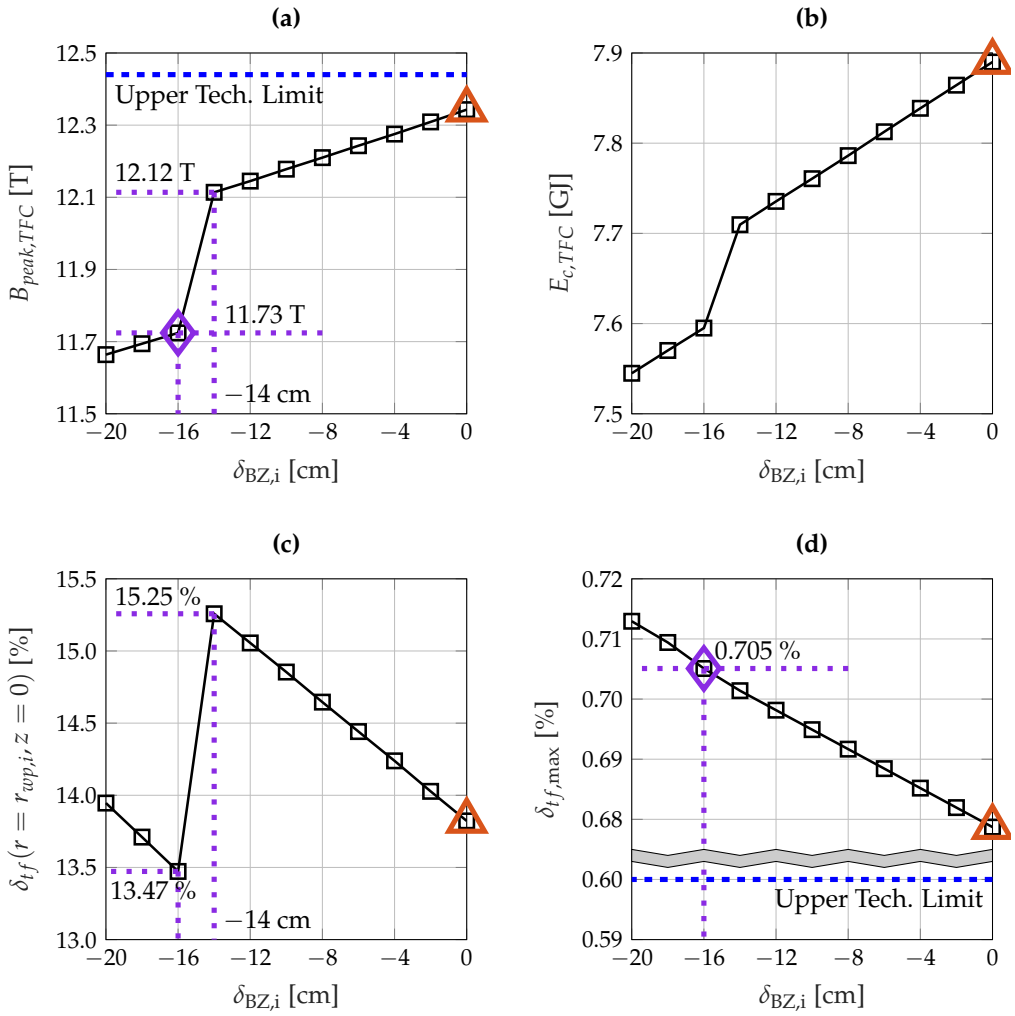

Figure 6.19.: Computed distributions of TF coil electromagnetic parameters for variations of the relative inboard BZ width $\delta_{BZ,i}$: (a) peak magnetic field $B_{peak,TFC}$, (b) stored magnetic energy $E_{c,TFC}$, (c) TF ripple δ_{tf} at the inner WP inboard poloidal location $(r = r_{wp,i}, z = 0)$ and (d) maximum TF ripple at plasma separatrix $\delta_{tf,\max}$. The triangle marks the reference DEMO1 2015 baseline modified to $l_i = 0.8$. The diamond marker denotes the largest BZ inboard thickness design point complying with the two-hour τ_{burn} design target.

Both appear to fall linearly in the examined $\delta_{BZ,i}$ and face a deflection at $\delta_{BZ,i} = -14$ cm, due to the modification of the WP winding scheme. A 4.3 % drop is observed for the global decay of $E_{c,TFC}$, hence of the dump voltage V_{dump} too.

Between -14 cm and -16 cm of $\delta_{\mathrm{BZ,i}}$ the ripple effects derived from the changing inboard leg position and conducting cross section play a central role. To elucidate such aspects δ_{tf} has been calculated on the inboard side of the inner TF coil WP, precisely at the radial/axial mid-equatorial plane location $r = r_{wp,i}$ and $z = 0$. The radial position $r_{wp,i}$ is illustrated in the TF coil inboard leg sketch of Figure 4.10. Beginning from the baseline configuration, δ_{tf} rises because of the wider toroidal opening between the TF coil inboard legs attributed to the increasing radial extensions. As δ_{tf} approaches the winding scheme transition point, a drastic collapse takes place in favour of toroidally-tighter winding packs, driven by the different winding arrangement. This pronounced shift of δ_{tf} explains the sharp deflection of $B_{peak,TFC}$ in the $[-16, -14]$ cm range of $\delta_{\mathrm{BZ,i}}$. The ripple effects associated with the inboard leg characteristics are softly experienced also on the plasma separatrix, whose maximum value $\delta_{tf,\max}$ has been found to linearly grow up to 0.705 %, i.e. $+4.4$ % from the baseline (see Figure 6.19−d). This denotes an enhanced distance from the upper 0.6 % maximum ripple upper limit, thus action must be taken acting directly on the outboard TF coil leg, as illustrated in the next section.

Analogous outcomes are observed to the in-plane radial inward and vertical separating forces, $F_{v,TFC}$ and out-of-plane bending force $F_{b,TFC}$, as illustrated in Figure 6.20.

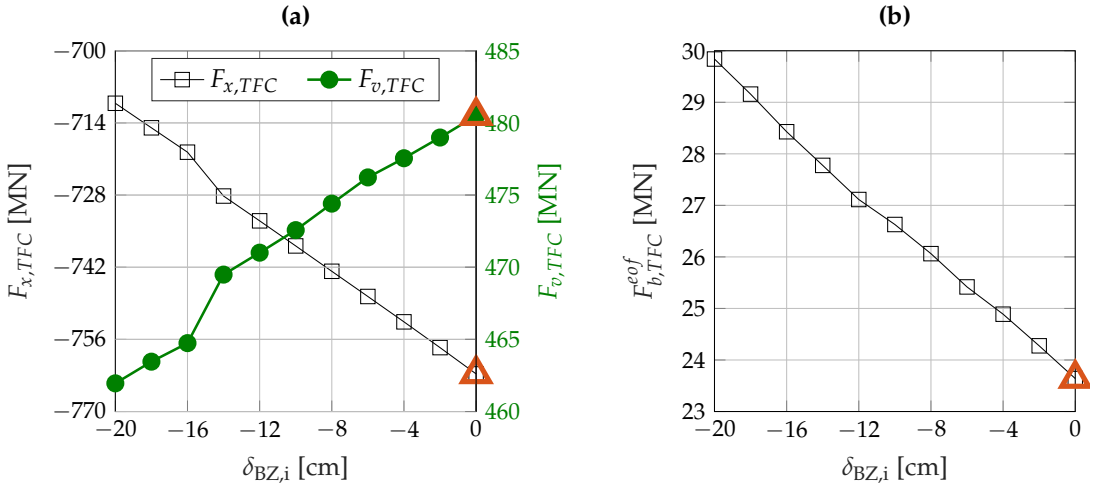

Figure 6.20.: Calculated values of TF coils total Lorentz parameters for variations of the relative inboard breeding zone thickness $\delta_{\mathrm{BZ,i}}$: (a) in-plane forces, given by inward net Lorentz force $F_{x,TFC}$ and vertical separating force $F_{v,TFC}$ and (b) out-of-plane bending force $F^{eof}_{b,TFC}$, calculated at plasma EOF. The triangles mark the reference DEMO1 2015 baseline modified to $l_i = 0.8$.

$F_{x,TFC}$ drops by nearly 52 MN for reduced $\delta_{\mathrm{BZ,i}}$, corresponding to approximately 7 % of the baseline design point. $F_{v,TFC}$ exhibits a very similar declining behaviour but with smaller decay ($\approx$ 3.7 %), due to the less important perturbations of B_ϕ in the top and the bottom regions of the coil. While $F_{x,TFC}$ and $F_{v,TFC}$ are conditioned by the modified B_ϕ regimes and WP volumes, $F_{b,TFC}$ is purely driven by the radial and vertical field B_r and B_z. The poloidal field is directly influenced by the toroidal currents derived from the plasma scenario model, which adapt itself to the different CS radial position governed by the BZ inboard width. The closer distance of the CS to the plasma and to the outboard TF coil leg (where the volumetric out-of-plane forces are larger), together with the calculated PF/CS coils currents features larger poloidal field, hence bigger bending forces.

The radial cut of the BZ domain has feedbacks to the neutronics as tritium breeding, neutron shielding and heat deposition. The reduction of the breeding zone is effectuated in the outer BB

region, where lower neutron flux densities and lower neutron energies are present. Therefore, the associated tritium breeding and nuclear heating contributions are much smaller than those obtained from the inner BZ region facing the plasma. Since HCPB and WCLL blankets rely on heterogeneous BZ thicknesses and breeding/multiplying materials, their sensitivities on the neutronic blanket parameters are different for both solutions. Furthermore, taking off BZ volume from the inboard side of the reactor enhances the neutron and gamma fluxes density in the vacuum vessel and the TF coils. This has important implications in the nuclear heating deposition and on the VV and TF coil radiation shielding criteria.

An important remark to make on the neutronic studies performed within frame of this parametric scan is about the prudential considerations which one shall take in evaluating the upcoming results, objectively and fairly. This sensitivity study was not meant to make a blind comparison on the nuclear performances of the HCPB and WCLL blanket concepts, for a very simple reason. The major reference baseline input specifications adopted for the system analyses rely on the HCPB and the WCLL DEMO 2015 blanket designs, which have been optimized on fixed inboard and outboard overall BB widths. The repartition of FW, BZ and manifold areas have emerged from the union of aspects going beyond a simple neutronic characterization, such as thermal-hydraulics, structural mechanics, electromagnetic loads, etc. Thus, changing $\Delta_{BZ,i}$ represents a perturbation of such an equilibrium of influences, which then ceases to hold. Henceforth, the outcomes of the illustrated trends shall be taken as design guidelines for improving a DEMO design as a whole, rather than quantitative assessments of radiation transport parameters.

The calculated profiles of the TBR for variations of $\delta_{BZ,i}$ are illustrated in Figure 6.21 for HCPB and WCLL blanket designs.

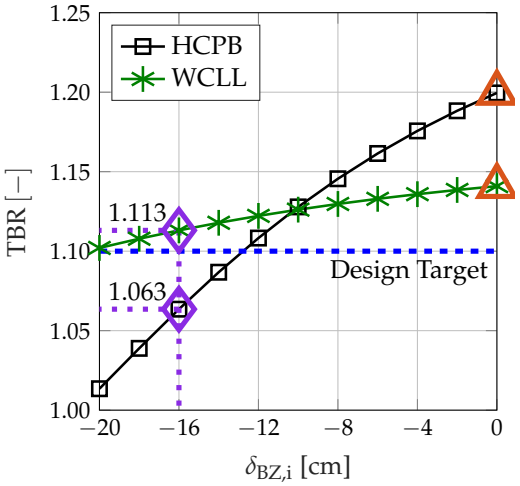

Figure 6.21.: Evaluated distribution of Tritium Breeding Ratio TBR for variations of the relative inboard BZ width $\delta_{BZ,i}$ and for two blanket concepts: HCPB (square marker line) and WCLL (asterisk marker line). The triangles mark the reference DEMO1 2015 baseline modified to $l_i = 0.8$. The diamond marker denotes the largest BZ inboard thickness situation complying with the two-hour τ_{burn} design target.

Both solutions features a decay of the TBR for the prescribed reduction of the inboard BZ radial domain. Because of the more favourable T breeding and neutron multiplications derived from Li_4SiO_4 and Be pebbles configuration the drop of the TBR in case of HCPB is larger than for the WCLL. The WCLL blanket still provides enough breeding material to cope with the 1.10 design target, unlike

the HCPB (see diamond markers).
In terms of global TBR sensitivity, the wide gap of relative TBR loss between HCPB and WCLL with respect to the variations of the BZ width has been confirmed by Pereslavtsev et al. [141], where some of the parameters affecting the TBR (e.g. steel fraction, ^{6}Li enrichment and FW thickness) have been investigated in details.

The calculated neutron radiation shielding outputs confirm the reduced shielding capabilities for all involved VV and TF coil reference local variables. The monitored parameters including their upper technological limits as peak nuclear volumetric heating $\mathcal{R}^{wp}_{heat,peak}$ at WP, fast neutron flux density $\Phi^{wp}_{fast,peak}$ at WP and peak displacement rate $\mathcal{R}^{vv}_{dpa,peak}$ at VV for the variations of $\delta_{\mathrm{BZ,i}}$ are visualized in Figure 6.22.

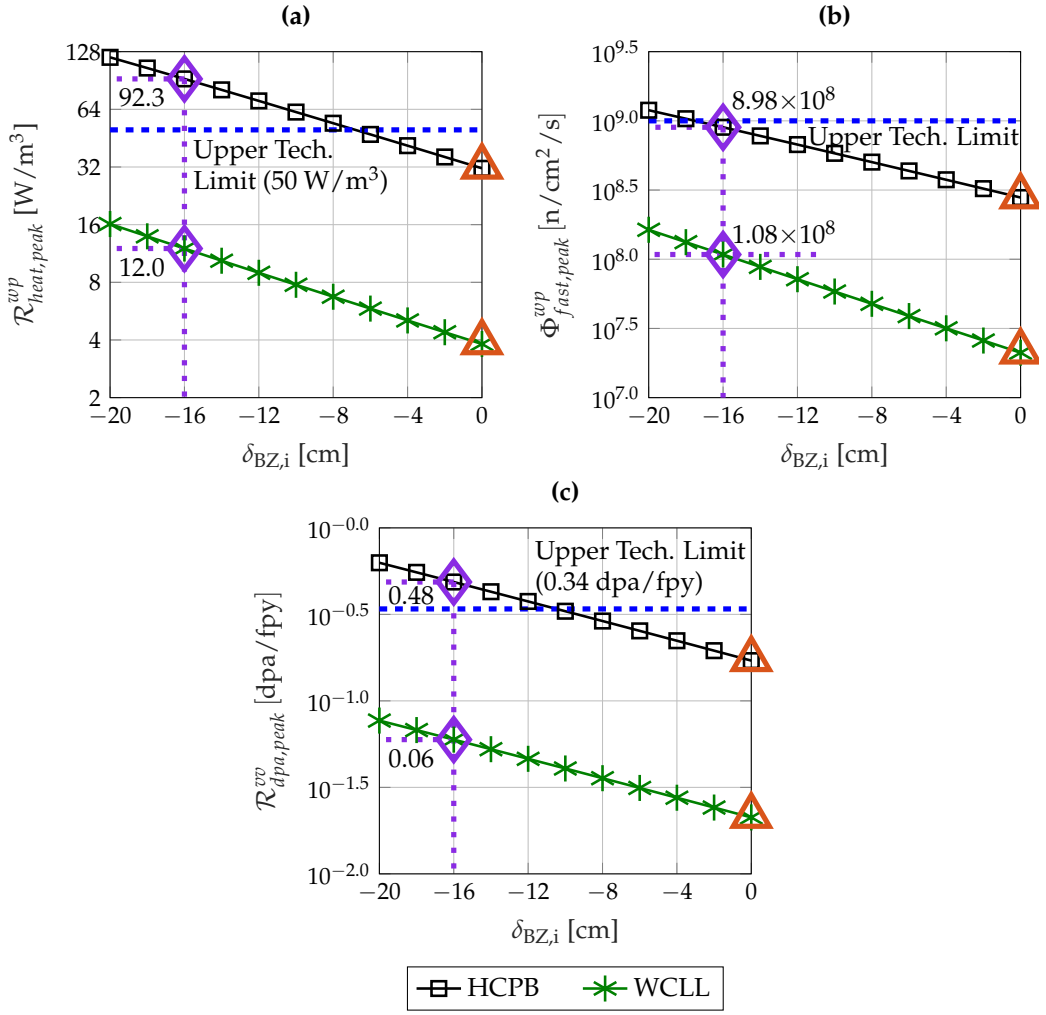

Figure 6.22.: Evaluated profiles of neutron radiation shielding parameters for variations of the relative inboard BZ width $\delta_{\mathrm{BZ,i}}$: (a) peak nuclear heating at TF coil winding pack $\mathcal{R}^{wp}_{heat,peak}$, (b) peak fast neutron flux density at TF coil winding pack $\Phi^{wp}_{fast,peak}$ and (c) peak dpa rate at VV $\mathcal{R}^{vv}_{dpa,peak}$. The triangles mark the reference DEMO1 2015 baseline modified to $l_i = 0.8$ and the diamond marker denotes the largest BZ inboard thickness situation complying with the two-hour τ_{burn} design target.

Since all shielding figures of merit span exponentially across several orders of magnitude (covering

both BB configurations), the lines are plotted in logarithmic scale. The greater neutron moderation and neutron adsorption capabilities of water compared to helium are visible in all reported curves, complying with all the imposed technological limits across the whole $\delta_{\mathrm{BZ,i}}$ range. As for the -16 cm $\delta_{\mathrm{BZ,i}}$ configuration, HCPB fails to match the volumetric heating and the dpa rate criteria and matches only the one on the fast neutron flux density.
In case of $\mathcal{R}^{wp}_{heat,peak}$ and $\mathcal{R}^{vv}_{dpa,peak}$, both HCPB and WCLL present rather similar growth rates, i.e. approximately 4 times and 3.6 times the baseline values, for $\delta_{BZ,i}$ spanning the whole examined range. Slightly different is the situation linked to $\Phi_{fast,peak}$, where the rise rate of the WCLL blanket has been found nearly three times larger than the HCPB's.
The different inclination the fast neutron flux density profiles between the two blankets are due to different neutron scattering and moderating capabilities, which are higher in the water/lead than the helium/beryllium mixture.

Removing breeding material provokes changes of the total nuclear energy deposition in the BZ and in the components radially placed outwards, in particular the blanket manifolds and VV. This is attributed to the combined effects of higher neutron flux densities and reduced volumes. The evaluated evolution of the nuclear heating in the BB and in the VV, R^{BB}_{heat} and R^{VV}_{heat}, for the imposed variations of $\Delta_{\mathrm{BZ,i}}$ are illustrated in Figure 6.23−a and b.

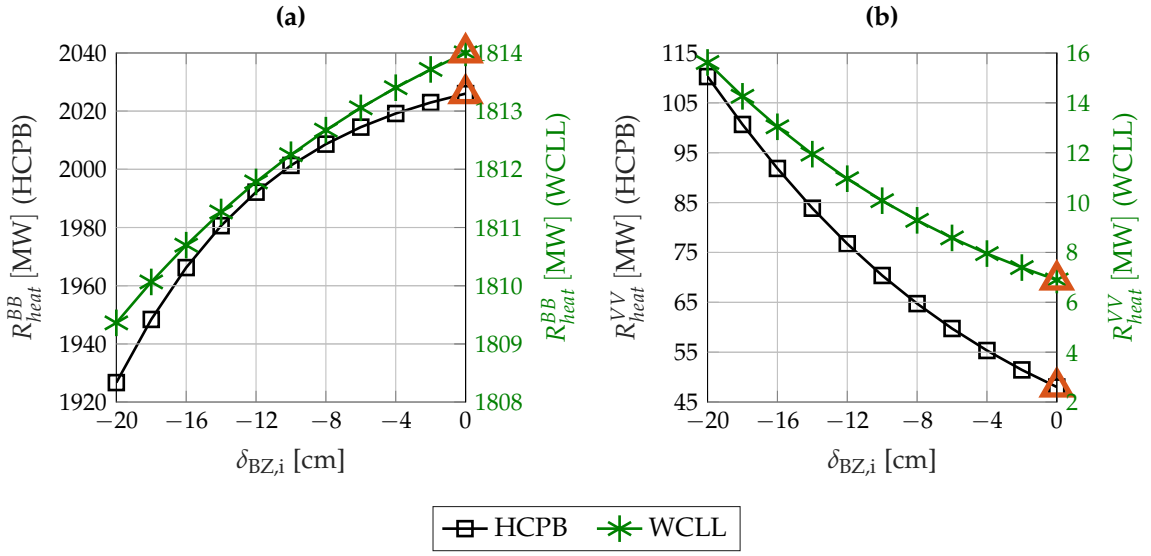

Figure 6.23.: Computed distribution of nuclear heating parameters for variations of the relative inboard BZ width $\delta_{\mathrm{BZ,i}}$: (a) total nuclear heating in the BB R^{BB}_{heat} and (b) total nuclear heating power in the VV R^{BB}_{heat}. The triangles mark the reference DEMO1 2015 baseline modified to $l_i = 0.8$.

The results show a larger sensitivity of HCPB, with a fall of R^{BB}_{heat} around 100 MW. The WCLL blanket does not largely suffer from the cut of inboard BZ, yielding around a 5 MW drop.
The growing conditions of R^{VV}_{heat} scaling up approximately by the same ratio ($\approx$ 2.3) throughout the entire $\delta_{\mathrm{BZ,i}}$ domain. In this case the volume of the VV remains fairly constant (except of minor poloidal effects), though the neutron flux density experiences a significant rise across the entire inboard domain, thereby leading to a rise of nuclear heating, both neutron and gamma-induced. In case of WCLL blanket, from the cumulative trend $R^{bz,i}_{heat}(r)$ of the NH calculated for the baseline's inboard BZ domain it has been verified that nearly 80 % of energy is deposited within the innermost 20 cm (out of 47) of innermost breeding zone, from the plasma outwards. As a result, the remaining 27 cm

are responsible only for the 20 %, providing a small contribution to the integral value and indicating a saturation behaviour of the NH against further increments of the radial width. Furthermore, the shrinking of the BZ implies higher neutron flux densities on the rear side, where the reduction is being performed. Accordingly, the diminishing of the NH is also partly compensated.
In case of HCPB the total BZ volume exploited more effectively, with the innermost 20 cm (out of 23) generating approximately 95 % of the total NH yield and with a steep cumulative curve at 100 % of the total heating rate. This indicates that the BZ reduction takes place in a very responsive region and explains the rather heterogeneous sensitivity of R^{BB}_{heat} to the variations of $\Delta_{\mathrm{BZ,i}}$ between the HCPB and the WCLL solutions.

Applying the definition of η_{gross} (Equation 4.146) to calculate $\dot{W}_{gross}$, the thermal powers $\dot{Q}_{BB}$, $\dot{Q}_{div}$ and $\dot{Q}_{VV}$ are energetically equivalent. But, from an exergetic standpoint they are not.
The thermal energy removed by the BB structures is a high grade heat contribution used in the PCS for electricity conversion. The heat generated in the double steel shell VV structures, instead, is exhausted by a low temperature coolant (e.g. water at 200 °C), used to pre-heat the secondary coolant in the PCS and not directly exploited for mechanical work purposes. Hence, since the plant power balance model currently implemented in MIRA does not reproduce the exergetic difference between BB and the VV thermal power the gross electric power has been calculated by conservatively keeping $\dot{Q}_{VV}$ fixed to the baseline value (48.1 MW for HCPB and 6.9 MW for WCLL). Therefore, the distribution of $\dot{Q}_{th}$ uniquely attains to that of $\dot{Q}_{BB}$, hence of R^{BB}_{heat}. Similarly, the gross and the recirculating electric powers $\dot{W}_{gross}$ and $\dot{W}_{rec}$ depend both on $\dot{Q}_{th}$ and its behaviour, as shown in Figure 6.24−a and b.

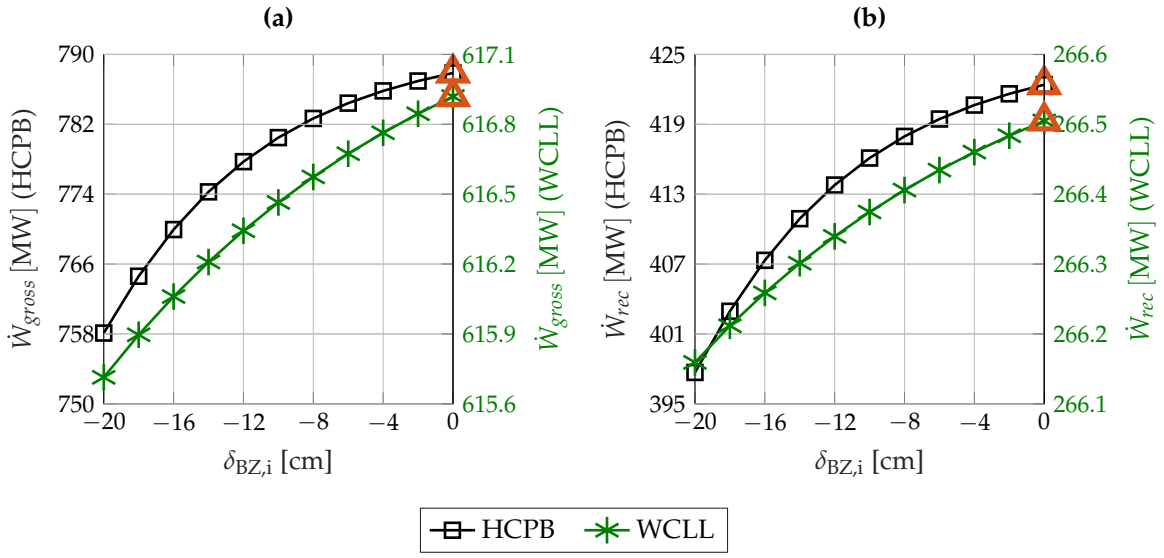

Figure 6.24.: Calculated values of plant power balance parameters for variations of the relative inboard BZ width $\delta_{\mathrm{BZ,i}}$: (a) gross electric power $\dot{W}_{gross}$ and (b) total recirculating power $\dot{W}_{rec}$. The triangles mark the reference DEMO1 2015 baseline modified to $l_i = 0.8$.

Both variables exhibit a similar behaviour with a marginal change compared to the baseline solution. $\dot{W}_{gross}$ linearly scales to $\dot{Q}_{th}$ and to η_{gross}, fixed to 26 % for WCLL and 30 % for HCPB. As a result, the nearly 100 MW thermal power lost in the BZ is equivalent to approximately 30 MW less of $\dot{W}_{gross}$ for the helium-cooled blanket. For the water-cooled blanket only 1.6 MW electric power is subtracted from $\dot{W}_{gross}$ upon the 5 MW diminution in the BZ.
The recirculating power benefits from the cubic dependency of $\dot{W}_{pump}$ on $\dot{Q}_{th}$, mitigating the cutting

effects on $\dot{W}_{gross}$. For WCLL, very low and negligible variations have been identified for $\dot{W}_{rec}$, around 0.5 MW. In case of HCPB the 20 MW drop of $\dot{W}_{rec}$ is primarily linked to $\dot{W}_{pump}$, being for helium-cooled blanket concepts a rather sensitive electric power consumption.

The evolution of the net electric power $\dot{W}_{net}$ for the two BB layouts are deduced straightforward by subtracting $\dot{W}_{rec}$ from $\dot{W}_{gross}$ and are visualized in Figure 6.25.

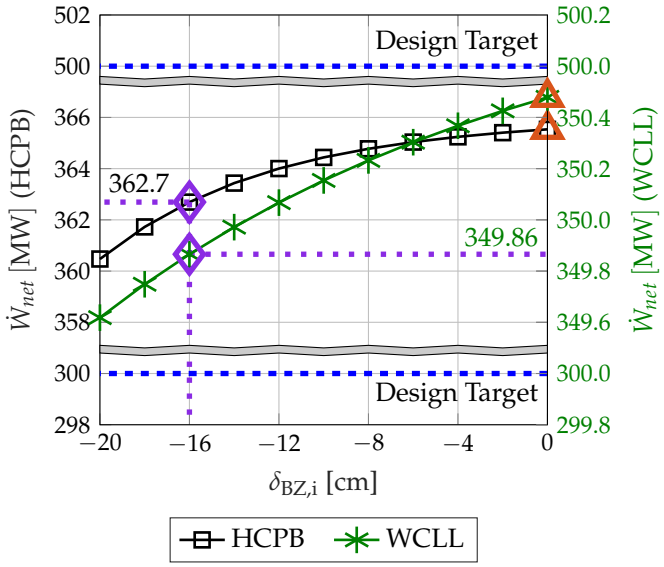

Figure 6.25.: Calculated net electric power $\dot{W}_{net}$ for variations of the relative inboard BZ width $\delta_{BZ,i}$. The orange triangles mark the reference DEMO1 2015 baseline modified to $l_i = 0.8$. The blue violet diamond marker denotes the largest BZ inboard thickness situation complying with the two-hour τ_{burn} design target.

Both blankets do not experience relevant changes of $\dot{W}_{net}$ from the different inboard BZ width offsets. The corresponding drops across the $\delta_{BZ,i}$ have been found around 6 MW for the helium-cooled BB and 0.8 MW for the WCLL BB. The HCPB blanket benefits more vividly from the more pronounced fall of the pumping power $\dot{W}_{pump}$, hence attenuating the effects derived from R_{heat}. In the WCLL the consequences of the BZ reduction are marginal within the BZ already, thereby generating effects hardly apprised from the BoP side.

This parametric study has produced a revisited DEMO baseline 2015, henceforth referred to as DEMO baseline. In addition to the abatement of l_i to 0.8, the BZ and BB inboard widths are being collapsed by 16 cm. This design modification has offered a wide spectrum of improvements, including softer loading and operating conditions in the TF coils and a better exploitation of the breeding blanket materials. Above all, the achievement of the two-hour τ_{burn} requirement represents the major accomplishment. However, the $\delta_{tf,\max}$ upper limit has further suffered this design change and it still denotes a violated constraint, to be addressed in the next section.

6.3. Parametric Scan of the Outboard VV-TFC Gap Thickness

A final study aims to quantify the influence of the TF coil geometric profile on design elements. Due to the violation of maximum TF ripple $\delta_{tf,\max}$ limit in the DEMO 2015 MIRA analysis further

pronounced by the inboard BZ reduction, the radial extension of the outboard TF coil leg has been identified as the most influencing factor responsible for the design nonconformity. In particular, the control variable used in the MIRA modelling frame is represented by the outboard width of the gap between the VV and the TF coil, $\Delta_{\mathrm{VV-TFC,o}}$ (see Figure 6.26).

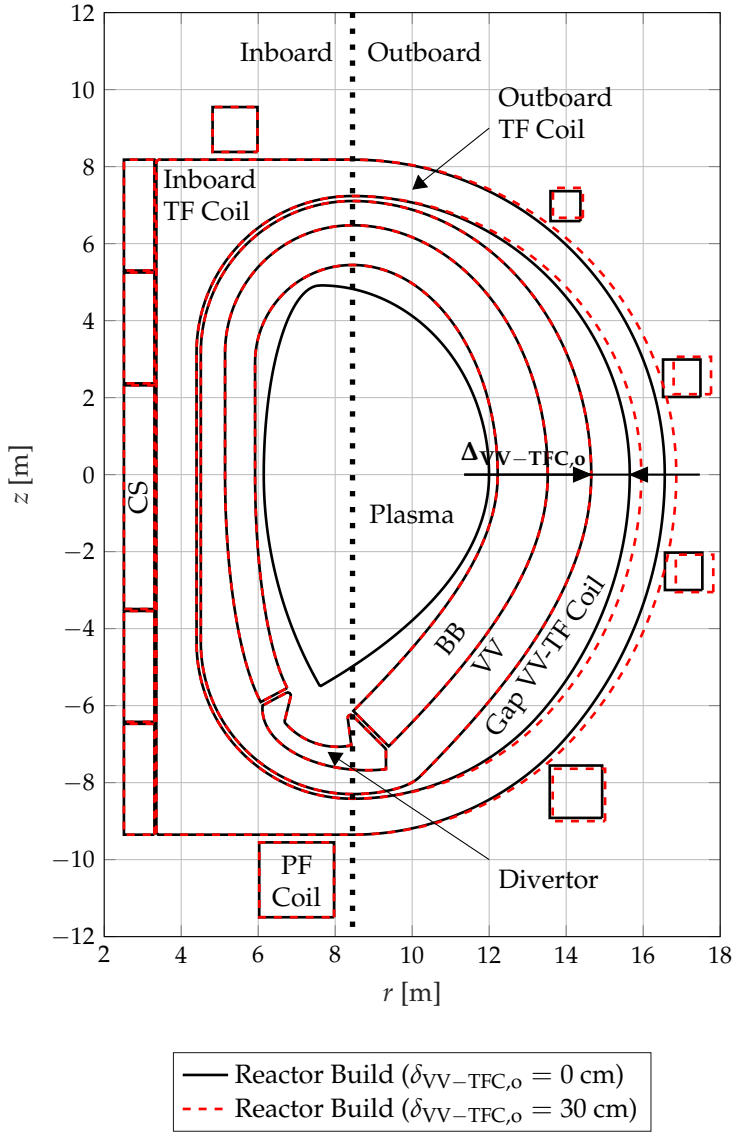

Figure 6.26.: Comparison of MIRA reactor builds related to two different values VV-TFC gap outboard relative thickness $\delta_{\mathrm{VV-TFC,o}}$: 0 cm (solid-black contours) and 30 cm (red-dashed contours).

In this parametric study $\delta_{\mathrm{VV-TFC,o}}$ has been varied from zero (i.e. the baseline point) to 30 cm, with $\Delta^{*}_{\mathrm{VV-TFC,o}} = 98$ cm. Each analysed point is spaced by a 2 cm increment and the $\delta_{\mathrm{VV-TFC,o}}$ interval upper limit is wide enough to observe the most relevant aspects. The reactor builds linked to lower and the upper bounds of $\delta_{\mathrm{VV-TFC,o}}$ are depicted in Figure 6.26 as per solid and dashed lines.

The calculated values of $\delta_{tf,\mathrm{max}}$ and τ_{burn} for the increment of $\delta_{\mathrm{VV-TFC,o}}$ are visualized in Figure 6.27−a and b. From the reference modified DEMO baseline (marked with a diamond) down to the widest TF coil outboard leg solution $\delta_{\mathrm{VV-TFC,o}} = 30$ cm, the peak TF ripple dumps approximately by 20 %. The fulfilment of the upper TF ripple limit criterion can be met for a $\Delta_{\mathrm{VV-TFC,o}}$

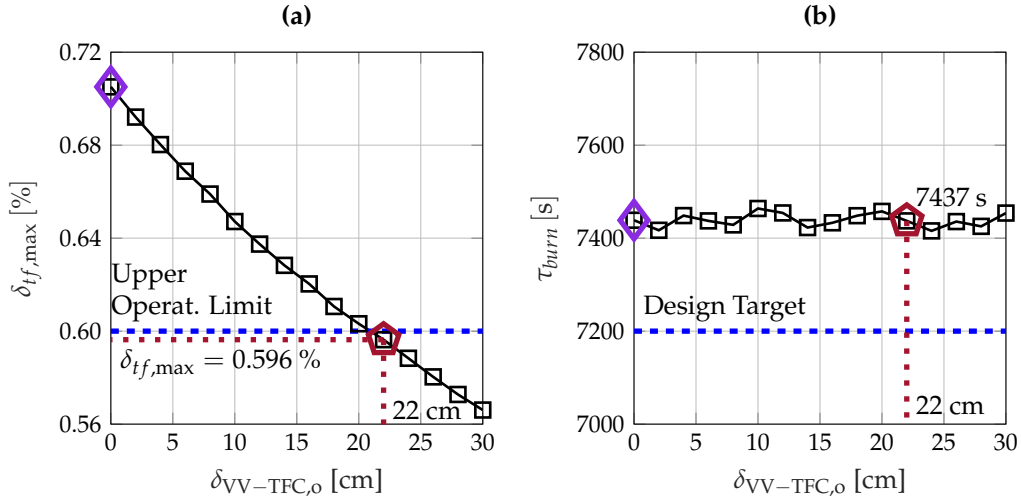

Figure 6.27.: Computed distribution of the maximum TF ripple $\delta_{tf,\max}$ (a) and of the burn time τ_{burn} (b) for incremental variations $\delta_{\mathrm{VV-TFC,o}}$ of the VV-TF coil gap outboard thickness $\Delta_{\mathrm{VV-TFC,o}}$. The blue violet diamonds mark the reference DEMO1 2015 baseline modified to $l_i = 0.8$ and $\delta_{\mathrm{BZ,i}} = -16$ cm. The purple pentagon markers denote the smallest VV-TF inboard thickness design point complying with the $\delta_{tf,\max}$ operational limit.

widening of 22 cm, leading to a 0.596 % peak value. Exploring $\delta_{\mathrm{VV-TFC,o}}$ allows to trace the effects on the maximum TF ripple without significantly perturbing the surrounding components, i.e. the PF and CS coils. The two mid-equatorial outer coils PF3 and PF4 are those which tangibly suffer from the imposed radial shift of the outboard TF coil leg. Broadening their average radius leads to a rise of their self-inductance, hence to a decrease of their maximum allowable current (quench stability limit in Equation 4.130). However, these two coils feature large margins from their admissible operating values, both at SOF and EOF. Moreover, if their radial mass center $r_m = 1700$ cm are pushed outwards up to 30 cm, the influence on the coil self-inductance appears to negligibly low, i.e. 2 %. In turn, their maximum achievable current remains almost constant. Hence, the PF/CS coils inductive and shaping capabilities remain approximately unaltered and no substantial impacts of $\delta_{\mathrm{VV-TFC,o}}$ on $\Psi_{b,eof}$ and on τ_{burn} are observed, as shown in Figure 6.27−b. In light of this situation, the two-hour design target keeps remaining satisfied.

Changing the geometry of the TF coil has a feedback on the TF coil operating conditions, scoping current, force and energy. Shaping the TF coil towards larger radial outboard extensions leads to larger coil volumes, hence to bigger total integral Lorentz forces. Moreover, the toroidal magnetic flux linked to the enlarged cross-sectional coil area proportionally increases as the TF coil self-inductance.
This is confirmed by the distributions of net inward radial force $F_{x,TFC}$, vertical separating force $F_{v,TFC}$ and bending out-of-plane force $F^{eof}_{b,TFC}$ (taken at EOF) and dump voltage V_{dump} shown in Figures 6.28−a to d. All Lorentz force components exhibit a growing behaviour. The amplitude is relatively small for $F_{x,TFC}$ and $F_{v,TFC}$, with around 6 and 7 MN, corresponding to the 0.7 and the 1.04 %, respectively. $F_{b,TFC}$ experiences a similar jump in amplitude, though much larger in relation to the reference design point, i.e. +16 %.
V_{dump} is proportional to the growth rate of the coil self-inductance L_c, whose slope gradually goes down. Sizing up the coil radially outwards yields a wider opening of the coil in toroidal direction associated with a loss of toroidal flux. This leads to a saturation of L_c, hence of V_{dump}. Nevertheless,

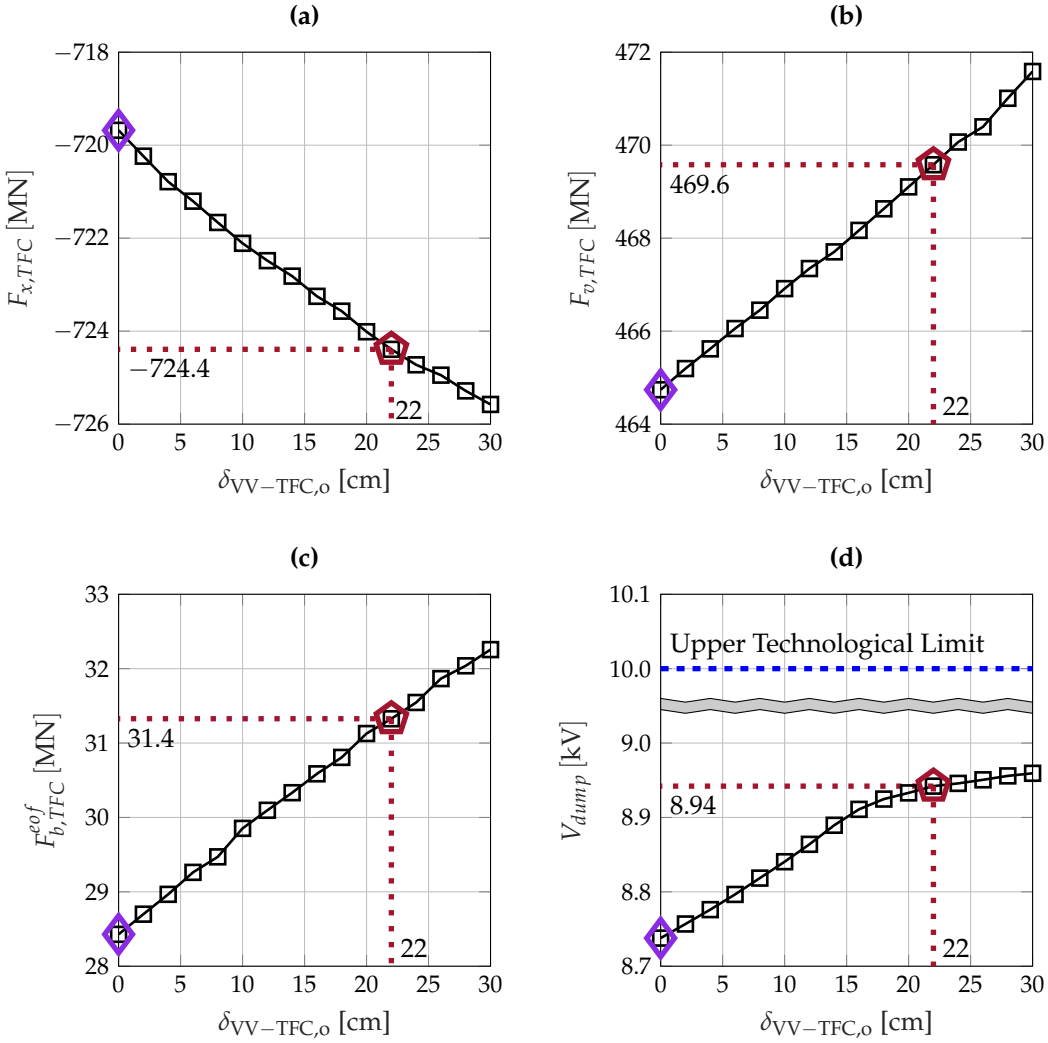

Figure 6.28.: Calculated values of TF coil Lorentz force components and engineering properties for incremental variations $\delta_{VV-TFC,o}$ of the VV-TF coil gap outboard thickness $\Delta_{VV-TFC,o}$: (a) net inward centering force $F_{x,TFC}$, (b) vertical separatrix force $F_{v,TFC}$, (c) net bending out-of-plane force and (d) coil dump voltage V_{dump}. The diamonds mark the reference DEMO1 2015 baseline modified to $l_i = 0.8$ and $\delta_{BZ,i} = -16$ cm. The pentagon markers denote the smallest VV-TF inboard thickness design point complying with the $\delta_{tf,max}$ operational limit.

the safety of the TF coil in relation to the quench stability is never at risk in the examined spectrum of TF coil geometries.

Despite of the rise of the mechanical loads and superconducting criteria, the obtained values have been found smaller as in the original MIRA baseline multiphysics approach (Table 5.22). This is valid for all parameters except for $F_{b,TFC}$, which globally grows from 23.64 to 31.32 MN in the final DEMO 2015 design point marked by a purple pentagon. However, compared to the in-plane force components, $F_{b,TFC}$ indicates a much smaller contribution to the total Lorentz force and should not represent a large concern in terms of induced stresses. Since the in-vessel and the VV radial build has not been affected by the introduced TF coil modifications and also the outboard leg only marginally impacts on the global neutron flux spectrum, no relevant influence has been noted on the neutron and gamma transport figures, nor on the plant power balance modelling part.

Based on this parametric study, a revisited DEMO 2015 baseline fully consistent with the imposed operational and technological limits and the design targets has been achieved. This relies on a reduced plasma internal inductance (from 1.155 to 0.8), a reduced inboard BB width (from 78 to 62 cm) and a larger VV-TF coil inter-gap $\Delta_{\mathrm{VV-TFC,o}}$ (from 98 to 120 cm).
The MIRA multiphysics reactor analysis approach can drive the future DEMO designs towards more consolidated assumptions. The DEMO 2015 baseline analysis shed light onto some of the modelling simplifications affecting the presently available system codes, which eventually affect the choices made by the designers of the individual components, too. A propagation of assumptions going against the designed-oriented guidelines, identified by the reported parametric scans, can be highlighted by comparing the revisited DEMO 2015 baseline to the 2017's [200] (see Table 6.2). The major system features of DEMO 2015 baseline are reported including the revised MIRA DEMO 2015 baseline and its original version issued by PROCESS.

Description (Symbol) [Unit]	DEMO 2015 MIRA	DEMO 2015 PROCESS	DEMO 2017 PROCESS
Plasma major radius (R_0) [m]	9.072	9.072	8.938
Plasma aspect ratio (A) [-]	3.1	3.1	3.1
Plasma elongation at separatrix (κ_X) [-]	1.779	1.781	1.848
Plasma triangularity at separatrix (δ_X) [-]	0.454	0.500	0.500
Plasma volume (V_p) [m^3]	2468	2502	2466
Safety factor at magnetic axis (q_0)	1.04	1.00	1.00
Toroidal field at plasma center (B_t) [T]	5.493	5.667	4.890
Plasma current (I_p) [MA]	19.261	19.600	19.075
Plasma internal inductance (l_i) [-]	0.800	1.155	1.096
Fusion power (P_{fus}) [MW]	2037	2037	1998
Additional heating power (P_{add}) [MW]	50	50	50
Total radiation power (P_{rad}) [MW]	304.1	305.5	275.2
Power transported across separatrix (P_{sep}) [MW]	154.1	154.1	156.4
BB ib/ob thickness $(\Delta_{\mathrm{BB,i/o}})$ [cm]	62/130	78/130	78/100
VV ib/ob thickness $(\Delta_{\mathrm{VV,i/o}})$ [cm]	62/112	62/112	60/110
VV-TFC gap ib/ob thickness $(\Delta_{\mathrm{VV-TFC,i/o}})$ [cm]	12/120	12/98	20/194
TFC ib/ob thickness $(\Delta_{\mathrm{TFC,i/o}})$ [cm]	100/87	105/105	96/96
TF coil current $(I_{c,TFC})$ [MA]	13.84	14.28	13.65
Number of TF coils (N_{TFC}) [-]	18	18	16
Burn time (τ_{burn}) [s]	7438	7200	7200
Tritium Breeding Ratio (TBR) [-]	1.113	n.a.	n.a.
Total thermal power $(\dot{Q}_{th})$ [MW]	2372	2436	2432
Gross electric efficiency (η_{gross}) [%]	26.0	37.5	37.5
Gross electric power $(\dot{W}_{gross})$ [MW]	616.1	913.0	987.1
Net electric power $(\dot{W}_{net})$ [MW]	349.9	500.0	500.0

Table 6.2.: Key features of the MIRA DEMO 2015 baseline and comparison to the reference 2015 and 2017 DEMO baselines issued by the PROCESS code.

The neutronic and the plant power balance-related results are listed assuming the WCLL blanket configuration. Additionally, the same set of parameters calculated for the DEMO 2017 baseline is reported aside. The newer DEMO design relies on similar geometric and power features, though based on two major modifications: a 30 cm reduction of the outboard BB thickness and of the number of reactor sector (or TF coil), from 18 to 16.

Based on observed implications of the inboard BB width and of challenges found to match the two-hour burn time requirement, a reduction of the outboard BB radial build appears in contrast with the modifications recommended by the parametric studies. Moreover, the l_i in the newer DEMO baseline (1.096) still presents a large amplitude, similarly to that of the 2015's. But, as shown in Figure 6.3, wide internal inductances imply small safety factor, thereby decreasing the plasma stability and yielding again the same issues on q_0 encountered in the l_i parametric study.

7. Summary and Outlook

To fill the gap between systems and the detailed transport and engineering codes the advanced system/design tool MIRA provides a refined and intermediate plant system analysis, with the primary goal of generating a more robust plant baseline.
The presently available fusion system codes attain to fairly simplified models, offering a spectrum of physics and engineering modelling solutions which can hardly cope with the theoretical and practical demands affecting such complex devices. As a result, the elaborated plasma physics simulation codes and engineering platforms suffer from the rudimentary state upon which the key design parameters are built in the presently available systems codes.

The largest share of the activities has been devoted to a substantial modelling campaign, tackling certain fusion research areas at a level of details so far unexplored within a system analysis environment. The efforts have been primarily devoted both to the development of physics and engineering system analysis elements.

An important milestone within the implemented physics modelling part is based on the solution to Grad-Shafranov static equilibrium problem in axisymmetric curvilinear coordinates system. By finding a magnetic configuration inside the confining region, positive aspects arise from establishing a consistency between plasma stored magnetic energy, pressure regime and stability, identified by the internal inductance l_i, poloidal plasma beta β_p and safety factor q_0. In the MIRA equilibrium module, the second order Grad-Shafranov partial differential equation is progressively solved such that the plasma toroidal current density $J_{\phi,p}$ fulfils also a set of requirements posed on l_i, β_p and q_0. This approach, being along the same line of presently conducted detailed plasma scenario analyses, exceeds in goals and sophistication any extent of equilibrium addressed in currently existing systems codes. For example, in fusion systems codes such as PROCESS and SYCOMORE q_0 is a fixed input parameter and l_i is calculated by means of simplified cylindrical plasma-based formulas.

The coupling between magnetic equilibrium and core plasma physics models represents an additional improvement of the MIRA multiphysics approach, due to the inter-dependences of the volume-averaged plasma density $\langle n_e \rangle$ and temperature $\langle T \rangle$ on the plasma magnetic flux profile. The core plasma physics module is characterized by the 0D core and mantle plasma power, particle and current balance laws, extracted from TREND system code. This physics modelling part has been complemented with a SOL/divertor physics sub-module for the evaluation of the peak heat fluxes on inner and outer divertor targets. The modelling frame is based on steady state power P_{sep} transported by charged particles across the separatrix through the SOL and depends on the magnetic configuration inside and outside the plasma separatrix.

MIRA provides a dedicated neutron and gamma transport model. This includes a solving algorithm for the streaming of high energy neutrons and photons generated inside the confining region and spreading across the plasma facing components. Therein, the Boltzmann transport equation is solved by means of a finite element method in 2D curvilinear coordinate systems and based on discontinuous elements. The neutron and gamma source terms are extracted from the core plasma physics module and based on the plasma profiles and the calculated magnetic configuration. Relying on such an improved modelling scenario, the neutron and photon wall loadings onto blanket first

wall and divertor structures are mapped consistently with the imposed BB and divertor geometric poloidal profiles.
The fulfilment of the neutronic requirements and technological constraints is achieved by means of the additional full reactor scale neutron and gamma transport sub-model, attaining the solution to the Boltzmann transport equation in one-dimensional cylindrical coordinate systems. The problem is solved for an arbitrary radial and material composition of the core physical reactor components, including BB, VV, gaps and TF coil. The model calculates the major neutronic-related design variables, such as TBR, nuclear energy deposition, peak fast neutron flux densities and volumetric heating at the TF coil superconducting cable and atomic displacement rates in materials.
Presently available fusion system codes disregard the neutronic features, thus excluding the abiding implications of the neutronic-related design variables.

The plasma magnetic equilibrium and stability effects coupled to the radial/poloidal/toroidal geometric influences of the physical components make the design of the toroidal and poloidal field coils systems a major task of system analysis tools. In tokamak magnetic configurations there are two and three-dimensional effects driving the engineering characterization of the TF and PF coils. But, in fusion system codes these are only partly foreseen within the full magnets modelling canvas, since most of the electromagnetic parameters are evaluated by means of rather simplified and idealized theories. For a more detailed evaluation of such elements within a system analysis tool, a Biot-Savart 3D magnetostatic analysis module has been integrated in MIRA static electromagnetic analysis, applied to arbitrary systems of PF and TF coils geometries and currents. This solving method allows for an evaluation of field profiles, Lorentz forces, stored energy and self and mutual inductances.
The external poloidal magnetic field configuration has been also addressed, considering the plasma scenario analysis. To that extent, a dedicated PF/CS coil current nonlinear solver has been implemented to characterize the combination of PF coil toroidal currents complying with plasma separatrix shape, equilibrium and stability requirements, coil currents and magnetic field technological limits and total vertical force operational constraints.
For both PF and TF coils, an engineering sub-module has been included to evaluate the superconducting cable packing layout and to verify the major superconducting criteria, given by the current sharing temperature margin, the quench stability protection and the critical current density limit.

A power balance model has been implemented in MIRA to map the power sources and sinks linked to the key reactor components. The computation starts from the source fusion and radiation powers, runs through the energy deposition into BB and VV goes down to the BoP and to the PCS, for the conversion of exhausted thermal energy into electricity.
A time cycle analysis model traces the timeline of a plasma pulse, from its creation at the breakdown to its death at the ramp-down. The coupling between the plasma equilibrium and the PF coil current solver permits a more advanced definition of the poloidal flux linked to the plasma current loop, hence of the plasma burn time τ_{burn}, too. The latter depicts the largest time slot over a pulsed cycle and identifies a top-level requirement for pulsed tokamak devices like EU-DEMO1.

The proposed multiphysics MIRA tokamak reactor analysis method has been applied to the EU-DEMO 2015 baseline, generated by means of the PROCESS system code. The analysis has been carried out by taking an identical set of input assumptions and requirements (such as same fusion power yield and reactor sizes) and observing the response on certain figures of merit.
The results have shown important implications derived from the more advanced modelling scenario addressed in the physics and the engineering parts. By replacing the modelling artefacts but keeping

unaltered the global assumptions and input specifications, the baseline configuration shows substantial deviations to the PROCESS outputs.
Apart from marginal deviations identified in some of the evaluated parameters, three major constraining conditions have been found in disagreement with the imposed upper or lower bounds, including:

- safety factor at plasma axis $q_0 = 0.55$, 45 % below its lower bound (1.0), to be addressed in light of sawtooth instability criterion;
- peak plasma boundary TF ripple $\delta_{tf,\max} = 0.68$ %, 13.3 % above its upper limit (0.6 %);
- plasma burn time $\tau_{burn} = 4768$ s, 33.8 % below its lower design target limit (7200 s).

The major causes for these discrepancies between the PROCESS and the MIRA analyses are attributed to the reduced spatial resolution, simplified physics modelling and limited engineering capabilities of PROCESS. As of the current state of MIRA, these variables no longer rely on prescribed input parameters (q_0), on 0D theories (τ_{burn}) nor on predefined scaling laws ($\delta_{tf,\max}$). They are rather based on the constrained solution of several multidimensional differential problems, incorporating high level physics, technological and operational limits and spanning from two up to three-dimensional geometric details.

The outcomes of the DEMO 2015 analysis have exhibited that drastic simplifications affecting the state-of-the-art systems codes impact the overall design of the reactor considerably. Therefore, the application of the MIRA approach to evaluate a FPP baseline generated by simplified codes like PROCESS can mitigate the lack of modelling instruments before sending the main reactor guidelines to detailed design.
To prove this applicative use of MIRA, a set of active measures has been addressed to steer certain reactor systems variables in favour of a design point which fulfils the imposed constraining conditions. Such measures have been reported in form of parameter scans, where three variables have been identified as the most sensitive ones in response to the q_0, $\delta_{tf,\max}$ and τ_{burn} non-conformities. These studies comprise of the following operations.

- Reduction of the plasma internal inductance l_i, in relation to its large rising influences on q_0 (with respect to sawtooth instability) and τ_{burn} and to the deviation of the baseline value (1.155) with respect to typical ITER and DEMO scenario analyses ($0.7 - 0.8$). The investigated l_i interval covers such a wide spectrum of solutions, ranging from 0.7 to 1.2.
- Decrement of the breeding zone inboard thickness $\Delta_{\mathrm{BZ,i}}$ by 20 cm, in view of the large TBR margins emerging from the baseline analysis and in relation to its indirect impact on τ_{burn}. The induced inward radial dislocations of the CS coils stack have been observed to provoke indeed tangible increments of τ_{burn}.
- Augmentation of the VV-TF coil gap outboard thickness $\Delta_{\mathrm{VV-TFC,o}}$ by 30 cm in response to the exceeding maximum TF ripple limits, being mitigated by moving the outboard leg of the TF coils outwards, further from the outer side of the plasma boundary.

The listed parameters have been studied by following a one-at-a-time approach, engaging the listing order and starting each scan from a given reference configuration. For the first parameter study on l_i, the reference DEMO 2015 baseline has been taken as the starting operating point. Consequently, each analysis has addressed a new revised DEMO design point, being also the reference configuration of the further parameter analysis.

The addressed sensitivity analyses have shed light onto some non-trivial inter-parametric dependencies, never explored in fusion system analyses. For example, important impacts of l_i on safety factor, plasma shape, density and temperature features, peak divertor flux and plasma burn time have been finally observed and quantified within a system analysis environment. Additionally, the physics correlations of l_i with τ_{burn}, already investigated for ITER but never fully addressed within fusion system analyses, have been brought to light. The effects of the plasma magnetic configuration on the burn time have emerged to be much deeper than ever accounted in currently operating fusion system codes, for as only the dependency on flux consumption at plasma ramp-up is being included.
The more elaborated plasma scenario analyses have illustrated predominant effects of l_i also during the plasma flat-top, precisely at its end. In this pulsed time frame, the poloidal flux at plasma boundary depends upon the shaping capabilities of the PF/CS coils, very much affiliated to the magnetic configuration inside the confining region, i.e. to l_i.

Another major outcome of the parametric studies concerns the burn time τ_{burn} and its relation to the overall inboard radial build configuration. From the inboard BZ width sensitivity study, it can be inferred that there is an optimal overall BB + TF coil inboard width, representing a meeting point between two opposing behaviours. From the one hand side there is the poloidal flux linkage, bound to scale quadratically with the CS radius $r_{CS,i}$. On the other hand, the maximum available currents in the CS modules drop fairly linearly with $r_{CS,i}$, because of the growing cable self-inductance, yielding hence smaller quench protections margins. Moreover, on top of these two predominant effects, the TF coil cabling layout positively experiences the advancement of the inboard straight leg towards the inner side of the tokamak. Accordingly, the TF coil winding pack exploits the enlarged available space to wind the cables in toroidal direction and to decrease the radial TF coil thickness. With respect to the total inboard BB thickness, τ_{burn} tends to reach a peak value, largely driven also by the current and field superconducting technological constraints.

A revised DEMO 2015 design that complies with all requirements and constraints has been generated by exploiting the main outcomes of the parametric analyses. The major differences with respect to the original PROCESS baseline are given by:

- l_i reduced from 1.155 to 0.8;
- $\Delta_{\mathrm{BZ,i}}$ decremented by 16 cm, yielding an overall BB thickness decreasing from 78 to 62 cm;
- $\Delta_{\mathrm{VV-TFC,o}}$ increased by 22 cm, from 98 to 120 cm.

Despite of these advised trends, within the most recent DEMO 2017 baseline l_i still features rather large values (1.096) and the outboard BB width has been reduced by 30 cm. The inboard extension, instead, has been left unaltered. One can argue that both modifications engage pretty opposing behaviour with respects to those indicated by the MIRA DEMO analyses. Some of the issues encountered both in the 2015 and in 2017 DEMO baselines could be prevented and corrected if this novel approach had been deployed.

The MIRA application study has brought up an important change in the way of designing a tokamak reactor like DEMO. The DEMO baselines have been generated over the years within the PPPT programme by fixing the BB inboard and outboard widths, neglecting the fundamental electromagnetic influences on the PF/CS coils, TF coils and on the plasma. More extended analyses on the blanket radial widths, going beyond the nuclear aspects, therefore should be addressed in future DEMO design analyses and MIRA provides a high fidelity computational to cope with such demands.

A continuation of this work should include further modelling activities to include the missing modules and refine the existing ones. Following a priority order, a model for the following fusion research areas should be considered for integration in the MIRA package.

1. Fuel cycle and vacuum pumping, for the temporal characterization of all hydrogen isotopes and plasma impurities exhausts inventories. The model should include key aspects linked to the different sub-system time scales and the technological features of the fuelling systems and vacuum pumps.

2. Plant availability, to calculate the plant availability factor in relation to the calculated components lifetime and the consequent remote maintenance schemes.

3. Cost estimation, to evaluate the capital and operation costs and extend the design analyses at a power plant scale.

4. Heating and current drive systems, incorporating more elaborated physics models about the current density distribution, energy deposition into the plasma and, possibly, engineering insights of the ongoing technological solutions.

As for the models already integrated in MIRA, there are still important margins of improvements that can be legitimated in view of a more robust design analyses. These comprise a model for the following item list of research fields, still in priority order.

1. Plasma MHD transport solver. Potentially, the core physics module could be complemented with a 1D transport model, to simulate at least the transport of charged fast and thermal particles and associated energy across the magnetic flux surface and to avoid prescribing the density and temperature profiles. A full coupling with the equilibrium would then allow a complete resolution of transport and Maxwell's equations, such that the free parametrization of the current density can be avoided. As a result $J_{\phi,p}$ can be consistently calculated, accounting for CD, bootstrap and ohmic current density terms, congruently with the temperature and density profiles.

2. Plant power balance. The current model is based on the definition of a fixed gross electric efficiency η_{gross}, whereas a more flexible characterization of the BoP subsystems would be more effective to calculate the thermodynamic cycles coordinates and the electric output.

3. Stress analysis in TF and PF coils structures. A complete magnet module shall include as well a stress analysis tool to verify the major stress criteria on the TF coil steel casing, on the TF and PF cable steel jacketing and the turn insulation.

4. Neutron and gamma transport model based on axisymmetric curvilinear coordinate systems for the full reactor scale. In this way, the calculation of the major integral T breeding and nuclear heating power would be conducted by refusing the cylindrical geometry approximation, and allowing a wider spectrum of geometric solutions for the core reactor components.

5. Optimization of TF and PF coil shape, position and number. Relying on a target plasma shape, the design of a tokamak reactor would benefit from a TF and PF coil system where the radial, toroidal and poloidal shapes, as well as the number can be optimized with respect to one or more figures of merit, such as minimum stored energy and best shaping capabilities.

A fusion power plant configuration solver and optimizer is needed to complete the set of architectural capabilities of a fusion design tool like MIRA. Accordingly, the optimization methods to find feasible plant design solutions minimizing or maximizing any given figure of merit should be investigated.

Appendix

A. Introduction to the Galerkin Finite Element Method

A finite number n_t of triangular elements, denoting the mesh $\mathcal{T}_h$, defines a generic physical component, where each mesh element T_k is composed of nodes connected by lines (or edges). The union of each element therefore defines the whole domain $\mathcal{D}$, such that $\bigcup_{k=1}^{n_t} T_k = \mathcal{D}_h \approx \mathcal{D}$. The size of a mesh is associated with the reference length h, which can be related to the diameter of a smallest circle (or sphere in 3D) which can enclose the element. From a more rigorous mathematical point of view, the metric h associated with a regular mesh $\mathcal{T}_h$ composed by n_t element T_k can be defined such that

$$h(\mathcal{T}_h) = \max\{\rho(T_k) \mid T_k \in \mathcal{T}_h\}, \tag{A.1}$$

where $\rho(T_k)$ is the diameter of circle inscribed in the triangular element T_k.
Any scalar function $u(\mathbf{x})$ defined in a multidimensional geometrical phase space $\mathbf{x} \in \mathcal{D} \subset \mathbb{R}^d$ with $d \geq 2$ and $\mathcal{D}$ denoting the spatial domain in $\mathbb{R}^d$ can be approximated as:

$$u(\mathbf{x}) \approx u_h(\mathbf{x}) = \sum_{k=1}^{M} u_k \phi_k(\mathbf{x}), \quad \forall \mathbf{x} \in \mathcal{D}, \tag{A.2}$$

where ϕ_k are canonical basis polynomial functions (also called hat function) of the finite element space $\mathcal{V}_h$ of continuous functions which are affine in $\mathbf{x}$ on each element of $\mathcal{T}_h$. The coefficients u_k are called degrees of freedom of ϕ and M is the number of degrees of freedom. Therefore, a finite element space $\mathcal{V}_h \subset H^1(\mathcal{D})$, is outlined as a functional subspace of the Sobolev space $H^1(\mathcal{D}) = \{v \in L^2(\mathcal{D}) : \nabla v \in L^2(\mathcal{D})\}$, with $L^2(\mathcal{D})$ being a Hilbert subspace in $\mathcal{D} \subset \mathbb{R}^d$ [134]. The hat functions ϕ_k are polynomials functions affine in $\mathbf{x}$.

The procedure known as Galerkin method is used to solve many differential problems. It is based on the derivation and the solution of the problem, when posed in weak form. A generic time-independent differential problem, where the unknown u is a function in the d independent variables $\mathbf{x} = (x_1, ..., x_d)$, can be defined in its strong form as

$$F\left(\mathbf{x}, \frac{\partial u}{\partial x_1}, ..., \frac{\partial u}{\partial x_d}, ..., \frac{\partial^{p_1+...p_d}}{\partial x_1^{p_1} ....\partial x_d^{p_d}}\right) = g(\mathbf{x}), \tag{A.3}$$

where q the order of the PDE is the maximum order of the partial derivative appearing in the equation, i.e. the maximum of $p_1 + ... + p_d$. If F is a linear combination of u and of its derivatives, the PDE is linear.
In heat conduction and structural mechanics a different arrangement of the strong formulation of Equation (A.3) is used to allow for more complex geometries and to reduce the order of the partial derivatives. This refers to as weak formulation, and it is obtained by multiplying the left and the right hand sides of the PDE in strong form times some test function $v \in \mathcal{V}$ and integrating over the volume domain $\mathcal{D}$, such that

$$\int_{\mathcal{D}} F\left(\mathbf{x}, \frac{\partial u}{\partial x_1}, ..., \frac{\partial u}{\partial x_d}, ..., \frac{\partial^{p_1+...p_d}}{\partial x_1^{p_1} ....\partial x_d^{p_d}}\right) v(\mathbf{x}) \mathrm{d}\mathbf{r} = \int_{\mathcal{D}} g(\mathbf{x})\, v(\mathbf{x}) \mathrm{d}\mathbf{r}, \tag{A.4}$$

where $\mathcal{V} \subset H^1$ is an appropriate Hilbert space, subspace of Sobolev space H^1, and $v = 0$ on $\partial\mathcal{D}$. Thus, the problem can be rearranged in finding $u \in \mathcal{V}$, so that

$$a(u, v) = \ell(v) \quad \forall v \in \mathcal{V}, \tag{A.5}$$

where $a(u, v)$ and $\ell(v)$ identify the bilinear and the linear form. The bilinear and the linear form normally include the information on boundary conditions. The Galerkin method for the numerical approximation of Equation (A.5) is to find an approximated solution $u_h \in \mathcal{V}_h \subset \mathcal{V}$, with $\mathcal{V}_h$ being a family of basis functions depending on the positive parameter h attaining to the mesh metric size (see Equation (A.1)) and defined such that

$$\mathcal{V}_h \subset \mathcal{V}, \ \dim \mathcal{V}_h = M < \infty, \ \forall h > 0. \tag{A.6}$$

The Galerkin method, therefore, yields the solution $u_h \in \mathcal{V}_h$ reformulated into the following form

$$a(u_h, v_h) = \ell(v_h) \quad \forall v_h \in \mathcal{V}_h. \tag{A.7}$$

Indicating ϕ_j with $j = 1, ...M$ a basis of the space V_h, Equation (A.7) has to hold for every basis ϕ_j, as all functions of $\mathcal{V}_h$ are linear combinations of ϕ_j. Therefore, taking into account the approximation of u_h of Equation (A.2), Equation (A.7) can be rearranged into a set of M linear equations leading to:

$$\sum_{j=1}^{M} u_j a(\phi_j, \phi_i) = \ell(\phi_i), \ \ i = 1, 2, ..., M, \tag{A.8}$$

where the elements $a_{ij} = a(\phi_j, \phi_i)$ are the stiffness matrix A and $f_i = \ell(\phi_i)$ the components of the vector $\mathbf{f}$. Solving the Galerkin problem of Equation (A.7), is equivalent to solve the linear system of equation

$$A\mathbf{u} = \mathbf{f}, \tag{A.9}$$

where the unknown vector of the degrees of freedom $\mathbf{u}$ represents the solution. Solving a PDE through finite element approximation implies defining the stiffness matrix A and the vector $\mathbf{f}$.
For second order PDEs the integrands of Equation (A.7) are recast by making use of the Green's first identity and becoming thus a linear combination of ∇u_h and ∇v_h, thereby the second order derivatives disappear. Moreover, the definition of a set of quadrature formula, such as Gauss quadrature formula, is necessary to express the integral terms as a linear combination of u_h, and define the linear system of Equation (A.9).
For every differential problem built and solved in MIRA environment making use of the Galerkin method, the definition of the A and $\mathbf{f}$, as well as the solution of Equation (A.9), are carried out by means of `Freefem++` solver, where the analytical expressions of $a(u_h, v_h)$ and $\ell(v_h)$ are specified by the user. The derivation of the weak formulation is therefore necessary.

For the applicative multidimensional differential problems solved by FEM and addressed within dedicated MIRA system/design code models, one can rely on both continuous ($\mathcal{V}_h$) and discontinuous ($\mathcal{W}_h$) piecewise finite elements of polynomial order r, associated with a quasi-uniform mesh $\mathcal{T}_h$ discretizing the space domain $\mathcal{D}$. According to the FE formalism, these can be expressed as:

$$\mathcal{V}_h(\mathcal{T}_h) = \left\{ v_h \in H^1(\mathcal{D}) \mid \forall T_k \in \mathcal{T}_h \ \ v_{h|T_k} \in \mathbb{P}_r \right\}, \tag{A.10}$$

and

$$\mathcal{W}_h(\mathcal{T}_h) = \left\{ v_h \in L^2(\mathcal{D}) \mid \forall T_k \in \mathcal{T}_h \ \ v_{h|T_k} \in \mathbb{P}_r \right\}, \tag{A.11}$$

where $\mathbb{P}_r$ is the set of polynomials of $\mathbb{R}^d$ of degrees lower or equal to r, with $d = 2$ for 2D and $d = 3$ for 3D mesh.
Continuous FEs are more suitable to solve elliptic or parabolic problems, or more generally, in presence of second-order partial derivatives (see for instance the plasma magnetic magnetic equilibrium problem of Section 3.1.2). Discontinuous FEs, instead, are being deployed to solve pure advection problems (see radiation transport model of Section 4.1.2), where first-order partial derivatives are for convective transport mechanisms and the polynomial basis functions are not necessarily continuous across the element edges. This choice is advocated by the fact that the solution hyperbolic problems (such as advection) may endure into discontinuities [134], which can be captured making use of such finite element spaces.
In case of linear FEs for each mesh triangle T_k, any generic function $v_h \in \mathcal{V}_h$ (or $v_h \in \mathcal{W}_h$) is defined on each mesh vertices, while for quadratic elements, the edge midpoints are included, too. Therefore, it can be inferred that for a given mesh, characterized by a number of elements n_t, $\mathbb{P}_2$ finite element functions provide a more accurate spatial mapping of v_h, though implying a larger size of the problem.

The solution of different multidimensional fusion-related problems have been conducted using the FE method, in order to extend the mathematical frame of their physics and engineering models to higher order two and three dimensional geometries. Interfacing a system code with a multidimensional numerical environment defines a new approach in integral power plant analysis, with the ultimate goal of achieving a more refined and reliable global reactor design, incorporating also response effects of the individual component of the global system. The problem considered for system analyses span from the simple calculation of integral parameters (e.g. domain volume or volume-averaged plasma properties) to the actual resolution of differential plasma equilibrium to neutron and photon transport in the tokamak vacuum chamber.

B. Interior Methods for Nonlinear Constrained Optimization

B.1. Introduction to Nonlinear Constrained Optimization Problems

A nonlinear optimization problem can be expressed in the form,

$$\begin{aligned} &\min_x f(x) \text{ subject to }, \\ &g_i(x) \leq 0, \;\; i = 1, ..., m, \\ &h_i(x) = 0, \;\; i = 1, ..., M, \end{aligned} \tag{B.1}$$

where $x \in \mathbb{R}^n$ is the solution vector and $f, g_i, h_i : \mathbb{R}^n \rightarrow \mathbb{R}$ are continuously differentiable functions. f depicts the function to minimize, while g_i and h_i denote the inequality and the equality constraining conditions. The interior-point method [92, 93, 94, 166], is an algorithm used to solve constrained minimization problems. It is based on the solution of a sequence of approximate minimization problems, which can be defined as:

$$\begin{aligned} &\min_{x,s} f_\mu(x, s) = \min_{x,s} f(x) - \mu \sum_{i=1}^{m} \ln(s_i) \text{ subject to }, \\ &g_i(x) + s_i = 0, \;\; i = 1, ..., m \\ &h_i(x) = 0, \;\; i = 1, ..., M \end{aligned} \tag{B.2}$$

where μ is a positive scalar (*barrier parameter*) and the logarithmic term is the *barrier function*. The s_i are restricted to be positive to keep the barrier function feasibly bounded and define the set of slack variables. Every s_i is associated with an inequality constraint g_i. The reason of such a modified problem resides in the behaviour of the logarithmic term for decreasing values of μ such that the minimum of f_μ should approach that of f. In other words, for very small $\mu > 0$, $f_\mu(x)$ acts like $f(x)$ such that the algorithm can be applied repeatedly to Equation (B.2) for decreasing values of μ, to approximate the solution of the original Equation (B.1).

To solve the sequence of these approximated problems, i.e. the values of x, s, the following conditions, also known as Karush-Kuhn-Tucker (KKT) conditions, shall be met

$$\begin{aligned} \nabla_x L(x, \lambda, y) = 0 \quad &\text{(stationary)}, \\ g_i(x) + s_i = 0, \; h_i(x) = 0 \quad &\text{(primal feasibility)}, \\ \lambda_i \geq 0 \quad &\text{(dual feasibility)}, \\ \lambda_i g_i(x) = 0 \quad &\text{(complementary slackness)}. \end{aligned} \tag{B.3}$$

The vector λ, being the concatenation of all λ_i and y of all y_i is the Lagrange multiplier vector; $L(x, \lambda, y)$ defines the auxiliary Lagrange function,

$$L(x, \lambda, y) = f(x) + \sum_{i=1}^{m} \lambda_i g_i(x) + \sum_{i=1}^{M} y_i h_i(x). \tag{B.4}$$

The KKT conditions are solved in the updated unknowns $X = [x, s, y, \lambda]$, where y identifies the vector of Lagrange multipliers associated with equality constraints y_i. Accordingly, one wishes to include the slack variables and the Lagrange multipliers, too. The problem of Equation (B.3) is solved via iterative Newton-Raphson method [121], where a generic system of nonlinear equations $F(x_k) = 0$, with $F : \mathbb{R}^n \to \mathbb{R}^n$ being continuously differentiable functions and k the iterative step, can be solved in the unknown vector of increment $\Delta x_k = x_{k+1} - x_k$,

$$J_F(x_k)\Delta x_k = -F(x_k), \tag{B.5}$$

where $J_F(x_k)$ denotes the $k \times k$ Jacobian matrix of F. Applying the same approach to the KKT conditions B.3, at each iterate k the solution $X_k = [x_k, s_k, y_k, \lambda_k]$ is expressed as a function of an increment of the solution $\Delta_k = [\Delta x_k, \Delta s_k, \Delta y, \Delta\lambda_k]$ so that $X_{k+1} = X_k + \Delta_k$. The KKT conditions formulated in Equation (B.3) can be recast in the matrix form of a linear system of algebraic equations,

$$\begin{bmatrix} H(x_k) & 0 & J_h^T(x_k) & J_g^T(x_k) \\ 0 & S_k\Lambda_k & 0 & -S_k \\ J_h(x_k) & 0 & I_M & 0 \\ J_g(x_k) & -S_k & 0 & I_m \end{bmatrix} \begin{bmatrix} \Delta x_k \\ \Delta s_k \\ -\Delta y_k \\ -\Delta\lambda_k \end{bmatrix} = \begin{bmatrix} \nabla f(x_k) - J_h^T(x_k)y_k - J_g^T(x_k)\lambda_k \\ S_k\lambda_k - \mu e \\ h(x_k) \\ g(x_k) + s_k \end{bmatrix}, \tag{B.6}$$

where the following variables are used in the definition of X_k:

- H denotes the Hessian of the Lagrange function L (see Equation B.4) and is defined as

$$H(x) = \nabla^2_{xx}L(x, \lambda, y) = \nabla^2 f(x) + \sum_{i=1}^{m} \lambda_i \nabla^2 g_i(x) + \sum_{i=1}^{M} y_i \nabla^2 h_i(x). \tag{B.7}$$

- $J_g(x_k)$ and $J_h(x_k)$ denote the Jacobian of the m inequality and M equality constraint functions g and h.
- $S_k = \text{diag}(s_k)$, with s identifying the vector of slack variables s_i at the iterate k.
- $\Lambda_k = \text{diag}(\lambda_k)$.
- λ_k and y_k denote the vector of Lagrange multipliers associated with g and h, respectively.
- I_m and I_M are the $m \times m$ and $M \times M$ identity matrices.
- e denotes the $m \times 1$ vector of ones, where m is the size of inequality constraints function g.

Even though the Newton method generally provides a fast convergence attention has to paid to the step size α for a complete Newton iteration. A common approach is to include a line search, so that the new iterate solution X_{k+1} is defined by

$$X_{k+1} = X_k + \alpha_k \Delta_k, \tag{B.8}$$

where α_k is a positive scalar selected such that some prescribed merit function $\mathcal{M}$ is reduced by moving to the new solution X_{k+1}. Such a merit function is chosen to minimize the objective function f_μ and the constraints violations, in the way

$$\mathcal{M} = f_\mu(x, s) + \nu \left\| h(x), g(x) + s \right\|. \tag{B.9}$$

The parameter ν is a scalar parameter which may increase with the iteration number in order to force the solution towards feasibility. The algorithm rejects the attempted step if this does not decrease the merit function and attempts a new step with a different value of α_k.

The interior-point optimization methods comes to a feasible solution when certain criteria are satisfied. In particular, the stationary, primal feasibility and complementary KKT conditions are usually used as optimality conditions, such that

$$\begin{aligned} \max\left(\left\|\nabla_x L(x_k,\lambda_k,y_k)\right\|, \left\|\lambda_k g(x_k)\right\|\right) &\leq \varepsilon_{foo}, \\ \max\left(\left\|h(x_k)\right\|, \max\left(g(x_k)\right)\right) &\leq \varepsilon_{cv}, \end{aligned} \tag{B.10}$$

where the operator $\|\cdot\|$ identifies the infinity norm, ε_{foo} and ε_{cv} denote the tolerances on the first-order optimality condition and on the constraints violations. The maximum value among the mentioned optimality definitions plays as stopping criteria for the method. In the following paragraph, the MATLAB optimization solver `fmincon`, used to solve many applicative problems described in this manuscript, is detailed with respect to its interfacing parameters.

B.2. The fmincon optimization tool.

`fmincon` [201] is a MATLAB built-in nonlinear programming solver which finds the minimum of a constrained problem specified by

$$\min_{\underline{w}} f(\underline{w}) \text{ subject to } \begin{cases} g(\underline{w}) \leq 0 \\ g_{eq}(\underline{w}) = 0 \\ A \cdot \underline{w} \leq b \\ A_{eq} \cdot \underline{w} = b_{eq} \\ l_b \leq \underline{w} \leq u_b \end{cases}, \tag{B.11}$$

where $\underline{w} \in \mathbb{R}^n$ is the solution vector and:

- $f : \mathbb{R}^n \to \mathbb{R}$, the function to minimize;
- b and b_{eq} are two m and m_{eq}-column vectors, with m and m_{eq} denoting the number of inequality and equality linear constraints, respectively;
- A and A_{eq} are the two $m \times n$ and $m_{eq} \times n$ matrices, associated with the m inequality and m_{eq} equality linear constraints, respectively;
- g and g_{eq}, represent the two functions defining the M inequality and M_{eq} equality non-linear constraints;
- u_b and l_b define the upper and lower bounds n column vector.

The above listed variables are all user-specified. By default, `fmincon` attempts to solve the Equation (B.11) as per interior-point method. Accordingly, the set of vector and matrices outlining the linear and nonlinear constraints together with upper and lower bounds are rearranged such that Equation (B.11) is recast into its "original" formulation, defined by Equation (B.2). As shown in Equation (B.6), first and second order differential operators are needed to find the optimal solutions, i.e. Jacobian and Hessian matrices. If not directly provided by the user, `fmincon` calculates numerically the gradients by means of finite difference method (FDM), either forward or central. The FD

step size v (`FiniteDifferenceStepSize`) can be also provided as input parameter, and the FD step δ are calculated as $\delta = v \cdot \text{sign}\,(\underline{w}) \cdot |\underline{w}|$. The Hessian matrix H, if not provided, is calculated by default as per quasi-Newton Broyden-Fletcher-Goldfarb-Shanno (BFGS) algorithm [202], which is a generalization of the secant method for the calculation of the root of first derivatives in multidimensional problems.

C. The Physics System Code TREND

In this chapter, some additional equations implemented in the system code TREND [10] and integrated in the core physics module of MIRA are reported.

C.1. Plasma current balance

The total toroidal plasma current I_p results from different processes occurring in tokamak plasma operation, both driven by external and internal phenomena. The following three contributions balance the plasma current at steady state, that is:

- inductive current I_{ind},
- external current drive I_{CD} and
- bootstrap current I_{BS}.

Those three terms hence yield the zero dimensional steady current balance as follows

$$I_p = I_{ind} + I_{CD} + I_{BS}, \tag{C.1}$$

which can be normalized with respect to the plasma current I_p and recast with respect to the related fractions

$$1 = f_{ind} + f_{CD} + f_{BS}. \tag{C.2}$$

The inductive currents are driven by means of magnetic induction, where the plasma and the central solenoid are acting as the primary and the secondary winding of a transformer. The time-dependent current driven by the CS induces a loop voltage U_{loop} in the plasma proportional to the time derivative of the induced magnetic flux Ψ. It scales with the inductive plasma current I_{ind} as per Ohm's law by

$$U_{loop} = R_p I_{ind}, \tag{C.3}$$

with R_p being the plasma resistance, referring to its surface-averaged specific electric conductivity $\langle\sigma\rangle_{S_p}$ and its toroidal length and poloidal cross section. The conductivity is calculated in TREND by first considering a pure cylindrical plasma as per Spitzer resistivity, then corrected by means of the resistivity enhancement factor γ_{NC}, which takes into account of neoclassical effects due to specific particles kinetics related to the radial variations of the toroidal magnetic field. The plasma temperature affects the conductivity in a relevant manner, showing therefore a connection between thermal and magnetic properties of plasma. The plasma resistance reads as

$$R_p = \frac{1}{\langle\sigma\rangle_{S_p}} \left(\frac{2\pi R_0}{S_p} \right), \tag{C.4}$$

and the surface-averaged plasma conductivity is given by,

$$\langle\sigma\rangle_{S_p} = \frac{\sigma_{S_p}}{\gamma_{NC}}, \tag{C.5}$$

where σ_{S_p} refers to an expression for the conductivity of a cylindrical plasma without considering neoclassical effects (Spitzer conductivity). These are taken into account by γ_{NC}, the so-called neoclassical resistivity enhancement factor. A scaling law for σ_{S_p} and γ_{NC} have been derived for ITER [87] and implemented in TREND. These are:

$$\sigma_{S_p} = 4.65 \times 10^8 \frac{(\langle T \rangle_n / 10)^{3/2}}{Z_{eff}} \left(\frac{2\pi\kappa_{95} a^2}{S_p} \right), \tag{C.6}$$

and

$$\gamma_{NC} = 4.3 - 0.6A. \tag{C.7}$$

It can be seen that plasma temperature and effective charge have a large influence on the plasma conductivity.

The bootstrap current is a neoclassical effect characterizing a beneficial contribution both for steady state and pulsed operational regimes. In tokamak fusion devices, this manifestation of plasma current occurs parallel to the magnetic field in the presence of a pressure gradient, leading to asymmetries in ion and electron velocity distributions. The latter result therefore into a net current, called bootstrap current. The TREND code allows calculating the bootstrap fraction $f_{BS} = I_{BS}/I_p$ by means of several scaling laws, each of them with both common and different independent variables and different levels of granularity. It can be seen that all of them include the information regarding the temperature, density and current profiles, the magnetic field and the plasma shape (e.g. aspect ratio). Most of them are of the following general form,

$$f_{BS} = c_{BS} \beta_p \sqrt{\varepsilon}, \tag{C.8}$$

where the bootstrap coefficient c_{BS} is derived from the different available scaling laws and $\varepsilon = 1/A$ is the inverse aspect ratio. The default expression of c_{BS} implemented in TREND is that found by Wilson [195], given by

$$c_{BS} = \sum_{i=1}^{12} a_i(\alpha_{jW}, Z_{eff}) b_i(\alpha_{TW}, \alpha_{pW}, \varepsilon) \tag{C.9}$$

and α_{jW}, α_{WT} and α_{pW} are three coefficients tied to the current density, temperatures and pressure profiles, expressed as:

$$\begin{aligned} \alpha_{jW} &= \frac{q_{cyl}}{q_0} \frac{2S_p}{a l_p} - 1 \\ \alpha_{TW} &= \frac{T_0}{\langle T \rangle} - 1 \\ \alpha_{pW} &= \frac{n_{e,0} T_0}{\langle T_n \rangle} - 1. \end{aligned} \tag{C.10}$$

S_p and l_p indicate the plasma cross sectional area and perimeter, respectively. The full definition of the coefficients a_i and b_i can be found in [195].

In tokamak fusion devices, the auxiliary heating systems can be potentially used (depending on the technology) to drive current, beside the intrinsic function of heating plasma. The driven current I_{CD} proportionally scales with the external current drive injected power P_{CD} as

$$I_{CD} = \frac{\langle \gamma_{CD} \rangle}{R_0 \langle n_e \rangle} P_{CD}, \tag{C.11}$$

with $\langle \gamma_{CD} \rangle$ defined as the global normalized current drive efficiency, $\langle n_e \rangle$ the average electron density and R_0 the plasma major radius. A scaling law for the normalized current drive efficiency (in case of NBI system) was proposed by Johner [15] and implemented in TREND, where the main dependency has been identified in the volume-averaged temperature.

$$\langle \gamma_{CD} \rangle = 0.035 \cdot \langle T \rangle . \tag{C.12}$$

C.2. Plasma pressure properties

As the magnetized plasma are usually assumed as ideal gases, the following state equation relates yields the radial profile thermal plasma pressure $p_{th}(\rho)$ as per ideal gas law

$$p_{th}(\rho) = \left[n_e(\rho) T_e(\rho) \cdot e + \sum_j n_j(\rho) T_j(\rho) \cdot e \right] = (1 + f_i)\, n_e(\rho) T(\rho) \tag{C.13}$$

with $e = 1.602 \times 10^{-19}$ [A·s] being the absolute value of electron charge, n_e and T the electron density and temperature, expressed in [m^{-3}] and [eV]. The index j designates the different ion species (fuel or impurities), where n_j and T_j identify the associated density and temperature, as described in Appendix C.3. Furthermore, the totality of ion species is incorporated in the total ion fraction f_i (see Equation (C.25)). The volume-averaged thermal pressure is given by:

$$\langle p_{th} \rangle = (1 + f_i) \langle n_e \rangle \langle T \rangle_n \cdot e. \tag{C.14}$$

Another parameter being of high importance for the stability of magnetically confined plasmas is the plasma beta β, indicating how the magnetic forces act against the plasma pressure to confine the plasma [106]. It defines the ratio between gas to magnetic pressure and is defined in TREND [10] as

$$\beta_{th} = \frac{\langle p_{th} \rangle}{B_{tot}^2 / 2\mu_0}. \tag{C.15}$$

B_{tot} denotes the total magnetic field, defined as

$$B_{tot} = \sqrt{B_t^2 + \langle B_p \rangle_l^2} \tag{C.16}$$

with B_t being the toroidal field at magnetic axis and $\langle B_p \rangle_l$ the poloidal field averaged on the plasma perimeter (Equation 3.11). The complete definition of the plasma beta includes the contribution of non-thermalized fast particles deriving from alpha particles $\gamma_{f\alpha}$ and the external heating systems, i.e. fast beam particles γ_{beam}. The sum of those contributions $\gamma_{fast} = \gamma_{f\alpha} + \gamma_{beam}$ is estimated in TREND via a modified scaling law $\gamma_{f\alpha}$ derived from ITER physics guidelines [87] and expressed as:

$$\gamma_{f\alpha} = \begin{cases} 0.029 f_{DT}^2 \left(\langle T \rangle_n - 3.7 \right), & \text{for } \langle T \rangle_n \leq 20 \text{ keV}, \\ 0.473 f_{DT}^2 & \text{for } \langle T \rangle_n > 20 \text{ keV}, \end{cases} \tag{C.17}$$

and γ_{beam} specified as input parameter (zero by default). Equivalently, the total plasma beta β is defined as

$$\beta = \left(1 + \gamma_{fast}\right) \cdot \beta_{th}. \tag{C.18}$$

The definition of total and thermal plasma beta relies on the magnetic pressure represented by the total field B_{tot}, being characterized by toroidal field B_t (on plasma axis) and poloidal field. Two

additional definitions of plasma beta referring to the individual magnetic field component exist and are implemented in TREND and in result in the thermal and total toroidal beta

$$\beta_{t,th} = \beta_{th} \left(\frac{B_{tot}}{B_t} \right)^2, \tag{C.19}$$

$$\beta_t = \beta \left(\frac{B_{tot}}{B_t} \right)^2, \tag{C.20}$$

and thermal and total poloidal plasma beta

$$\beta_{p,th} = \beta_{th} \left(\frac{B_{tot}}{\langle B_p \rangle_l} \right)^2, \tag{C.21}$$

$$\beta_p = \beta \left(\frac{B_{tot}}{\langle B_p \rangle_l} \right)^2, \tag{C.22}$$

where B_t is the the toroidal component of the magnetic field and is calculated at the plasma geometric centre axis ($r = R_0, z = 0$) by Equation (3.17), whilst the poloidal field $\langle B_p \rangle_l$ is calculated by Amperes law in combination of Stokes theorem applied to the plasma current and generated poloidal field, yielding

$$\langle B_p \rangle_l = \frac{1}{L} \mu_0 I_p. \tag{C.23}$$

C.3. Plasma particle balance properties

The plasma particles handled by TREND in case of DT fusion reaction include:

- electrons (denoted by e),
- fuel ions, i.e. deuterium D and tritium T (for DT reaction),
- fusion reaction-induced helium (He),
- impurity ions, including all the ion species not directly involved in the fusion reaction, for instance coming from plasma-wall interactions or other processes based on external seeding by gas puffing.

The charge state and the transport processes associated with each of these atomic species are modelled in a rather simplified manner via integral parameters such as global fractions f_j defined as:

$$f_j = \frac{\langle n_j \rangle}{\langle n_e \rangle}, \tag{C.24}$$

where $\langle n_j \rangle$ and $\langle n_e \rangle$ are the volume-averaged densities for the atomic species j and electrons. The former are calculated from the profiles across the magnetic surfaces within the core plasma region. Thereby, the total ion fraction can be defined as

$$f_i = \frac{1}{\langle n_e \rangle} \sum_j \langle n_j \rangle = f_D + f_T + f_{He} + \sum_j f_j. \tag{C.25}$$

Assuming the quasi-neutrality of plasma $\langle n_e \rangle \approx \sum_j \langle n_j \rangle Z_j$, with Z_j designating the charge number of the ion species j, the total fuel fraction $f_{DT} = f_D + f_T$ can be outlined as

$$f_{DT} = 1 - 2f_{He} - \sum_j f_j Z_j. \tag{C.26}$$

Each ion species j is associated with a charge number Z_j, where $Z = 1$ for fuel ions, whose density is designated with the variable n_{DT}, being calculated as the sum of those of deuterium and tritium. The listing of atomic species actually taking place in fusion processes shows that the plasma is not a pure "hydrogen plasma" but it is diluted by helium (as a product of a fusion reaction) and additional impurities. For this reason, an important parameter (to be calculated both for core and mantle SOL regions) defining the fuel dilution is the effective ion charge number Z_{eff}, defined as:

$$Z_{eff} = \sum_j \langle n_j \rangle Z_j^2 \Big/ \sum \langle n_j \rangle Z_j = 1 + 2f_{He} + \sum_j f_j (Z_j^2 - Z_j) \tag{C.27}$$

The helium fraction f_{He}, as well as all the impurity fraction f_j and charge number Z_j can be either fixed or used as iteration variables to fulfil the plasma operational limits, as described in Section 3.2.4.

Whilst the electron and impurities densities are specified as input parameters for the plasma module, the fuel ions and helium densities are calculated in the plasma physics module by solving two particle balances, i.e. the quasi neutrality of plasma and the integral steady state mass conversation law for helium, turning into the rate equation for the helium density $\langle n_{He} \rangle$.
The volume-averaged helium density $\langle n_{He} \rangle$, and the related He fraction f_{He}, can be obtained from the steady stated He mass balance equation applied to the confining region, where losses are due to transport mechanism (equivalently to power losses), and sources to the fusion rate. Accordingly, it can be recast as

$$\frac{\mathrm{d} \langle n_{He} \rangle}{\mathrm{d}t} = 0 = \frac{P_{fus}}{E_{fus} V} - \frac{\langle n_{He} \rangle}{\tau_p^*}, \tag{C.28}$$

where the first terms frames the He source rate due to fusion reaction, the second depicts the transport loss rate. Similarly to heat transport loss, a time scale τ_p^* named global particle confinement time has been introduced to count for the diffusive and convective transport mechanisms as well as for finite pumping leading to particle losses. The implicit assumption, taken in TREND as well as in other systems codes (e.g. HELIOS [15] and PROCESS [17]) is that the He confinement time τ_{He} is similar to τ_p^*, $\tau_{He} \approx \tau_p^*$. Furthermore, it is normally assumed in 0D systems codes [10, 15] that the particle confinement time τ_p^* is apportioned directly with the energy confinement time τ_E, hence defining a particle-to-energy ratio f_{P2E} written as

$$f_{P2E} = \frac{\tau_p^*}{\tau_E}, \tag{C.29}$$

where $f_{P2E} \approx 5$ has been found to be a reasonable value [10].

C.4. Plasma power balance properties

Energy confinement time. The ITER IPB98(y,2) scaling [108, 111] has been implemented in TREND and to calculate the energy confinement time τ_E. It is defined as:

$$\tau_E \equiv \tau_{E,th}^{IPB98(y,2)} = 0.05621\ H\ I_p^{0.93} B_t^{0.15}\ P_{con}^{-0.69} \overline{n}_e^{0.41} M^{0.19} R_0^{1.97} \epsilon^{0.58} \kappa_x^{0.78}, \tag{C.30}$$

where H is the confinement enhancement (H) factor, I_p is the plasma current, B_t the vacuum toroidal field at plasma axis, M the averaged mass number, P_{con} the transport loss, $\langle n_e \rangle$ the volume-averaged electron density (in $10^{19}\mathrm{m}^{-3}$), R_0 the major radius, $\epsilon = a/R_0$ the inverse aspect ratio. κ_x is the elongation defined as $\kappa_x = S_p/(\pi a^2)$, with S_p the plasma cross sectional area and a the plasma minor radius. τ_E is expressed in s, while the remaining parameters are defined in (MA, T, MW, $10^{19}\mathrm{m}^{-3}$, AMU, -, m). Compared to the original scaling [111], the so-called H-factor is already included in the above equation in order to consider enhancements or degradations of the confinement [10, 112].

Synchrotron radiation. The power loss related to the synchrotron radiation is calculated in TREND as

$$P_{syn} = C_{syn} \frac{\left(1 - r_{syn}\right)^{0.62} T_0 (16 + T_0)^{2.61}}{\left[1 + 0.12 \frac{T_0}{p_{a0}^{0.41}(1-r)^{0.41}}\right]^{1.51}} R_0 a^{1.38} \kappa_{syn}^{0.79} B_t^{2.62} n_{e,0}^{0.38} G(A) K\left(\alpha_T^{syn}, \alpha_n^{syn}, \beta_T^{syn}\right), \tag{C.31}$$

where

$$\begin{aligned} p_{a0} &= 6.04 \times 10^3 \frac{a \cdot n_{e,0}}{B_t}, \\ G(A) &= 0.93\left[1 + 0.85 \exp\left(-0.82A\right)\right], \\ K(\alpha_n, \alpha_T, \beta_T) &= \frac{(1.98 + \alpha_T)^{1.36}}{(\alpha_n + 3.87\alpha_T + 1.46)^{0.79}} \frac{\beta_T^{2.14}}{(\beta_T^{1.53} + 1.87\alpha_T - 0.16)^{1.33}}, \end{aligned} \tag{C.32}$$

and $C_{syn} = 3.84 \times 10^{-9.6}$, κ_{syn} is the elongation defined as $\kappa_{syn} = V/2\pi^2 R_0 a^2$, $\alpha_n^{syn} = c_n - 1$, $\alpha_T^{syn} = c_T - 1$, $\beta_T^{syn} = \beta_T$. $G(A)$ is a correction factor that consider different aspect ratios and $K(\alpha_n^{syn}, \alpha_T^{syn}, \beta_T^{syn})$ is a profile correction factor. The reflection of radiation at the first wall can be taken into account by r_{syn}, the synchrotron reflection coefficient. The specific value of r_{syn} has to be assessed for metal walls. So far, $r_{syn} = 0.6 - 0.7$ is assumed.

D. Solution of the Boltzmann Radiation Transport Equation

D.1. The Boltzmann Equation

The equation describing the neutron kinetics is the Boltzmann equation [129] which depict the balance between the neutron gains and losses within a macroscopic domain. The steady state form is given by the integro-differential equation defined as:

$$\begin{aligned}&[\mathbf{\Omega}\cdot\nabla+\Sigma_t(\mathbf{r},E)]\,\psi(\mathbf{r},\mathbf{\Omega},E)=\\&\quad=q_{ex}(\mathbf{r},\mathbf{\Omega},E)+\int \mathrm{d}E'\int \mathrm{d}\mathbf{\Omega}'\Sigma_s(\mathbf{r},\mathbf{\Omega}'\cdot\mathbf{\Omega},E'\to E)\psi(\mathbf{r},\mathbf{\Omega}',E'),\end{aligned} \tag{D.1}$$

where the solution is the angular neutron flux density $\psi(\mathbf{r},\mathbf{\Omega},E)$, whose phase space is characterized by the spatial coordinates $\mathbf{r}$, the angular streaming direction $\mathbf{\Omega}$ and the kinetic energy E. In order to solve the kinetics equation, several functions describing the interactions of neutrons and photons with matter are needed. These functions are the microscopic σ_x (cm^2) and macroscopic Σ_x (neutron cm^{-1}) cross sections, which differ by means of the the atomic density $n(\mathbf{r})$ of the material which the neutrons are interacting with, i.e. $\Sigma_x(\mathbf{r},E)=n(\mathbf{r})\cdot\sigma_x(\mathbf{r},E)$. Excluding multiplying materials inducing fission reactions, the cross section terms appearing in Equation (D.1) include:

- the macroscopic total cross section $\Sigma_t(\mathbf{r},E)$, representing the probability of collision (grouping all the reactions) per unit path length;
- the differential macroscopic scattering $\Sigma_s(\mathbf{r},\mathbf{\Omega}'\cdot\mathbf{\Omega},E'\to E)$, where $\Sigma_s(\mathbf{r},\mathbf{\Omega}'\cdot\mathbf{\Omega},E'\to E)\cdot\mathrm{d}E\mathrm{d}\mathbf{\Omega}$ represents the probability per unit path length that particles at position $\mathbf{r}$ with energy E' travelling in direction $\mathbf{\Omega}'$ scatter into $\mathrm{d}E$ about E and into the cone of direction $\mathbf{d\Omega}$ about $\mathbf{\Omega}$.

The external source $q_{ex}(\mathbf{r},\mathbf{\Omega},E)$ is a known distribution of source particles independent of the angular flux distribution Ψ. The neutron phase of Equation (D.1) is therefore defined as:

$$\mathcal{X}:=\left\{(\mathbf{r},\mathbf{\Omega},E):\mathbf{r}\in\mathcal{D}\subset\mathbb{R}^3,\mathbf{\Omega}\in\mathcal{S}_2,E\in[E_{min},E_{max}]\right\}, \tag{D.2}$$

and its inflow boundary subsets:

$$\partial\mathcal{X}_-:=\left\{(\mathbf{r},\mathbf{\Omega},E)\in\partial\mathcal{D}\times\mathcal{S}_2\times[E_{min},E_{max}],\ \text{s.t. }\mathbf{\Omega}\cdot\boldsymbol{n}(\mathbf{r})<0\right\}, \tag{D.3}$$

where $\mathcal{D}$ is the volume domain bounded by the boundary $\partial\mathcal{D}$ (oriented at each point $r\in\mathcal{D}$ by its unit outward normal vector $\mathbf{n}(\mathbf{r})$) and $\mathcal{S}_2$ is the unit sphere upon which the the angular coordinate $\mathbf{\Omega}$ represents the angular direction of neutrons.

The boundary conditions for this equation are:

- Incoming boundary condition

$$\Psi(\mathbf{r},\mathbf{\Omega},E)|_{\partial\mathcal{X}^0} = \Psi_{in}, \tag{D.4}$$

  where Ψ_{in} is a known function. In case of $\Psi_{in} = 0$ ones refers to as *vacuum boundary conditions*.

- Albedo boundary condition

$$\Psi(\mathbf{r},\mathbf{\Omega},E) = \beta(\mathbf{r})\Psi(\mathbf{r},\mathbf{\Omega}_R,E), (\mathbf{r},\mathbf{\Omega},E) \in \partial\mathcal{X}_-, \mathbf{\Omega}_R = \mathbf{\Omega} - 2\mathbf{n}\left(\mathbf{\Omega}\cdot\mathrm{n}\right), \tag{D.5}$$

  where $\beta = 1$ corresponds to purely reflective boundary, while $\beta = 0$ is again the vacuum boundary conditions. Intermediate situations $0 < \beta < 1$ are equivalent to situations where only fractions of neutrons are leaving the domain and while the remaining part is being reflected.

The transport equation can be solved by two kinds of computational methods: deterministic and Monte Carlo. The latest involves the tracking of neutrons along their random walks, assuming therefore a statistical approach. In systems analyses a neutronics tool requires relatively low computational times, making therefore the Monte Carlo technique not suitable. For this reason only deterministic techniques are investigated by analysing the numerical techniques addressed over the last decades for specific reactor physics studies.

The numerical solution of Equation (D.1) demands the discretization of the independent variables $\mathcal{X}$. Concerning the energy, the energy multigroup technique is elaborated in Appendix D.2. With regard the angular nodalization, a large number of methods have been proposed and implemented in many transport codes. The angular approximation techniques, can be basically split in two main categories:

- methods based on the integral form of the neutron transport equation;
- methods based on the integro-differential neutron transport equation (see Equation (D.1)).

The first category [129, 203] known as methods of characteristics (MoC) consists of a global neutron balance over the domain by integrating out the angular dependence from the transport equation. This technique allows to treat the angular variable with perfect accuracy but requires high computational efforts for a large number of spatial nodes. These methods, though, are not well suited for highly anisotropic scattering [129], being a key feature in fusion reactors neutronics [140, 144]. The latter kind of angular approximations applies to the angular variable certain approaches aiming to construct a set of spatial-dependent Partial Differential Equations (PDE). Two methods are implemented in transport codes as the $\mathrm{P_L}$ [204, 205, 206, 207] and the $\mathrm{S_N}$ methods [129, 206, 207]. As discrete ordinate approximation theory coupled to curvilinear geometries represent to iron-cast points for tokamak system design, these are of interest for integration in MIRA system design code, as outlined in Appendix D.3.

D.2. Energy discretization

The majority of deterministic computational methods apply the multi-energy-group approximation, where the energy domain $E \in [E_G, E_0]$ is divided into G energy intervals, as shown in Figure D.1, where $E_G = 0$ and E_0 is an energy value above which the neutrons contribution is negligible. According to this formalism, the neutrons in the group g feature energies between E_g

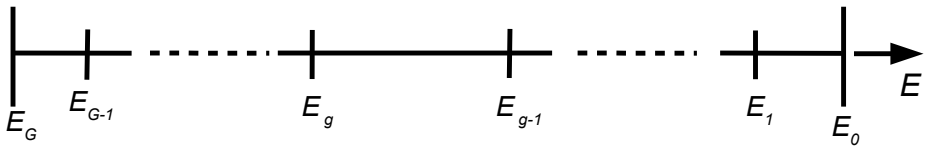

Figure D.1.: Multi-energy-group discretization

and E_{g-1} increasing therefore the group number as the energy decreases. The use of the multigroup discretization allows the elimination of the energy variable from the transport equation due to the approximation of angular flux defined within the energy group g:

$$\psi_g(\mathbf{r},\mathbf{\Omega}) = \int_{E_g}^{E_{g-1}} \mathrm{d}E\ \psi_g(\mathbf{r},\mathbf{\Omega},E) = \int_g \mathrm{d}E\ \psi_g(\mathbf{r},\mathbf{\Omega},E)\,. \tag{D.6}$$

According to the assumption of energy separability within each energy group and to the definition of the multigroup cross sections [129], the BTE for fixed source and no fission term can be expressed in the multigroup form:

$$\left[\mathbf{\Omega}\cdot\nabla + \Sigma_{t,g}(\mathbf{r})\right]\psi_g(\mathbf{r},\mathbf{\Omega}) = \sum_{g'=1}^{G}\int \mathrm{d}\mathbf{\Omega}'\Sigma_{gg'}(\mathbf{r},\mathbf{\Omega}'\cdot\mathbf{\Omega})\psi_g\left(\mathbf{r},\mathbf{\Omega}'\right) + q_g^e(\mathbf{r},\mathbf{\Omega}) \tag{D.7}$$

where Σ_g, $\Sigma_{gg'}$ and q_g^e are the total cross section, the differential scattering cross section from energy group g' to group g and the external neutron source, all defined within the interval $[E_{g-1}, E_g]$.

D.3. Discrete Ordinate Approximation in Curvilinear Coordinates

The discrete ordinate method, also called S_N method, has been implemented in numerous deterministic transport tools, such as ANISN [146], TORT-TD [208], TRIDENT [138] and FEMRZ [139]. The procedure consists of solving the transport problem of Equation (D.1) only for a number of distinct angles Ω_n and applying the spherical harmonics expansion to the angular in the integral scattering term. Thereby, the angular dependence on the variable Ω is replaced by a set of $K(N) = N(N+2)$ PDEs (three dimensional case), having the form:

$$\left[\mathbf{\Omega_n}\cdot\nabla + \Sigma_{t,g}(\mathbf{r})\right]\Psi_{n,g}(\mathbf{r}) = q^s_{n,g}(\mathbf{r},\mathbf{\Omega_n}) + q^{ex}_{n,g}(\mathbf{r}), \tag{D.8}$$

where $\Psi_g(\mathbf{r},\mathbf{\Omega_n})$ is written as $\Psi_{n,g}(\mathbf{r})$ and:

$$q^s_{n,g}(\mathbf{r},\mathbf{\Omega}) = \sum_{l=0}^{L}\sum_{m=0}^{l}\sum_{g'=1}^{G}\Sigma_{l,gg'}(\mathbf{r})\phi^m_{lg'}(\mathbf{r})Y^e_{lm}\left(\mathbf{\Omega_n}\right), \tag{D.9}$$

is the scattering source term in one and two-dimensional cylindrical geometry from group g' to g and $q^{ex}_{n,g}(\mathbf{r})$ is the external source of our transport problem. According to this formalism $\phi^m_{lg'}(\mathbf{r})$ relates the scattering moment

$$\phi^m_{lg}(\mathbf{r}) = \int Y^e_{lm}(\mathbf{\Omega})\Psi_g(\mathbf{r},\mathbf{\Omega}), \tag{D.10}$$

$\Sigma_{l,gg'}$ indicates the $l-$th moment of the differential cross section from group g' to g and Y^e_{lm} the even terms of the spherical harmonics Y_{lm} [129] read to:

$$\begin{aligned} Y_{lm}(\mu,\omega) &= Y^e_{lm}(\mu,\omega) + i\, Y^o_{lm}(\mu,\omega), \\ Y^e_{lm}(\mu,\omega) &= C^{1/2}_{lm} P_l(\mu)\cos(m\omega), \\ Y^o_{lm}(\mu,\omega) &= C^{1/2}_{lm} P_l(\mu)\sin(m\omega), \end{aligned} \tag{D.11}$$

with

$$C_{lm} = \frac{(2l+1)(l-m)!}{(l+m)!}. \tag{D.12}$$

The presence of a discrete set of angular ordinates implies also a quadrature formula for the evaluation for each energy group g of the angular flux moments ϕ^m_{lg}, the total flux $\Phi_g(\mathbf{r})$, and the current $\mathbf{J_g}(\mathbf{r})$. Therefore, having a set of $K(N)$ discrete angular ordinates Ω_n, an equivalent number of weights w_n is required, yielding:

$$\phi^m_{lg}(\mathbf{r}) = \sum_{n=1}^{K(N)} w_n Y^m_l(\mathbf{\Omega_n})\Psi_n(\mathbf{r}), \tag{D.13}$$

$$\Phi_g(\mathbf{r}) = \sum_{n=1}^{K(N)} w_n \Psi_{n,g}(\mathbf{r}), \tag{D.14}$$

$$\mathbf{J_g}(\mathbf{r}) = \sum_{n=1}^{K(N)} \mathbf{\Omega_n} w_n \Psi_{n,g}(\mathbf{r}). \tag{D.15}$$

A transport calculation using the S_N method requires an adequate choice of angular coordinates and weights, that is the order N and its related quadrature set. For general multidimensional applications, such as two and three dimensional geometry, two angular coordinates are required to specify the angular dependency on Ω. These are related to a certain spatial coordinates system (e.g. x, y, z Cartesian coordinates).
For general $n-\gamma$ transport problems the *level symmetric quadratures*, with ordinates arranged on a unit octant, are widely applied [129]. This quadrature set adopts the same set of $N/2$ positive values of the direction cosines μ, η, ξ, with respect to each of the three Cartesian axes x, y, z. In practice, one has $\mu_1 = \eta_1 = \xi_1, \mu_2 = \eta_2 = \xi_2, ...\mu_{N/2} = \eta_{N/2} = \xi_{N/2}$. As shown by Lewis [129], due to the symmetry condition, the directional cosines μ_n can be chosen with one degree of freedom only, i.e. for a given value of μ_1 the remaining coordinates are directly calculated. For the calculation of weights w_n one first considers the normalization conditions on the $N(N+2)/8$ coordinates on one octant, and the remaining degrees of freedom are used to correctly integrate the Legendre polynomials in each of the angular variables. Other techniques to discretize the variable Ω, such as such as quadrature set with reduced symmetry, are also available [129].
Level-symmetric sets may be too restrictive, thus one might need to loosen the symmetry with respect to one or more axis. In case of (r, ϕ, z) curvilinear geometry selecting the direction cosines μ_n on constant levels of ordinates ξ_n offers the ability to accurately write the angular derivative with respect to ω [129], being a necessary condition. In this case, for a unit sphere octant the discrete ordinates cosines and weights are then defined for $N/2$ levels of ξ polar levels. Level-symmetric and reduced symmetry discrete ordinate sets have been considered as the two discrete ordinate quadratures solutions for solving the core plasma radiation transport problem. In one dimensional geometry

$\Psi_g(x,\mu) \equiv \Psi_g(x,\mu_n) \equiv \Psi_{n,g}(x)$, only one directional cosine μ is needed to simulate the neutron streaming toward the direction x (except of cylindrical coordinates where two variables are needed). In this specific reference geometry, the quadrature formulas are based on an even number of ordinates which are symmetric to $\mu = 0$, i.e. neutrons flow with equal importance toward left and right coordinates. The advantage coming from this choice is that the reflective boundary conditions can be easily set as:

$$\Psi_n(0) = \Psi_{N+1-n}(0),\ n = 1,2,...\frac{N}{2}. \tag{D.16}$$

The ordinates μ_n are taken to be the N roots of the Legendre polynomials (P_N quadrature), and the weights w_n are determined so that the quadrature formula correctly integrates the Legendre polynomials P_0 through P_{N-1}.

Unlike the Cartesian coordinate frame, the angles specifying the angular flux do change as the neutrons travel in curvilinear coordinates [129]. This phenomenon known as *angular redistribution* makes the mathematical treatment of the streaming operator more elaborated, because angular derivatives are needed for its description. According to the reference space-angle system of Figure D.3, $\hat{e}_z$ represents the polar axis, $\cos^{-1}\xi$ the polar angle and the azimuthal angle ω is measured from the positive r axis. The angular variable $\mathbf{\Omega}$ can be expressed in terms of μ and η or ξ and ω, with the condition of symmetry on the emission density at $\omega = 0$, i.e.

$$\psi_g(r,z,\xi,\omega) = \psi_g(r,z,\xi,-\omega). \tag{D.17}$$

The system of curvilinear coordinates here defined leads to the following relations among the angular variables ξ and ω and the direction cosines μ and ξ.

$$\mu = \sqrt{1-\xi^2}\cos\omega, \tag{D.18}$$

$$\eta = \sqrt{1-\xi^2}\sin\omega. \tag{D.19}$$

Therefore the transport problem, defined in two-dimensional curvilinear coordinates, without the energy dependency and across without adsorbing or scattering can be recast as:

$$\left(\frac{\mu}{r}\frac{\partial}{\partial r}r - \frac{1}{r}\frac{\partial}{\partial\omega}\eta + \xi\frac{\partial}{\partial z} + \Sigma_{t,g}(r,z)\right)\psi_g(r,z,\xi,\omega) = q_g^{ex}(r,z\xi,\omega). \tag{D.20}$$

A level-symmetric or a reduced-symmetry quadrature set can be chosen for the curvilinear system of coordinate (r,ϕ,z) [129], where the directions are identified by the pairs $(\pm\mu_i,\pm\xi_i)$, for $i = 1,...,N/2$. The quadrature points are taken on constant levels of η_i about the z axis so that the derivative term on ω can be numerically calculated. Following the terminology pursued by [129], the direction $\mathbf{\Omega_n}$ is identified by means of two indices $\mathbf{\Omega_n} \rightarrow \mathbf{\Omega_{pq}} = \left[\xi_p,\mu_{pq}\right]$ (see Figure D.2 for a S_6 discrete ordinate set). The first one indicates the value ξ_p associated to $\mathbf{\Omega_n}$, having $\xi_1 < \xi_2 < ... < \xi_N$. The index q refers to the value of μ associated with the value of ξ_p. Therefore for a fixed value of ξ_p one finds the set of μ values, so that $\mu_{p1} < \mu_{p2} < ... < \mu_{pN_p}$, where $1 < N_p < N$. The treatment of the angular derivative requires particular attention, as the phenomenon of angular redistribution together with the presence of quadrature set of angular coordinates make this operation elaborated. Omitting here the mathematical procedure, one can state that imposing the radiation particle balance in case of infinite medium and flux distribution both uniform and isotropic the streaming terms should vanish. This can be achieved by introducing the angular differencing coefficients $\alpha^p_{q+1/2}$ so that:

$$\alpha^p_{q+1/2} = \alpha^p_{q-1/2} - \mu_{pq}w_{pq}, \tag{D.21}$$

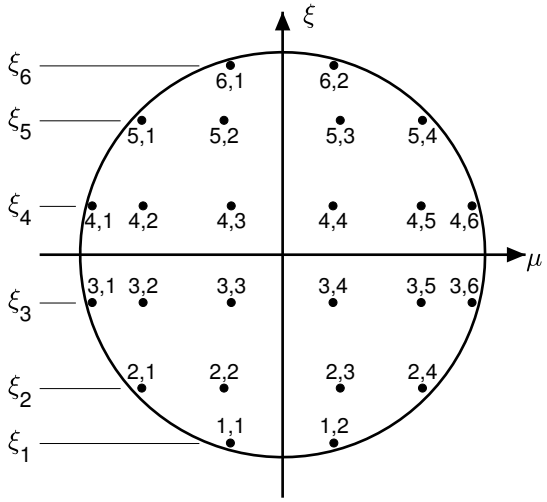

Figure D.2.: Schematic view of an S_6 quadrature set on the projection plane $\mu - \xi$, as per DSNQUAD utility program [209]. The calculated cosines μ_{pq} are associated with a polar angle cosine ξ_p. The figure is inspire to a similar representation of level-symmetric quadrature set reported in Ref. [129].

combined to the condition $\alpha^p_{1/2} = 0$ for $p = 1, 2, ...N$ [129], to progressively calculate $\alpha^2_{q+1/2}$ for $q = 1, 2, ..., N_p$. For a calculated value of $\alpha^2_{q+1/2}$, the so-called angular diamond difference approximation is introduced to the half-integer angular fluxes $\psi_{p,q+1/2}$ and $\psi_{p,q-1/2}$ to ψ_{pq}, yielding

$$\psi_{pq} \approx \frac{1}{2}\left(\psi_{p,q+1/2} + \psi_{p,q-1/2}\right) \quad p = 1, 2, ..., N, \;\; q = 1, 2, ..., N_p, \tag{D.22}$$

where the energy group index q has been suppressed for the sake of simpler notation. The discrete ordinate approximation applied to Equation (D.20) requires a recasting of the angular derivative $\frac{\partial}{\partial\omega}\eta$ to account for the angular redistribution.
An approximated formulation of Equation (D.20), combined to the diamond difference approximation of Equation (D.22), outlines the partial differential equation in the domain $\mathbf{r}(r, z)$ for solving the particle transport equation along a set of directions $\boldsymbol{\Omega_{pq}} = \left[\mu_{pq}, \xi_p\right]$, such that [129]:

$$\begin{aligned}\left(\frac{\mu_{pq}}{r}\frac{\partial}{\partial r}r + \frac{2\alpha^p_{q+1/2}}{r\, w_{pq}} + \xi_p\frac{\partial}{\partial z} + \Sigma_t(r,z)\right)\psi_{pq}(r,z) \\ - \frac{(\alpha^p_{q+1/2} + \alpha^p_{q-1/2})}{r\, w_{pq}}\psi_{p,q-1/2}(r,z) = q_{pq}(r,z).\end{aligned} \tag{D.23}$$

To solve Equation (D.23) for $q = 1$, the term $\psi_{p,1/2}$ needs to be treated separately, i.e. establishing a starting direction method. One can solve Equation (D.20) in the direction $\omega = \pi$, with $\xi = \xi_p$. A simpler (and faster) alternative, is to use the step differencing approximation, such that [129]

$$\psi_{p,1/2}(r,z) = \psi_{p,1}(r,z), \tag{D.24}$$

and Equation (D.23), for $q = 1$, then becomes:

$$\left(\frac{\mu_{p,1}}{r}\frac{\partial}{\partial r}r + \frac{\alpha^p_{3/2} - \alpha^p_{1/2}}{r\, w_{p,1}} + \xi_p\frac{\partial}{\partial z} + \Sigma_t(r,z)\right)\psi_{p,1}(r,z) = q_{p,1}(r,z). \tag{D.25}$$

A utility program called DSNQUAD [209] included in the 1D transport code ANISN [146] generates the reduced-symmetry quadrature set for a specified S_N order N. The calculation of the S_N constants [210], considers a quadrant of a unit sphere divided into $N(N+2)/4$ solid angles, each with a particular weight w. The S_N cosines μ_{pq} are measured from the $r-$axis (see Figure D.3) and the weights w_{pq} are the fraction of the surface area of the sphere which surrounds the intersection of the vector associated with the direction cosine and the surface of the sphere.

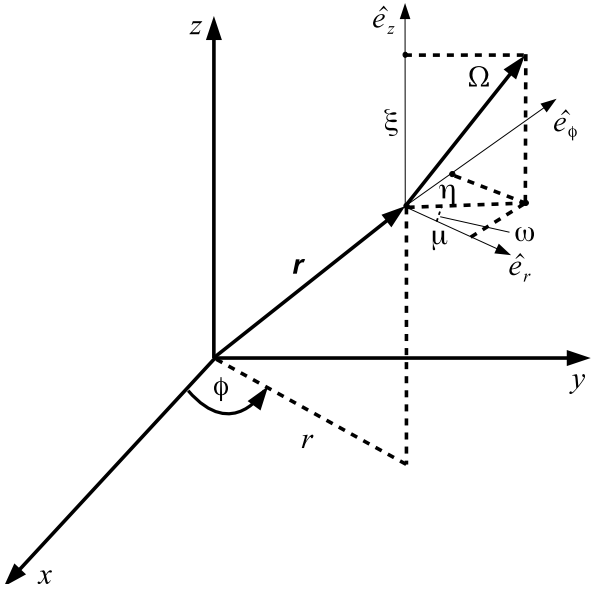

Figure D.3.: Cylindrical and Cartesian space-angle coordinate systems associated with the spatial-angle phase space of the Boltzmann transport equation $(\mathbf{r}, \mathbf{\Omega})$ (see Equation (D.1)). The (x, y, z) coordinates refers to the Cartesian coordinate system, whereas (r, ϕ, z) to the curvilinear ones.

Taking $\omega = \pi$ to measure the first direction cosine μ_{p0}, corresponding to $\xi_p = -\sqrt{1-\mu_{p0}^2}$ and $w = 0$, the solution of Equation (D.25) for $q = 1$ (with $\alpha^p_{1/2} = 0$), and of Equation (D.23) for increasing $q > 1$, advances for each level p upgrading $\alpha^p_{q+1/2}$, $\alpha^p_{q-1/2}$ and $\psi_{p,q-1/2}$ based on Equations (D.21) and (D.22).
Once all the angular flux distributions $\psi_{pq}(r,z)$ are known for all the $K(N) = N(N+2)/2$ ordinates, then the major integral parameters, such as scalar flux Φ and radial and vertical net currents, J_r and J_z, outlined in Equations (D.14) and (D.15), can be expressed as [129]:

$$\begin{aligned}
\Phi(r,z) &= \frac{1}{4}\sum_{pq}^{K(N)} w_{pq}\,\psi_{pq}(r,z), \\
J_r(r,z) &= \frac{1}{4}\sum_{pq}^{K(N)} w_{pq}\mu_{pq}\,\psi_{pq}(r,z), \\
J_z(r,z) &= \frac{1}{4}\sum_{pq}^{K(N)} w_{pq}\xi_p\,\psi_{pq}(r,z).
\end{aligned} \tag{D.26}$$

D.3.1. Solution of the Boltzmann Equation in One-Dimensional Cylindrical Geometry

The 1D model reduces its geometry detail to one radial coordinate $\mathbf{r} \equiv r$, considering therefore all quantities to be independent from the coordinate z. Moreover, the angular flux applies the reflection condition on the plane perpendicular to the direction z, i.e.:

$$\psi(r,\mu,\xi) = \psi(r,\mu,-\xi). \tag{D.27}$$

From the above relation it can be seen that Equations (D.23) and (D.25) can be solved considering only the two octants $\mu > 0, \xi > 0$ and $\mu < 0, \xi > 0$, where the whole geometric domain is approximated as an infinite cylinder. Accordingly, all components are represented by cylindrical layers having a given homogenized material composition.
Applying the same criteria one obtains the neutron balance equation for an infinite cylindrical geometry:

$$\left(\frac{\mu_{pq}}{r}\frac{\mathrm{d}}{\mathrm{d}r}r + \frac{2\alpha^p_{q+1/2}}{r\,w_{pq}} + \Sigma_t(r)\right)\psi_{pq}(r) - \frac{(\alpha^p_{q+1/2} + \alpha^p_{q-1/2})}{r w_{pq}}\psi_{p,q-1/2}(r) = q_{pq}(r), \tag{D.28}$$

where the angular differencing coefficients $\alpha^p_{q\pm1/2}$ obey to the same recursive rule reported in Equation (D.21). The resolution of this differential equation goes through the spatial differencing of the radial coordinate r into a grid characterized by N mesh points, as seen in Figure D.4, as per *diamond difference scheme* [129].

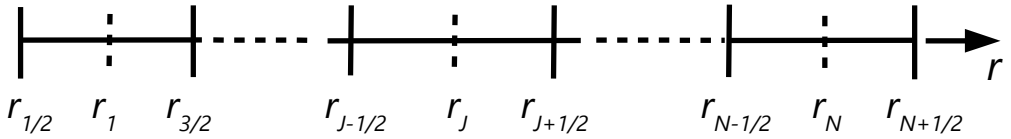

Figure D.4.: Diamond differencing scheme for cylindrical geometry

The cross section values Σ_t, angular flux ψ and emission density q are piecewise constant and they are considered to vary their value only at half-mesh point r_J, defined as:

$$r_J = \frac{r_{J+1/2} + r_{J-1/2}}{2}. \tag{D.29}$$

Hence, integrating Equation (D.28) between $r_{J-1/2}$ and $r_{J+1/2}$ (within the volume of a cylinder with a unitary height h) $V_J = \pi h(r^2_{J+1/2} - r^2_{J-1/2})$ and removing the energy group index g one obtains the following discrete set of algebraic equations in the unknowns $\psi_{pq,i}$:

$$\begin{aligned}\psi_{pq,J} = {} & \psi^{shell}_{pq,J} + \\ & \left\{(A_{J+1/2} - A_{J-1/2})\left[|\mu_{pq}| + \frac{\left(\alpha^p_{q+1/2} + \alpha^p_{q-1/2}\right)}{w_{pq}}\right] + \Sigma_{t,J}V_J\right\}^{-1} \times \\ & \left\{(A_{J+1/2} - A_{J-1/2})\left[|\mu_{pq}|\,\psi_{p,q,J+1/2} + \frac{\left(\alpha^p_{q+1/2} + \alpha^p_{q-1/2}\right)}{w_{pq}}\psi_{p,q-1/2,J}\right] + V_J \cdot q_{pq,J}\right\},\end{aligned} \tag{D.30}$$

which needs to be coupled to the two diamond difference relationships:

$$\psi_{pq,J} = \frac{1}{2}\left(\psi_{p,q-1/2,J} + \psi_{p,q+1/2,J}\right), \tag{D.31}$$

and

$$\psi_{pq,J} = \frac{1}{2}\left(\psi_{p,q,J+1/2} + \psi_{p,q,J-1/2}\right). \tag{D.32}$$

Solving for increasing values of μ_{pq} one finds:

$$\psi_{p,q+1/2,i} = 2\psi_{pq,J} - \psi_{p,q-1/2,J}, \tag{D.33}$$

and for negative values of μ_{pq} the procedure starts from the outer boundary and moves inward. Equation (D.33) then yields

$$\psi_{pq,J-1/2} = 2\psi_{pq,J} - \psi_{pq,J+1/2}. \tag{D.34}$$

$\psi^{shell}_{pq,J}$ indicates an arbitrarily source term (if any) named shell source for the angular neutron flux along the direction μ_{pq} in the interval J. That is a mathematical formalism introduced in the ANISN 1D transport code to allow for an angular description of the neutron source in one or more radial intervals. Once the angular and spatial grids are established (setting up the order N and the number of radial nodes) the algorithm to calculate the angular flux for the energy group g, angular coordinate μ_{pq} and the radial node r_J is straightforward and can be easily implemented in computer codes.

The truncation error coming from the diamond spatial differencing is $\mathcal{O}((\Sigma^J_t\Delta_J/2|\mu_{pq}|)^2)$ [129], where $\Delta_J = r_{J+1/2} - r_{J-1/2}$ denotes the mesh spacing of the interval J. The allowable mesh spacing is determined by the smallest $|\mu_{pq}|$ and must obey to:

$$\Delta_J \ll \frac{2|\mu_{pq}|}{\Sigma^J_t}, \tag{D.35}$$

where the largest value of Σ^J_t among all energy groups has to be considered. If $\Delta_J > \frac{2|\mu_{pq}|}{\Sigma^J_t}$ negative angular fluxes will result. In transport problems with highly anisotropic scattering (requiring high-order S_N and small μ_{pq}) and highly adsorbing material (large Σ^J_t) this criterion may not always feasible, leading to mesh spacings that are small fractions of centimeter [129]. In these cases, there are alternative difference schemes which guarantee the non-appearance of negative angular flux densities disregarding the size of Δ_J. These are based on lower accuracies, with truncation errors $\mathcal{O}(\Sigma^J_t\Delta_J/2|\mu_{pq}|)$ [129].

The solution algorithm to solve a neutron transport problem using the discrete ordinate method is based on the iteration on the scattering source $q_{n,g}(\mathbf{r})$, as it is dependent on the angular flux value for all the $K(N)$ angular coordinates on the point r. Therefore, for discrete ordinate method the within group neutron transport equation has the form:

$$\left[\boldsymbol{\Omega_n}\cdot\nabla + \Sigma_t(\mathbf{r})\right]\psi^{l+1}_{n,g}(\mathbf{r},\boldsymbol{\Omega_n}) = q^l_{n,g}(\mathbf{r},\boldsymbol{\Omega_n}), \tag{D.36}$$

where l indicated the iteration index. The solution algorithm normally starts with an initial guess of the solution $\psi^0_{n,g}$ and updates the emission density $q^l_{n,g}$ until the solution converges to a constant value with a fixed tolerance ϵ, given for instance on the scalar flux Φ_g (see Equation (D.14)). The solution algorithm stops when the following condition is verified:

$$\frac{\left|\Phi^{l+1}_g - \Phi^l_g\right|}{\Phi^l_g} \leq \epsilon, \tag{D.37}$$

which needs to be verified in all points of the spatial domain $\forall\mathbf{r}\in\mathcal{D}$.

D.4. Important Nuclear Cross Section in Fusion Applications

The following plots display some trends of important nuclear microscopic cross sections σ for variations of the incident neutron energy E_n. These include:

- tritium production (Figure D.5);
- neutron multiplication (Figure D.6);
- elastic scattering (Figure D.7);
- neutron-induced gamma production (Figure D.8);

The plots have been produced extracting the microscopic cross section from the FENDL3.1 nuclear libraries [149, 150] with the NEA software JANIS (Java-based nuclear information software) [211].

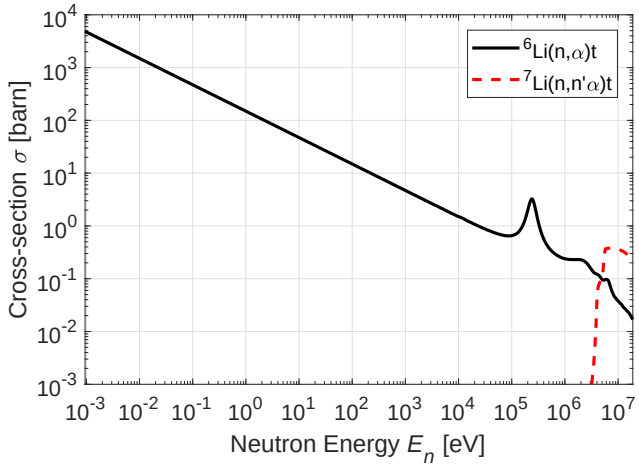

Figure D.5.: Microscopic cross section σ of T production for ^{6}Li and ^{7}Li vs. incident neutron energy E_n.

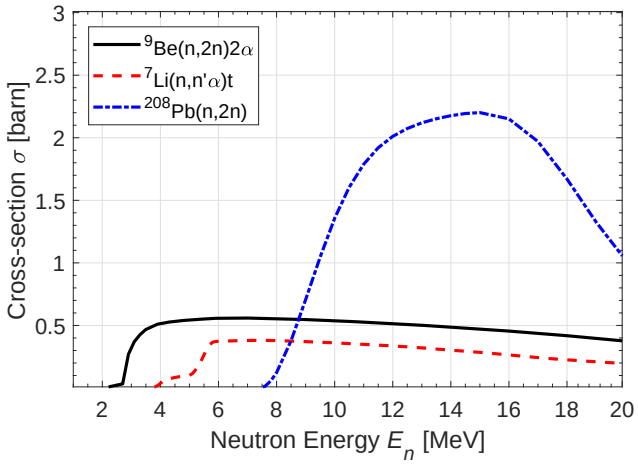

Figure D.6.: Microscopic cross section σ of neutron multiplication for ^{9}Be, ^{7}Li and ^{208}Pb vs. incident neutron energy E_n.

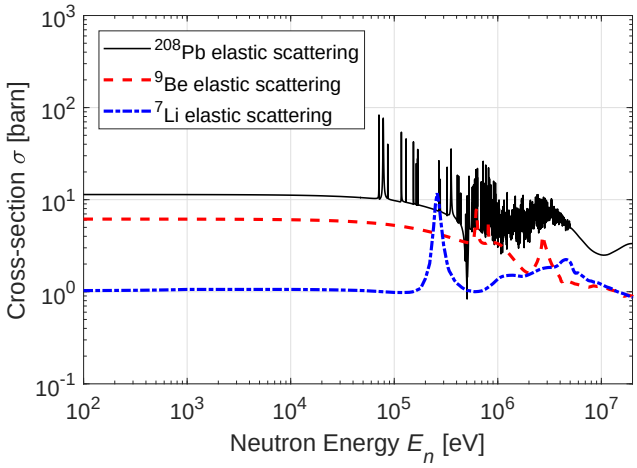

Figure D.7.: Microscopic cross section σ of elastic scattering for ^{208}Pb, ^{9}Be and ^{7}Li vs. incident neutron energy E_n.

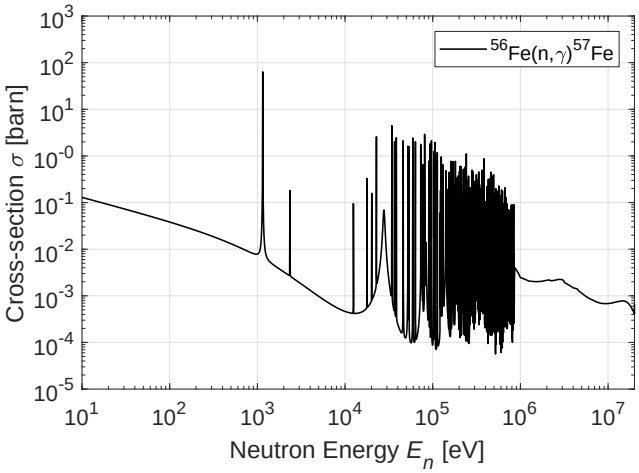

Figure D.8.: Microscopic cross section σ of ^{56}Fe$(n,\gamma)^{57}$Fe incident neutron energy E_n.

E. Verification and Benchmark of New System Code Models

The implementation of a mathematical model simulating a physical process necessitates:

- a verification study to assess the correctness of the problem definition and
- a benchmark against the solution considered to be exact or proven to be experimentally validated.

In this section, three newly developed models are being verified and (if possible) benchmarked against some reference solutions. The analysed models are:

- 2D plasma magnetic equilibrium (see Section 3.1),
- 2D core neutron/gamma radiation transport radiation in plasma vacuum chamber (see Section 4.1.2) and
- 1D global reactor neutron/photon radiation transport (see Section 4.1.3).

E.1. Verification Study of the Grad-Shafranov Equilibrium Model

Due to the current lack of running DEMO (or ITER)-like devices, the proposed numerical method is compared with analytical formulae available in literature. The simplest solution to the inhomogeneous GSE is the Solov'ev equilibrium [91] based on the linear dependence on Ψ of the functions included in the current density source term, i.e. pressure $p(\Psi)$ and poloidal current $f(\Psi)$. Such equilibria are used to study different transport and stability conditions. However, these are somewhat overconstrained in shape, poloidal beta and plasma current, and thus not entirely transferable to tokamak equilibria configurations. But, they allow to cross-check the correct implementation of the model and the interpretation of the results.

Due to its simplicity, the set of formulae detailed by Zheng et al. [212] has been chosen to verify the numerical solution of Equation (3.27) against the exact analytical solution Ψ_e of the GSE, under Solov'ev equilibrium. This special equilibrium configuration implies a linear dependency on Ψ of the source functions p and f, and can be expressed as [212]

$$\begin{aligned} A_1 &= -\mu_0 \frac{\mathrm{d}p}{\mathrm{d}\Psi}, \\ A_2 &= \frac{1}{2}\frac{\mathrm{d}f^2}{\mathrm{d}\Psi}. \end{aligned} \tag{E.1}$$

The two coefficients A_1 and A_2 denoting the current density distribution represent two degrees of freedom of the problem and can be determined so that the requirements on plasma current and poloidal beta are met. As a result $J_{\phi,p} \equiv J_{\phi,p}(r, I_p, \beta_p) \equiv 1/\mu_0 \left(A_1 r - A_2/r\right) \forall z \in \mathcal{D}_p$, with $\mathcal{D}_p$

being any arbitrary domain in the (r,z) poloidal coordinate system. Based on this definition of $J_{\phi,p}$ the GSE becomes

$$\Delta^*\Psi_e = r^2 A_1 - A_2, \tag{E.2}$$

where $\Delta^* = r\frac{\partial}{\partial r}\left(\frac{1}{r}\frac{\partial}{\partial r}\right) + \frac{\partial^2}{\partial z^2}$ is the elliptic operator identified by the LHS of Equation (3.6). The solution of Equation (E.2) defines the radial-poloidal distribution of the poloidal flux $\Psi_e(r,z)$ (divided by 2π) and yields

$$\Psi_e(r,z) = c_1 + c_2 r^2 + c_3\left(r^4 - 4r^2z^2\right) + c_4\left(r^2\ln r - z^2\right) + \frac{A_1}{8}r^4 - \frac{A_2}{2}z^2 \tag{E.3}$$

where the four coefficients $c_1, ..., c_4$ can be obtained assuming the plasma to be mirror symmetric and imposing four bounding Dirichlet boundary conditions ($\Psi = 0$), dictated by the plasma parameters R_0, a, κ and δ. These are outlined by the mid-equatorial innermost and outermost radial coordinates $r_i = R_0 - a$ and $r_o = R_0 + a$ and by the top elongated radial and vertical coordinates $r_t = R_0 - \delta a$ and $z_t = \kappa a$. On the latter, due to its definition of most elongated point, a null radial gradient condition $\frac{\partial\Psi}{\partial r} = 0$ is imposed. R_0 and a denote here the major and minor radii, while κ and δ relate to the plasma elongation and triangularity at the LCMS. In summary, the four conditions for the determination of $c_1, ..., c_4$ become then

$$\begin{aligned}
&c_1 + c_2 r_i^2 + c_3 r_i^4 + c_4\ln(r_i) = -\frac{A_1}{8}r_i^4,\\
&c_1 + c_2 r_o^2 + c_3 r_o^4 + c_4\ln(r_o) = -\frac{A_1}{8}r_o^4,\\
&c_1 + c_2 r_t^2 + c_3 r_t^2(r_t^2 - 4z_t^2) + c_4\left[r_t^2\ln(r_t) - z_t^2\right] = -\frac{A_1}{8}r_t^4 + \frac{A_2}{2}z_t^2,\\
&2c_2 + 4c_3(r_t^2 - 2z_t^2) + c_4\left[r_t^2\ln(r_t) - t_z^2\right] = -\frac{A_1}{2}r_t^2,
\end{aligned} \tag{E.4}$$

and the two coefficients A_1 and A_2 can be extracted from the total current I_p and poloidal beta β_p such that

$$\begin{aligned}
I_p &= \int_{\mathcal{D}_p} J_{\phi,p}\mathrm{d}r\mathrm{d}z = -\frac{1}{\mu_0}\int_{\mathcal{D}_p}\left(rA_1 - \frac{A_2}{r}\right)\mathrm{d}r\mathrm{d}z,\\
\beta_p &= 2\mu_0\frac{\langle p\rangle_V}{\langle B_p\rangle_l^2} = -\frac{2A_1\left(\oint_{\partial\mathcal{D}_p}\mathrm{d}l\right)^2}{\mu_0^2 I_p^2}\frac{\int_{\mathcal{D}_p}\Psi r\mathrm{d}r\mathrm{d}z}{\int_{\mathcal{D}_p} r\mathrm{d}r\mathrm{d}z}.
\end{aligned} \tag{E.5}$$

Calculating the exact solution for a homogeneous rectangular mesh boxed within the radial interval $r \in [r_i, r_o]$ and poloidal interval $z \in [-z_t, z_t]$, the poloidal contour depicting the null-poloidal magnetic flux surface is extracted and imposed as plasma boundary $\partial\mathcal{D}_p$ for the weak problem formulated in Equation (3.27). Adapting the same equilibrium solving methodology of Figure 3.3, the target vector $\underline{v}$ is reduced to two parameters only (I_p, β_p) and the Picard iterations are simply avoided, due to the linearity of Equation (E.2) and to the absence of the normalized flux $\overline{\Psi}$. Under these conditions, the outgoing distribution of Ψ_h, together with the parameters A_1 and A_2 can be compared to the analytical solution given by Equation (E.3).

In elliptical partial differential equations (PDE), such as Equation (E.2), two notations are adopted to quantify the deviation of the approximated numerical solution $\Psi_h(\mathbf{r})$ from its exact solution $\Psi_e(\mathbf{r})$, where $\mathbf{r} \in \mathcal{D}$ identifies the spatial variable and $\mathcal{D}$ the space domain. These are the error

in the L^2 norm

$$\|\epsilon\|_{L^2} = \sqrt{\frac{\int_{\mathcal{D}} (\Psi_h - \Psi_e)^2 \, \mathrm{d}\mathbf{r}}{\int_{\mathcal{D}} \Psi_e^2 \, \mathrm{d}\mathbf{r}}}, \tag{E.6}$$

and the in H^1 norm

$$\|\epsilon\|_{H^1} = \sqrt{\frac{\int_{\mathcal{D}} \left[(\nabla\Psi_h - \nabla\Psi_e)^2 + (\Psi_h - \Psi_e)^2 \right] \mathrm{d}\mathbf{r}}{\int_{\mathcal{D}} \left[(\nabla\Psi_e)^2 + \Psi_e^2 \right] \mathrm{d}\mathbf{r}}}. \tag{E.7}$$

The first bases on the solution function directly involved in the PDE, whereas the latter takes into account of the error affecting the gradients. The H^1-error is of relevance, as the poloidal magnetic field is directly associated with the gradient of Ψ. The subscript h of the FE solution denotes that the solution (and its numerical error) is affected by the mesh size h, i.e. the maximum distance from two adjacent mesh nodes. In order to identify the optimal mesh size to adopt in a reactor system analysis, this dependence has been examined for a plasma Solov'ev equilibrium configuration applied to the EU-DEMO 2015 design [30] assuming $R_0 = 9.07$ m, $A = 3.1$, $\kappa = 1.7$, $\delta = 0.5$, $I_p = 19.6$ MA, $\beta_p = 1.107$ and $B_t = 5.67$ T. The mesh size h has been scanned starting from $h = 1$ m and halving its value five times, thus down to $h = 0.03125$ m. The L^2 and the H^1-norm error has been evaluated for each scanned mesh metric is depicted in Figure E.1, both for piecewise linear and quadratic continuous finite elements P_1 and P_2.

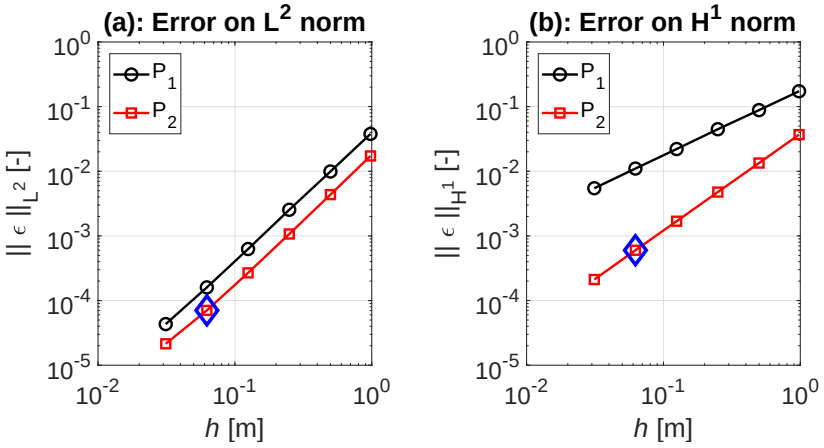

Figure E.1.: Convergence rates for the mesh metric h related to the two-dimensional plasma equilibrium problem defined by the Grad-Shafranov and solved numerically as per finite element method. Subfigures (a) and (b) display the error in L^2- and H^1 norm. For each plot, the black-circled and the red-squared marker curves base respectively on the piecewise linear and quadratic finite element functions adopted for the poloidal flux Ψ, solution of Equation (E.2). The blue diamond markers indicate the metric size yielding a selected optimal accuracy.

The finite element approximation for elliptical problems, where the calculated solution Ψ_h reproduces the exact solution Ψ_e converges in the H^1 norm if $\|\epsilon\|_{H^1} \leq Ch^p$ for $p > 0$, where p is called the rate of convergence [213]. The rate depends on the degree of the polynomial used to approximate Ψ, the order of the highest derivative of Ψ in the weak form, and whether there are local singularities in the domain. The constant C is independent of Ψ and depends on the domain shape and boundary

conditions. Typically one finds $p = k + 1 - m > 0$, where k is the degree of the polynomial used in the interpolation and m is the order of the highest derivative of Ψ in the weak form, i.e. $m = 1$ for Equation (3.28).
As a result, the H^1-norm error is excepted to converge with h and h^2 for P_1 and P_2, respectively. This trend has found positive confirmation in Figure E.1−b, where the black-circle marker line, designating the P_1 FE approximation, linearly scales with h, whereas the P_2 elements (red-squared marker line) feature a higher convergence rate ($p \approx 1.7$) and a rather smaller error.
The L^2-norm error (Figure E.1−a) drops quadratically with h, i.e. $(p = 2)$ both for linear and quadratic piecewise continuous functions. The error convergence rate results found for the numerical solution of our elliptical problem are in line with the literature guidelines of Ref. [134] on a priori estimate of the error on L^2 and H^1 norm.
The same verification study has been conducted likening the finite element solution Ψ_h of Equation (3.27) to the exact solution Ψ_e for a wide range of major radius $R_0 = 6 - 12$ m and aspect ratio $A = 2 - 4$ fixing elongation and triangularity and calculating I_p and B_t according to Equations (3.15) and (3.17). Based on this more extended study and observing the mesh convergence rates of Figure E.1 any equilibrium problem postulated in weak form and based on P_2 elements and mesh metric $h = 0.10 - 0.20$ m was found to be a good compromise between H^1-norm error amplitude (always around 10^{-3}) and computing time ($\approx$ 2-5 sec, including mesh generation).

In order to extend the proposed solving method to any tokamak a relation for the optimal mesh size h as a function of the plasma minor radius a, playing the dominant role of this function, is evaluated. With P_2 FE several analyses have been carried out for increasing values of a. A linear scaling on a has been found for a fixed value of $\|\epsilon\|_{L^2}$ and $\|\epsilon\|_{H^1}$ with 10^{-4} and 10^{-3} based on grid-independence criteria. Therefore, referring to blue diamond marker on L^2-norm curve of Figure E.1, yielding $\|\epsilon\|_{L^2} \approx 7 \times 10^{-4}$ and $\|\epsilon\|_{H^1} \approx 6 \times 10^{-4}$ for $h \approx 0.06$ m, one can infer that a first rule-of-thumb law to extract h for a given plasma minor radius a can be written as

$$0.1 \times a[\mathrm{m}] \leq h[\mathrm{m}] \leq 0.05 \times a[\mathrm{m}], \tag{E.8}$$

which can be applied safely to any general system code analysis.

A further verification has been performed for the error η_h on the integral balance equations, which the GSE is derived from. With reference to the static equilibrium of plasma (Equation (3.1)) and the integral form of Ampere's law (Equation (3.14)), one wishes to observe the following conditions:

$$\begin{aligned}
\eta_{h,r} &= \int_{\mathcal{D}_p} \left[\frac{\partial p}{\partial r} - \left(J_\phi B_z - J_z B_\phi \right) \right] \mathrm{d}\mathbf{r} \approx 0, \\
\eta_{h,z} &= \int_{\mathcal{D}_p} \left[\frac{\partial p}{\partial z} - \left(J_r B_\phi - J_\phi B_r \right) \right] \mathrm{d}\mathbf{r} \approx 0, \\
\eta_{h,\phi} &= \int_{\mathcal{D}_p} \left(J_r B_z - J_z B_r \right) \mathrm{d}\mathbf{r} \approx 0, \\
\eta_{h,A} &= \frac{1}{\mu_0} \oint_{\partial\mathcal{D}_p} \left(B_r \hat{n}_z - B_z \hat{n}_r \right) \mathrm{d}l - I_p \approx 0,
\end{aligned} \tag{E.9}$$

where J_r and J_z denote the radial and vertical plasma current density and are expressed as in Equation (3.5) as function of the poloidal current f, as well as the toroidal magnetic field $B_\phi = \mu_0 f / (2\pi r)$. B_r and B_p are the radial and the vertical magnetic field component and hinge on the poloidal magnetic flux Ψ according to Equation (3.4). Finally, $\hat{n}_r$ and $\hat{n}_z$ point to the radial and vertical normal

vectors on the LCMS contour enclosing the plasma boundary $\partial\Omega_p$. The four listed integrals can be easily performed within a finite element environment. The maximum residual error on the three momentum balance equations does not exceed a few kN ($|\eta_{h,r}| \approx 2$ kN), thus much smaller compared to the total Lorentz force $F_L = \left\| \int_{\mathcal{D}_p} (\mathbf{J} \times \mathbf{B}) \mathrm{d}\mathbf{r} \right\| \approx 100$ MN. The residual error on the plasma current loop integral features similar figures, i.e. $|\eta_{h,A}| \approx 3$ kA $\ll I_p$. Therefore, one can conclude that the errors associated with implemented equilibrium model are related mainly to numerical issues, caused by finite element interpolation and/or numerical precision.

The spatial distribution of the poloidal magnetic flux $\Psi(r,z)$ is depicted in Figure E.2. The results have been obtained for a mesh spacing of $h = 0.15$ m and imposing the Solov'ev equilibrium conditions (see Equation (E.1)) and for the symmetric plasma parameters associated with the DEMO 2015 design. The topology of nested close magnetic flux surfaces is underlined by the black-line contours, where the coloured region delimit the different flux regions. Ψ increases from the plasma periphery (where the null flux boundary condition is applied) towards the plasma magnetic axis, where it reaches its maximum values and the radial and vertical magnetic field components vanish. An important aspect, in view of an integration in system codes, bases on the radial and vertical distributions of Ψ and on the impact on the major plasma parameters affecting the global plasma performances, such as density and temperature. As seen in Figure E.2, larger flux regions are located around the plasma center, where density and temperatures are found larger, so does the fusion yield. As a result, the volume integration of the fusion power density over a spatially distributed magnetic configuration can be somewhat beneficial in view of a deeper and more accurate estimation of the key reactor parameters.

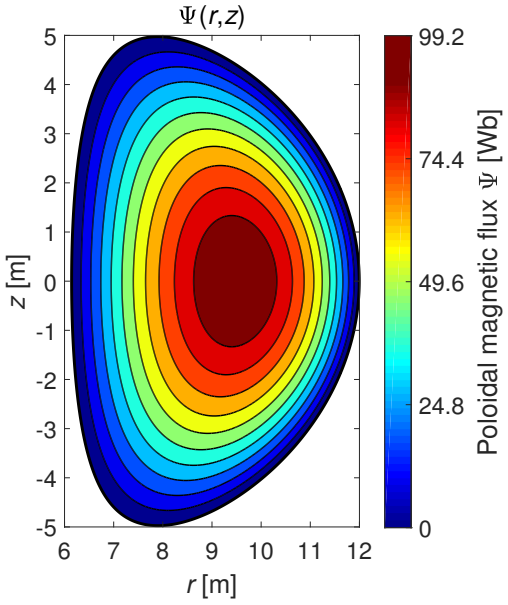

Figure E.2.: Contour plot of the poloidal magnetic flux inside the plasma domain (finite element solution). The Solov'ev equilibrium conditions and the main DEMO 2015 design specifications are imposed, such as: $R_0 = 9.07$ m, $A = 3.1$, $\kappa = 1.7$, $\delta = 0.5$, $I_p = 19.6$ MA, $\beta_p = 1.107$. The solution is obtained for a uniform triangular mesh, whose metric h has been set equal to 15 cm.

E.2. Verification and Benchmark of the 2D Core Plasma Radiation Transport Model

In order to verify the weak formulation of Equations (4.22) and (4.23) (attaining to the discontinuous Galerkin method) and to evaluate the error derived from the S_N discrete ordinate approximation, a verification and a benchmark (V&B) study has been carried out by means of two separate techniques:

- verification against a manufactured exact analytical solution $\psi_e(x,y)$ on an arbitrary L-square two-dimensional Cartesian domain $(x,y) \in \mathcal{D} = [0,L] \times [0,L]$;
- benchmark against a Monte Carlo transport model of a DEMO-like plasma vacuum chamber and neutron volumetric source.

E.2.1. Verification against analytical solution

With reference to Figure E.3−a a square geometry domain has been deployed for obtaining a simple analytical solution $\psi_e(x,y)$, fulfilling the vacuum boundary condition on the inflow boundary $\partial\mathcal{D}^0$. In two-dimensional Cartesian coordinate system (x,y) the transport problem of Equation (D.1) for monoenergetic particles in void media and the angular variable $\mathbf{\Omega} = [\mu,\eta]$ becomes:

$$\begin{cases} \left(\mu\dfrac{\partial}{\partial x} + \eta\dfrac{\partial}{\partial y}\right)\psi(x,y) = S(x,y) \\ \psi(x,y) = 0 \text{ on } \partial\mathcal{D}_- \end{cases}, \tag{E.10}$$

which, for $\mu > 0$ and $\eta > 0$ admits the following exact solution $\psi_e(x,y)$ [207]

$$\psi_e(x,y) = xy \quad \text{for } \mu > 0 \wedge \eta > 0, \tag{E.11}$$

artificially produced to meet the boundary condition of Equation (E.10) on $\partial\mathcal{D}^0 = \{(x,y) \mid x = 0, y = 0\}$ (see red lines of Figure E.3). The 2D colormap of ψ_e is displayed in Figure E.3-b and it has been calculated on a unit-square domain ($L = 1$ m), for $\mu = \frac{\sqrt{2}}{2}$ and $\eta = \frac{\sqrt{2}}{2}$, which corresponds to a 45° azimuthal angle ϕ (see Figure D.3). Substituting $\psi_e(x,y)$ to $\psi(x,y)$ in Equation (E.10) yields the following source term

$$S(x,y) = \mu y + \eta x \quad \text{for } \mu > 0 \wedge \eta > 0. \tag{E.12}$$

Having $\mathcal{T}_h$ as a structured mesh, composed by n_t elements T_k, to approximate the domain $\mathcal{D}$ in Cartesian coordinate (x,y), the approximated solution $\psi_h(x,y) \approx \psi(x,y)$ is sought in the piecewise linear discontinuous finite element space $\mathcal{W}_h(\mathcal{T}_h)$ (see Equation (A.11)) and obtained by solving the following weak formulation of Equation (E.10), derived from Equations (4.22) and (4.23)

$$\begin{aligned} &\int_{\mathcal{T}_h}\left(\mu\frac{\partial}{\partial x} + \eta\frac{\partial}{\partial y}\right)\psi_h\, v_h \,\mathrm{d}x\mathrm{d}y + \\ &\quad + \sum_{T_k\in\mathcal{T}_h}\sum_{e\in\partial T_k}\int_e \mathcal{H}(\psi_h,\mathbf{\Omega},\mathbf{n}_k)v_h \,\mathrm{d}\ell = \int_{\mathcal{T}_h} S\, v_h \,\mathrm{d}x\mathrm{d}y \qquad \forall v_h \in \mathcal{W}_h \end{aligned} \tag{E.13}$$

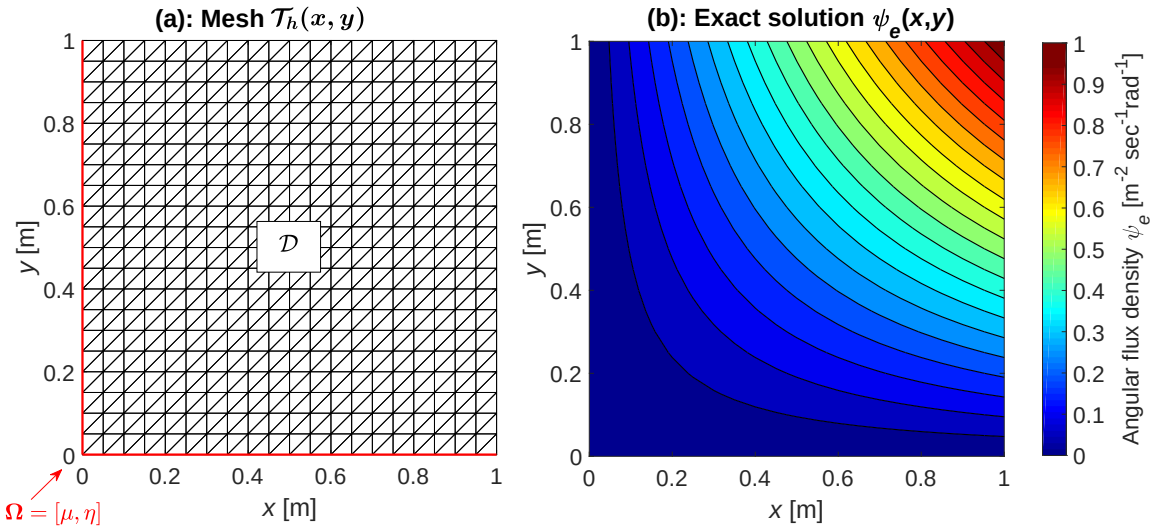

Figure E.3.: Exact solution for the 2D advection problem of Equation (E.10). Sub-figure (a) displays the structured triangular mesh $\mathcal{T}_h$ ($h = 5$ cm for the visualized case), associated with the unit-square domain $\mathcal{D}$ in (x,y) Cartesian system, whose side L is as long as one meter. Having assumed $\mathbf{\Omega} = [\mu, \eta]$, with $\mu > 0$ and $\eta > 0$, the inflow boundaries $\partial\mathcal{D}_-$ are represented by the red edges, located at $x = 0$ and $y = 0$. Sub-figure (b) shows the 2D colormap of manufactured exact solution $\psi_e(x,y) = xy$, which fulfils the vacuum boundary conditions on $\partial\mathcal{D}_-$.

where all v_h are test functions on $\mathcal{W}_h$ and $\mathcal{H}(\psi_h, \mathbf{\Omega}, \mathbf{n}_k)$ is the upwind numerical flux of ψ_h for the direction $\mathbf{\Omega} = [\mu, \eta]$ along the oriented versor $\mathbf{n}_k = \left[n_x, n_y\right]_{\partial T_k}$ on the mesh element edge ∂T_k (see Equation (4.24)). Similarly to the reference case in curvilinear (r,z) coordinates, the mesh $\mathcal{T}_h$ has been created with the built-in `Freefem++` mesh generator and Equation (E.13) has been implemented. The integral operators acting on all mesh elements of $\mathcal{T}_h$ (`int2d(Th)`) and on the all element edges `intalledges(Th)`, together with the `jump` function, make the implementation of Equation (E.13) rather straightforward. The convergence of the error $\epsilon = \psi_h - \psi_e$ of the solution of Equation (E.13) is evaluated for an increasing number of mesh nodes (or number degrees of freedom - NDOF), reduced to h. Assuming the reference case of Figure E.3, i.e. $L = 1$ m and $\mathbf{\Omega} = \frac{\sqrt{2}}{2}[1,1]$, different values of $\|\epsilon\|_{L^2}$ and $\|\epsilon\|_{H^1}$ haven been calculated for h spanning from 0.5 m to 1 cm; the results are reported in Figure E.4.
Analysing the data on both curves, a situation for as $p = 2$ and $p = 1$ is found for $\|\epsilon\|_{L^2}$ and $\|\epsilon\|_{H^1}$, which finds confirmation L^2 and H^1-norm a-priori error estimates available in literature [134, 214]. Next a relation for the optimal mesh size h as a function of the plasma minor radius a, and ensuring a feasibly low error for any possible fusion power plant plasma/SOL domain scenario is elaborated. Carrying out the error analysis for increasing values of L, hence for a, a linear scaling trend on h is observed for a fixed value $\|\epsilon\|_{L^2}$ with 10^{-3} being assumed to be reasonably low. Therefore, taking the plasma minor radius a scaling to L, such that $a \approx L/2$, and referring to blue diamond on the L^2-norm curve of Figure E.4 (yielding $\|\epsilon\|_{L^2} \approx 10^{-3}$ for $h \approx 0.05$ m), one can infer that a first rule-of-thumb law to extract h for a given plasma minor radius a can be written as

$$h[\mathrm{m}] = 0.05 \times a[\mathrm{m}], \tag{E.14}$$

where a safety factor 2 has been conservatively applied. As none of the parameters of interest attaining to the transport refers to the partial derivatives of ψ, those considerations have been made only on the L^2-norm error estimate. An additional verification exercise concerns the conservativeness

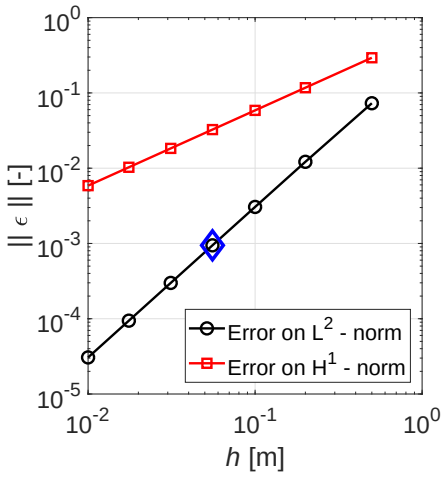

Figure E.4.: Error convergence curves for decreasing values of mesh size h for the two-dimensional plasma advection problem of E.10, solved numerically as per discontinuous Galerkin method (see Equation (E.13)). The blue diamond indicates the metric size yielding a selected optimal accuracy for the transport problem

of the proposed method. Accordingly, the surface integral over the whole outflow boundary $\partial\mathcal{D}_+ = \{(x,y) \in \partial\mathcal{D} \,|\, \mathbf{n}\cdot\boldsymbol{\Omega} > 0\}$, shall equate the volume integral of the fixed source $S(x,y)$. As a result, the verification of the mass conservation is performed, leading to following expression of the global mass balance error $\eta_{h,\psi}$, defined as:

$$\eta_{h,\psi} = \int_{\mathcal{D}} S(x,y)\mathrm{d}x\mathrm{d}y - \int_{\partial\mathcal{D}_+} \mathbf{n}\cdot\boldsymbol{\Omega}\psi_h(x,y)\mathrm{d}\ell, \tag{E.15}$$

where, based on Equation (E.12), the integral on S, can be easily obtained analytically, leading to

$$\eta_{h,\psi} = \frac{L^3}{2}(\mu+\eta) - \int_{\partial\mathcal{D}_+} \left[n_x(x,y)\mu + n_y(x,y)\eta\right]\psi_h(x,y)\mathrm{d}\ell, \tag{E.16}$$

with n_x and n_y denoting the $x-$ and $y-$ component of the normal versor $\mathbf{n}$ on every mesh element edges on $\partial\mathcal{D}_+$. The aforementioned error estimate used to verify the mass balance conservation, has been applied for several values of L, and applying a metric size h, as per Equation (E.14). The results confirmed the correctness of the implemented methods, with residual errors of $|\eta_{h,\psi}| \sim 10^{-16}$ s^{-1} for $L = 1$ m, resulting into an infinitesimal fraction of the integral particle volume source $\int S(x,y)\mathrm{d}x\mathrm{d}y = L^3/2(\mu+\eta) \approx 0.7$ s^{-1}.

E.2.2. Benchmark against Monte Carlo solution

A benchmark of the model has been also performed with respect to a more realistic tokamak radiation transport situation, i.e. based on a two-dimensional axisymmetric curvilinear coordinate system. The results of the discontinuous finite element radiation transport model, described in Section 4.1.2 and integrated in the MIRA system/design code, have been obtained for a typical DEMO-like neutron source and geometry situation, referred to the EU-DEMO 2015 baseline [30]. The angular flux density outcome of problem (4.21) (basing on a deterministic numeric approach), is

post-processed by means of Equation (D.26) in terms of wall loading poloidal distribution $\Gamma_{\perp}^{n}(\alpha_w)$ (see Equation (4.17)) and compared to the same distribution calculated as per a statistic approach, i.e. based on Monte Carlo method. The Monte Carlo N-Particle (MCNP) code has been used to simulate the neutron transport problem. As the verification study has been performed attaining to an analytical solution on a very simplified (Cartesian) geometry configuration, the benchmark against Monte Carlo solution allows to assess the error associated with the discrete ordinate approximation, essentially due the quadrature formula (see Equation (D.26)) and to the angular diamond difference scheme (see Equation (D.22)).

A mathematical formalism is needed to represent the geometrical topology of the magnetic flux surfaces (MS), such that the spatial profile of the volumetric neutron source can be reproduced in both numerical and statistic environments. Defining the variable $\varrho = \rho \cdot a$, with $\rho \in [0,1]$ being the normalized magnetic flux coordinate (see Equation (3.34)), having the plasma electron density n_e and temperature T both constant on a magnetic flux surface identified by $\varrho = \varrho_i$, one can infer that the generic isotropic volumetric source $q_{pq} \equiv q$, along the direction $\mathbf{\Omega_{pq}} = [\mu_{pq}, \xi_p]$, can be expressed as a function of ϱ, too. A formulation has been proposed by Fausser et al [194], yielding

$$q(\varrho) \propto \left[1 - \left(\frac{\varrho}{a}\right)^2\right]^P, \tag{E.17}$$

with P being a user-defined peaking factor. This profile assumes a L-mode confinement configuration, with null pedestal electron density and temperature (see Equation (3.35)). In conjunction with such a notation a set of parametric equations is being utilized to manufacture the shape of a genetic magnetic surface identified by $\varrho = \varrho_i$ in (r,z) curvilinear coordinate system (see Figure E.5. As a result, any point $P(r',z')$ laying on such curve can be localized by means of the independent variables α and ϱ, such that

$$\begin{cases} r'(\varrho,\alpha) = R_0 + \varrho\cos(\alpha + \delta \cdot \sin\alpha), \\ z'(\varrho,\alpha) = \kappa \cdot \varrho \sin\alpha, \end{cases} \tag{E.18}$$

with R_0, δ and κ denoting the plasma major radius, triangularity and elongation. The polar coordinate coordinate $\alpha \in [0, 2\pi]$ (not to be confused with a geometrical angle) is simply a parametric variable, conveniently chosen for magnetic surface profiling purposes. With reference to Figure E.5, the plasma chamber region $\mathcal{D}$ is composed of the union of SOL domain $\mathcal{D}_{sol}$ and the confining region. According to this approach, the latter is split into a finite number N_{MS} of region $\mathcal{D}_i$, with $i = 1, ..., N_{MS}$. To this series of concentric plasma confining sub-domains, corresponds an identical amount of magnetic surfaces, where each domain cell $\mathcal{D}_i$ is delimited by the adjacent MS profile at ϱ_{i-1} and ϱ_i, and ϱ_0 denoting the plasma center at $r = R_0$ and $z = 0$. The whole vacuum chamber domain $\mathcal{D} = \bigcup_{i=1}^{N_{MS}} \mathcal{D}_i \cup D_{sol}$, is enclosed by the boundary $\partial\mathcal{D}$, assumed to be of elliptical shape. For simplicity the divertor profile is simply omitted. The Cartesian coordinates of a generic point $P_w(r_w, z_w)$, laying on $\partial\mathcal{D}$, can be parametrically determined making use of the independent variable α_w, and defined as:

$$\begin{cases} r_w(\alpha_w) = R_0 - \delta \cdot a + (a + \Delta_{\mathrm{SOL,k}})\cos\alpha_w, \\ z_w(\alpha_w) = (\kappa \cdot a + \Delta_{\mathrm{SOL,t}})\sin\alpha_w, \end{cases} \qquad k = i/o, \tag{E.19}$$

with $\Delta_{\mathrm{SOL,t}}$ denoting the vertical top SOL thickness from the top and bottom most elongated LCMS points, i.e. at $r = R_0 - \delta \cdot a$ and $z = \pm\kappa \cdot a$. Similarly, $\Delta_{\mathrm{SOL,k}}$ indicates the SOL thickness k on the mid-equatorial plane, with $k = i/o$. According to the notation of Figure E.5, if $k \equiv i$, the inboard

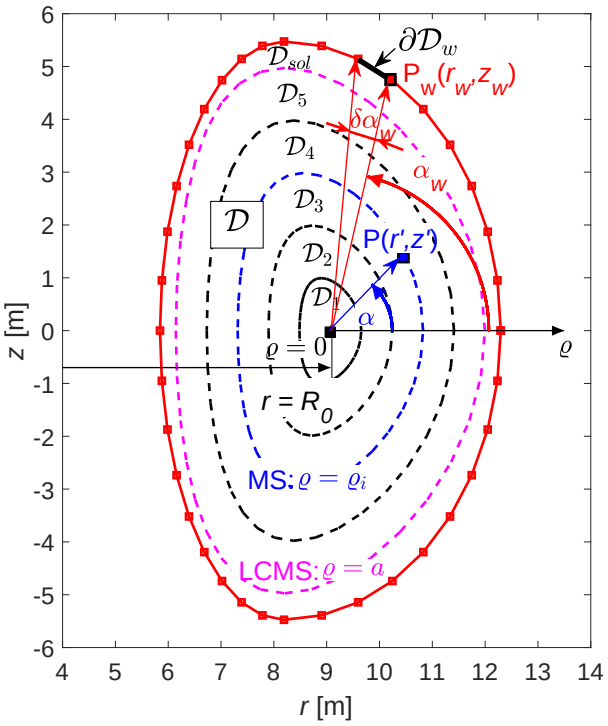

Figure E.5.: Schematic view of the plasma chamber $\mathcal{D}$ adopted for the benchmark of the deterministic two-dimensional radiation transport model of Equation (4.30) against MCNP solution. The magnetic flux coordinate ϱ is used to manufacture the shape of a tokamak-like magnetic flux surface, following the parametrization of Equation (E.18). A prescribed number N_{MS} of MSs discretizes the plasma confining region into a set of as many concentric sub-domains $\mathcal{D}_i$. The plasma chamber boundary $\partial\mathcal{D}$, approximating the surrounding first wall, is also parametrized in two-dimensional coordinates by means of the parametric ellipse formulation of Equation (E.19). The boundary is discretized in a finite set of wall elements $\partial\mathcal{D}_w$, each mapped on the poloidal angle α_w and set as a targeting boundary panel for the poloidal wall loading profile $\Gamma_\perp(\alpha_w)$.

side of $\partial\mathcal{D}$ is obtained for the second and the third quadrant (with respect to the plasma center) and $\alpha_w \in [\pi, \frac{3}{2}\pi]$. Analogously, if if *kequivo* the outboard leg is calculated for the fourth and the first quadrants, i.e. $\alpha_w \in [\frac{3}{2}\pi, 2\pi] \vee [0, \frac{\pi}{2}]$.
To map the poloidal distribution of the neutron wall loading $\Gamma_\perp(\alpha_w)$ (see Equation (4.17)), the boundary $\partial\mathcal{D} = \bigcup_{w=1}^{N_W} \partial\mathcal{D}_w$ is split into a finite number $N_W = 2\pi/\delta\alpha_w$ of surface elements $\partial\mathcal{D}_w$, with $w = 1, 2, ...N_W$ and $\delta\alpha_w$ a specified increment of the poloidal angle α_w. The poloidal wall loading is therefore calculated element-wise for each boundary surface $\partial\mathcal{D}_w$ mapped on the variable α_w, where SOL region is then found in the domain region among $\partial\mathcal{D}$ and the last closed magnetic surface (LCMS), i.e. at $\varrho = a$.

To facilitate the reproduction of a tokamak-like neutron source shape $q(\varrho)$ in both reference deterministic and statistic configurations, two separate (tough analogous) approaches are followed. In FE environment, taking $\mathcal{D}_i$ the generic plasma region pertaining to two adjacent and concentric MSs, ϱ_{i-1} and ϱ_i, a volume-averaged neutron source $q(\varrho_{i-1/2}) \equiv q_{i-1/2}$ in $\mathcal{D}_i$ is calculated to approximate the continuous two-dimensional distribution of the source term $q(\varrho)$, for solving the transport problem of Equation (4.21). Making use of the parametrization of Equation (E.18), the

$q_{i-1/2}$ can be defined as:

$$q_{i-1/2} \equiv q(\varrho_{i-1/2}) = \frac{\int\limits_{\mathcal{D}_i} q(\varrho)\mathrm{d}\mathbf{r}}{\int\limits_{\mathcal{D}_i} \mathrm{d}\mathbf{r}} = \frac{\int\limits_0^{2\pi}\int\limits_{\varrho_{i-1}}^{\rho_i} q(\varrho)\ |\mathbf{J}(\varrho,\alpha)|\, r'(\varrho,\alpha)\mathrm{d}\varrho\,\mathrm{d}\alpha}{\int\limits_0^{2\pi}\int\limits_{\varrho_{i-i}}^{\varrho_i} |\mathbf{J}(\varrho,\alpha)|\, r'(\varrho,\alpha)\mathrm{d}\varrho\,\mathrm{d}\alpha}, \tag{E.20}$$

where $\mathbf{J}(\varrho,\alpha)$ outlines the Jacobian matrix of the change of parametrization reported in Equation (E.18), reading as:

$$\mathbf{J}(\varrho,\alpha) = \begin{pmatrix} \frac{\partial r'}{\partial \varrho} & \frac{\partial r'}{\partial \alpha} \\ \frac{\partial z'}{\partial \varrho} & \frac{\partial z'}{\partial \alpha} \end{pmatrix} = \begin{pmatrix} \cos(\alpha+\delta\sin\alpha) & -\varrho\cdot\sin(\alpha+\sin\alpha)(1+\delta\cos\alpha) \\ \kappa\sin\alpha & \kappa\varrho\cos\alpha \end{pmatrix}. \tag{E.21}$$

The determinant of $\mathbf{J}(\varrho,\alpha)$ is being used to performed the outlined double integral over the volume $\mathrm{d}\mathbf{r}$, which making use of variable change of Equation (E.18) can be written as $\mathrm{d}\mathbf{r} = 2\pi \mathrm{d}r\mathrm{d}z$ $\equiv 2\pi r'(\varrho,\alpha)\ |\mathbf{J}(\varrho,\alpha)|\ \mathrm{d}\varrho\mathrm{d}\alpha$. In a `Freefem++` finite element environment the scalar field denoting the external neutron volumetric source q is, hence, defined region-wise, i.e. meshing on the borders outlining the specified magnetic surfaces ϱ_i and assigning the value of $\varrho_{i-1/2}$, calculated as per Equation (E.20). In a Monte Carlo arrangement, the neutron source is modelled such that the probability of generation $f_{i-1/2}$ pertaining to the domain region $\mathcal{D}_i$ is calculated as:

$$f_{i-1/2} \equiv f(\varrho_{i-1/2}) = \frac{\int\limits_{\mathcal{D}_i} q(\varrho)\mathrm{d}\mathbf{r}}{\sum\limits_{i=1}^{N_{MS}} \int\limits_{\mathcal{D}_i} q(\varrho)\mathrm{d}\mathbf{r}} = \frac{\int\limits_0^{2\pi}\int\limits_{\varrho_{i-1}}^{\varrho_i} q(\varrho)\ |\mathbf{J}(\varrho,\alpha)|\, r'(\varrho,\alpha)\mathrm{d}\varrho\,\mathrm{d}\alpha}{\int\limits_0^{2\pi}\int\limits_0^{a} q(\varrho)\ |\mathbf{J}(\varrho,\alpha)|\, r'(\varrho,\alpha)\mathrm{d}\varrho\,\mathrm{d}\alpha}, \tag{E.22}$$

where the numerator and the denominator indicate the total neutron source in $\mathcal{D}_i$ and in the whole chamber $\mathcal{D}$. The double integrals of Equations (E.20) and (E.22) are performed numerically by means of trapezoidal numerical integration.

The goal is to validate the solution of the discrete ordinate finite element transport model against that obtained by means of Monte Carlo technique, in the same geometry (Figure E.5), source (Equations (E.20) and (E.22)) and boundary conditions. This operation is performed by making use of dedicated numerical codes for both approaches (`Freefem++` and `MCNP5`).
The input specifications to the benchmark are listed in Table E.1. Due to the vertical symmetry the elongation and triangularity at 95 % poloidal flux (κ_{95} and δ_{95}) have been assumed. The number N_{MS} of magnetic flux surfaces and the increment $\delta\alpha_w$ have been assessed such that the complexity of the `MCNP5` model is kept reasonably low; especially $\delta\alpha_w$, which directly affects the number of plasma surrounding wall elements N_W, hence the number of random walk to run to achieve a reliable statistics. Due to technical limitations of MCNP when deploying this methodology, for $\delta\alpha_w < 10$ deg the generation of the surfaces used to tally the neutron streaming fails to succeed. With regard to the source peaking factor P, Peaking factor in the neutron source formulation reported in Equation (E.20), the values is based on the relation proposed by Fausser et al [194] and derived from the volumetric neutron source formulation of Equation (3.44), such that $P = \gamma\alpha_T + 2\alpha_n$, with $\gamma = 2$ for

Parameter (symbol) [unit]	Value	Remarks
Plasma major radius (R_0) [m]	9.07	
Plasma aspect ratio (A) [-]	3.1	
Plasma triangularity (δ) [-]	0.33	Triangularity at 95 % flux (δ_{95})
Plasma elongation (κ) [-]	1.59	Elongation at 95 % flux (κ_{95})
Number of magnetic surface (N_{MS}) [-]	5	
Poloidal angle wall step size ($\delta\alpha_w$) [deg]	10	Limited by MCNP capabilities
ib/ob SOL thickness ($\Delta_{\mathrm{SOL,i/o}}$) [m]	0.225	
top SOL thickness ($\Delta_{\mathrm{SOL,t}}$) [m]	0.53	
Fusion neutron power P_{neut} [MW]	1629	Equation (3.46)
Source peaking factor (P) [-]	4.9	Equation (E.20)

Table E.1.: Input parameters used for the benchmark of the numerical core radiation transport model against Monte Carlo solution. The data for the transport simulation refers to EU-DEMO 2015 design [30] and for each parameter the variable name, the symbol (in round bracket), the unit (in square brackets) and additional remarks are reported.

average temperatures closed to 15.1 keV, $\alpha_T = 1.45$ and $\alpha_n = 1$ are the EU-DEMO1 2015 design [30] plasma temperature and density α factors (see Equation (3.35)).

The Monte Carlo `MCNP5` model has been built-it in a parametric way, such that multiple reactor configurations can be benchmarked as well. The magnetic flux surfaces, as well as the wall boundary $\partial\mathcal{D}$ have been reproduced in `MCNP5` exploiting the surface cards of type Z, for as a curvilinear axisymmetric surface (around Z-axis) in Cartesian three-coordinate system can be generated by imposing the coordinates of two adjacent points on the poloidal plane in r,z. Therefore, for a discrete set of $\alpha \in [0,2\pi]$, a finite set of points calculated as per Equation (E.18), the whole MS can be implemented in `MCNP5` repeating for as many times as the number of point pairs $P_i(r_i,z_i) - P_{i+1}(r_{i+1},z_{i+1})$ the surface card Z, following the prescribed format. In order to have an accurate spatial resolution of the manufactured magnetic configuration, for each MS the number of ordinates along α are determined such that, on the r,z poloidal plane, the geometrical length of each segment does not exceed 0.1 m. With regard to the boundary $\partial\mathcal{D}$, each pair of coordinates defining the surface $\partial\mathcal{D}_w$ on the (r,z) poloidal plane (see also Figure 4.2), pertaining to the poloidal angles α_i and $\alpha_{w,i+1}$, is obtained assuming a fixed increment of $\delta\alpha_w$ (see Table E.1) and making use of Equation (E.19) for the radial and vertical coordinates of such point couplets.
As `MCNP5` cannot simulate the particle transport in 2D geometries, a 20° toroidal sector has been imposed, with reflective boundary conditions on the two toroidal surfaces. The neutron source is fixed assuming isotropic and monoenergetic 14.1 MeV neutrons, where the generation probability is assigned to each cell according to Equation (E.22).

The comparison analyses the deviation between the FE `Freefem++` and the `MCNP5` models in terms of the poloidal distribution of the neutron wall loading $\Gamma_{\perp}^{\mathrm{neut}}(\alpha_w)$. Having labelled each of the surfaces $\partial\mathcal{D}_w$ in the surface section of the input file, the wall loading poloidal profile is obtained by imposing the `MCNP5` tally type 1 on each of the boundary complement, i.e. the *Surface Tally* F1. The tally $\mathrm{F1}|_{\partial\mathcal{D}_w}$ calculates the integral particle (or energy) surface current on $\partial\mathcal{D}_w$, analogously to the inflow total power definition of Equation (4.16). The results from the specified `MCNP5` tallies are normalized to the total source of the problem. To convert the information from the total surface $\mathrm{F1}|_{\partial\mathcal{D}_w}$ to the actual wall loading $\Gamma_{\perp}^{\mathrm{MC}}|_{\partial\mathcal{D}_w}$, the tally values need to be multiplied with the total fusion neutron power P_{neut} and divided by the surface $S|_{\partial\mathcal{D}_w}$ of the surface element $\partial\mathcal{D}_w$ to yield the wall

loading definition of Equation (4.17). Thus, in mathematical form, therefore one finds:

$$\Gamma_{\perp}^{\mathrm{MC}}(\alpha_w)|_{\partial\mathcal{D}_w} = \mathrm{F1}|_{\partial\mathcal{D}_w} \cdot \frac{P_{neut}}{S|_{\partial\mathcal{D}_w}}, \tag{E.23}$$

where the surface $S|_{\partial\mathcal{D}_w}$ is outlined by the following set of formulas

$$\begin{aligned} S|_{\partial\mathcal{D}_w} &= 2\pi \cdot \overline{r_w} \cdot l_w, \\ \overline{r_w} &= \frac{r_w(\alpha_{w,i}) + r_w(\alpha_{w,i-1})}{2}, \\ l_w &= \sqrt{\left[r_w(\alpha_{w,i}) - r_w(\alpha_{w,i-1})\right]^2 + \left[z_w(\alpha_{w,i}) - z_w(\alpha_{w,i-1})\right]^2}. \end{aligned} \tag{E.24}$$

The FE solution of $\Gamma_{\perp}^{\mathrm{FE}}(\alpha_w)|_{\partial\mathcal{D}_w}$ is calculated with `Freefem++`. The MSs and the wall boundary are parametrized and meshed according to Equations (E.18) and (E.19) and the metric size h defined in Equation (E.14) is imposed to build a quasi-uniform mesh $\mathcal{T}_h$ characterizing the domain of the plasma vacuum chamber $\mathcal{D}$. The transport problem of Equation (4.30) is solved by means of the discontinuous Galerkin method with an isotropic neutron source sampled for each of the anular region between two adjacent MSs. The acquisition of $\Gamma_{\perp}^{\mathrm{FE}}$ goes first through the computation of the net radial and vertical neutron currents and then to the application of the wall loading definition, to be verified against that of Equation (E.23) yielded by the `MCNP5` Monte Carlo model.

To validate the FE against the reference MC solution a couple of definitions directly connected to such concept are first introduced. A deviation is conceived as a difference between the values predicted by a model, $\hat{y}$, and those actually observed, y. A common definition hinges upon *relative error* $RE(\hat{y})$, reading as:

$$\mathrm{RE}(\hat{y}) = \frac{\hat{y} - y}{y}. \tag{E.25}$$

For a set of N predicted values $\hat{Y} = [\hat{y}_1, \hat{y}_2, ..., \hat{y}_N]$ and of N actually observed values $Y = [y_1, y_2, ..., y_N]$, two scalar definitions of error are being used. The first refers to the *normalized-root-mean-square error* $\mathrm{NRMSE}(\hat{Y})$, and reads as:

$$\mathrm{NRMSE}(\hat{Y}) = \sqrt{\frac{1}{N}\sum_{i=1}^{N}\left[\mathrm{RE}(\hat{Y}_i)\right]^2} = \sqrt{\frac{1}{N}\sum_{i=1}^{N}\left(\frac{\hat{Y}_i - Y_i}{Y_i}\right)^2}, \tag{E.26}$$

while the second simply refers to the *maximum relative error*

$$\mathrm{MRE}(\hat{Y}) = \max\left[\left|\mathrm{RE}(\hat{Y}_1)\right|, \left|\mathrm{RE}(\hat{Y}_2)\right|, ... \left|\mathrm{RE}(\hat{Y}_N)\right|\right]. \tag{E.27}$$

The predictor and observer correspond to the FE and to the MC model. Using the neutron wall loading definition of Equation (4.17) for each of the N_W wall surface elements $\partial\mathcal{D}_w$ poloidally distributed along the ordinate α_w, the following data sets are introduced to calculate the deviation from the finite element and the Monte Carlo models, respectively addressed with FE and MC superscript.

$$\begin{aligned} \hat{Y} &= \Gamma_{\perp}^{\mathrm{FE}}(\alpha_w) \equiv \left[\Gamma_{\perp}^{\mathrm{FE}}|_{\partial\mathcal{D}_1}, \Gamma_{\perp}^{\mathrm{FE}}|_{\partial\mathcal{D}_2}, ..., \Gamma_{\perp}^{\mathrm{FE}}|_{\partial\mathcal{D}_{N_W}}\right], \\ Y &= \Gamma_{\perp}^{\mathrm{MC}}(\alpha_w) \equiv \left[\Gamma_{\perp}^{\mathrm{MC}}|_{\partial\mathcal{D}_1}, \Gamma_{\perp}^{\mathrm{MC}}|_{\partial\mathcal{D}_2}, ..., \Gamma_{\perp}^{\mathrm{MC}}|_{\partial\mathcal{D}_{N_W}}\right]. \end{aligned} \tag{E.28}$$

The deterministic approach relies on the discrete ordinate $\mathrm{S_N}$ method (Appendix D.3). The continuous angular coordinate $\boldsymbol{\Omega}$ is replaced by a finite number $K(N) = N(N+2)/4$ of angular

ordinates $\mathbf{\Omega}_n$, each associated with quadrature weight w_n. It is important to establish the required quadrature order N minimizing the error associated with the angular discretization. The S_N method introduces a numerical error attributed to the quadrature formula used to approximate the integral over the angular independent variable $\mathbf{\Omega}$ (see Equation (D.26)).
Quadrature weights and ordinates indirectly point to an additional complication of the S_N method, the so-called ray effects. It raises from the physical interpretation of the discrete ordinate approximation, which "forces" particles to travel only along a reduced number of directions. Hence, the solution of the transport equation is "right" just along these discrete directions $\mathbf{\Omega}_n$ and the quadrature formula may experience inability to adequately approximate the scalar flux. Exploiting the exactness of the Monte Carlo method, one can assess the discrete ordinate quadrature order N minimizing the numerical error due to the angular discretization.

For an increasing value of N, the number of angular directions $K(N)$ increase (quadratically) and the error is therefore expected to diminish, as shown in Figure E.6.

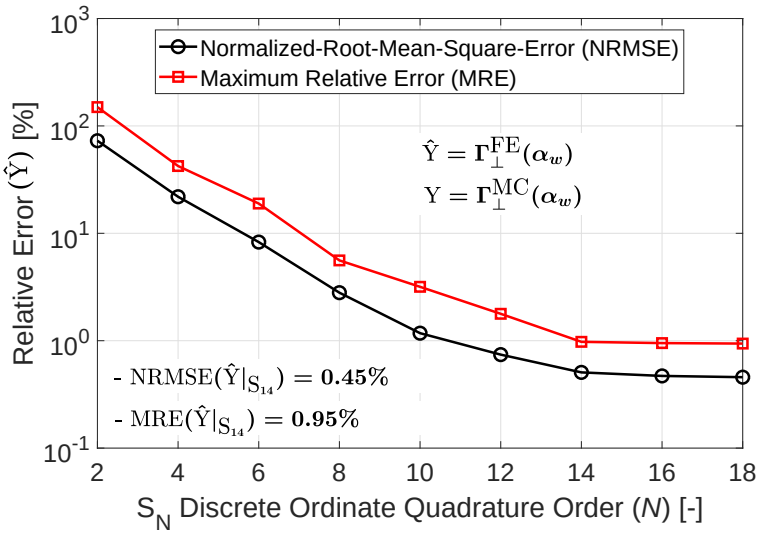

Figure E.6.: MRE and NRMSE error convergence curves of the void plasma/SOL radiation transport model for increasing values of the discrete ordinate quadrature order S_N. The values predicted by the FE model ($\hat{\mathrm{Y}}$) in terms of poloidal neutron wall loading profile $\Gamma_{\perp}|_{\partial\mathcal{D}_w}$ are correlated to those calculated by the Monte Carlo MCNP 5 particle transport code (Y).

The model deviation, in terms of MRE and the NRMSE definitions has been calculated for quadrature orders N spanning from 2 (the lowest possibly applicable) to 18. The result show a damping behaviour of both MRE (squared-marker line) and NRMSE (circled-marker) from vastly large errors for lower quadrature order to a nearly steady value around the S_{14} quadrature, where the MRE and NRMSE appraise figures which can be simply accepted. The MRE for $N \geq 14$ lays around 0.97 %, whereas the global NRMSE places near 0.5 %. Such a flattening behaviour of the error illustrates the physical limitations of such angular discretization method (at least with the adopted quadrature ordinates and weights).
The deviation has been measured on the net neutron current on the boundary, where the discontinuous finite element method suffers the most, due to the vacuum boundary condition and the lack of the neutron source. If a comparison were carried out on the 2D distribution on the scalar flux across the vacuum chamber, the global error (e.g. definition on the L^2-norm of Equation (E.6)) would perhaps yield lower scales. As this would not entail any implications within a fusion reactor code, this study

has been omitted and any evaluation has been carried out on $\Gamma_{\perp}(\alpha_W)$ only.
If a mesh size h as of Equation (E.14) and a discrete ordinate approximation at least S_{14} are prescribed the overall numerical error on the poloidal mapping of the wall loading distribution lower than 1 % on its NRMSE and MRE definitions. For a system code transport module this can be considered as satisfactory and makes this model worthwhile for integration in a multiphysics fusion system analysis package.

To depict the numerical deviations, the poloidal profile of $\Gamma_{\perp}(\alpha_w)$ is visualized in Figure E.7 for both the FE and the MC approaches, $\Gamma_{\perp}^{\mathrm{FE}}$ and $\Gamma_{\perp}^{\mathrm{MC}}$. The trend of the relative error $\mathrm{RE} = (\Gamma_{\perp}^{\mathrm{FE}} - \Gamma_{\perp}^{\mathrm{MC}})/\Gamma_{\perp}^{\mathrm{MC}}$ is also reported to map the local behaviour across the α_w domain.

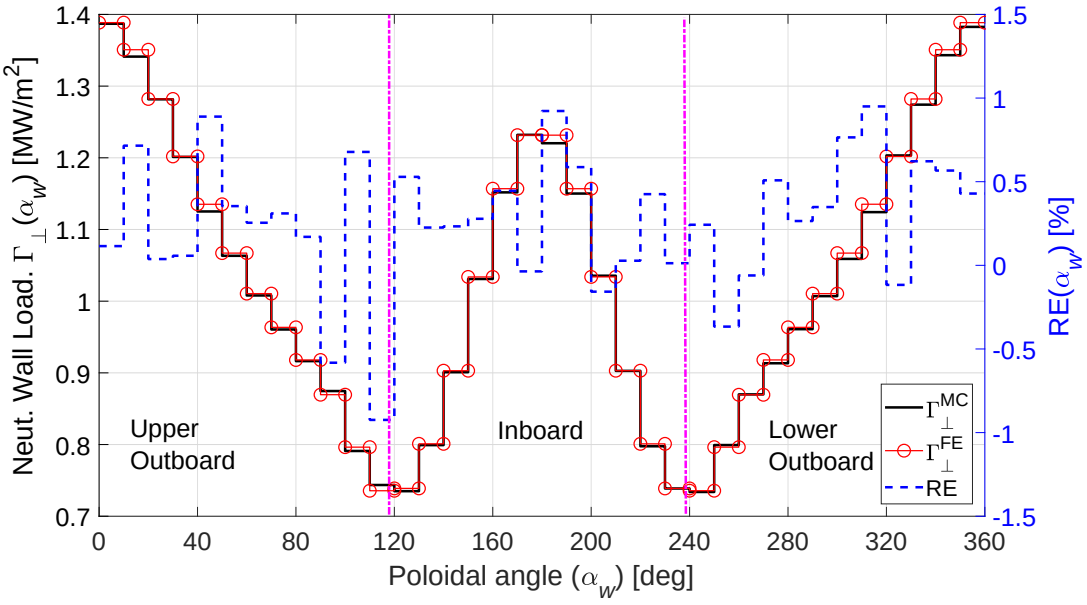

Figure E.7.: Neutron wall loading $\Gamma_{\perp}$ vs. plasma vacuum chamber poloidal angle α_w (see Figure E.5) for the EU-DEMO 2015 plasma vacuum chamber. The solid line refers to the `MCNP5` solution, while the circles are derived from the numerical discontinuous finite element radiation transport model implemented in the `Freefem++` FE solver. The dashed line denotes the RE of FE related the MC solution.

The largest distance between the FE and the MC solutions MRE = 0.95 % is located in the lower outboard region close to the mid-equatorial plane and RE is below 1 % through the whole α_w domain. Mapping the outflow particle streaming currents along the poloidal coordinate α_w allows identifying the most critical locations on the surrounding walls and thereby to implement design solutions to mitigate them.
In case of radiation and in absence of adsorbing and scattering media, neutrons (or photon) particles spread over the plasma vacuum chamber rather uniformly, thus not inducing large concerns in terms of localized heat fluxes. Due to the closest vicinity to the core region, the largest wall loadings are observed in the outboard near the mid-equatorial plane, with the highest amplitude on the outboard region as a consequence of the toroidal effects.

The proposed model has to prove its versatility to diverse tokamak scenarios, such as to different geometry configurations. A system/design code might be used to compare different tokamak devices featuring different sizes. Having established some key rules for the mesh size h and for the quadrature order N, the evaluation of the error shall be carried out by scanning various reactor geometries. In

particular, with reference to the EU-DEMO-2015 design, whose specifications are listed in Table E.1, the attention has been directed towards two of the most representative key geometry parameters, such as major radius R_0 and aspect ratios A. Taking the reference DEMO design (i.e. $R_0|_{\text{ref}} = 9.07$ m, $A|_{\text{ref}} = 3.1$), a parametric scan has been performed simulating a ranging of cases such that $R_0 = R_0|_{\text{ref}} \pm 1.5$ m and $A = A|_{\text{ref}} \pm 0.5$. With such applicative it is assumed that this would cover a broad range of plausible DEMO machine configurations, in a near-term future [19]. The results for each analysed case are reported in Table E.2, where each cell relates to the normalized-root-mean-square and maximum relative error definitions (NRMSE [%] / MRE [%] format for each table cell). The figures confirm the versatility expected for a transport model to use for reactor system design,

	$R_0 = 7.5$ m	$R_0 = 9.0$ m	$R_0 = 10.5$ m
$A = 2.6$	0.463 / 0.990	0.4911 / 1.160	0.459 / 1.083
$A = 3.1$	0.519 / 1.108	0.4913 / 1.116	0.455 / 0.877
$A = 3.6$	0.509 / 1.101	0.5177 / 1.237	0.479 / 0.978

Table E.2.: NRMSE and MRE of the numerical radiation transport model for varying amplitudes of plasma major radius R_0 and aspect ratio A. The values appearing in each cell, separated by the indicate the NRMSE [%] on the left and the MRE [%] on the right of the slash symbol.

as the deviations are found nearly constant (disregarding negligible fluctuations) for a wide range of applicative reactor geometry situations. Such an outcome not only confirms the finding highlighted in Figure E.6 for the reference DEMO 2015 design, but can be broadly generalized to any arbitrary reactor plasma layout.

E.3. Verification and Benchmark of the Global Reactor Radiation Transport Model

The design of a FPP relies on a credible neutronic assessment of each core reactor components, from the plasma to the superconducting magnets. In Section 4.1, a dedicated neutron transport model has been proposed for integration in MIRA. In order to run in feasible low times, it is based on a set of simplifying assumptions, which, together with the two following simplifying assumptions, introduces a certain error in the solution:

- discrete ordinates and energy multigroup approximations, for numerically solving the Boltzmann transport equation;
- one-dimensional cylindrical transport;
- homogenization of material mixes for reactor components.

The model therefore yields a set of results which unfortunately are affected by uncertainties, due to the simplifications and the numerical techniques deployed to solve the radiation transport problem. This requires error quantification to have a more reliable prediction of the obtained results, for using in a system analysis environment.
For benchmarking the model is compared to the Monte Carlo technique for the EU-DEMO 2015 design and analysed for the following parameters:

- scalar fast/total neutron flux $\Phi_{fast,n} / \Phi_{tot,n}$ (Equation 4.12), where fast neutrons feature kinetic energy larger than 0.1 MeV;

- scalar total gamma flux $\Phi_{tot,\gamma}$;
- total deposited nuclear heating power on each reactor component m, R^m_{heat};
- total tritium production rate in the breeding zone region R^{bz}_{nt}.

The benchmark analysis is conducted in two phases:

- verification study against 1D cylindrical Monte Carlo solution, to evaluate the deviations arising from the numerical approximations deduced from the deterministic solving techniques;
- comparison to 2D MCNP DEMO-like to quantify the second main (and most probably largest) deviation share.

The third part arising from material homogenization is assessed by making use of 3D detailed MCNP neutronic analyses, performed for DEMO design and available in literature.

For both 1D and 2D cases the radial build composition of the EU-DEMO 2015 design [30, 32] has been chosen for the benchmark, i.e. major radius $R_0 = 9.07$ m and aspect ratio $A = 3.1$, yielding 2037 MW fusion power. The reactor layout is based on Helium-Cooled Pebble Beds (HCPB) [34] blanket concept, water-cooled stainless steel vacuum vessel (VV) and Nb_3Sn-based superconducting TF coils. For simplicity, the latter has been to be uniquely homogenized between inner and outer steel case and winding pack, so that it is modelled as an individual component. As the divertor is not yet part of the core radiation transport model, it has been removed from the reactor build, thus assuming vertical symmetry. Inboard ($\Delta_{m,i}$), outboard ($\Delta_{m,o}$) and top thickness ($\Delta_{m,t}$), alongside with the material composition of each reactor system subsystems are reported in Table E.3.
Every row depicts a radially discretized component, where the material mix contents associated with the BB subsystems (i.e. W armour, FW, BZ, back plates and manifold) have been obtained from Ref. [215], whereas for VV and TFC, they have been derived from the MCNP DEMO 2015 model [190]. The original values have featured a slight re-visitation to take into account of the toroidal and poloidal gaps between the blanket boxes (a 1 % void fraction has been assumed everywhere) and the presence of additional Eurofer of the box caps. Moreover, the amount of Be and Li_4SiO_4 have been adjusted to match the total reactor material inventories, reported in the Design Description Document of the HCPB DEMO blanket [216]. For both, the indicated values include the void fraction of empty gaps between the pebbles, characterized by the so-called *packing factor*, found in the range of 63-64 % for pebble beds in fusion blankets and for the current HCPB design [216], too.
The VV is being modelled as a three layer homogenized system, with a typical double inner and outer SS316 stainless steel shell structure, with low pressure water coolant in between (see Section 2.2.4).
In the following, the verification study performed on a manufactured cylindrical geometry frame precedes the more elaborated benchmark study against against two-dimensional Monte Carlo solution, outlining the main deviations affecting the proposed model.

E.3.1. Verification against 1D Monte Carlo solution

In order to quantify the accuracy of the numerical approximation introduced by energy, angular and spatial nodalization, a one-to-one benchmark is executed by building a cylindrical reactor model. Each reactor component is simulated as a straight infinitely long cylinder characterized by a prescribed inboard and outboard thickness and material make-up, as indicated in Table E.3. To reproduce such conditions reflecting boundary conditions are imposed on the top and bottom planes, denoted by t^* and b^*. In the outermost and innermost cylinders, indicated by r^* and l^* vacuum

Component	$\Delta_{m,i}$ [cm]	$\Delta_{m,o}$ [cm]	$\Delta_{m,t}$ [cm]	Material	Vol. Fract [%]
Plasma Core	291.7	291.7	466.7	Void	100.0
SOL	20.0	20.0	50.0	Void	100.0
W Armour	0.2	0.2	0.2	Tungsten	99.0
				Void	1.0
First Wall	2.5	2.5	2.5	Eurofer	64.9
				Helium	35.1
				Void	1.0
Breeding Zone	23.0	52.0	37.5	Li_4SiO_4	19.5
				Eurofer	12.0
				Be pebbles	55.7
				Helium	11.8
				Void	1.0
Back Plates	8.5	8.5	8.5	Eurofer	44.5
				Helium	53.5
				Void	1.0
Manifold	43.0	60.0	56.5	Eurofer	60.1
				Helium	38.9
				Void	1.0
Gap BB-VV	2.0	5.0	5.0	Void	100.0
VV Inner Shell	5.0	5.0	5.0	SS316	99.0
				Void	1.0
VV Coolant Shell	50.0	100.0	47.0	SS316	59.5
				Water	39.5
				Void	1.0
VV Outer Shell	5.0	5.0	5.0	SS316	99.0
				Void	1.0
Gap VV-TFC	10.0	85.0	10.0	Void	100.0
TF Coil	102.0	93.0	85.0	Epoxy resin	18.0
				Nb_3Sn	2.9
				Bronze	7.3
				Copper	11.7
				Liquid He	15.8
				SS316	41.2
				Void	1.0

Table E.3.: EU-DEMO 2015 design: radial-vertical build and material composition (% vol.) for each radially discretized core reactor component [30, 32].

boundary conditions are considered. The neutron source is isotropically distributed inside the core plasma region $r \in [R_0 - a, R_0 + a]$, where a is the plasma minor radius. Hence, the angular sampling from the 2D transport model is not affected here. Across this domain, the volumetric source is assumed constant and equal to $q_{neut}(r) = P_{neut}/V_p$ where P_{neut} is the neutron fusion power V_p is the plasma volume calculated of the adopted DEMO design ($\sim$ 2400 m^3). In order to obtain comparable power density across the reactor systems, the height of the cylinder has been chosen as the average vertical build of all components.
In MCNP environment, to reproduce such a source spatial distribution within a cylinder, the source

probability shall indicate a sampling scheme based on a specific power of the radius variable. In this case, the sampling is a linear function of the cylinder radius $p(r) = c|r|^{\alpha}$, with $\alpha = 1$, resulting in a uniform spatial distribution over the cylinder cross section. A schematic view of the cylindrical model implemented in MCNP is visualized in Figure E.8.

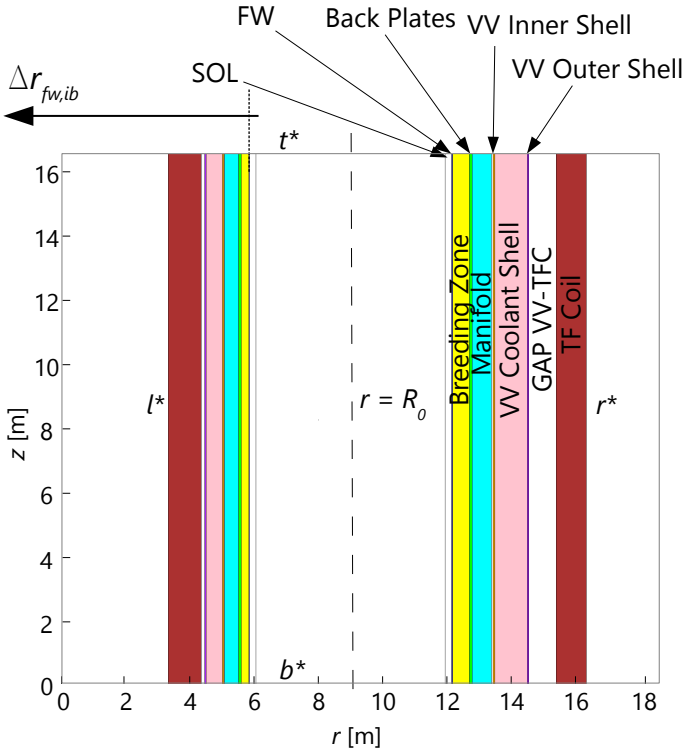

Figure E.8.: Radial-Vertical view of the EU-DEMO 2015 MCNP cylindrical homogenized model adopted for verifying the 1D deterministic model integrated in the MIRA system/design code.

The FENDL/MG-3.1b neutron cross section libraries have been deployed for this study, featuring a Vitamin J+ energy structure with 211 groups for neutron and 42 groups for gamma. Another important parameter concerns with the L-th order of P_L Legendre expansion of the scattering cross sections. A $L = 4$ expansion has been found reasonably adoptable for such material and space reactor configurations.
Based on the findings derived from Appendix E.2, a S_{16} discrete ordinate quadrature is being used for all the simulations performed in this V&B study. Higher orders have nor exhibited any noticeable variations in the observed results.
The mesh spacing Δ_J for determining the number N_m of inboard and outboard intervals for each zone m has to be also evaluated. For a given accuracy, Δ_J is evaluated from the smallest value of the ordinate cosines μ_n and the largest macroscopic total cross section Σ_t^J within the radial coordinate interval r_J of the node J (see Equation D.35).

In Figure E.9, the profiles for $\Phi_{fast,n}$, $\Phi_{tot,n}$ and $\Phi_{tot,\gamma}$ are depicted as functions of the distance from the inboard FW $\Delta r_{fw,ib}$ (see Figure E.8). The results derived from the deterministic model, as per ANISN 1D transport code and referred to as "1D, MIRA" are overlapped to those obtained by MCNP simulations, assumed the actual comparison matter and indicated as "1D, MCNP". The relative error RE of the MIRA solution from the reference MCNP profile is visualized in dot-dashed

line.

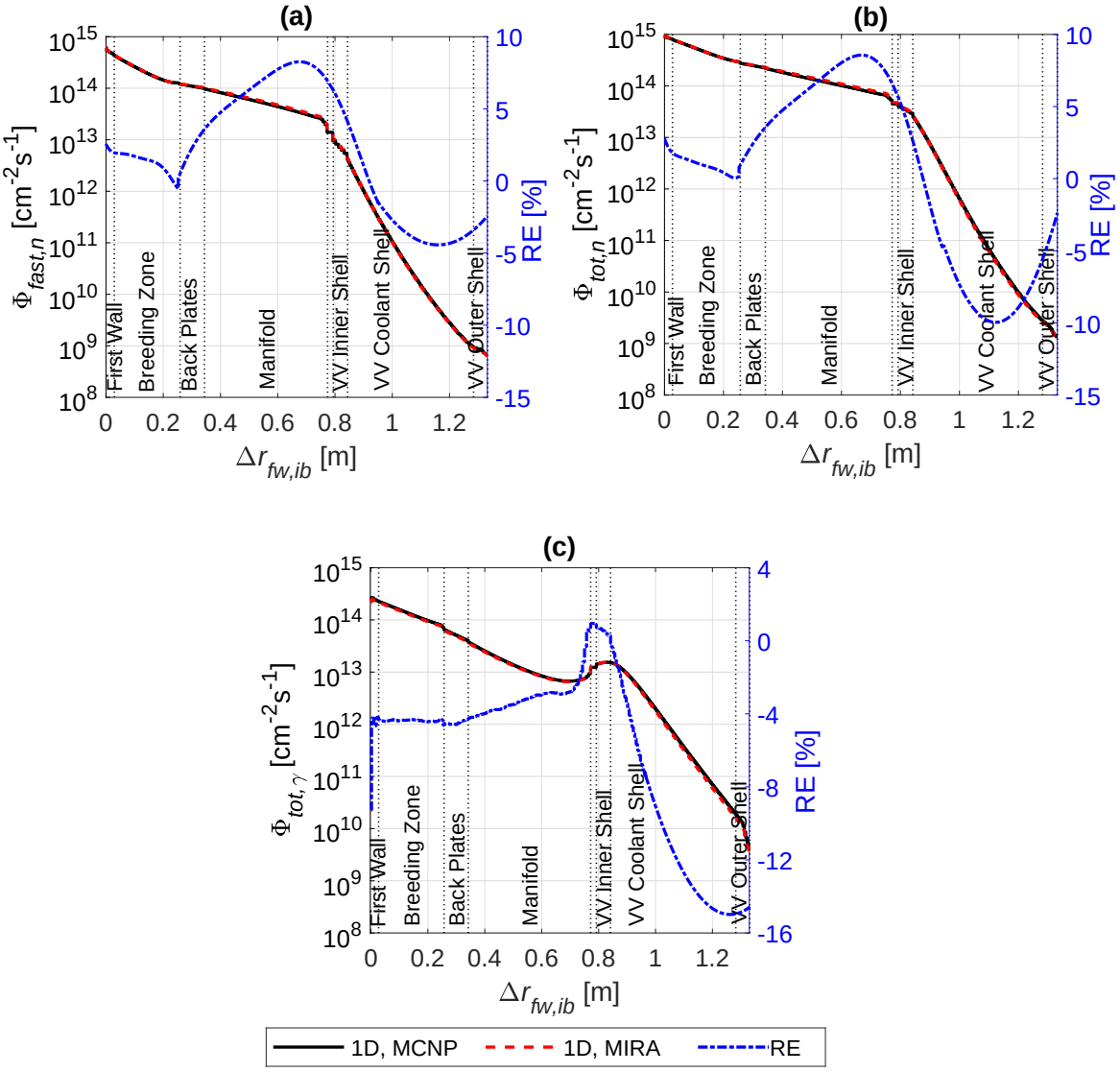

Figure E.9.: Radial profiles of fast neutron flux density $\Phi_{fast,n}$ (a), total neutron flux density $\Phi_{tot,n}$ (b) and total gamma flux density $\Phi_{tot,\gamma}$ (c) on inboard mid-plane. The curves relate to the MIRA and MCNP solutions (solid and dashed) to the 1D transport problem depicted by Figure E.8. The relative error RE is depicted by the dot-dashed line.

In the benchmark of the MIRA neutron/gamma transport model, $\hat{Y}$ relates to the MIRA solution and Y to MCNP, in terms of RE, MRE and NRMSE. Globally, a relatively good match is found across the whole reactor radial domain, with NRMSE around 5 % for $\Phi_{fast,n}$ up to 8 % for $\Phi_{tot,\gamma}$. The largest deviations between MIRA and MCNP models lay in ranges spanning from $+8.25$ % for $\Phi_{fast,n}$, $+8.55$ % for $\Phi_{tot,n}$ down to -14.7 % for $\Phi_{tot,\gamma}$. The RE of $\Phi_{fast,n}$ on the outer VV shell, used to establish the shielding of the superconducting TF coils (Table 4.1), shows smaller amplitudes compared to its peak in the manifold region, with -2.7 % deviations.
All curve exhibit several local minima and maxima, all attributed to the group-wise sampling of the energy domain. As shown in Figure D.8, large resonances are observed for neutron energy between 0.01 and 1 MeV in the capture reaction of ^{56}Fe yielding a photon particle, i.e. $^{56}\mathrm{Fe}(n,\gamma)^{57}\mathrm{Fe}$. The

deterministic solution tends to underestimate the effects of the Fe neutron captures for high neutron energies, characterizing the main volumetric source for photons. The largest amplitudes of RE are observed in the FW, manifold and VV regions, where larger fractions of steel are found and neutrons feature important kinetic contributions. The RE in all variables yields a local minimum inside the VV coolant shell because neutrons are slowed down by water, and the self-shielding effect are smaller.
The same considerations can be deduced from neutron captures in tungsten isotopes [217], explaining also the large peak of RE of $\Phi_{tot,\gamma}$ at $\Delta r_{fw,ib} = 0$ m, i.e. on the FW tungsten armour.
In fusion application the accuracy of the transport solution obtained by deterministic multigroup approach is dependent on the material composition, in particular on the steel content. Consequently, the adopted energy group structure features certain limitations, hence an adaptation to highly ferritic materials should be considered.

When a resonance isotope is present in a dilute mixture the reaction rate affected by such a resonance is reduced and then self-shielded [148, 218]. Different methods are available to mitigate the self-shielding effects, such as the Bondarenko method or Background cross section method [218]. All make use of the definition of the so-called escape cross section, relating to the probability of a neutron to by-pass the resonance region. This is constructed from a mean chord length ℓ, which for cylindrical geometry is defined by the volume V and the surface S of the cylindrical region affected including the resonant material and given by $\ell = 4V/S$ [148]. The Bondarenko method is deployed in TRANSX by imposing ℓ for each subregion.

Table E.4 lists the nuclear heating powers R^m_{heat} for each reactor component m. The peak deviations (~ 9 %) are found in the inner VV shell, where similar figures have been obtained for the radial scalar flux profiles and finding confirmation in the justifications given above. The nuclear heating contribution from the induced gamma rays suffers from the limitations of the energy group structure in highly resonant regions. For all other regions, in particular for the BB sub-domains, the relative errors are globally reduced to near ~ 1 %. This last result represents a major achievement for a neutronic module to adopt in systems codes, as these are the most sensitive locations for global FPP power performance evaluation purposes.

Component	1D, MIRA [MW]	1D, MCNP [MW]	RE [%]
W Armour	86.9	87.5	−0.82
Firs Wall	239.2	240.1	−0.36
Breeding Zone	1362.5	1353.8	+0.65
Back Plates	96.8	96.3	+0.49
Manifold	176.6	172.4	+2.47
VV Inner Shell	23.1	21.2	+8.99
VV Coolant Shell	60.1	56.8	+5.86
VV Outer Shell	0.0122	0.0121	+0.29
TF Coil	0.0058	0.0059	−1.55

Table E.4.: Global nuclear heating power R^m_{heat} in all m listed core reactor physical components. The results obtained via 1D deterministic ANISN model implemented in MIRA (1D, MIRA) are correlated, in terms of relative error, to those procured by means of reference MCNP calculations in 1D cylindrical geometry (1D, MCNP).

In Table E.5 the breeding zone T production rate are listed for inboard, outboard and total contribution. Again the transport assumptions, nuclear cross section libraries and numerics settings

T breeding contribution	1D, MIRA [g/d]	1D, MCNP [g/d]	RE [%]
Inboard	238.9	236.6	+1.00
Outboard	747.2	744.8	+0.31
Total	986.10	981.4	+0.48

Table E.5.: Global tritium generation rate R_{nt}^{bz} for inboard, outboard and BZ contribution. The results obtained via coupled 2D plasma + 1D reactor MIRA transport model are correlated to those derived from reference MCNP simulations in 1D cylindrical geometry.

provide a reliable estimation of the T breeding capabilities in the BZ region, with global deviations below 1 %. As seen from Table E.4, the integral parameters are largely overestimated by the deterministic models, which places problems when imposing lower limits for T-self sufficiency (Table 4.1). Moreover, splitting inboard and outboard finds its ground in the next section, where the toroidal effects play a crucial role in such distinction. For 1D cases, the reported figures exhibit a wider gap between MIRA and MCNP in the inboard than outboard. However, the global error in the total share is redistributed, down to $\sim$ 0.5 %.

To summarize, the proposed model is capable of simulating the radial streaming of neutron and gamma radiation in fusion-like functional materials correctly. In the BB sub-systems the error introduced by angular quadrature formula, energy multigroup structure and spatial truncation is only $\sim$ 1-2 % for the integral nuclear heating and tritium breeding rates. In the VV regions near the BB the deviation increases up to 8 % due to the highly ferritic materials and their large resonances in the neutron capture reaction.

E.3.2. Benchmark against 2D Monte Carlo Solution

The goal of this subsection is to outline the global error of introduced by the pure one dimensionality of the radiation streaming assumed for the coupled 2D plasma chamber + 1D reactor transport model. Here, the neutron source specifications are derived from Table E.1 adopting the same approach and spatial distributions, both for the numerical finite element and Monte Carlo models. Each component is vertically symmetric with respect to the mid-equatorial plane (see Figure E.10), thus only the upper-half of the reactor is simulated, with reflecting boundary condition imposed on the plane mp^*. The TF coil has been shaped uniquely in a singular homogenized component, neglecting the corner in the inboard outer region.
Inboard, outboard and top thicknesses and material compositions are reported in Table E.3. The transport settings for ANISN transport simulations are kept unchanged from the previous verifications study, i.e.

- S_{16} discrete ordinate approximation;
- P_4 scattering moment Legendre expansion;
- Mesh spacing Δ_J calculated by Equation (D.35);
- FENDL3.1b cross section libraries with Vitamin J+ multigroup energy structure, consisting of 211 n + 42 γ groups.

Figure E.11 illustrates the radial profiles of $\Phi_{fast,n}$ and $\Phi_{tot,n}$ and Figure E.12 the trends of $\Phi_{tot,\gamma}$ as function of the radial distance from the inboard FW $\Delta r_{fw,ib}$ at mid-equatorial plane ($z = 0$). The results from the 1D MIRA neutronic module are locally diagnosed against those obtained by

MCNP simulations.

The outcomes outlined for the 1D verification study are confirmed here with peak local relative

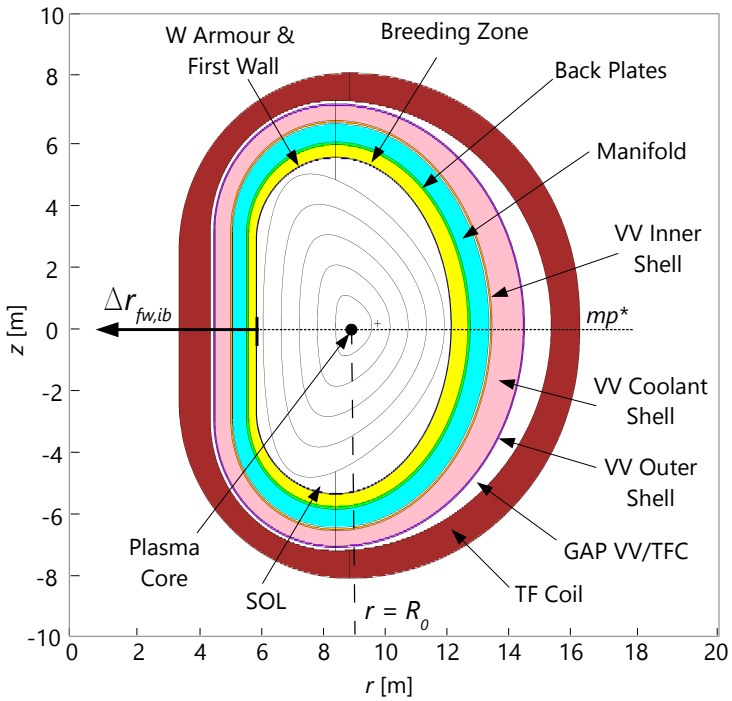

Figure E.10.: Radial-Vertical cut of the EU-DEMO 2015 MCNP homogenized model adopted for benchmarking the 2D core plasma + 1D reactor deterministic model integrated in the MIRA system/design code.

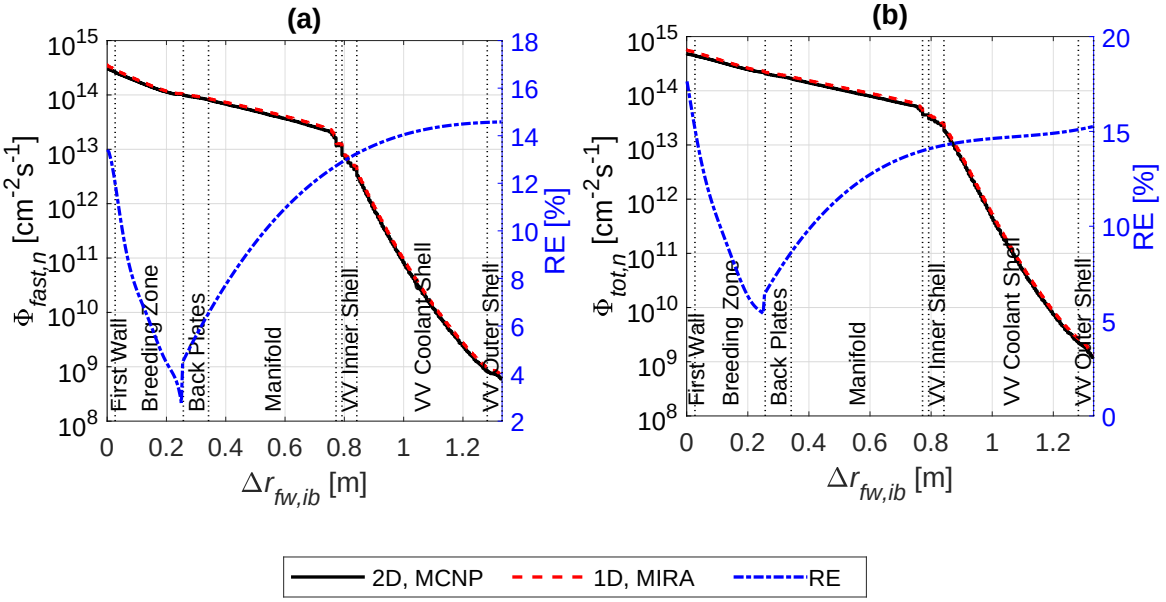

Figure E.11.: Radial profiles of fast neutron flux density $\Phi_{fast,n}$ (a) and total neutron flux density $\Phi_{tot,n}$ (b). The curves relate to the MIRA and MCNP solutions (solid and dashed) to the 2D transport problem depicted by Figure E.10. The relative error RE is depicted by the dot-dashed line.

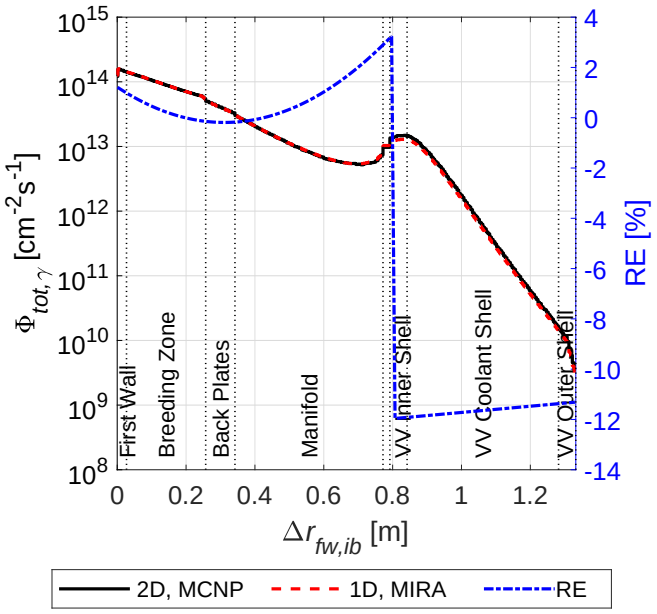

Figure E.12.: Radial profiles of total gamma flux density $\Phi_{tot,\gamma}$. The curves relate to the MIRA and MCNP solutions (solid and dashed) to the 2D transport problem depicted by Figure E.10. The relative error RE is depicted by the dot-dashed line.

errors occurring in highly ferritic regions, such as first wall, manifold and vacuum vessel. In this case, the toroidal effect add an additional contribution, radially increasing up to + ∼15-16 % on the inner side of the TFC towards the outer VV shell, while for the global NRMSE definition of the error is approximately ∼11-13 %. Similar values (∼14-15 %) are present for peak total and fast neutron fluxes on the inboard first wall, where also the dpa rate on the Eurofer steel are computed to assess the blanket lifetime. The limitations of the multigroup energy approach in accounting for the self-shielding effects of neutron captures in iron are again manifested in the RE trend of $\Phi_{tot,\gamma}$, exhibits a drastic collapse of $\Phi_{tot,\gamma}$ on the inner VV shell and leads to a negative 12% MRE.
For a neutronic variable parameter spanning by 6-7 orders of magnitude across its spatial domain, these figures can be evaluated for a systems code module, assuming that these uncertainties are also extended to the local nuclear power density and atomic displacement rates. Since fast and total neutron fluxes tend to overestimate their actual values in the those reactor regions where the neutron radiation damage and shielding criteria are being evaluated, such figures can be conservatively used for radial build design purposes.

Table E.6 reports the nuclear heating powers R^m_{heat} for each reactor component m. The integral energy deposition shows an increasing error moving radially outwards, with very good predictions on the first three BB subregions, up to 15 % in the manifold region. Moving further towards the outer part of the tokamak, the toroidal effects and the limited capabilities of energy grouping prevail and the deviations amplifies up to 76 % in the TF coil region. Such large distances between actual and predicted solutions occur where the contribution to the overall plant thermal power are nearly negligible, while rather accurate estimations are yielded in those region driving the nuclear engineering design of the plant, such as the breeding blanket components.

In Table E.7 the breeding zone T production rates are listed for inboard, outboard and total BZ contributions. The predictions are affected by a pronounced unbalance between inboard and outboard shares to the total T generation rate, with around ∼ 5% less and nearly 9 % more than

Component	1D, MIRA [MW]	2D, MCNP [MW]	RE [%]
W armour	66.9	66.2	+1.02
First Wall	206.2	204.1	+1.07
Breeding Zone	1738.2	1675.4	+3.72
Back Plates	56.8	50.8	+11.71
Manifold	112.9	97.8	+15.44
VV Inner Shell	14.3	9.94	+43.92
VV Mid Shell	38.3	27.1	+41.87
VV Outer Shell	0.0071	0.0047	+50.96
TFC	0.0039	0.0023	+76.14

Table E.6.: Global nuclear heating power R^m_{heat} in all m listed core reactor physical components. The results obtained via 1D MIRA neutronic model (1D, MIRA) are correlated to those procured by means of reference MCNP calculations in 2D toroidal geometry (2D, MCNP).

T breeding contribution	1D, MIRA [g/d]	2D, MCNP [g/d]	RE [%]
Inboard	115.5	122.8	-5.97
Outboard	316.9	290.8	+8.95
Total	432.4	413.6	+4.52

Table E.7.: Global tritium generation rate R^{bz}_{nt} for inboard, outboard and BZ contribution. The results obtained via coupled 2D plasma + 1D reactor MIRA transport model are correlated to those derived from reference MCNP simulations in 2D axisymmetric geometry.

the actual value for inboard and outboard. Similar trends have been also found in the inboard and outboard nuclear heating power terms for all the core reactor components, as of Table E.6 (omitted here). Such behaviour is associated with the poloidal effects due to the actual curvature of the components in poloidal direction, affecting the radiation streaming. Such different responses cancelling partially out, with lower and relatively good prediction around the 5 % with respect to MCNP 2D homogenized solution.
In the previous verification study the "blind" comparison between deterministic and Monte Carlo showed a $\sim$ 1 % error on the global tritium generation rate derived from the spatial, angular and energy discretization of the solving technique (see Table E.5). Therefore, the remaining 4 % can be linked to the one-dimensional assumption.

To investigate more thoroughly such geometric effects the error analysis on the tritium breeding rate, being the most important integral parameter, has been conducted for multiple reactor configurations.
The limit of the cylindrical approximation for actual toroidal geometries holds for very large values of aspect ratio, i.e. $A \gg 1$. Based on Equation (2.1) such a configuration can be either achieved for high major radius R_0 or small minor radius a. Relying on the same feasibility ranges for R_0 and A followed already for benchmarking the 2D plasma core transport model. In Table E.8 is listed the RE calculated on the total T generation rate in the BZ region R^{bz}_{nt}. The deviations are observed to grow (nearly linearly) for increasing aspect ratios and decreasing major radius amplitudes, finding a match in the expected considerations on the limits of the cylindrical "Ansatz" of the problem. The uncertainties lay in a relatively narrow range (from 3.5 to 6 %) for very diverse reactor configurations. This suggests that the effects induced by other factors, such as the reactor component radial and vertical builds, can be restrained to a few percentage points.
Therefore, for the reactor layouts currently investigated in the ongoing system design activities a 5 %

error contribution on assessed tritium breeding and nuclear heating integral terms can be attributed to the cylindrical approximation, while a 15 % to the local radial profile used for shielding and neutron damage requirements evaluations.

	$R_0 = 7.5$ m	$R_0 = 9.0$ m	$R_0 = 10.5$ m
$A = 2.6$	+4.74	+4.03	+3.56
$A = 3.1$	+5.38	+4.52	+3.99
$A = 3.6$	+5.92	+4.96	+4.39

Table E.8.: RE [%] on the global tritium generation rate predicted by the 1D deterministic neutron transport module for varying plasma major radius R_0 and aspect ratio A. The error is measured as a relative deviation from the reference MCNP 2D axisymmetric model

Compared to actual DEMO blanket situations, where material heterogeneities and void gaps between the different subsystems impact on the overall neutron and photon streaming, the reactor configurations addressed so far rely on a homogenized material mixtures in regions delimited by their radial domain. The final step for assessing the global error introduced by the simplifying assumptions of the transport model is to estimate the net contribution coming from the material mix.
Locally, the particle kinetics is influenced rebalancing the particles towards certain preferential paths. As a result, the spatial distribution of scalar neutron and photon fluxes can be highly heterogeneous and the volume integration of local reaction rates are consequentially influenced. To predict these effects on the global parameters, such as heating power and tritium breeding rate, the current EU-3D DEMO MCNP heterogeneous transport simulations [130, 131] are taken as the reference set of parameters upon which the predictions of less refined simulators are evaluated. To establish the distance to the "actual" solution and to confine the error only to heterogeneous and further 3D effects the benchmark is carried out between the "2D, MCNP" and the actual three-dimensional cases. The key comparison parameter is the Tritium Breeding Ratio (TBR, see 4.33), relating the global tritium production rate R_{nt} and the tritium burn-up in the core plasma. The input specifications of radial build and material compositions (see Table E.3) are indeed derived from the DEMO HCPB 2015 design, whose calculated TBR is 1.205 [131, 181] for a breeding zone layout with 15.5 mm breeder 40 mm Be pebble beds poloidally piled-up. For a fair comparison the the T generation rate calculated by the 2D MCNP model and reported on Table E.7 (413.6 [g/d]) needs to be rescaled accounting for the neutron leaking through the divertor openings. Such neutrons cannot breed tritium as they get unavoidably lost. For the tight divertor layout implemented in the EU-DEMO 2015 baseline (see 2.10) only 4-5 % of fusion neutrons are lost. Thus, the effective T generation rate amounts to 392 g/d, corresponding to a TBR = 1.25 and deviating from the reference 1.205 TBR value by approximately $\sim$4 %. Similar figures have been obtained comparing also the deposited nuclear heating power in BB subsystems ($\sim$3 %). The deviations from 3D MCNP results on the local dpa rate ($\sim$20 %), fast neutron flux ($\sim$18 %) and power density ($\sim$15 %) have been roughly extracted from Refs. [131, 181].

To summarize, the relative error of the MIRA neutronic module on the neutronic parameters used to verify the neutronic design criteria (see Table 4.1) are reported in Table E.9 for each identified contribution.
Although local deviations may appear relatively large, the deployment of this model in systems codes is capable of comparing reliably design solutions, studying the global impact not only at a level of the individual components, though to the reactor as a whole. However, as the results exhibit in all cases overestimating figures they can be conservatively deployed for shielding design applications, where a 30 % roof on a parameter diminishing by orders of magnitude across its domain can be

Error source	TBR	R_{heat}^{bb+vv}	$\mathcal{R}_{dpa}(r_{1,i}^{fw})$	$\mathcal{R}_{dpa}(r_{1,i}^{vv})$	$\Phi_{fast}(r_{1,i}^{wp})$	$\mathcal{R}_{heat}(r_{1,i}^{wp})$
Numerics	+0.5	+1.0	+2.5	+10.5	+3.5	+5.0
1D geometry	+3.5	+3.0	+7.0	+5.0	+15.0	+10.0
Homogenization	+4.0	+3.0	+1.5	+22.0	+18.5	+15.0
Total	+8.0	+7.0	+10.0	+37.5	+37.0	+30.0

Table E.9.: RE [%] of the MIRA neutronic module affecting the assessment of: (i) TBR, (ii) global nuclear heating power in BB and VV R_{heat}^{bb+vv}, (iii) peak atomic displacement rate on inboard blanket FW $\mathcal{R}_{dpa}(r_{1,i}^{fw})$ and (iv) vacuum vessel $\mathcal{R}_{dpa}(r_{1,i}^{vv})$, (v) fast neutron flux density $\Phi_{fast}(r_{1,i}^{wp})$ and (vi) nuclear power density power $\mathcal{R}_{heat}(r_{1,i}^{wp})$ at inboard TF Coil winding pack. The global error is broken down into different contributions, associated with different simplifying assumptions.

genuinely judged in range and not too conservative. The errors on TBR and nuclear heating are found in an acceptable range of deviations, providing overestimating guesses. In this case the error shall be always taken into account when using these parameters for breeding blanket radial build design, where the operational requirements are based on imposed lower limits.

F. Complementary Parametric Scans

F.1. Parametric Scan of the Plasma Internal Inductance

The plots reported in this section provide a set of additional trends to support the parametric scan on the plasma internal inductance l_i addressed in Section 6.1.

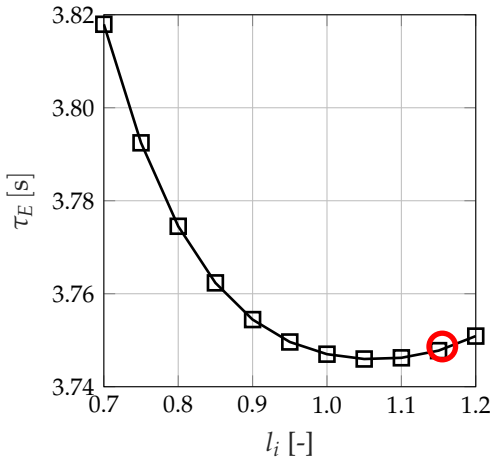

Figure F.1.: Evaluated plasma energy confinement time τ_E for constrained variations of the plasma internal inductance l_i. The red circle marks the DEMO1 2015 baseline, as per MIRA analysis.

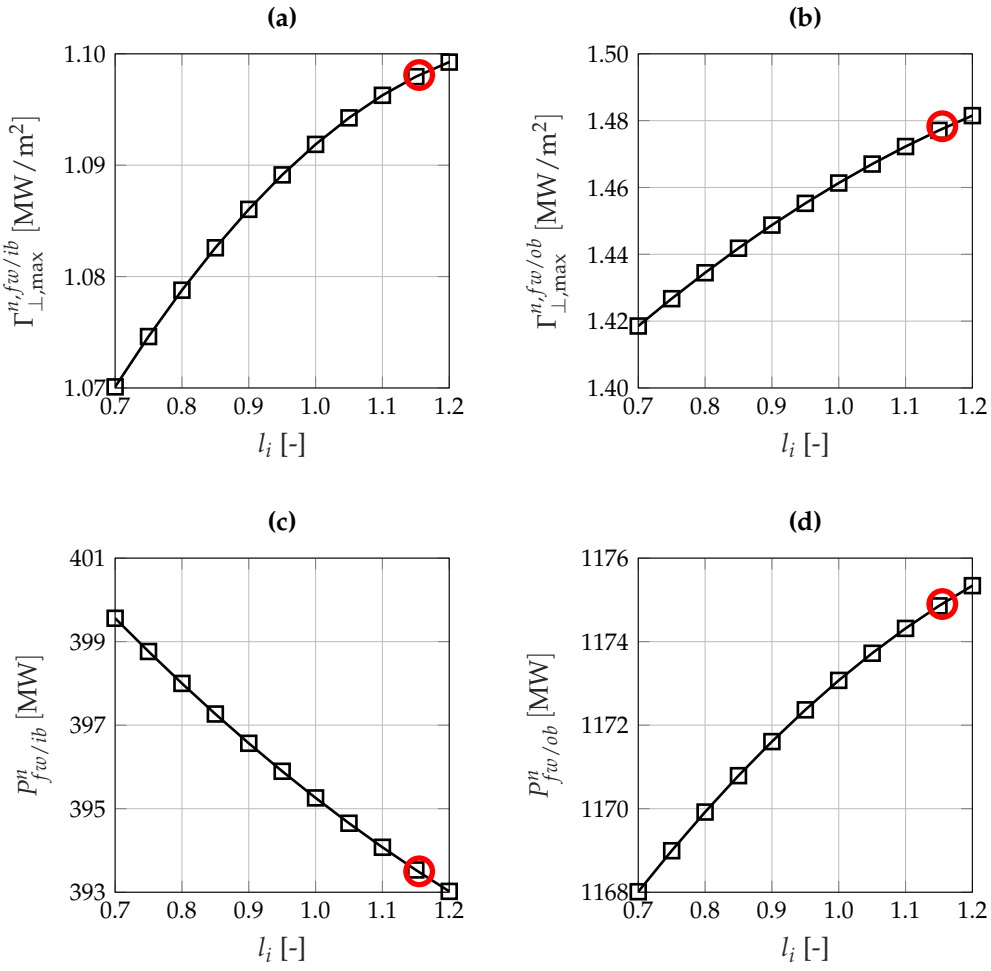

Figure F.2.: Computed distributions of neutron radiation wall loading properties for constrained variations of the plasma internal inductance l_i: (a) inboard FW peak neutron wall loading $\Gamma^{n,fw/ib}_{\perp,\max}$, (b) outboard FW peak neutron wall loading $\Gamma^{n,fw/ob}_{\perp,\max}$, (c) total incident neutron power onto inboard FW $P^{n}_{fw/ib}$ and (d) total incident neutron power onto outboard FW $P^{n}_{fw/ob}$. The red circle marks the DEMO1 2015 baseline, as per MIRA analysis.

F.2. Parametric Scan of the Inboard Breeding Zone Thickness

This section provides a set of complementary plots in support to the parametric scan on the inboard BZ thickness $\Delta_{BZ,i}$ addressed in Section 6.2.

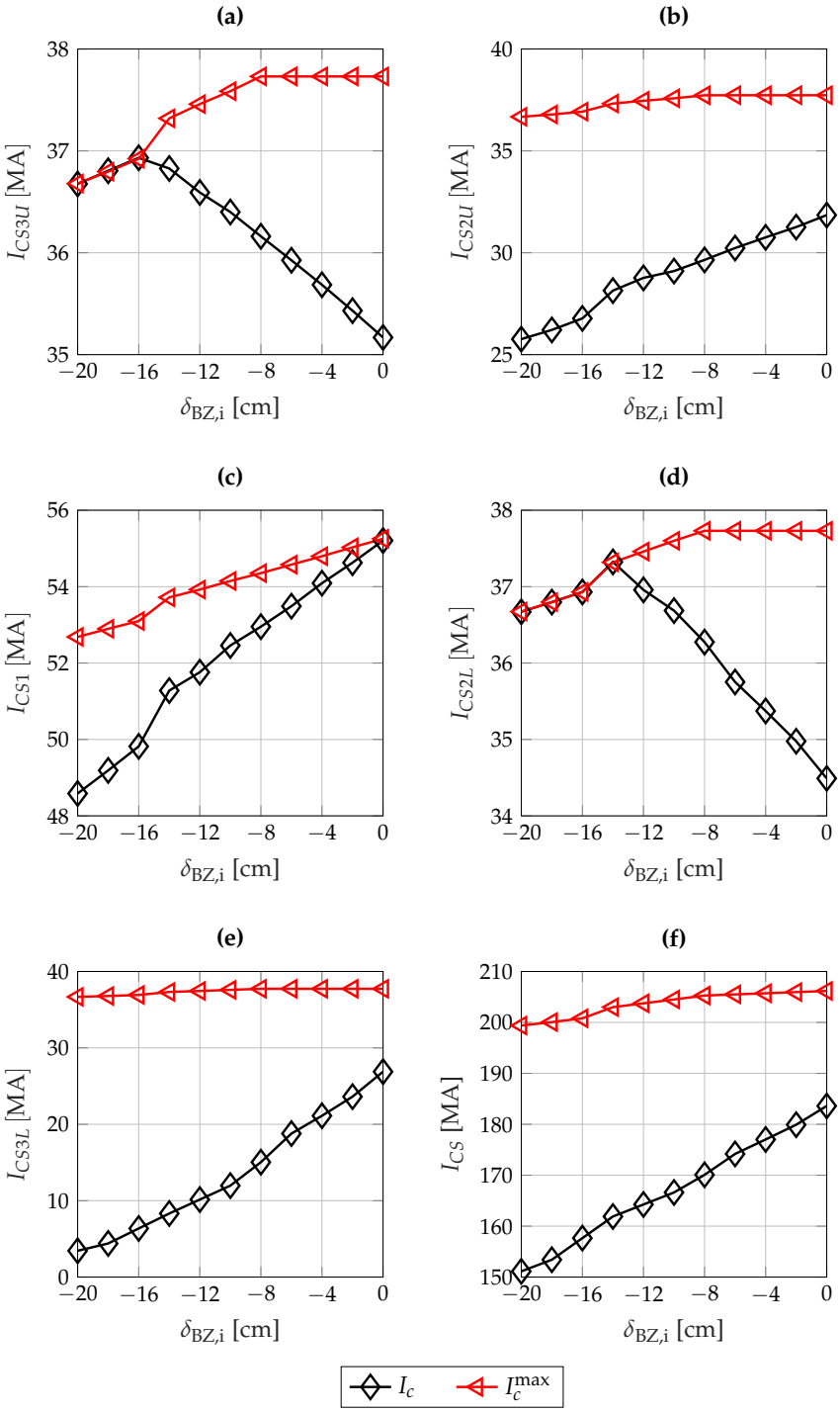

Figure F.3.: Calculated CS coils total and maximum currents for variations of the relative inboard breeding zone thickness $\delta_{BZ,i}$.

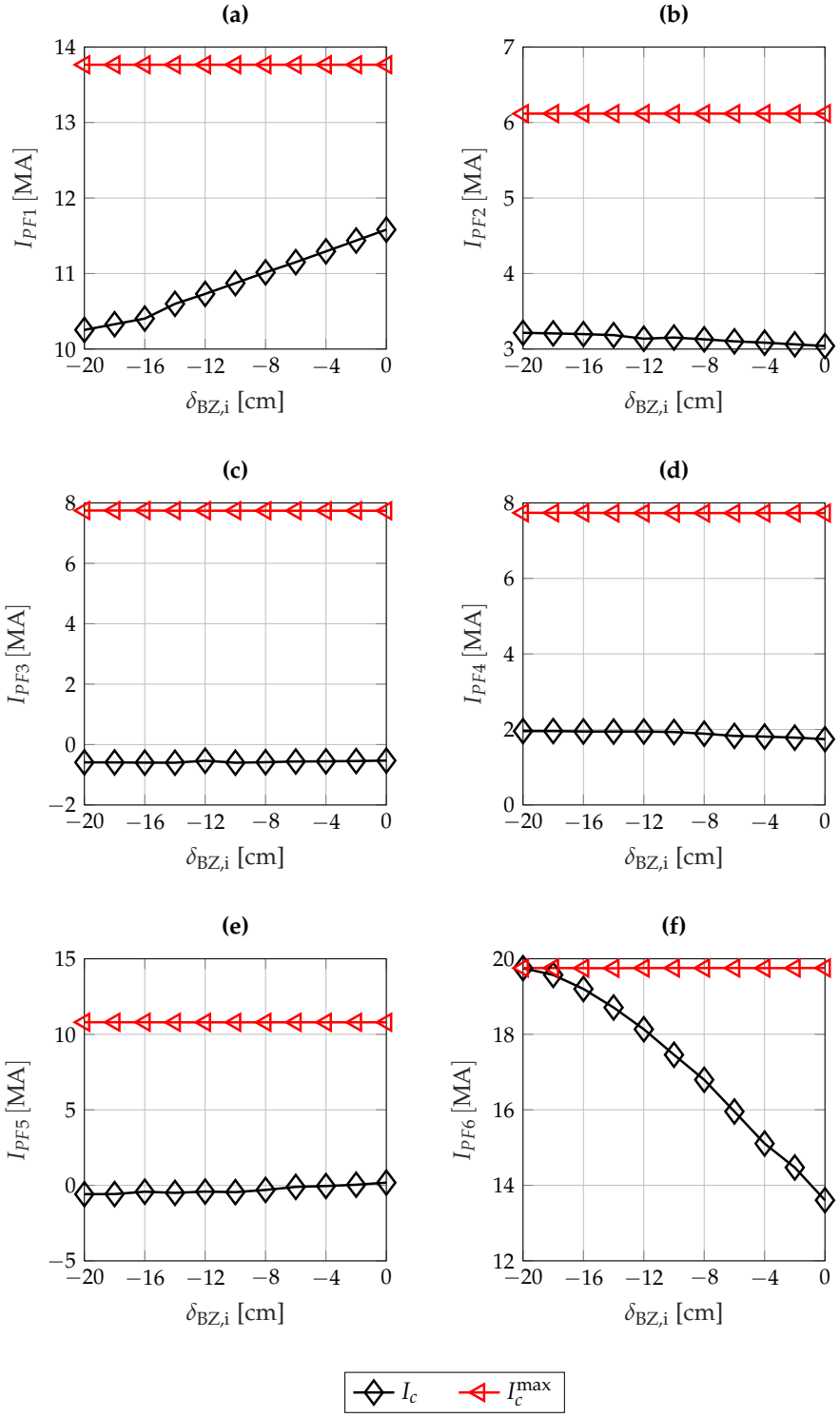

Figure F.4.: Computed profiles of PF coils total and maximum currents for variations of the relative inboard breeding zone thickness $\delta_{BZ,i}$.

References

[1] United Nations, Department of Economic and Social Affairs, Population Division (2017). World Population Prospects: The 2017 Revision, Key Findings and Advance Tables. Working Paper No. ESA/P/WP/248, https://esa.un.org/unpd/wpp/Publications/Files/WPP2017_KeyFindings.pdf. Last accessed on 11.06.2019.

[2] U.S. Energy Information Administration. International Energy Outlook 2017 (2017). https://www.eia.gov/outlooks/ieo/pdf/0484(2017).pdf. Last accessed on 11.06.2019.

[3] International Energy Agency. World Energy Outlook 2016. Executive Summary (2016). https://www.iea.org/publications/freepublications/publication/WorldEnergyOutlook2016ExecutiveSummaryEnglish.pdf. Last accessed on 11.06.2019.

[4] P. Muehlich, T. Hamacher. Global transportation scenarios in the multi-regional EFDA-TIMES energy model. *Fusion Engineering and Design*, 84:1361–1366, 2009.

[5] P.H. Rebut, R.J. Bickerton, B.E. Keen. The Joint European Torus: installation, first results and prospects. *Nuclear Fusion*, 25(9):1011, 1985.

[6] ASDEX Upgrade Design Team and Tokamak Theory Group. ASDEX-Upgrade. Definition of a tokamak experiment with a reactor compatible poloidal divertor. Technical Report IPP 1/197, Max-Planck-Institut für Plasmaphysik, Garching(DE), 1982.

[7] R. Aymar, P. Barabaschi, Y. Shimomura. The ITER design. *Plasma Physics and Controlled Fusion*, 44:519–565, 2002.

[8] T. Donne, W. Morris, X. Litaudon, C. Hidago, D. McDonald, H. Zohm et al. *European Research Roadmap to the Realisation of Fusion Energy*. EUROfusion, November 2018. ISBN: 978-3-00-061152-0.

[9] Jeffrey P. Friedberg. *Plasma Physics and Fusion Energy*. Cambridge Unversity Press, 2007. ISBN:978-0-521-85107-7.

[10] Tobias Hartmann. *Development of a Modular System Code to Analyze the Implications of Physics Assumptions on the Design of a Demonstration Fusion Power Plant*. PhD thesis, Technische Universitaet Muenchen, 2013.

[11] D. Maisonnier, D. Campbell, I. Cook, L. Di Pace et al. Power plant conceptual studies in Europe. *Nuclear Fusion*, 47:1524–1532, 2007.

[12] G. Federici, R. Kemp, D.Ward, C. Bachmann et al. Overview of EU DEMO design and R&D activities. *Fusion Engineering and Design*, 89:882–889, 2014.

[13] U. Fischer, C. Bachmann, J.P. Catalan, T. Eade et al. Methodological approach for DEMO neutronics in the European PPPT programme: Tools, data and analyses. *Fusion Engineering and Design*, 123:26 – 31, 2017.

[14] F. Najmabadi, The ARIES Team. The ARIES-AT advanced tokamak, Advanced technology fusion power plant. *Fusion Engineering and Design*, 80:3–23, 2006.

[15] J. Johner. HELIOS: A Zero-Dimensional Tool for Next Step and Reactor Studies. *Fusion Science and Technology*, 59:308–349, 2011.

[16] B.G. Hong, D. Lee, S.-K. Kim, Y. Kim. Development of a tokamak reactor system code and its application for concept development of a demo reactor. *Fusion Engineering and Design*, 83:16151618, 2008.

[17] M. Kovari, R. Kemp, H. Lux, P. Knight et al. PROCESS: A systems code for fusion power plants - Part 1: Physics. *Fusion Engineering and Design*, 89:3054–3069, 2014.

[18] M. Kovari, F. Fox, C. Harrington, R. Kembleton et al. PROCESS: A systems code for fusion power plants - Part 2: Engineering. *Fusion Engineering and Design*, 104:9–20, 2016.

[19] G. Federici, C. Bachmann, W. Biel, L.V. Boccaccini et al. Overview of the design approach and prioritization of R & D activities towards an EU DEMO. *Fusion Engineering and Design*, 109-111:1464–1474, 2016.

[20] C. Reux, L. Di Gallo, F. Imbeaux, J.F. Artaud et al. DEMO reactor design using the new modular system code SYCOMORE. *Nuclear Fusion*, 55:073011 (10pp), 2015.

[21] J.-C. Jaboulay, A. Li Puma, J. Martinez Arroyo. Neutronic predesign tool for fusion power reactors system assessment. *Fusion Engineering and Design*, 88:2336–2342, 2013.

[22] A. Li-Puma, J.-C. Jaboulay, B. Martin. Development of the breeding blanket and shield model for the fusionpower reactors system SYCOMORE. *Fusion Engineering and Design*, 89:1195–1200, 2014.

[23] J.-L. Duchateau, P. Hertout, B. Saoutic, J.-F. Artaud et al. Conceptual integrated approach for the magnet system of a tokamak reactor. *Fusion Engineering and Design*, 89:2606–2620, 2014.

[24] H. Fujieda, Y. Murakami, M. Sugihara. Tokamak Plasma Power Balance Calculation Code (TPC Code) Outline and Operation Manual. Technical Report JAERI-M 92-178, Japan Atomic Energy Agency, Japan, 1992.

[25] M. Nakamura, R. Kemp, H. Utoh, D.J. Ward et al. Efforts towards improvement of systems codes for the Broader Approach DEMO design. *Fusion Engineering and Design*, 87:864–867, 2012.

[26] K. Okano, G. Federici, K. Tobita. DEMO design activities in the broader approach under Japan/EU collaboration. *Fusion Engineering and Design*, 89:2008–2012, 2014.

[27] R. Wenninger, R. Kembleton, C. Bachmann, W. Biel et al. The physics and technology basis entering European system code studies for DEMO. *Nuclear Fusion*, 57:016011 (11pp), 2017.

[28] C. Bustreo, G. Casini, G. Zollino, T. Bolzonella et al. FRESCO, a simplified code for cost analysis of fusion power plants. *Fusion Engineering and Design*, 88:3141–3151, 2013.

[29] B. Meszaros. EU DEMO1 2015 DEMO-Tokamak-Complex (CAD Model). Technical Report EFDA_D_2M9AJJ, EUROfusion, 2015.

[30] R. Wenninger. Reference Design - 2015 April (EU DEMO1 2015) PROCESS Full Output. Technical Report EFDA_D_2MDKFH, EUROfusion, 2015.

[31] L.V. Boccaccini, G. Aiello, J. Aubert, C. Bachmann et al. Objectives and status of EUROfusion DEMO blanket studies. *Fusion Engineering and Design*, 109-111:1199–1206, 2016.

[32] G. Federici, W. Biel, M.R. Gilbert, R. Kemp et al. European DEMO design strategy and consequences for materials. *Nuclear Fusion*, 57:092002 (26 pp), 2017.

[33] C. Bachmann. DEMO Plant Description Document. Technical Report EFDA_D_2KVWQZ, EUROfusion, 2015.

[34] F. Hernandez, P. Pereslatsev, Q. Kang, P. Norajitra et al. A new HCPB breeding blanket for the EU DEMO: Evolution, rationale and preliminary performances. *Fusion Engineering and Design*, 124:882–886, 2017.

[35] A. Del Nevo, E. Martelli, P. Agostini, P. Arena et al. WCLL breeding blanket design and integration for DEMO 2015: status and perspectives. *Fusion Engineering and Design*, 124:682–686, 2017.

[36] A. Tassone, A. Del Nevo, P. Arena, G. Bongiovi et al. Recent Progress in the WCLL Breeding Blanket Design for the DEMO Fusion Reactor. *IEEE Transaction on Plasma Science*, 46:1446–1457, 2018.

[37] J. Aubert, G. Aiello, N. Jonqueres, A. Li Puma et al. Development of the water cooled lithium lead blanket for DEMO. *Fusion Engineering and Design*, 89:1386–1391, 2014.

[38] G. Ambrosino, R. Albanese. Magnetic control of plasma current, position, and shape in Tokamaks: a survey or modeling and control approaches. *IEEE Control Systems*, 25(5):76–92, Oct 2005.

[39] C. Sborchia, A. Bonito Oliva, T. Boutboul, K. Chan et al. The ITER magnet systems: progress on construction. *Nuclear Fusion*, 54(1):013006, 2014.

[40] L. Zani, C.M. Bayer, M.E. Biancolini, R. Bonifetto et al. Overview of Progress on the EU DEMO Reactor Magnet System Design. *IEEE Transactions on Applied Superconductivity*, 26(4):1–5, June 2016.

[41] P.V. Gade, C. Bayer, W.H. Fietz, R. Heller et al. Electromagnetic and mechanical analysis of a toroidal field coil winding pack for EU DEMO. *Fusion Engineering and Design*, 98–99:1068–1071, 2015.

[42] ITER Organization. Design Description Document - TF Coils and Structures. Technical Report ITER_D_2MVZNX v2.2, 2009.

[43] P. Bruzzone, K. Sedlak, B. Stepanov. High current superconductors for DEMO. *Fusion Engineering and Design*, 88(9):1564 – 1568, 2013.

[44] P. Bruzzone, K. Sedlak, B. Stepanov, L. Muzzi et al. Design of Large Size, Force Flow Superconductors for DEMO TF Coils. *IEEE Transactions on Applied Superconductivity*, 24(3):1–4, June 2014.

[45] P. Bruzzone. Pre-conceptual studies and R & D for DEMO superconducting magnets. *Fusion Engineering and Design*, 89(7):1775 – 1778, 2014.

[46] A. Torre, D. Ciazynski, P. Hertout, L. Zani. Tools Used at CEA for Designing the DEMO Toroidal Field Coils Winding Pack. *IEEE Transactions on Applied Superconductivity*, 26(4):1–5, June 2016.

[47] A. Torre, D. Ciazynski, L. Zani. EU-DEMO TF and CS Magnet Systems Design and Analyses Performed at CEA. *IEEE Transactions on Applied Superconductivity*, 27(4):1–5, June 2017.

[48] R. Wesche, K. Sedlak, N. Bykovsky, P. Bruzzone et al. Winding Pack Proposal for the TF and CS Coils of European DEMO. *IEEE Transactions on Applied Superconductivity*, 26(3):1–6, April 2016.

[49] R. Wesche, N. Bykovsky, X. Sarasola, K. Sedlak et al. Central solenoid winding pack design for DEMO. *Fusion Engineering and Design*, 124:82 – 85, 2017.

[50] ITER. Design Description Document - Magnets - Conductors. Technical Report ITER_D_2NBKXY v1.2, 2009.

[51] L. Bottura, B. Bordini. $J_C(B, T, \varepsilon)$ Parameterization for the ITER Nb_3Sn Production. *IEEE Transactions on Applied Superconductivity*, 19(3):1521–1524, June 2009.

[52] M. Lewandowska, K. Sedlak, L. Zani. Thermal-Hydraulic Analysis of the Low- T_c Superconductor (LTS) Winding Pack Design Concepts for the DEMO Toroidal Field (TF) Coil. *IEEE Transactions on Applied Superconductivity*, 26(4):1–5, June 2016.

[53] P.V. Gade, C. Barth, C. Bayer, W.H. Fietz et al. Conceptual Design of a Toroidal Field Coil for a Fusion Power Plant Using High Temperature Superconductors. *IEEE Transactions on Applied Superconductivity*, 24:4202705, 2014.

[54] P. Bruzzone, K. Sedlak, D. Uglietti, N. Bykovsky et al. LTS and HTS high current conductor development for DEMO. *Fusion Engineering and Design*, 96-97:77 – 82, 2015.

[55] W.H. Fietz, R. Heller, M.J. Wolf, P.V. Gade. High temperature superconductor cables for EU-DEMO TF-magnets. *Fusion Engineering and Design*, 125:290 – 293, 2017.

[56] L. Zani, D. Ciazynski, B. Lacroix, M. Coleman et al. Status of CEA Magnet Design Tools and Applications to EU DEMO PF and CS Magnets. *IEEE Transactions on Applied Superconductivity*, 28(3):1–5, April 2018.

[57] L. Bottura. A practical fit for the critical surface of NbTi. *IEEE Transactions on Applied Superconductivity*, 10(1):1054–1057, March 2000.

[58] Peter C. Stangeby. *The Plasma Boundary of Magnetic Fusion Devices*. IOP Publishing Ltd, 1999. ISBN:0-7503-0559-2.

[59] K.J. Dietz, S. Chiocchio, A. Antipenkov, G. Federici et al. Engineering and design aspects related to the development of the ITER divertor. *Fusion Engineering and Design*, 27:96–108, 1995.

[60] ITER Organization. `https://www.iter.org/img/crop-2000-90/all/content/com/img_galleries/com_media_photos_06.jpg`. Last accessed on 05.12.2018.

[61] T.R. Barrett, G. Ellwood, G. Perez, M. Kovari et al. Progress in the engineering design and assessment of the European DEMO first wall and divertor plasma facing components. *Fusion Engineering and Design*, 109-11, Part A:917–924, 2016.

[62] J.H. You, G. Mazzone, E. Visca C. Bachmann et al. Conceptual design studies for the European DEMO divertor: Rationale and first results. *Fusion Engineering and Design*, 109-11 Part B:1598–1603, 2016.

[63] J.H.You, G. Mazzone, C. Bachmann, D. Coccorese. Progress in the initial design activities for the European DEMO divertor: Subproject "Cassette". *Fusion Engineering and Design*, 124:364–370, 2017.

[64] B. van der Schaaf, F. Tavassoli, C. Fazio, E. Rigal et al. The development of EUROFER reduced activation steel. *Fusion Engineering and Design*, 69:197–203, 2003.

[65] J.H. You, E. Visca, T. Barrett, B. Boeswirth et al. European divertor target concepts for DEMO: Design rationales and high heat flux performance. *Nuclear Materials and Energy*, 16:1 – 11, 2018.

[66] Weston M. Stacey. *Fusion - An Introduction to the Physics and Technology of Magnetic Confinement Fusion*. WILEY-VCH Verlag GmbH & Co. KGaA, Weinheim, 2010. ISBN:978-3-527-40967-9.

[67] C.Bachmann, F. Arbeiter, L.V. Boccaccini, M. Coleman et al. Issues and strategies for DEMO in-vessel component integration. *Fusion Engineering and Design*, 112:527–534, 2016.

[68] R. Mozzillo, D. Marzullo, A. Tarallo, C. Bachmann et al. Development of a master model concept for DEMO vacuum vessel. *Fusion Engineering and Design*, 112:497–504, 2016.

[69] A. Loving, O. Crofts, N. Sykes, D. Iglesias et al. Pre-conceptual design assessment of DEMO remote maintenance. *Fusion Engineering and Design*, 89:2246–2250, 2014.

[70] F. Franza, L.V. Boccaccini, U. Fischer, P.V. Gade et al. On the implementation of new technology modules for fusion reactor systems codes. *Fusion Engineering and Design*, 98-99:1767–1770, 2015.

[71] B. Meszaros, C. Bachmann, R. Kemp, G. Federici. Definition of the basic DEMO tokamak geometry based on systems code studies. *Fusion Engineering and Design*, 98-99:1556–1560, 2015.

[72] R. Kemp, R. Wenninger, G. Federici, H. Reimerdes et al. Exploring a broad spectrum of design options for DEMO. *Fusion Engineering and Design*, 2018.

[73] F. Maviglia, G. Federici, R. Wenninger, R. Albanese et al. Effect of the engineering constraints on charged particle wall heat loads in DEMO. *Fusion Engineering and Design*, 124:385–390, 2017.

[74] W.-H. Qian, K. Qian. Optimising the four-arc approximation to ellipses. *Computer Aided Geometric Design*, 18:1–19, 2001.

[75] J. File, R.G. Mills, G.V. Sheffield. Large superconducting magnet designs for fusion reactors. *IEEE Transactions on Nuclear Science*, 18:277 – 282, 1971.

[76] R.W. Moses. Analytic expressions for magnetic forces on sectored toroidal coils. In *Proceedings of Sixth Symposium on Engineering Problems for Fusion Research*, pages 917–921. San Diego, US, 1975.

[77] J. Erb, W. Maurer. Method for Determining the Magnet Shape in Toroidal Arrangements. In *Proceedings of the 5th International Conference on Structural Mechanics in Reactor Technology*, volume 2.1/6, pages 1–7. Berlin, Germany, 1979.

[78] C.V. Atanasiu, S. Guenter, K. Lackner, I.G. Miron. Analytical solutions to the Grad-Shafranov equation. *Physics of Plasmas*, 11:3510–3518, 2004.

[79] H. Grad, H. Rubin. Hydromagnetic Equilibria and Force-Free Fields. In *Proceedings of the Second United Nations Conference on the Peaceful Uses of Atomic Energy*, volume 31, page 190, 1958.

[80] C.E. Kessel, D. Campbell,, Y. Gribov, G. Saibene et al. Development of ITER 15 MA ELMy H-mode inductive scenario. *Nuclear Fusion*, 49:085034 (19pp), 2009.

[81] M.C.R. Andrade, G.O. Ludwig. Scaling of bootstrap current on equilibrium and plasma profile parameters in tokamak plasmas. *Plasma Phys. Control. Fusion*, 50:065001 (18pp), 2008.

[82] J.A. Romero, JET-EFDA Contributors. Plasma internal inductance dynamics in a tokamak. *Nuclear Fusion*, 50:115002 (9pp), 2010.

[83] Weston M. Stacey. *Fusion Plasma Physics*. WILEY-VCH Verlag GmbH & Co. KGaA, Weinheim, 2005. ISBN:3-527-40586-0.

[84] H.R. Koslowski. Operational limits in tokamaks. *Transactions of Fusion Science and Technology*, 49:147–154, 2006.

[85] Hartmut Zohm. *Magnetohydrodynamic Stability of Tokamaks*. Wiley-VCH Verlag GmbH & Co. KGaA, 2014. ISBN:978-3-527-67736-8.

[86] N.A. Uckan. Relative merits of size, field and current ignited tokamak performance. *Fusion Technology*, 14:299–319, 1988.

[87] N.A. Uckan. ITER Physics Group. ITER Physics Design Guidelines: 1989. Technical Report ITER documentation series No. 10, International Atomic Energy Agengy, Japan, 1990.

[88] F. Franza, I.S. Landman, S. Pestchanyi. Development of an advanced magnetic equilibrium model for fusion reactor system codes. *Fusion Engineering and Design*, 136:309 – 313, 2018.

[89] A. Bermúdez, D. Gómez, P. Salgado. *Mathematical Models and Numerical Simulation in Electromagnetism - Volume 74*. Springer, 2009. ISBN:978-3-319-02948-1.

[90] F. Hecht. New development in freefem++. *Journal of Numerical Mathematics*, 20(3-4):251–265, 2012.

[91] L.S. Solov'ev. The theory of hydromagnetic stability of toroidal plasma configurations. *Soviet Physics JETP*, 26:400–407, 1968.

[92] R.H. Byrd, J.C. Gilbert, J. Nocedal. A trust region method based on interior point techniques for nonlinear programming. *Mathematical programming*, 89:149–185, 2000.

[93] I. Polik, T. Terlaky. Interior Point Methods for Nonlinear Optimization. In: G. Di Pillo, F. Schoen Nonlinear Optimization. Lecture Notes in Mathematics, vol 1989. Springer, Berlin, Heidelberg, 2010.

[94] A. Forsgren, P.E. Gill, M.H. Wright. Interior Methods for Nonlinear Optimization. *SIAM Rev.*, 44(4):525597, 2006.

[95] R. Albanese, R. Ambrosino, M. Mattei. CREATE-NL+: A robust control-oriented free boundary dynamic plasma equilibrium solver. *Fusion Engineering and Design*, 96-97:664–667, 2015.

[96] R.R. Khayrutdinov, V.E. Lukash. Studies of Plasma Equilibrium and Transport in a Tokamak Fusion Device with the Inverse-Variable Technuque. *Journal of Computational Physics*, 109:193–201, 1993.

[97] F. Villone, L. Barbato, S. Mastrostefano, S. Ventre. Coupling of nonlinear axisymmetric plasma evolution with three-dimensional volumetric conductors. *Plasma Physics and Controlled Fusion*, 55:1–15, 2013.

[98] S.C. Jardin, N. Pomphrey, J. De Lucia. Dynamic Modeling of Transport and Positional Control of Tokamaks. *Journal of Computational Physics*, 66:481–507, 1986.

[99] H. Zohm, C. Angioni, E. Fable, G. Federici et al. On the physics guidelines for a tokamak DEMO. *Nuclear Fusion*, 53:073019 (6pp), 2013.

[100] H. Zohm. On the minimum size of DEMO. *Fusion Science and Technology*, 58:613–624, 2010.

[101] G.V. Pereverzev, P.N. Yushmanov. ASTRA Automated System for Transport Analysis. Max-Planck-Institut für Plasmaphysik, Garching bei München. Report Nr. 5/98, February, 2002.

[102] R.Zagorski, R.I. Ivanova-Stanik, R.Stankiewicz. Simulations with the COREDIV code of DEMO discharges. *Nuclear Fusion*, 53:073030 (6pp), 2013.

[103] A.V. Chankin, D.P. Coster, R. Dux, C. Fuchs et al. SOLPS modelling of ASDEX upgrade H-mode plasma. *Plasma Physics and Controlled Fusion*, 48(6):839–868, 2006.

[104] I.S. Landman. Tokamak Code TOKES: Models and Implementation. Scientific Report FZKA 7496, Karlsruhe Institute of Technology (formerly Forschungszentrum Karlsruhe), September 2009.

[105] F. Wagner, G. Becker, K. Behringer, D. Campbell et al. Regime of Imyroved Confinement and High Beta in Neutral-Beam-Heated Divertor Discharges of the ASDEX Tokamak. *Physical Review Letters*, 57:1408–1412, 1982.

[106] M. Kikuchi, K. Lackner, M. Q. Tran. *Fusion Physics*. International Atomic Energy Agency, 2012. ISBN:978-92-0-130410-0.

[107] H.-S. Bosch, G.M. Hale. Improved formulas for fusion cross-sections and thermal reactivities. *Nuclear Fusion*, 32:611–631, 1992.

[108] M. Shimada, D.J. Campbell, V. Mukhovatov, M. Fujiwara et al. Progress in the ITER Physics Basis. Chapter 1: Overview and summary. *Nuclear Fusion*, 47:S1–S17, 2007.

[109] ADAS Atomic Data and Analysis Structure, H.P. Summers. ADAS User manual 2.6. http://www.adas.ac.uk/manual.php. Last accessed on 07.04.2018.

[110] T. Puetterich, R. Neu, R. Dux, A.D. Whiteford et al. Calculation and experimental test of the cooling factor of tungsten. *Nuclear Fusion*, 50:025012 (9 pp), 2010.

[111] ITER Physics Expert Group on Confinement and Transport et al. Chapter 2: Plasma confinement and transport. *Nuclear Fusion*, 39:2175 (76pp), 1999.

[112] D.J. Ward. The physics of DEMO. *Plasma Physics and Controlled Fusion*, 52:124033 (13pp), 2010.

[113] H. Lux, R. Kemp, D.J. Ward, M. Sertoli. Impurity radiation in DEMO systems modelling. *Fusion Engineering and Design*, 101:42 – 51, 2015.

[114] H. Lux, R. Kemp, E. Fable, R. Wenninger. Radiation and confinement in 0D fusion systems codes. *Plasma Physics and Controlled Fusion*, 58(7):075001, 2016.

[115] M. Greenwald, J.L. Terry, S.M. Wolfe, S. Ejima et al. A new look at density limits in tokamaks. *Nuclear Fusion*, 28:2199–2207, 1988.

[116] P.T. Lang, W. Suttrop, E. Belonohy, the ASDEX Upgrade Team et al. High-density H-mode operation by pellet injection and ELM mitigation with the new active in-vessel saddle coils in ASDEX Upgrade. *Nuclear Fusion*, 52(2):023017, 2012.

[117] F. Troyon, R. Gruber, H. Sauremann, S. Semenzato, S. Succi. MHD-Limits to Plasma Confinement. *Plasma Physics and Controlled Fusion*, 26:209–215, 1994.

[118] O. Sauter, R.J. La Haye, Z.Chang, D.A. Gates et al. Beta limits in long-pulse tokamak discharges. *Physics of Plasmas*, 4:1654–1664, 1997.

[119] Y.R. Martin, T. Takizuka, ITPA CDBM H-mode Threshold Database Working Group. Power requirement for accessing the H-mode in ITER. *Journal of Physics: Conference Series*, 123:012033 (11 pp), 2008.

[120] A. Kallenbach, M. Bernert, T. Eich, J.C. Fuchs et al. Optimized tokamak power exhaust with double radiative feedback in ASDEX Upgrade. *Nuclear Fusion*, 52:122003 (4pp), 2012.

[121] A. Ben-Israel. A Newton-Raphson Method for the Solution of Systems of Equations. *Journal of Mathematical Analysis and Applications*, 15:243–252, 1966.

[122] R.P. Wenninger, M. Bernert, T. Eich, E. Fable et al. DEMO divertor limitations during and in between ELMs. *Nuclear Fusion*, 54:063003 (7pp), 2014.

[123] M.A. Makowski, D. Elder, T.K. Gray, B. LaBombard et al. Analysis of a multi-machine database on divertor heat fluxes. *Physics of Plasmas*, 19:056122 (9pp), 2012.

[124] T. Eich, B. Sieglin, A. Scarabosio, W. Fundamenski et al. Inter-ELM Power Decay Length for JET and ASDEX Upgrade: Measurement and Comparison with Heuristic Drift-Based Model. *Physical Review Letters*, 107:215001 (4pp), 2011.

[125] B. Sieglin, T. Eich, M. Faitsch, A. Herrmann, et al. Investigation of scrape-off layer and divertor heat transport in ASDEX Upgrade L-mode. *Plasma Physics and Controlled Fusion*, 58(5):055015, 2016.

[126] A. Scarabosio, T. Eich, F. Hoppe, I. Paradela et al. Scaling of the divertor power spreading (S-factor) in open and closed divertor operation in JET and ASDEX Upgrade. *Journal of Nuclear Materials*, 463:49–54, 2015.

[127] T. Eich, A.W. Leonard, R.A. Pitts, W. Fundamenski et al. Scaling of the tokamak near the scrape-off layer H-mode power width and implications for ITER. *Nuclear Fusion*, 53:093031 (7pp), 2013.

[128] A. Kallenbach, N. Asakura, A. Kirk, A. Korotkov et al. Multi-machine comparisons of H-mode separatrix densities and edge profile behaviour in the ITPA SOL and Divertor Physics Topical Group. *Journal of Nuclear Materials*, 337-339:381–385, 2005.

[129] E.E. Lewis, W.M. Miller. *Computational Methods of Neutron Transport*. Wiley-Interscience, 1984. ISBN:0-471-09245-2.

[130] P. Pereslavtsev, L. Lu, U. Fischer, O. Bitz. Neutronic analyses of the HCPB DEMO reactor using a consistent integral approach. *Fusion Engineering and Design*, 89:1979–1983, 2014.

[131] P. Pereslavtsev, U. Fischer, F. Hernandez, L. Lu. Neutronic analyses for the optimization of the advanced HCPB breeder blanket design for DEMO. *Fusion Engineering and Design*, 124:910 – 914, 2017.

[132] F. Arbeiter, C. Bachmann, Y. Chen, M. Ilic, et al. Thermal-hydraulics of helium cooled First Wall channels and scoping investigations on performance improvement by application of ribs and mixing devices. *Fusion Engineering and Design*, 109-111:1123 – 1129, 2016.

[133] W.H. Reed, T.R. Hill. Triangular mesh methods for the neutron transport equation. Technical Report LA-UR-73-479, Los Alamos Scientific Laboratory of the University of California, 1973.

[134] A. Quarteroni. *Modellistica numerica per problemi differenziali*. Springer-Verlag Italia, 2006. ISBN:10 88-470-0493-4.

[135] S. Adjerid, T.C. Massey. A posteriori discontinuous finite element error estimation for two-dimensional hyperbolic problems. *Computer Methods in Applied Mechanics and Engineering*, 191:5877–5897, 2002.

[136] A. Ern, J.-L. Guermond. Discontinuous Galerkin Methods for Friedrichs' Symmetric Systems. I. General Theory. *SIAM Journal on Numerical Analysis*, 44:753–778, 2005.

[137] Ralf Hartmann. Numerical Analysis of Higher Order Discontinuous Galerkin Finite Element Methods. VKI Lecture Series 2008-0, pp. 1-107, ISBN 13-978-2-930389-88-5, October 2008.

[138] T.J. Seed, W.F. Miller Jr., F.W. Brinkley Jr. TRIDENT: A Two-Dimensional, Multigroup, Triangular Mesh Discrete Ordinates, Explicit Neutron Transport Code. Technical Report LA-6735-M, Los Alamos Scientific Laboratory of the University of California, 1977.

[139] T. Fujimura, T. Tsutsui, K. Horikami, Tadahiro Ohnischi et al. FEMRZ Program for Solving Two-Dimensional Neutron Transport Problems in Cylindrical Geometry by the Finite Element Method. Technical Report JAERI-1253, JAERI, 1978.

[140] K. Furuta, Y. Oka, S. Kondo. Accuracy of Multi-Group Transport Calculation in D-T Fusion Neutronics. *Journal of Nuclear Science and Technology*, 24:333–339, 1987.

[141] P. Pereslavtsev, C. Bachmann, U. Fischer. Neutronic analyses of design issues affecting the tritium breeding performance in different DEMO blanket concepts. *Fusion Engineering and Design*, 109-111:1207 – 1211, 2016.

[142] T.A. Gabriel, J.D. Amburgey, N.M. Greene. Radiation-Damage Calculations: Primary Knock-On Atom Spectra, Displacement Rates, and Gas Production Rates. *Nuclear Science and Engineering*, 61(1):21–32, 1976.

[143] D.G. Doran. Neutron displacement cross sections for stainless steel and tantalum based on a lindhard model. *Nuclear Science and Engineering*, 49(2):130–144, 1972.

[144] M. Akiyama. *Design Technology of Fusion Reactors*. Word Scientific, 1991. ISBN:9971-50-727-7.

[145] J.G. Issa, N.S. Riyait, A.J.H. Goddard, G.E. Stott. Multigroup Application of the Anisotropic FEM Code FELTRAN to One, Two, Three-Dimensions and R-Z Problems. *Progress in Nucleer Energy*, 18:251–264, 1986.

[146] W.W. Engle. A User Manual for ANISN, a One Dimensional Discrete Ordinates Transport Code with Anisotropic Scattering. Technical Report K-1693, Union Carbide Corporation, 1967.

[147] R.E. MacFarlane, D.W. Muir, R.M. Boicourt, A.C. Kahler. The NJOY Nuclear Data Processing System, Version 2012. Technical Report LA-UR-12-27079, Los Alamos National Laboratory - Theoretical Division, December 2012.

[148] R.E. MacFarlane. TRANSX 2: A Code for Interfacing MATXS Cross-Section Libraries to Nuclear Transport Codes. Technical Report LA-12312-MS, Los Alamos Scientific Laboratory of the University of California, June 1992.

[149] International Atomic Energy Agency, Nuclear Data Service. FENDL-3.1d: Fusion Evaluated Nuclear Data Library Ver.3.1d. `https://www-nds.iaea.org/fendl/index.html`. Last accessed on 12.06.2018.

[150] U. Fischer, M. Angelone, T. Bohm, K. Kondo et al. Benchmarking of the FENDL-3 Neutron Cross-section Data Starter Library for Fusion Applications. *Nuclear Data Sheets*, 120:230 – 234, 2014.

[151] U. Fischer. Neutronic Characterization of various Blanket Concept in the geometrical Configuration of a Tokamak Reactor. In B.E. Keen, and M. Huguet, R. Hemsworth, editor, *Fusion Technology 1990*, pages 787 – 791. Elsevier, Oxford, 1991.

[152] U. Fischer, C. Bachmann, I. Palermo, P. Pereslavtsev et al. Neutronics requirements for a DEMO fusion power plant. *Fusion Engineering and Design*, 98-99:2134 – 2137, 2015.

[153] M.E. Sawan, M.A. Abdou. Physics and technology conditions for attaining tritium self-sufficiency for the DT fuel cycle. *Fusion Engineering and Design*, 81(8):1131 – 1144, 2006.

[154] M. Abdou, N.B. Morley, S. Smolentsev, A. Ying et al. Blanket/first wall challenges and required R&D on the pathway to DEMO. *Fusion Engineering and Design*, 100:2–43, 2015.

[155] L.A. El-Guebaly, S. Malang. Toward the ultimate goal of tritium self-sufficiency: Technical issues and requirements imposed on ARIES advanced power plants. *Fusion Engineering and Design*, 84(12):2072 – 2083, 2009.

[156] G. Federici, C. Bachmann, L. Barucca, W. Biel et al. DEMO design activity in Europe: Progress and updates. *Fusion Engineering and Design*, 136:729 – 741, 2018.

[157] S.J. Sackett. Calculation of Elecromagnetic Fields and Forces in Coil Systems of Arbitrary Geometry. Proc. Sixth Symposium on Engineering Problems of Fusion Research (San Diego, California), IEEE No. 75CH1097-5-NPS, pp. 935-939, 1975.

[158] S.J. Sackett. A Code for Calculating the Electromagnetic Field, Force, and Inductance in Coil Systems of Arbitrary Geometry. User's Manual. Technical Report UCID-17621, University of California, 1977.

[159] B. Manes. TOKEF: A Tokamak input generator for EFFI. Technical Report KfK-3854, Kernforschungszentrum Karlsruhe, December 1984.

[160] R. Ambrosino, R. Albanese. Reference Flat Top Equilibria for DEMO with Aspect Ratio 3.1. Technical Report EFDA_D_2AQ5GP, EUROfusion, 2015.

[161] R. Albanese, R. Ambrosino, A. Castaldo, V.P. Loschiavo. Optimization of the PF coil system in axisymmetric fusion devices. *Fusion Engineering and Design*, 133:163 – 172, 2018.

[162] R. Albanese, F. Villone. The Linearized CREATE-L Plasma Response Model for the Control of Current, Position and Shape in Tokamaks. *Nuclear Fusion*, 38:723–738, 1998.

[163] ITER. Plant Description Document - ITER 2009 Baseline, Chapter 5 - Tokamak - ITER_D_2X6K67 v1.1, 2009.

[164] F. Maviglia, R. Albanese, M. de Magistris, P.J. Lomas et al. Electromagnetic Models of Plasma Breakdown in the JET Tokamak. *IEEE Transactions on Magnetics*, 50(2):937–940, 2014.

[165] M. Mattei. Ramp down and breakdown studies AR = 3.1. Technical Report EFDA_D_2CYDTB, EUROfusion, 2015.

[166] F.A. Potra, S.J. Wright. Interior-point methods. *Journal of Computational and Applied Mathematics*, 124(1):281 – 302, 2000. Numerical Analysis 2000. Vol. IV: Optimization and Nonlinear Equations.

[167] S. Ejima, R.W. Callis, J.L. Luxon, R.D. Stambaugh et al. Volt-second analysis and consumption in Doublet III plasmas. *Nuclear Fusion*, 22:1313–1319, 1982.

[168] F. Villone. Toroidal field ripple analysis. Technical Report EFDA_D_2M97UY, EUROfusion, 2016.

[169] Alexander Winkler. *Transient Behaviour of ITER Poloidal Field Coils*. PhD thesis, Universität Karlsruhe, 2010.

[170] L. Muzzi. Design of TF Winding Pack Option 2 (WP2) and of ENEA LTS cable. Technical Report EFDA_D_2MR47U, EUROfusion, 2016.

[171] K. Sedlak. Common operating values for DEMO TF WP design for 2016. Technical Report EFDA_D_2MMDTG, EUROfusion, 2016.

[172] R. Wesche. CS Winding Pack Design and Analysis. Technical Report EFDA_D_2MRPVA, EUROfusion, 2017.

[173] D. Ciazynski. CEA TF and CS winding pack optimization. Technical Report EFDA_D_2N48SV, EUROfusion, 2017.

[174] D. Ciazynski. CEA PF5 winding pack preliminary design. Technical Report EFDA_D_2MLPYG, EUROfusion, 2017.

[175] L. Muzzi. Report on PF Coil Design and Analysis. Technical Report EFDA_D_2N9VKL, EUROfusion, 2017.

[176] L. Zani, E. Mossang, M. Tena, J.P. Serries et al. $J_C(B,T)$ characterization of NbTi strands used in ITER PF-relevant insert and full-scale sample. *IEEE Transactions on Applied Superconductivity*, 15(2):3506–3509, June 2005.

[177] G. Zollino, G. Casini, D. Pierobon, V. Antoni et al. A comparison between a steady state and a pulsed fusion power plant. *Fusion Engineering and Design*, 86(9):2787 – 2790, 2011.

[178] K. Battes, C. Day, V. Rohde. Basic considerations on the pump-down time in the dwell phase of a pulsed fusion DEMO. *Fusion Engineering and Design*, 100:431 – 435, 2015.

[179] J. Morris, M. Kovari. Time-dependent power requirements for pulsed fusion reactors in systems codes. *Fusion Engineering and Design*, 124:1203 – 1206, 2017.

[180] R. Wenninger, R. Albanese, R. Ambrosino, F. Arbeiter et al. The DEMO wall load challenge. *Nuclear Fusion*, 57(4):046002, 2017.

[181] F.H. Hernandez. HCPB Design Report. Technical Report EFDA_D_2MNBH9, EUROfusion, 2016.

[182] L. Barucca, S. Ciattaglia, M. Chantant, A. Del Nevo et al. Status of EU DEMO heat transport and power conversion systems. *Fusion Engineering and Design*, 2018.

[183] E. Bubelis, W. Hering, S. Perez-Martin. Conceptual designs of PHTS, ESS and PCS for DEMO BoP with helium cooled BB concept. *Fusion Engineering and Design*, 2018.

[184] I. Moscato, L. Barucca, S. Ciattaglia, P.A. Di Maio et al. Preliminary design of EU DEMO helium-cooled breeding blanket primary heat transfer system. *Fusion Engineering and Design*, 2018.

[185] E. Martelli, F. Giannetti, G. Caruso, A. Tarallo et al. Study of EU DEMO WCLL breeding blanket and primary heat transfer system integration. *Fusion Engineering and Design*, 2018.

[186] L. Malinowski, M. Lewandowska, F. Giannetti. Analysis of the secondary circuit of the DEMO fusion power plant using GateCycle. *Fusion Engineering and Design*, 124:1237 – 1240, 2017.

[187] M.A. Boles Y.A. Çengel. *Thermodynamics: An Engineering Approach*. McGraw-Hill series in mechanical engineering. McGraw Hill, 1998. ISBN:978-0-070-11927-7.

[188] A. Li-Puma, J. Bonnemason, L. Cachon, J.L. Duchateau et al. Consistent integration in preparing the helium cooled lithium lead DEMO-2007 reactor. *Fusion Engineering and Design*, 84(7):1197 – 1205, 2009.

[189] U. Fischer. Material compositions for PPPT neutronics and activation analyses. Technical Report EFDA_D_2MM3A6, EUROfusion, 2017.

[190] P. Pereslavtsev. 2016 DEMO HCPB MCNP model. Technical Report EFDA_D_2MK7GG, EUROfusion, 2018.

[191] A. Del Nevo. WCLL Design Report 2016. Technical Report EFDA_D_2MU2ZL, EUROfusion, 2017.

[192] K. Sedlak. Report on TF Winding Pack Design and Analysis. Technical Report EFDA_D_2MT93A, EUROfusion, 2017.

[193] C. Harrington. Thermodynamic modelling of the balance of plant for a water-cooled DEMO using Apros. Technical Report EFDA_D_2MBUKD, EUROfusion, 2017.

[194] C. Fausser, A. Li Puma, F. Gabriel, R. Villari. Tokamak D-T neutron source models for different plasma physics confinement modes. *Fusion Engineering and Design*, 87:787–792, 2012.

[195] H.R. Wilson. Bootstrap current scaling in tokamaks. *Nuclear Fusion*, 32:257–263, 1992.

[196] O. Sauter, C. Angioni, Y.R. Lin-Liu. Neoclassical conductivity and bootstrap current formulas for general axisymmetric equilibria and arbitrary collisionality regime. *Physics of Plasmas*, 6(7):2834–2839, 1999.

[197] R. Villari. Neutronic Analysis Report for Divertor Cassette and PFC 2015. Technical Report EFDA_D_2MN2H3, EUROfusion, 2016.

[198] F. Villone. Toroidal field ripple Final Report v1.1. Technical Report EFDA_D_2ANZQQ, EUROfusion, 2014.

[199] D. Maisonnier, I. Cook, P. Sardain, L.V. Boccaccini et al. DEMO and fusion power plant conceptual studies in Europe. *Fusion Engineering and Design*, 81(8):1123 – 1130, 2006.

[200] R. Wenninger. DEMO1 Reference Design - 2017 March ("EU DEMO1 2017") - PROCESS Full Output. Technical Report EFDA_D_2NDSKT, EUROfusion, 2017.

[201] MathWorks Documentation. The *fmincon* nonlinear constrained optimization tool. `https://de.mathworks.com/help/optim/ug/fmincon.html`. Last accessed on 21.07.2018.

[202] D.G. Luenberg, Y. Ye. *Linear and Nonlinear Programming - Fourth Edition*. Springer, 2015. ISBN:978-0-387-74502-2.

[203] A. Talamo. Numerical Solution of the Time Dependent Neutron Transport Equation by the Method of the Characteristics. *Journal of Computational Physics*, 240:248–267, 2013.

[204] J.K. Fletcher. The solution of the Time-Independent Multi-Group Neutron Transport Equation Using Spherical Harmonics. *Annals of Nuclear Energy*, 4:401–405, 1977.

[205] J.K. Fletcher. The solution of the Multigroup Transport Equation Using Spherical Harmonics. *Nuclear Science and Engineering*, 84:33–46, 1983.

[206] R. Sanchez, N.J. McCormick. A Review of Neutron Transport Approximations. *Nuclear Science and Engineering*, 80:481–535, 1982.

[207] Milan Hanus. *Mathematical Modelling of Neutron Transport*. PhD thesis, University of West Bohemia, Pilsen, 2014.

[208] S. Goluoglu, H.L. Dodds. A Time-Dependent, Three-Dimensional Neutron Transport Methodology. *Nuclear Science and Engineering*, 139(3):248–261, 2001.

[209] Nuclear Energy Agency, Computer program services. DSNQUAD, Angular Quadrature Weights and Cosines for ANISN. `www.oecd-nea.org/tools/abstract/detail/psr-0251`. Last accessed on 23.05.2018.

[210] C.E. Lee. The Discrete Sn Approximation to Transport Theory. Technical Report LA-2595, Los Alamos Scientific Laboratory of the University of California, June 1961.

[211] N. Soppera, M. Bossant, E. Dupont. JANIS 4: An Improved Version of the NEA Java-based Nuclear Data Information System. *Nuclear Data Sheets*, 120:294 – 296, 2014.

[212] S.B. Zheng, A.J. Wootton, E.R. Solano. Analytical tokamak equilibrium for shaped plasmas. *Physics of Plasmas*, 3:1176 (3pp), 1996.

[213] J.E. Akin. *Finite Element Analysis with Error Estimators*. Elsevier Butterworth-Heinemann, 2005. ISBN:0-7506-6722-2.

[214] D. Fournier, R. Herbin, R. Le Tellier. Discontinuous Galerkin Discretization and hp-Refinement for the Resolution of the Neutron Transport Equation. *SIAM Journal on Scientific Computing*, 35(2):A936–A956, 2013.

[215] A.G. Spagnuolo. Blanket Material Composition For Neutronics. Technical Report EFDA_D_2MU2ZL, EUROfusion, 2016.

[216] F.H. Hernandez. DDD 2015 for HCPB (Update of DDD 2014). Technical Report EFDA_D_2MRQ4E, EUROfusion, 2016.

[217] J.-Ch. Sublet, M.E. Sawan. Self-shielding effects in a tungsten layer in a fusion device. *Fusion Engineering and Design*, 45(1):65 – 73, 1999.

[218] C.L. Dembia, G.D. Recktenwald, M.R. Deinert. Bondarenko method for obtaining group cross sections in a multi-region collision probability model. *Progress in Nuclear Energy*, 67:124 – 131, 2013.

Acknowledgements

I would like to express my most sincere gratitude to Prof. Dr.-Ing. Robert Stieglitz and Dr. Lorenzo Virgilio Boccaccini for giving me the opportunity to carry out my PhD work at the Institute of Neutron Physics and Reactor Technology and Prof. Dr. Hartmut Zohm for taking over the co-refereeing of my thesis. To all I am deeply grateful for their valuable guidance, for their tireless reviewing work and for their unconditional trust they put on me for the accomplishment of this challenging project.

I am very grateful to Dr. Ivan Alessio Maione for his unlimited help and support (as a friend, a colleague and a supervisor) including many inspiring conversations and an unlimited endorsement of my work initiatives.

I am truly thankful to Dr. Fabio Cismondi for seeing in me the potential to carry out this challenging work, my colleagues Mr. Gandolfo Alessandro Spagnuolo and Dr. Gaetano Bongioví for carrying out also on my behalf our join activities during the thesis drafting and to Dr. Marigrazia Moscardini for her prompt assistance in the procedural aspects of the thesis submission.

I am also really beholden to the following persons for their active contribution to some of the system modules implemented in MIRA:

- Dr. Igor Landman and Dr. Sergey Pestchanyi for their valuable contribution to the plasma physics and magnetic equilibrium parts, as well as for the fruitful scientific discussions and for their categorical availability to help me whenever I needed.
- Dr. Tobias Hartmann for passing me on the architectural logics and the functional aspects of the plasma physics code TREND, eventually leading to a successful integration in MIRA.
- Dr. Yuefeng Qiu and Dr. Ulrich Fischer for their worthwhile backing regarding the neutron transport modelling part.
- Mr. Gade Pattabhi Vishnuvardhan for his valuable guidance through the fundamentals of magnetostatics and superconducting cable engineering design, contributing to magnet systems' module currently implemented in MIRA.
- Mr. Eric Brünner for his patient and engaging guidance through object-oriented programming, making our collaboration very stimulating and eventually inspiring the current architecture of MIRA.

Special thanks go to my family for their outright support throughout my whole educational path, encouraging me to think always positive and to endure. Last but most certainly not least I would like to thank my fiancée Dr. Dimitra Xenioti for her unending support and firm encouragement, even during the toughest times.